博士論文

Evaluation of Liquefaction Potential of Partially Saturated Heap of Iron Ore Fines during Maritime Transportation

(部分飽和条件下における船積み鉄鉱粉の液状化ポテンシャルの評価)

Hailong Wang
王　海龍

A thesis submitted in partial fulfillment of the requirements for degree of

Doctor of Philosophy

Department of Civil Engineering
The University of Tokyo
Tokyo, Japan

September, 2014

Abstract

The problem of liquefaction has raised concerns with the International Maritime Organization (IMO) and their country members due to several accidents and loss of life during the transportation of liquefiable cargoes at sea. In 2009 two vessels capsized and sank following liquefaction of iron ore fines, which were loaded in the Indian ports. In October and November 2010, three vessels sank during the carriage of nickel ore from Indonesia to China with the loss of forty four seafarers, which was very possibly induced by cargo liquefaction. Several vessels had also experienced cargo liquefaction problems after loading bauxite in the Amazon region in northern Brazil.

To avoid the occurrence of liquefaction of iron ore fines during maritime transportation, the IMO has launched investigations since 2009 to study the responses of heaps of iron ore fines. Following four years of cooperation and discussions between related industrial groups, research groups and committee members of the IMO, a draft individual schedule for iron ore fines, which gives instructions to ship operators or masters when transporting iron ore fines, was proposed in 2013. The draft is now under voluntary implementation and is expected to be adopted in the International Maritime Solid Bulk Cargoes (IMSBC) Code in 2015, and would become mandatory from the beginning of 2017.

In order to reveal the liquefaction potential of iron ore fines, this thesis is an independent study from a point view of geotechnical engineering focusing on two types of iron ore fines. The primary objective of this study was to understand the responses of the heap of iron ore fines through characterizing the geotechnical properties of iron ore fines. Delicate laboratory tests were performed focusing on the geotechnical properties of both saturated and unsaturated iron ore fines, such as soil water characteristic curve (SWCC), permeability, undrained shear strength, liquefaction resistance etc. The overall responses, such as the seepage in the heap, the dynamic responses of the heap were studied by employing numerical tools. The major outcomes from this study are summarized as follows:

1. Soil water characteristic curve (SWCC) of iron ore fines

Iron ore fines are usually loaded into a vessel with relatively uniform nature water content; however, the saturated and unsaturated zones may be soon formed due to the seepage of water in the heap. The properties, such as shear strength, water retention ability, permeability, deformation of the unsaturated soil are largely relied on its SWCC, which indicates the relationship between suction and water content of the unsaturated soil.

SWCCs of two types of iron ore fines were measured in this study not only in the low suction range (0.1 kPa -100 kPa) but also in the high suction range (up to 10^6 kPa). A new testing technique, the membrane filter technique, was employed in the SWCC test to study the effect of void ratio on the SWCCs of iron ore fines. In addition, comparisons of SWCCs were made between iron ore fines and common geo-materials mixture. Scanning electron microscope (SEM) observations were also conducted to reveal the characteristics of SWCC of iron ore fines.

2. Permeability of iron ore fines

The property of permeability, which is essential to analyze the seepage, dynamic responses etc. in the heap, was measured for the saturated and unsaturated iron ore fines. To increase the accuracy of measurements, the test was conducted on a triaxial system under constant water head. The system head loss consumed by the surface friction of the water flow paths was estimated in order to obtain more reliable results. Regarding the permeability test of the unsaturated soils, it was found that the filter clogging problem induced by both dust in the flow water and the fines content in the soils affects the test procedures significantly. By following strict rules of evaluation, the system head loss of the measurement system was estimated. As a reference, soil for comparison with iron ore fines, the permeability of saturated and unsaturated Toyoura sand was also evaluated.

3. Liquefaction resistance of iron of fines

Considering the partially saturated condition of the heap of iron ore fines, the liquefaction resistance of the saturated and unsaturated iron ore fines was studied by conducting undrained cyclic loading tests. The test was performed on a specially manufactured triaxial apparatus, on which the measurement systems of pore air pressure, pore water pressure, volume change of the unsaturated specimens were equipped. Research on the liquefaction resistance of unsaturated soils has been undertaken since the 1970s, of which mostly focused on the clean sands. Previous studies show that the resistance of liquefaction of unsaturated soils is higher than that of saturated soils and the increase was recently well linked to the potential volumetric strain of unsaturated clean sands. However, it was found from this study that the relationship between the potential volumetric strain and the increase in liquefaction resistance induced by degree of saturation (Sr) could not well explain the results of sands with fines content (Fc, particle size ≤0.075 mm), such as iron ore fines (Fc=24%) and Inagi sand (Fc=30%) used in this study. Efforts were taken to explain the combined effect of Sr and Fc on the liquefaction resistance of soils from the fundamental

behavior of deformation. A volumetric strain ratio of the potential volumetric strain to the volumetric strain caused by the reduction in effective stress was proposed to be the new parameter to correlate the increase in liquefaction resistance induced by Sr and Fc. Associating with the results of the consolidation tests, the new parameter showed better correlation than previously proposed parameters.

4. Seepage analysis

The saturated zone of the heap of iron ore fines was expected to be the area with the highest liquefaction potential. Thus, the moment, when the highest water table was formed for a given initial Sr, was thought to be the critical condition of the heap to resist the rolling motion. On the other hand, the liquefaction potential of the unsaturated zone of the heap also needs to be considered in order to evaluate the overall responses of the heap under the rolling motion. Seepage analysis was carried out by employing a FEM code to unveil the time-dependent water table and distribution of Sr in the heap. The Van Genuchten model was used in the simulation to establish the relationship between suction, Sr and permeability. The effects of density of iron ore fines, boundary conditions of the heap and parameter setting of the Van Genuchten model were examined through the analysis. An envelope, which indicates the maximum height of water table in the heap for a given initial Sr, and the distribution of Sr in the unsaturated zone were obtained.

5. Dynamic responses analysis

The two dimensional responses of the heap of iron ore fines was evaluated by employing a commercial software, UWLC Ver. 2. A generalized elasto-plastic model was employed to simulate the behavior of liquefiable zone of the heap. Three cases, which focus on the effects of liquefaction potential and low permeability of the unsaturated zone on the overall response of the heap, were studied. In each case, the response of the heap was examined under different rolling angles from 5° to 30°. The simulation results show that the properties of the unsaturated zone have significant effect on the overall responses of the heap, such as the strain distribution, the liquefaction potential etc., which imply the importance of considerations of the unsaturated zone.

While following the research stream addressed above, discussions on the testing techniques, such as the membrane filter technique used in the SWCC test, the calibration of system head loss and filter clogging problems in the permeability test etc., were also involved in the tests performed in this study. Particularly in the undrained cyclic loading test for the unsaturated

soils, the cell pressure control system, which ensures the constant total principle stress during vertical cyclic loading by adjusting the cell pressure, was examined. The test results confirm good performance of the system and validate the necessity of the cell pressure control system in the triaxial system in order to evaluate the liquefaction resistance of the unsaturated soils in a more accurate manner.

Acknowledgement

I would like to extend my deep gratitude to my supervising professor, Prof. Junichi Koseki, IIS, The University of Tokyo for his kind instruction. He extended my vision to the problem faced by our human being in the world and stimulated my self-confidence to bravely challenge the frontier research. In this three years, what I leant from him is not limited to the professional knowledge but more importantly the attitude to work, life and myself. He allowed me to explore the unknown world from my own naive thoughts and led me in the right direction when I went too far.

I sincerely acknowledge the following PhD thesis committee members, Prof. Ikuo Towhata and Associate Prof. Taro Uchimura at Geotechnical Engineering Laboratory, The University of Tokyo, Prof. Tomoyoshi Nishimura from Ashikaga Institute of Technology, Associate Prof. Takashi Kiyota, at Geo-disaster Mitigation Engineering Laboratory, IIS, The University of Tokyo for their valuable comments, criticisms and suggestions for my study. In particular, I would like to express my gratitude to Prof. Tomoyoshi Nishimura for his extraordinary help on the testing skill of the unsaturated soils and warmhearted care during my study.

My special appreciation goes to Associate Prof. Fei Cai at Geotechnical Engineering Laboratory, Gunma University, who gives me great help on the works of numerical analysis.

I would like to express my appreciation to Prof. Kenji Ishihara from Chuo University and Dr. Atsuo Onoue from International Geotechnical Institute for their kind care during site inspections.

I sincerely acknowledge The Japan Iron and Steel Federation who provided the testing materials.

Mr. Takeshi Sato, Geotechnology Institute Ltd., not only gives me unbelievable helps on my experimental works but also establishes intimate friendship with me. He lights my crazy passion to the testing equipment and feeds my hungry mind to the unknown knowledge. I would like to send my deep acknowledgement to him.

I would like to express my gratitude to Dr. Laura Banasiak for her careful review of my thesis and many great suggestions.

I would like to send my regards to Prof. Reiko Kuwano, IIS, The University of Tokyo and Prof. Jiro Kuwano from Geosphere Research Institute of Saitama University for their instruction and care during site visits as well as Lab. trips.

I would like to express my acknowledge to all the teachers in the Japanese Language Class in the Department of Civil Engineering and in the School of Engineering, The University of Tokyo. Their kind help gives me confidence of learning a blend of new languages and colors my PhD live. Because of them, I can continuously improve my Japanese, 誠に有難う御座いました。

Great help also from Mrs. Ayuko Akaike and Miyake family (Shunzo San, Yasuko San, Yuta San and Mayuko San) and Mrs. Akiko Suzuki. I am proud of being a member of our Host family program. It gives me much deeper understanding about Japanese culture and society.

I obtained valuable help from Mr. Seiichi Kaneko and Mr. Masakuni Tsuji from Shimizu Corporation, Mr. Kenji Shinkawa and Mr. Shinya Ishimatsu from Kajima Corporation, and Mr. Sekimoto Tsunehiro and Mr. Isao Michishita from Penta-Ocean Construction Corporation during my job hunting. Thank you for giving me knowledge about work culture in Japan.

Special thanks to Yukika Miyashita san for her help on my experimental works, to Satoko Kichibayashi san for her help on many troublesome documenting works, to my tutor and good friend Takenaka san for his help on my life in Japan and his kindness.

Thanks Araki san, Ko san and Suwal sand for their initial instructions of my research; Aoyama sand, Otsubo sand, Yu san, Yolanda san, Han san for their kind care and pure friendship; Seto san, Mari san, Usama san, Yangyang san, Sasaki san, Nguyen san, Abilash san, Ikeya san, Hoshino san, Aoyagi san for having great time with time.

I would like to express my thanks to all members mentioned or not mentioned above in Koseki Laboratory, Kuwano Laboratory, Kiyota Laboratory and Geotechnical Engineering Laboratory in The University of Tokyo. They give me such a good environment to study and to enjoy life.

Thank also given to members from JR East Co. Hirano san for your kind help in my job hunting.

My sincerely acknowledge gives to Ministry of Education, Science and Culture, Japan for providing the financial assistance for my study.

Last, gives thanks to my lovely family for their support.

Table of contents

Chapter 1. Introduction

Contents

1.1 Objective of study

The main concern of this study is the liquefaction problem of heaps of iron ore fines during transportation in the ocean. This problem was caught the eye because of two accidents which are reported in the section 1.2. To find a solution of this problem from standpoint of a geotechnical engineer, section 1.3 illustrate the process of problem simplification and research configuration.

The objectives of this study are: a) characterization of geotechnical properties of iron ore fines, focusing on SWCC, permeability and liquefaction resistance; b) numerical evaluation of responses of heaps of iron ore fines during maritime transportation.

1.2 Background

1.1.1 Accidents

In 2009 two vessels, the 'Asian Forest' and the 'Black Rose', capsized and sank following liquefaction of iron ore fines cargoes which had been loaded in the Indian ports of Mangalore and Paradip (Isacson, 2010 a). In October and November 2010, three vessels, the 'Jian Fu star', the 'Nasco Diamond' and the 'Hong Wei' sank during the carriage of nickel ore from Indonesia to China with a loss of forty four seafarers, which were very possibly induced by cargo liquefaction (Isacson, 2010 b). Several vessels had also experienced cargo liquefaction problems after loading bauxite in the Amazon region in northern Brazil (Gard, 2012). These accidents caused serious concern of P&I Clubs[1] and their members on the liquefaction problem associated with maritime transportation of solid bulk cargo.

1.1.2 How to deal with

On the issue of cargo transportation in the ocean, there is a convention, International Convention for the Safety of Life at Sea (SOLAS). This convention provides a general framework for the carriage of all cargoes. For a specific issue of cargoes to be transported, the main reference for any ship operator or master is the International Maritime Solid Bulk Cargoes (IMSBC) Code which is of the similar function as industrial standards. In the IMSBC Code, all cargoes are classified into four groups, A, B, A&B and C[2]. Cargoes belonging to Group A

1. P&I Club: International Club of Protection and Indemnity
2. Group A consists of cargoes which may liquefy if shipped at a moisture content in excess of their transportable moisture limit (TML); Group B consists of cargoes which possess a chemical hazard which could give rise to a dangerous situation on a ship; Group C consists of cargoes which are neither liable to liquefy (Group A) nor to possess chemical hazards (Group B).

are believed to have potential of liquefaction under certain conditions. For Group A cargoes, provisions are given in Section 7 of IMSBC Code to avoid liquefaction of cargoes during a voyage. The general way to do so is to control the actual moisture content of a Group A cargo under its TML value[3] before being loaded to a ship. There are more than 200 types of cargoes listed by IMSBC Code, each of which has an individual schedule describing cargo properties, group, caution issues, etc. to instruct any ship operator or master (IMSBC Code, 2012).

Regarding the liquefaction problem of a cargo, a ship operator or master can directly find the schedule of this cargo and check if this cargo belongs to Group A or not. If it is, check if the actual moisture content of this cargo is lower than its TML value. If it is, this cargo can be allowed to load, otherwise, it should not be allowed to load to a ship.

1.1.3 Liquefaction of iron ore fines

One would naturally think that a master of ship operator can search for the individual schedule of iron ore fines when they transport it. Unfortunately, there is no such a schedule specifically for iron ore fines in the IMSBC Code. There is a schedule for “IRON ORE”, which covers the iron ore with particle size up to 250mm and is classified as Group C cargo (non-liquefiable cargo). Under such a description, iron ore fines was in some cases declared as Group C cargo in the past. The two accidents related to carriage of the iron ore fines happened in 2009 (the ‘Asian Forest’ and the ‘Black Rose’) urged the IMO and related organizations to take actions on making an amendment to IMSBC Code for iron ore fines, namely, they need to re-consider the descriptions of “IRON ORE” and make a more proper schedule(s) for “IRON ORE” and/or iron ore fines.

1.1.4 How to make an amendment

On the issue of making an amendment to IMSBC Code for iron ore fines, several steps were followed (DSC 18/INF.11, 2013; Ota 2013).

3. TML (Transportable moisture limit) of a cargo means the maximum moisture content of the cargo which is considered safe for carriage in ships. The IMSBC Code in Appendix 2 describes test procedures to determine TML value. One of the tests is Proctor/Fagerberg test (compaction test) and TML value is the intersection of the compaction curve and the line Sr (degree of saturation) = 70%. The TML value may also take the 85%-90% of FMP value, which is determined by flow table test as described in Appendix 2 of the IMSBC Code. FMP (Flow Moisture point) means the percentage moisture content at which a flow state develops under the prescribed method of test in a representative sample of the material.

1. TWG (Technical Working Group)[4] was established to study the problem and to prepare reports.
2. External exports[5] in the relevant disciplines was appointed by TWG to verify prepared reports.
3. Verified reports was evaluated by an independent scientific group[6] under the direction of the International Group of P&I Clubs[7].
4. Evaluated and verified reports were submitted to Correspondence Group (CG)[8] for examination.
5. Examined reports, comments and reports of CG were submitted to Sub-Committee on DSC[9] of MSC[10] for discussion.
6. Final decisions (draft of amendment) of Sub-Committee on DSC are going to be reported to MSC of IMO[11] for approval and making into force. A brief introduction of IMO and related issues are given in Appendix A.

1.1.5 Events related to decision making

The above addressed procedure of making a decision by IMO involves many events for discussions to give a simple idea of this process for better understanding of the problem, rough summaries of events related are sorted by date of events.

2009. 07 & 2009. 10: Two vessels capsized and sank following liquefaction of iron ore fines cargoes which they had loaded in the Indian ports (Isacson, 2010 a)

2010.09: 15th session of The Sub-Committee on DSC. The Sub-Committee approved a DSC circular on Carriage of iron ore fines which gives advice on the transportation of iron ore fines and admits iron ore fines as the hazards of cargoes that may liquefy (DSC, 2010) [12] . The sub-committee on DSC concludes in its followed DSC circular (DSC.1/Circ.63, 2010) that iron ore fines which is not specifically listed in IMSBC Code

4 TWG concerning on iron ore fines consists of three largest iron ore producers in the world with the support of their respective competent authorities

5 Prof. Kenji Ishihara, Prof. Junichi Koseki and Dr. Kourosh Koushan

6 Imperial College of London (Dr. Stephen Neethling, Prof. Dracos Vassalos and Prof. Velisa Vesovic)

7 International Group of P&I Clubs represents a group of industry NGOs that includes BIMCO, Intercargo, International Chamber of Shipping and IFAN.

8 CG (Correspondence Group) was participated by 19 member governments and 7 international organizations.

9 Sub-Committee on DSC (Dangerous Goods, Solid cargoes and Containers), one of the sub-committees of MSC

10 MSC: Maritime Safety Committee, one of committees of IMO

11 IMO: International Maritime Organization, the United Nations (UN) specialized agency with responsibility for the safety and security of shipping and the prevention of marine pollution by ships.

12 All the documents with DSC or MSC can be free downloaded at IMO website after free registration. https://webaccounts.imo.org/Common/WebLogin.aspx?App=IMODOCS&ReturnUrl=http%3A%2F%2Fdocs.imo.org%2F

may liquefy and should be treated as such materials that may liquefy as described in section 7 of the IMSBC Code; if this cargo is shipped with moisture content in excess of its transportable moisture limit (TML) there is a risk of cargo shift, which may result in capsizing of a ship; some shippers have in the past declared the iron ore fines cargo under the "IRON ORE" schedule in the IMSBC Code, which is classified as a Group C cargo.

2011.09: 16th session of The Sub-Committee on DSC. The Sub-Committee on DSC agreed an interim revised draft DSC circular (DSC.1/Circ.66, 2011) on carriage of iron ore fines, reiterating the dangers of liquefaction associated with carriage of iron ore fines (DSC 2011). The Sub-committee established a correspondence group (CG) to develop schedule for iron ore fines for inclusion in the IMSBC Code with particular reference to the phenomenon of liquefaction in some types of iron ore fines (DSC.1/Circ.66, 2011). In addition, until a definition of iron ore fines is incorporated into the IMSBC Code and for the purpose of providing reference, the Sub-Committee on DSC took note that iron ore fines is considered to be a cargo mainly constituted by iron bearing minerals with a size up to 6.35 mm (DSC.1/Circ.66, 2011).

2012.09: 17th session of The Sub-Committee on DSC. The Sub-Committee discussed the report of the correspondence group (CG) which provided a new individual schedule for iron ore fines. However, it was felt that it was important to await the outcome of significant research being carried out in Australia and Brazil on carriage of iron fines (DSC 2012). The Sub-Committee on DSC also update circular DSC.1/Circ.66 (new circular: DSC.1/Circ.66/Rev.1, 2012) so that it would continue to be applied until the finalization of the schedule.

2012.10: 91st session of The Maritime Safety Committee. In the regard of the content in 17th session of the Sub-Committee on DSC, the MSC (Maritime Safety Committee), at its 91st session, authorized DSC 18 to issue a circular on early implementation of the draft schedule for iron ore fines (MSC 91/13 2012).

2012.12-2013.06 Correspondence Group (CG). CG disseminated the research plan and results of Technical Working Group (TWG).

2013.09: The ministry of Land, Infrastructure, Transport and Tourism and the National Maritime Research Institute. A workshop on carriage of iron ore fines in bulk was organized to facilitate the understanding on the results of the research and the draft individual schedule prepared by the correspondence group (CG) on the transport of iron ore fines in bulk (Ota, 2013; Ishihara, 2013; Herff and Baker, 2013; Hudson, 2013; Policarpo and Maney, 2013; Linden, 2013 and Evans, 2013). On the workshop, the TWG

(Technical Working Group) reported the findings of their studies and gave recommendations to CG on the issue of preparation of a draft schedule for iron ore fines. The CG summarized agreements on TWG's recommendations among CG participants and proposed a draft individual schedule of iron ore fines.

2013.09: 18th session of The Sub-Committee on DSC. The Sub-Committee considered the reports of the correspondence group (CG) on transport of iron ore fines in Bulk (DSC 18/6/13, 2013, DSC 18/6/14, 2013 and DSC 18/INF.9, 2013) together with the related documents (e.g. reports from TWG etc.) submitted to the session, and approved the report in general (DSC 18/13, 2013). The main conclusions of DSC 18/13 (2013) are cited hereunder:

1. Reports of the TWG (Technical Working Group) assessed the adequacy of current IMSBC Code methods for determining TML; described the characteristics of vessel motions and forces affecting iron ore fines during transit; explored potential adjustments to one of the existing routine iron ore fines tests; provided further evidence to substantiate the applicability of the adjusted routine iron ore fines test (DSC 18/INF.10, 2013; DSC 18/INF.11, 2013; DSC 18/INF.12, 2013; DSC 18/INF.13, 2013).
2. Agreed to include the new test procedure for determining TML of iron ore fines.
3. Agreed, in principle, to the draft amendment to appendix 2 of the IMSBC Code on the new test procedure, while some reservations were raised regarding the need for two different individual schedules for iron ore fines depending on their TML.
4. Decided to use goethite content of 35 percent as a threshold for exemption from requirements for group A cargoes (the author's note: iron ore fines with not less than 35% goethite content are not regarded as liquefiable)
5. Agreed on the criteria for identification of IRON ORE (Group C) and IRON ORE FINES (Group A) based on grain size. IRON ORE FINES contains 10% or more of fine particles less than 1mm and 50% or more particles less than 10mm. (DSC.1/Circ.71, 2013).

2013.11: The Sub-Committee on DSC. A draft schedule for iron ore fines was issued in DSC.1/Circ.71 (2013). It is expected to be adopted as part of amendment to the IMSBC Code by Maritime Safety committee at its 95th session, in 2015. Therefore, taking into account that the mandatory entry into force date of these amendments would be 1 January 2017, DSC 18 agreed to invite SOLAS contracting governments to voluntarily implement the draft schedules and test procedure as soon as possible.

1.3 Research stream

1.1.6 Technical issues related to the problem

There are two main issues that the IMO and related organizations concern: 1. How to avoid liquefaction of a heap of iron ore fines; 2. How to avoid loss (life and/or commodity) even after liquefaction of heaps in a ship. The second question is out of the scope of author's knowledge and will not be discussed in this thesis. Regarding the first question, it involves another two issues: 1. What kind of motions may a heap/a ship experience in one/multiple voyages; 2. How will a heap response under expected motions.

1. What kind of motions may a heap/a ship experience in one/multiple voyages?

   The motions a ship may experience depends mostly on its voyage route (e.g. from Australia to Japan or from Brazil to China etc.), weather conditions of each zone along the voyage (e.g. a ship may suffer from storm in some seasons at some sea areas), the period of extreme weather condition and how to statistically consider, the normal period, height and mode of ocean waves, the size and arrangement of a ship and so on. Some studies have been published on the report of IMO (DSC 18/INF.11 2013) on these issues. In this study instead of finding solutions in these unfamiliar research fields, simple assumptions are adopted base on study results of IMO reports and inquiries to related professionals. Assumptions:

   1) Only consider the effect of predominant motion, the rolling motion (six motion components of a ship, Surge, Sway, Heave, Roll, Pitch and Yaw are shown in Fig. 1-1);
   2) Only consider the shear stress induced by rolling motion, effect of acceleration is not considered;
   3) Assuming the period of rolling motion is 10 second (0.1 Hz);
   4) A ship/a heap is assumed to experience a certain number of circles of roll in a voyage;
   5) Only analyze response of one heap in a ship (there could be 2-9 holds in a ship depending on the size of a ship and there is on heap in each hold).

2. How will a heap response under expected motions

   1) Saturation condition of a heap

   Fig. 1-2 shows typical photo of the heap of iron ore fines. The material is usually piled up in natural ground without protection from weathering. It usually contains certain

amount of water before loading. The water content in a heap is expected to be roughly uniform at the moment right after loading to a ship. The water content distribution is believed to be change from a uniform distribution to a non-uniform one because of movement of water in the heap during one voyage (0.5-1.5 months). The movement of water results in a time-dependent water distribution in the heap, where a saturated or nearly saturated zone at the lower part and dryer condition at the upper part of the heap may form as shown in Fig. 1-3.

2) Stress applied on a heap

The motion a heap is assumed to suffer from is rolling motion as shown schematically in Fig. 1-4. Because of the rolling motion, a cyclic shear stress is applied on the heap induced by rotation of center of gravity. Under such a shear stress, the whole heap or part of the heap may liquefy.

1.1.7 Specific objective of this study

After simplification of the real conditions, general assumptions and study configuration have been depicted in Section 1.3.1. It transforms the original problem involving a wide range of professional knowledge to a general problem of geotechnical engineering: the evaluation of the response of a partially saturated heap of iron ore fines subjected to the rolling motion.

1.1.8 Works done for the problem

The experimental study and numerical simulation are carried out for the evaluation of the response of a heap of iron ore fines. Basic properties of saturated and/or unsaturated iron ore fines, such as water retention ability, water permeability and resistance against cyclic shear stress/liquefaction were studied by conducting laboratory element tests; the overall responses of a heap of iron ore fines, such as time-dependent water distribution in the heap and response of a heap under rolling motion were carried out by numerical simulation. The more detailed works are addressed as follows:

1. SWCC (Soil Water Characteristic Curve) test. This test describes a relationship between suction and water content for an unsaturated soil and indicates water retention ability of a soil. As shown an element of an unsaturated soil in Fig. 1-5, pore water in a soil will naturally flow from one place with high elevation potential (P_E) to another place with low P_E. The magnitude of P_E only depends on the position of pore water in the element (to know more about potential composed in soil, Chapter 4 of Tindall et al.

(1999) is recommended). On the other hand, there is another component of potential, matric potential (or capillary potential, which usually termed as suction/matric suction=pore air pressure – pore water pressure in geotechnical engineering, osmotic suction is assumed to be 0 herein for simplicity and is introduced in Section 2.1.2 of Chapter 2) works on pore water. The magnitude of suction depends on the amount of water in soil matrix (soil skeleton) and property of soil particle, namely, the fewer water in the soil matrix and/or the more hydrophilic the soil particle, the higher the suction in soil becomes to retain the rest of pore water. Suction is of the same meaning as tension T (attraction force between soil particle and pore water induced by meniscus effect as shown in Fig. 1-5). Subsequently, the reduction of pore water driven by P_E induces the increase of T which tries to stop pore water from leaving. As a results, the combined effect of each potential component produces an equilibrium state in the element. SWCC exactly describes the equilibrium state of a soil element. An arbitrary position in the heap of iron ore fines can be considered as an element like the one in Fig. 1-5. Through proper estimation of suction distribution in the heap and utilization of SWCC of iron ore fines, the equilibrium water distribution in the heap can be evaluated. Since iron ore fines is not usually encountered in geotechnical engineering, comparison is also made on water retention ability between iron ore fines and common materials in low suction range as well in very high suction range.

2. Permeability test. Coefficient of permeability of a soil element indicates the water flow velocity in this element. It is another important aspect for estimation of time-dependent water distribution in a heap of iron ore fines. In this study, efforts are taken to develop testing techniques of permeability test for both saturated and unsaturated soils in a triaxial apparatus. The test was conducted in a triaxial system to reduce the interface effect between the specimen and the confining wall and to freely control the confining stress. Constant water head system was applied to both saturated specimen and unsaturated specimen. Since the used triaxial system is unable to directly measure the water head difference at the two ends of a specimen, it is necessary to consider the system head loss induced by friction in the water flow path, especially for materials with relatively high permeability, for instance, with the order of 10^{-2}-10^{-3} cm/s. Calibration relationship between flow speed through the system and system head loss is established to evaluate the system head loss during seepage of the saturated specimen. For the unsaturated specimen, it is found that filter clogging problem severely affect the calibration process because even the distilled water could clog the membrane filter

used for the unsaturated test. Through strict test procedure, a family curves of calibration relationship are established. The permeability of two material under both saturated and unsaturated states is discussed.

3. Undrained cyclic loading test. Resistance against cyclic shear stress/liquefaction of an element of iron ore fines provides basic properties for analysis of the response of a heap of iron ore fines. In this study, tests were conducted on a triaxial apparatus. Considering the partially saturated condition a heap of iron ore fines may form, proper evaluation of the liquefaction resistance of unsaturated iron ore fines became one of tasks of this study. The work in this aspect was further extended to the effects of degree of saturation and fines content on the resistance against liquefaction of iron ore fines and other common materials. Except the undrained cyclic loading test, consolidation test to obtain the volumetric change of soils induced by change of confining pressure was also conducted to better understand the effect of fines content on liquefaction resistance.
4. Seepage analysis. The analysis of seepage of water in the heap of iron ore fine is important to estimate the saturation condition in the heap. Saturated zone and unsaturated zone may form during the voyage for the heap with an initially uniform water content. The extent of the saturated zone and the degree of saturation of the unsaturated zone are crucial information for the dynamic analysis of the heap. Numerical tool was utilized to simulate the seepage in the heap of iron ore fines based on the results of SWCC test and permeability test. Van Genuchten model (Van Genuchten, 1980; Kool et al., 1985 and Parker et al., 1985) was introduced to a FEM code for simulation. The effects of initial water content, density of iron ore fines and boundary on the saturation distribution are discussed. The critical conditions when the maximum height of saturated zone for a given initial degree of saturation are estimated and the distribution of degree of saturation of unsaturated zone in the heap under critical conditions is evaluated.
5. Dynamic response analysis. The final objective of this study is to evaluate the liquefaction potential of the heap of iron ore fines. The two dimensional response analysis of the heap is performed numerically. The liquefaction potential of both saturated zone and unsaturated zone are taken into consideration. The area with high liquefaction potential, the strain distribution and shear stress distribution in the heap are plotted out. The liquefaction potential of the heap under different angles of rolling motion are discussed.

1.4 Organization of the thesis

Chapter 1	**Introduction** The background of the intended research was described. To understand the problem the international organizations faced, simplifications of the problem were made from the point view of geotechnical engineering. The objective and research aspects were presented
Chapter 2	**Apparatus and measurement system** The test apparatus and measurement system mainly used in this study was presented. Test system features and measurement mechanism was described.
Chapter 3	**Test materials** The materials tested in this study and some of their physical properties were revealed.
Chapter 4	**SWCC test and permeability test** The water retention ability and permeability of iron ore fines and the other materials were covered. Testing techniques and challenges are discussed.
Chapter 5	**Undrained properties of saturated and unsaturated materials** Undrained behavior of soils under both saturated condition and unsaturated condition were examined. The resistance against liquefaction for unsaturated soils with or without fines content were discussed. A new parameter to correlate the resistance against liquefaction of unsaturated soil was proposed.
Chapter 6	**Seepage analysis of the heap of iron ore fines** Numerical study on the seepage in the heap of iron ore fines was presented.
Chapter 7	**Dynamic response analysis of the heap of iron ore fines** The responses of the heap of iron ore fines was analyzed based on experimental studies and seepage analysis.
Chapter 8	**Conclusions and recommendations** Conclusions of current study and recommendations for the further studies were presented

Appendix A	**Introduction of issues about IMO** Introduction about international maritime organization and issues related to this study are presented

Appendix B	**Membrane filter technique** The membrane filter technique used in this study is presented.
Appendix C	**Volume measurement system** The system to measure volume change of soil specimens used in triaxial system is presented
Appendix D	**Time histories of SWCC test in high suction range** The time histories of all specimen tested in high suction range using vapor pressure equilibrium technique is presented
Appendix E	**Undrained cyclic loading test for Toyoura sand** Results of undrained cyclic loading test on saturated and unsaturated Toyoura sand are presented
Appendix F	**Undrained cyclic loading test for Inagi sand** Results of undrained cyclic loading test on saturated and unsaturated Inagi sand are presented
Appendix G	**Undrained cyclic loading test for Iron ore fines B** Results of undrained cyclic loading test on saturated and unsaturated for Iron ore fines type B are presented

Reference

1. DSC. (2010) Sub-Committee on Dangerous Goods, Solid cargoes and Containers (DSC)-15th session. International Maritime Organization.
2. DSC. (2011). Sub-Committee on Dangerous Goods, Solid cargoes and Containers (DSC)-16th session. International Maritime Organization.
3. DSC. (2012). Sub-Committee on Dangerous Goods, Solid cargoes and Containers (DSC)-17th session. International Maritime Organization.
4. DSC.1/Circ.63. (2010). Carriage of iron ore fines that may liquefy. International Maritime Organization.
5. DSC.1/Circ.66. (2011). Carriage of iron ore fines that may liquefy. International Maritime Organization.
6. DSC.1/Circ.66/Rev.1. (2012). Carriage of iron ore fines that may liquefy. International Maritime Organization.
7. DSC.1/Circ.71. (2013). Early implementation of draft amendments to the IMSBC Code related to the carriage and testing of iron ore fines. International Maritime Organization.

8. DSC 18/6/13. (2013). Report of the correspondence group on transport of iron ore fines in bulk (Part 1). International Maritime Organization.
9. DSC 18/6/14. (2013) Report of the correspondence group on transport of iron ore fines in bulk (Part 2) Research synopsis and recommendations by the technical working group (TWG Report #5. International Maritime Organization.
10. DSC 18/13. (2013) Report to the maritime safety committee. International Maritime Organization.
11. DSC 18/INF.9. (2013) Report of the Correspondence Group on Transport of Iron Ore Fines in Bulk (Part 3) Comments in the final round of the correspondence group. International Maritime Organization.
12. DSC 18/INF.10. (2013). The Technical Working Group (TWG) Report #1 Terms of Reference .1. International Maritime Organization.
13. DSC 18/INF.11. (2013). The Technical Working Group (TWG) Report #2 Marine Report. International Maritime Organization.
14. DSC 18/INF.12 (2013). The Technical Working Group (TWG) Report #3 Iron Ore Fines Proctor-Fagerberg Test. International Maritime Organization.
15. DSC 18/INF.13. (2013). The Technical Working Group (TWG) Report #4 Reference Test. International Maritime Organization.
16. Evans, T. (2013) Goethite and its liquefaction resistance. Workshop on Carriage of Iron Ore Fines in Bulk, IMO headquarters, London.
17. Gard. (2012). Brazil-liquefaction of bauxite cargoes. Gard.
18. Herff, M. and Baker, D. (2013) Overview of the technical working group process Workshop on Carriage of Iron Ore Fines in Bulk, IMO headquarters, London.
19. Hudson, A. (2013) Iron ore fines: context for the TWG research. Workshop on Carriage of Iron Ore Fines in Bulk, IMO headquarters, London.
20. IMSBC Code (2012) International Maritime Solid Bulk Cargoes Code. IMO.
21. Isacson, C. (2010a). Re: India- safe shipment of iron ore fines from Indian ports. International Group Member Circular No.16
22. Isacson, C. (2010b). Re: Indonesia and the Philippines – Safe Carriage of Nickel Ore Cargoes. International Group Member Circular No.23
23. Kool, J.B., Parker, J.C. and Van Genuchten (1985). Determining soil hydraulic properties from one-step outflow experiments by parameter estimation: I. Theory and numerical studies. Soil Sci. Soc. AM. J., Vol. 49, pp: 1348-1354.

24. Ishihara, K. (2013) Fundamental of liquefaction and associated risks. Workshop on Carriage of Iron Ore Fines in Bulk, IMO headquarters, London.
25. Linden, D. (2013) Validation of modified proctor fagerberg test Workshop on Carriage of Iron Ore Fines in Bulk, IMO headquarters, London.
26. MSC 91/13 (2012) Dangerous goods, solid cargoes and containers- Urgent matters emanating from the seventeenth session of the Sub-Committee. International Maritime Organization.
27. Ota, S. (2013) Results of the Correspondence Group on transport of iron ore fines in bulk. Workshop on Carriage of Iron Ore Fines in Bulk, IMO headquarters, London.
28. Parker, J.C., Kool, J.B. and Van Genuchten, M.Th. (1985). Determining soil hydraulic properties from one-step outflow experiments by parameter estimation: II. Experimental studies. Soil Sci. Soc. AM. J., Vol. 49, pp: 1354-1359.
29. Policarpo, D and Maney, P. (2013) TML test procedure- the case of iron ore fines. Workshop on Carriage of Iron Ore Fines in Bulk, IMO headquarters, London.
30. Tindall, J.A. & Kimkel, J.R. 1999. Unsaturated zone hydrology for scientists and engineers. New Jersey: Prentice Hall. pp: 95-122.
31. Van Genuchten, M.Th. (1980). A closed-form equation for predicting the hydraulic conductivity of unsaturated soils. Soil Sci. Soc. AM. J., Vol. 44, pp: 893-898.

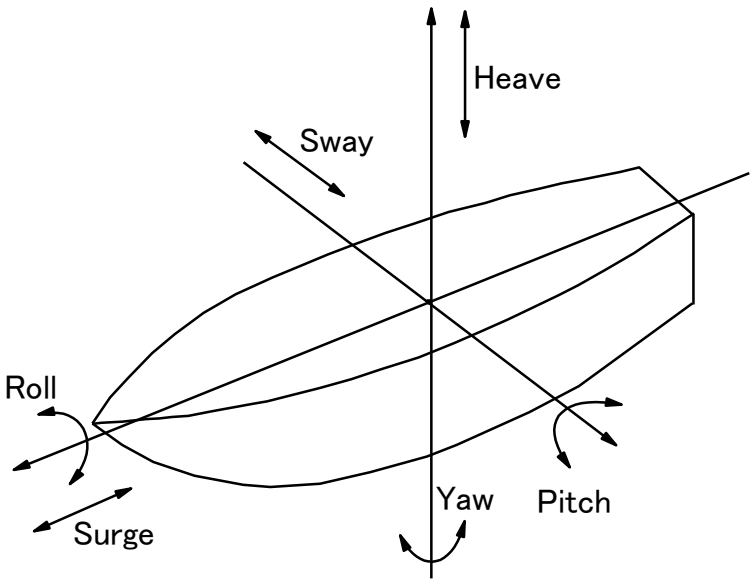

Fig. 1-1 Six motion components of a ship

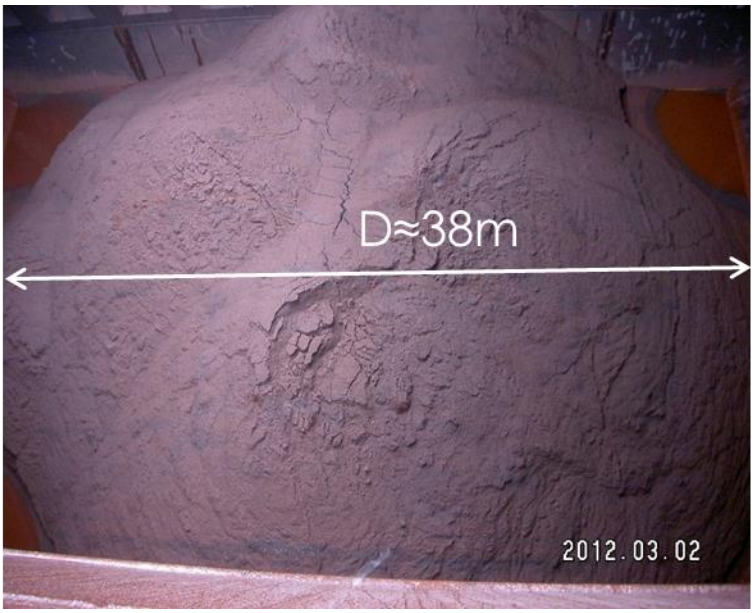

Fig. 1-2 A typical image of the heap of iron ore fines

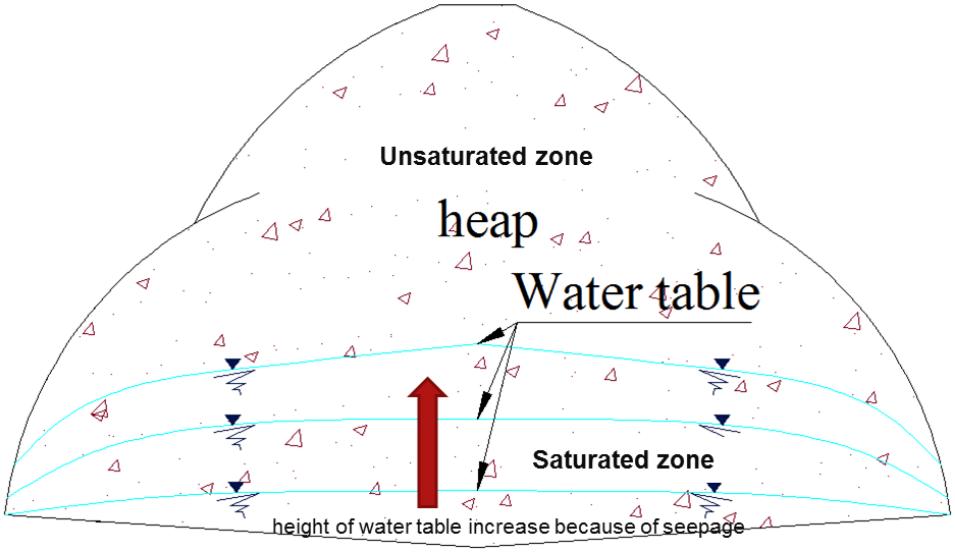

Fig. 1-3 Saturation condition of a heap

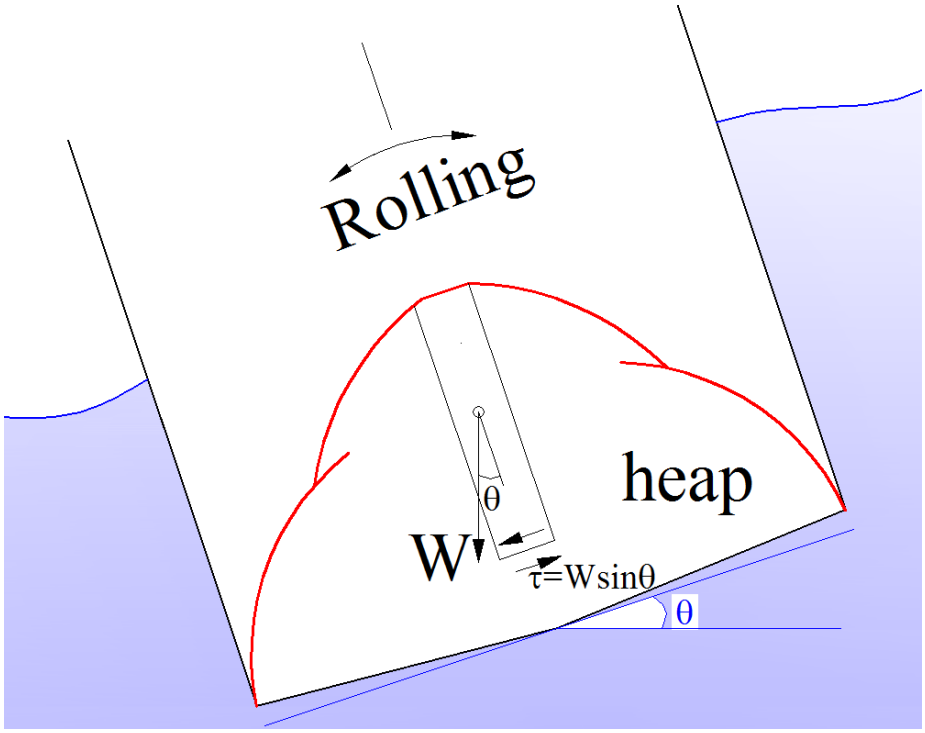

Fig. 1-4 The condition of a heap under rolling motion

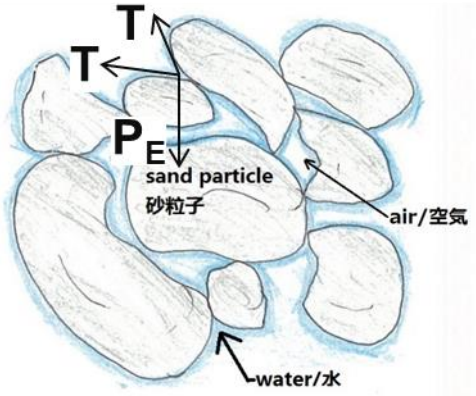

Fig. 1-5 Forces worked on pore water of an unsaturated soil element

Chapter 2. Apparatus and measurement system

Contents

In this chapter, the measurement systems for the SWCC tests and test apparatus for undrained cyclic loading test are described in detail. The apparatuses for other tests e.g. permeability test are introduced in Chapters where corresponding test results are presented.

2.1 Measurement systems for SWCC test

Two types of equipment were employed in this study to measure SWCC (Soil water characteristic curve, a relationship between suction and amount of water in soil) in low suction range (0.1 kPa -100 kPa) and in very high suction range (10^3 kPa-10^6 kPa), respectively.

2.1.1 Low suction range

Pressure plate apparatus is a common device to measure SWCC of materials for suction less than 1500 kPa. For this type of apparatus, a ceramic disk is conventionally installed as a filter. The principle of measuring SWCC by pressure plate apparatus is described in many books or papers, for instance, Fredlund and Rahardjo (1993), thus it is not repeated herein. A pressure plate apparatus on which a ceramic disk with air entry value (AEV) of about 200 kPa was installed was prepared for this study and will be referred to as ceramic disk apparatus hereafter in this Chapter. Another pressure plate apparatus on which the membrane filter was installed as the filter was also prepared and will be referred to as membrane filter apparatus (the membrane filter technique is introduced in Appendix B).

Fig. 2-1 shows layouts of the two types of pressure plate apparatuses used. There is a very small hole on the cap of the ceramic disk apparatus considering evaporation effect in a probably long test period. For the membrane filter apparatus, evaporation effect was not considered to be severe because the test period was much shorter and evaporation effect should be minor. The thickness of the ceramic disk used is 4 mm, while the thickness of the membrane filter is 0.14 mm (for each test a new membrane filter was placed). Suction was introduced by axis-translation technique for the ceramic disk apparatus. For the membrane filter apparatus, the applied suction with a maximum value of around 20 kPa (water elevation difference of 2 m) was introduced by elevation difference between the specimen and water level in a burette (H in Fig. 2-1 b). A differential pressure transducer (DPT) was used for each apparatus to record the volume of water flowing in/out during a test.

2.1.2 High suction range

Vapor equilibrium technique

To measure SWCC in very high suction range (10^3 kPa-10^6 kPa), the vapor equilibrium technique is introduced. The vapor equilibrium technique is a way to control humidity (or relative humidity) of a sealed space by using a saturated chemical solution. Fig. 2-2 shows the leak proof chamber used in this study and a typical specimen tested.

To intuitively understand this technique, Fig. 2-3 (a) illustrates the phenomenon of vapor–liquid equilibrium. In a sealed bottle with some pure water inside, there are two states for water, water in liquid state and water in the form of water vapor. The phenomenon of water diffusion always exists in this system, namely, some liquid water (ΔW_l) transforms into water vapor meanwhile some water vapor (ΔW_v) returns to liquid water. In this sealed system, a dynamic equilibrium (vapor–liquid equilibrium) of water diffusion is the final state that the water in the bottle tries to achieve, which means it is the final goal for the water to make $\Delta W_v = \Delta W_l$ in this system. Under the dynamic equilibrium state, the water vapor is said to be saturated ("saturated" does not mean air in the bottle is fully filled by water vapor, it is a state that no extra liquid water can change into water vapor without the return of an equivalent amount of water vapor to the liquid state). If we assume the molecule number of water vapor in any state is N and in a saturated state is N_s, N will never exceed N_s ($N \leq N_s$) without any change in the system. If there is a way to keep N value as a constant N_c ($N_c < N_s$) without disturbing any other parts of the system, for instance using an imaginary hand to take water vapor out when $N > N_c$, the liquid water will continuously try to evaporate more water vapor to achieve dynamic equilibrium until there is no liquid water anymore, unless there are some other forces (or a more general term, potential) to stop liquid water from doing so. No matter if there are some other forces in the system or not, a final equilibrium will form, of which the number of molecule of water vapor is N_c. The chemical solution in vapor equilibrium technique used for SWCC test is just like the imaginary hand.

Some chemical solutions are sensitive to the humidity (or relative humidity, a term describing the amount of water vapor in a space) of their surrounding space. If the air surrounding a chemical solution is too dry, the chemical solution will release more water vapor until the humidity is just right for the solution, and vice versa. Now we call the relative humidity (RH) just right for a chemical solution as its controlled RH (RH_c). Considering the SWCC test in high suction range, as shown in Fig. 2-2, if we store a chemical solution in the leak-proof

chamber, the final equilibrium in the test chamber will be RH= RH_c (or N=N_c). On the other hand, water in a soil specimen will not completely diffuse to the air because there are some other forces in the soil water i.e. matric suction and osmotic suction to stop soil water from doing so (total suction = matric suction + osmotic suction).

In Section 1.3.3 of Chapter 1, two components of potential in an unsaturated soil element are introduced to illustrate the working principle of matric suction (matric potential). The equilibrium between liquid water and water vapor addressed in the last two paragraphs is fundamentally controlled by potential equilibrium. For example a chemical solution is actually a mixture of pure water and soluble salt(s), as shown in Fig. 2-2 (b). If a salt dissolves in pure water, it will lower the potential of the pure water and consequently urge the salt solution (mixture of salt and pure water) to absorb more water vapor to dilute the salt. The potential component induced by dissolved salt is called osmotic potential (or osmotic suction). In a soil specimen, some soil particles (e.g. soluble salt crystal) may dissolve in soil water and form a salt solution (soil water). The matric suction and osmotic suction in soil water can retain a certain volume of water within the specimen. Thus, the potential (suction) in the soil water and the potential in the chemical solution will eventually establish a state of equilibrium in a system such as that shown in Fig 2-3 (b). Based on this equilibrium, the total suction of a soil specimen can be theoretically calculated from a function of controlled relative humidity (Eq. 4-1 in Chapter 4). The variable we are interested in in the SWCC test is matric suction, so osmotic suction is estimated by the other method introduced in Chapter 4.

Vapor equilibrium technique is a common way to apply very high total suction in a SWCC test (Fredlund and Rahadjo, 1993; Nishimura and Fredlund, 2000; Marcial et al., 2002; Tang and Cui, 2005 and Salager et al., 2013). In this study, seven different saturated chemical solutions (i.e. K_2SO_4, KNO_3, $NH_4H_2PO_4$, NaCl, $Mg(NO_3)_2 \cdot 6H_2O$, $MgCl_2 \cdot 6H_2O$, LiCl) recommended by JGS0151-2000 (JGS: Japanese test standard of Japanese Geotechnical Society) were prepared to control RH. Before determining the controlled RH (RH_c) of each chemical solution, the effect of temperature on RH_c of a chemical solution needs to be noted. Firstly, the RH_c of a chemical solution changes in different room temperature. With an increase in room temperature, for example, the RH_c of some solutions may increase, while some may decrease. Secondly, the increase/decrease rate may change even for the same solution in different room temperature ranges. Thirdly, when the room temperature exceeds certain values, RH_c may not be properly evaluated because, for instance, a chemical reaction may happen in a solution and the substance in the solution may change fundamentally. Thus,

RH_c of a chemical solution is a function of temperature and ways of evaluation of RH_c may be only valid in a certain temperature range.

Measurement system

The test of SWCC in high suction range was conducted at constant room temperature (15.6± 0.5°C). To control the temperature of the room, two sets of electronic remote control systems (Sanyo cooling unit controller) were installed in the room. Twenty leak-proof chambers as shown an example in Fig. 2-2 (a) with dimensions of 30cm × 30cm × 50cm (length × width × height) are stored in the room.

To confirm the stability of controlled relative humidity (RH_c), the RH values in chambers were measured by a resistance change type sensor, SK-LTH II α-2 (Sato Keiryoki MFG.CO., LTM.), as shown in Fig. 2-4. The relative humidity values were maintained relatively stable. Relative humidity is a physical value that is very difficult to be measured precisely. The accuracy of transducer SK-LTH II α-2 is ±3% for RH between 30% and 90%. It is out of the scope of measurement for the sensor when RH is under 25%. The accuracy is ±5% for the rest of the RH ranges. This means that measured data in Fig. 2-4 should be used with caution.

According to authoritative literatures, RH_c for each used chemical solution are also calculated. Table 2-1 summarizes results according to Young (1967), CRC handbook (Haynes 2010-2011) and JGS 0151-2000 (at 20°C) together with measured RH_c by the SK-LTH II α-2 sensor. The two columns named as "T-range" indicate the applicable temperature range for calculation recommended by referred literatures. The last column in Table 2-1 are RH_c values used in this study, which were chosen according to calculated RH_c from CRC handbook (Haynes 2010-2011) considering its authoritativeness and wide acceptance.

It is very difficult to decide the RH_c of the LiCl solution. Anhydrous LiCl solid and distilled water mixture was used to produce the saturated solution in this study. While there are four other solid lithium chloride hydrates, with 1, 2, 3 and 5 water molecules, respectively (Monnin et al., 2002), hydration and dehydration could happen in the LiCl solution (Skolunov and Serkov, 1995; Masset, 2009). On the other hand, the equations for calculating RH_c in Young (1967) and CRC handbook (Haynes 2010-2011) are not strictly for anhydrous LiCl solution (see notes 2&3 below Table 2-1). The true RH_c value of LiCl solution may not be correctly measured by the RH transducer (it is out of the scope of measurement of the RH transducer used when RH is less than 25%). According to the summarized experimental data

of vapor pressure of water above saturated LiCl solution by Gokcen (1951), a RH=10.8% at 18°C was obtained. Thus, an RH_c value of 11.0% for the LiCl solution was chosen.

Table 2-1 RH_c summary

Saturated chemical solution	CRC handbook at 15.6°C		Young (1967) at 15.6°C		JGS 0151-2000 at 20°C	Measured value at 15.6°C	Chosen RH_c
	RH	T range (°C)	RH	T range (°C)			
K_2S0_4	97.6	10-50	98.2	15-60	98	96.7	97.6
KNO_3	94.2	0-50	--	--	95	92.2	94.2
$NH_4H_2PO_4$	--	--	93.2[1)]	18-46	93.1	90.9	93.2
$NaCl$	75.5	10-40	75.3	5-60	75	72.6	75.5
$Mg(NO_3)_2 \cdot 6H_2O$	54.2	5-35	55.5	0-50	54	53.5	54.2
$MgCl_2 \cdot 6\ H_2O$	32.9	5-45	33.3	10-50	33	33.3	32.9
$LiCl$	11.2/ 20.8[2)]	20-65/ 15-65[2)]	11.4/ 12[3)]	20-70/ -10-15[3)]	11.0	23.5	11.0

Note: 1) There was not enough information for calculation, the value was picked directly from the figure of the reference at 18°C; 2) Calculated value and temperature range are for $LiCl \cdot H_2O$/ $LiCl \cdot 3H_2O$ solution; 3) Calculated value and temperature range are for $LiCl \cdot H_2O$/ $LiCl \cdot 2H_2O$ solution

2.2 Apparatus for undrained cyclic loading test

A specially manufactured double-cell triaxial apparatus, as shown schematically in Fig. 2-5, was employed to conduct undrained cyclic loading tests. This layout is specifically designed for testing unsaturated soil, while tests on saturated specimens can be also easily performed after slight modification. The introduction of the apparatus is mostly focused on the setup for conducting test on unsaturated soil. This configuration contains three main parts, e.g. the pneumatic power system, the main body of the apparatus and the measurement system.

1. Pneumatic power system.

   A double action cylinder was installed to apply cyclic loading. Two sides of the double action cylinder were connected to two pressure regulators, respectively. The pressure at the bottom of the cylinder is kept constant and the pressure at the top of the cylinder is controlled by an E/P regulator converting electric signal to pneumatic signal. The electric signal sent to the E/P regulator is triggered by a function generator. In such a way, the frequency, amplitude etc. of vertical cyclic loading can be precisely applied by adjusting the output electric single of the Function Generator. A relatively small double action cylinder, Fujikura SCD-40-48-B0, having a stroke of 48 mm and a friction free ball bearing (without seal at bearing), is used in this system to further increase the accuracy of the applied loading.

   Another power system for cell pressure (hereafter, cell pressure control system) including a Function Generator and an E/P regulator, as shown in Fig. 2-5, is also equipped particularly for tests on unsaturated soils. During applying vertical cyclic loading to a saturated specimen normally the cell pressure is kept constant. Though the total mean principle stress (p) changes because of the vertical cyclic loading, it does not significantly affect the effective stress of a saturated specimen because pore pressure parameter B of the specimen is near unity. While in the case of an unsaturated specimen, a change of p results in a change in effective mean principle stress (p') which is not desired in this kind of test (more details are discussed in Chapter 5). Thus, in a test on an unsaturated specimen, the cell pressure is also controlled by the cell pressure control system simultaneously while applying vertical cyclic loading. The change in cell pressure is set as -1/3 of the change in q, the deviator stress as schematically shown in Fig. 2-6. Under such a configuration, p is kept constant and the effect of p on the test result can be eliminated. Some discussions about the effect of p on the test results are addressed in Chapter 5.

2. Apparatus

   The main body of the triaxial apparatus was designed by Koseki Lab, IIS, Univ. of Tokyo. The membrane filter technique (Nishimura et al. 2012) is introduced to the pedestal instead of the traditional ceramic disk. A very thin porous membrane filter paper (0.14 mm in thickness) is sandwiched between a stainless steel plate and the main part of the pedestal and was tightened by six flat head screws (MB in Fig. 2-5). Details about the membrane filter technique are discussed in Appendix B. On the top cap, a hydrophobic filter was glued on the surface to keep pore water from entering into it. Another set of pedestal and top cap were used for test on saturated specimen.

3. Measurement systems

   A load cell with a unique shape was installed inside the cell of the apparatus. A linear variable differential transformer type displacement transducer (LVDT) is equipped to measure vertical displacement of a specimen. In order to measure suction of an unsaturated specimen, two pressure transducers were installed to measure pore air pressure and pore water pressure from the top cap and from the pedestal, respectively. To measure the volume change of a specimen during undrained cyclic loading, a double cell system similar with that used by Ng et al. (2002) is introduced. This system contains an inner cell, a reference burette and a DPT. The reference burette is connected to the pressure cell by a tube to guarantee the same pressure in the cell and in the reference. Details of this system are given in Appendix C.

Reference

1. Fredlund, D.G. & Rahardjo, H. 1993. Soil mechanics for unsaturated soils. New York: John Wiley and Sons, Inc..
2. Gokcen, N.A. 1951. Vapor pressure of water above saturated lithium chloride solution. J. Am. Chem. Soc. 73: 3789
3. Haynes, W. M. (eds.) 2010-2011. Handbook of Chemistry and Physics (91st ed.). Boca Raton, Florida: CRC Press: 15-33 - 15-34.
4. Marcial, D., Delage, P., Cui, Y.J. 2002. On the high stress compression of bentonites. Can. Geotech. J. 39:812-820.
5. Masset, P.J. 2009. Thermogravimetric study of the dehydration reaction of LiCl・H_2O. Journal of Thermal Analysis and Calorimetry 96: 439-441
6. Monnin, C., Dubois, M., Papaiconomou, N., Simonin, J.P. 2002. Thermodynamics of the LiCl+H_2O system. J. Chem. Eng. Data 47: 1331-1336
7. Nishimura, T. & Fredlund, D.G. 2000. Unconfined compressive strength of a silty soil and kaolin below the residual state. Advances in Unsaturated Geotechnics: pp. 262-274.
8. Salager, S., Nuth, M., Ferrari, A., Laloui, L. 2013. Investigation into water retention behavior of deformable soils. Can. Geotech. J. 50: 200-208.
9. Skolunov, A.V. & Serkov, A.T. 1995. Study of hydration of lithium ion in lithium chloride solution in active membrane transfer. Fibre Chemistry 27 (4): 234-239.
10. Tang, A.M. & Cui, Y.J. 2005. Controlling suction by the vapour equilibrium technique at different temperatures and its application in determining the water retention properties of MX80 clay. Can. Geotech. J. 42:287-296.
11. Young, J.F. 1967. Humidity control in the laboratory using salt solutions- A review. Journal of Applied Chemistry 17: 241-245.

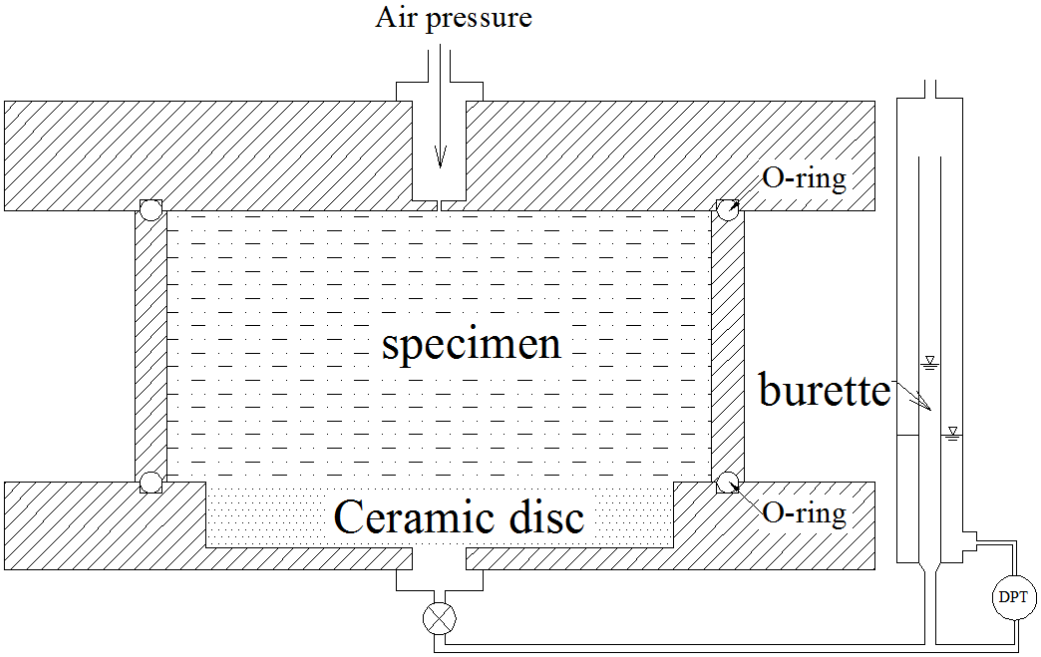

Fig. 2-1 (a) Pressure plate apparatus equipped with ceramic disk

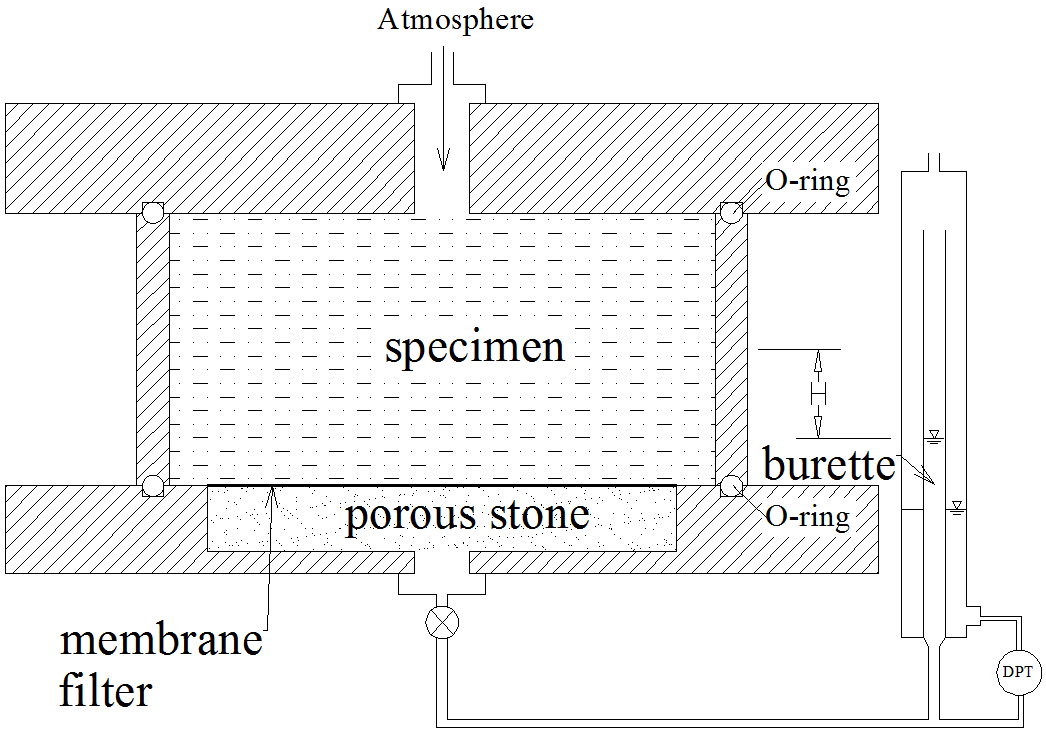

Fig. 2-1 (b) Pressure plate apparatus equipped with membrane filter

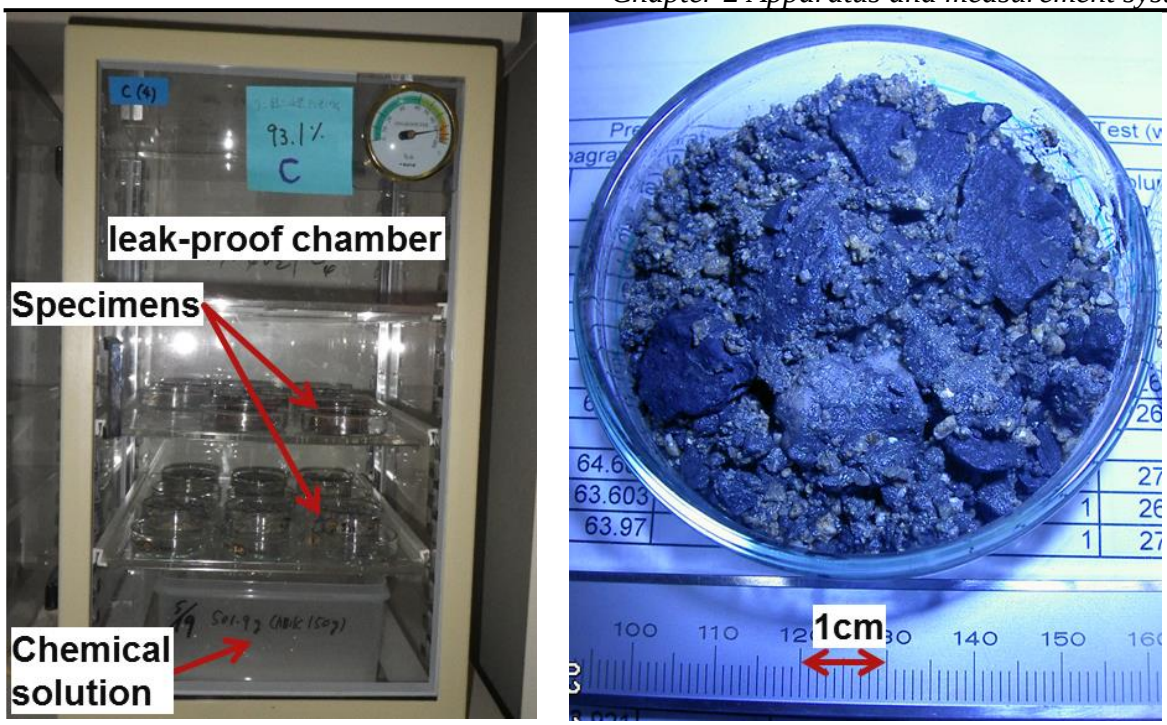

Fig. 2-2 (a) Sealed chamber to store specimens; (b) a typical specimen

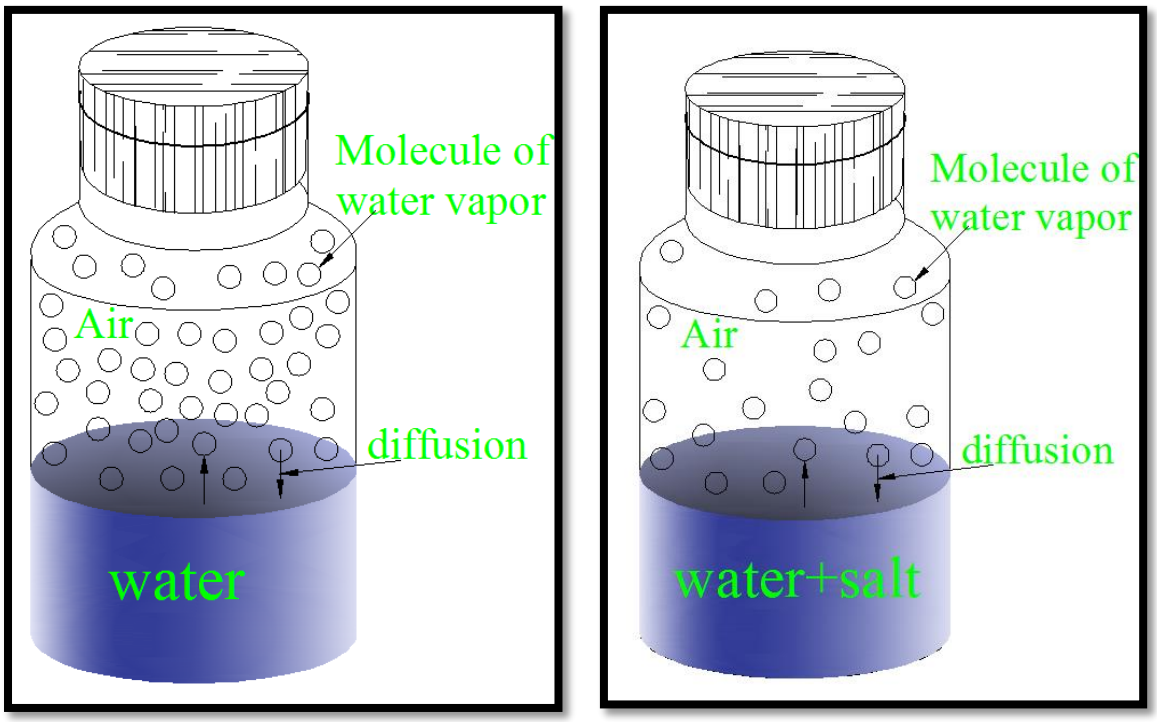

Fig 2-3 Vapor–liquid equilibrium of (a) pure water; (b) pure water with soluble salt

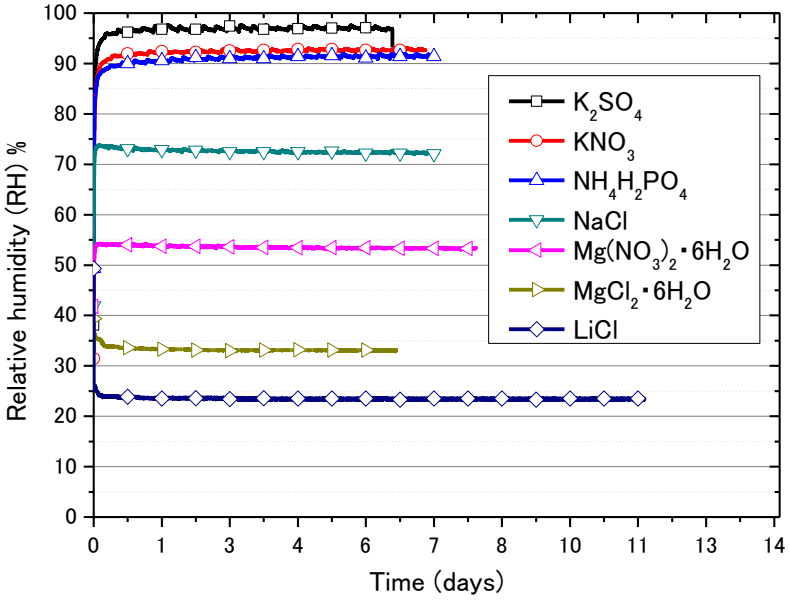

Fig. 2-4 Relative humidity measured in chambers

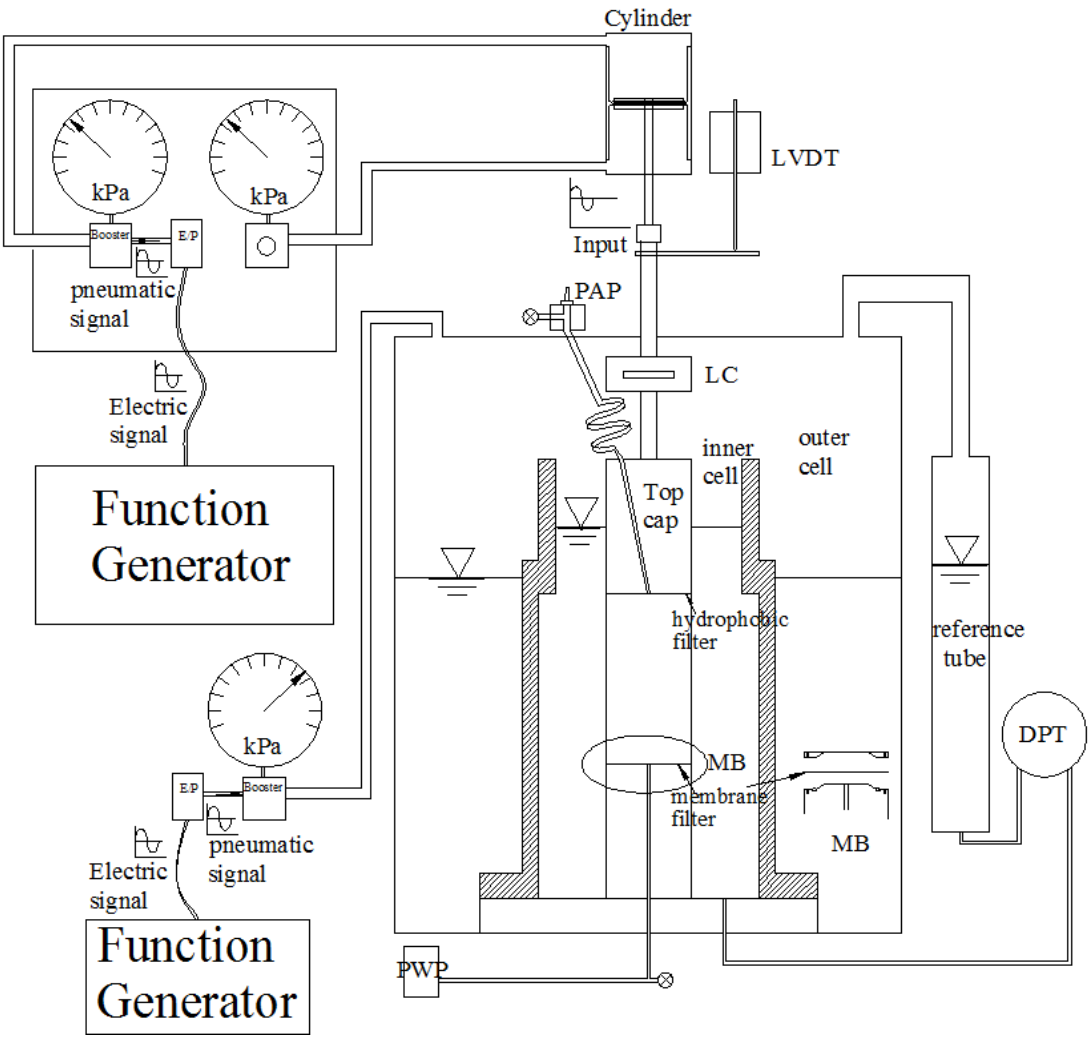

Fig. 2-5 Triaxial apparatus scheme for test of unsaturated specimen

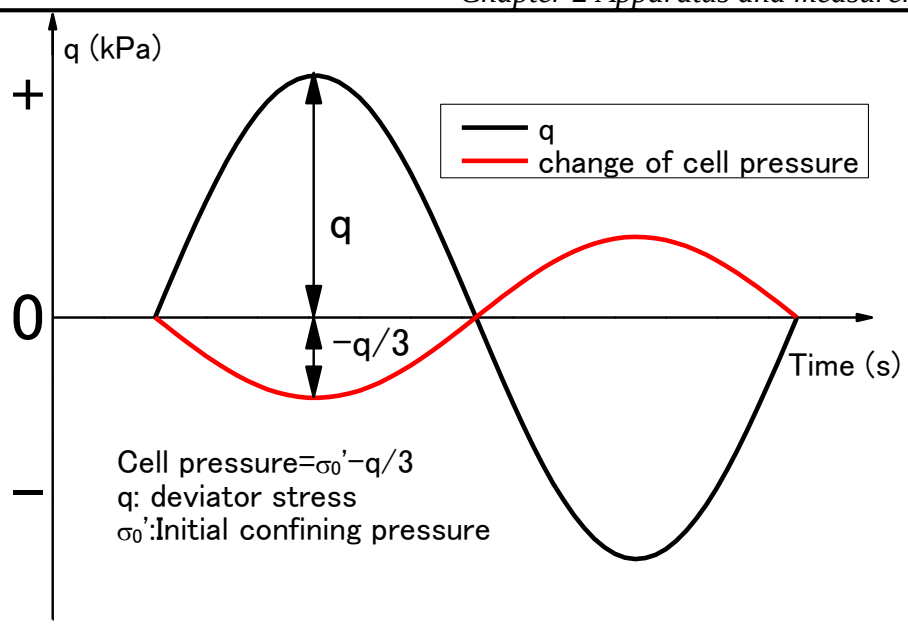

Fig. 2-6 Control of cell pressure to keep p constant

Chapter 3. Test materials

Contents

3.1 Introduction

In this study, more than one material (e.g. iron ore fines, sand, gravel, clay) was used in each test program. The basic properties of these materials are described in this chapter. In the last section of this chapter, SEM images of some materials are also displayed.

Before a detailed description of each material is given, Table 3-1 summarizes the values of some parameters determined in this study. The materials used were:

1. Iron ore fines type B (IOF-B): used for all tests in this study;
2. Iron ore fines type A (IOF-A): used mainly for SWCC test;
3. Iron ore fines passing 4.75 mm (IOF-4.75) and 2 mm (IOF-2) sieves: used mainly for SWCC test;
4. Mixtures of Nashime sand, Chiba gravel and DL clay to simulate gradations of IOF-B (NCD-B) and IOF-A (NCD-A): used mainly for SWCC test;
5. Inagi sand (ING): used mainly for undrained cyclic loading test;
6. Toyoura sand batch J (T): used mainly for undrained cyclic loading test.

Table 3-1 Properties of materials used

Materials	IOF-B	IOF-A	IOF-A-4.75	IOF-A-2	NCD-B	NCD-A	ING	T
Gravel (%)	33.5	56.8	27.9	0	33.5	56.8	0	0
Sand (%)	42.9	25.4	42.3	58.7	42.9	25.4	70.5	99.9
Silt (%)	17.1	14.6	24.4	32.4	--	--	18.2	--
Clay (%)	6.5	3.2	5.4	8.9	--	--	11.3	--
Fc (%)	23.6	17.8	29.8	41.3	23.6	17.9	29.5	0.1
G_s	4.444	4.835	4.859	4.859	2.678	2.694	2.656	2.659
D_{60} (mm)	1.382	--					0.136	--
D_{50} (mm)	0.715	--					0.115	0.16
D_{30} (mm)	0.136	--					0.076	--
D_{10} (mm)	0.013	--					0.004	--
U'c	1.0	--					10.6	--
Uc	106.3	--					34.0	--
e_{max}	--	--					1.65	0.99
e_{min}	--	--					0.91	0.63
ρ_{dmax} (g/cm^3)	2.79	--					--	--
ω_{opt} (%)	12.04	--					--	--

Notes: Gravel, Sand, Silt and Clay: Percentage of particle size in the range of 2-75 mm, 0.075-2 mm, 0.005-0.075 mm and < 0.005 mm, respectively; Fc: fines content, particle size <0.075 mm; D_{60}, D_{50}, D_{30} and D_{10}: sizes passed by 60%, 50%, 30% and 10% of a material by weight, respectively; Uc and U'c: Coefficient of uniformity and coefficient of curvature, respectively. $Uc=D_{60}/D_{10}$; $U'c=D_{30}^2/(D_{10}*D_{60})$; G_s: specific gravity; e_{max} and e_{min}: Maximum and minimum void ratio; ρ_{dmax} and ω_{opt}: Maximum dry density and optimum water content obtained from compaction test.

3.2 Iron ore fines type B (IOF-B)

3.2.1 Appearance

Fig. 3-1 shows the overall and close-up view of a typical relatively large particle of IOF-B. Large particles of IOF-B are normally covered by dull brownish-yellow fines and possess a multi-layer structure like shale. The top view is the view shown perpendicular to each layer and the lateral view is the view parallel to the layers. In Fig. 3-1 (b), a rather smooth surface of the top layer is observed, while some substance with a similar color as the fines appears sandwiched between the layers.

3.2.2 Gradation

To ensure uniformity of IOF-B for all the tests, around 100 kg of IOF-B passing through a 9.5 mm sieve was mixed with water and stored in one box. Fig. 3-2 shows the gradation of IOF-B. It is classified as a SFG material containing 33.5% gravel, 42.9% sand, 17.1% silt and 6.5% clay according to the test standard of Japanese Geotechnical Society (JGS 0051-2000). Non-plastic fines content is about 24%.

3.2.3 Specific gravity

Iron ore fines are normally rich in iron oxides, of which the specific gravity is usually higher than other common soils encountered in geotechnical engineering. Open or closed pores, which may exist in IOF-B, as shown in Fig. 3-1 (b) and SEM photos in Section 3.6, may also affect its self-weight. To determine a representative specific gravity (G_s) for this material, seven tests were conducted by employing pycnometers of 100 ml following the JIS A 1020:1999 (JIS: Japanese Industrial Standard). Fig. 3-3 shows the measured G_s values, which is of an average value of 4.444. In addition, G_s values of IOF-B scatters in between 4.4 and 4.5 which may be attributed to possible closed pores within the large particles. The air inside the closed pores may not be expelled by boiling the samples in the test. Another possible reason is that IOF-B may contain different mineral components such as hematite, goethite etc., which may have different values of G_s. The average value, 4.444, was used for all the related calculations for this material.

3.2.4 Maximum dry density and optimum water content

The compaction test was conducted for IOF-B according to method A (similar as “Standard proctor method” with compaction energy of 550 kJ/m^3) specified in JIS A-1201:1990 (JIS: Japan Industrial Standard). Not exactly the same as instructed in the standard, three sets of

new material were prepared. After obtaining the first three data points, as shown in Fig. 3-4, they were re-used to produce another three points. A maximum dry density of 2.79 g/cm^3 was obtained with an optimum water content of about 12%, under which the degree of saturation (Sr) is 90%. The parameter compaction degree Dc, which is used to indicate the density of a specimen of IOF-B, is defined as:

$$\mathrm{Dc} = \frac{\text{dry density of a specimen}}{\text{maximum dry density of IOF-B } (2.79\ \mathrm{g/cm^3})} \times 100\% \quad \text{(Eq. 3-1)}$$

3.3 Iron ore fines type A (IOF-A)

3.3.1 Appearance

The overall and close-up views of typical particles of IOF-A are shown in Fig. 3-5. This material is a dark red color. Similar to IOF-B, the relatively large particle shows a layered structure, while pores can be observed from both top and lateral sides (top view and lateral view are defined in the same manner as those for IOF-B shown in Fig. 3-1).

3.3.2 Gradation

Fig. 3-6 shows the gradation of IOF-A. Another two gradation curves for materials IOF-A-4.75 and IOF-A-2, which are IOF-A cut off by 4.75 mm and 2 mm sieves, respectively, are also shown in the same figure. The maximum size of IOF-A passes the 19 mm sieve. It is classified as GFS material containing 56.8% gravel, 25.4% sand, 14.6% silt and 3.2% clay according to JGS 0051-2000.

3.3.3 Specific gravity

Several tests were conducted to determine G_s for this material, as shown in Fig. 3-7. It seems that G_s of IOF-A is larger and scattered in a wider range than that of IOF-B. Interestingly, G_s values of relatively small particles (IOF-A-4.75 and IOF-A-2) seem to be more stable than those of IOF-A, which implies that the fluctuation of G_s may be induced by pores inside relatively large particles, as shown in Fig. 3-5. The average values of 4.835, 4.859 and 4.859 for IOF-A, IOF-A-4.75 and IOF-A-2, respectively, were used for other related calculations.

3.4 Sands mixtures: NCD-B and NCD-A

One of the motivations of this study was to show the difference in properties of iron ore fines and common materials usually encountered in geotechnical engineering. For this purpose, three types of common materials (Nashime sand, Chiba gravel and DL clay) were mixed to

represent common materials. The principle of mixing these materials was to achieve a similar gradation to IOF-B or IOF-A. For instance, NCD-B (hereafter used as a reference material for IOF-B), which was composed of 33.1% Nashime sand, 50.9% Chiba gravel and 16.0% DL clay by weight, was made to simulate the gradation of IOF-B. The gradation curves of common materials are shown in Fig. 3-8 and curves of the reference materials together with those of iron ore fines are shown in Fig. 3-9. Since the maximum grain size of IOF-B and IOF-A are 9.5 mm and 19 mm, respectively, some larger particles were cut off from the original Chiba gravel as shown for Chiba gravel-1 (for IOF-B) and Chiba gravel-2 (for IOF-A) in Fig. 3-8. The G_s values for NCD-B and NCB-A material mixtures are 2.678 and 2.694, respectively.

3.5 Inagi sand and Toyoura sand

Inagi sand and Toyoura sand were used for undrained cyclic loading tests. Inagi sand is composed of 70.5% sand, 18.2% silt and 11.3% clay, classified as SF material according to JGS0051. Its specific gravity is 2.656, and the maximum and minimum void ratios are 1.65 and 0.91, respectively. Fig. 3-10 shows the gradation of Inagi sand. Toyoura sand is a widely used clean sand with a G_s value of 2.656 and the maximum and minimum void ratios of 0.99 and 0.63, respectively.

3.6 SEM observations

The possible existence of open or closed pores in iron ore fines was the motivation to observe the surface information on iron ore fines and common materials, since pores may affect properties of a material such as G_s, water retention ability etc. Scanning electron microscope (SEM) observations were carried out on two types of iron ore fines (IOF-B and IOF-A) and two types of common materials (Chiba gravel and DL clay) to reveal their surface information. Observation results of relatively large particles of IOF-B and IOF-A are compared with that of Chiba gravel, and in a similar manner the fines content of IOF-B, IOF-A and DL clay are compared.

3.6.1 Large particles of IOF-B, IOF-A and Chiba gravel

Figs. 3-11~3-13 show images of observed materials with different magnifications. For IOF-B and IOF-A, both top and lateral views were observed. The following observations were made: (1) The surface of IOF-B from the top view is smoother than that of IOF-A (Fig. 3-11a and Fig. 3-12a); (2) Crystals of different shape for two types of iron ore fines from the top view

are shown in the red triangles marked in Fig. 3-11b and Fig. 3-12b; (3) Pores can be seen in the lateral view of both iron ore fines (Fig. 3-11c and Fig. 3-12c); (4) The surface of Chiba gravel is very smooth and no pore was observed (Fig. 3-13 a, b). Though it is not known whether pores in both types of iron fines are connected to each other via a network or not, the existence of pores should affect some of their physical properties e.g. G_s, water retention ability, etc.

3.6.2 Fines content of IOF-B, IOF-A and DL clay

Fig. 3-14 shows the observation of fines content of two types of iron ore fines and DL clay. While it is difficult to distinguish any micro pores in these three materials, it can be seen that the fines content of IOF-B seems larger than the other two materials and the shape of IOF-B is rather spherical.

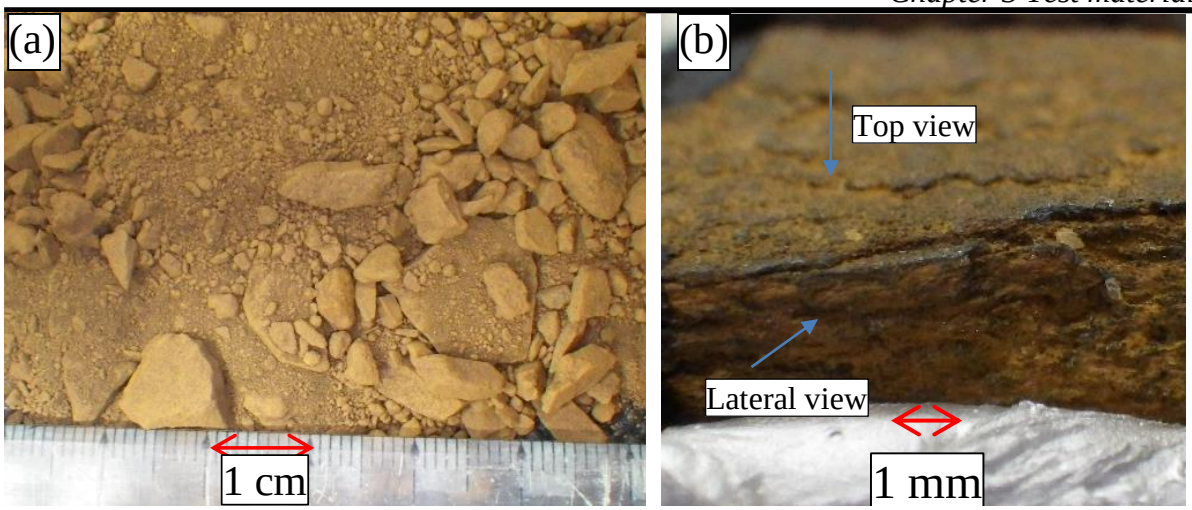

Fig. 3-1 (a) Overview and (b) typical particle of IOF-B

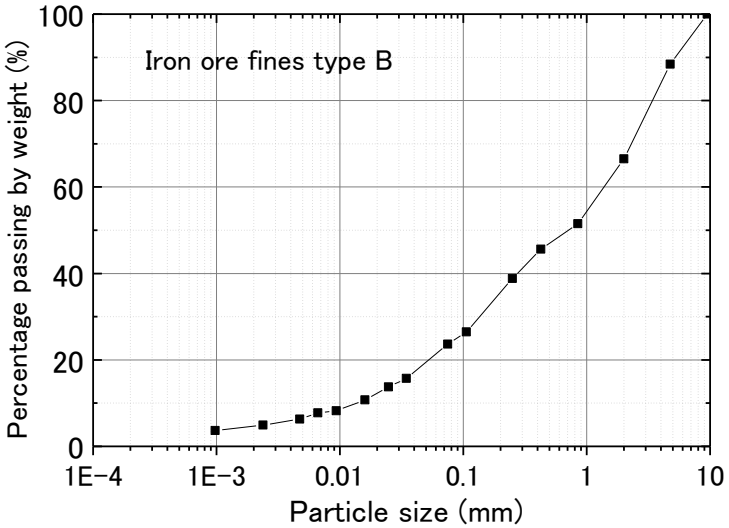

Fig. 3-2 Gradation of IOF-B

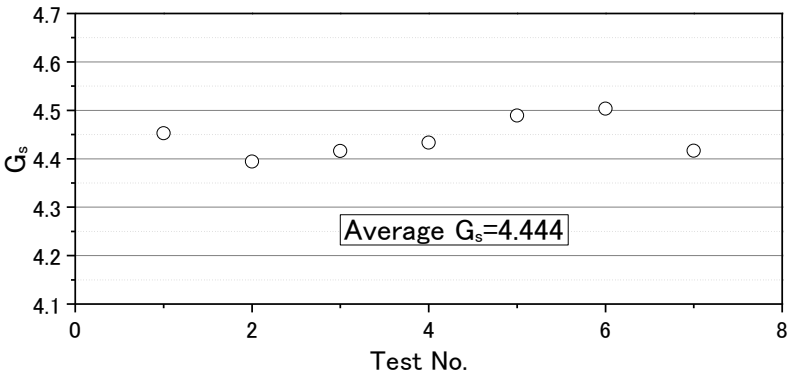

Fig. 3-3 Specific gravity (G_s) of IOF-B

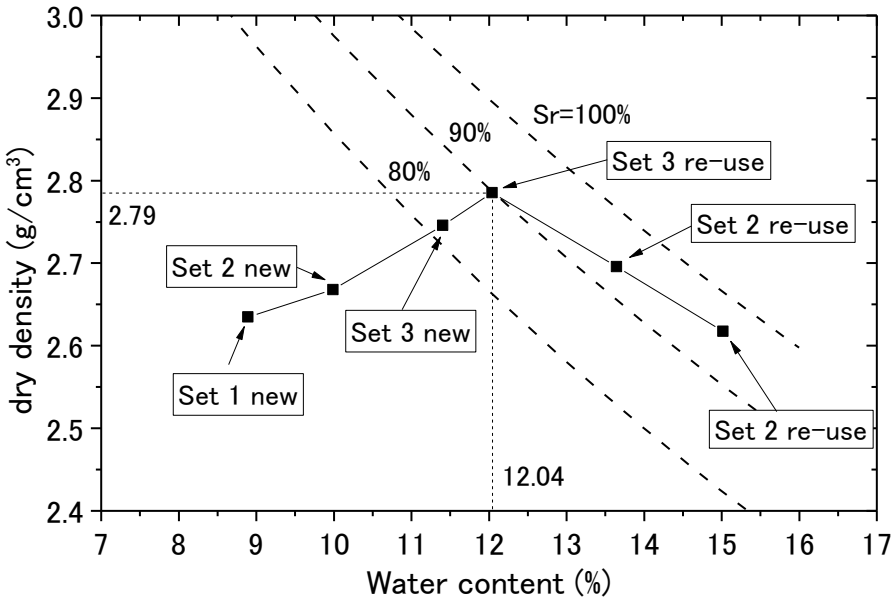

Fig. 3-4 Compaction test of IOF

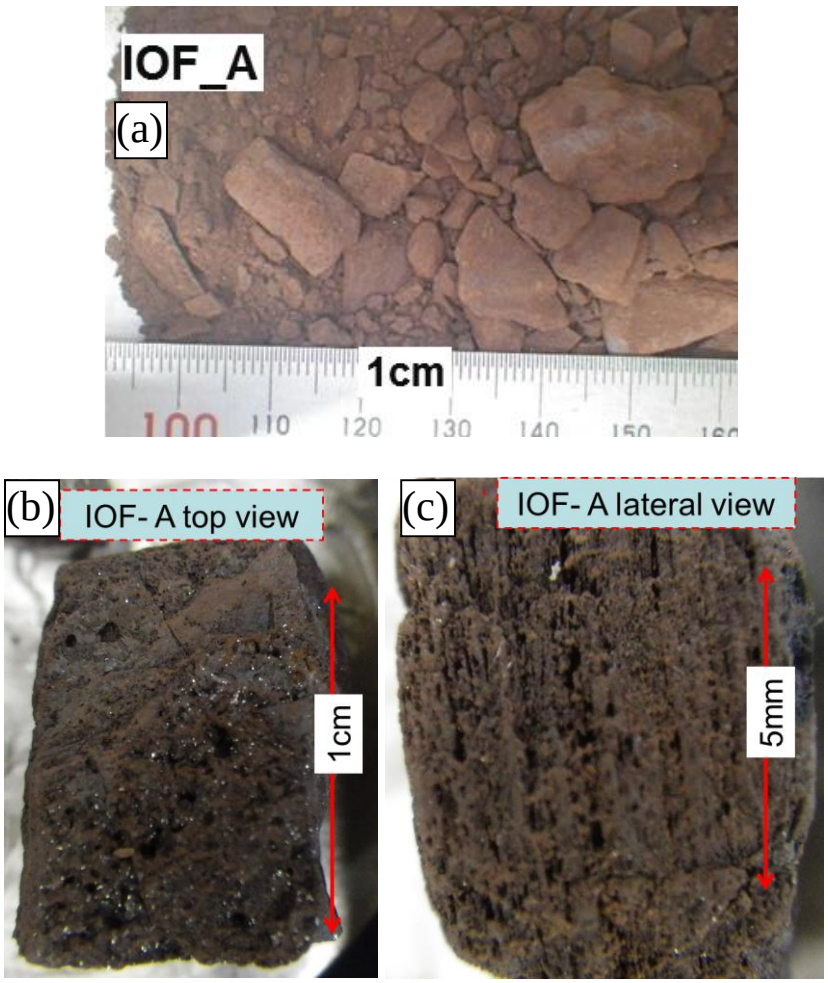

Fig. 3-5 (a) Overview, (b) top view and (c) lateral view of IOF-A

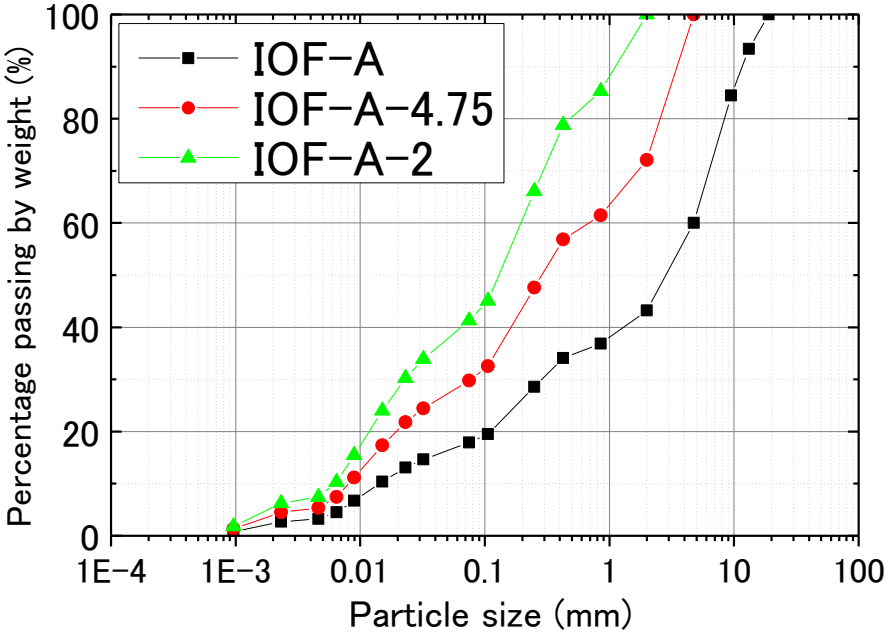

Fig. 3-6 Gradation of iron ore fines type A

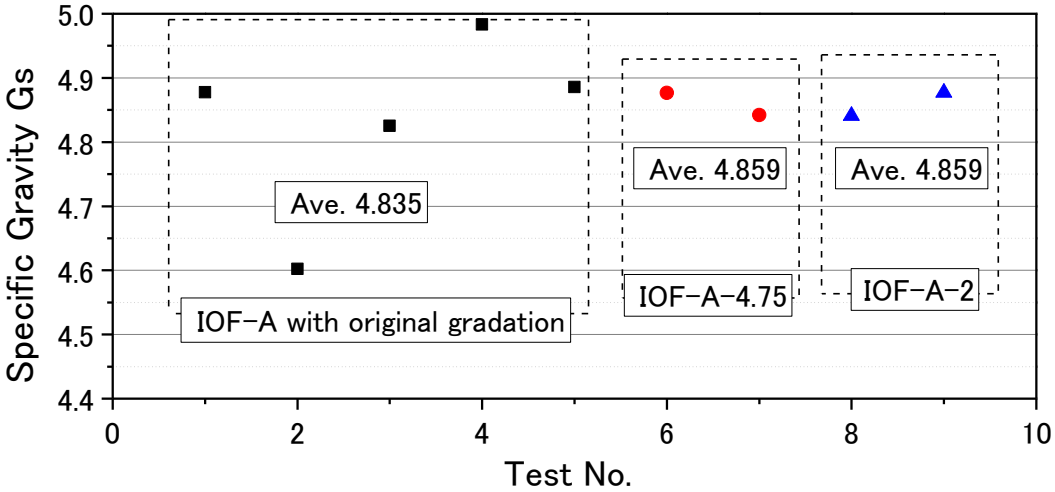

Fig. 3-7 Specific gravity of iron ore fines type A

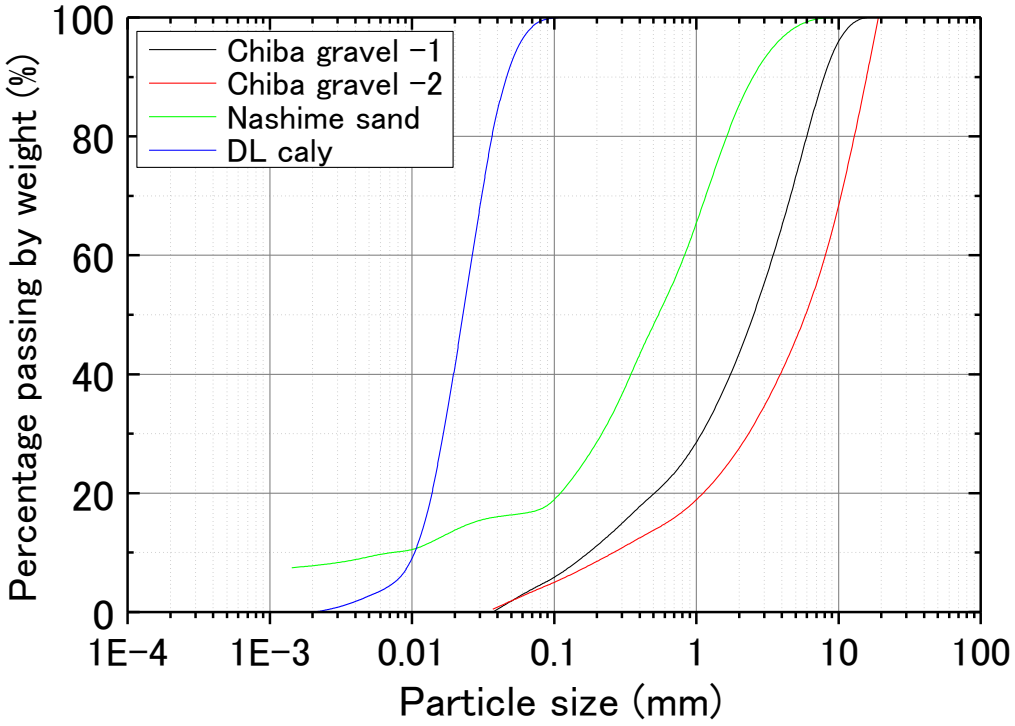

Fig. 3-8 Gradation of common materials

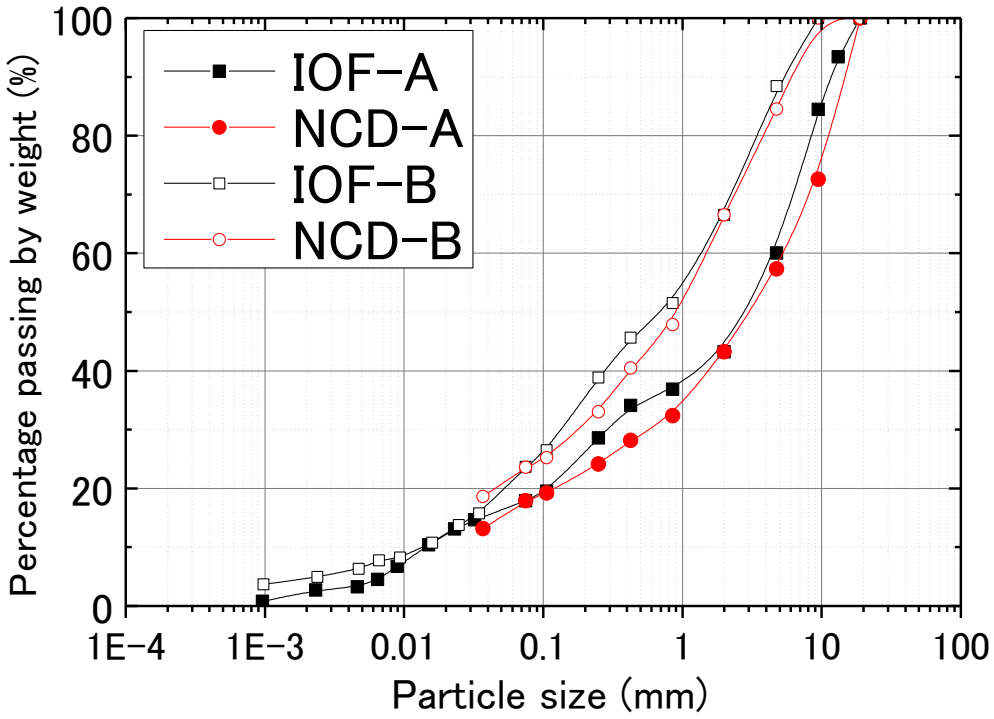

Fig. 3-9 Gradation of material mixtures and iron ore fines

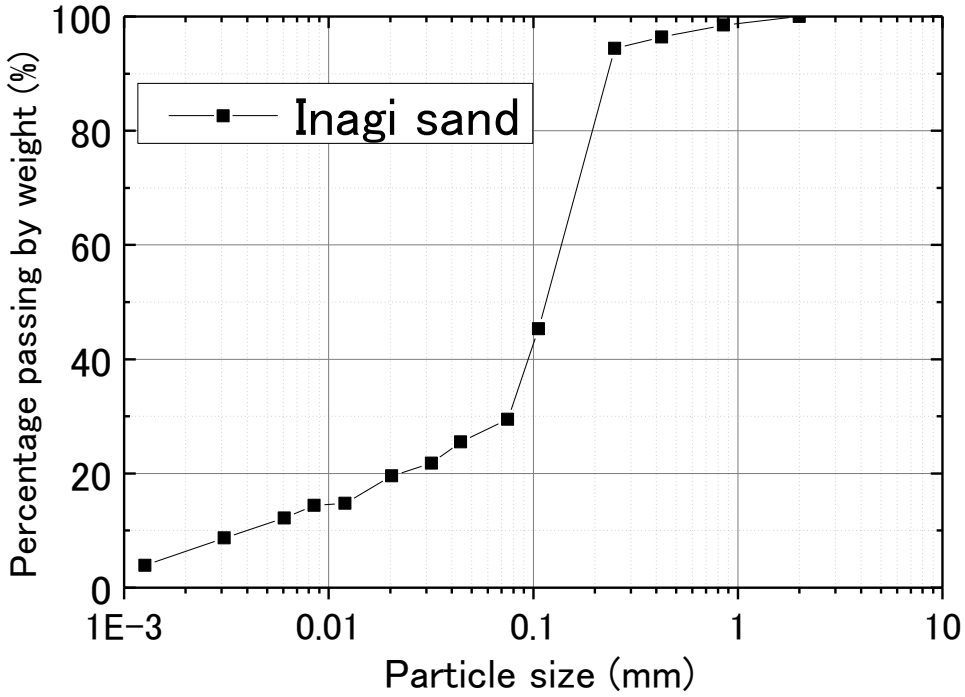

Fig. 3-10 Gradation of Inagi sand

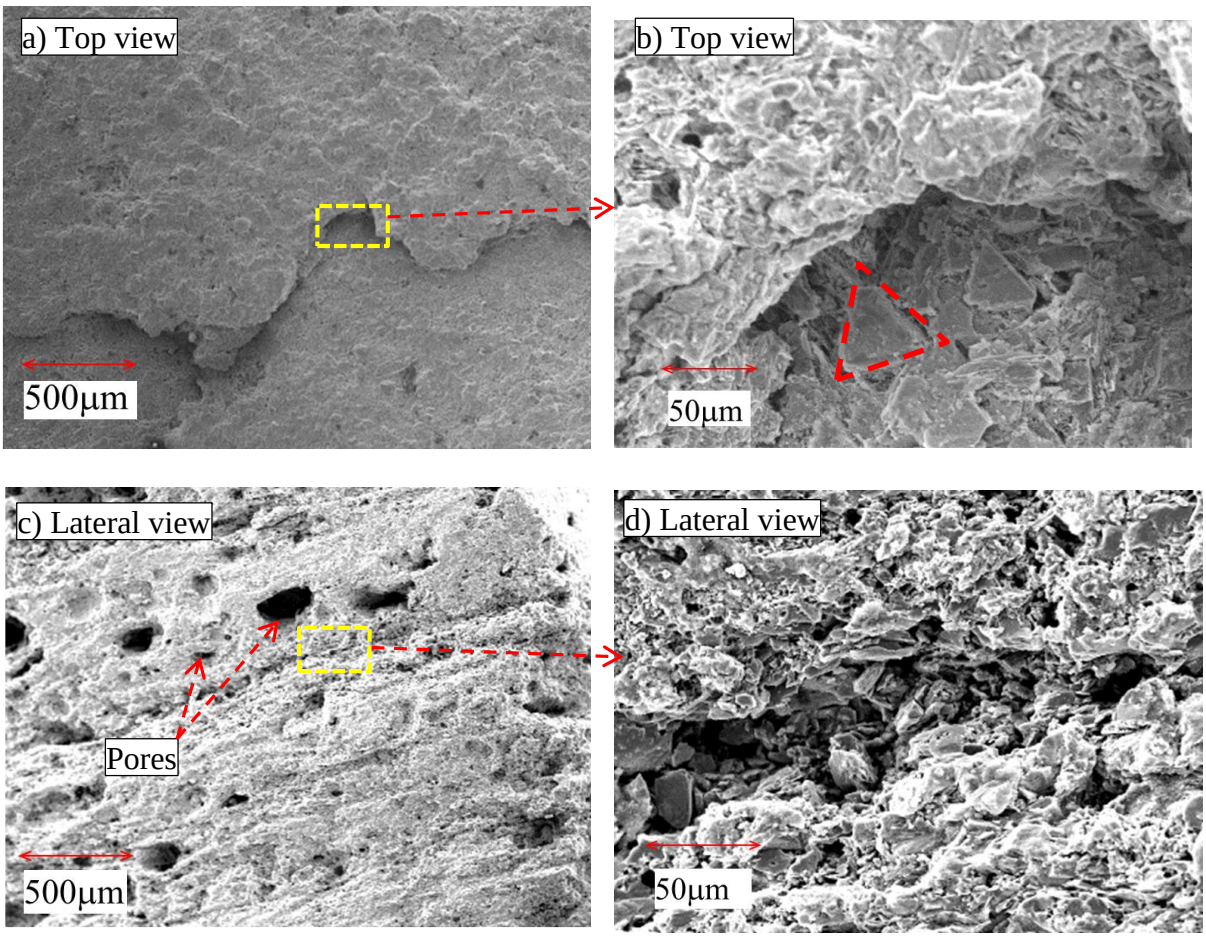

Fig. 3-11 SEM images of large particles of IOF-B

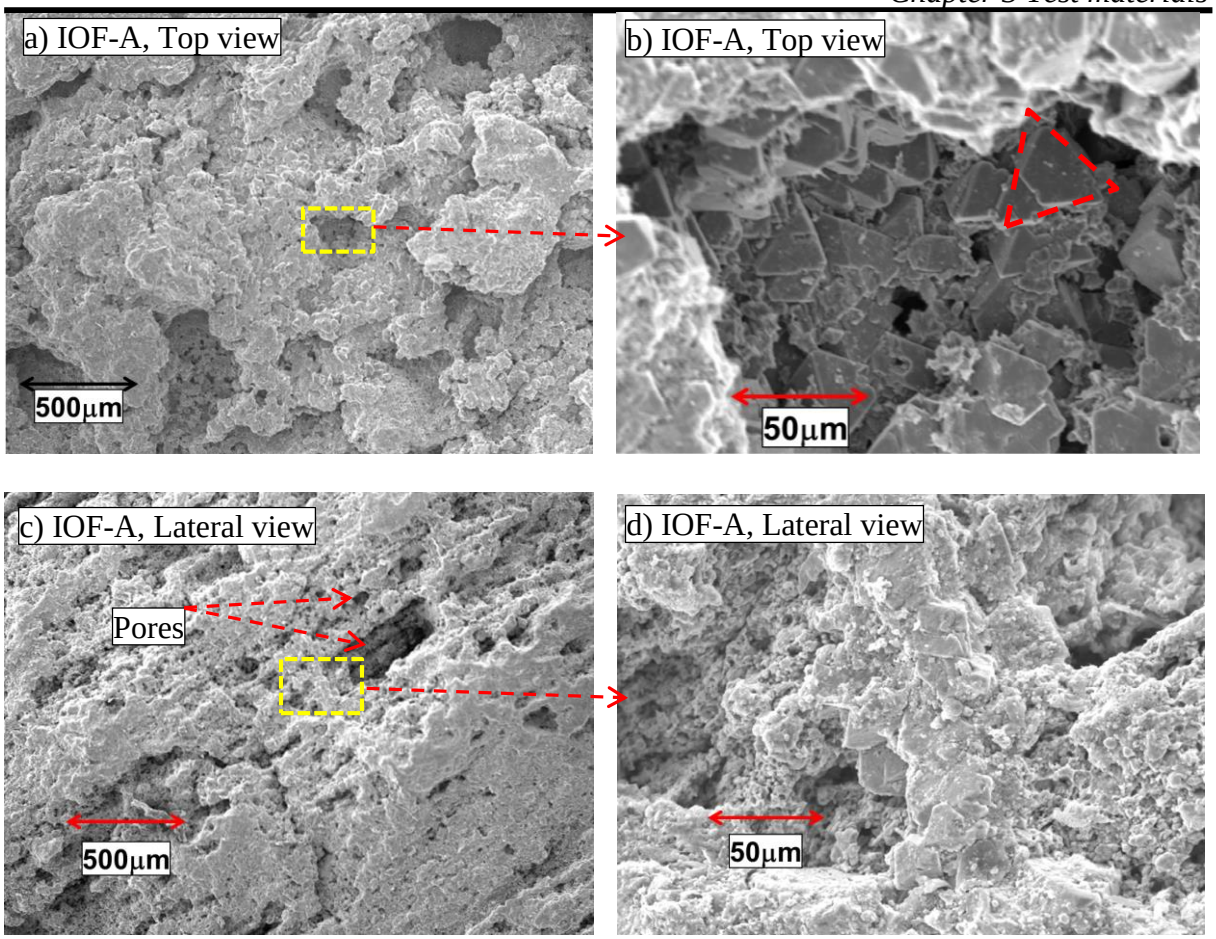

Fig. 3-12 SEM images of large particles of IOF-A

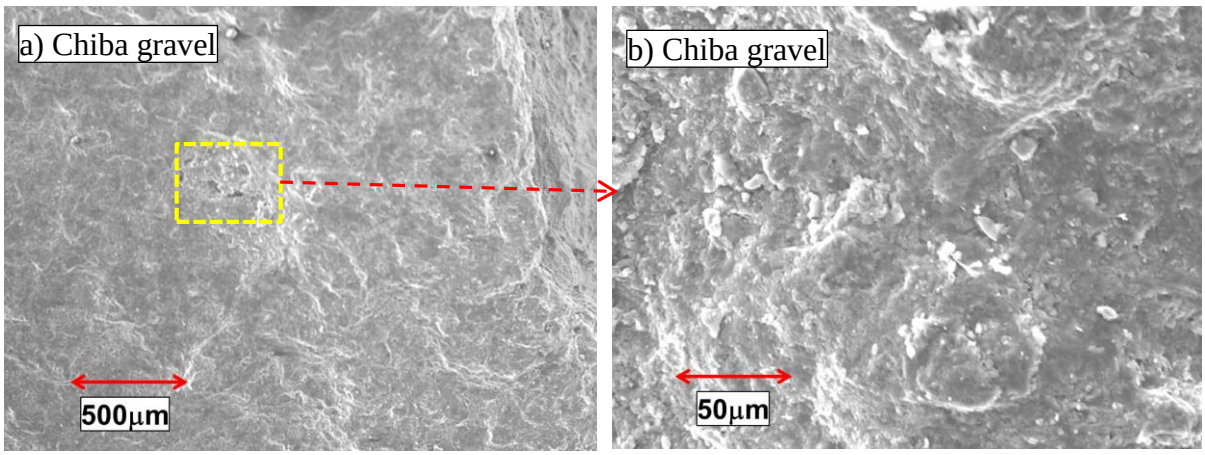

Fig. 3-13 SEM images of Chiba gravel

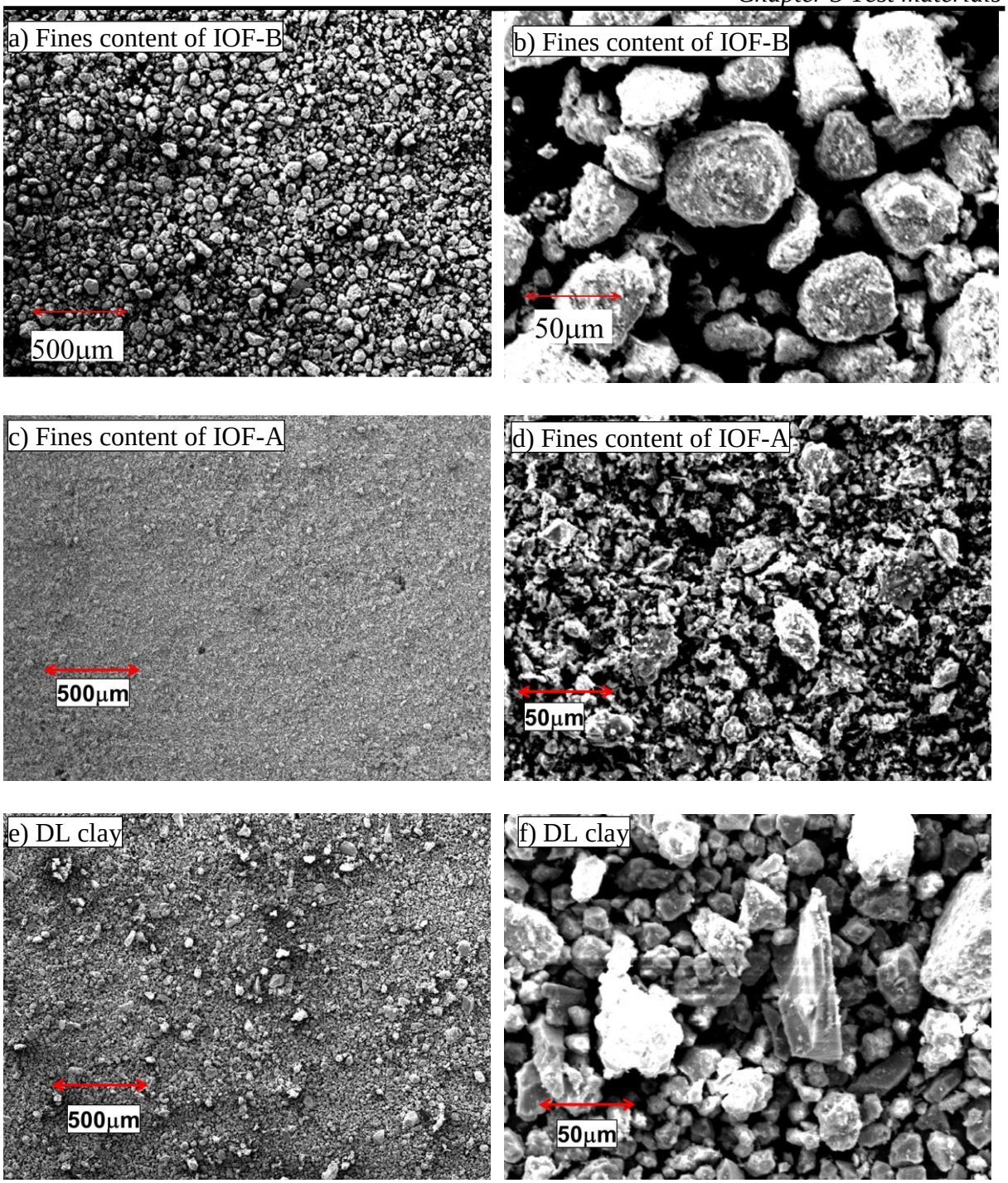

Fig. 3-14 SEM images for fines content of IOF-B, IOF-A and DL clay

Chapter 4. SWCC test and permeability test

Contents

4.1 Introduction

Iron ore fines when being loaded into a vessel usually contains a certain amount of water. The water content distribution in a heap of iron ore fines would be relatively uniform at the moment of loading. If we take an unsaturated element of iron ore fines from the heap as schematically shown in Fig. 4-1 (a), because of gravity force (W), pore water in the element would naturally flow to a position lower than its current position. On the other hand, the tension force (T), caused by the meniscus effect existed at contact points between particles and/or in the micro-porous structure of individual particles, would retain a certain amount of water within the iron ore fines. The combined effect of W and T as well as some other forces such as van der Waals force produced by attraction forces between water and soil molecules, osmotic force because of soluble salt in soil water and force induced by vapor pressure etc. determine the final water content or equilibrium water content in the element (Tindall et al., 1999). In the saturated element, all of the above-mentioned forces are either not related to effective stress (e.g. gravity force of water) or vanished (e.g. tension force); while for the unsaturated element the situation becomes much more complicated. The classical principle of effective stress, which governs the strength and deformation properties of the saturated element, is challenged in the unsaturated field. In the unsaturated soil element, which may be regarded as a four-phase structure, the combined effect of the gas phase (e.g. pore air), the liquid phase (e.g. pore water), the solid phase (e.g. soil particles) and contractile skin results in a pressure difference between pore air and pore water. This pressure difference is usually termed as suction. To find the fundamental variables governing the strength and deformation properties of the unsaturated soils, some efforts are taken to find the parameters depending on the saturation condition to correlate the term of suction such as Bishop (1959), while some focused on the establishment of a more general configuration to consider suction as an independent term such as Fredlund and Morgenstern (1977). No matter which variables should be used, suction has become one of the most important components in the unsaturated field.

Suction or matric suction is often defined as the subtraction of pore water pressure (PWP) from pore air pressure (PAP) i.e. PAP-PWP, and SWCC describes the relationship between suction and the equilibrium water content. One of the usages of SWCC in this study is to evaluate the water distribution in the heap of iron ore fines since if the suction distribution is properly estimated it becomes possible to analyze the equilibrium water content distribution in the heap. Fig. 4-1 (b) schematically shows a typical SWCC. A SWCC usually includes two curves: a drying curve, which shows that soil water content reduces as suction increases, and a wetting

curve, which shows that water content increases as suction decreases. There is hysteresis between drying and wetting curves induced by reasons such as the non-uniform pore size distribution in the voids, and a difference in the contact angle at the advancing interface during the drying process and wetting process etc. (Fredlund and Rahardjo, 1993). For a single drying curve or wetting curve, an opposite "S" shape of SWCC is rather typical, while the shape may change depending on the density of the soil element, soil type, particle structure etc. (Standing, 2011). Burger and Shackelford (2001) mentioned a double "S" shape SWCC observed from their experimental work on soils with micro-pores in individual particles. The double "S" shape SWCC is caused by the difference of air entry values (AEV) between interpellet porosity formed by the network of pores in the soil element and intrapellet porosity, which is micro pore within the individual particles.

It is possible to estimate the final water distribution in the heap of the iron ore fines by utilizing the SWCC, while time-dependent water distribution also needs to be evaluated to find the critical water distribution in the heap of iron ore fines. Thus, the permeability property of iron ore fines under both saturated and unsaturated condition is another aspect to reveal the critical condition for the heap. In ASTM Special Technical Publication N0. 163, principle of permeability test (Burmister, 1954), permeability tests on sand-gravel mixtures, granular materials, sands and fine-grained soils (Yemington, 1954; Chu et al., 1954; Lambe, 1954; Jones, 1954) were addressed and discussed. For the traditional test of permeability, a rigid model is usually used to confine the specimen to be tested, while one of the drawbacks of using the rigid mold is the interface effect between the soil specimen and the mold, where permeability may be significantly different from that of the tested specimen. Attempts were made to use the flexible confining wall, such as rubber membrane on triaxial system (Olsen et al., 1985; Carpenter et al., 1986; Aiban and Znidarcic, 1989; Uno et al., 1990 and Hatanaka et al., 1997). Another advantage of using the triaxial system is that the stress state of the specimen can be adjusted freely.

When dealing with the permeability of unsaturated soils, the primary consideration would be the distinction between flow of the gas phase (pore air) and flow of the liquid phase (pore water). To measure solely the permeability of pore water, filters preventing air drainage have to be installed. Klute (1972), Dirksen (1991) and Masrouri et al. (2008) summarized permeability testing techniques for unsaturated soils. Masrouri et al. (2008) concluded that constant head steady state flow would be the most accurate way to reveal the permeability of unsaturated soils, though it is relatively expensive. To determine the permeability of

unsaturated soil in a more efficient manner, many studies focus on unsteady-state methods, such as the outflow-inflow method, the instantaneous profile and the thermal method (Bruce and Klute, 1956; Jackson, 1964; Vachaud, 1967; Whisler et al., 1968; Selim et al., 1970; Arya et al., 1975; Clothier and Scotter, 1982; Smettem and Kirkby, 1990; Toorman et al., 1992; Simunek and Nimmo, 2005).

A series of tests to obtain the SWCC and coefficient of permeability were conducted in this study. For the SWCC test, suction ranged from 0.1 kPa to 10^6 kPa were applied by introducing different techniques. In the low suction range (0.1-100 kPa), the effect of density and testing techniques (membrane filter technique (Nishimura, 2012) and ceramic disk technique) on SWCC of iron ore fines type B (IOF-B) are discussed. In the high suction range (10^3-10^6 kPa), the vapor equilibrium technique was applied and the combined effect of void ratio and gradation on SWCC of iron ore fines type A (IOF-A) was studied. Water retention ability of two types of iron ore fines were compared with common materials in the full range of suction.

For the permeability tests, the main purpose was to measure the coefficient of permeability of IOF-B under both saturated and unsaturated conditions. As a reference, the permeability of Toyoura sand was also measured. The specimens were confined by the flexible membrane in the triaxial system to reduce the interface effect. A constant water head was applied to the testing system. Since the water head applied on the specimens was unable to be measured directly using current measurement system, the head loss consumed in the water flow path was calibrated. Another problem associated with the permeability test is filter clogging. Fines content in the specimens and dust in water may accumulate in the filters used in the tests, which causes a reduction in water flow speed. In addition, the hydraulic gradient in the specimens also needs to be considered since it affects the flow type in the specimen and Darcy laminar flow is required to apply Darcy's law. The effects of system head loss, filter clogging as well as hydraulic gradient on the permeability of tested materials are discussed in this chapter.

4.2 SWCC test in low suction range

The SWCC test of IOF-B conducted in the low suction range (0.1-100 kPa) is studied in this section. In the following three sub-sections, the test procedures, the effect of density and testing techniques are addressed, respectively. Fig.4-2 shows the gradation of IOF-B. This material contained 33.5% gravel and 24% fines content, is classified as SFG material according to the test standard of the Japanese Geotechnical Society (JGS 0051-2000). More details about this material are presented in Chapter 3. To study the effect of density, four specimens with

different densities were tested by using a pressure plate apparatus where the membrane filter technique (Nishimura et al. 2012) was introduced. For the testing technique, three SWCC tests of specimens with similar densities were conducted on pressure plate apparatuses equipped with either the membrane filter or the ceramic disk. The membrane filter is a thin and micro-porous filter paper made from a hydrophilic acrylic copolymer. The work principle is the same as the ceramic disk and more details about this technique is addressed in Appendix B.

4.2.1 Test apparatuses and specimen preparation

A traditional pressure plate apparatus, in which a ceramic disk with thickness of 4 mm was installed, was employed (ceramic disk apparatus, hereafter) to conduct the SWCC test in the suction range of 0.1-100 kPa. Another specially manufactured apparatus (membrane filter apparatus), in which the membrane filter technique was introduced instead of the ceramic disk, was also employed to apply suction up to 20 kPa. A commercial membrane filter, Supor 450 was used in this test (See Appendix B for further details). A burette and a differential pressure transducer were connected to the water compartment of each apparatus to monitor the volume of water drainage (a schematic illustration of used apparatuses are shown in Fig. 2-1 of Chapter 2). The method for applying suction with these two types of apparatus is different. For the ceramic disk apparatus, in the suction range of 0.1-2 kPa, suction was applied by the hanging column method, in which the tested specimen is placed at a higher position than the water surface elevation in the burette connected to the apparatus. By doing so, a negative pore water pressure was applied to the specimens. In the suction range of 2-100 kPa, the axis-translation technique was used, in which positive air pressure was applied to the air phase of the tested specimens. For the membrane filter apparatus, suction was applied by the hanging column method solely (the maximum elevation difference is about 2 m).

All the specimens tested in the low suction range were made by static compression. Attention was paid to guarantee good contact between the specimen and the pedestal of the apparatus. The specimens were saturated by soaking them in a vacuum water tank. The test conditions discussed in Sections 4.2.2 and 4.2.3 are listed in Table 4-1 and test conditions of some other tests are given in the section where they are discussed.

Table 4-1 Test conditions of specimens discussed in Section 4.2

Test name	Specimen size Radius/Height (cm)	Initial Sr (%)	Specific gravity G_s	Void ratio e	Dry density ρ_d (g/cm3)	Apparatus
SW_L_IOF-B_1_3	2.49/2.05	105.6	4.444	1.194	2.03	Ceramic disk
SW_L_IOF-B_1_5		108.5		1.260	1.97	
SW_L_IOF-B_2_2	2.51/2.57	100.0		1.214	2.01	Membrane Filter
SW_L_IOF-B_4_3		104.2		0.814	2.45	
SW_L_IOF-B_3_3		102.7		0.727	2.57	
SW_L_IOF-B_5_1		103.3		0.629	2.73	

Notes: In column "Initial Sr", most values exceed 100% because there was some water remained in top cap of apparatuses after saturation

4.2.2 Effect of density on SWCC at low level suction

Figs. 4-3 (a), (b) and (c) show the relationship between suction and volumetric water content (θ), degree of saturation (Sr) and gravimetric water content (ω), respectively. All four tests with different density conditions were conducted using the membrane filter apparatus. Figs. 4-3 (a) and (b) show that under the same suction, θ and Sr increases with a decrease in specimen void ratio for either drying or wetting curves, and the drying and wetting curves seem to be parallel with each other when suction exceeded 1.5 kPa. Fig 4-3 (c) shows that ω values on the drying or wetting curves converge together when the suction value exceeds 1.5 kPa regardless of specimen void ratio, which implies that the void ratio may not affect ω significantly when suction exceeds certain values. Similar results were also reported on clayey silty sand (Salager et al. 2013) and bentonite (Romero et al. 1999, Lloret et al. 2003). Regarding the clayey material, this phenomenon can be explained by the existence of a large portion of intraaggregate water, which exists inside the clay particle layer structures and actually becomes a part of the clay minerals. The amount of intraaggregate water in clay depends mostly on the clay particle itself and, thus, the void ratio has less effect on ω (Bradbury & Baeyens 2002, Jacinto et al. 2012). For granular materials, the amount of water retained by particle surface due to van der Waals force and by micro-pores in individual soil particles should not be significantly affected by a change in relatively low suction range. Thus, the amount of water in the specimens may still be controlled by void ratio. When the granular materials are densified, the volume of relatively large pores is easier to be compressed than that of relatively small pores. While the amount of water retained between particles is governed by relatively small pores, for specimens of IOF-B with different densities, it is possible that the volumes of relatively small pores in the specimens with different densities is similar. Thus, the relationship between suction and gravimetric water content ω was not significantly affected by void ratio.

4.2.3 Effect of testing technique on SWCC

Fig. 4-4 (a) shows the drainage time history of the first several steps of two tests conducted with ceramic disk apparatus and membrane filter apparatus, respectively. The blue line shows that water flowed out from the membrane filter apparatus very fast due to the much thinner membrane filter used (i.e. 0.14 mm for membrane filter compared to 4 mm for ceramic disk). For the membrane filter apparatus, it normally takes several hours for each step of suction to be stabilized. Under similar conditions, it is common to wait for several days for each step of the test conducted on the ceramic disk apparatus, as shown by the black line. More importantly, it was found that during the test conducted on the ceramic apparatus, sometimes it is very difficult to determine where the equilibrium of each suction step is. In Fig. 4-4 (a), with the ceramic disk apparatus (black line), we may empirically think that equilibrium was achieved in the second step. However, what would it be if we waited for a longer time? The drainage time history of test with ceramic disk apparatus was re-plotted in Fig. 4-4 (b) together with the result of another repeated test, as shown by the red line. For the two tests, the same apparatus and similar procedures were employed. For test SW_L_IOF-B_1_5 (red line), after more than one month of waiting for Step 3, it seemed that equilibrium of drainage was achieved. By comparing the time histories of the two tests, it is difficult to say that the waiting time was sufficient for some steps of the test SW_L_IOF-B_1_3 (black line). For drainage histories obtained from tests using the membrane filter apparatus, such phenomenon was not observed.

Fig. 4-5 compares the SWCCs of the three tests discussed in Fig. 4-4. It shows that for the drying curves, the gravimetric water content during the second test with the ceramic disk apparatus (red line) is higher than that of the test using the membrane filter apparatus (blue line) when suction is less than 1.5 kPa. These two curves converged when suction exceeds 1.5 kPa. If considering the effect of void ratio, as discussed in Fig. 4-3 (c), the SWCCs measured by membrane filter technique and ceramic disk technique are consistent. For the two wetting curves, though suction values at initial points are different, it seems they approached each other when suction reduces to 3 kPa. On the other hand, the drying curve for the first test with ceramic disk apparatus (black line) shown in Figure 4-5 joins the other two curves when suction exceeds 6 kPa approximately, which implies that the waiting time for equilibrium at each step before 6 kPa may be not sufficient.

Through discussion on time histories of water drainage and SWCC results obtained by employing membrane filter technique and ceramic disk technique, it can be concluded that the membrane filter technique is efficient and reliable to measure SWCC.

4.3 SWCC test in high suction range

Results of the SWCC test in the very high suction range (e.g. 10^3kPa-10^6kPa) are described in this section. A description of the equipment built specifically for this test in Koseki Lab, IIS, The University of Tokyo is given in Chapter 2. There are two purposes in this test program, 1. Examination of effects of density and gradation effect on SWCC in high suction range (Section 4.3.4); 2. Comparison of water retention ability of iron ore fines with that of the common materials (Section 4.4).

4.3.1 Suction determination

The vapor equilibrium technique, which uses the saturated chemical solution to control relative humidity (RH), is a common way to apply very high total suction (e.g. 10^3-10^6 kPa) (Fredlund & Rahadjo, 1993; Nishimura & Fredlund, 2000; Marcial et al., 2002; Tang & Cui, 2005 and Salager et al. 2013). The working principle is addressed in Section 2.1.2 of Chapter 2. Total suction can be calculated as a function of RH (Fredlund and Rahardjo, 1993):

$$\text{suction}_{\text{total}}(\text{kPa}) = -0.46 \times \text{T} \times \rho_{\text{w}} \times \ln\frac{RH}{100} \qquad \text{(Eq. 4-1)}$$

where, T is the absolute temperature (T=273.16+t°, t° is the room temperature, 15.6°C in this study); ρ_w is the density of water (i.e. 999 kg/m3 at t°=15.6°C); and RH is the relative humidity (%).

The suction applied by using the vapor equilibrium method is total suction (=matric suction + osmotic suction), while matric suction is what we desired in SWCC, thus osmotic suction (explained in Section 2.1.2 of Chapter 2) has to be subtracted from total suction. Electric conductivity (κ) of the suspended soils were measured for the tested materials according to JGS0212-2000 and osmotic suction were estimated by Eq. 4-2, which is recommended by JGS 0151-2000.

$$Suc_O\,(\text{kPa}) = 0.36 \times \kappa \qquad \text{(Eq. 4-2)}$$

where, κ is the electric conductivity of suspended soils (mS/m). The κ values of six types of soils, SW_H_IOF-A, SW_H_IOF-A_4.75, SW_H_IOF-A_2, SW_H_NCD-A, SW_H_IOF-B and SW_H_NCD-B, which were tested in SWCC test high suction range and are introduced in

the following sections, are 0 mS/m, 0 mS/m, 0 mS/m, 0.24 mS/m, 0.09 mS/m and 0.44 mS/m, respectively. Since the κ values are very small, the osmotic suction are not considered in this study.

Seven saturated chemical solutions (i.e. K_2SO_4, KNO_3, $NH_4H_2PO_4$, NaCl, $Mg(NO_3)_2 \cdot 6H_2O$, $MgCl_2 \cdot 6H_2O$, LiCl) recommended by JGS0151-2000 were chosen to control RH. The solutions were stored in leak-proof chambers, as shown in Fig. 2-1a in Chapter 2. Room temperature was controlled at 15.6±0.5°C. The RH values controlled by the chemical solutions are functions of temperature. In Section 2.1.2 of Chapter 2, the process for determining the RH values for the used chemical solutions at the temperature of 15.6°C is given. The determined RH values and their corresponding suction values are given in Table 4-2.

Table 4-2 RH summary and suction calculation

Chemical solution	K_2SO_4	KNO_3	$NH_4H_2PO_4$	NaCl	$Mg(NO_3)_2 \cdot 6H_2O$	$MgCl_2 \cdot 6H_2O$	LiCl
Controlled RH (%)	97.6	94.2	93.2	75.5	54.2	32.9	11.0
Suction ($\times 10^3$ kPa)	3.2	8.0	9.4	37.4	81.5	148.0	293.8

4.3.2 Specimen preparation and test procedure

For each specimen, dry material and water (equivalent of gravimetric water content of 10%) was mixed directly in the specimen container (petri dish with inner diameter of 59 mm). Then, very small energy was applied by raising the petri dish by 10 mm from ground and allowing it to free fall 10 times. The applied energy was calculated as the summation of elevation potential energy without considering energy loss during free fall. Since the specimen made by the above mentioned process is of an uneven surface, it is difficult to determine the density of the specimen directly. Thus, the density of the specimens was estimated separately by making a specimen in the same fashion using a constant volume mold.

Both drying and wetting curves of SWCCs of the test materials were measured. For each point on the SWCCs, three identical specimens were prepared. For the drying process, specimens were stored in the RH-controlled chambers and the mass of the specimens were measured every specific time interval (e.g. 2 weeks or so) by a balance with resolution of 1 mg. The equilibrium of the specimens was thought to be achieved when the mass of the specimens didn't or only slightly changed in at least two successive measurement time intervals. For the wetting process, specimens were first stored in the chamber with the lowest RH (i.e. 11.0%). After equilibrium

of the specimens was achieved, they were delivered to chambers with higher RH values to start the wetting process.

4.3.3 Typical time history of test

Time histories for all tested soils specimens are presented in Appendix D. Several typical time histories of specimens of IOF-A are reproduced in Fig 4-6 to illustrate features of this test:

1. Equilibrium duration of the specimens in the chambers with relatively high RH values (e.g. RH=97.6%, 94.2% and 93.2%) is usually longer than those with relatively low RH (RH=75.5%, 54.2%, 32.9% and 11.0%). It seems that the lower the RH of the testing chambers, the faster equilibrium of the specimens in the chambers is achieved. For instance, it took more than 6 months for the specimens with RH of 97.6% to reach equilibrium and 1 month for those with RH of 11.0% for drying process (Figs. 4-6 a and b).
2. The water content time histories for identical specimens are not necessary close to each other before achievement of equilibrium e.g. Fig. 4-6 (a). It is found that the distance to the chemical solution controlling RH in the testing chamber affects the rate of water diffusion.
3. Slight change in the circumstance of the chamber may affect the equilibrium of the specimens. For instance, as shown in Fig. 4-6 (c), when new specimens were stored in the chamber, equilibrium of old specimens were disturbed.
4. Slight fluctuation in water content was observed especially for the specimens in the wetting process as shown for example in Fig. 4-6(d).

4.3.4 Effects of gradation and density on SWCC in high suction range

The combined effect of gradation and density is studied on SWCCs of IOF-A with original gradation (IOF-A), that passing 4.75mm sieve (IOF-A-4.75) and that passing 2mm (IOF-A-2). Table 4-3 lists test conditions and Fig. 4-7 shows the gradation curves of tested materials (details about these materials are given in Chapter 3). Fig 4-8 shows the relationship between suction and water content. The drying curves or wetting curves are very close to each other though their gradation and void ratio are very different. From the results of IOF-B shown in Fig. 4-3, it is expected that void ratio may also not affect SWCC of IOF-A significantly. While in the high suction range, the water retained by van der Waals forces and by micro pores in individual soil particles may prevail. The van der Waals force relates to the surface area of the materials (or fines content) and micro pores were observed in relatively large particles as shown

by SEM images in Chapter 3, thus the combined effect of these two items may result in the closeness of SWCC curves for IOF-A.

Table 4-3 Test conditions of specimens of IOF-A

Test name	Specific gravity G_s	Void ratio e	Dry density ρ_d (g/cm3)	Compaction energy (kJ/m^3)
SW_H_IOF-A	4.835	0.592	3.03	3.27
SW_H_IOF-A-4.75	4.859	0.817	2.67	2.88
SW_H_IOF-A-2	4.859	1.138	2.27	2.45

Denotation of test name, SW_H_XXX_D/W_XX: SW_H_: stands for SWCC test in high suction level by vapor equilibrium technique; XXX_: stands for material tested; IOF-A_: iron ore fines type A with original gradation; IOF-A-4.75_: iron ore fines type A passing 4.75 mm sieve; IOF-A-2_: iron ore fines type A passing 2 mm sieve;

4.4 Comparison of SWCCs of iron ore fines and common materials

In this section, the water retention ability of iron ore fines was compared with those of common materials in both the low and high suction ranges. Two types of soil mixtures NCD-A (reference materials for IOF-A) and NCD-B (reference materials for IOF-B) are of the similar gradation with IOF-A and IOF-B, respectively. They were composed of mixtures of three common materials: Nashime sand, Chiba gravel and DL clay (properties of these three materials are addressed in Chapter 3). The mixtures are regarded as representatives of common geo-materials encountered in this study. The gradation of iron ore fines and their reference materials is shown in Fig. 4-9.

Table 4-4 Test condition summary for iron ore fines and their reference materials

	Test name	Specimen Radius/Height (cm)	Initial water content ω (%)	Specific gravity G_s	Void ratio e	Dry density ρ_d (g/cm3)
Low suction	SW_L_IOF-B_1_5	2.49/2.05	30.76	4.444	1.260	1.97
	SW_L_NCD-B	2.49/2.50	31.98	2.678	0.821	1.47
	SW_L_IOF-A	2.50/6.01	9.98	4.835	0.636	2.96
	SW_L_NCD-A	2.50/6.01	11.86	2.694	0.356	1.99
High suction	Test name	Compaction energy (kJ/m^3)	Initial water content ω (%)	Specific gravity G_s	Void ratio e	Dry density ρ_d (g/cm3)
	SW_H_IOF-B	2.16	10	4.444	1.221	2.00
	SW_H_NCD-B	2.19	10	2.678	0.841	1.45
	SW_H_IOF-A	3.27	10	4.835	0.592	3.03
	SW_H_NCD-A	3.26	10	2.694	0.336	2.01

Denotation of test name SW_L/H_XXX:SW_: stands for SWCC test; L_: stands for test in low suction level (0.1 kPa-100 kPa); H_: stands for test in high suction level (10^4 kPa-10^6 kPa); XXX_: stands for material tested.

The SWCCs in the low suction range presented in this section were measured by ceramic disk apparatus. Test procedures in the low and high suction ranges were the same (see Sections 4.2 and 4.3 for details, respectively). In addition, since the G_s values of two types of iron ore fines are much larger than those of common materials, volumetric water content is used to show the water retention ability of materials. Table 4-4 summarizes the test conditions of the specimens discussed in this section.

Figs. 4-10 (a) and (b) show SWCCs for iron ore fine type B and type A respectively, together with their reference materials. The SWCCs in the high suction range are also plotted in the inserted figures. The column of void ratio in Table 4-4 shows that specimens of iron ore fines have a higher void ratio (looser condition) than their reference materials. Based on the results shown in Fig. 4-3(a), it can be expected that iron ore fines with higher void ratio may have lower volumetric water content for the same material under the same suction value. The results in Fig. 4-10 show that: (1) In the low suction range, both iron ore fines have higher water retention ability than their reference materials; (2) In the high suction range, IOF-B still retains the higher water retention ability except for some points on its wetting curve, while SWCC of IOF-A falls below that of its reference material; however, the difference in water contents under the same suction is very small. Generally speaking, iron ore fines may have a higher water retention ability in the low suction range and similar water retention ability in the high suction range compared to materials commonly encountered in geotechnical engineering.

4.5 Permeability test on saturated materials

The permeability of saturated IOF-B and Toyoura sand was measured in a triaxial apparatus. Many trial tests and modification had been done on the test apparatus in order to obtain good results. The final version of test apparatus is introduced in Section 4.5.1, on which the permeability of saturated IOF-B was measured. For the system on which permeability of saturated Toyoura sand was measured, it is slightly different concerning the length of water flow paths, the position of water head measurement etc. The permeability test described in this section mainly focuses on the results of the specimen of IOF-B.

4.5.1 Test apparatus

The apparatus used for the permeability test undertaken on saturated specimens is shown in Fig.4-11. The main body of the apparatus is the same as the one used for undrained cyclic loading test as described in Chapter 2, with some new additions for permeability test, namely:

1. The water supply part (I). It consists of two water tanks and a water cell. If the valve V1 is kept open, water in tank 1 will flow into the water cell and the overflowed water will be collected by tank 2. On the other hand, water in the water cell will flow through the system, as shown by the arrows.
2. The water used for the permeability test was is first distilled from tap water, then filtered by a membrane filter (Supor 450, details about the membrane is addressed Appendix B), then de-aired before being injected into water tank 1 and finally filtered again by a coarse membrane filter (Versapor 1200, Pall Corp.) glued at the bottom of tank 1. The water processed in this way is to reduce the effect of filter clogging problem, which is discussed in Section 4.6.2, and the water is named as processed water hereafter.
3. The water receiver part (II). It bears two main functions in this system, keeping a constant water head and measuring the volume change during consolidation of the specimen. It consists of two water containing pipes, P1 and P2. a) In P1, another smaller pipe B1 is installed. The water initially from the water cell in water supply part (I) is collected by B1 first and stored in P1 by overflow from B1. In this way, the water head on the receiver side is also constant. b) The volume change of the saturated specimen during consolidation can be measured by a calibrated burette B2, which is installed in P2.
4. The total head applied to the system is measured by connecting a DPT to the water cell in the water supply part (I) at one side and to the inside of B1 at the other side. The tubes connected to the water cell and burette B1 are inserted into the containers to avoid disturbance from joints.
5. The accumulated volume of water flowed into P1 during seepage is measured by connecting another DPT to the bottom of P1 at one side and to a reference water level, for instance P2 at the other side. The volume change of the specimen during consolidation is also measured by the same DPT by turning the valve V2 to the side of calibrated burette B2.
6. The tubes with a diameter of 1.5mm are used inside the apparatus (length 0.6m in total approximately) and the tubes with diameter of 4.5mm are used outside the apparatus with length of 1.5m in total approximately.

4.5.2 System head loss calibration

As illustrated in Fig. 4-11, the applied water head is the total water head including the head consumed in the system drainage paths (system head loss) and in the specimen (real water

head). It is necessary to subtract the system head loss from the total head in order to calculate the permeability of the specimen because the real water head cannot be directly measured. An accurate estimation of the system head loss is significantly important for the specimens with relatively high permeability since system head loss may consume a large portion of the total water head.

To calibrate the system head loss, a clean acrylic pipe was substituted for the specimen between the top cap and pedestal. In addition, two filter papers were also fixed on the pedestal to take into account the head consumed by filter papers in the test (trial tests show that the number of filter papers used could affect the head loss significantly in current system). On both sides of the acrylic pipe, rubber rings were placed and vertical loading was applied to the pipe to prevent leakage from two ends of the pipe. Processed water was injected to saturate the pipe and water drainage paths. Head loss in the acrylic pipe was assumed to be zero.

The calibration test includes several steps. In one step, the water head was kept constant and a certain amount of water was allowed to flow through the system. Then the water head was changed to a different level in the next step. Fig. 4-12 (a) shows the relationship between accumulated volume of water drained in each step and the measured total head. In the legend of the figure, the “Step No.” indicates the order of each step performed. The water head was set at the lowest level in the first step and increased in the following steps. After Step 7, the water head of Step 8 was lowered to the level the same as Step 5 to examine the repeatability of the system. Step 9 was performed one night later than Step 8 with the same water head as that of Step 5 and 8 to check the time dependence of the system.

Fig. 4-12 (b) shows the relationship between accumulated volume of water in each test step and the calculated flow speed in every 0.5 ml (flow speed=0.5ml/time duration for water drainage of 0.5ml). It seems that the flow speed is rather stable at relatively low water head; while water head fluctuates severely when flow speed exceeds a certain value (e.g. 0.06 ml/s). It also shows that the flow speed slightly reduces with an increase in the accumulated volume of water. The results of Steps 5, 8 and 9 show that the flow speeds under the same water head are consistent between Steps 5 and 8, while it is lower for Step 9. This result implies that flow speed is repeatable when test duration is not very long (e.g. within 2 hours), while the flow speed may reduce when test duration is longer. The flow speed reduction and time-dependence may be induced by filter clogging, which is discussed in Section 4.6.2.

Fig. 4-12 (c) shows the relationship between system head loss and flow speed (the data of Steps 8 and 9 are not included). As also shown in Fig 4-12 (b), variation was observed when flow speed exceeds a certain value (e.g. 0.06 ml/s). It suggests that the flow speed of the permeability test should not be too large otherwise the evaluated system head loss may be with unacceptable error. A linear fitting line is drawn in Fig. 4-12 (c) based on the average value of flow speed in each step to estimate the system head loss. By using the fitting curve, the real water head (H_{real}) applied to a specimen can be calculated as:

$$H_{real}=H_{total}-H_{loss} \quad \text{(Eq. 4-2)}$$

where, H_{total} is the total water head measured directly from DPT; and H_{loss} is a function of flow speed in Fig. 4-12 (c).

4.5.3 Test conditions

The coefficients of permeability of saturated IOF-B and Toyoura sand were measured in the triaxial system. The IOF-B specimen, with dimensions shown in Fig. 4-11, was molded by one dimensional compaction in a constant volume mold. After saturation by double vacuuming method, it was consolidated under 50 kPa and 100 kPa, successively. After each stage of consolidation, permeability was measured under different water head (or hydraulic gradient H_{real}/L), respectively. The specimen of Toyoura sand with the same dimensions as those of the specimen of IOF-B was made by air pluviation and saturated by flushing with CO_2 and de-aired water, respectively. It was consolidated under 50 kPa and 100 kPa, successively. Similar to IOF-B, permeability of the specimen of Toyoura sand under different water heads was measured after each stage of consolidation.

4.5.4 Test results

Figs. 4-13 and 4-14 show changes of applied total water head, flow speed and calculated *k* value with the accumulated water volume under confining pressure of, respectively, 50kPa and 100kPa for the specimen of IOF-B. The legends in Figs. 4-13 and 4-14 show the confining pressure and step order. It can be seen that the applied water head was kept constant (Figs. 4-13a and 4-14a); while the flow speed reduces with the accumulated water volume regardless of applied water head and confining pressure (Figs. 4-13b and 4-14b). It is not very clear though that the flow speed seems to have a trend of entering into a steady state (black dash lines in Figs. 4-13b and 4-14b). As flow speed decreases, the calculated system head loss decreased and consequently the calculated real water head H_{real} applied to the specimen increased and the permeability reduced, as shown in Figs. 4-14 (c) and 4-15 (c). Though *k* values vary initially,

each set of data under the same confining pressure is or tends to converge to a unique value. Similar results for sand, sandy silt as well as silty clay are reported by Tavenas et al. (1983) and Olsen et al. (1985). Moreover, they show that soils with low permeability (e.g. clay) need a long time to achieve steady state and suggest that constant head should be applied to reasonably evaluate the permeability.

The duration needed for stabilization may be caused by:

1. Structure change of the specimen due to reconsolidation (the effective stress changes as applying a hydraulic gradient) (Pane et al., 1983 and Hatanaka et al. 1997).
2. Migration of soil particles during seepage (Pane et al., 1983 and Hatanaka et al. 1997).
3. Increase of system head loss due to filter paper clogging

The measured density of the specimen of IOF-B changed from 2.54 g/cm^3 (Dc=91.3%) at 50 kPa confining pressure to 2.55 g/cm^3 (Dc=91.7%) at 100 kPa confining pressure. Although the volume change during seepage was not taken into account, the density may not change significantly since the applied total water head was less than 5 kPa during seepage.

Even after consolidation, there would be some particles weakly contacted with others. They may easily be swept away by water flow during seepage. The particles flowing with water may be stopped by soil structure downstream or by filter paper, either of which would increase the resistance to the water flow and consequently induce the decrease in flow speed. After particles at weak points were swept to somewhere in the flow system, the flow speed may tend to stabilize, as shown by the black slash lines in Fig. 4-13 b. While if the water head was increased, for instance, from Step 50-1 to Step 50-2, some weak zones for the higher water head would be swept away further and flow speed reduce again in Step 50-2. The Steps 100-1~100-3 were performed after Step 50-5 under 100 kPa confining pressure, from which it can be seen that the reduction of flow speed became slower under the same water head (i.e., Step 50-2 vs 100-1; Step 50-3 vs 100-2 or Step 50-5 vs 100-3).

Filter clogging, which is described in detail in Section 4.6.2, is another possible reason for flow speed reduction. If fine particles in the water are blocked by the filter paper downstream or if fine particles enter the filter paper during consolidation, the permeability of the filter paper may reduce and consequently the flow speed reduces. Unfortunately, filter clogging should be regarded as a system defect, which is not considered in the calibration of system head loss described in Section 4.5.2.

Fig. 4-15 shows the relationship between the average value of *k* for each step and hydraulic gradient applied on the specimen. It can be seen that *k* reduces significantly as the hydraulic gradient increases with confining stress of 50kPa. The reduction would be much milder if the stabilized *k* values in each step are used. In addition, the reasons of flow speed and *k* value reduction explained above mainly focused on each individual step, the effect of hydraulic gradient has not been considered.

The red points in Fig. 4-15, which is the case with the confining pressure of 100 kPa, are a good example to explain the effect of hydraulic gradient since the effect of particle migration may not be very significant. It can be seen that *k* decreases as the hydraulic gradient increases. Under a high gradient, Darcy laminar flow, which is one of the requirements in applying Darcy's law, may change to turbulent flow. The turbulent flow usually consumes more energy (or head) because of non-uniform flow direction and consequently reduces the apparent value of *k* (Burmister 1954). Carpenter and Stephenson (1986) also observed the reduction of *k* with an increase in hydraulic gradient for clay. They suggested that the reduction may also relate to the length of the tested specimens.

Fig. 4-16 shows the relationship between calculated *k* values for Toyoura sand and accumulated flow volume under confining pressures of 60 kPa and 100 kPa. The *k* values seem consistent under the same confining pressure regardless of applied water head. Though the data fluctuates severely especially for the test with confining pressure of 60kPa, the fluctuation seems to reduce with the accumulated flow volume. The *k* values seem to approach 0.02 cm/s and 0.008 cm/s for confining pressure of 60 kPa and 100 kPa, respectively. This means that the permeability of the specimen of Toyoura sand decreased 2.5 times due to the increase in confining pressure from 60 kPa to 100 kPa. Hatanaka et al. (1997) also observed the decrease of *k* with an increase in confining pressure and suggested that this was due to the volume change in the tested specimens during seepage. However, the dry density of the specimen of Toyoura sand after consolidation at 60 kPa is 1.55g/cm^3 (Dr=78.1%) and Dr changed to 78.4% after consolidation under 100kPa. Though the volume change of the specimen during seepage was not measured, the volume change of the specimen may not be very high. One of the possible reasons for the reduction of *k* measured on the specimen of Toyoura sand may relate to the interface between the soil specimen and membrane. The membrane penetration may become more severe under the higher confining pressure.

Fig. 4-17 shows the average *k* values of each step for the specimen of Toyoura sand. It shows that the average *k* values of steps under the same confining pressure are generally consistent.

In addition, the average values may be overestimated because of fluctuation in data as shown in Fig. 4-16.

Fig 4-18 shows the system head loss calculated from the calibration curve in Fig. 4-12 (c) under different hydraulic gradient for the specimens of IOF-B and Toyoura sand. For the case of Toyoura sand under confining pressure of 60 kPa, the system head loss was higher than 80%. This may introduce certain calculation errors for the result of permeability. For most cases, the system head loss is in the range of 50% to 65%. This suggests that setup of the apparatus during head loss calibration and during the tests, such as the type and number of filter paper and porous stones in a test, the way of tube connection in the system, water quality etc. needs to be maintained the same carefully in order to obtain reliable results.

4.6 Permeability test for unsaturated materials

4.6.1 Test apparatus

Some modifications were made on the apparatus shown in Fig. 4-11 to conduct permeability tests for unsaturated soil, as shown in Fig. 4-19.

1. The structure of the water supply tank and receiver pipes were kept the same as those in Fig. 4-11, while the connection joints to DPT were moved to inside of the cell to reduce measured system head loss.
2. A new top cap with two paths for water and air drainage, respectively, was employed. A pore air pressure transducer (PAP transducer) was connected to the air drainage path to monitor the pore air pressure of the unsaturated specimens.
3. Membrane filter papers were fixed on both the top cap and the pedestal to avoid pore air drainage and to measure suction during the test (details of the membrane filter can be found in Appendix B).

4.6.2 Filter clogging

Similar as the case for the saturated specimen, the system head loss has to be measured in this system, while before showing the system head loss, the filter clogging problem is addressed first.

Filter clogging is that very small particles in soil or dust in water may invade the used filter papers in the saturated test or the membrane filters used in the unsaturated test. This problem may directly cause the reduction of permeability of the filter, namely it becomes more difficult

for water to pass though the filter and the system head loss increases as clogging problem becomes more severe. In Section 4.5.2, the filter clogging problem of filter paper is examined in the calibration test of system head loss. It shows that the flow speed is repeatable if the test duration is short, while the flow speed may reduce if the test duration is relatively long. In this section, clogging of the membrane filter is focused on.

Fig. 4-20 shows the configuration of a special test. The pedestal on which the membrane filter was installed is emerged by de-aired water and water in the water cell can flow into the burette at the left hand side through the pedestal. The head difference between the water cell and the burette is measured by the DPT1. The volume of water flowed through the pedestal is measured by DPT2. The water level in the burette is a constant head and that in the water cell is a falling head. Fig. 4-21 (a) shows the relationship between measured water head by DPT1 and measured flow speed by DPT2 for several steps of the test:

Step 1. A new membrane filter (No.1) was installed and the black points in Fig 4-21 (a) are the relationship between water head difference and flow speed for the first time flow (virgin flow). As water level in the water cell lowered, the measured water head decreased.

Step 2. After Step 1, extra water was added to the water cell to reach the original level and the second time flow for the membrane filter No. 1 was followed. Red points are the result in Fig. 4-21 (a). As compared with the results of Step 1 (black points), the flow speed reduced in the second flow under the same water head difference.

Step 3. Membrane filter (No.1) was removed and a new membrane filter (No.2) was installed immediately after Step 2. Extra water was then added to reach the original level and the green points show the data of virgin flow of membrane No.2. They overlap the results of virgin flow of membrane No.1.

Step 4. After Step 3, a certain amount of fines content of IOF-B was added to simulate the possible effect of fines content in permeability tests. The water level was kept the same as that after Step 3 (blue points are the results). The flow speed seems to be slightly slower than virgin flow of No. 1 membrane (black points), which implies that fines content may not significantly affect water flow speed. However, the effects of test duration and confining pressure were not considered in Step 4.

Test results imply that the water flow speed decreases as the amount of water flowing out increases. The test was repeated in a similar manner several times and it was confirmed that the flow speed does become slower as water flows through the system.

Test results in Fig. 4-21 (a) indicate that certain changes happened during water drainage, which was expected to be caused by clogging of the membrane filter. To verify this idea, another test was conducted with the same configuration and the same procedure as those used in the test mentioned above except the water quality. Distilled and de-aired water was used for test in Fig. 4-21 (a). This kind of water may still contain some fine particles, thus the water used for the verification test was processed water, as described in Item 2 of Section 4.5.1. The membrane filter used in the verification test was numbered as No.3. Results of virgin flow and second flow of the No.3 membrane were compared with that of membranes No.1 as shown in Fig. 4-21 (b). It shows that the flow speed increased by using the processed water (virgin flows of No.1 and No.3 membranes). The speed difference between first flow and second flow of No. 3 membrane is smaller compared with those measured for No.1 membrane filter. The last part of second flow of No.3 membrane filter in the red dash circle is the data after one night waiting while keeping the test setup the same as that of the earlier stage of the second flow of No.3 membrane filter. It shows a large drop in flow speed which may be caused by settlement of fine particles in water overnight. This test result implies that water quality and test duration are very important factors for the permeability test by using the membrane filter.

The filter clogging problem also exists for common filter papers, which were used in the saturated test as discussed in Section 4.5.4. Several photos of new and used membrane filter and filter paper (used in permeability tests of specimens of IOF-B) were taken by a digital microscope VHX-5000 (Keyence Corp.), as shown in Fig. 4-22. The pore size of the membrane filter is about 0.45μm, so it is difficult to observe clearly the pores on the membrane filter and the clogging inside the membrane filter becomes even more difficult to observe, as shown in Figs. 4-22(a) and (b). While it may generally be distinguished that the color of the used membrane filter is yellow in color (controlling parameters such as RGB, brightness etc. of two photos were adjusted to be the same values), which may be resultant of flushing of water containing IOF-B during permeability test. Though in the test to show filter clogging problem (Fig. 4-21a), adding fines content does not affect the water flow speed significantly (blue triangles), the effect of fines content may be intensified by the consolidation process. For filter paper in Photos 4-2 (c) and (d), they clearly show that fine particles are inside of texture of the filter paper, which may result in a reduction in flow speed, as discussed in Section 4.5.4.

4.6.3 System head loss calibration

Due to the filter clogging problem, the processed water as described in Section 4.5.1 was used for system head loss calibration as well as for the tests on unsaturated specimens. The system head loss was measured by using the configuration shown in Fig 4-19. Water paths connecting the top cap and the pedestal were first saturated by flushing with processed water under a negative pressure of -100 kPa. Then pre-saturated membrane filters were immediately fixed on the pedestal and the top cap. After mounting the acrylic pipe on the pedestal, processed water was injected into the pipe from the top end of the pipe until water overflowed. The top cap was then placed on the top end of the pipe by applying a large vertical force to avoid leakage from two ends of the pipe. After connection of all necessary parts, the apparatus was left for 3 hours to simulate the period spent on preparation and consolidation of the specimen in the permeability test. Following this, a certain amount of water was allowed to flow through the system. Three tests with different total water head were conducted with new membranes and Fig. 4-23 (a) shows the relationship between volume of water flow and flow speed. Apparently, the flow speed is affected by the volume of accumulated water flow because of filter clogging. To ascertain the system head loss, a triple relationship, flow volume-flow speed-measured water head has to be established. Fig. 4-23 (b) shows the relationship between system head loss (measured water head in calibration test) and flow speed in every flow volume of 3 ml (flow speed = 3ml/time required for drainage of 3 ml water). It shows that system head loss was initially linear to flow speed and curved as flow volume increased. Though more data would be required to improve the accuracy of the relationships shown in Fig. 4-23 (b), additional test could not be conducted due to the fact that it was very time-consuming. Thus, in this study, the system head loss are estimated according to the relationship in Fig. 4-23 (b).

4.6.4 Coefficient of permeability of unsaturated material

The coefficient of permeability for unsaturated specimens of Toyoura sand and IOF-B with the same dimensions of 50 mm in diameter and 100 mm in height were measured in the triaxial system. The specimen of Toyoura sand was made by compacting 5 layers in a volume constant mold. After molding the specimen, extra water was added from the top of the specimen and then the specimen was cured for 2 hours to increase its initial water content uniformly. The specimen was consolidated under 100 kPa by only allowing pore air drainage. The dry density and degree of saturation after consolidation were 1.47 g/cm^3 (Dr=51.8%) and 69.8%,

respectively. Initial suction after consolidation was about 1.6 kPa. The specimen of IOF-B with initial water content of approximately 12% was molded in the constant volume mold by one dimensional compaction. In a similar manner, the specimen was cured overnight for water content uniformity after the addition of extra water. The specimen was consolidated under 100 kPa by only allowing pore air drainage. The dry density and degree of saturation after consolidation were 2.58 g/cm^3 (Dc=92.7%) and 84.3%, respectively. Initial suction after consolidation was approximately 0.3 kPa. After consolidation the valve of pore air drainage path was closed. The water receiver side (II in Fig. 4-16) was adjusted to a position lower than the specimens to apply a negative pore water pressure to the specimens (with a value equivalent to suction of the specimens).

The system head loss evaluated according to measured average flow speed in every flow volume of 3 ml during tests of Toyoura sand and IOF-B were plotted together with calibration curves of system head loss relationship, as shown in Fig. 4-24. In the test with Toyoura sand (red points) the flow speed decreased as accumulated flow volume increased. The flow speed of the unsaturated specimen of IOF-B (black pionts) was too low that the calibration curves of system head loss had to be extrapolated. After estimation of system head loss, the real head applied on the specimens and the coefficient of permeability were calculated, as shown in Fig. 4-25. The *k* value of the specimen of Toyoura sand are was quite stable at about 2×10^{-4} cm/s. For the permeability of the unsaturated specimen of IOF-B, because the estimated system head loss is very small, the results may not be significantly affected by filter clogging. The average *k* value for the unsaturated IOF-B specimen was 1.5×10^{-5} cm/s.

4.7 Discussion on permeability

4.7.1 Permeability of Toyoura sand

Fig. 4-26 compares the permeability of Toyoura sand studied by Uno et al (1990) and test results from this study. In the test program of Uno et al (1990), a rigid mold was used to confine the specimens of Toyoura sand. To stop pore air drainage of the unsaturated Toyoura sand, two types of filters, glass filer G4 and glass filter G3, were used. Both filters have a thickness of 6 mm, while G4 has a pore size of 5-10 μm and it is 25-30 μm for G3 filter (the pore size of the membrane filter used in this study is 0.45 μm). In order to guarantee a good contact between the specimens and the pedestal, vertical load was applied to the specimens (the magnitude of load was not described). Uno et al (1990) also referred to test results by Kawanishi et al (1987) obtained by the instantaneous profile method. Detailed information on these tests is unknown

since the reference Kawanishi et al (1987) is not available to the author. The blue triangles are test data obtained in this study with confining pressure of 100kPa.

Fig. 4-26 shows that the *k* values for saturated Toyoura sand obtained in this study are slightly lower than that of Kawanishi et al (1987). For the unsaturated condition of Toyoura sand, the results of Uno (1990) obtained by using coarse filter (G3) are consistent with results of Kawanishi et al (1987) and the measured permeability seems to reduce as the used filter becomes finer (G3 filter →G4 filter →membrane filter). It implies that the filter used in the permeability test may significantly affect the test results, although the effect of head loss of filters was considered for both Uno et al (1990) and this study. There might be some other reasons, for instance, filter clogging, which may be not properly considered in this study. In addition, the sidewall effect caused by contact between the specimen and the confining wall (flexible wall or rigid wall) may be another factor.

4.7.2 Permeability of IOF-B

It was difficult to find well-documented reference data of iron ore fines for comparison, thus, permeability of IOF-B is evaluated by using a prediction model. Mualem (1976) proposed a model for predicting the permeability of unsaturated porous media from the knowledge of SWCC. This proposed model includes a dimensionless water content, Θ:

$$\Theta = \frac{\theta - \theta_r}{\theta_s - \theta_r} \qquad \text{(Eq. 4-3)}$$

where, θ stands for volumetric water content and, subscripts '*s*' and '*r*' indicate the saturated and residual volumetric water content, respectively. To solve the model proposed by Mualem (1976), Van Genuchten (1980) proposed an equation to correlate Θ with pressure head *h*:

$$\Theta = \begin{cases} \frac{1}{[1+|\alpha h|^n]^{1-1/n}} & h < 0 \\ 1 & h \geqq 0 \end{cases} \qquad \text{(Eq. 4-4)}$$

where, α and n are model parameters, and α is a unit of (m^{-1}) when unit of *h* is (m); *h* is pressure head (m). It is assumed that the suction (kPa)=$\gamma_w \times h$, γ_w is the unit weight of water in this study.

By introducing Eq. 4-4, the model proposed by Mualem (1976) was converted to:

$$k = k_s \Theta^{1/2} \left[1 - \left(1 - \Theta^{n/(n-1)}\right)^{1-1/n}\right]^2 \qquad \text{(Eq. 4-5)}$$

where, *k* is permeability of unsaturated soil; k_s is permeability of saturated soil; and *n* is the parameter in Eq. 4-4.

Eq. 4-5 involves 5 parameters: (1) θ_s, which is known when the density of soil is given; (2) θ_r, which has to be evaluated from SWCC result; (3) α and (4) n, which are determined by fitting SWCC using Eq. 4-4; and (5) k_s, which is determined by the permeability test of the saturated specimen.

Eqs. 4-3~4-5 were further extended to predict permeability of unsaturated soil by using drainage histories during one or several steps in SWCC test (Kool et al., 1985 and Parker et al., 1985). Though this process may need only a few experimental works and some programing works, it is not straightforward to obtain the unique values for the parameters (α and n), which are suitable for every drainage history. In this study, the k value was estimated according to SWCC result and Eqs. 4-3~4-5 following the process below:

1. Result obtained from permeability test: k_s=1.008*10^{-3} cm/s for the saturated specimen with density of 2.54 g/cm^3 (Dc=91.7%) under confining pressure of 100 kPa; k is in the range (1.2-1.9)×10^{-5} cm/s for the unsaturated specimen with density of 2.58 g/cm^3 (Dc=92.5%) under confining pressure of 100 kPa. The measured suction during consolidation is in the range of 0.2-0.4kPa.
2. SWCC of test SW_L_IOF-B_3_3 (Table 4-1) is used to determine the two parameters because the density of the specimen test SW_L_IOF-B_3_3 (2.57 g/cm^3) is similar with that of the specimens in the permeability tests. The saturated volumetric water content θ_s, experimental result of SWCC and fitting results are shown in Fig. 4-27. θ_r is set to be the point corresponding to the highest suction value on the SWCC.
3. After determining the α and n values, permeability is calculated from Eq.4-5. The results and measured values are plotted in Fig. 4-28.

Fig. 4-28 indicates that the measured k value is close to the wetting prediction curve. As illustrated in Section 4.6.4, after molding the specimen, extra water was added to the unsaturated specimen. Therefore, the specimen may be in the wetting process. Though the experimental result and model prediction are consistent, it does not mean that the test result is accurate. Firstly the suitability of the prediction model for IOF-B is not discussed and secondly with different value of some parameters, such as the residual volumetric water content, the prediction results may vary severely. The results shown in Fig. 4-28 may only imply that the accuracy of measured permeability of the unsaturated IOF-B specimen in this study is acceptable.

4.8 Chapter conclusions

From the discussion on the SWCC test results and permeability test result, several points can be concluded:

1. Regarding the effect of void ratio on the water retention ability of IOF-B, the test result shows that the volumetric water content θ and degree of saturation Sr on SWCCs increases with a decrease in void ratio under the same suction (Fig. 4-3 a, b). On the other hand, the gravimetric water content ω increases with an increase in void ratio when suction is less than 1.5 kPa, while the effect of void ratio on ω vanishes when suction exceeds 1.5 kPa (Fig. 4-3 c).
2. The membrane filter technique is efficient and reliable to measure SWCC within the suction range up to 20 kPa (Fig. 4-4 and 4-5)
3. The vapor pressure equilibrium technique, used for determination of SWCC in high suction range (10^3-10^6 kPa) is very sensitive to the test circumstance and time consuming (Fig. 4-6).
4. Results of SWCC test in high suction range shows that SWCCs tend to converge together regardless of gradation and void ratio as well as the type of soil tested (Figs. 4-8 and 4-10).
5. Two types of iron ore fines possess higher water retention ability than the reference soil mixtures in the low suction range and similar retention ability in the high suction range (Fig. 4-10).
6. The problems of system head loss and filter clogging need to be considered carefully in order to evaluate the permeability of sandy soils in an accurate manner (Figs. 4-12, 4-21, 4-22 and 4-23).
7. The measured permeability of the saturated specimens (Toyoura sand and IOF-B) may be rather accurate, while more tests on the permeability of unsaturated soils may be needed (Figs. 4-15, 4-17, 4-25, 4-26 and 4-28). In addition, system head loss of the triaxial system may need to be reduced further in future studies (Fig. 4-18).

Reference

1. Aiban S.A. and Znidarcic D. (1989) Evaluation of the flow pump and constant head techniques for permeability measurements. Geotechnique, vol. 39, No. 4, 655-666.

2. Arya, L.M., Farrell, D.A. and Blake, G.R. (1975) A field study of soil water depletion patterns in presence of growing soybean roots: I. determination of hydraulic properties of the soil. Soil Sci. Soc. Proc., Vol. 39, pp: 424-430.
3. Bishop, A.W. (1959). The principle of effective stress. Lecture delivered in Oslo, Norway, in 1955; published in Teknisk Ukeblad, Vol. 106, No. 39, pp: 859-863.
4. Bradbury, M.H. & Baeyens, B. 2003. Porewater chemistry in compacted re-saturated MX-80 bentonite. J. Contam. Hydrol.,61: 329-338.
5. Bruce, R.R. and Klute A. (1956) The measurement of soil moisture diffusivity. Soil science society proceedings, Vol. 20, pp: 458-462.
6. Burger, C.A. and Shackelford, C.D. (2001) Evaluating dual porosity of pelletized diatomaceous earth using bimodal soil-water characteristic curve functions. Can. Geotech. J. 38:53-66.
7. Burmister, D.M. (1954) Principles of permeability testing of soils. ASTM special technical publication No. 163, pp: 3-26.
8. Carpenter, G.W. and Stephenson R.W. (1986). Permeability testing in the triaxial cell. Geotechnical Testing Journal, Vol. 9, No. 1, pp: 3-9.
9. Chu, T.Y., Davidson, D.T. and Wickstrom, A.E. (1954) Permeability test for sands. ASTM special technical publication No. 163, pp: 43-55.
10. Clothier B.E. and Scotter D.R. (1982) Constant-flux infiltration form a hemispherical cavity. Soil Sci. Soc. AM. J., Vol. 46, pp: 696-700.
11. Dirksen, C., Unsaturated hydraulic conductivity, In: Soil Analysis: Physical methods, K.A. Smith and C.E. Mullins (eds.), 209-269, Marcel Dekker, Inc., New York, 1991.
12. Fredlund, D.G. and Morgenstern, N.R. (1977). Stress state variables for unsaturated soil. ASCE J. Geotech. Eng. Div. GT5, Vol 103, pp: 447-466.
13. Fredlund, D.G. and Rahardjo, H. (1993). Soil mechanics for unsaturated soils. John Wiley & Sons, Inc.
14. Hatanaka, M., Uchida, A. and Takehara, N. (1997) Permeability characteristics of high-quality undisturbed sands measured in triaxial cell. Soils and Foundations, Vol. 37, No. 3, 129-135.
15. Jacinto, A.C., Villar, M.V., Ledesma, A. 2012. Influence of water density on the water-retention curve of expansive clays. Geotechnique 62 (8): 657-667.
16. Jackson R.D. (1964) Water vapor diffusion in relatively dry soil: I. Theoretical considerations and sorption experiments. Soil science society proceedings, pp: 172-176.

17. Jones, C.W. (1954) The permeability and settlement of laboratory specimens of sand and sand-gravel mixtures. ASTM special technical publication No. 163, pp: 68-78.
18. Klute, A. (1972). The determination of the hydraulic conductivity and diffusivity of unsaturated soils. Soil Science, Vol. 113, No. 4, pp: 264-276.
19. Kool, J. B., Parker, J. C., and M. Th. van Genuchten. (1985) Determining soil hydraulic properties from one step outflow experiments by parameter estimation: I. Theory and numerical studies, Soils Sci. Soc. Am. J., 49, 1348-1354.
20. Lambe, T.W. (1954) The permeability of compacted fine-grained soils. ASTM special technical publication No. 163, pp: 56-67.
21. Lloret, A., Villar, M.V., Sanchez, M., Gens, A., Pintado, X., Alonso, E.E. (2003). Mechanical behaviour of heavily compacted bentonite under high suction changes. Geotechnique 53 (1): 27-40.
22. Marcial, D., Delage, P., Cui, Y.J. (2002). On the high stress compression of bentonites. Can. Geotech. J. 39:812-820.
23. Masrouri, F., Bicalho, K.V. and Kawai, K. (2008) Laboratory hydraulic testing in unsaturated soils. Geotechnical and Geological Engineering, Vol. 26, No. 6, 691-704.
24. Mualem, Y. (1976). A new model for predicting the hydraulic conductivity of unsaturated porous media. Water Resources Research, 12: 513-522.
25. Nishimura, T. & Fredlund, D.G. (2000). Unconfined compressive strength of a silty soil and kaolin below the residual state. Advances in Unsaturated Geotechnics: pp. 262-274.
26. Olsen, H.W., Nichols, R.W. and Rice T.L. (1985). Low gradient permeability measurements in a triaxial system. Geotechnique, vol. 35, No. 2, 145-157.
27. Pane, V., Croce, P., Znidarcic, D., Ko, H.Y., Olsen, H.W. and Schiffman, R.L. (1983). Effects of consolidation on the permeability measurements for soft clay. Geotechnique, vol. 33, No. 1, 67-72.
28. Parker, J. C., J. B. Kool, and M. Th. van Genuchten. (1985) Determining soil properties from one-step outflow experiments by parameter estimation, II. Experimental studies, Soil Sci. Soc. Am. J., 49, 1354-1359.
29. Romero, E., Gens, A., Lloret, A. (1999). Water permeability, water retention and microstructure of unsaturated compacted Boom clay. Engineering Geology 52: 117-127.
30. Salager, S., Nuth, M., Ferrari, A., Laloui, L. (2013). Investigation into water retention behavior of deformable soils. Can. Geotech. J. 50: 200-208.

31. Selim, H.M., Kirkham, D. and Amemiya, M. (1970) A comparison of two methods for determining soil water diffusivity. Soil Sci. Soc. Proc., Vol. 34, pp: 14-18.
32. Simunek, J. and Nimmo, J. (2005) Estimating soil hydraulic parameters form transient flow experiments in a centrifuge using parameter optimization technique. Water Resources Research, Vol. 41, Wo4015, doi: 10.1029/2004WR003379.
33. Smettem, K.R.J. and Kirkby, C. (1990) Measuring the hydraulic properties of a stable aggregated soil. J. Hydrology, Vol. 117, pp: 1-13.
34. Standing, J.R. (2011). The development of unsaturated soil mechanics at Imperial College, London. Unsaturated soils: Theory and practice 2011, pp: 119-138.
35. Tang, A.M. & Cui, Y.J. (2005). Controlling suction by the vapour equilibrium technique at different temperatures and its application in determining the water retention properties of MX80 clay. Can. Geotech. J. 42:287-296.
36. Tavenas, F., Leblond, P., Jean, P. and Leroueil, S. (1983). The permeability of natural soft clays. Part I: Methods and laboratory measurement. Can. Geotech. J. 20: 629-644.
37. Tindall, J.A., Kimkel, J.R. and Kunkel, J.R. 1999. Unsaturated zone hydrology for scientists and engineers. New Jersey: Prentice Hall. pp: 95-122.
38. Toorman, A.F., Wierenga, P.J. and Hills, R.G. (1992) Parameter estimation of hydraulic properties from one-step outflow data. Water Resources Research, Vol. 28, No. 11, pp: 3021-3028.
39. Uno, T., Sato, T., Sigii, T. and Tsuge, H. (1990) Method of test for permeability of unsaturated sandy soil with controlled air pressure. Proc. of the Japan Society of Civil Engineers, No. 418, III-13, pp: 115-124.
40. Vachaud, G. (1967) Determination of the hydraulic conductivity of unsaturated soils from and analysis of transient flow data. Water resources research, Vol. 3, No. 3, pp: 697-705.
41. Van Genuchten, M. Th. (1980) A closed-form equation for predicting the hydraulic conductivity of unsaturated soils, Soil Sci. Soc. Am. J., 892-898.
42. Whisler, F.D., Klute A. and Peters, D.B. (1968) Soil water diffusivity from horizontal infiltration. Soil Sci. Soc. Proc., Vol. 32, pp: 6-11.
43. Yemington, E.G. (1954) A low-head permeameter for testing granular materials. ASTM special technical publication No. 163, pp: 37-42.

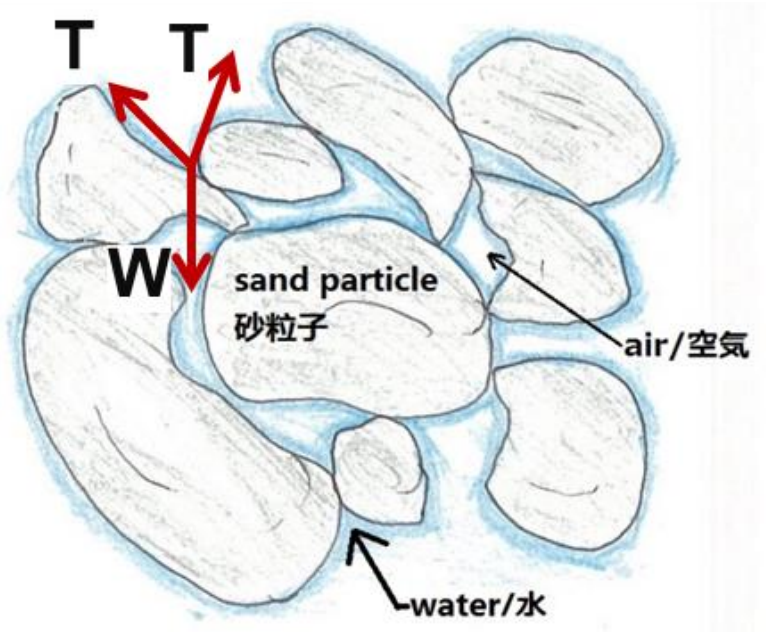

Fig. 4-1 (a) An element of unsaturated soil

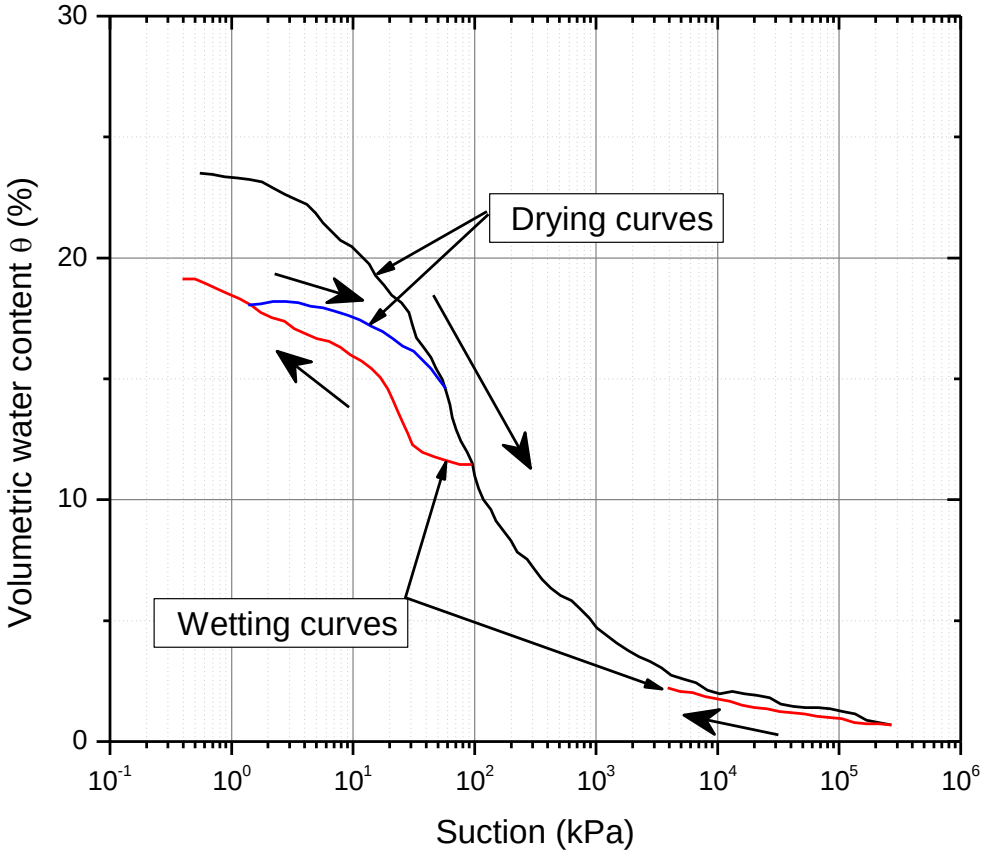

Fig. 4-1 (b) Schematic SWCCs for illustration

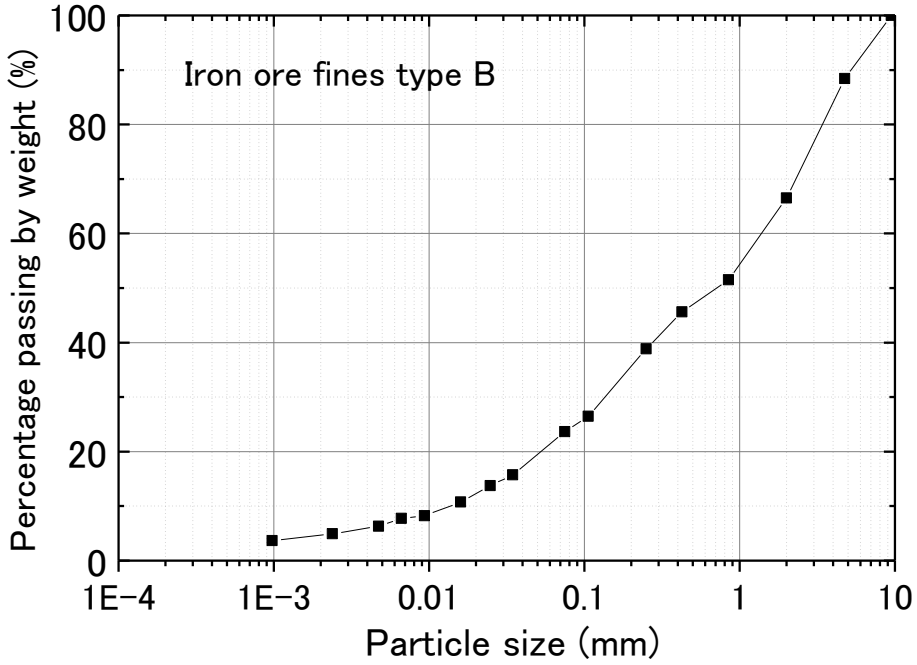

Fig. 4-2 Gradation of IOF-B

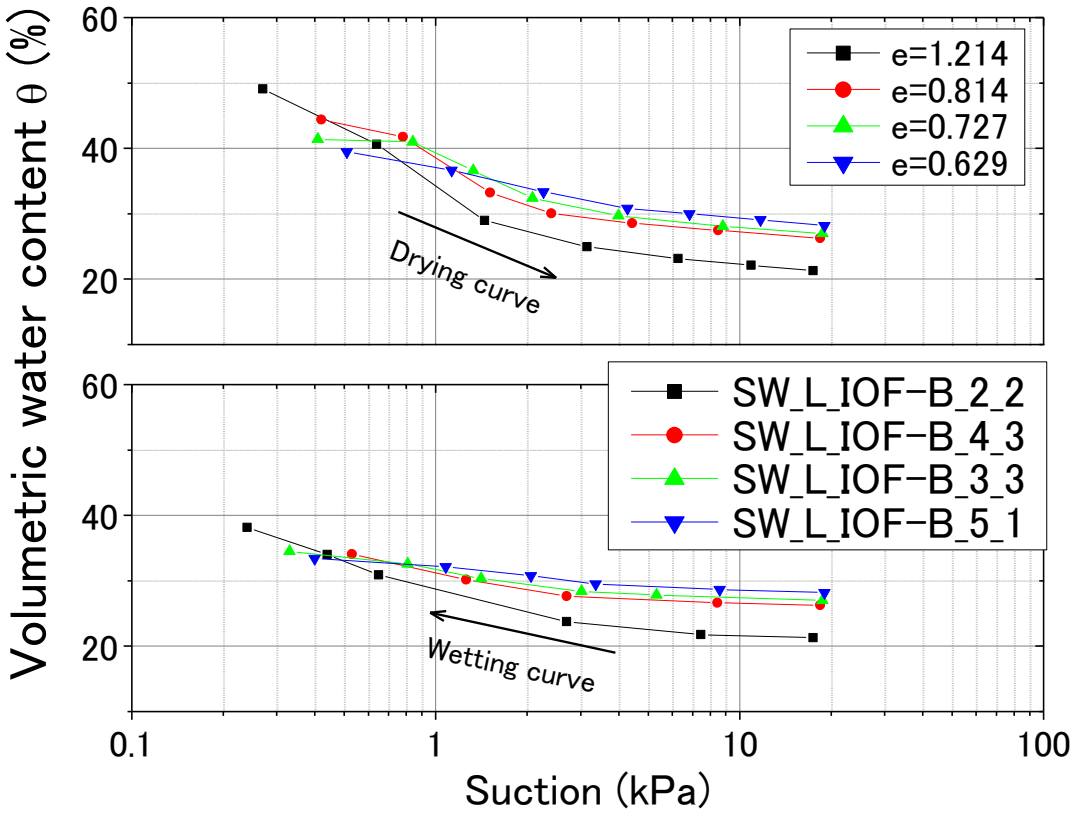

(a) Suction vs volumetric water content

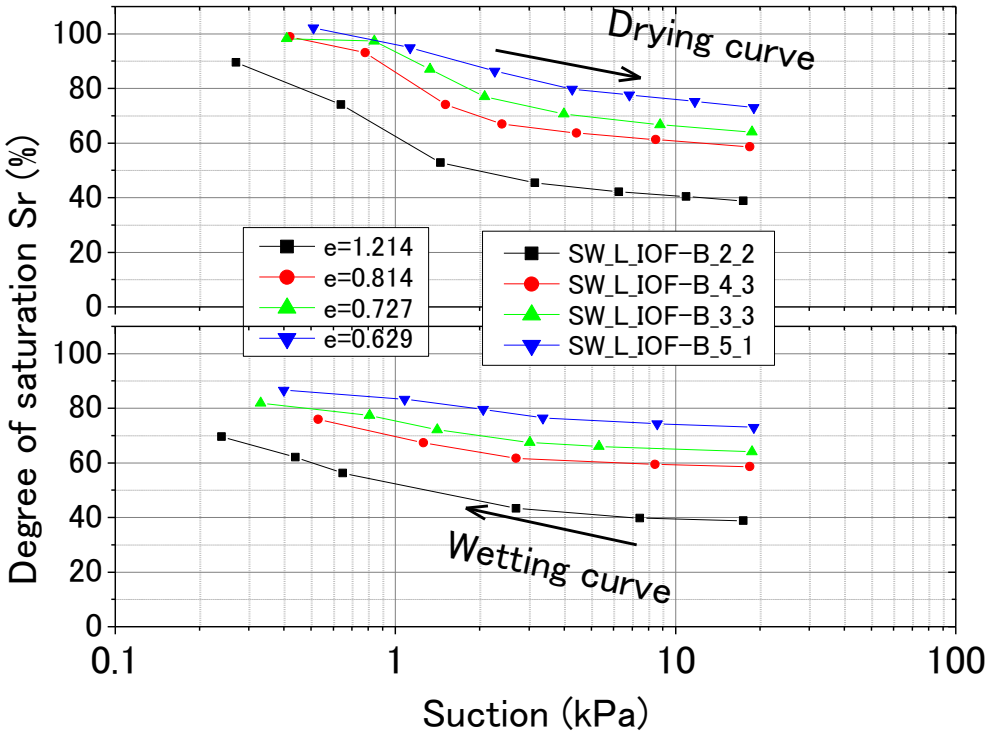

(b) Suction vs degree of saturation

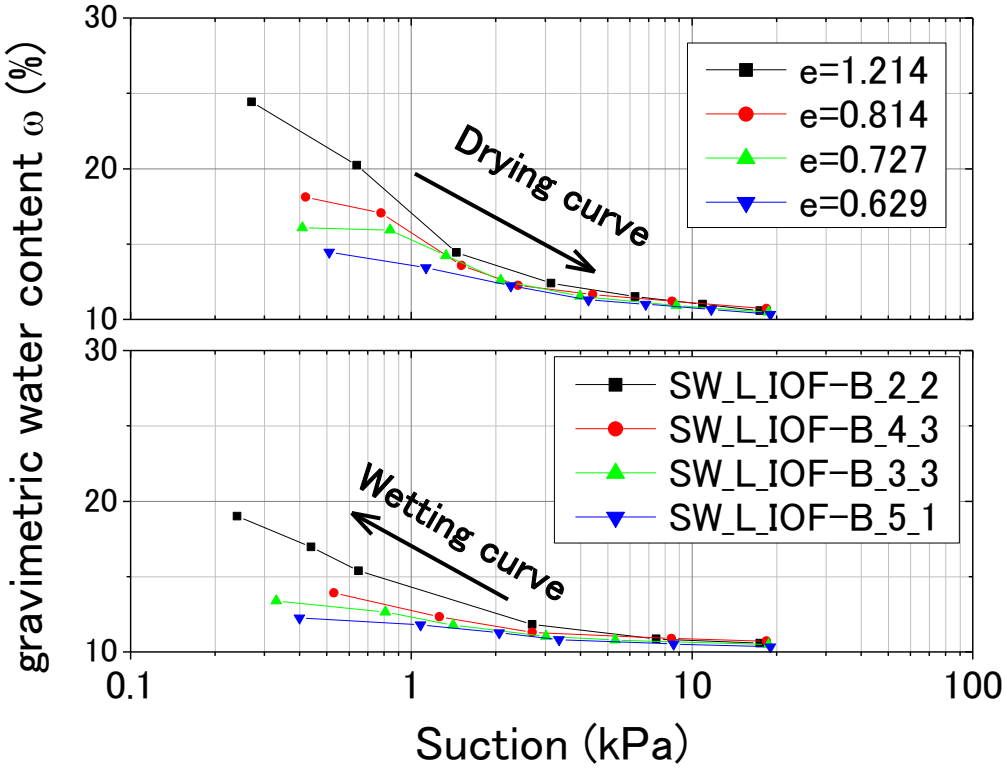

(c) Suction vs gravimetric water content

Fig. 4-3 SWCC of IOF-B with different density

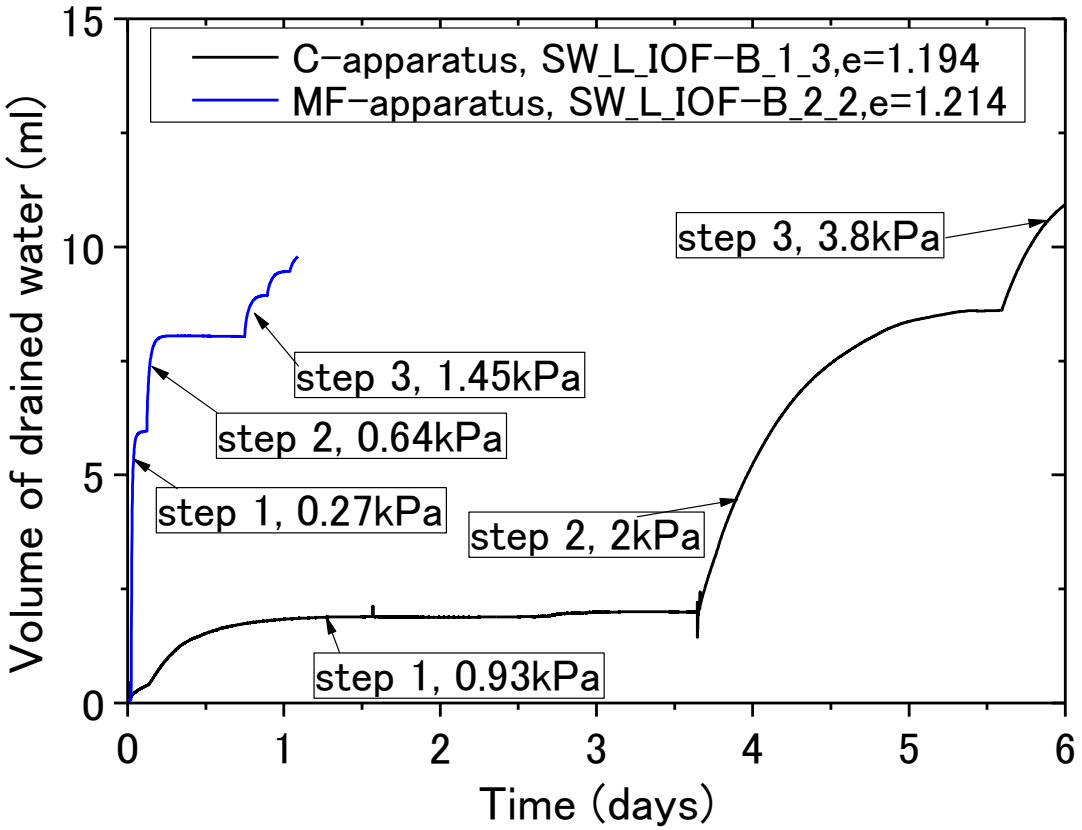

Fig. 4-4 (a) Time histories of tests on Ceramic disk apparatus and membrane filter apparatus

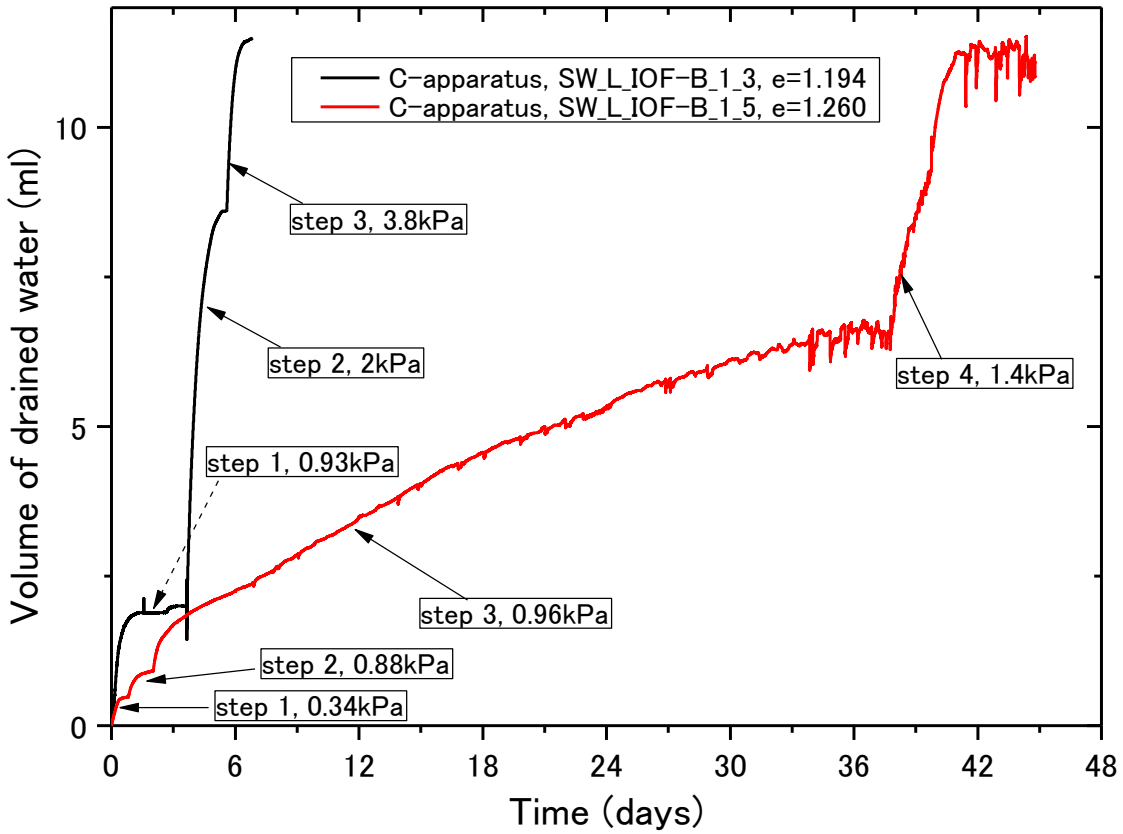

Fig. 4-4 (b) Time histories of tests on Ceramic disk

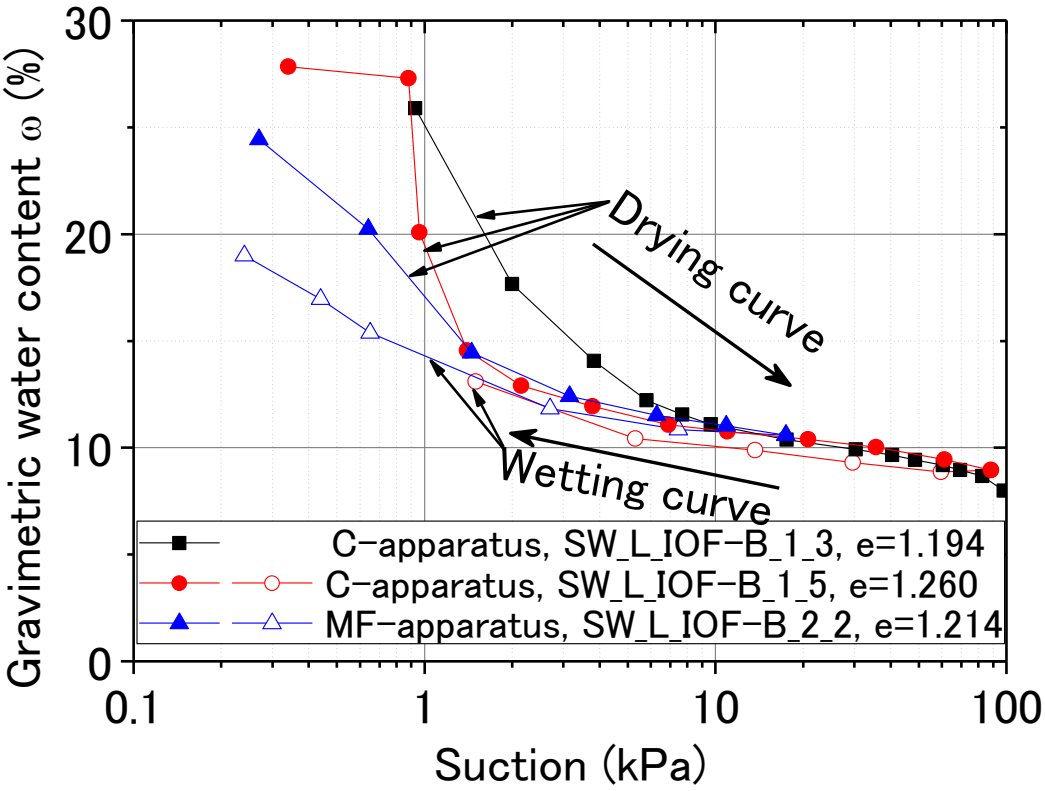

Figure 4-5. SWCCs performed on different apparatus

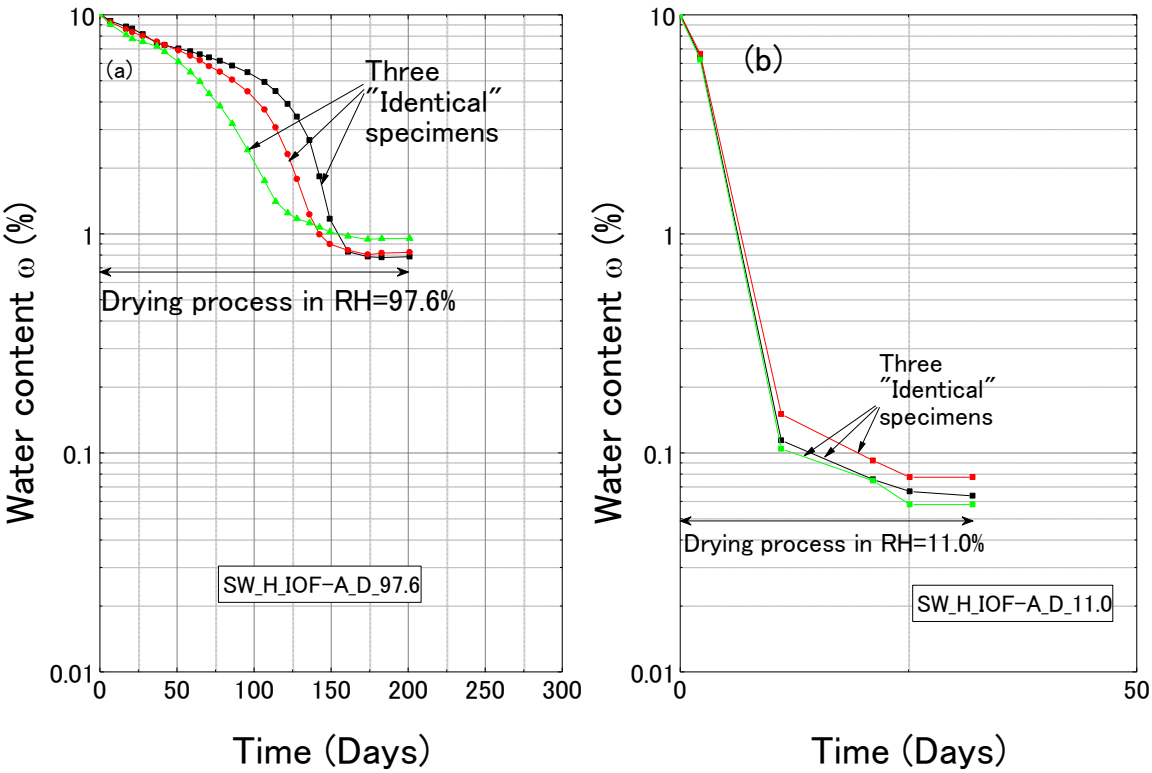

a) Drying process in RH of 97.6% b) Drying process in RH of 11.0%

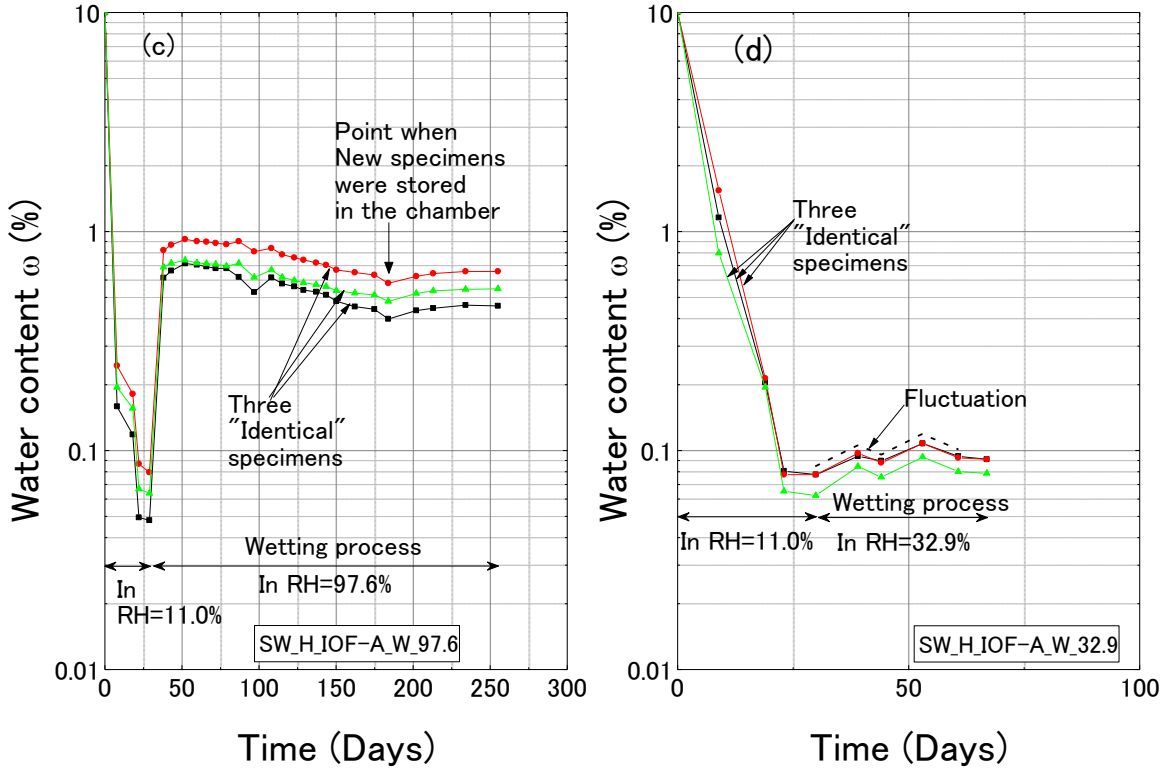

c) Wetting process in RH of 97.6% d) Wetting process in RH of 32.9%

Fig.4-6 Time history of specimens

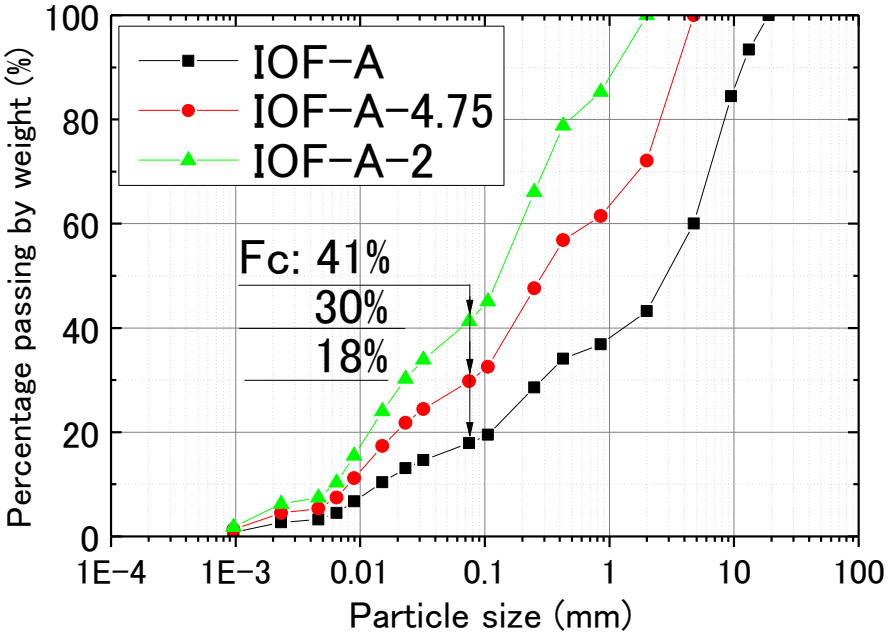

Fig. 4-7 Gradation of iron ore fines type A

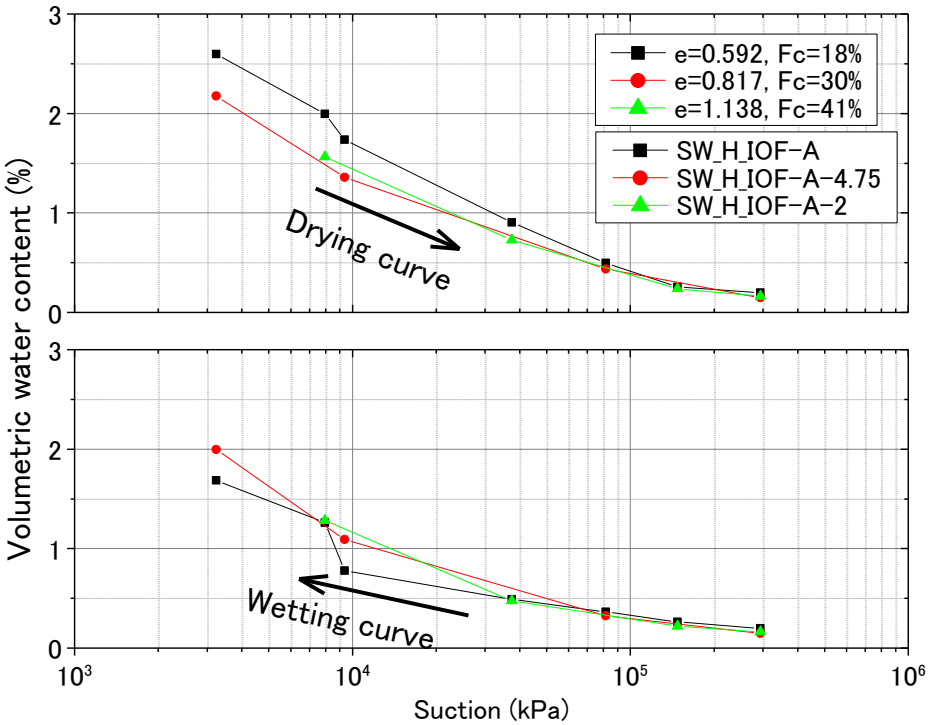

(a) Suction vs volumetric water content

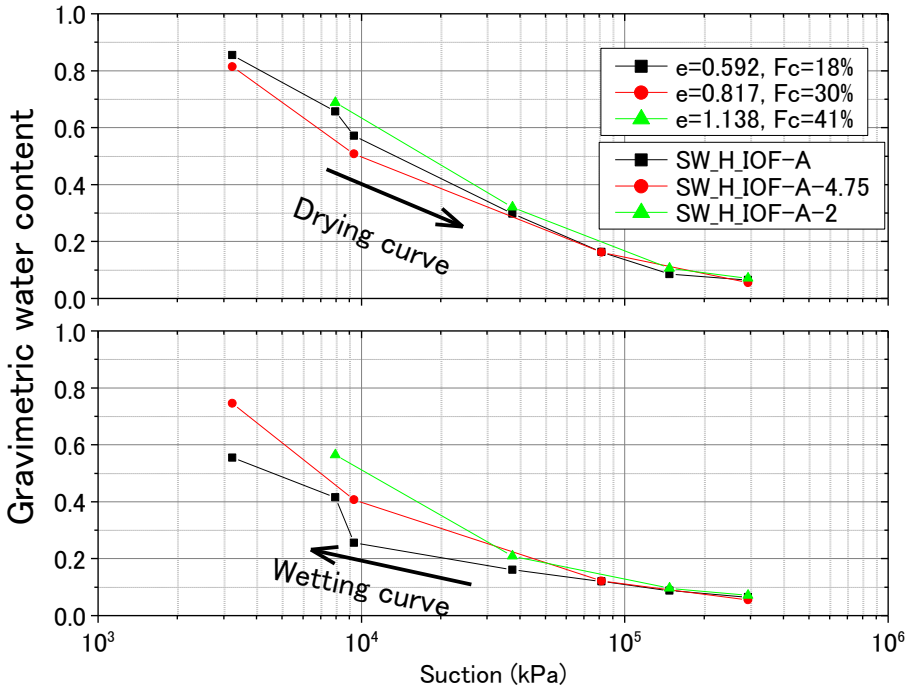

(b) Suction vs gravimetric water content

Fig. 4-8 SWCC of IOF-A with different density and gradation

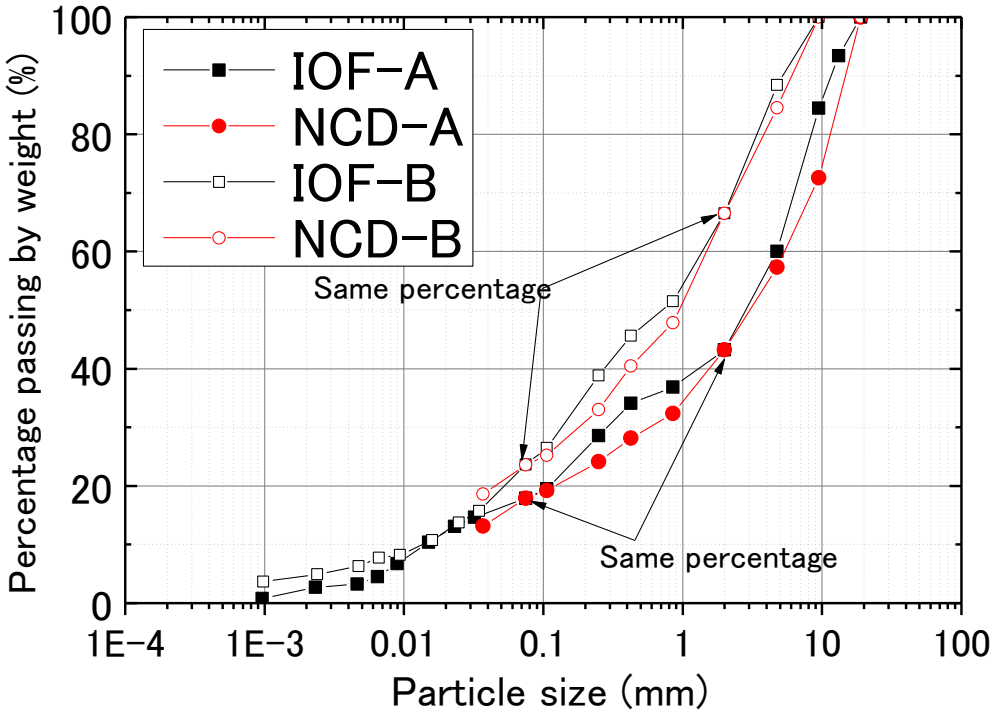

Fig. 4-9 Gradation of iron ore fines and mixed common materials

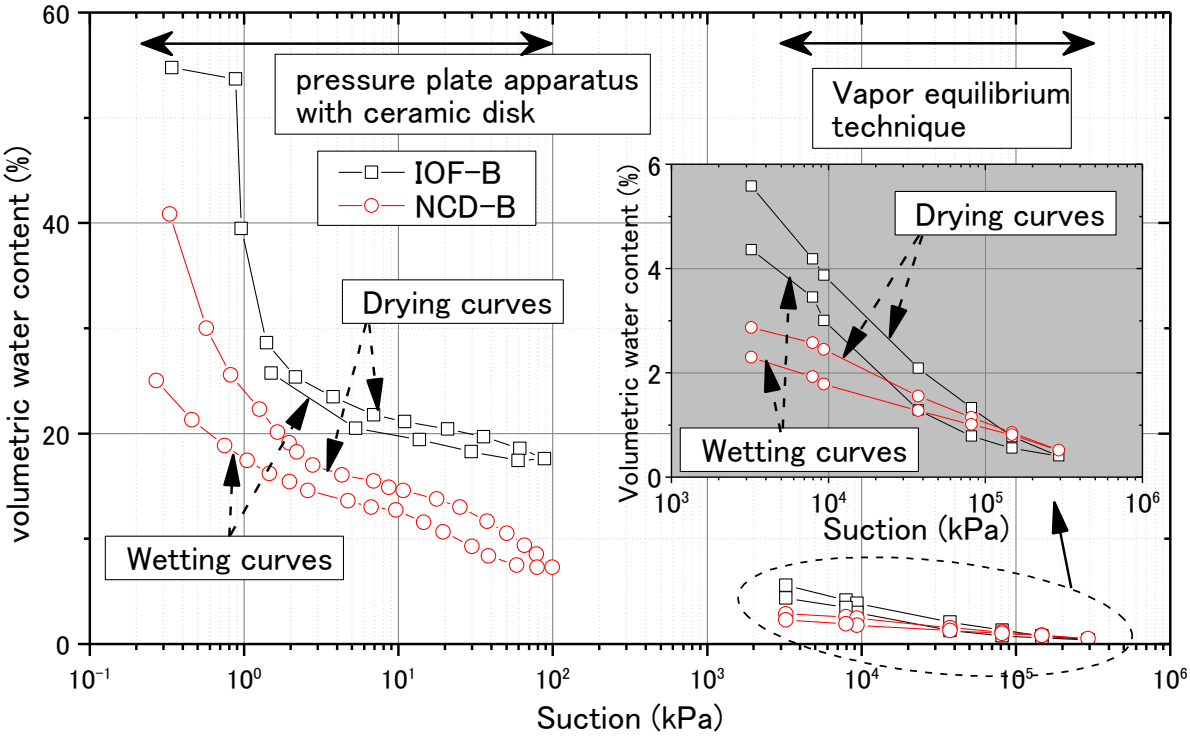

Fig. 4-10 (a) SWCC of IOF-B and its reference material mixing

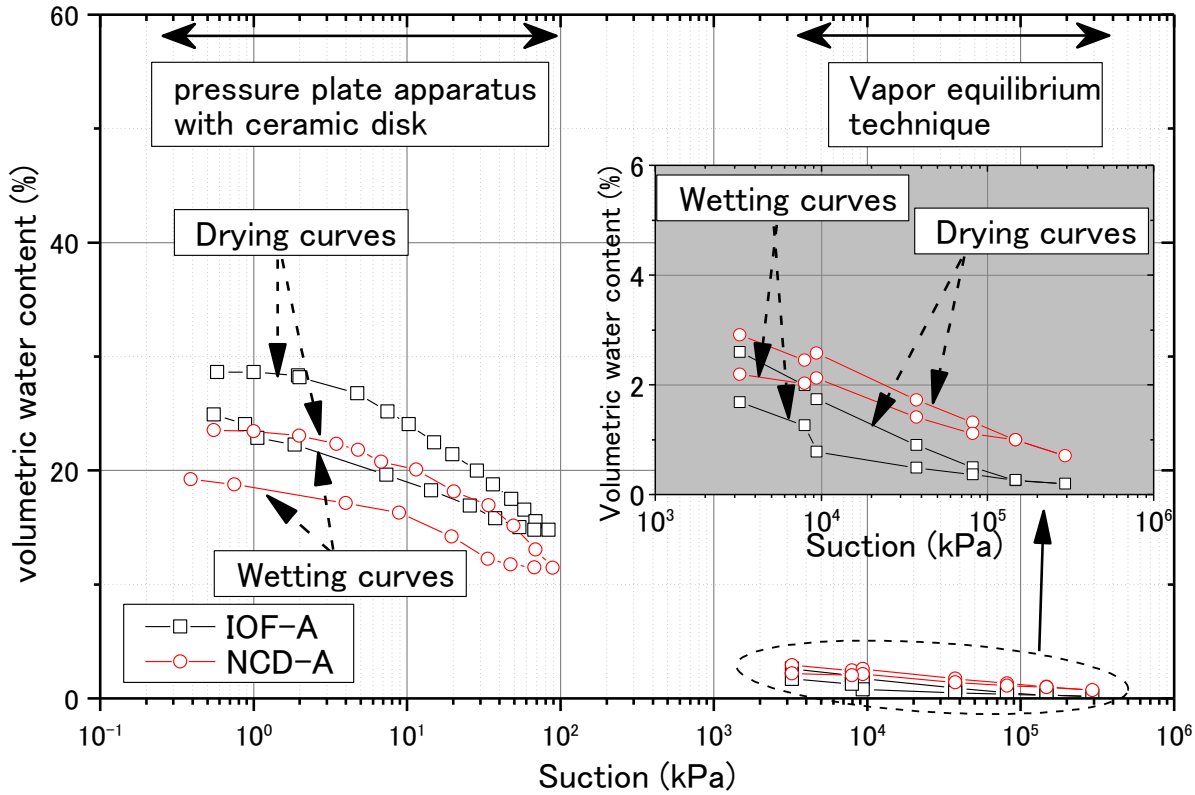

Fig. 4-10 (b) SWCC of IOF-A and its reference material mixing

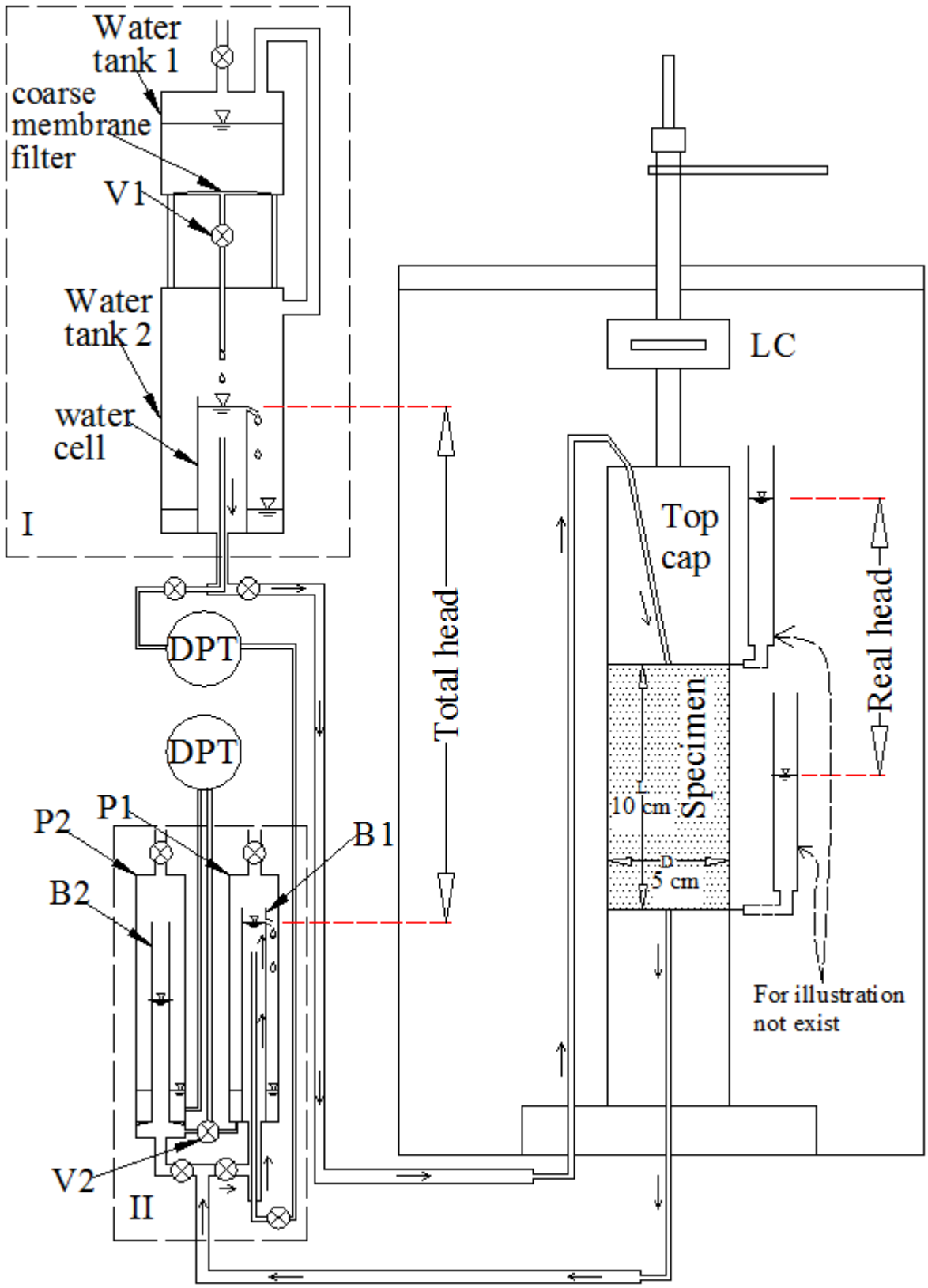

Fig. 4-11 Apparatus of permeability test for a saturated specimen

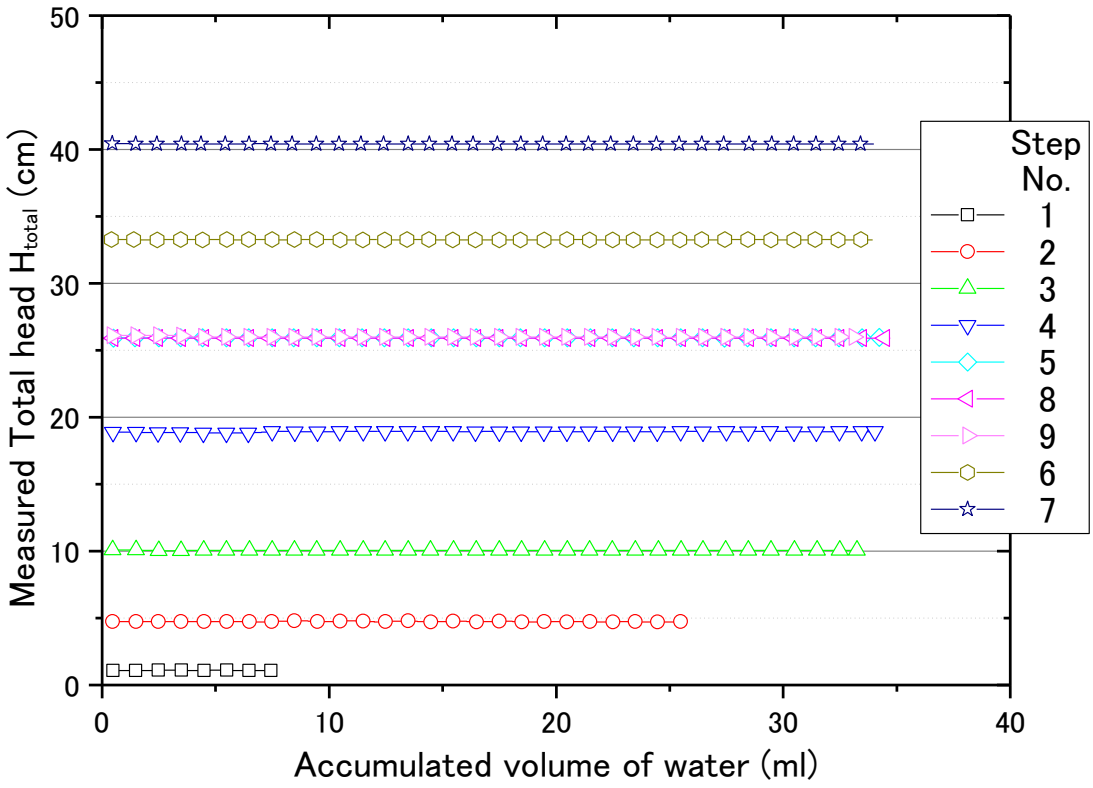

Fig. 4-12 (a) Applied total water head

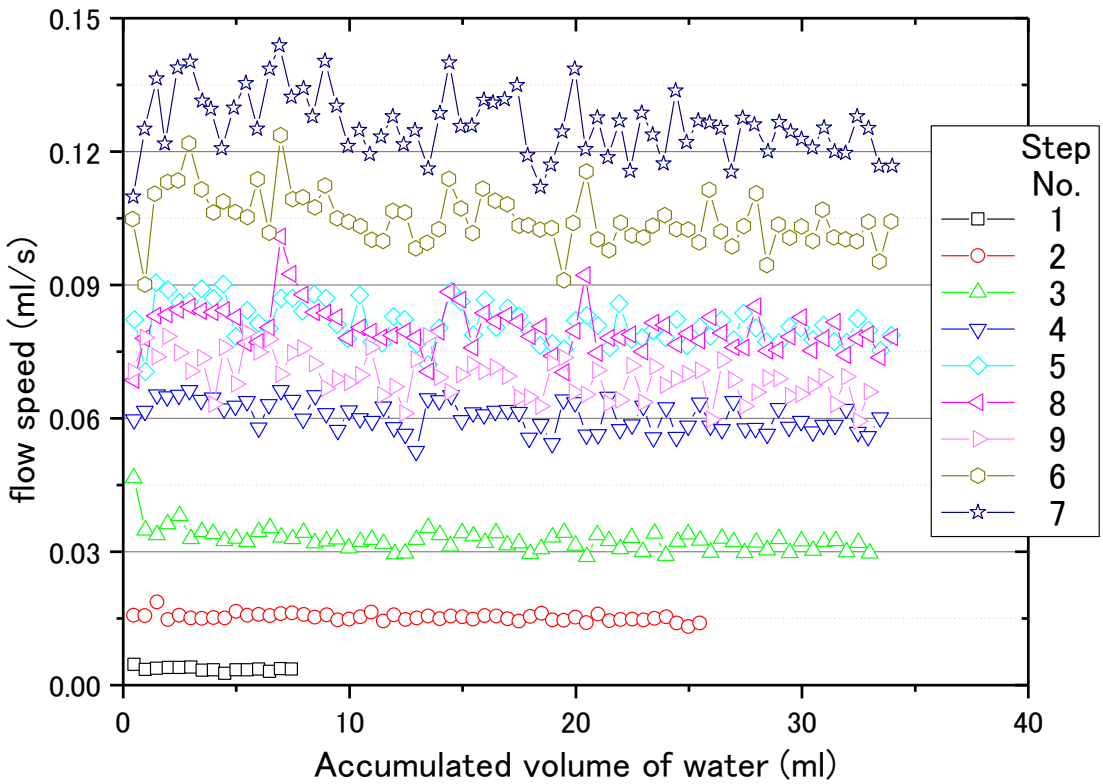

Fig. 4-12 (b) Flow speed vs volume of water seeped

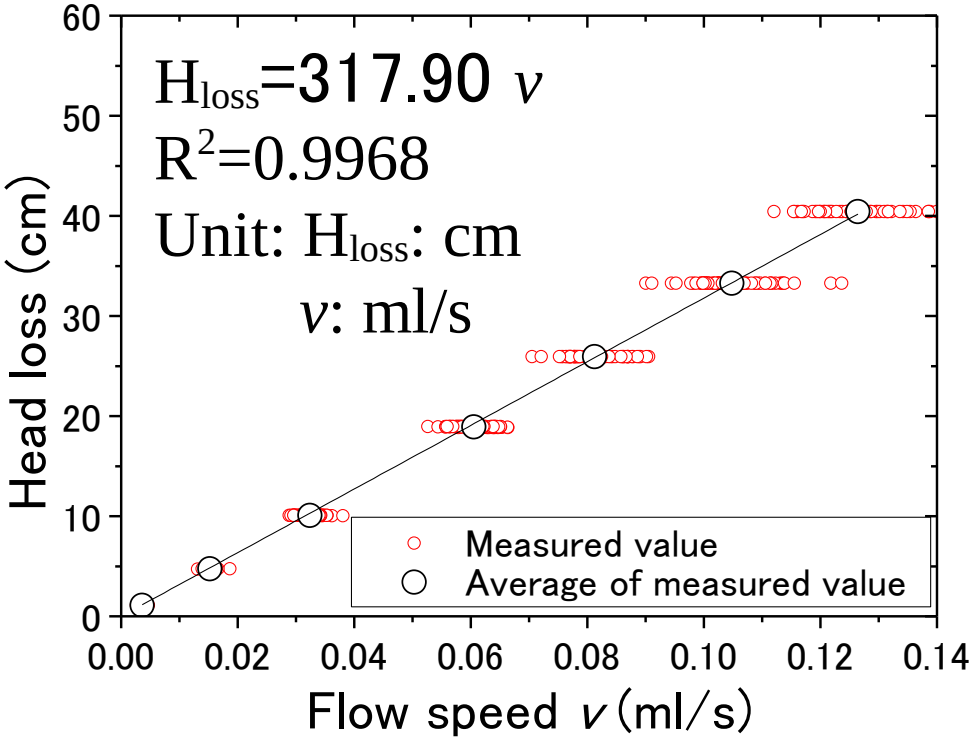

Fig. 4-12 (c) Calibration of system head loss

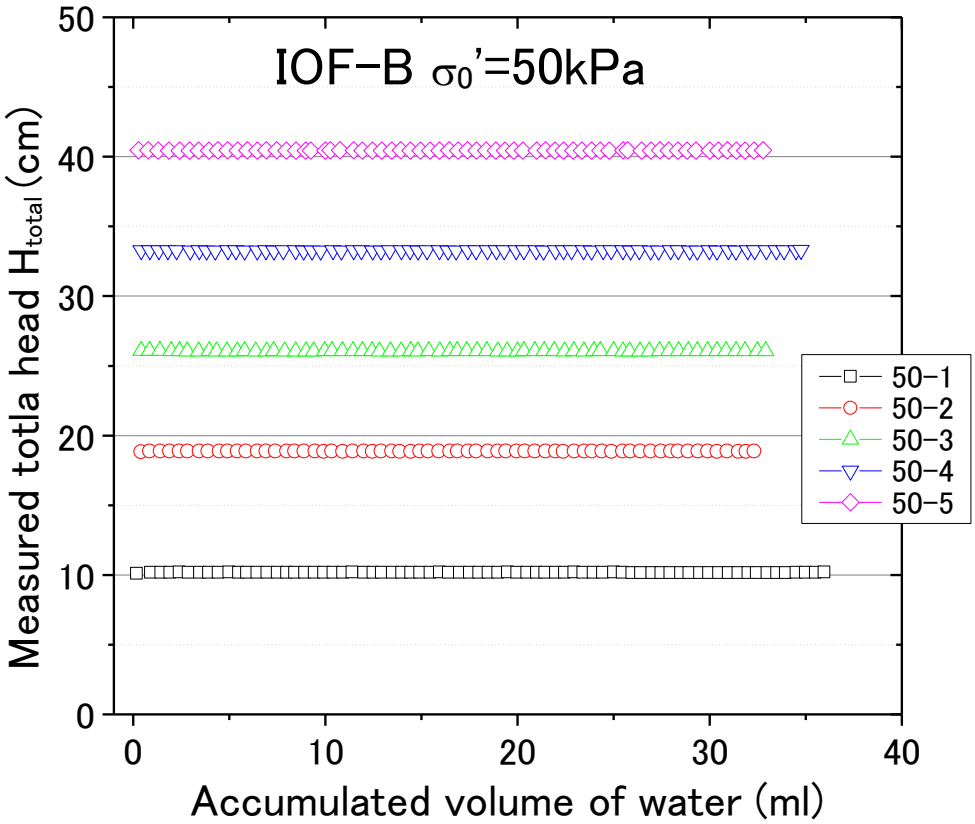

Fig. 4-13 (a) Changes of applied total water head

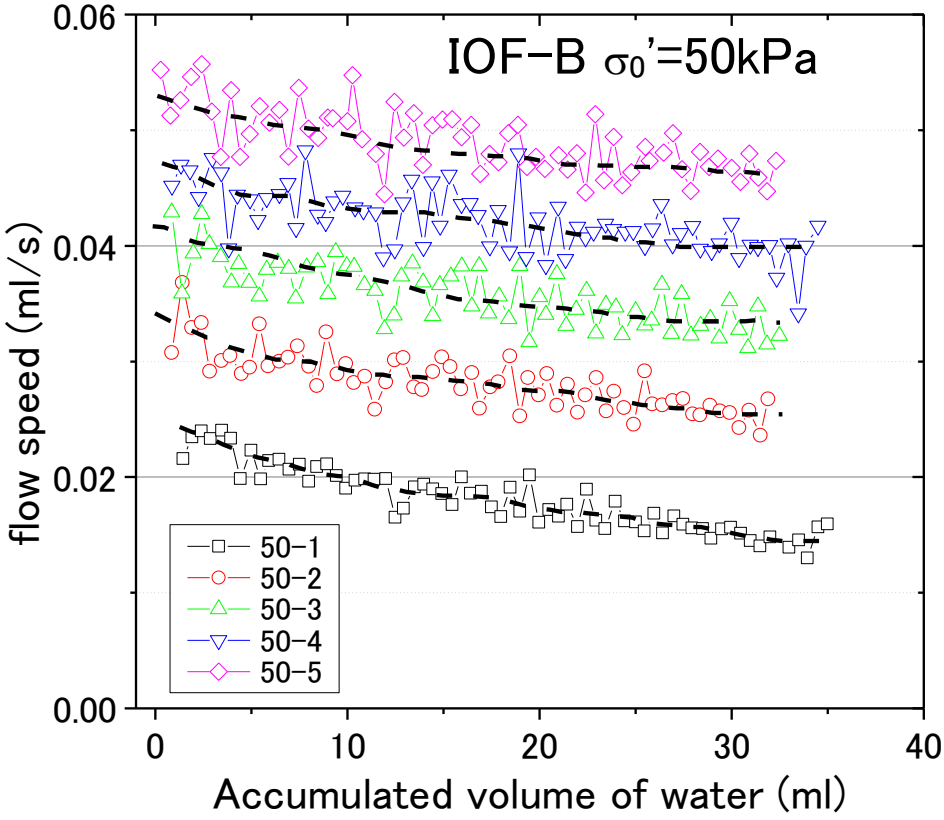

Fig. 4-13 (b) Change calculated k value

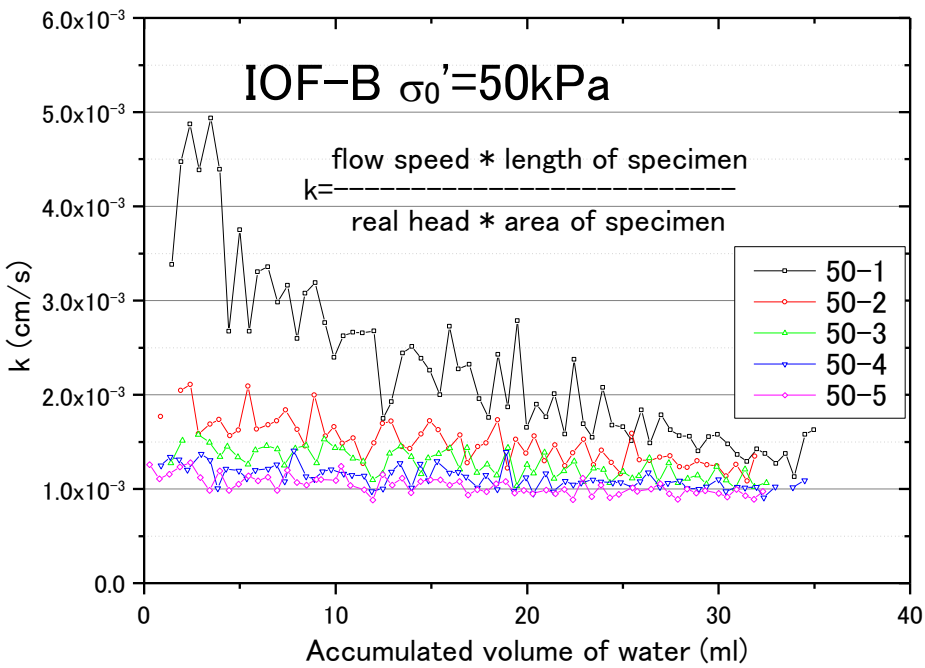

Fig. 4-13 (c) Change calculated k value for IOF-B under confining pressure of 50 kPa

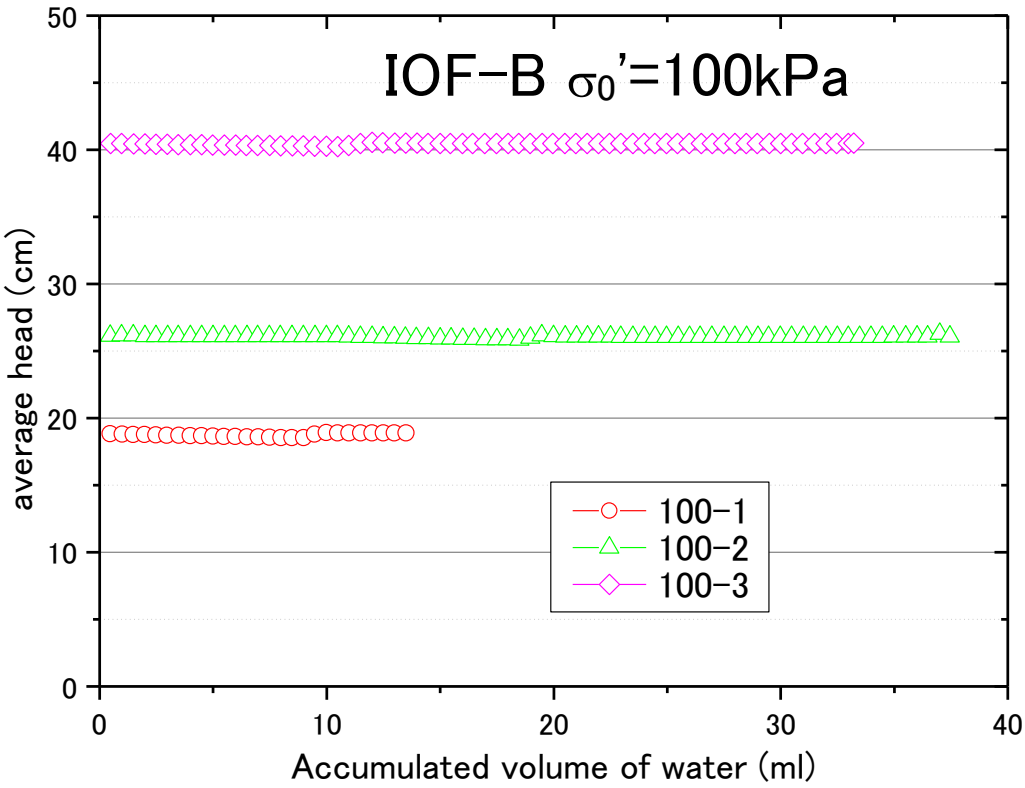

Fig. 4-14 (a) Changes of applied total water head

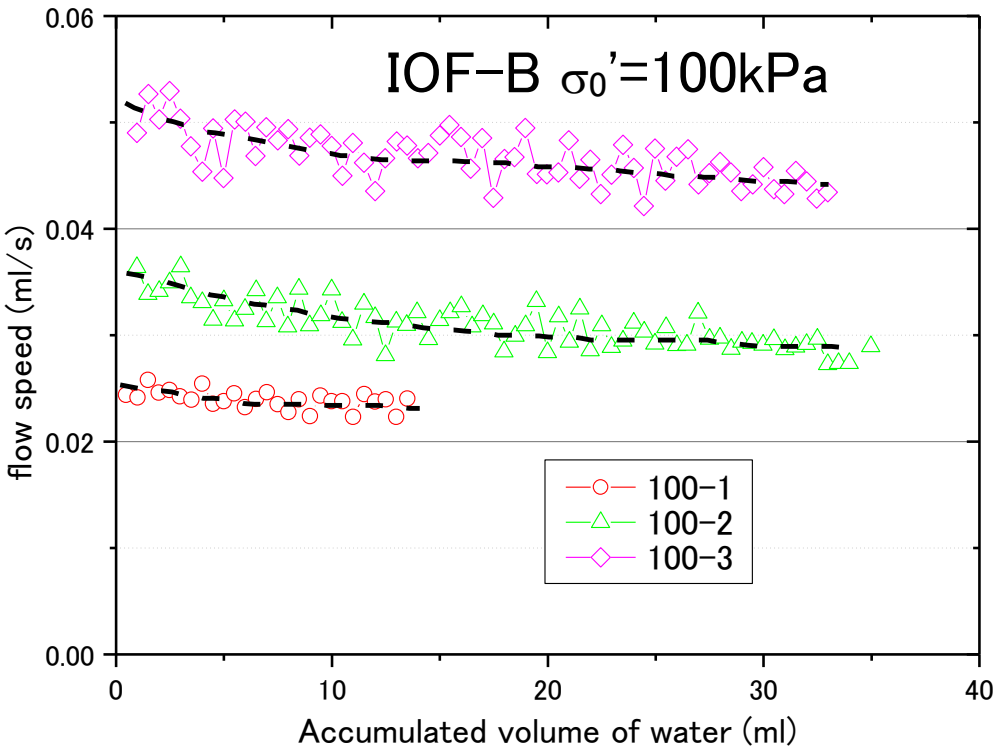

Fig. 4-14 (b) Changes of flow speed

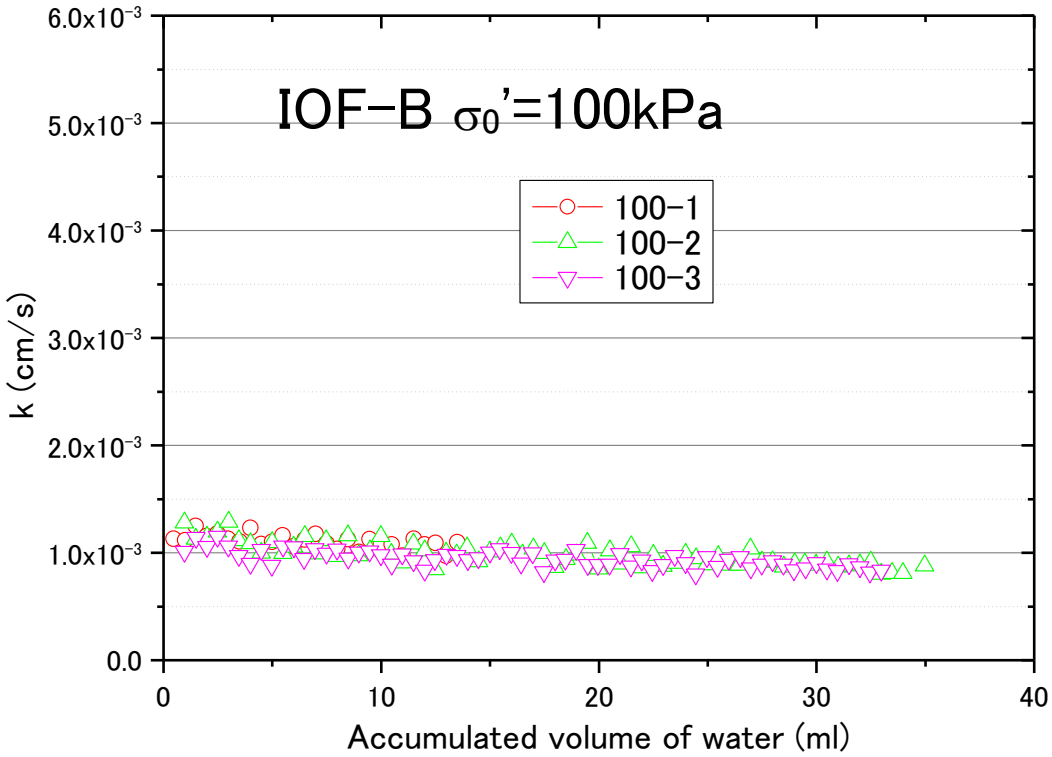

Fig. 4-14 (c) Change calculated k value for IOF-B under confining pressure of 100 kPa

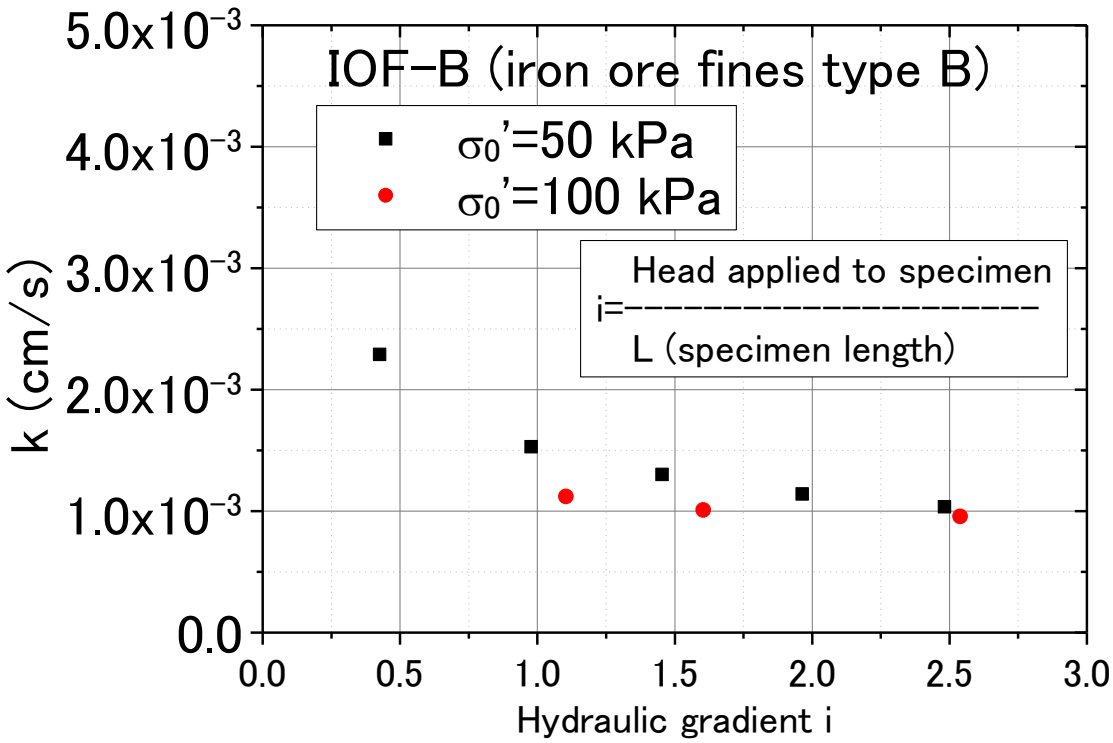

Fig. 4-15 Coefficient of permeability of iron ore fines type B

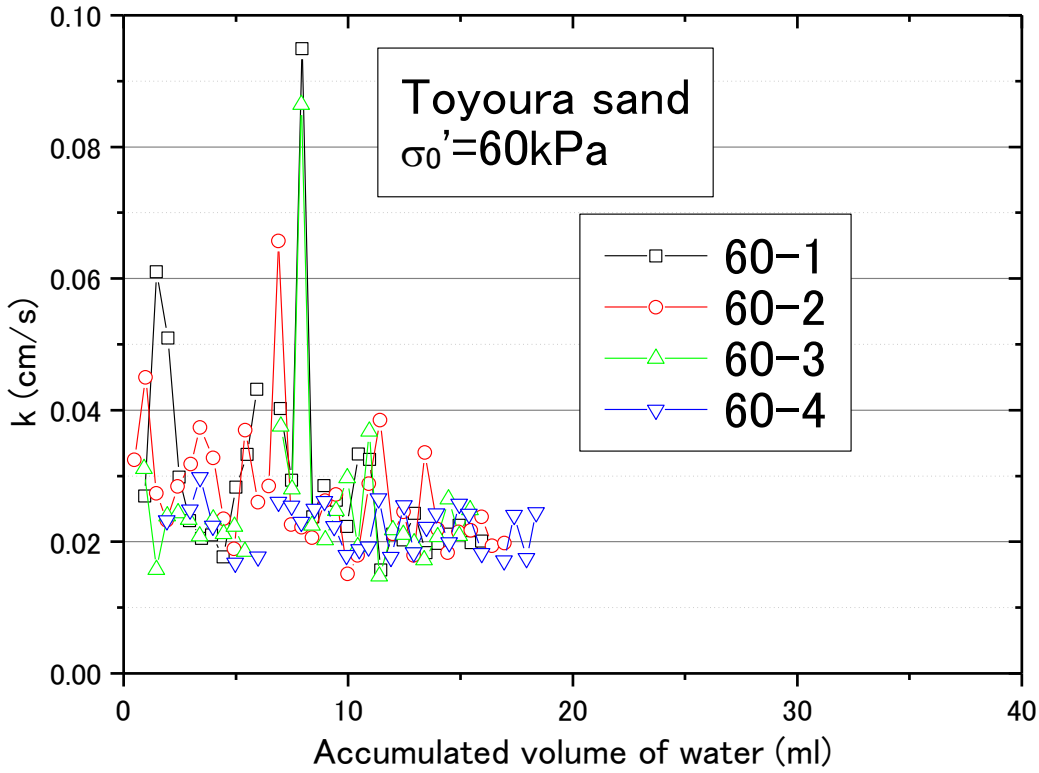

Fig. 4-16 (a) Change calculated k under confining pressure of 60 kPa

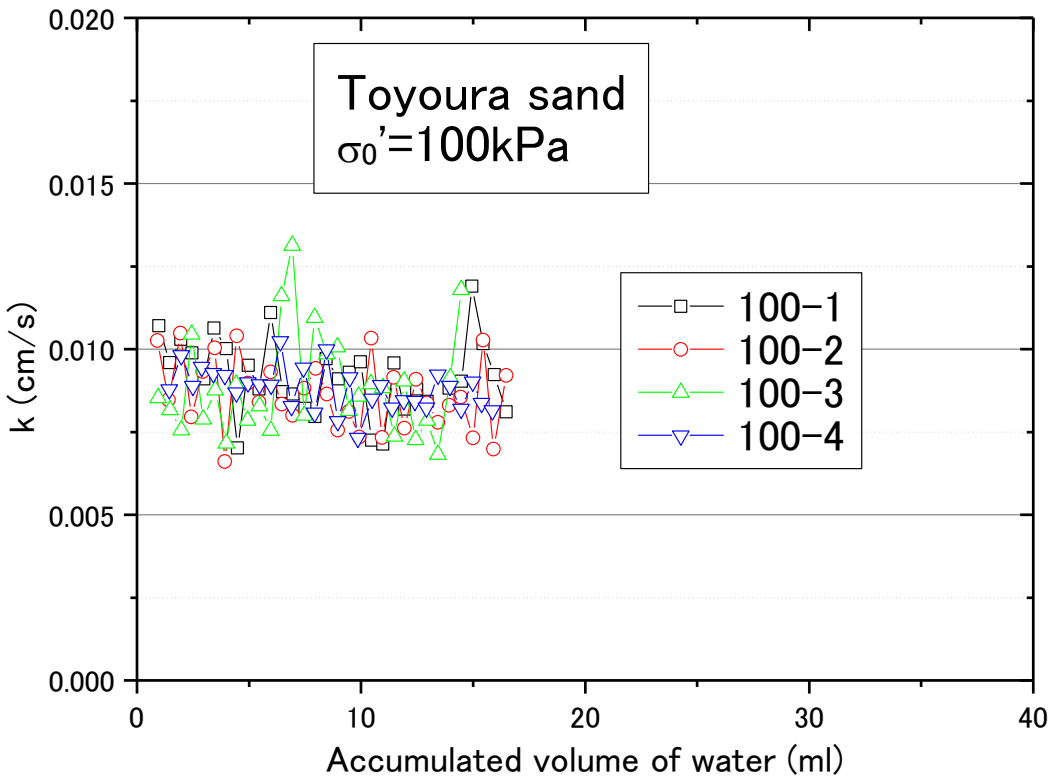

Fig. 4-16 (b) Change calculated k under confining pressure of 100 kPa

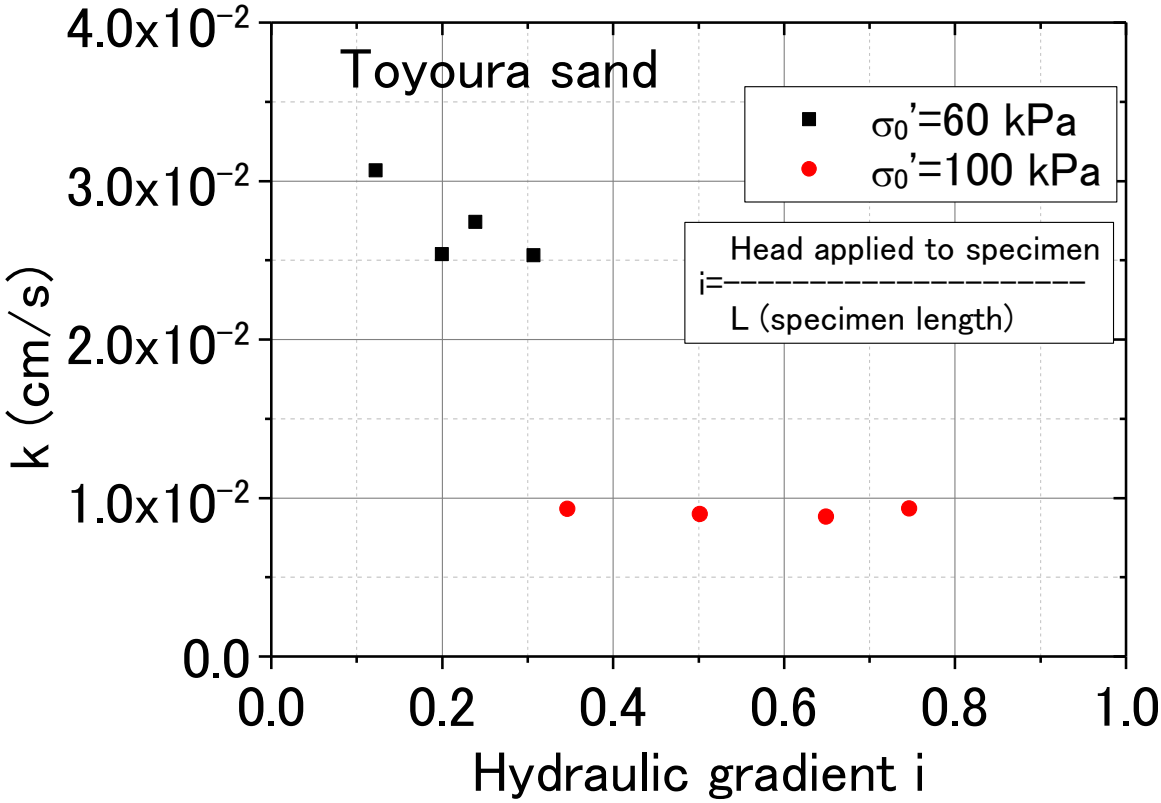

Fig. 4-17 Coefficient of permeability of Toyoura sand

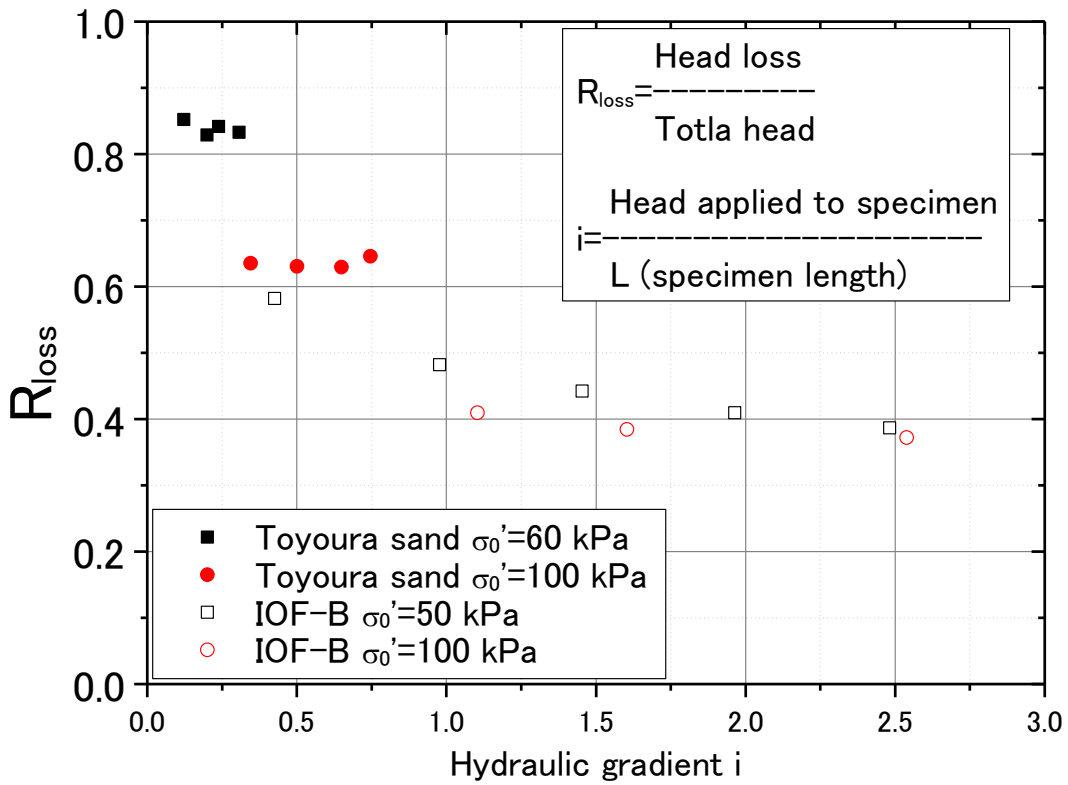

Fig. 4-18 System head loss in tests

Fig. 4-18 System head loss in tests

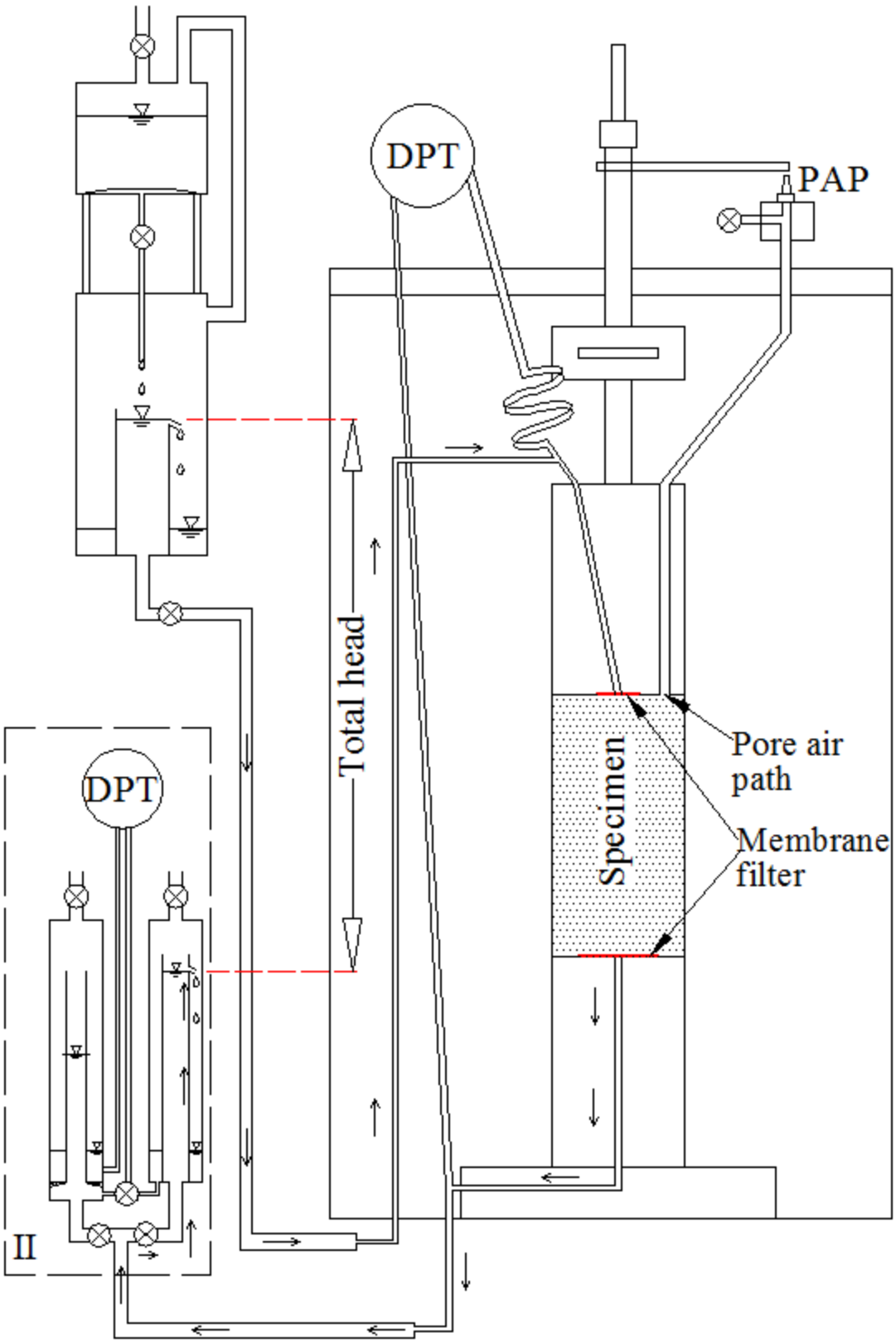

Fig. 4-19 Apparatus layout for an unsaturated specimen

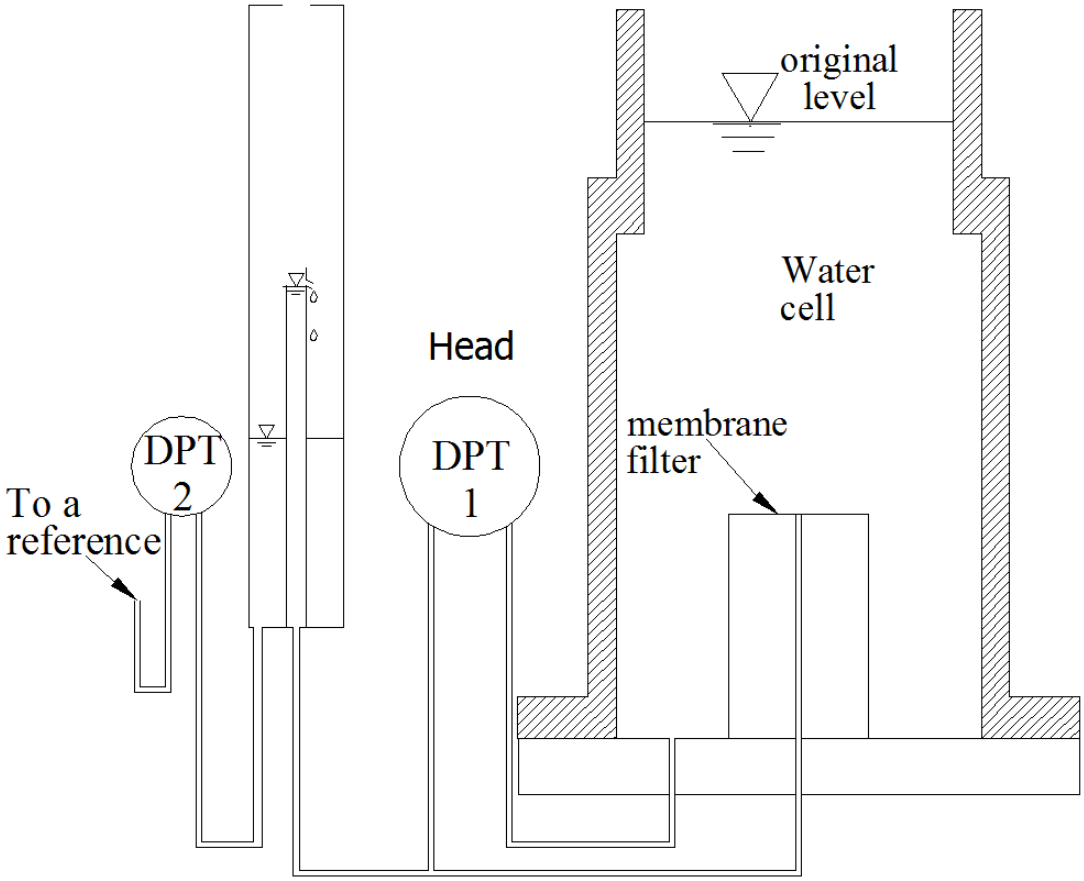

Fig. 4-20 Layout for filter clogging

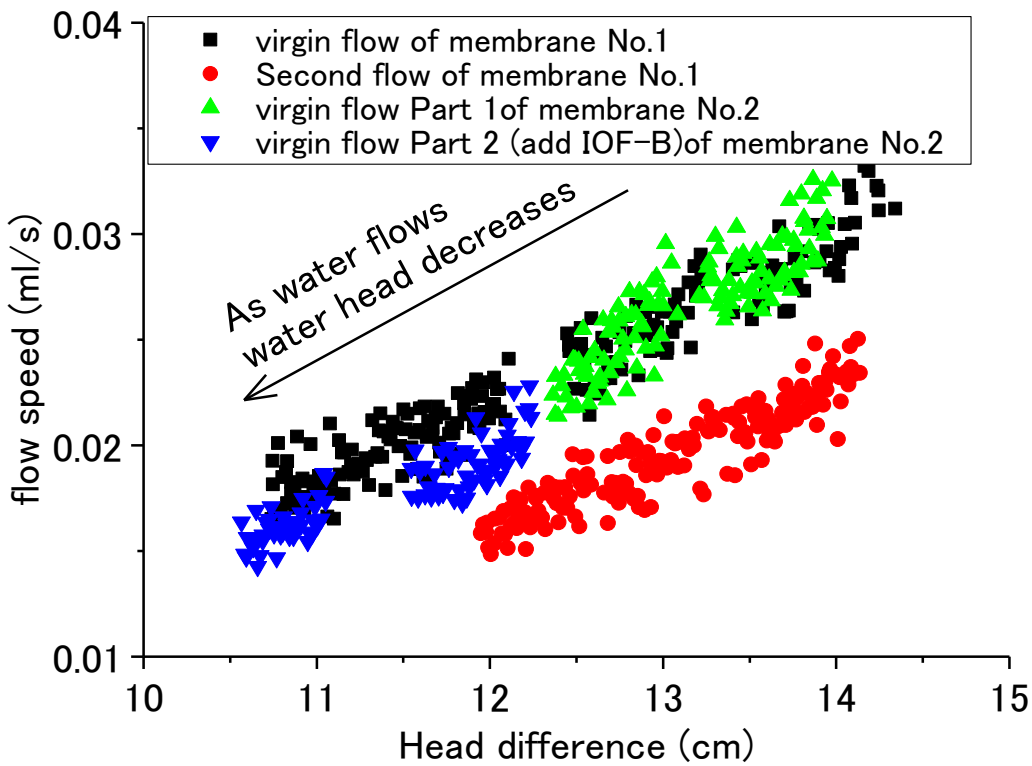

Fig.4-21 (a) Filter clogging problem

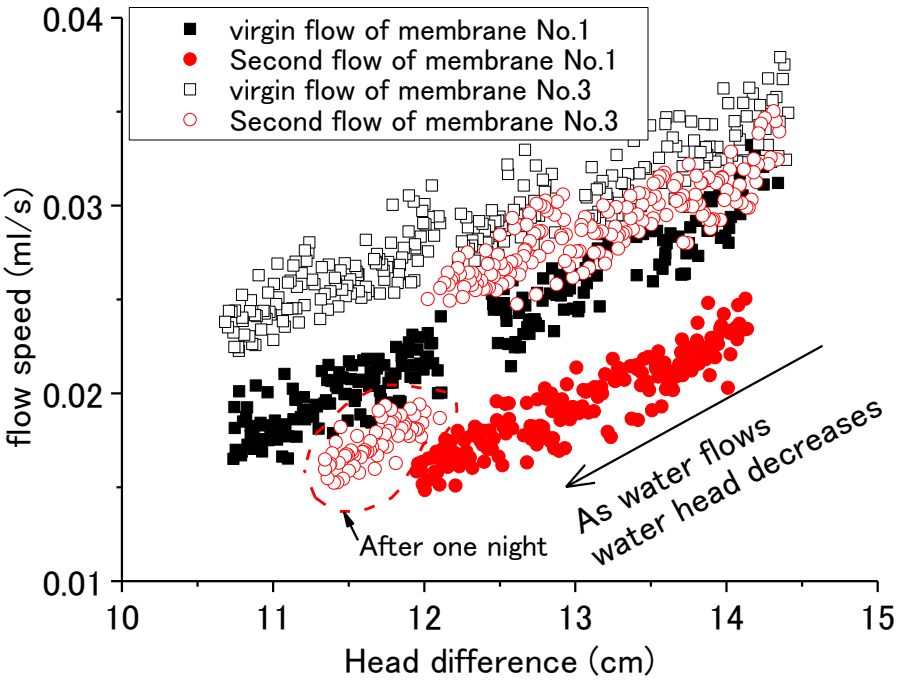

Fig.4-21 (b) Verification of filter clogging problem

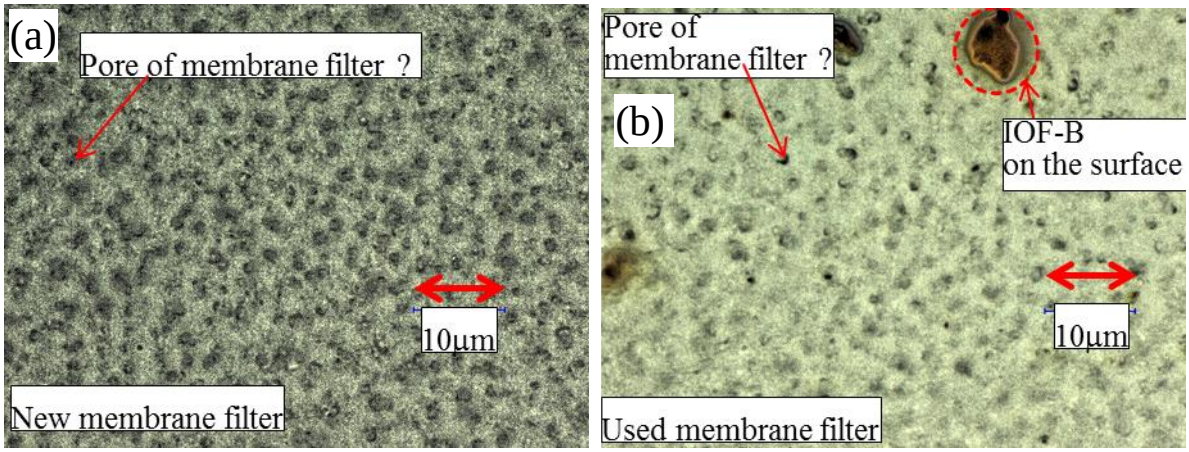

Fig. 4-22(a) New membrane filter (b) used membrane filter

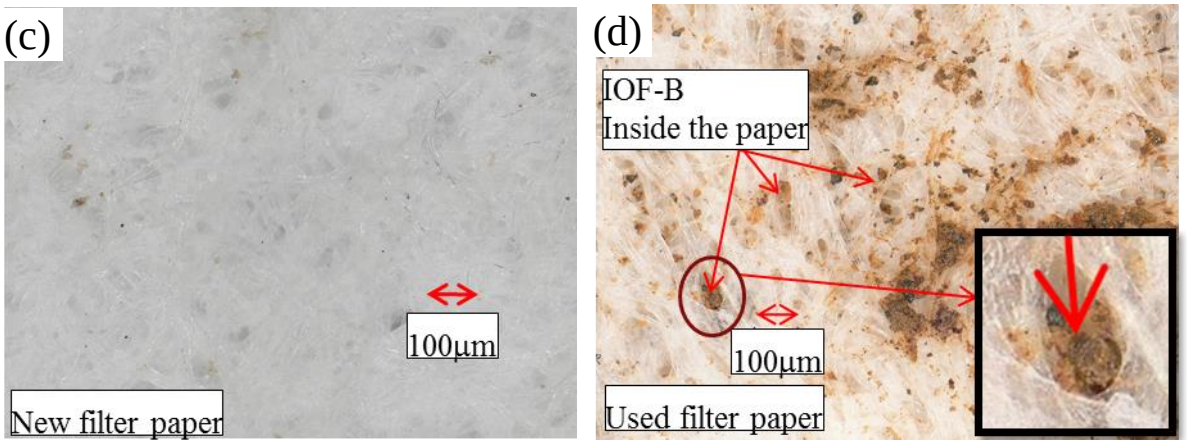

Fig. 4-22(c) New filter paper (d) used filter paper

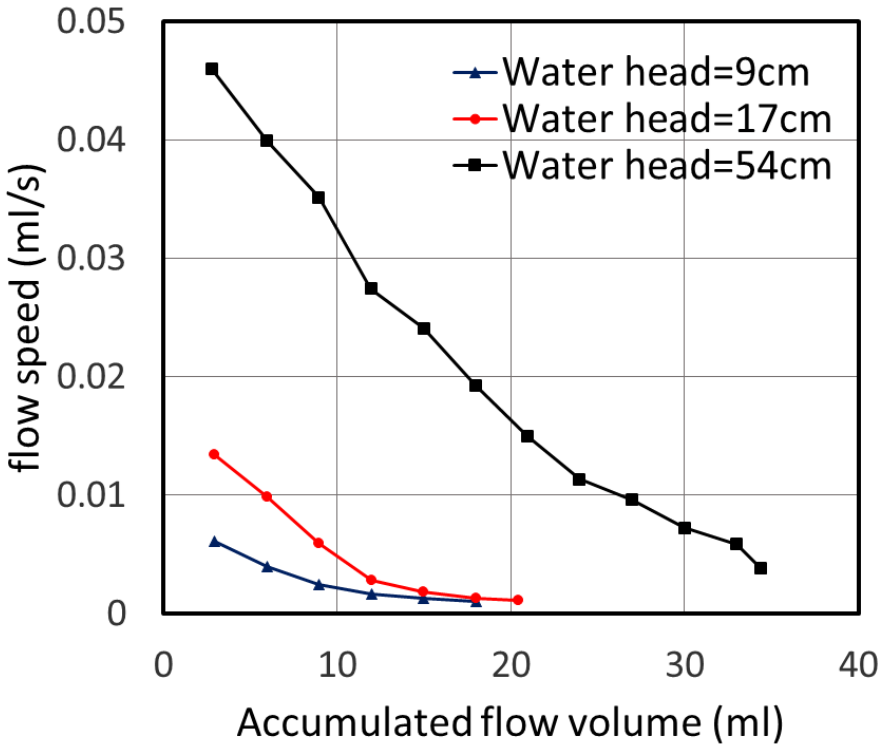

Fig. 4-23 (a) Relationship between flow volume and flow velocity

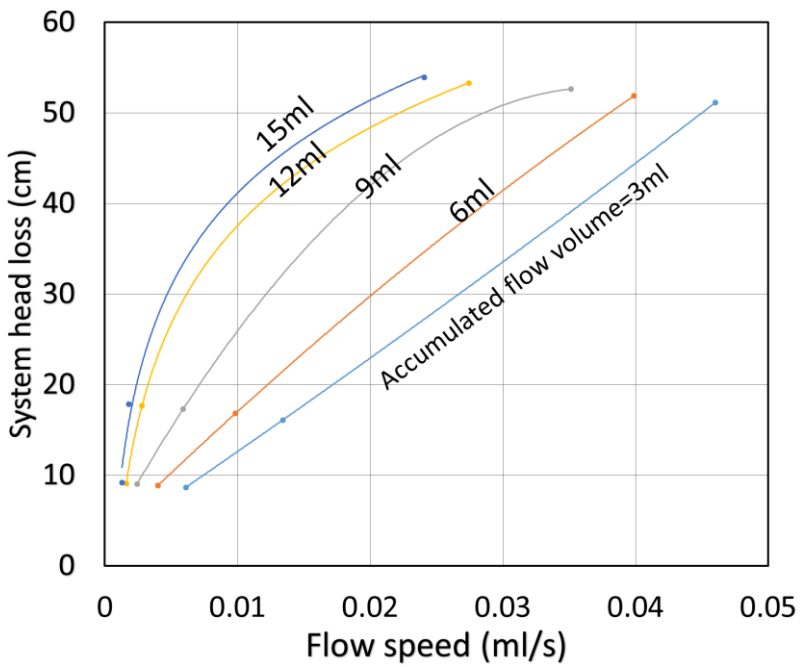

Fig. 4-23 (b) System head loss of set for unsaturated permeability test

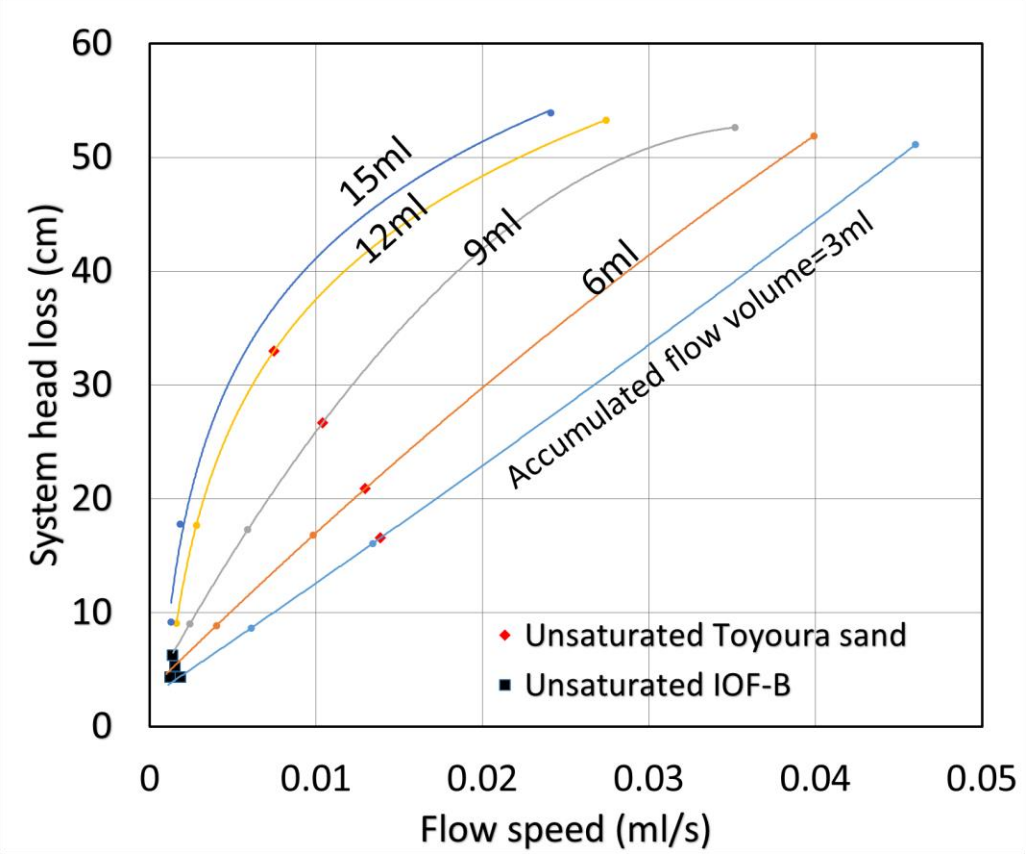

Fig. 4-24 System head loss estimation of unsaturated specimens

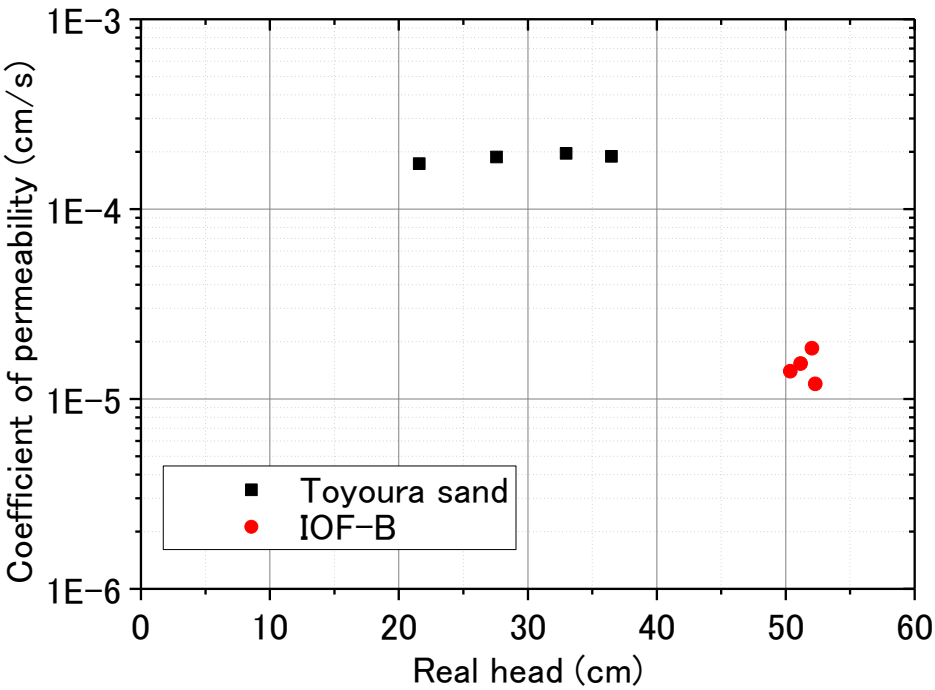

Fig. 4-25 Coefficient of permeability of unsaturated Toyoura sand and IOF-B

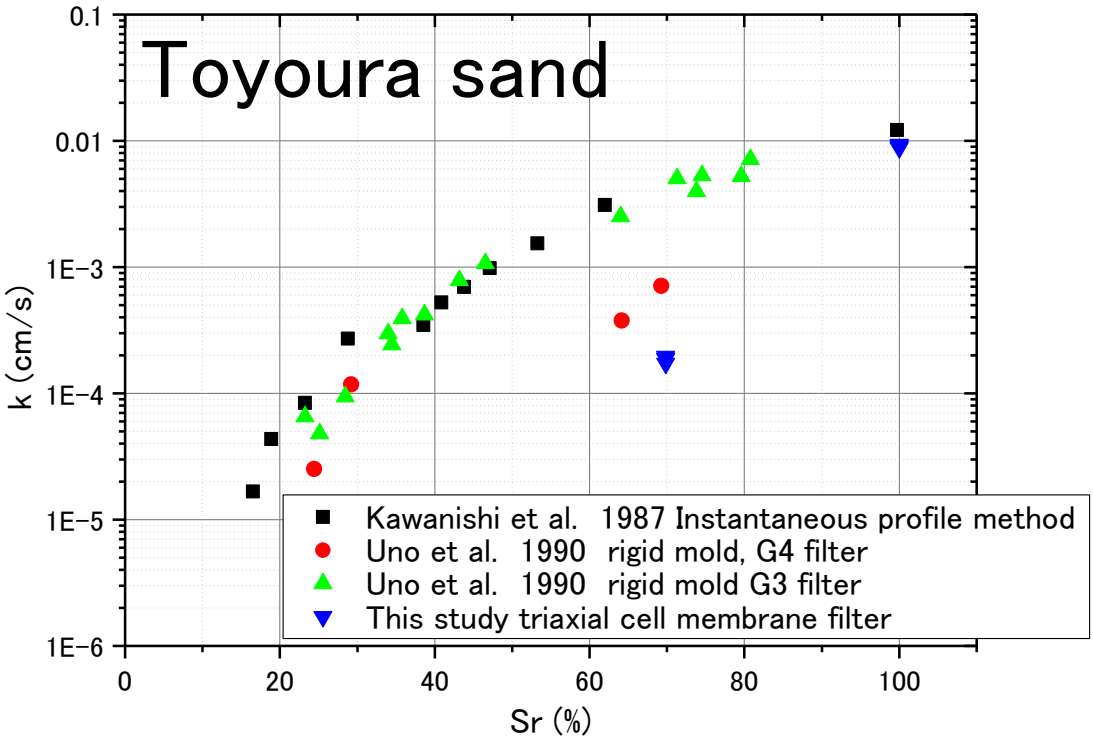

Fig. 4-26 Coefficient of permeability of unsaturated Toyoura sand

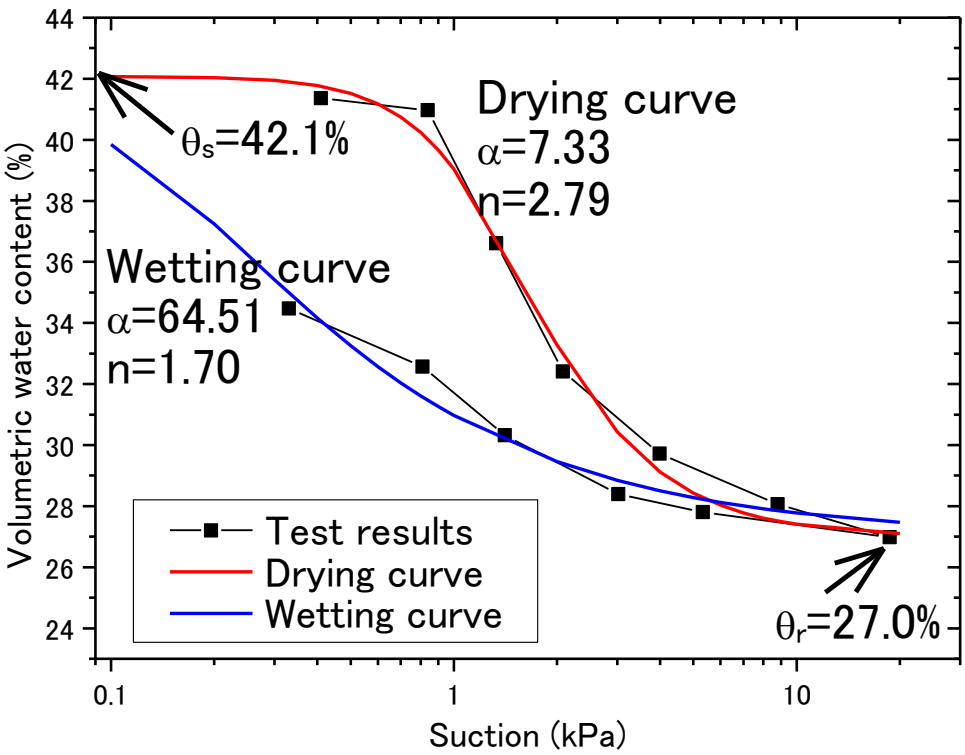

Fig. 4-27 Fitting SWCC by Van Genuchten model

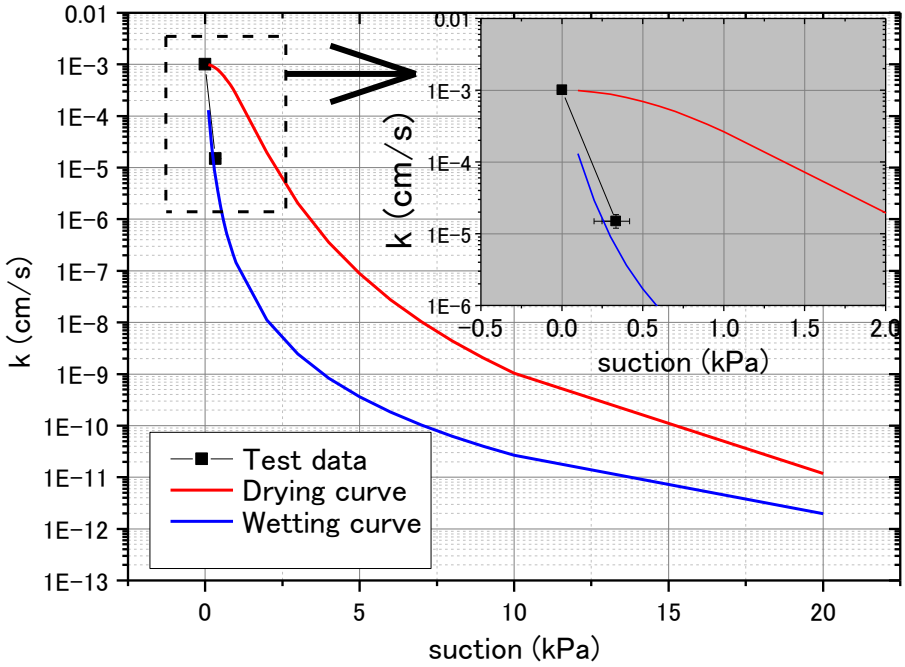

Fig. 4-28 Measured and predicted k values

Chapter 5 Undrained properties of saturated and unsaturated sandy soils

Contents

5.1 Introduction

In this chapter, the undrained properties of soil elements are studied. Three types of tests are described, namely undrained monotonic loading test, consolidation test and undrained cyclic loading test. Undrained monotonic loading tests were conducted on saturated iron ore fines type B (IOF-B) to understand its behavior under undrained conditions and to provide data for numerical analysis described in Chapter 7. Consolidation tests were carried out on saturated IOF-B, Inagi sand and Toyoura sand to find the volume change induced by change of confining stress and to link the volume change to liquefaction resistance. Undrained cyclic loading tests were performed on saturated and unsaturated IOF-B, Inagi sand and Toyoura sand to estimate the liquefaction resistance and to analysis the effects of degree of saturation (Sr) and fines content (Fc) on the liquefaction resistance.

The main purposes of these three types of tests were to: (1) try to find a parameter to explain the effects of degree of saturation (Sr) and fines content (Fc) on liquefaction resistance; (2) provide data to support the dynamic response analysis of the heap of iron ore fines under rolling motion.

5.1.1 Liquefaction

Liquefaction is a broad topic relating to many issues in geotechnical engineering, such as dam failure under static loading, level ground and slope deformation during earthquakes, ground collapse under ocean waves etc.

The terminology ‘liquefaction’ was defined by Castro et al. (1977) as a phenomenon wherein a saturated sand loses a large percentage of its shear resistance (due to monotonic or to cyclic loading) and flows in a manner resembling a liquid until the shear stresses acting on the mass are as low as its reduced shear resistance. A framework evaluating the resistance against liquefaction or liquefaction potential of the soils was established based on this concept (Poulos et al. 1985). The general idea of this framework was to establish a steady state line through the monotonic loading test, which indicates the relationship between void ratio, effective stress and shear stress of a soil. The steady state of the soil has a similar meaning to critical state (Roscoe et al. 1958; Sladen et al. 1985), both of which imply a unique state of the soil in which large deformation is driven by the small residual shear stress. Since monotonic tests are often performed to follow the framework, ‘liquefaction’ defined by Castro et al. (1977) is also sometimes referred as static liquefaction or static instability (Lade, 1993; Yamamuro and Lade 1997a, b and 1998; Vaid and Eliadorani 1998). It is important to distinguish the concept of

'liquefaction' from the concept of 'cyclic mobility'. The definition of cyclic mobility in Castro et al. (1977) is the progressive softening of the saturated sand specimen when subjected to cyclic loading at constant water content. The cyclic mobility often involves the increase in shear stress during development of shear strain, of which steady state is difficult to be defined. From this aspect, the 'liquefaction' defined by Castro et al. (1977) may also be referred to as 'flow liquefaction' (Yoshimine, 1999).

The concepts of "liquefaction" and "cyclic mobility" were also defined by Seed (1979) as:

"Liquefaction: *a condition where a soil will undergo continued deformation at a constant low residual stress or with low residual resistance, due to the buildup and maintenance of high pore water pressure, which reduce the effective confining pressure to a very low value; pore pressure buildup leading to liquefaction may be due either to static or cyclic stress applications and possibility of its occurrence will depend on the void ratio or relative density of a sand and the confining pressure; it may also be caused by critical hydraulic gradient during an upward flow of water in a sand deposit*".

"Cyclic mobility or Peak cyclic pore pressure ratio of 100% with limited strain potential: *a condition in which cyclic stress applications develop a peak cyclic pore pressure ratio of 100% and subsequent cyclic stress applications cause limited strains to develop either because of remaining resistance of the soil to deformation or because the soil dilates, the pore pressure drops, and the soil stabilized under the applied loads. Cyclic mobility may also be used in a broader sense to describe the cyclic straining that may occur even with pore pressure ratios less than 100% in which case the actual peak value of pore pressure ratio may simply be stated*".

These concepts (Seed, 1979) are mostly defined according to the undrained behaviors of the soils under cyclic loading. The corresponding evaluation procedure of liquefaction resistance was also established by Seed and Peacock (1971). The idea of this procedure is, through the undrained cyclic loading test, to relate the applied cyclic loading with the number of cycles which causes certain strain (liquefaction resistance curve), on which the liquefaction resistance of the soils can be defined. This procedure didn't particularly distinguish the difference between liquefaction and cyclic mobility and many well documented field tests were summarized in order to link this procedure to the evaluation of liquefaction potential of ground (Tokimatsu and Yoshimi 1983; Youd et al. 2001; Yang 2002; Hossain et al. 2013; Kayen et al. 2013).

Since understanding the responses of the heap of iron ore fines under cyclic motion is the objective of this study, the liquefaction potential of iron ore fines are evaluated according to the procedure proposed by Seed and Peacock (1971) in this study.

5.1.2 Effects of degree of saturation (Sr) and fines content (Fc) on the liquefaction property of soils

Many factors such as confining pressure, initial shear stress, density, Fc diagenetic processes (e.g. aging, cementation, stress history etc.) and Sr are believed to affect the resistance of soils against liquefaction. In this study, two factors, Sr and Fc are studied. For the effect of Sr, both laboratory (Sherif et al. 1977, Grozic et al. 2000, Bouferra et al. 2007) and field investigations (Okamura et al. 2006, Kayen et al. 2013) have been conducted. As far as the authors' knowledge, all literature indicates a higher resistance of the soils against liquefaction under unsaturated condition compared to fully saturated conditions. Many researchers have tried to uncover the key factors which gives unsaturated soils the resistance against liquefaction. Attempts were made on Sr (Yoshimi et al. 1989, Goto et al. 2002), pore-pressure coefficient B value (Yoshimi et al. 1989, Unno et al. 2008, Arab et al. 2011), wave velocity (Huang et al. 1999, Ishihara et al. 2001, Tsukamoto et al. 2002, Yang 2002 and Yang et al. 2004) and potential volumetric strain (Okamura and Sugo, 2006). The relationship between resistance against liquefaction and Sr are not unique even for the same soil as summarized by Okamura and Sugo (2006). Although B value and wave velocity (P-wave or S-wave), which can be closely related to pore water pressure generation by elasticity theory were thought to be a good indicator, it is difficult to measure them in relatively low Sr. For example under unsaturated conditions, B values dropped to 0.2 for Sr = 96% and 0 for Sr < 90% (Yoshimi et al. 1989, Ishihara et al. 2001). Okamura and Sugo (2006) proposed a parameter, potential volumetric strain, which is actually the theoretical maximum volumetric stain of pore air compression under the test conditions employed. This parameter shows a unique correlation with increase of liquefaction resistance of unsaturated Toyoura sand with Fc of 0.1% and soils with Fc < 5%. Since the Inagi sand and IOF-B used in this study contain a certain amount of fines, the verification of potential volumetric strain is examined for the soil with fines. The effect of fines content on liquefaction resistance of saturated soils have been studied extensively, however, a very good parameter has not been determined (Yamamuro and Covert, 2001; Monkul and Yamamuro, 2011; Nakazawa and Hradah, 2012). Since most tests in this study are focused on unsaturated soils, the effect of fines content is only discussed in Section 5.5.10.

5.2 General test procedures

Three types of tests, undrained monotonic loading test, consolidation test and undrained cyclic loading test are described in this chapter. In undrained monotonic loading test, only saturated specimens of IOF-B was tested. In the consolidation tests, saturated specimens of IOF-B, Inagi sand and Toyoura sand were tested. In the undrained cyclic loading tests, saturated and unsaturated specimens of IOF-B, Inagi sand and Toyoura sand were tested. To avoid confusion, details of some properties of the tested soils (which were addressed in Chapter 3) in this chapter are re-addressed.

Fig. 5-1 shows the gradation curves of IOF-B and Inagi sand.

IOF-B with a maximum particle size of 9.5 mm contains gravel, sand and fines content of 33%, 43% and 24%, respectively. Its Gs value is 4.444 and maximum dry density obtained from compaction test is 2.79 g/cm^3 with corresponding optimum water content ω_{opt} of 12%. In all tests on IOF-B in this chapter, compaction degree Dc, defined by Eq. 3.1 in Chapter 3, is used to show its density state.

Inagi sand passing through a 2mm sieve contains about 30% fines content. Its Gs, e_{max} and e_{min} values are 2.656, 1.96 and 0.91, respectively.

For the widely known clean Toyoura sand, its Gs, e_{max} and e_{min} values are 2.659, 0.99 and 0.63, respectively. The used Toyoura sand contains 0.1% fines content. For Inagi sand and Toyoura sand, relative density Dr (Dr= $(e_{max}-e)/(e_{max}-e_{min}) \times 100\%$) is used to represent their density state.

The methods for molding the specimen vary for different soils.

For IOF-B and Inagi sand, oven dried materials were first mixed with a certain amount of water (corresponding to approximately water content of 12% for IOF-B and 22% for Inagi sand) and cured for at least 24 hours before use. All specimens of IOF-B and Inagi sand were made by one dimensional compression in a constant volume mold. First, a pre-decided amount of wetted soil specimen was poured into a steel mold with an inner diameter of 50 mm. Then the soil was compressed from two sides of the mold by using two cylindrical steel blocks with slightly smaller diameters than the inner diameter of the mold. The specimens of Inagi sand and the loose specimens of IOF-B were easily shaped by this method, while it was difficult to shape the medium dense specimens of IOF-B. To achieve desired density, relatively uniform blows were applied to the two blocks iteratively using a wooden hammer.

For Toyoura sand, air pluviation and moisture tamping were used and the specific method used is addressed in Section 5.5.2. The dimensions of the specimens described in this chapter were 50 mm in diameter and 100 mm in height.

To saturate the specimens, the technique of CO_2 flushing followed by de-aired water flushing was applied to all Toyoura sand specimens, while the double vacuuming method (Tatsuoka 1987, Ampadu and Tatsuoka 1993) was applied to all IOF-B and Inagi sand specimens in this chapter. By applying back pressure after saturation, the specimens with b values higher than 0.95 are regarded as fully saturated. Treatment of the unsaturated specimens is introduced in Section 5.5.

5.3 Undrained monotonic loading tests on IOF-B

5.3.1 Test apparatus and methods

A triaxial apparatus with a strain control axial loading system was employed for the undrained monotonic loading tests. The strain rate was 0.1%/min. Tests were terminated either when the specimens achieved steady state where the specimens deformed under the constant deviator stress and the effective stress, or when the axial strain of the specimens surpassed a certain value, say 20%. Table 5-1 lists conditions of six tests on IOF-B, three of which are of medium dense condition and the other three are of loose condition

Table 5-1 Test conditions of undrained monotonic loading test on IOF-B

Test name	Void ratio e	Compaction degree Dc (%)	Confining pressure σ_0' (kPa)	q_{peak} (kPa)	p'_{peak} (kPa)	q_{res} (kPa)	p'_{res} (kPa)
UM_Mar19	0.734	92.0	50	379.0	195.8	283.2	143.0
UM_Mar18	0.682	94.9	100	516.4	270.6	401.8	202.5
UM_Mar24	0.679	95.0	200	621.0	335.6	481.7	244.4
UM_Apr25	1.173	73.5	50	5.6	17.6	4.1	7.0
UM_Apr23	1.106	75.6	100	13.1	35.4	10.0	13.9
UM_Apr27	1.224	71.8	200	22.3	63.7	18.3	28.8

Note: Void ratio e and compaction degree Dc are values after consolidation; q_{peak} and p'_{peak} are peak q value and the value of p' at peak q, respectively; q_{res} and p'_{res} are minimum residual q value and value of p' at minimum residual q, respectively.

5.3.2 Results for medium dense IOF-B specimens

Fig. 5-2 shows the stress paths and stress strain relationships of the three tests conducted on the medium dense IOF-B specimens. The dash lines in Fig. 5-2 (a) are q=3p' lines or total stress path in the triaxial test. Initially, all specimens show contraction properties (or negative

dilatancy) and positive pore water pressure is generated, while effective stress paths go or tend to go to the dilatant side with the increase in deviator stress q. However, the shear stresses drop to residual stress levels after passing the phase transformation line distinguishing dilative and contractive behaviors which is not usually observed for clean sands (Ishihara, 1993),. It seems that the dilative behavior is more apparent for the specimen under lower confining pressure, which is consistent with classical studies on steady state for clean sand (e.g. Ishihara, 1993).

For the peak shear stress (or peak deviator stress q_{peak}) and residual stress, both increased as the confining pressure increased. The peak deviator stresses (q_{peak}), residual deviator stresses (q_{res}), and p'_{peak} and p'_{res}, which are the effective mean principal stress at q_{peak} and q_{res}, respectively, are listed in Table 5-1. For the stress stain relationship under medium dense condition, as shown in Fig. 5-2 (b), all the specimens display softening behavior as the shear stress reduced after the peak shear stress. Interestingly, the values of axial strain at which the peak shear stresses are achieved are similar (axial strain = 2.5%) for the three tests. Moreover, the residual shear stresses at residual state are achieved also at similar values of axial strain, approximately starting from 13%.

The normalization method described by Sladen et al. (1985) was applied to the three test results of medium dense IOF-B to attempt to find the collapse line. Both q and p' were normalized by p'_{res}. The normalized stress paths and stress strain relationships are shown in Fig. 5-3. Interestingly, after normalization, the peak deviator stress $(q/ p'_{res})_{peak}$ and residual deviator stress $(q/ p'_{res})_{res}$ converge to one point for the three tests with different confining pressure. The collapse line is drawn with a slope M_L of 1.6. For normalized stress strain curves in Fig. 5-3 (b), all three curves are very similar, which implies that for the medium dense IOF-B, q/ p'_{res} may govern the vertical deformation behavior under undrained condition.

5.3.3 Results for loose IOF-B specimens

Effective stress paths and stress strain relationships of the saturated loose specimens of IOF-B are plotted in Fig.5-4 in a similar manner as those of the medium dense specimens. The loose specimens show extensive contractive behavior and there is no sign of turning to the dilatant side. Similar to the medium dense specimens, the increase in confining pressure raises both peak shear stress and residual shear stress. For the stress strain relationship, the peak deviator stress and residual deviator stress were achieved at around 1% and 10%, respectively, earlier than those of the medium dense specimens. The normalized relationships are depicted in Fig.

5-5. A collapse line with a slope of 0.2 is obtained and normalized stress strain relationships (Fig. 5-5b) of the three specimens roughly converge.

5.3.4 Discussion

As illustrated in Section 5.3.2, the normalized effective stress path at the peak and residual points seem not to be affected by confining stress and the stress strain relationship seems to be governed by normalized deviator stress and density. Though only limited data are available from this test program, a rough prediction for the undrained behavior of the saturated IOF-B specimens under monotonic loading was made, as shown in Fig. 5-6. For the stress path of IOF-B, at medium dense condition, IOF-B still shows contractive behavior although it may turn to the dilatant side. If the density of the IOF-B specimen is reduced, the contraction property may prevail. Meanwhile, the normalized peak and residual deviator stresses may consequently reduce, namely the specimen may become weaker to resist shear stress. On the other hand in Fig. 5-6 (b), as the density reduces, the axial strain where the peak shear stress is achieved appears earlier. Moreover, the normalized peak deviator stress, after which the large deformation may develop suddenly under a smaller shear stress, may reduce significantly.

5.4 Isotropic consolidation tests

5.4.1 Test apparatus and methods

The stress strain relationship is always one of the most fundamental properties for geotechnical engineers. Though in the undrained test, there is no apparent volumetric strain for the saturated specimen if the compressibility of pore water and system compliance are ignored, the volumetric strain caused by shear ($\varepsilon_{vol,shear}$) and volumetric strain caused by change in effective confining pressure ($\varepsilon_{vol,p'}$) are believed to be with the different mechanisms. $\varepsilon_{vol,shear}$ is induced by the dilatancy property of the soil, while $\varepsilon_{vol,p'}$ is attributed to ambient pressure. In this section, the isotropic consolidation tests including the loading and unloading process for three materials, IOF-B, Inagi sand and Toyoura sand are discussed to understand the difference in $\varepsilon_{vol,p'}$ for the different materials and for the same material with various densities.

The test was conducted on a triaxial apparatus. All specimens were fully saturated under low confining pressure (5 kPa for one of the tests on Toyoura sand and 20 kPa for the remaining tests). For each test, isotopic confining pressure was increased or decreased stepwise. The increment of each step was either 5 kPa or 10 kPa. After one loading or unloading step, 120 minutes for IOF-B specimens and Inagi sand, and 30 minutes for Toyoura sand were set for the

consolidation process. The confining pressure was controlled by an E/P control system and it was monitored by a differential pressure transducer (DPT), by which the confining pressure can be precisely adjusted (the adopted tolerance was ± 0.2 kPa). The vertical loading was regulated by a mechanical loading system, which can easily control the vertical loading with a tolerance of ± 0.1 kPa. Drainage was always allowed during loading or unloading. Volume change in the specimens was measured by a calibrated burette and another DPT.

Table 5-2 lists the test conditions in the test program. The specimen preparation process and saturation process are introduced in Section 5.2. Particularly for the Toyoura sand specimens with different densities, two methods of molding the specimens were applied. For the specimen C_T_Apr2, the air pluviation method was used. In order to make the C_T_Apr15 specimen with very loose condition, the moisture tamping method was used following the descriptions of Ishihara (1993). The pre-wetted Toyoura sand with water content 5% was placed in a constant volume mold in 10 layers, careful tamping was applied to each layer to achieve the desired dry density.

Table 5-2 Test conditions of isotropic consolidation test

Test name	Void ratio e at p'_{max}	Compaction degree Dc/ Relative density Dr (%)	Maximum confining pressure p'_{max} (kPa)	$\varepsilon^{e}_{vol,0.1p'}$ (%)
C_T_Apr2	0.707	Dr 79.2	60	0.33
C_T_Apr15	0.982	Dr 2.8	60	0.47
C_IOF-B_Apr5	0.728	Dc 92.3	100	0.79
C_IOF-B_May7	0.726	Dc 92.4	50	0.73
C_IOF-B_Apr23	1.111	Dc 75.6	100	1.25
C_IOF-B_Apr18	1.137	Dc 74.7	50	1.54
C_ING_Apr7	1.171	Dr 64.3	60	1.37

XX in test name, C_XX_: stands for material of the tests. T: Toyoura sand; ING: Inagi sand; IOF-B: iron ore fines type B. Void ratio e, Dc and Dr are the values after consolidation by maximum confining pressure (p'_{max}).

5.4.2 Results

Fig. 5-7 shows the typical time histories of measured volume change, effective mean principal stress p' and deviator stress. Relatively large volume change was observed during the loading process when confining pressure was relatively low. Very small volume change was measured at the early stage of the unloading process, while relatively large volume change with high fluctuation was observed in the later stage of the unloading process (e.g. p'< 20 kPa). The results imply that the volume change is very sensitive under low confining pressure.

Fig. 5-8 (a) shows the typical relationship between applied confining pressure and volumetric strain obtained in each step. To calculate the volumetric strain, the volumes of the specimens after consolidation at the maximum confining pressure (point A in Fig 5-8 a) was used, thus

volumetric strains are negative values for both the loading and unloading curves. As can be seen from Fig. 5-8 (a), the shapes of the loading and unloading curve are very different from the loading curve being an almost straight line while the unloading curve is curved. The elastic volumetric strain ($\varepsilon^{e}_{vol,p'}$) and plastic volumetric strain ($\varepsilon^{p}_{vol,p'}$) caused by the change in confining pressure are defined according to the loading and unloading curve, as shown in Fig. 5-8 (a). The main purpose of the test program is to compare the difference in the volumetric strain induced by the change in confining stress for the different soils. To do so, the confining pressure is normalized by the maximum confining pressure at point A (p'_{max}), as shown in Fig. 5-8 (b).

The loading curves of all seven tests conducted on the three types of soils are plotted in Fig. 5-9. The loading curves are generally straight lines. The dense Toyoura sand specimen has the lowest volumetric strain during loading and the difference in the volumetric strain between the dense and loose Toyoura sand specimens is very small compared with that of the dense and loose IOF-B specimens. The volumetric strains of the medium dense IOF-B specimens are similar with that of the loose Toyoura sand. The loose IOF-B specimen displays larger volumetric strains than the dense IOF-B specimens. The largest volumetric strain during the loading process is observed for the Inagi sand.

The unloading curves of the consolidation tests are shown in Fig. 5-10. For most tests, the minimum confining pressure in the unloading process was kept to 3 kPa, while for some cases it may be lower than 1 kPa. Under very low effective stress, irregular deformation (collapse) of the specimens was observed. Thus, in order to not introduce unnecessary error, this discussion is only focused on the range where p'/p'_{max} is larger than 0.1. It seems that the volumetric strain of Toyoura sand is very low level regardless of density compared with the other materials. While for the medium dense IOF-B specimens, volumetric strain in the unloading process becomes much higher than that of the loose Toyoura sand specimen. In addition, the volume change in Inagi sand is still very high in the unloading process.

The results of this test program imply that the volumetric strain induced by the change in confining pressure may be significantly different for different soils. The unloading process in this test is similar with the process in the undrained cyclic loading test. In this test, the effective stress was decreased by reducing the confining pressure; in the undrained cyclic loading test, the effective stress was decreased by the generation of excess pore pressure. Though the reduction in effective stress is caused by a different loading pattern (monotonic or cyclic

loading), the values of $\varepsilon^{e}_{vol,p'}$ obtained in this program may generally represent the $\varepsilon^{e}_{vol,p'}$ induced during the undrained cyclic loading test. Since the values of $\varepsilon^{e}_{vol,p'}$ are not available when p' reaches zero, the values of $\varepsilon^{e}_{vol,0.1p'}$, which is the $\varepsilon^{e}_{vol,p'}$ when p'/p'_{max} reaches 0.1 as indicated by the red dash line in Fig.5-10, are summarized in Table 5-2 to indicate the magnitude of the volumetric strain caused by the reduction in effective stress.

5.5 Undrained cyclic loading test

5.5.1 Test apparatus

A specially designed triaxial apparatus was employed to carry out tests on the specimens with saturated and unsaturated conditions. While detailed information on the apparatus is given in Chapter 2, some important points of the apparatus are repeated herein. Fig. 5-11 is a duplication of Fig. 2-5 in Chapter 2. The pore water pressure (PWP) was measured by a pressure transducer through the pedestal on which the membrane filter was used instead of a traditional ceramic disk (for details of the membrane filter see Appendix B). Pore air pressure (PAP) was measured through the top cap, on which a hydrophobic filter was glued to avoid pore water entering the pore air pressure measurement system. The volume change in the unsaturated specimen subjected to undrained loading was measured by the double cell system, which measures the overall volume change in the specimens (See Appendix C for details of the double cell system). Vertical cyclic loading with a frequency of 0.1 Hz was applied by the pneumatic loading system. Another pneumatic pressure control system (cell pressure control system) was used to keep the total mean principal stress (p) constant.

5.5.2 Test methods

The soils tested in this test program were Toyoura sand with fines content (Fc) of 0.1%, Inagi sand with Fc of 30% and IOF-B with Fc of 24%. The general test conditions are summarized in Table 5-3. All the tests were divided into three series (Series 1, Series 2 and Series 3) according to the type of soil. Tests in each series were again divided into groups (Group1, Group 2…) accord to the confining pressure of the tests and finally the tests in each group were further divided into sets (Set1, Set2…) according to density conditions. In the column of the test name in Table 5-3, the characters UC_T, UC_ING or UC_IOF-B are the first characters of the name of the individual test, which indicates the test type (undrained cyclic loading test) and the test name of the tested soil, as shown in the brackets of the first column of Table 5-3. The second and third columns are the initial confining pressure and the average density indicators after consolidation, respectively. Both the saturated and the unsaturated tests were conducted

in each set of test, of which cell pressure was constant (total mean principal stress, p, changed) during the application of vertical loading for the saturated tests. While p was kept constant by employing the cell pressure control system for most cases during vertical cyclic loading. The states of p during vertical cyclic loading are indicated by circles in Table 5-3. The solid circles means p-changed condition and hollow circle means p-constant condition. The red solid circle indicates a special case, in which the p-changed condition was applied to the unsaturated specimens. The symbol σ_0' stands for the (final) consolidation stress before applying cyclic loading. The specimens may be consolidated during setting up the test or preparation for saturation etc. with a small confining pressure. However, σ_0' hereafter will be termed 'initial confining pressure' or 'initial consolidation stress'. The σ_0' specified in the results Section 5.5.4 is the more accurate value for each individual test, while the values of σ_0' listed in Table 5-3 are the designed or desired value before conducting the tests. Those in the column "R_L" and "LRR" are defined in the later sections.

The methods of making the specimens have been described in Section 5.2, while some other issues specific to this test program are addressed herein. In test program Set 1, the saturated Toyoura sand specimens were made by the air pluviation method, while the moisture tamping method was employed for the unsaturated specimens. The main concern of changing the method for the unsaturated specimens was that the air pluviation method may affect the saturation condition of the membrane filter fixed on the pedestal since extremely large suction in dry sand may absorb water in the initially saturated membrane filter in a very short time and induce cavity in the membrane filter. However, possible effect on liquefaction resistance by the means of preparation methods of the specimen (Mulilis et al 1977) was not examined in this study. For the moisture tamping method used for the unsaturated specimens in Set1 (medium dense condition), pre-wetted Toyoura sand with an initial water content of 17.5% was compacted by five layers in the mold. Some extra water was injected later to the specimen to increase its Sr. As the water injection process may affect water distribution in the specimen, a relatively high initial water content (17.5%) was chosen to prepare the specimen. It should be noted that, if the initial water content was further increased, water may flow out from the specimen because of reduction in suction.

Table 5-3 Summary of test conditions

Test name	σ_0' (kPa)	Dr or Dc (%)	Sr (%)	p	R_L	LRR
Series 1 UC_T (Toyoura sand)	Group1 60	Set1 Dr: 65	100	●	0.160	1
			91	○	0.351	2.19
		Set2 Dr: -4	100	●	0.079	1
			79	○	0.221	2.78
Series 2 UC_ING (Inagi sand)	Group2 60	Set3 Dr: 64-78	100	●	0.140	1
			84	○	0.202	1.44
			73	○	0.267	1.91
			69	●	0.252	1.80
Series 3 UC_IOF-B (IOF-B, iron ore fines type B)	Group3 100	Set4 Dc: 93	100	●	0.315	1
			84	○	0.475	1.51
			72	○	0.546	1.73
		Set5 Dc: 81	100	●	0.131	1
			76	○	0.201	1.66
	Group4 50	Set6 Dc: 93	100	●	0.337	1
			77-82	○	0.529	1.57
		Set7 Dc: 80	100	●	0.120	1
			71	○	0.200	1.67

In test program Set 2, extremely loose specimens were made by the moisture tamping method for both saturated and unsaturated specimens. The initial water content of pre-wetted Toyoura sand was 5%. Trial tests show that Toyoura sand with 5% water content can achieve a very loose state, thus it is relatively easy to make the loose specimens with uniform density. They were molded in the mold which was fixed on the pedestal of the apparatus and the procedure is similar to that described in Section 5.4.1.

For the saturation process of the specimens, the method used, which are described in Section 5.2, depended on the tested soils. For tests on the unsaturated specimens, the Sr value of 72% in Set 4 corresponds to the initial water content (12%) of IOF-B during the making of the specimens, while for all the other cases extra water was injected into the specimens to increase their Sr values. In the case of Inagi sand in Series 2, extra water was placed on the top of the specimen and then the open side of the mold was covered by plastic wrap. The specimen was cured for one night in order to create uniformity of water distribution in the specimen. This method can accurately create the specimen with the desired water content. However, a limitation of this method is that the amount of water added to the specimen cannot be higher than a certain value otherwise it won't be retained by the specimen because of loss of suction. When the suction in the specimen reduced to a certain level, water in the specimen may flow out. To overcome the limitation of this method, for the unsaturated Toyoura sand specimens in

Series 1, after setting up the apparatus and applying small confining pressure to the specimen, water was injected from the valve connecting the pedestal and received from the valve connecting to the top cap until no air bubbles were observed in the water flow paths. A relatively high water content can be achieved by this method, while water content could not be controlled to the value desired. Test results show that the Sr value after water injection by this method depends on the density of the specimens, for which the denser the specimens, the higher the Sr value can be achieved. According to this finding, the unsaturated IOF-B specimens in Series 3, except the case in Set 4 with Sr of 72%, were first consolidated under the confining pressure listed in the 2nd column of Table 5-3 and then water was injected into the specimens by the same means applied to the specimens in Series 1.

Considering the extremely loose condition for specimens in Set 2, the volume change in the specimens during saturation or during water injection was taken into account by measurement of the double cell system, which was prepared for measurement of volume change in the unsaturated specimens during undrained cyclic loading. Besides, since the particle size of IOF-B is relatively large and under very loose condition such as the specimens in Set 5 and Set 7, the membrane usually penetrates to the specimens under certain confining pressure. The membrane penetration results in an uneven surface of the specimens, which makes it difficult to measure the initial diameter of the specimens by Pi-tape. Thus, the diameters of the specimens in Set 5 and Set 7 were measured under 'zero' confining pressure (the confining pressure applied by membrane was not considered) and the change in volume of the specimen after applying confining pressure was taken into account through measurement of the double cell by the same means applied to the specimen in Set 2.

5.5.3 Terminology and Formulations

Terminology and formulations used for calculation include:

1. Deviator stress q: Output of load cell divided by the area of the specimen after consolidation under σ_0'.
2. Total mean principal stress p: $p=q/3+p_{cell}$, where p_{cell} is the cell pressure measured from the cell pressure transducer.
3. Effective mean principal stress p'=p-PWP: In the saturated test, it is a common definition to represent the mean value of the effective stress. In the unsaturated test, it is used to represent the difference between the total mean stress p and pore water pressure PWP.

4. Net mean principal stress p-PAP: The difference between total mean principal stress p and pore air pressure PAP.
5. Suction: It equals to PAP minus PWP.
6. Axial strain ε_a: Change in height divided by height after consolidation.
7. Measured volumetric strain $\varepsilon_{vol,m}$: Calculated according to data measured by the double cell system and the vertical displacement transducer (for details of the calculation method, see Appendix C). The volume used for calculation is the volume of the specimen after consolidation under σ_0'.
8. Theoretical volumetric strain $\varepsilon_{vol,air}$: represents the volumetric strain calculated from measured data of PAP based on the Boyle's law. Strictly speaking, this value is the theoretical volumetric strain of the specimen caused by air compression. PWP was used for the calculation when PAP was not available. Its maximum value, $\varepsilon^*_{vol,air}$, for one specific test is calculated by assuming that PAP is equal to the cell pressure.
9. CSR: Cyclic stress ratio, CSR=$\sigma_d/2\sigma_0$', σ_d is single amplitude of the cyclic loading.
10. $N_{DA=5\%}$: Number of cycles that causes double amplitude of 5% of axial strain.
11. R_L is evaluated resistance against liquefaction which is defined as the value of CSR which causes 5% double amplitude of axial strain of the specimen at 20th cycle.

5.5.5 Typical test results

In this section, typical time histories, effective stress path, stress strain relationship, etc. in each set of tests are presented. In Appendices E, F and G, time histories, stress strain relationship etc. are plotted for each individual test. There is a basic information bar of each individual test at the bottom of each figure showing in the section and in Appendices E-G which includes the test name, confining pressure (σ_0'), cyclic stress ratio (CSR), relative density (Dr) or compaction degree (Dc) and degree of saturation (Sr). The name of the test shown in the information bar is unique for each individual test, through which more details can be found in Tables at the beginning of Appendixes E, F and G.

1. Toyoura sand, Set 1 (Dr = 65%)

Figs. 5-12 and 5-13 are typical results of tests on Toyoura sand in Set 1. The behavior of both the saturated and the unsaturated specimens are rather similar, for example, the PWP increases gradually and axial strain biases to the extension side under the cyclic loading. Cyclic mobility was observed with both specimens, of which the shear stress increases along the failure envelopes after reaching the state of initial liquefaction (i.e., p'=0 kPa). However, the slope of

failure envelopes slightly decreased for the unsaturated specimen as shown the red lines in the plots of stress path. Another difference that can be observed is that there is a sudden jump in PWP, axial strain and effective mean stress for the saturated specimen when the p′ value reduced from its initial value by about two thirds, which is not observed in the unsaturated case.

2. Toyoura sand, Set 2 (Dr = -4%)

Figs. 5-14 and 5-15 are typical results of Toyoura sand in Set 2, for the specimens with extremely loose condition. From the stress strain relationship in Fig. 5-14 (b), liquefaction or flow liquefaction is observed, of which resistance against shear stress apparently didn't increase during the development of axial strain. In the case of cyclic mobility, deviator stress q may increase in the manner as shown by the red arrow. On the other hand, the decrease in Sr may induce the change of behavior from liquefaction to cyclic mobility compared with the stress strain relationships of the unsaturated case in Fig. 5-15 (b). This comparison implies that Sr may be a factor that affects the behaviors of liquefaction and cyclic mobility.

3. Inagi sand, Set 3 (Dr = 64-78%)

Fig. 5-16 and Fig. 5-17 depict typical results of Inagi sand in Set 3. Similar behaviors with those discussed for Toyoura sand are observed such as the progressive deformation and the fact that dilatancy behavior becomes more apparent for the unsaturated specimen than those of the saturated specimen. While unlike the case of unsaturated Toyoura sand, for the unsaturated specimen of Inagi sand, the net mean stress (p-PAP) didn't reduce to zero.

4. IOF-B, Set 4 and Set 5 (Dc = 93% and 81%, respectively)

For IOF-B, the conditions between Group 3 (σ_0' = 100 kPa) and Group 4 (σ_0' = 50 kPa) are very similar, and thus, representative plots are only shown for Set 4 and Set 5 in Group 3 in Figs. 5-18~5-21. Similar as the medium dense Toyoura sand, behaviors of the medium dense IOF-B specimens (Dc = 93%) shows dilatant behavior for the saturated and unsaturated specimens (Figs. 5-18 and 5-19, respectively). While for the unsaturated case, extension failure was observed during the test, of which the specimen broke into two parts from the middle height as indicated by the sudden change of the axial strain in Fig. 5-19. For the loose IOF-B specimens, it seems that the stress stain relationship is closer in behavior to liquefaction rather than cyclic mobility. Even for the unsaturated case, the dilatant behavior is not very apparent (Figs. 5-20 and 5-21).

5.5.6 Effect of change of p during cyclic loading

The change in pore water pressure (ΔPWP) of the soil specimen in the triaxial system with undrained condition can be expressed as:

$$\Delta PWP=B\,[\Delta\sigma_3+A\,(\Delta\sigma_1-\Delta\sigma_3)]=B\,[\Delta p+(A-1/3)\,\Delta q] \qquad \text{(Eq.5-1)}$$

where, A and B are pore pressure coefficients (Skempton, 1954); $\Delta\sigma_1$, $\Delta\sigma_3$, Δp and Δq are the change in major principal stress, minor principal stress, total mean principal stress and deviator stress, respectively. Eq. 5-1 implies that excess PWP can be generated by both normal stress (e.g. p) and shear stress (e.g. q). The undrained cyclic loading test carried out in this study is to understand the soils behavior under the shear stress, for instance, the change in excess PWP and the change in effective stress induced by cyclic shear stress. It is desired to study the effect of shear stress on the effective stress without involving any other variables. The change in effective stress can be written as:

$$\Delta p'=\Delta p-\Delta PWP=(1-B)\,\Delta p-B\cdot(A-1/3)\,\Delta q \qquad \text{(Eq. 5-2)}$$

For the saturated specimens, the value of B is very close to unity and any change in Δp will not significantly affect the effective stress according to Eq. 5-2, while for the unsaturated specimens, its B value is usually much smaller than unity (The B values measured in this study for extremely loose Toyoura sand in Set 2 are near 0.1, more details are shown in Table E-2 in Appendix E). For very small B values, any change in Δp will directly result in a change in effective stress (e.g. Δp') according to Eq. 5-2, which is not desired. In order to eliminate the effect of Δp for the unsaturated specimens, the cell pressure, p_{cell}, was controlled to change simultaneously as illustrated in Fig. 5-22 by employing the cell pressure control system.

Cell pressure was controlled to maintain a p-constant condition for all unsaturated tests except those conducted on Inagi sand with a Sr of 69% in Set 3. Figs. 5-23~5-25 show stress paths and strain histories of three typical tests in Set 3 for the saturated specimen with p-changed (Fig. 5-23) , the unsaturated specimen with p-changed (Fig. 5-24) and the unsaturated specimen with p-constant (Fig. 5-25), respectively. The slope angles of peak to peak stress paths (blue lines) of saturated specimen and the unsaturated specimen with p-constant condition are larger compared with that of the unsaturated specimen with p-changed condition. A failure line (red double line) is drawn from the compression side of the saturated specimen and the angle of internal friction of 39.2° is obtained. The friction angle is assumed to be valid regardless of stress directions (compression or extension) and saturation conditions, etc. for the three tests.

According to Mohr-Coulomb failure criterion, failure lines were drawn in all three stress paths. Red solid circles in figures indicate effective stress, after which the stress paths touched or nearly touched the failure lines for the first time at the next appeared peak shear stress, as indicated by the red arrows. It shows that the stress paths always firstly touch the failure line on the extension side and followed by the compression side, which explains why the axial strain on the extension side for the three tests always developed faster than that on the compression side as shown in Fig. 5-23(b) ~5-25 (b). However, the effective stress (red solid circle) prior to touching the failure line on the extension side is larger for p-change condition of the unsaturated specimen (Fig. 5-24a) than the ones with p-constant condition (Fig. 5-25a). When the stress path approaches the failure line, relatively large strain will normally be triggered. If the liquefaction resistance is defined based on the deformation, the resistance of specimen with p-changed condition may be lower than the specimen with constant p because the former case may touch the failure line earlier. In addition, for the saturated specimen and the unsaturated specimen with p-constant condition, the two red solid points are very “close” (within one stress cycle) while they are “far” (several stress cycles) for the unsaturated specimen with p-change condition. These observations explain that the axial stain is relatively uniformly developed in Figs. 5-23(b) and 5-25 (b), while it biases to the extension side significantly in the earlier stage for case in Fig. 5-24(b).

5.5.7 Suction and its effect on effective stress

PWP and PAP were usually measured for the unsaturated tests before and during the application of cyclic loading, while because of the limitation in the ways of increasing the water content of the unsaturated specimens introduced in Section 5.5.2, PAP was not always properly measured. The main reason for this is that water may enter into the PAP measurement system when the water content is too high or water may enter the PAP measurement system during the water injection process. Typical measurements are described in this section to illustrate the performance of the membrane filter technique (Nishimura et al., 2012) on the measurement of PWP and to study the effect of suction on effective stress.

Figs. 5-26 (a) and (b) show the typical measurements of PAP and PWP as well as the calculated suction before applying cyclic loading for the tests in Set 3 (Inagi sand) with Sr of 69% and 84%, respectively. For the case with low Sr (Fig. 5-26a), it can be seen that the suction value is very stable and only a slight change is induced by consolidation. On the other hand, for the case with high Sr (Fig. 5-26b), the measured pore pressures are rather stable before

consolidation, while PWP increases rapidly with increasing cell pressure. During consolidation of the unsaturated specimens of Inagi sand, only pore air is allowed to drain, during which, as the air volume in the specimen reduces, suction may gradually vanish. On the other hand, some pore water may drain out from the pore air drainage path, which may block the air drainage path resulting in PWP increase. In many cases with relatively high Sr (not only restricted to Inagi sand), a positive PWP value was observed, which may be due to a similar reason.

It would be interesting to compare the suction values measured during or before consolidation (H indicated in Fig. 5-26) with SWCC measured by pressure plate apparatus. SWCCs of Inagi sand were measured by both the membrane filter apparatus and ceramic disk apparatus. The SWCCs together with suction measured by the triaxial apparatus are plotted in Fig. 5-27. The SWCCs measured by the membrane filter apparatus and the ceramic disk apparatus are consistent, which is also concluded in Chapter 4. It is interesting that all suction values for the unsaturated specimens of Inagi sand measured on the triaxial apparatus distribute along the wetting curve of SWCC. This may be resultant from the specimen preparation process. The water content of the specimen of Inagi sand used for the undrained cyclic loading test was deliberately increased to the desired value from the initial water content of 22% by adding more water, thus the specimen may be in a wetting process when being mounted on the pedestal. An imagined wetting curve (red dash line in Fig. 5-27) was drawn which started wetting from somewhere on the water content = 22% line (red solid line). Though the initial values of water content of the wetting curves for the imagined one (ω = 22%) and for the one measured by membrane filter apparatus (ω = 27%) are different, these two curves may converge at low suction values. The SWCC measurements of IOF-B discussed in Fig. 4-5 of Chapter 4 also show a similar conclusion.

In the test program of the undrained cyclic loading test, the suction of Inagi sand specimens in Set 3 with Sr of 73% and 69% and in Set 4 with Sr of 72% are properly measured during cyclic loading, although the suction values are rather small. Figs. 5-28 (a) and (b) show the typical suction measurements of IOF-B and Inagi sand during undrained cyclic loading. It shows that generally suction values are rather stable under cyclic loading and a slight reduction is observed with the increase in pore pressure. Fluctuation appears near the end of the tests where the change in pore pressure is also large. The sustainability of suction under cyclic loading may somehow affect the behavior of the unsaturated soils though the magnitude of the measured suction is very small. In most cases in this study, the (p-PAP) or (p-PWP) are used to represent the effective stress of the unsaturated specimens, neither of which considers the effect of

suction. To show the effect of suction, another term, Bishop effective stress (Bishop, 1959) is used in this section:

$$p'_{Bishop} = p\text{-}PAP + \chi\,(PAP\text{-}PWP),\quad \chi = (Sr - Sr_0)/(100 - Sr_0) \qquad \text{(Eq. 5-3)}$$

where, χ is a parameter proposed by Vanapalli et al. (1996); Sr_0 denotes the residual degree of saturation. By taking Sr_0 as 57.7% according to the last point of SWCC measured by membrane filter apparatus, the stress paths of four tests of Inagi sand (test with Sr of 73% in Set 3) in terms of p-PAP and p'_{Bishop} are drawn in Fig. 28 (c). It shows that under the same deviator stress (q), p'_{Bishop} is generally higher than p-PAP obviously because of the positive value of suction. However, generally the effect of suction on the effective stress is minor due to the small values of measured suction.

5.5.8 Measured volume change during cyclic loading

The volume change of the unsaturated specimens during undrained cyclic loading was measured for some tests by the double cell system. The measurement system is discussed in Appendix C in detail. Fig. 5-29 shows the typical result of measured volumetric strain of Inage sand with Sr of 67.3% together with the theoretical volumetric strain as defined in Section 5.5.4. There was a problem of output delay from the DPT used to measure volume change of the unsaturated specimens. The output of DPT cannot follow the input signal during the application of cyclic loading, and more importantly it is very difficult to reduce the error caused by this problem when large deformation of the specimen was triggered suddenly. Thus, large fluctuation appeared as shown in Fig. 5-29. As also discussed in Appendix C, the measured data during large deformation of the specimen have to be abandoned. For the volumetric strain before relatively large deformation, the measured value is slightly larger than the calculated value, which may be caused by error in the measurement system, such as that caused by the meniscus effect.

5.5.9 Resistance against liquefaction

There is a common way to define the resistance against liquefaction on the liquefaction resistance curve, which is a relationship between cyclic stress ration (CSR, defined in Section 5.5.4) and the number of cycles to cause a certain stain obtained from the laboratory test, for example, triaxial test, torsional shear test etc. The relationship is plotted for Toyoura sand, as shown in Fig. 5-30, in which $N_{DA=5\%}$ stands for the number of cycles that causes 5% double amplitude of axial strain. The resistance against liquefaction R_L is defined for the saturated and

unsaturated soils as the CSR value that causes 5% double amplitude of axial strain (DA = 5%) at the 20th cycle. The values of R_L were also listed in Table 5-3 for each set of test.

A similar relationship is plotted for Inagi sand in Fig. 5-31. For Inagi sand, the effects of density and consolidation duration on the liquefaction resistance curve were studied for saturated specimens. As shown the black squares in Fig. 5-31, the Dr value ranged from 64% to 75%, while it seems the density in the tested range didn't affect the liquefaction resistance significantly. On the effect of consolidation duration, there are three tests of the saturated specimens in pink triangle shown in in Fig. 5-31 which were consolidated for one night while the remaining specimens regardless of Sr were consolidated for 2 hours. It seems that a longer duration of consolidation may increase liquefaction resistance. In addition, as discussed in Section 5.5.6, because of the change in total mean principal stress, the liquefaction resistance may reduce. As shown the results in Fig. 5-31, the liquefaction resistance for the specimens with p-changed (red circle) is smaller than those with p-constant (blue triangle).

Fig. 5-32 shows a similar relationship for the IOF-B specimens. For the saturated test, it seems that the relationship between CSR and $N_{DA=5\%}$ was not affected by confining pressure as significantly compared with the result of the saturated specimen in Set 4, and Set 6, Set 5 and Set 7. For the medium dense specimens, the liquefaction resistance curve of the saturated specimen is not parallel with those of the unsaturated specimens, which causes variations in LRR (defined in Section 5.5.10). Since all the other curves between the saturated case and the unsaturated are rather parallel for other soils tested and for IOF-B with loose condition, the effect of the definition of the R_L on the LRR is not discussed. In addition, it shows that the liquefaction resistance of IOF-B for the medium dense condition is much higher than that of loose IOF-B, which implies that the density condition may be very important for evaluation of the resistance against liquefaction for IOF-B.

5.5.10 Discussion on the effects of Sr and Fc

The results of the undrained cyclic loading tests as discussed in Section 5.5.9 imply that the resistance against liquefaction can be increased by decreasing the Sr value of the soils. The liquefaction resistance ratio induced by Sr is now defined in this study as

$$\mathrm{LRR} = \frac{L_R \text{ of an unsaturated soil}}{L_R \text{ of the saturated soil}} \qquad \text{(Eq. 5-4)}$$

A relationship between LRR and Sr is plotted in Fig. 5-33, in which results from previous studies by other researchers are also included. It seems that the test results for Toyoura sand from this study are consistent with those from other studies, while the plotted relationship is not very unique even for Toyoura sand. This may imply that Sr is not a very good parameter to represent the effect of Sr on the resistance against liquefaction. Okamura and Sugo (2006) proposed another parameter, the maximum volumetric strain caused by pore air compression, $\varepsilon^*_{vol,\ air}$ (original name is potential volumetric strain). The $\varepsilon^*_{vol,\ air}$ is the maximum value of theoretical volumetric strain, with $\varepsilon_{vol,air}$, defined in Section 5.5.4. The relationship between $\varepsilon^*_{vol,\ air}$ and LRR is shown in Fig. 5-34, which shows that the trend for Toyoura sand and a type of Masa sand containing less than 5% fines content is rather unique while the results for Inagi sand and IOF-B are distributed at much lower positions under the trend line. The results in Fig. 5-34 implies that volumetric strain caused by pore air compression may be one factor affecting the resistance against liquefaction for unsaturated soil, while there may be other factors which may also affect it (e.g. fines content Fc).

The combined effect of Sr and Fc from the fundamental point of view was analyzed. Fig. 5-35 schematically shows a soil element and the change in element volume due to shear stress. Regardless of Sr of this element, 3 types of deformation happen when it is subjected to undrained cyclic shear stress:

1. The volumetric strain of the soil particle skeleton $\varepsilon_{vol,shear}$ induced by dilatancy of soil particles;
2. The volumetric strain of the soil particle skeleton $\varepsilon_{vol,p'}$ induced by reduction in effective stress p'. Under cyclic shear stress, the pore pressure normally increases and effective stress consequently reduces. The reduction in p' is just like the unloading process of the consolidation test described in Section 5.4. Some elastic energy stored in connections between particles has to be released because of the reduction in p';
3. The volumetric strain of voids, which is a summation of the volumetric strain of pore air compression $\varepsilon_{vol,air}$ and pore water compression $\varepsilon_{vol,water}$ induced by increase of pore pressure. Due to the much higher bulk modulus of pore water compared with that of the soil skeleton and pore air, $\varepsilon_{vol,water}$ is ignored in this study.

There are three states for this element: (1). Initial state when there is no excess pore pressure. In this state, the confining pressure is applied to the soil particle skeleton; (2). Final state when the element is fully liquefied. In this state, the confining pressure is applied to the void; (3) A

state in-between the initial state and final state. In this state, the confining pressure is applied to both the soil particle skeleton and void. Under State 3, the net volume of the soil particle skeleton should be the same as the net volume of the void. The word "net volume" herein means the area of black square boundary in Fig. 5-35 (b) or (c), or the blue square boundary in Fig. 5-35 (d). Otherwise, the confining pressure will be applied only to either the soil particle skeleton or the void. From the inference above, we can get:

$$\varepsilon_{vol,shear}\ (+) + \varepsilon_{vol,p'}\ (-) = 0\ (Sr = 100\%) \qquad \text{(Eq. 5-5)}$$

$$\varepsilon_{vol,shear}\ (+) + \varepsilon_{vol,p'}\ (-) = \varepsilon_{vol,air}\ (+)\ (Sr < 100\%) \qquad \text{(Eq. 5-6)}$$

Eq. 5-5 was inferred by Martin et al (1975) and Eq. 5-6 is actually an extension under unsaturated condition. Eq. 5-6 shows that the volumetric stress induced by shear stress, $\varepsilon_{vol,shear}$ links with two items, volume change by reduction of effective stress ($\varepsilon_{vol,p'}$) and volume change of air compression ($\varepsilon_{vol,air}$). The relationship shown in Fig. 5-34 only considers one item, the $\varepsilon_{vol,air}$, however, $\varepsilon_{vol,p'}$ may be another parameter for liquefaction resistance of the unsaturated soils. Thus, a new parameter, volumetric strain ratio $R_{Vol,\ air/p'}$ is proposed in this study:

$$R_{Vol,air/p'} = \frac{\varepsilon^{*}_{vol,air}}{\varepsilon^{e}_{vol,0.1p'}} \qquad \text{(Eq. 5-5)}$$

where, $\varepsilon^{*}_{vol,\ air}$ is defined in Section 5.5.4 and can be expressed as:

$$\varepsilon^{*}_{vol,air} = \frac{\sigma'_0}{p_b+\sigma'_0}(1 - s_r)\frac{e}{1+e} \qquad \text{(Eq. 5-6)}$$

where, p_b: absolute value of back pressure applied before cyclic loading (kPa); $\varepsilon^{e}_{vol,0.1p'}$ is the volumetric strain caused by 90% effective stress reduction estimated by consolidation test introduced in Section 5.4 (last column in Table 5-2 shows the values of tested materials).

Fig. 5-36 shows the relationship between proposed parameter, $R_{Vol,\ air/p'}$ and LRR. It shows that the proposed parameter significantly improved the uniqueness of the correlation with LRR; while the data are still scattered somehow, which may need to be further verified in future studies.

5.6 Chapter conclusions

Three types of tests are discussed in this chapter focusing on the undrained behavior of the saturated and the unsaturated soils. Several conclusions are summarized as follows:

1. The undrained behavior of saturated IOF-B specimens under monotonic loading are studied in this chapter. The results show that the undrained shear strength of saturated IOF-B may be closely related to the initial confining pressure and residual effective stress (Fig. 5-3 a, Fig. 5-5 a); the axial strain may be governed by the ratio of shear stress to the residual effective stress (Fig. 5-3 b, Fig. 5-5 b); the undrained shear strength of the saturated IOF-B may reduce significantly with the decrease in density of the material (Fig. 5-6).
2. The volume changes of the saturated Toyoura sand, Inagi sand and IOF-B specimens during isotropic loading and unloading consolidation processes were studied. The results show that the volume changes caused by consolidation may significantly differ depending on the type and density of the soils (Fig. 5-9, Fig. 5-10).
3. The results of the undrained cyclic loading tests on the saturated and the unsaturated Toyoura sand, Inagi sand and IOF-B are reported in this chapter. The results show that compared with the soils under saturated conditions, the decrease in Sr may induce the reduction in the rate of pore pressure generation; the conversion of the behavior of the soils from liquefaction to cyclic mobility; the significant increase in liquefaction resistance (Figs. 5-14~5-23 and Figs. 5-30~5-32).
4. Testing techniques used in the undrained cyclic loading test are discussed in this chapter. Discussions show that efficient control of total mean principal stress p is very important to evaluate the resistance against liquefaction of the unsaturated soils and the cell pressure control system employed performs very well (Figs. 5-25 and 5-31); membrane filter technique used to measure negative pore water pressure on the triaxial system performs very well for tested soils (Figs. 5-26~5-28); the measured volumetric strain for the unsaturated specimens are generally consistent with the theoretical value, while the measurement system of volume of the unsaturated specimens during cyclic loading may need to be improved in the future (Fig. 5-29).
5. Regarding the effect of Sr and Fc on the liquefaction resistance, a new parameter, volumetric strain ratio $R_{Vol,\ air/p'}$, is proposed which is better correlated with the liquefaction resistance ratio induced by Sr and Fc than other parameters, while more studies may need be done to verify the proposed parameter (Figs. 5-33~5-36).

Reference

1. Ampadu, S.K. and Tatsuoka, F. (1993) Effect of setting method on the behavior of clays in triaxial compression from saturated to undrained shear. Soils and Foundations, Vol. 33, No. 2, 14-34.
2. Arab, A., Shahrour, I. and Lancelot, L. (2011) A laboratory study of liquefaction of partially saturated sand. Journal of Iberian Geology, Vol. 37, No. 1, 29-36.
3. Bishop, A.W. (1959). The principle of effective stress. Lecture delivered in Oslo, Norway, in 1955; published in Teknisk Ukeblad, Vol. 106, No. 39, 859-863.
4. Bouferra, R., Benseddiq, N. and Shahrour, I. (2007). Saturation and preloading effects on the cyclic behavior of sand. Int. J. Geomech., Vol. 7, No. 5, 396-401.
5. Castro, G. & Poulos, S.J. (1977). Factors affecting liquefaction and cyclic mobility. Journal of the Geotechnical Engineering Division, ASCE, Vol. 103, No. GT6, 502-516.
6. Goto, S. and Shamoto, Y. (2002). Estimation method for the liquefaction strength of unsaturated sandy soil (part 2) (in Japanese). Proc., 37th Jpn. Nat. Conf. Geotech. Eng., 1987-1988.
7. Grozic, J.L.H., Robertson, P.K. and Morgenstern, N.R. (2000). Cyclic liquefaction of loose gassy sand. Can. Geotech. J., Vol. 37, 843-856.
8. Hossain, A.M., Andrus, R.D. and Camp, W.M. (2013). Correcting liquefaction resistance of unsaturated soil using wave velocity. J. Geotech. Geoenviron. Eng., Vol. 139, 277-287.
9. Huang, Y., Tsuchiya, H and Ishihara, K. (1999). Estimation of partial saturation effect on liquefaction resistance of sand using P-wave velocity (in Japanese). Proc. JGS Symp., 113, 431-434.
10. Ishihara, K. (1993). Liquefaction and flow failure during earthquakes. Geotechnique, Vol. 43, No. 3, 351-415.
11. Ishihara, K., Tsuchiya, H., Huang, Y. and Kamada, K. (2001). Recent studies on liquefaction resistance of sand- effect of saturation. Proc. 4th Int. Conf. Recent Advance in Geotech. Earthquake Eng. and Soil Dynamics, 1-7.
12. Kayen, R. et al. (2013). Shear-wave velocity-based probabilistic and deterministic assessment of seismic soil liquefaction potential. J. Geotech. Geoenviron. Eng., Vol. 139, 407-419.
13. Lade, P.V. (1993). Initiation of static instability in the submarine Nerlerk beam. Can. Geotech. J., Vol. 30: 895-904.

14. Martin, G.R., Fin, W.D.L. and Seed, H.B. (1975). Fundamentals of liquefaction under cyclic loading. J. Geotech. Eng. Div., ASCE, Vol. 101, No. GT5, 423-438.
15. Monkul, M.M. and Yamamuro, J.A. (2011). Influence of silt size and content on liquefaction behavior of sands. Can. Geotech. J., Vol. 48, 931-942.
16. Mulilis, J.P., Seed, H.B., Chan, C.K., Mitchell, J.K. and Arulanandan, K. (1977). Effects of sample preparation on sand liquefaction. J. . Geotech. Eng. Div., ASCE, Vol. 103, No. GT2, 91-108.
17. Nakazawa, H. and Hradah, K. (2012). Revision of relative density and estimation of liquefaction strength of sandy soil with fine content (in Japanese). Journal of Japan Society of Civil Engineers, Ser. A1 Vol. 68, No. 4: I_282-I_292.
18. Nishimura, T., Koseki, J., Fredlund, D.G. and Rahardjo, H. (2012). Microporous membrane technology for measurement of soil-water characteristic curve. Geotech. Testing J., Vol.35, 201-208.
19. Okamura, M. Ishihara, M. and Tamura, K. (2006). Degree of saturation and liquefaction resistances of sand improved with sand compaction pile. J. Geotech. Geoenviron. Eng., Vol. 132, No. 2, 258-264.
20. Okamura, M. and Soga, Y. (2006). Effects of pore fluid compressibility on liquefaction resistance of partially saturated sand. Soils and Foundations, Vol. 46, No. 5, 695-700.
21. Poulos, S.J., Castro, G. and France, J.W. (1985) Liquefaction evaluation procedure. J. Geotech. Eng., Vol. 111, 772-792
22. Roscoe, K.H., Schofield, A. N. and Worth, C.P. (1958). On the yielding of soils. Geotechnique, Vol. 8, No. 1: 22-53.
23. Seed, H.B. (1979). Soil liquefaction and cyclic mobility evaluation for level ground during earthquakes. J. Geotech. Eng. Div., ASCE, Vol. 105, No. GT2, 201-255.
24. Seed, H.B. and Idriss, M. (1971). Simplified procedure for evaluating soil liquefaction potential. J. Geotech. Eng. Div., ASCE, Vol. 97, No. SM9, 1249-1273.
25. Sherif, M.A., Ishibashi, I. and Tsuchiya, C. (1977) Saturation effects on initial soil liquefaction. J. Geotech. Eng. Div., ASCE, Vol. 103, No. GT8, 914-917.
26. Skempton, A. W. (1954). The pore-pressure coefficients A and B. Geotechnique, Vol. 4, No. 4, 143-147
27. Sladen, J. A., D'Hollander, R.D. and Krahn, J. (1985a). Back analysis of the Nerlerk berm liquefaction slides. Can. Geotech. J., Vol. 22: 579-588.
28. Tatsuoka, F. (1987) Report of the 3rd technical seminar on the triaxial compression tests (in Japanese), Tsuchi to Kiso, Vol. 35, No. 11, 89-93.

29. Tokimatsu, K. and Yoshimi, Y. (1983). Empirical correlation of soil liquefaction based on SPT N-value and fines content. Soils and Foundations, Vol. 23, No. 4, 56-74.
30. Tsukamoto, Y., Ishihara, K., Nakazawa, H., Kamada, K. and Huang, Y. (2002). Resistance of partly saturated sand to liquefaction with reference to longitudinal and shear wave velocities. Soils and Foundations, Vol. 42, No. 6, 93-104.
31. Unno, T., Kazama, M., Uzuoka, R. and Sento, N. (2008). Liquefaction of unsaturated sand considering the pore air pressure and volume compressibility of the soil particle skeleton. Soils and Foundations, Vol. 48, No. 1, 87-99.
32. Vaid, Y.P. and Eliadorani, A. (1998). Instability and liquefaction of granular soils under undrained and partially drained states. Can. Geotech. J., Vol. 35: 1053-1062.
33. Vnanpalli, S.K.; Fredlund, D.G., Pufahl, D.E. and Clifton, A.W. (1996). Model for the prediction of shear strength with respect to soil suction. Can. Geotech. J. 33:379-392.
34. Yamamuro, J.A. and Lade, P.V. (1997a). Instability of granular materials at high pressures. Soils and Foundations, Vol. 37, No. 1: 41-52.
35. Yamamuro, J.A. and Lade, P.V. (1997b). Static liquefaction of very loose sands. Canadian Geotechnical Journal, Vol. 34, 905-917.
36. Yamamuro, J.A. and Lade, P.V. (1998). Steady-state concepts and static liquefaction of silty sands. J. of Geotech. Geoenviron. Eng., Vol. 124, 868-877.
37. Yamamuro, J.A. and Covert, K.M. (2001). Monotonic and cyclic liquefaction of very loose sands with high silt content. J. Geotech. Geoenviron. Eng., Vol. 127, 314-324.
38. Yang, J. (2002) Liquefaction resistance of sand in relation to P-wave velocity. Geotechnique, Vol. 5, No. 4, 295-298.
39. Yang, J., Savidis, S. and Roemer, M. (2004). Evaluating liquefaction strength of partially saturated sand. J. Geotech. Geoenviron. Eng., Vol. 130, No. 9, 975-979.
40. Yasuda, S., Kobayashi, T., Fukushima, Y., Kohari, M. and Simazaki, T. (1999). Effect of degree of saturation on the liquefaction strength of Masa (in Japanese). Proc., 34th Jpn. Nat. Conf. Geotech. Eng., 2071-2072.
41. Yoshimi, Y., Tanaka, K. and Tokimatsu, K. (1989). Liquefaction resistance of a partially saturated sand. Soils and Foundations, Vol. 29, No. 3, 157-162.
42. Yoshimine, M., Robertson, P.K. and Wride, C.E. (1999). Undrained shear strength of clean sands to trigger flow liquefaction. Can. Geotech. J., Vol. 36, 891-906.
43. Youd, T.L. et al. (2001). Liquefaction resistance of soil: summary report from the 1996 NCEER and 1998 NCEER/NSF workshops on evaluation of liquefaction resistance of soils. J. Geotech. Geoenviron. Eng., Vol. 127, No. 10, 817-833.

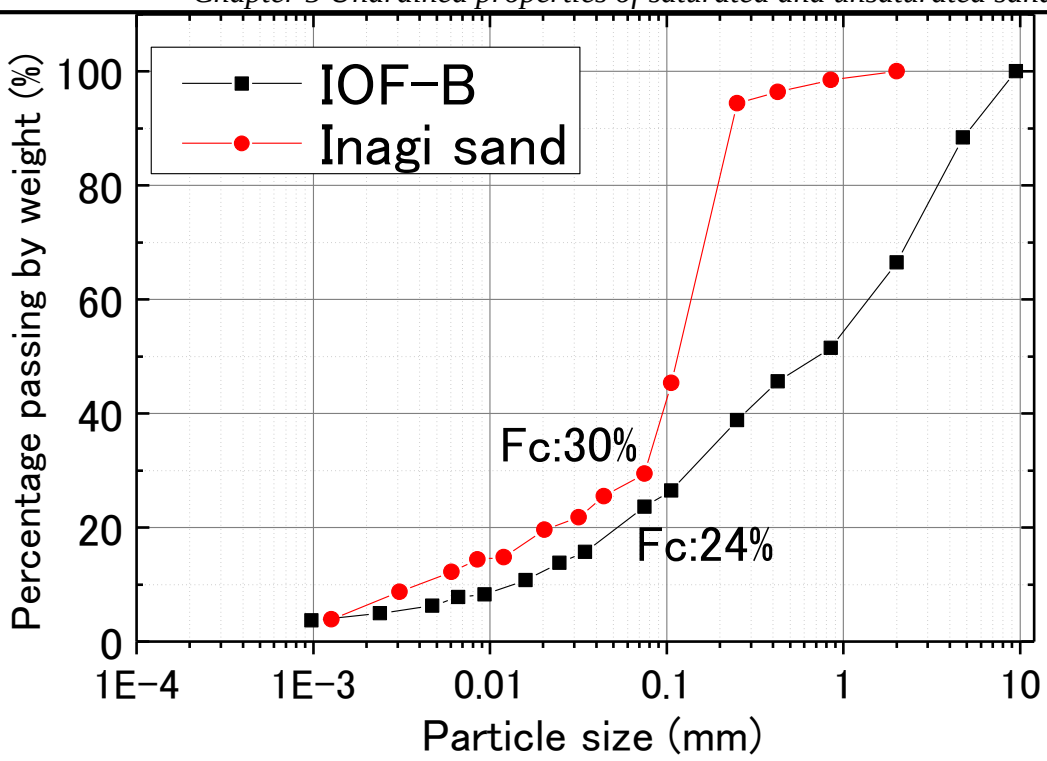

Fig. 5-1 Gradation of IOF-B and Inagi sand

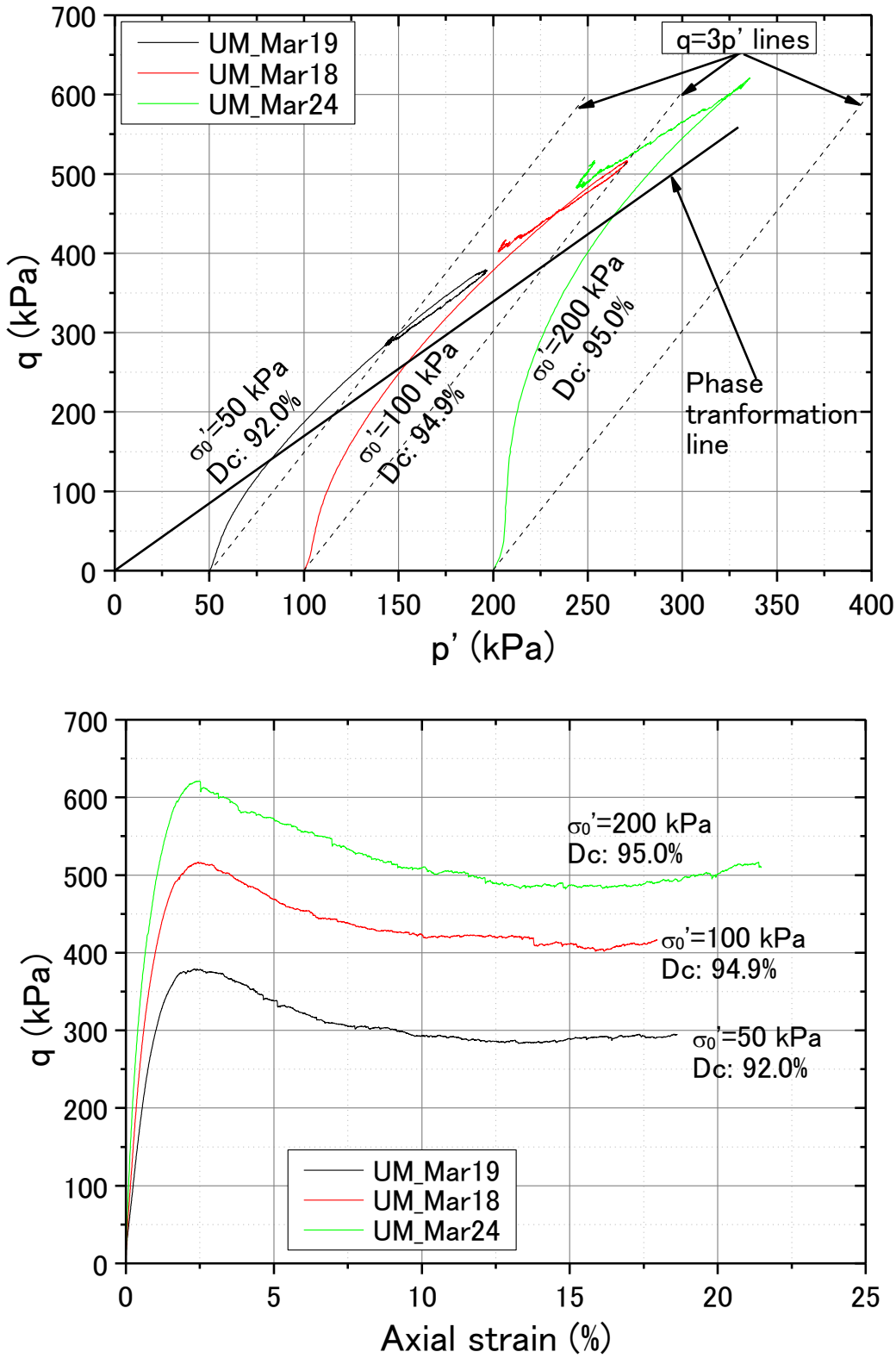

Fig. 5-2 (a) Stress paths of medium dense IOF-B; (b) Stress strain relationship of medium dense IOF-B

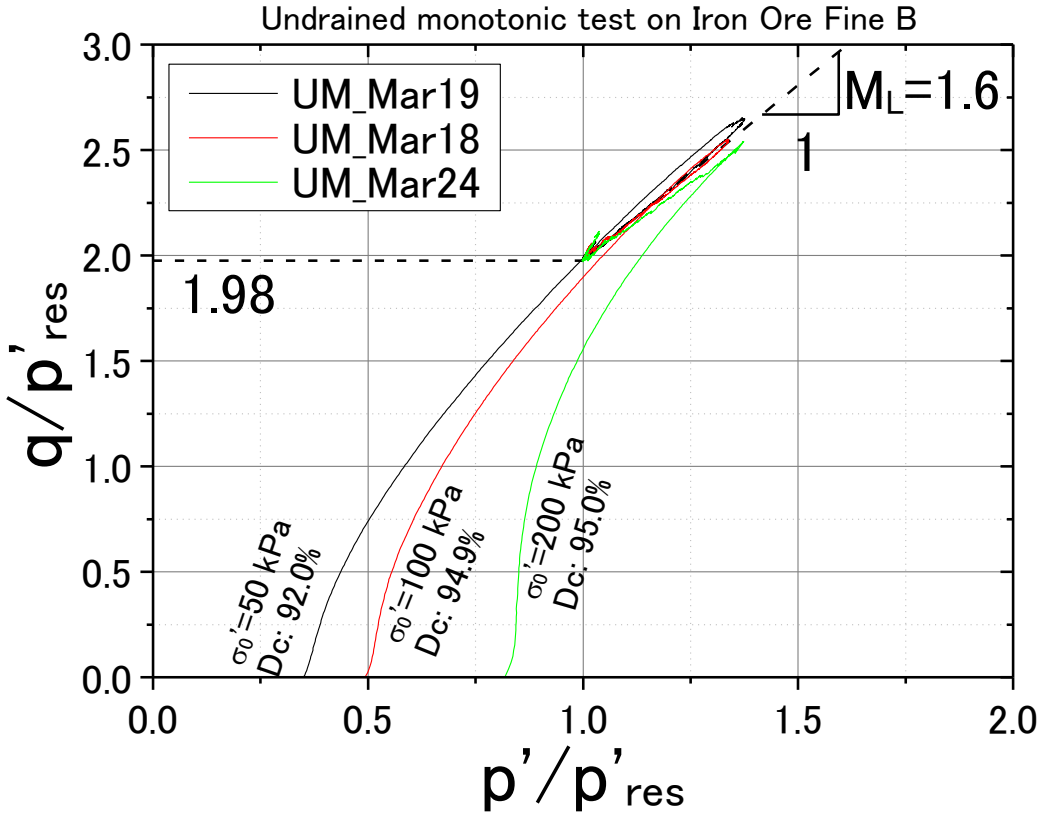

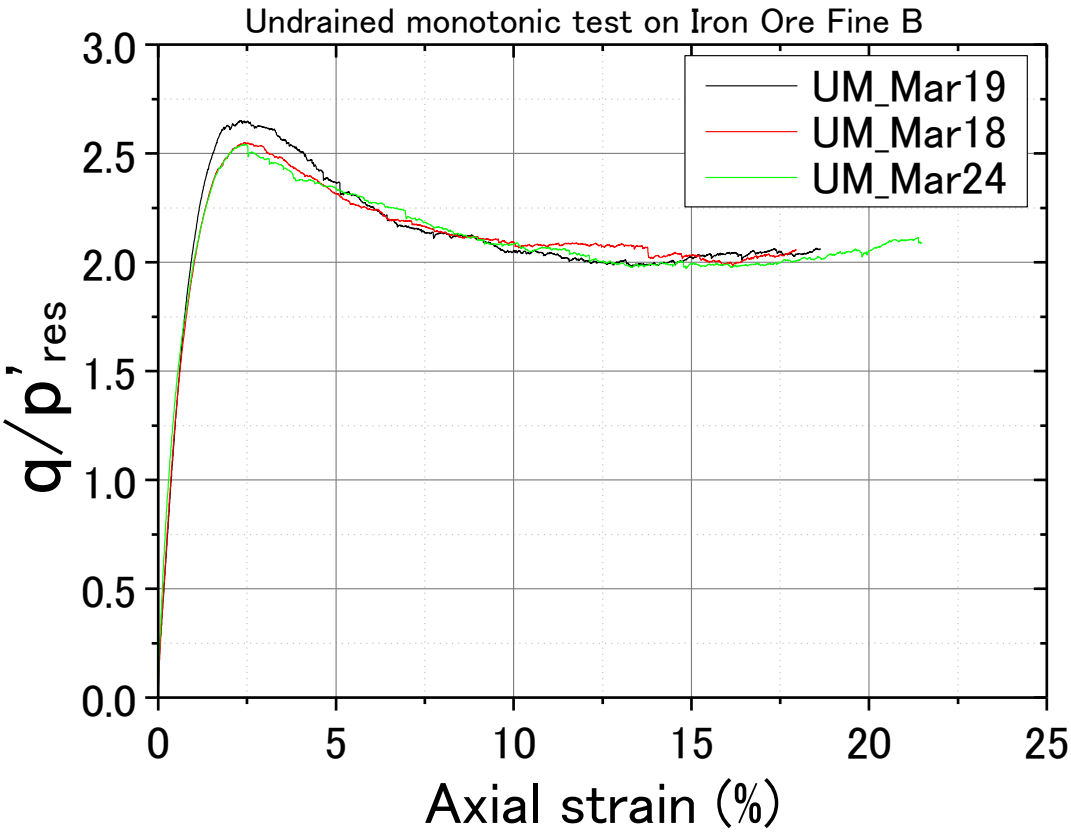

Fig. 5-3 (a) Normalized Stress paths of medium dense IOF-B; (b) Normalized stress strain relationship of medium dense IOF-B

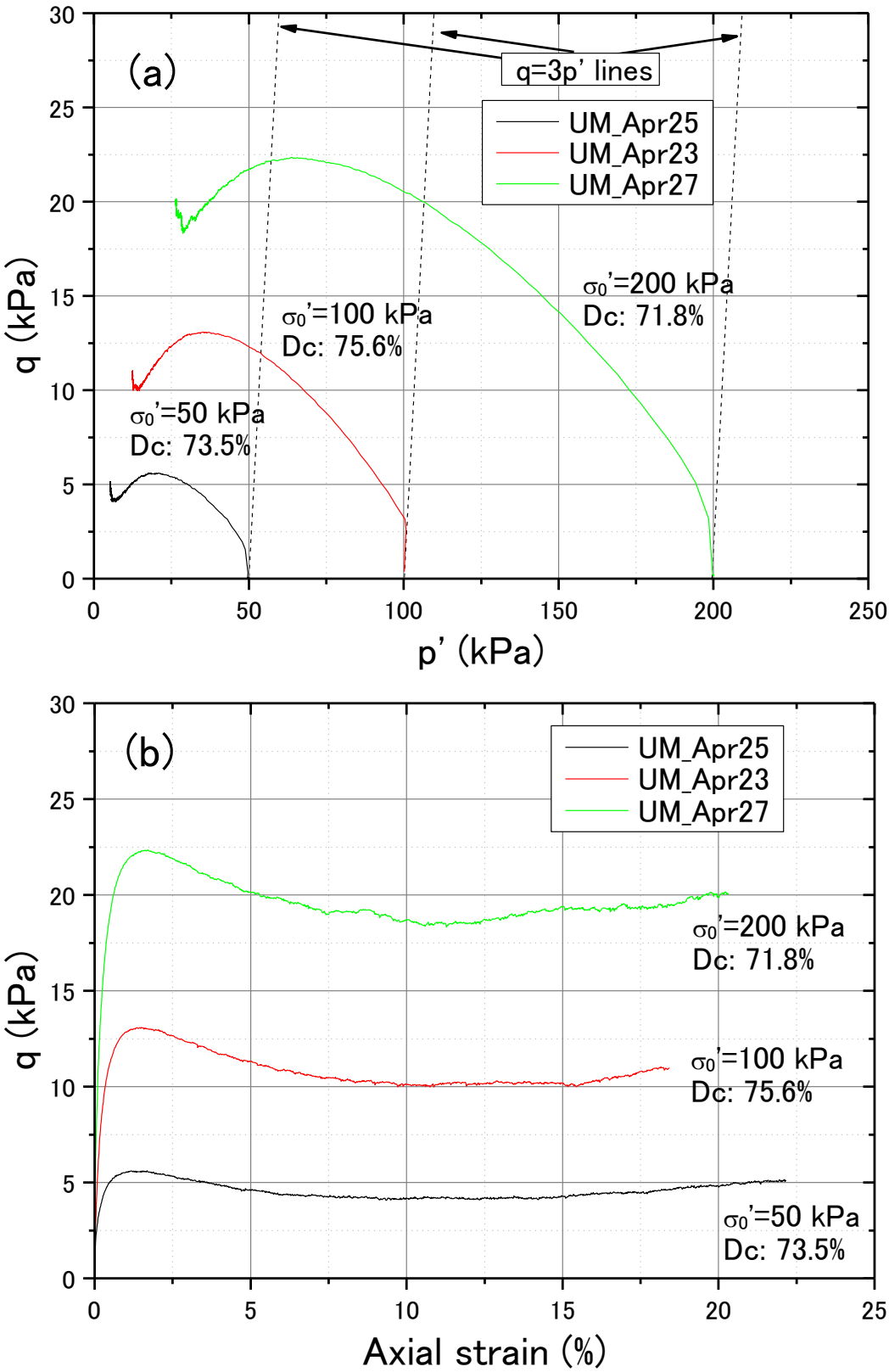

Fig. 5-4 (a) Stress paths (b) Stress strain relationship of loose IOF-B

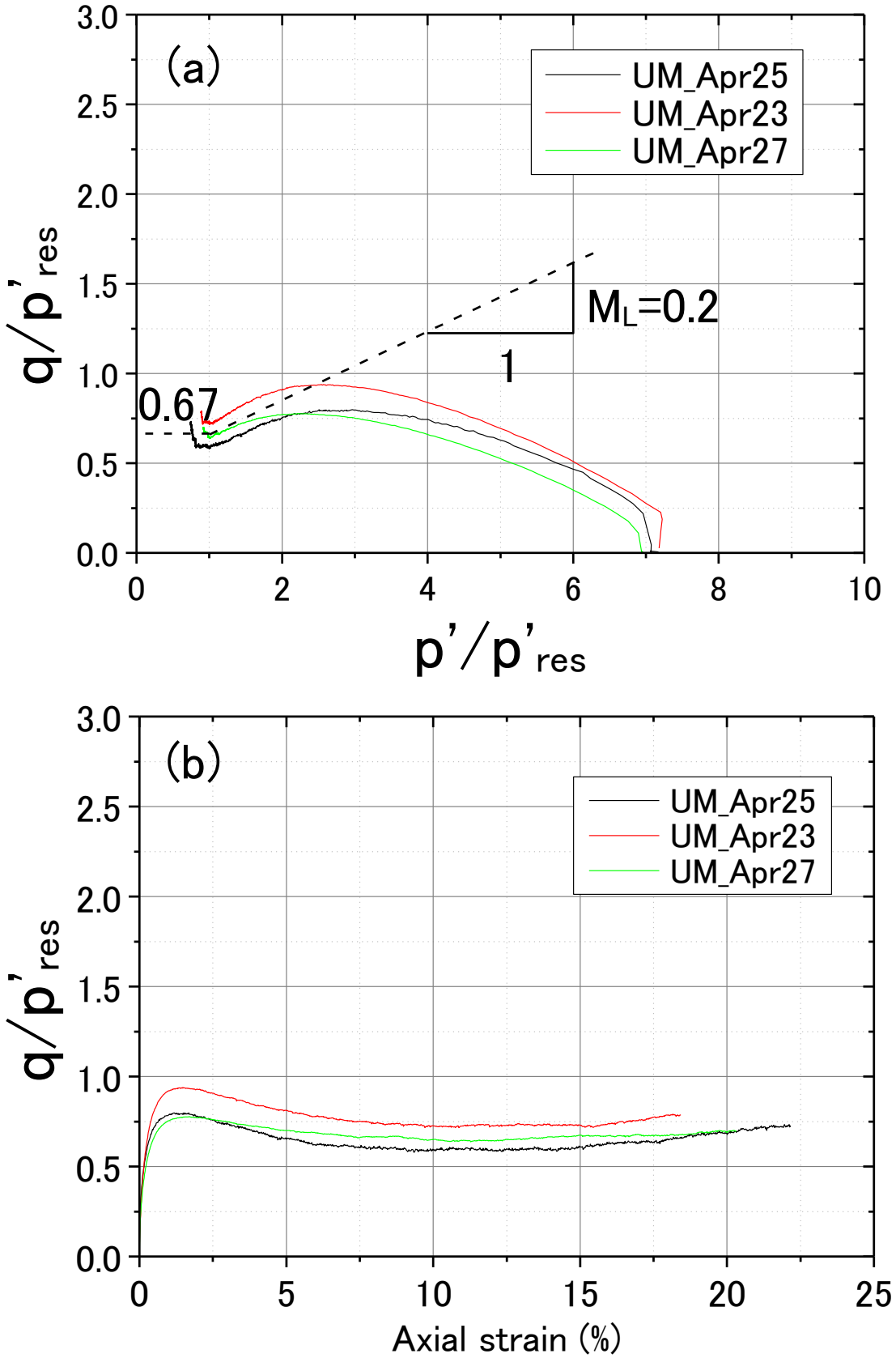

Fig. 5-5 (a) Normalized stress paths (b) Normalized stress strain relationship of loose IOF-B

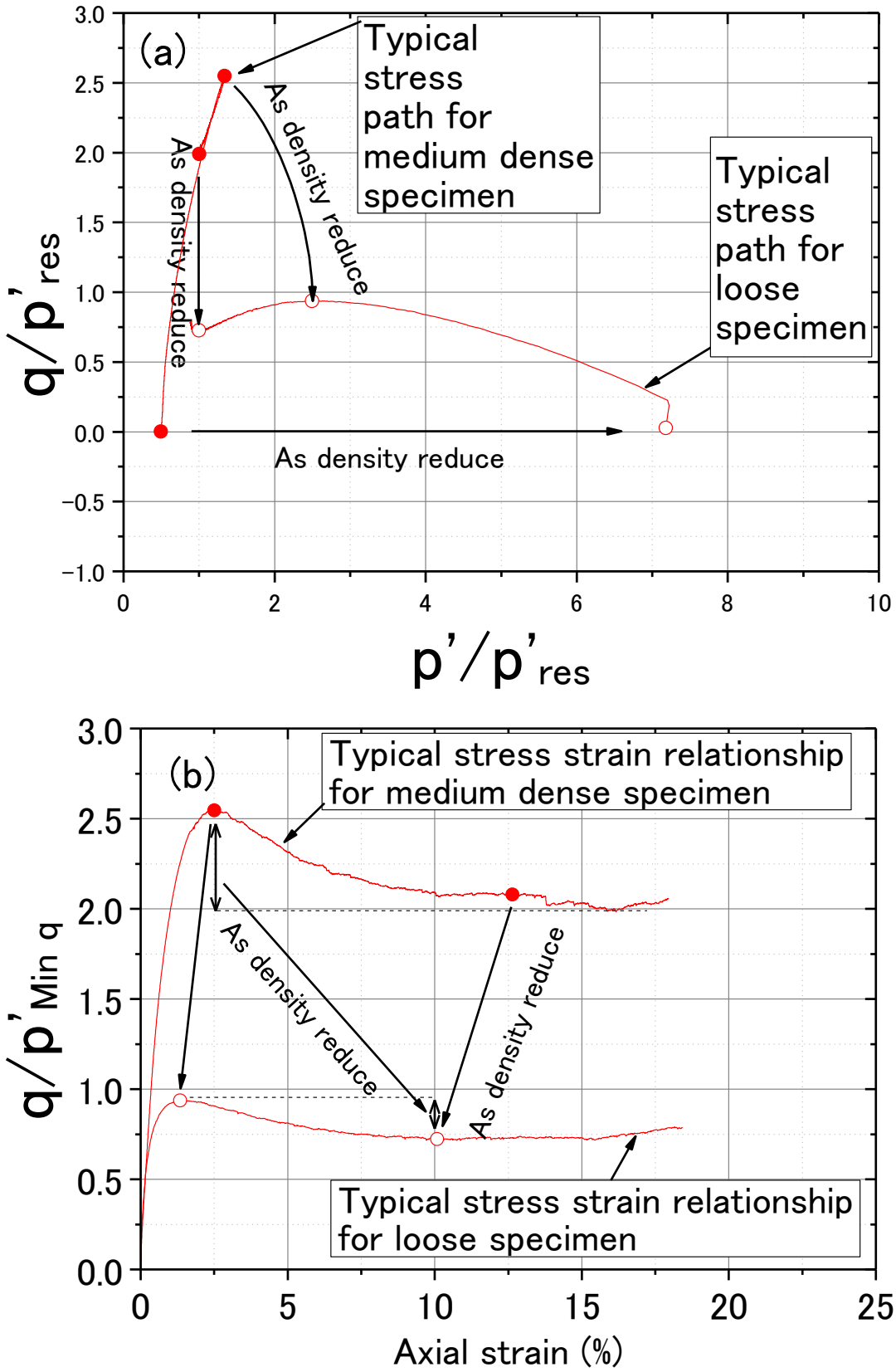

Fig. 5-6 Prediction of undrained behavior of IOF-B under monotonic loading (a) Normalized stress paths (b) Normalized stress strain relationship

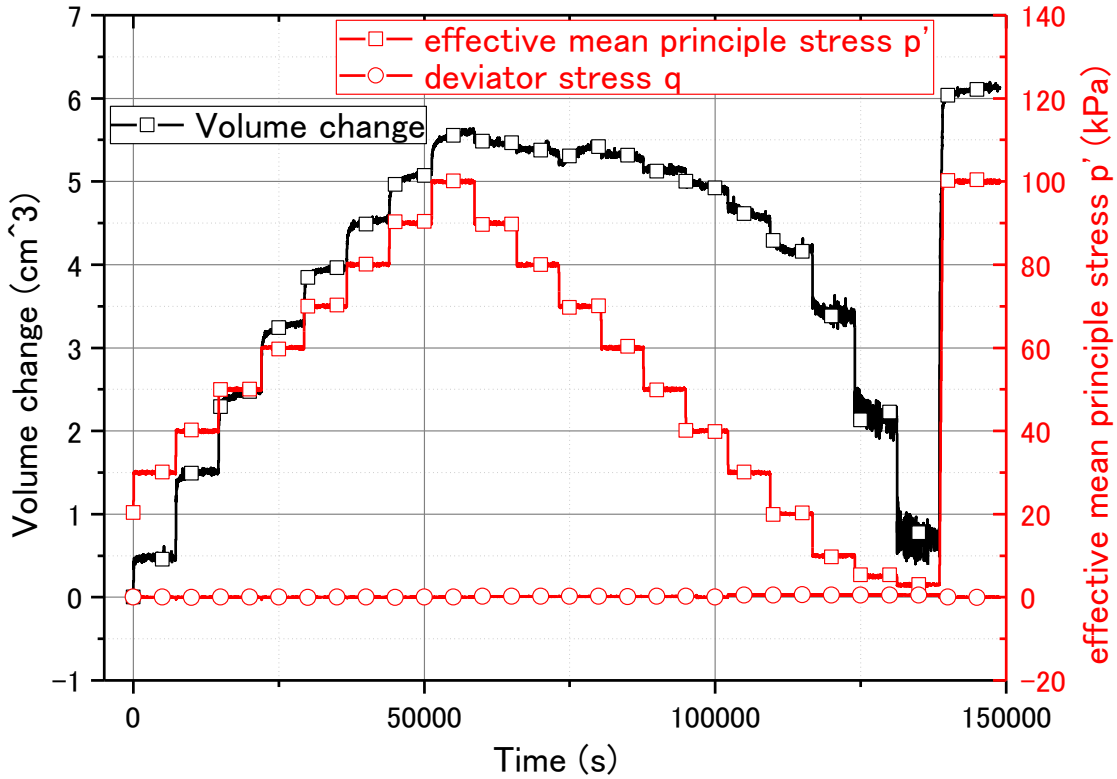

Fig. 5-7 Typical time histories of p' and q and volume change

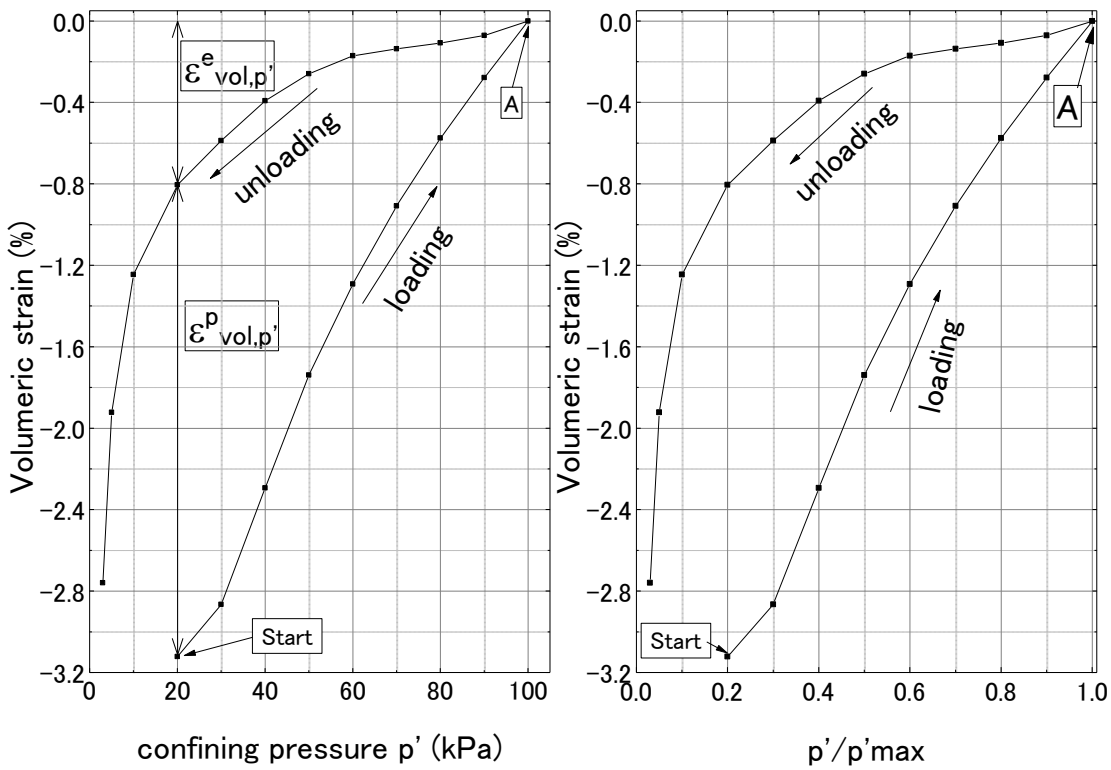

Fig. 5-8 (a) Volumetric strain (b) Normalized volumetric strain

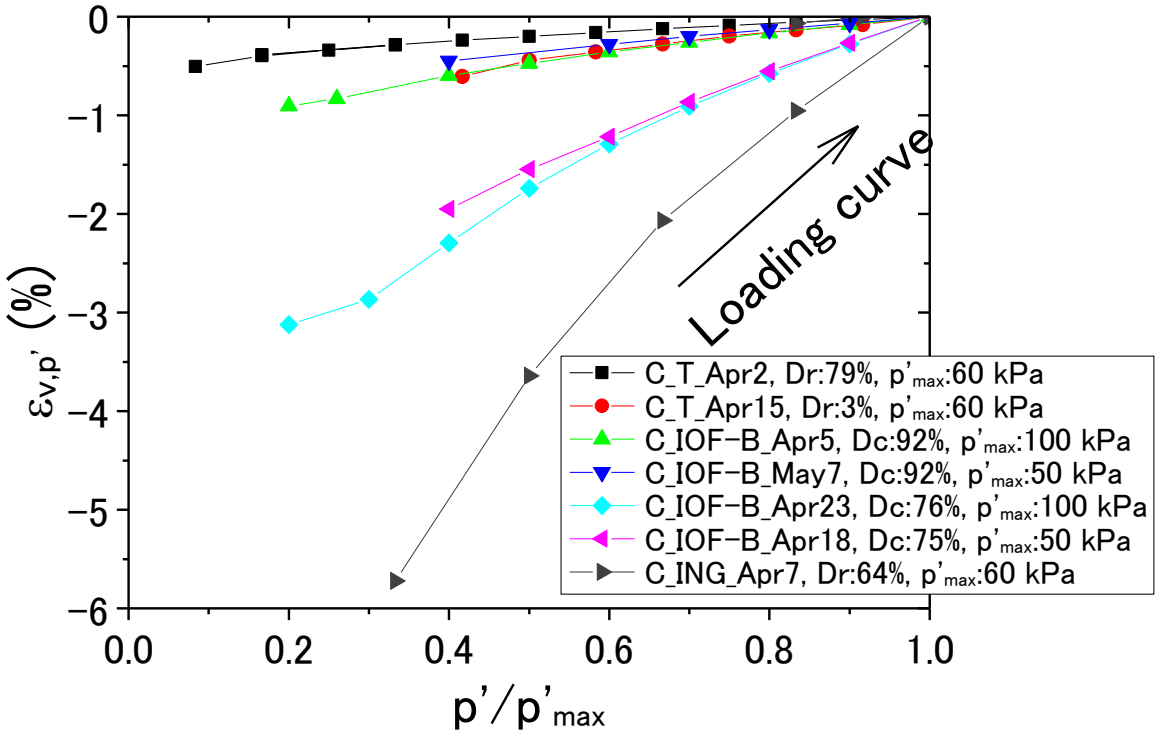

Fig. 5-9 Normalized volumetric strain (loading) for all tested specimens

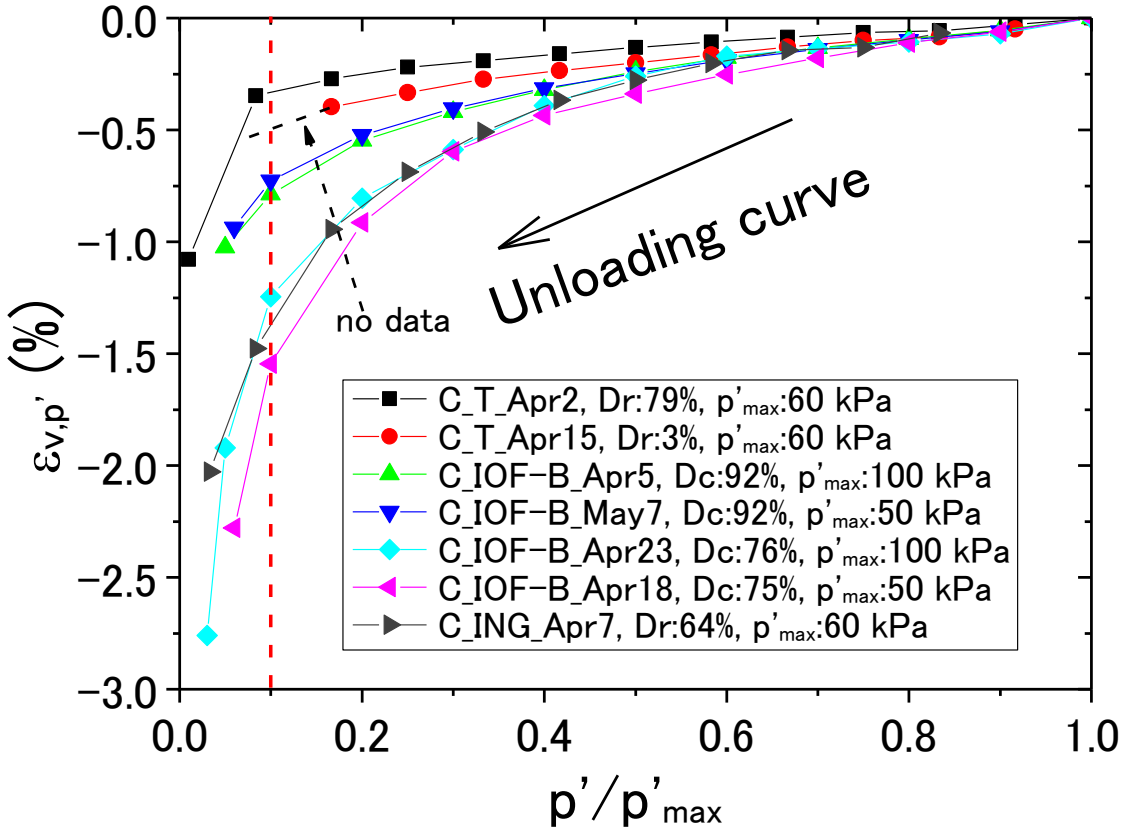

Fig. 5-10 Normalized volumetric strain (unloading) for all tested specimens

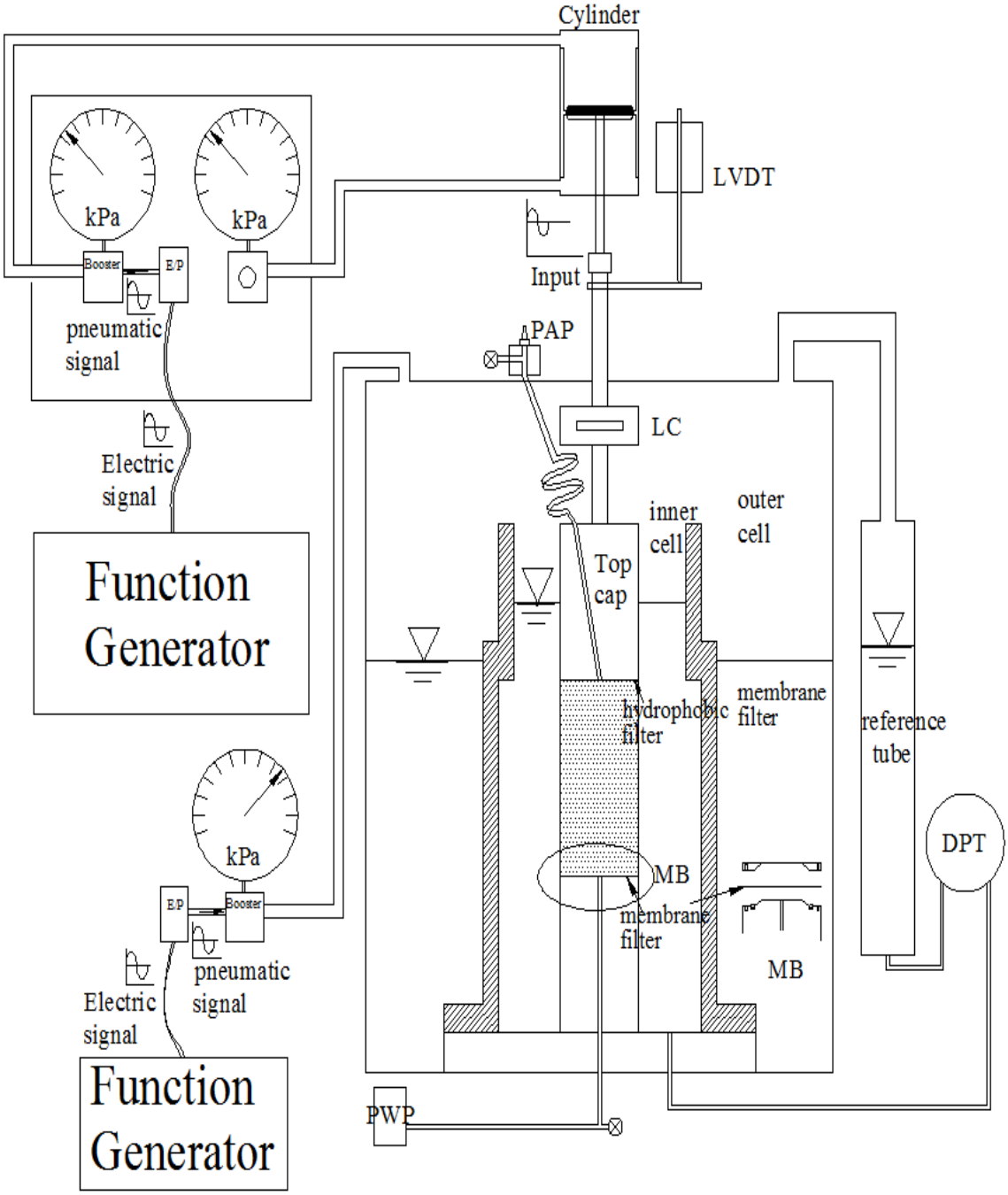

Fig. 5-11 Layout of triaxial apparatus for unsaturated test

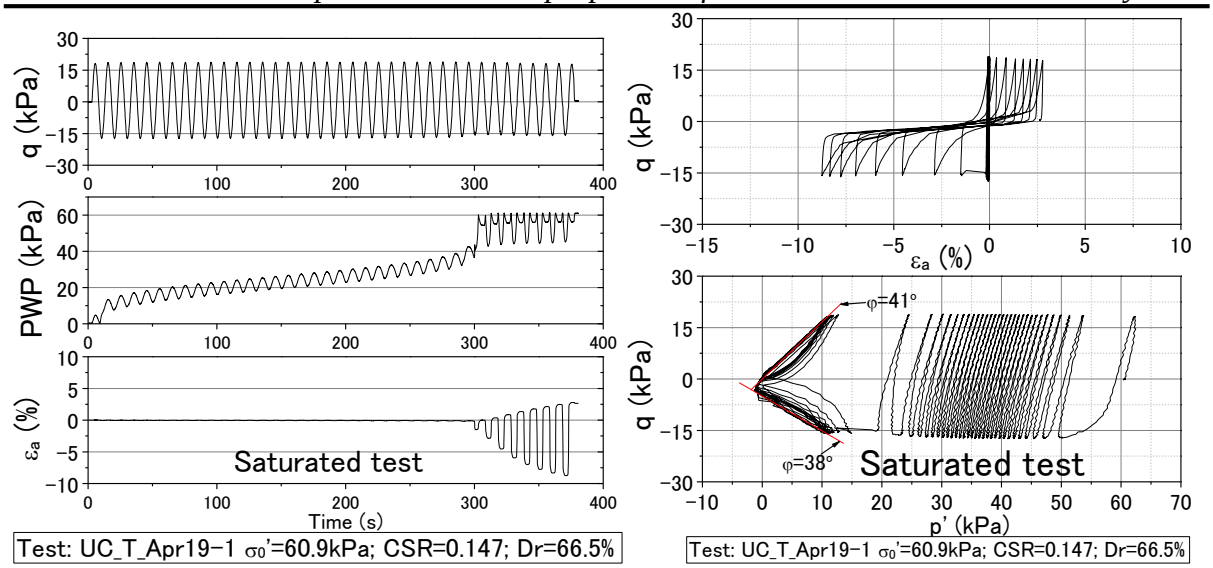

(a) Time histories; (b) Stress strain relationship and stress path

Fig. 5-12Typical results of saturated condition of Set 1 (medium dense Toyoura sand)

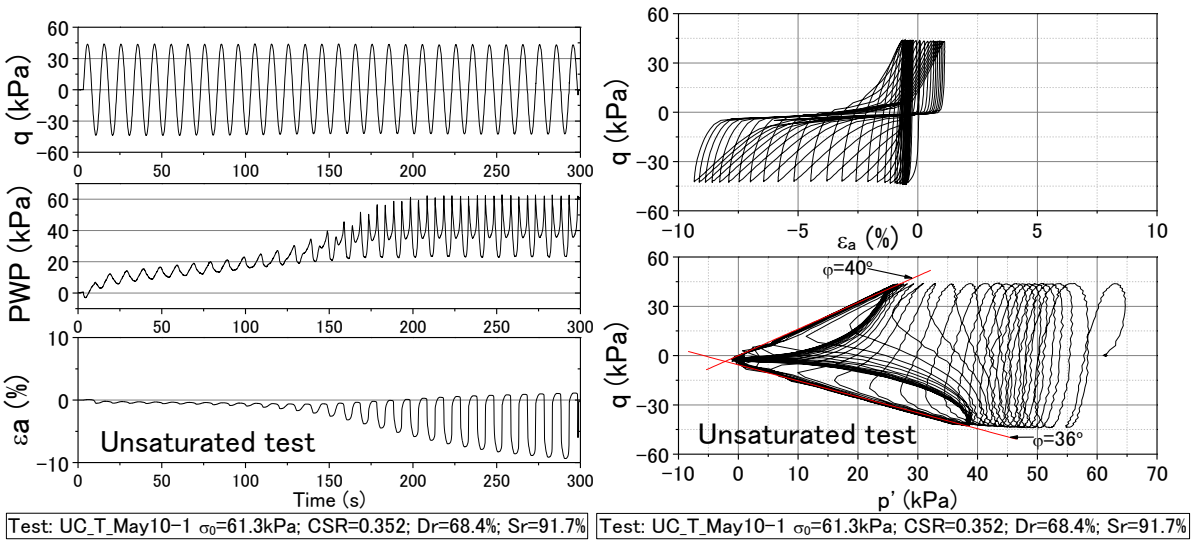

(a) Time histories; (b) Stress strain relationship and stress path

Fig. 5-13 Typical results of unsaturated condition of Set 1(medium dense Toyoura sand)

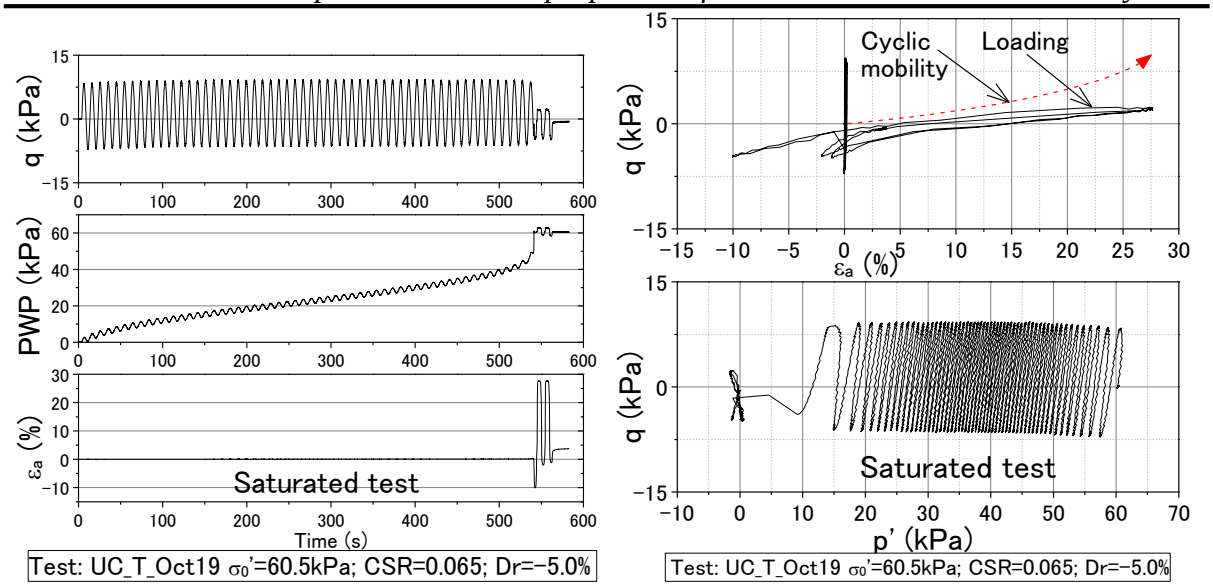

(a) Time histories; (b) Stress strain relationship and stress path

Fig. 5-14 Typical results of saturated condition of Set 2 (extremely loose Toyoura sand)

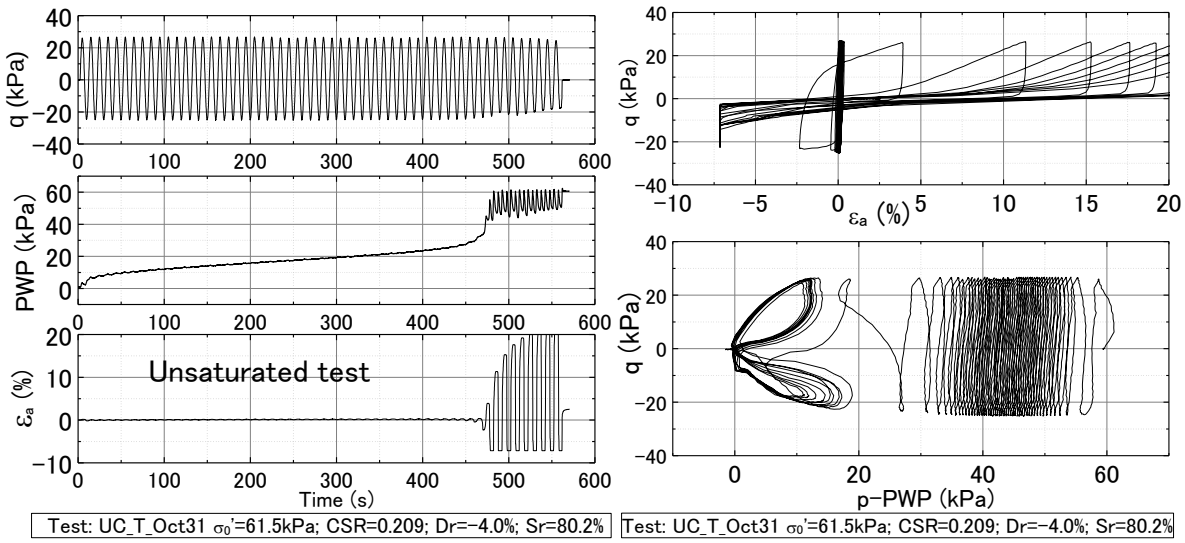

(a) Time histories; (b) Stress strain relationship and stress path

Fig. 5-15 Typical results of unsaturated condition of Set 2 (extremely loose Toyoura sand)

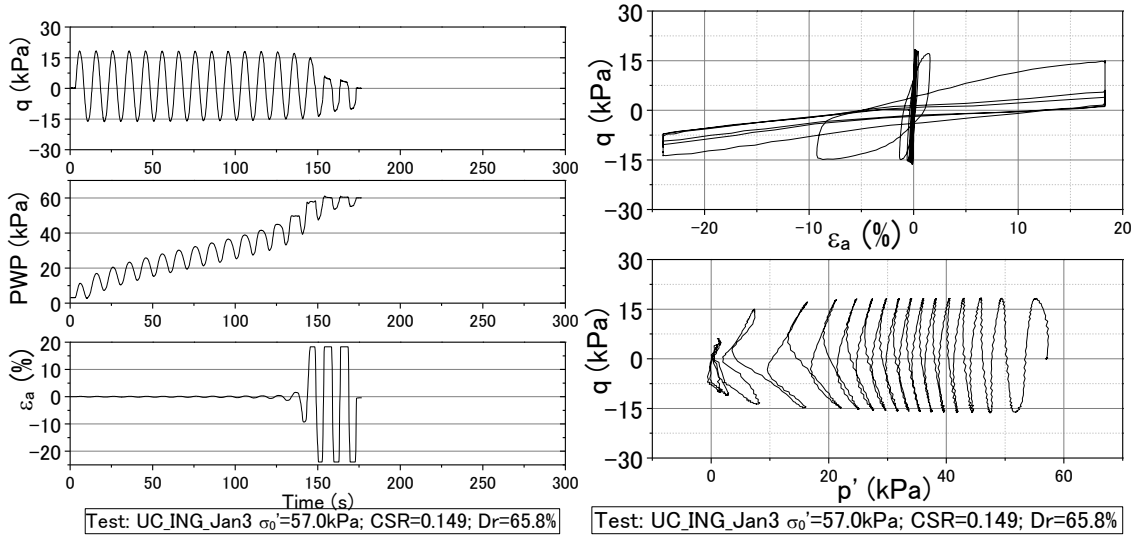

(a) Time histories; (b) Stress strain relationship and stress path

Fig. 5-16 Typical results of saturated condition of Set 3 (Inagi sand)

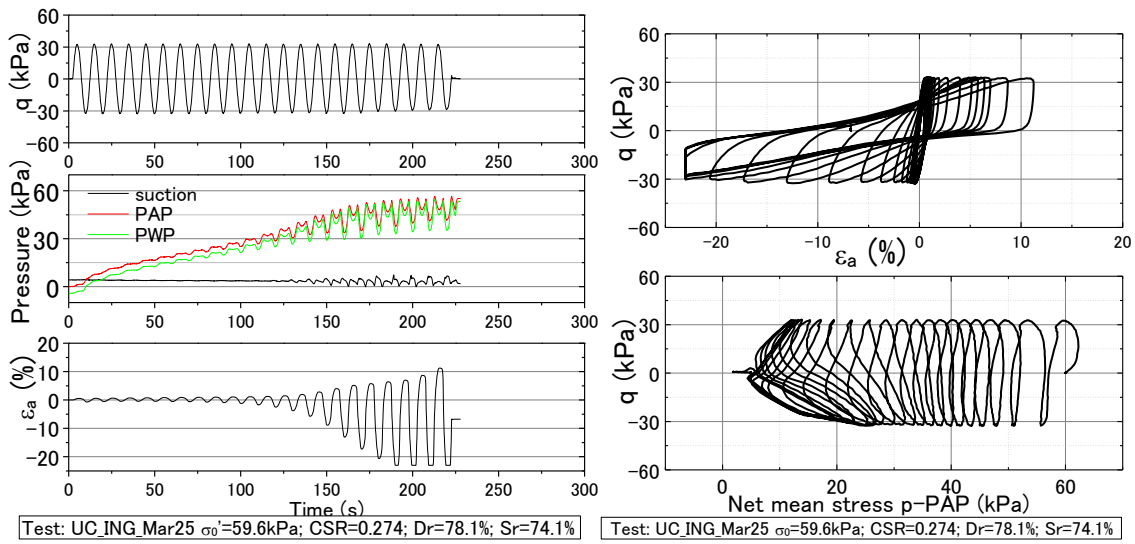

(a) Time histories; (b) Stress strain relationship and stress path

Fig. 5-17 Typical results of saturated condition of Set 3 (Inagi sand)

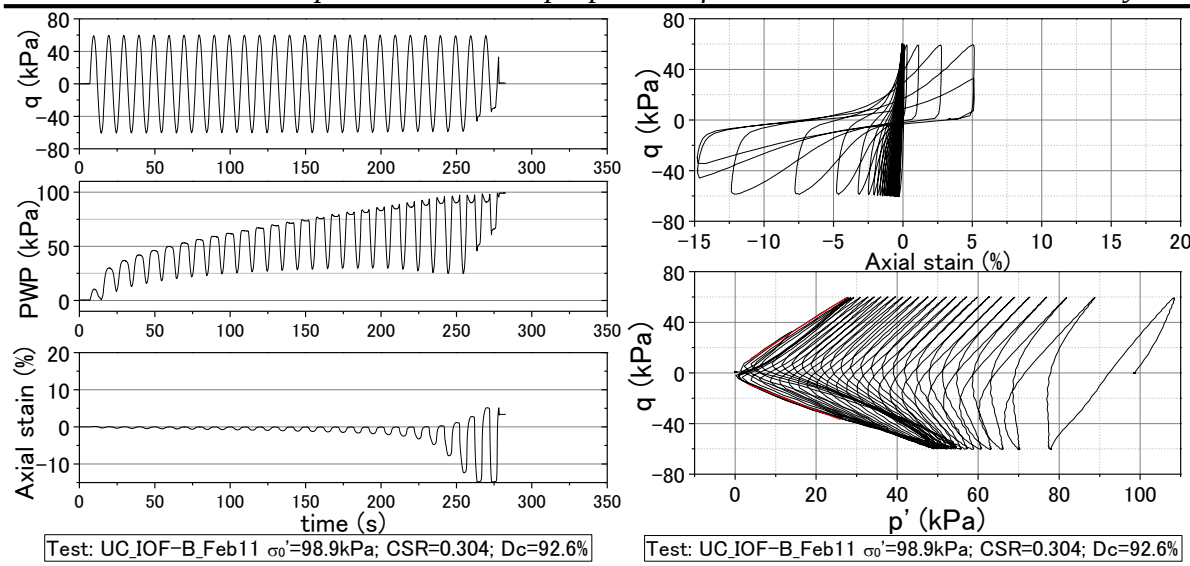

(a) Time histories; (b) Stress strain relationship and stress path

Fig. 5-18 Typical results of saturated condition of Set 4 (IOF-B)

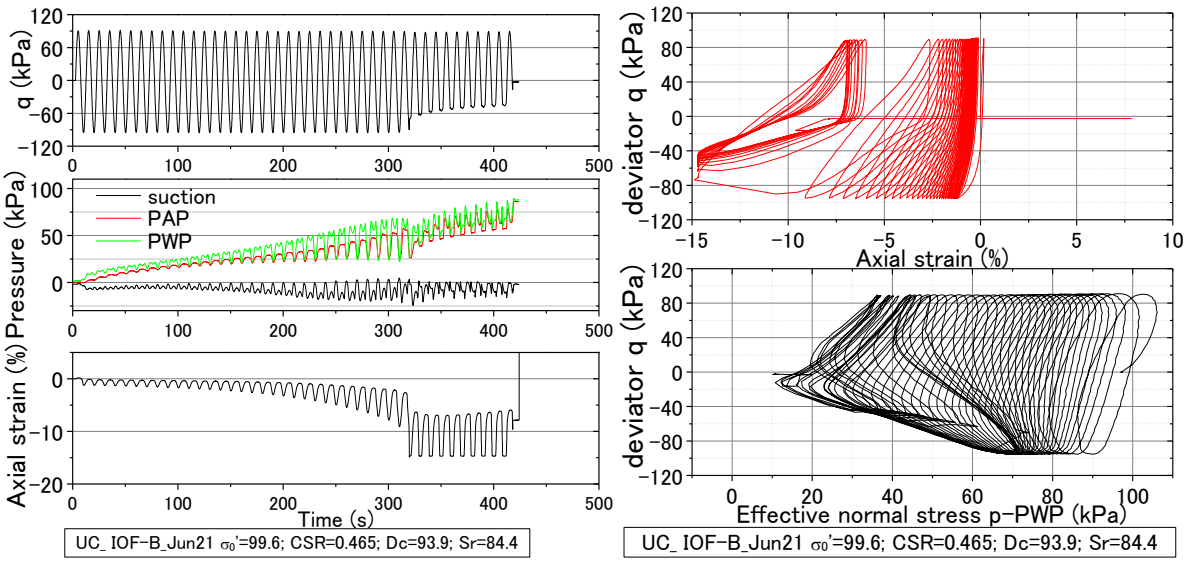

(a) Time histories; (b) Stress strain relationship and stress path

Fig. 5-19 Typical results of unsaturated condition of Set 4 (IOF-B)

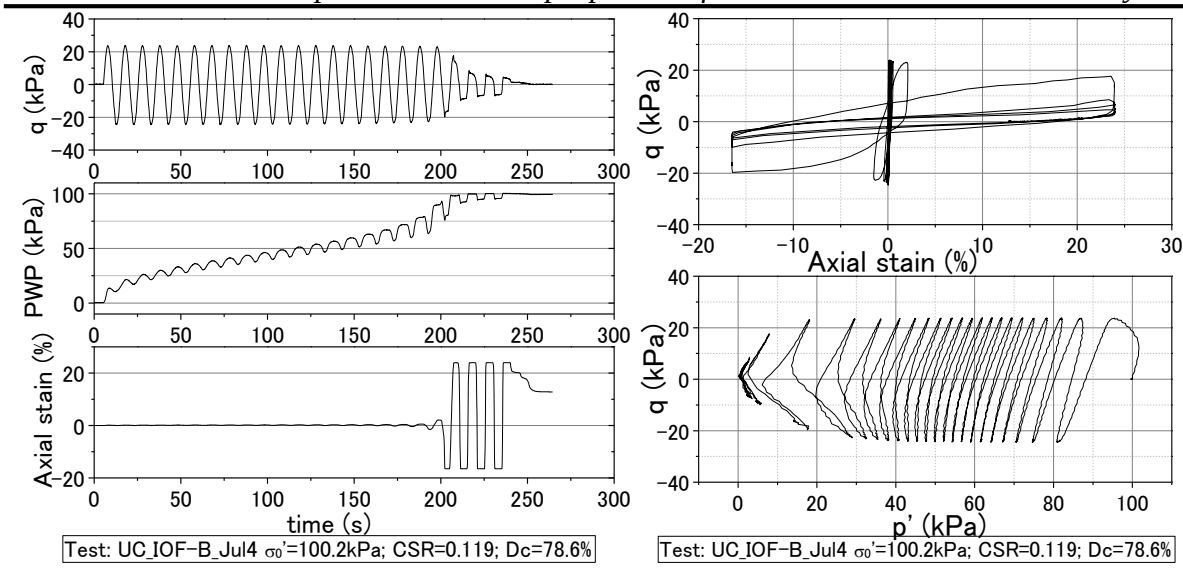

(a) Time histories; (b) Stress strain relationship and stress path

Fig. 5-20 Typical results of saturated condition of Set 5 (IOF-B)

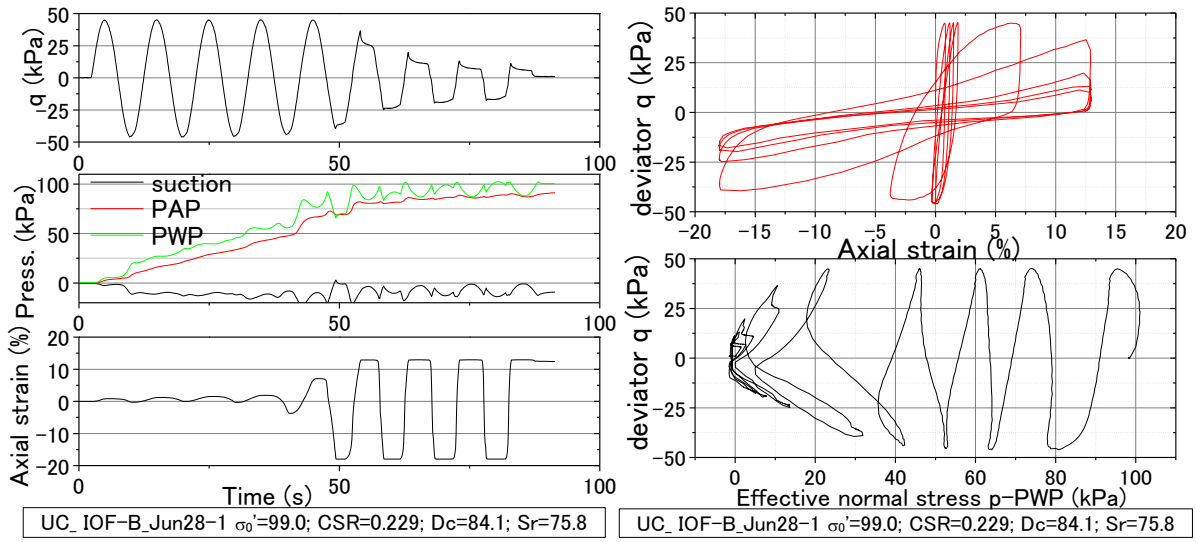

(a) Time histories; (b) Stress strain relationship and stress path

Fig. 5-21 Typical results of unsaturated condition of Set 5 (IOF-B)

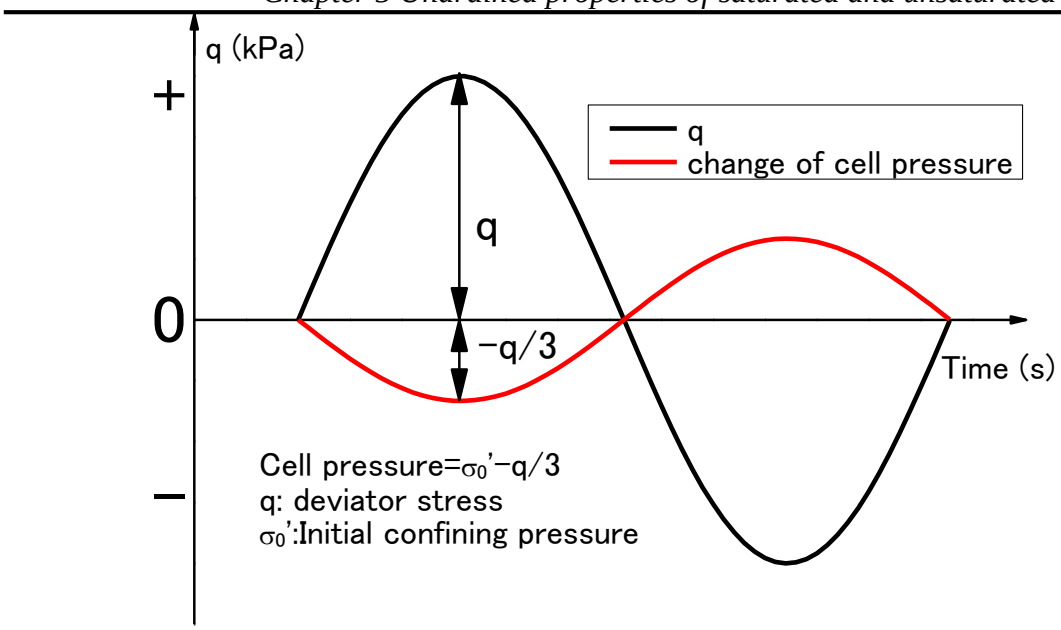

Fig. 5-22 Illustration of cell pressure control principle

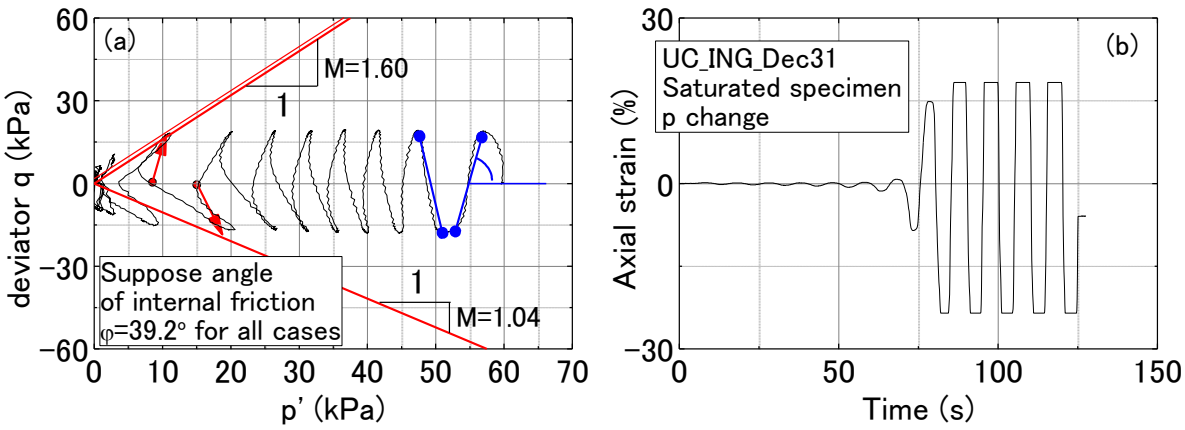

Figure 5-23 (a) Stress path and (b) strain history of a saturated Inagi sand specimen

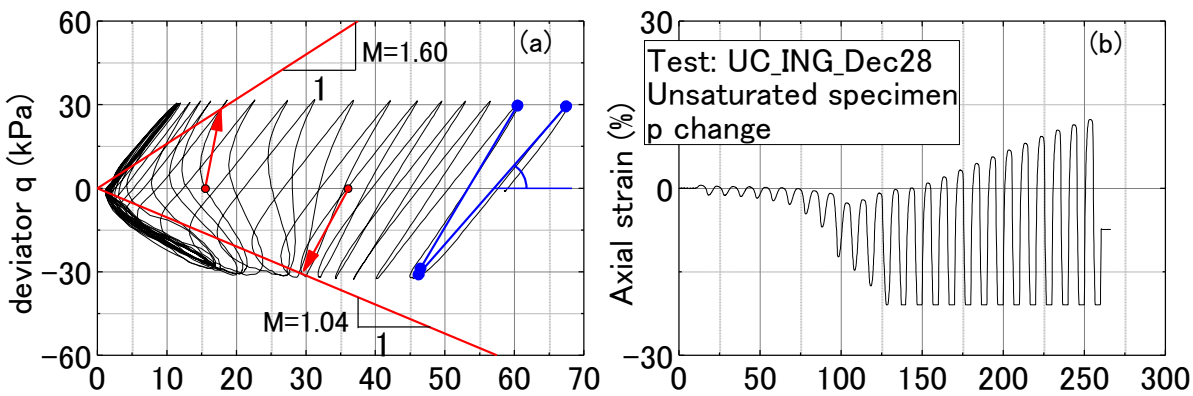

Figure 5-24 (a) Stress path and (b) strain history of an unsaturated Inagi sand specimen with p-change condition

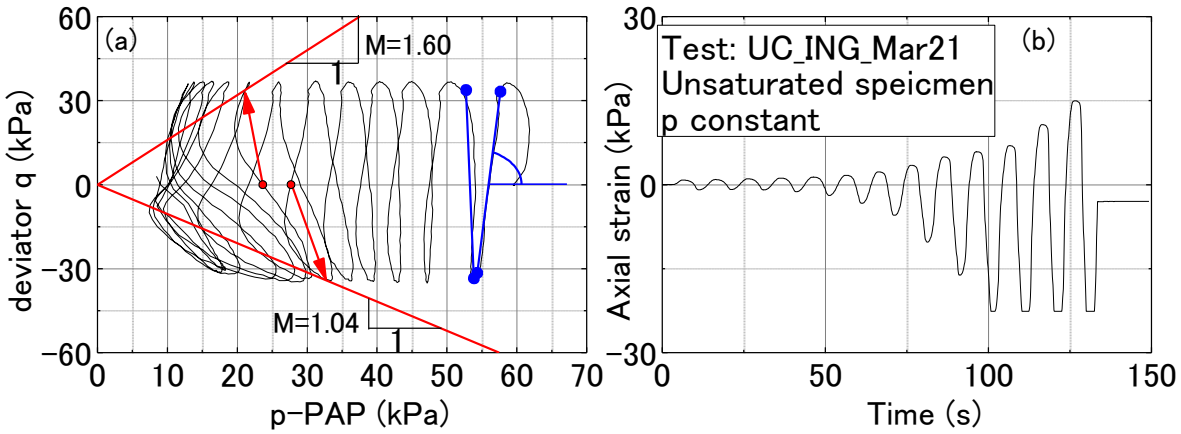

Figure 5-25 (a) Stress path and (b) strain history of an unsaturated Inagi sand specimen with p-constant condition

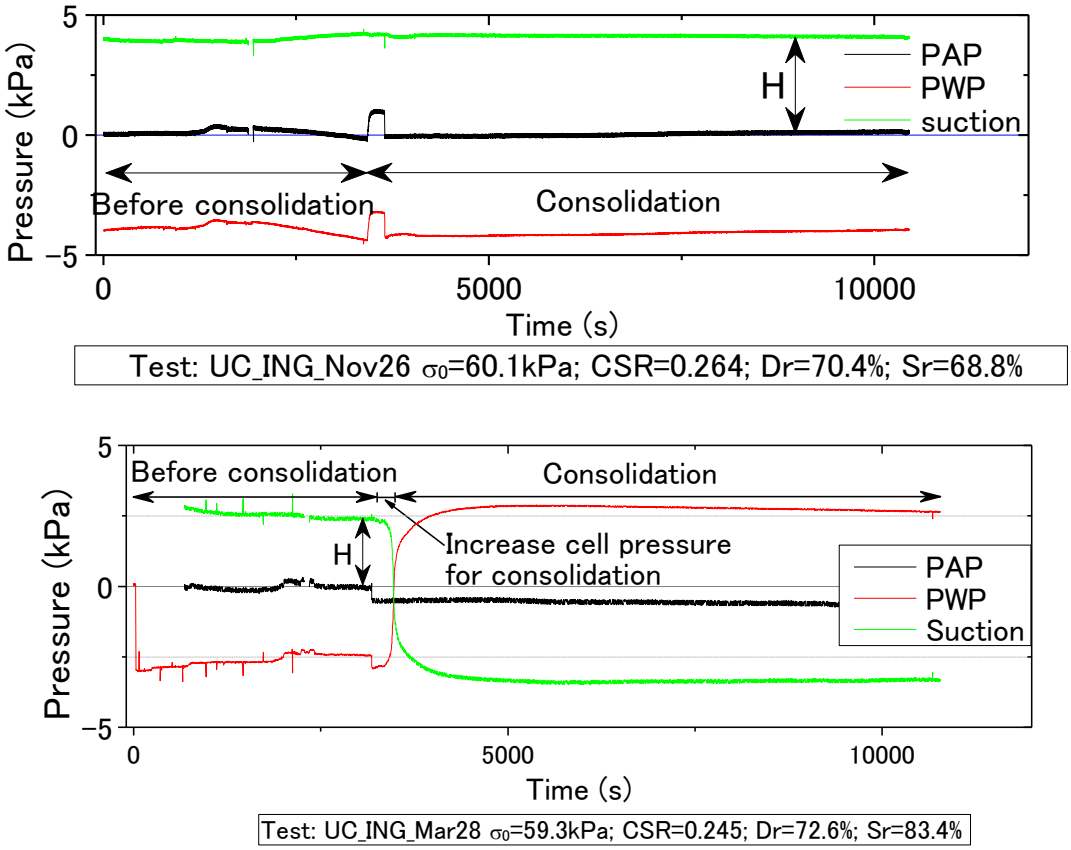

Fig. 5-26 Pore pressure measurement before applying cyclic loading

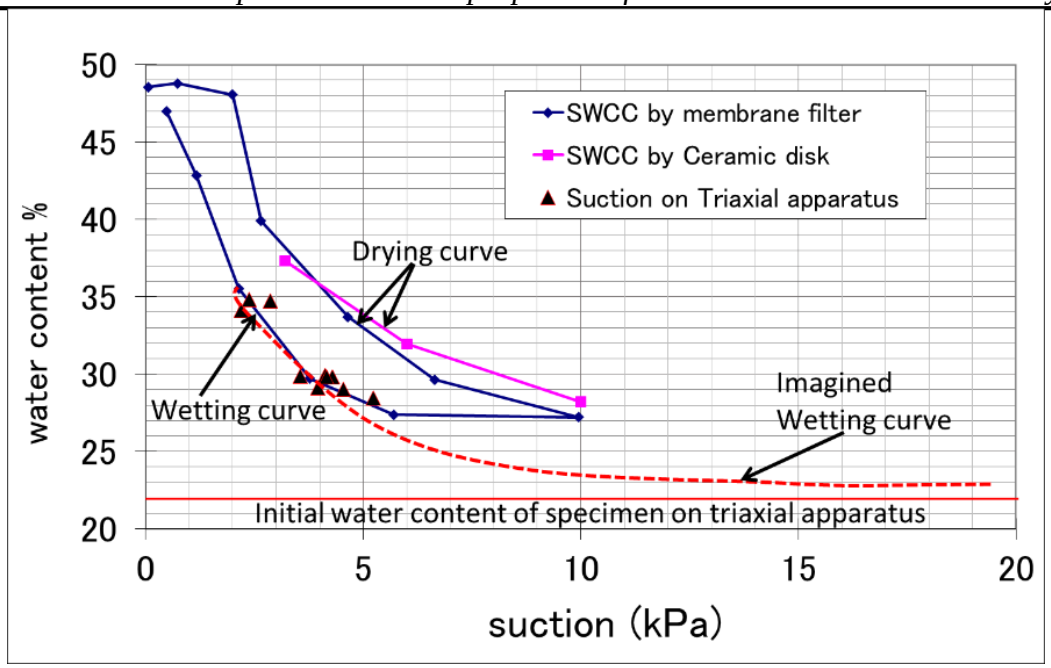

Fig. 5-27 SWCC measurement of Inagi sand

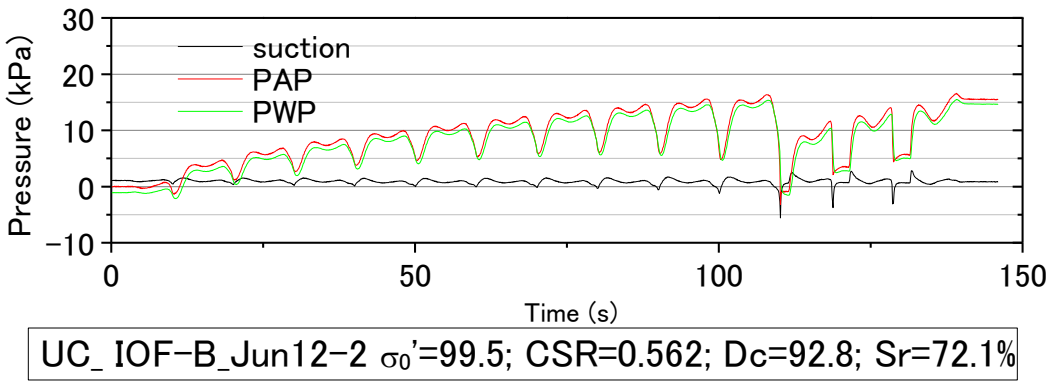

Fig. 5-28 (a) Typical measurement of pore pressure during cyclic loading for IOF-B with Sr of 72%

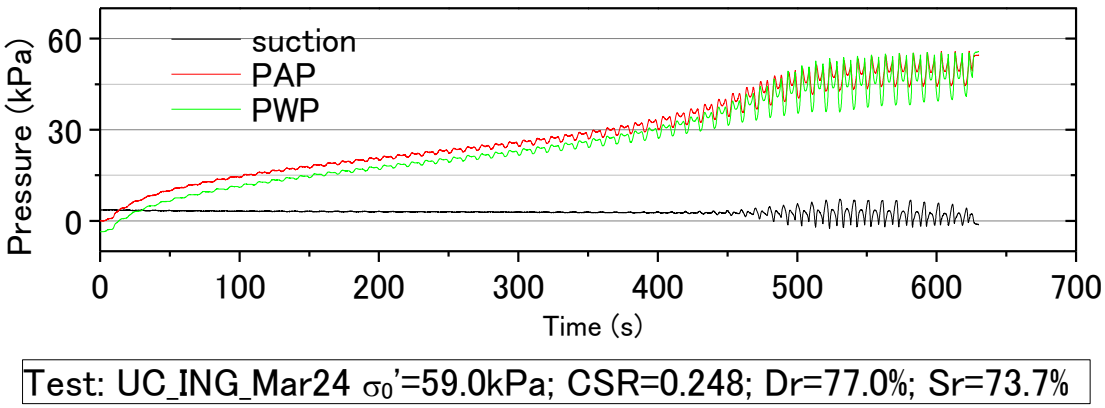

Fig. 5-28 (b) Typical measurement of pore pressure during cyclic loading for Inagi sand with Sr of 74%

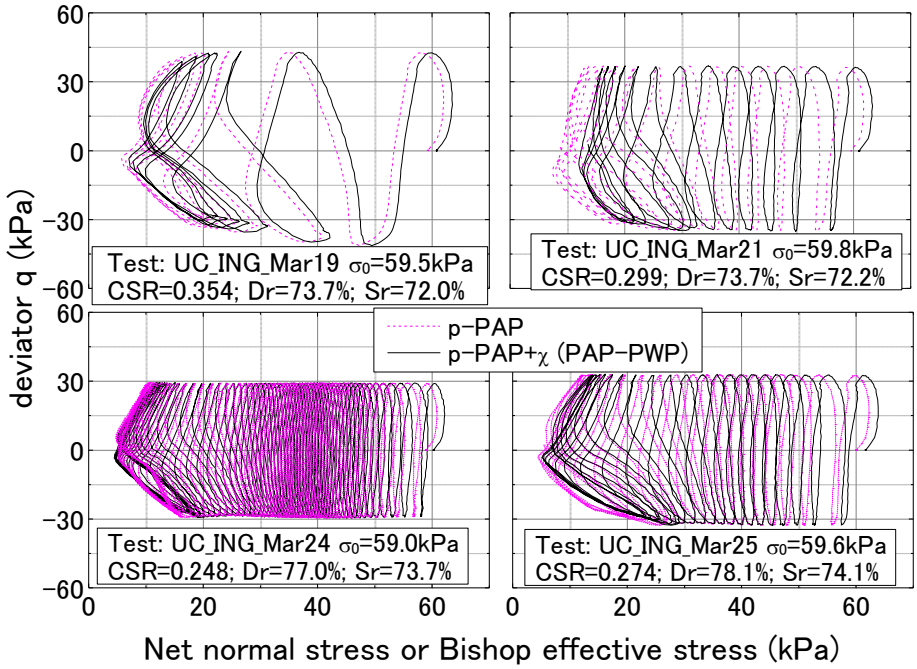

Fig. 5-28 (c) Effect of suction on effective stress paths

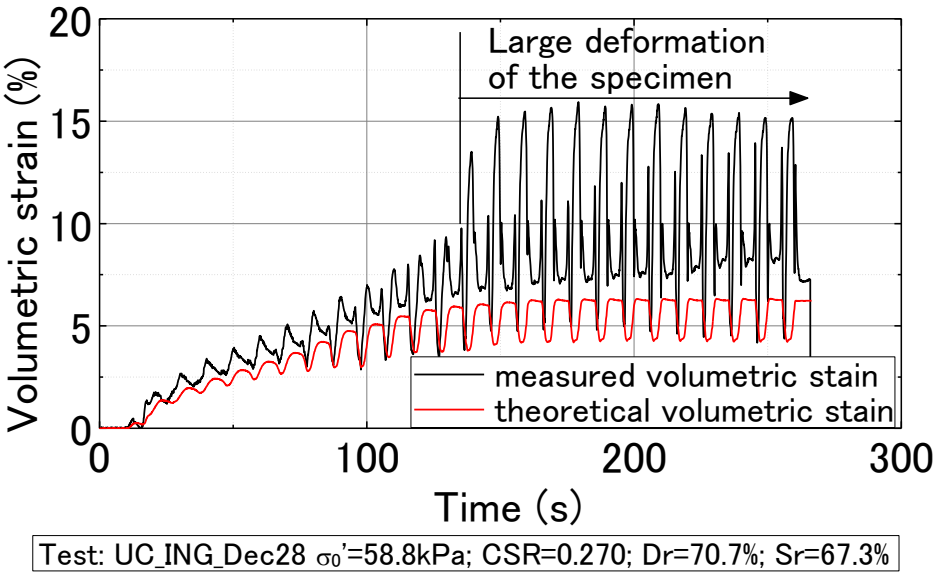

Fig. 5-29 Typical measurement of volumetric strain (Inagi sand)

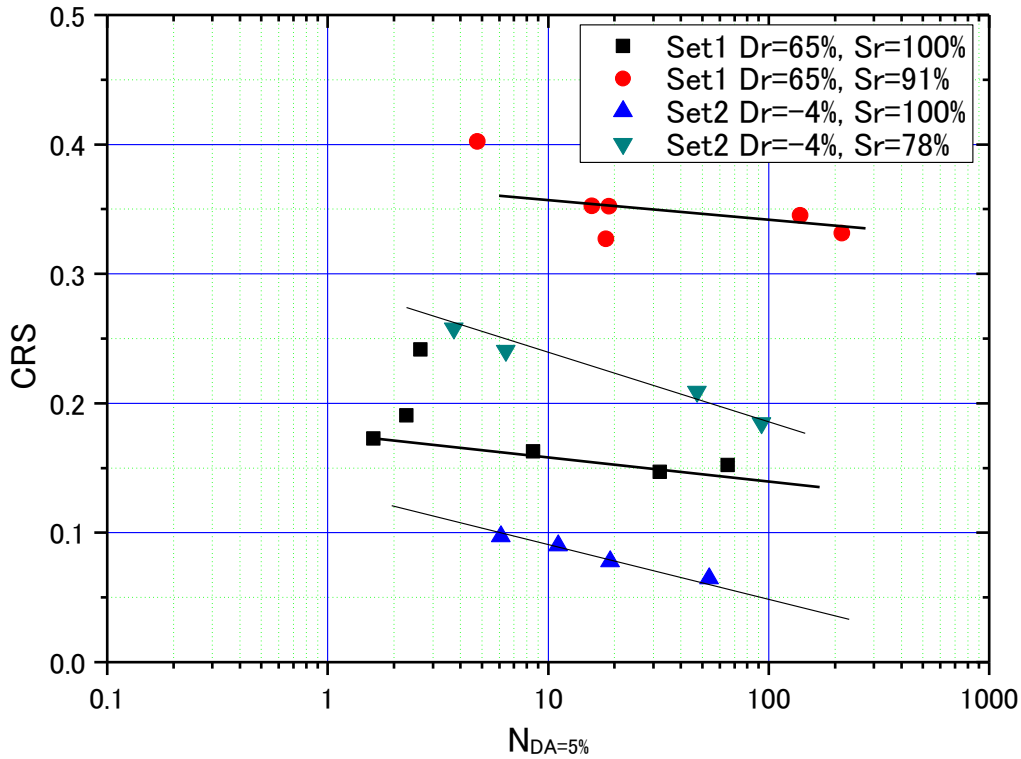

Fig. 5-30 CSR vs No. of cycles of Toyoura sand

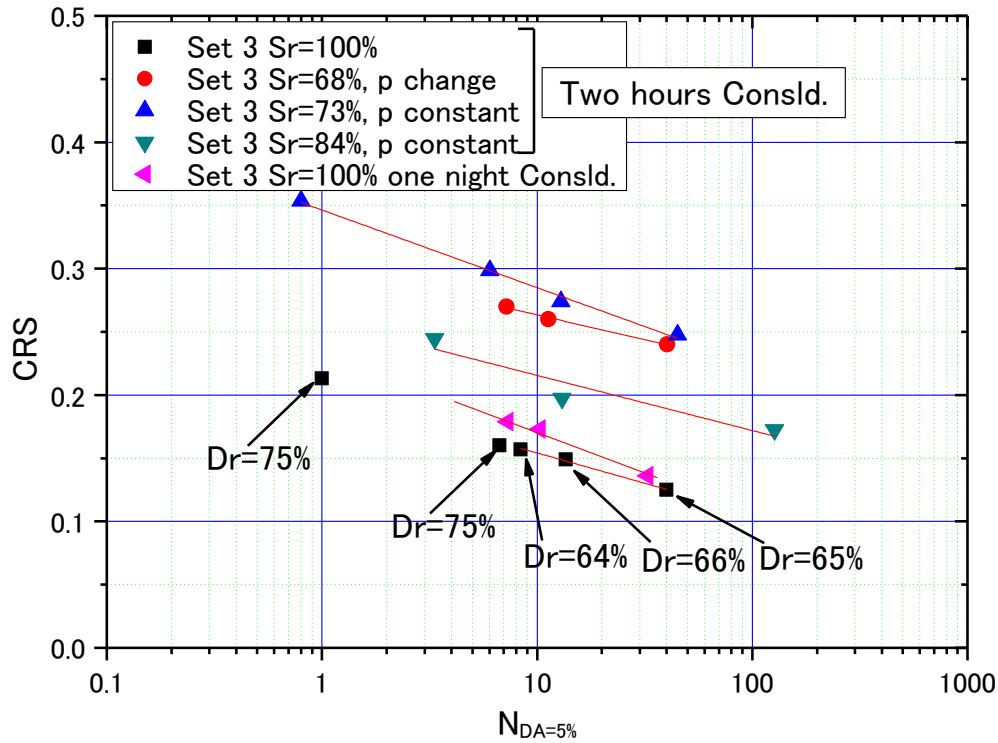

Fig. 5-31 CSR vs No. of cycles of Inagi sand

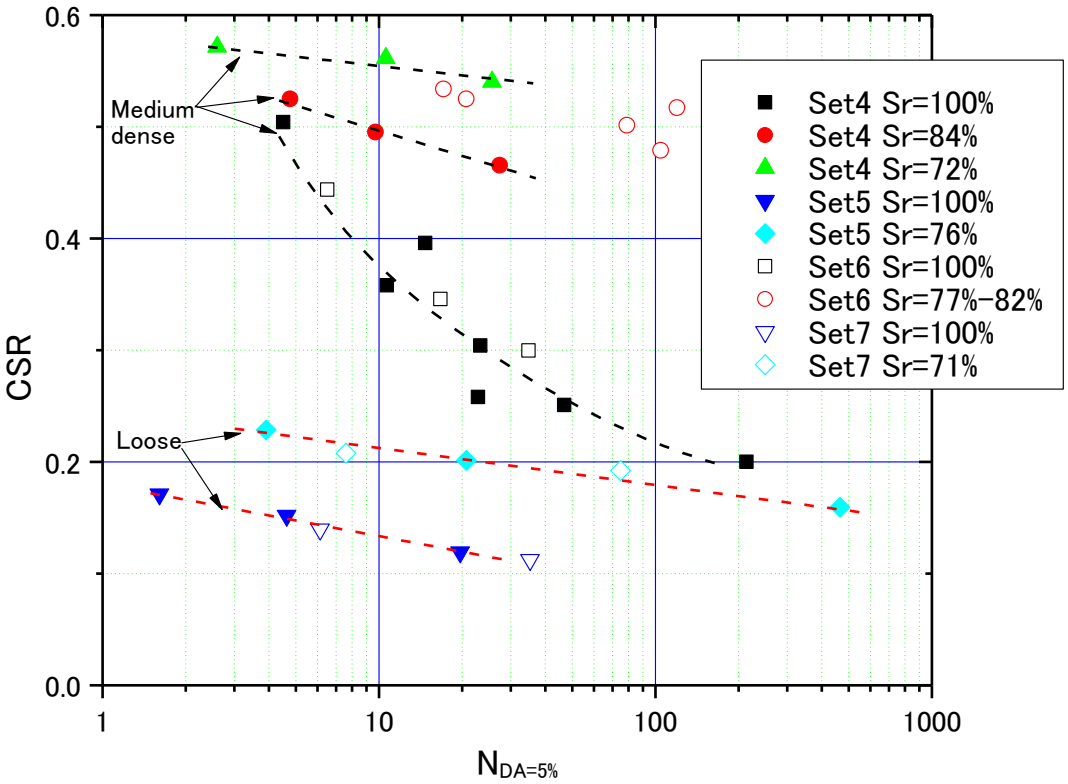

Fig. 5-32 CSR vs No. of cycles of IOF-B

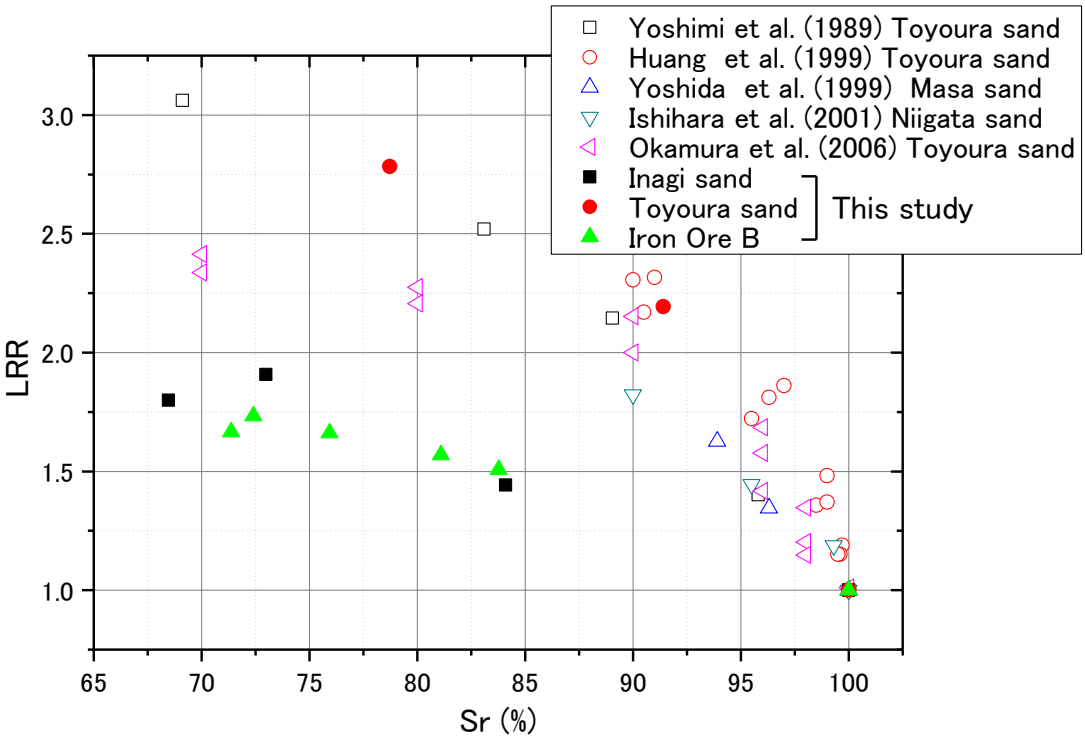

Fig. 5-33 Relationship between Sr and LRR

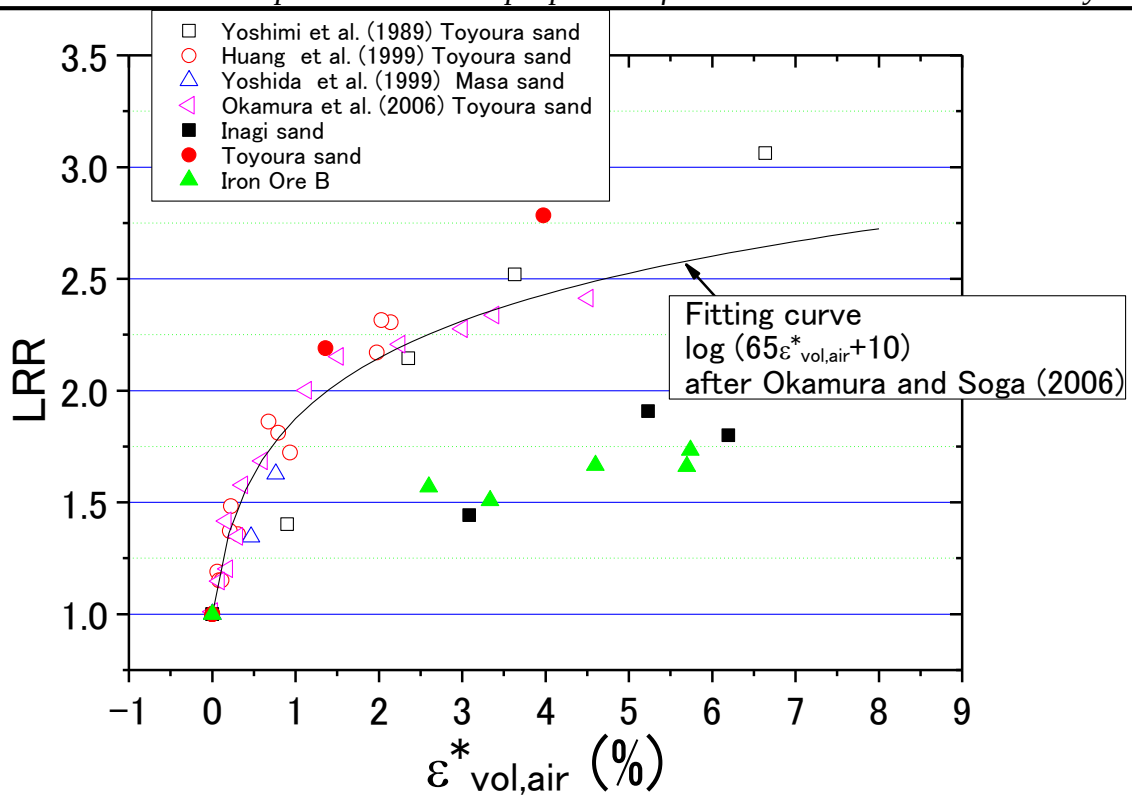

Fig. 5-34 Relationship between $\varepsilon^*_{vol,\ air}$ and LRR

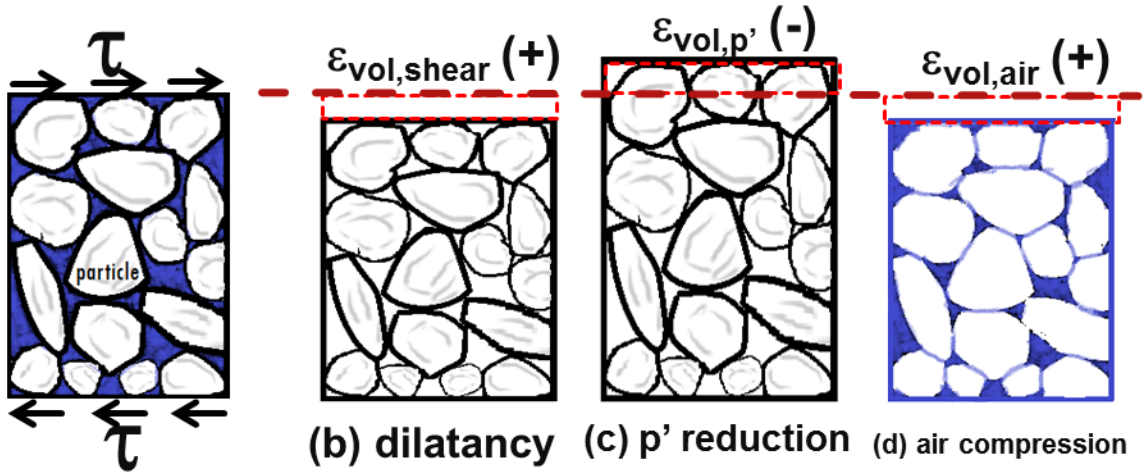

Fig. 5-35 Volume change during cyclic shear stress

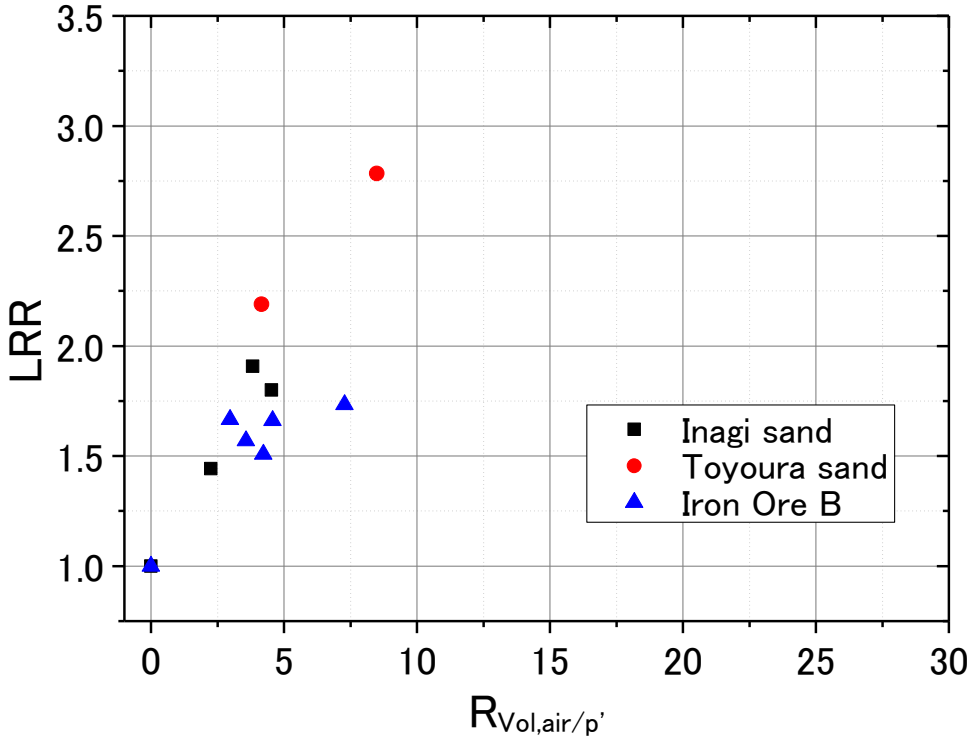

Fig. 5-36 Correlation of LRR with proposed parameter

Chapter 6. Seepage analysis of the heap of iron ore fines

Contents

6.1 Introduction

In Chapter 5, the undrained behaviors of the saturated and the unsaturated iron ore fines type B (IOF-B) are discussed. One of the conclusions is that the liquefaction resistance of IOF-B is closely related to its degree of saturation (Sr). The saturated elements of IOF-B are liquefiable for both the medium dense condition and the loose condition, meanwhile, the liquefaction or the liquefaction potential of the unsaturated elements of IOF-B are observed though their liquefaction resistance may be higher than that of the saturated condition under otherwise similar condition. Thus, the overall liquefaction resistance of the heap of IOF-B would be closely related to the distribution of Sr in the heap. The heap with a large saturated zone may be easier to liquefy than that with a small saturated zone; on the other hand, analysis considering the effect of the liquefaction potential of the unsaturated zone on the overall resistance of the heap against liquefaction should be more realistic than that without considering it. In this Chapter, distribution of Sr in the heap of IOF-B is evaluated through seepage analysis. The seepage analysis was performed based on the knowledge of water retention ability and permeability of IOF-B which are evaluated from the SWCC test and permeability test as discussed in Chapter 4. The goal of this chapter is to find the extent of the saturated zones and the distribution of Sr in the unsaturated zone of the heap under a given initial condition

6.2 Program and model

6.2.1 FEM program

A FEM program, Guslope, coded by Geotechnical Lab, Gunma Univ., Japan, is employed for the seepage analysis. This program is capable of analyzing two dimensional movement of water of the unsaturated material and giving a result of water head distribution.

6.2.2 Initial and boundary conditions

The dimensions of the heap to be simulated are shown in Fig. 6-1, which are very typical for the heaps of iron ore fines loaded on the Capesize type carriers (typically 150 kDWT or more) bulk carriers. The initial water content in the heap of iron ore fines after being loaded to a ship is thought to be rather uniform generally. To simulate this condition in the seepage analysis, as shown in Fig. 6-2, the initial water table is set at the bottom boundary of the heap, a transition phase with thickness of 0.1m is set above the water table and the rest part of the heap (from the

height of 0.1m to the height of 14m) is set to be of the same initial degree of saturation (Sr_{ini}). The density of IOF-B is assumed to be uniform everywhere in the heap. Possible change of the density caused by the seepage, the rolling motion, etc. is not considered in the simulation. The effect of rolling motion on the seepage in the heap is not taken into account due to the limitation of the software.

There are 4 boundaries for this heap, B1-B4 as shown in Fig. 6-1. B3 and B4 are always set to be impervious in all simulation conditions. B1 and B2 are set to be either impervious or pervious depending on the simulation conditions. The condition with fully impervious boundaries is expected to produce a result with the highest level of water table for a given Sr_{ini}, which may be the most critical condition. On the other head, the condition with pervious boundaries corresponds to the real condition of the heap during transportation.

6.2.4 Simulation duration and results conversion

The duration of seepage is set to be 1000 hours (about 42 days) which corresponds to a voyage from Brazil to China, while the distribution of Sr for a shorter voyage, for instance, from Australia to Japan (17 days approximately), can also be known. The duration of the voyages is referred from maritime report (DSC 18/INF.11., 2013). The water head of the point O at the bottom center of the heap as shown in Fig. 6-2 is traced to show the time history of water head at the point O.

The output results of the program is water head with unit of meter. A point with the positive water head in the heap is considered to be saturated and that with the negative value is thought to be unsaturated. The water table is assumed to be the contour line with water head of zero and it can be located through the water head at the bottom boundary. Since the Sr of the unsaturated zone is not directly given, it was determined with the help of SWCC curve which can be expressed as a relationship between suction and Sr (assuming suction=9.81 kN/m^3×water head).

6.3 Simulation conditions

Determination of permeability of the unsaturated IOF-B (k_{Uns}) is one of the key issues for the seepage analysis. The built-in Van Genuchten model (Van Genuchten 1980) is used to predict the permeability of the unsaturated IOF-B since only limited experimental data of k_{Uns} are available. The Van Genuchten model is introduced in detail in Section 4.7.2 of Chapter 4.

Basically the permeability of the unsaturated soils is proposed to be a function of water head (h) with 5 parameters:

$$k_{Uns}=f\ (k_s,\ \theta_s,\ \theta_r,\ \alpha,\ n,\ h) \qquad \text{(Eq. 6-1)}$$

where, k_s: coefficient of permeability of the soil in saturated condition;

θ_s: saturated volumetric water content;

θ_r: residual water content;

α and n: model parameters;

h: water head.

The parameter, k_s, is set as 1.008×10^{-3} cm/s which is obtained from permeability test of the medium dense specimen of IOF-B (Dc=91.7% and ρ_d=2.55 g/cm^3) under the confining pressure of 100 kPa as discussed in Chapter 4. Parameters, θ_s and θ_r, are determined by the density and SWCC of IOF-B. Parameters, α and n, can be determined by fitting SWCC of IOF-B. Three SWCCs of IOF-B for different densities are used. Fig. 6-3 shows the comparison of fitting curves and test results. Table 6-1 lists the conditions of SWCC tests and obtained parameters. It shows that for one SWCC, there are two sets of parameters, one is obtained from the drying curve of SWCC and another is from the wetting curve because of the hysteresis effect of SWCC. Since the built-in Van Genuchten model could not consider the hysteresis effect in the simulation, the effect of different parameter settings on the results are examined.

Table 6-1 SWCC tests and Van Genuchten model fitting

Test name	G_s	e	ρ_d (g/cm3)	θ_s (%)	θ_r (%)	Drying curve		Wetting curve	
						a (/m)	n	A (/m)	n
SW_L_IOF-B_3_3	4.444	0.727	2.57	42.1	27.0	7.3	2.79	65.5	1.70
SW_L_IOF-B_4_3	4.444	0.814	2.45	44.9	26.3	9.4	2.89	39.1	2.03
SW_L_IOF-B_2_2	4.444	1.214	2.01	54.8	21.3	22.2	2.14	81.5	1.79

In Table 6-2, simulation conditions performed in the seepage analysis are listed. Cases 1 and 2 are conditions with fully impervious condition. Cases 3 and 4 are conditions with pervious boundaries of B1 and B2 (Fig. 6-1). The effect of parameters α and n obtained by either the drying curve or the wetting curve of SWCC is examined in Cases 1-4. Cases 3, 5 and 6 examine the effect of density.

Table 6-2 Conditions of seepage analysis

Case No.	Corresponding Test	e	θ_s (%)	θ_r (%)	k_s $\times 10^{-3}$ cm/s	Sr_{ini} (%)	Boundary B1 and B2	SWCC Curve
1	SW_L_IOF-B_3_3	0.727	42.1	27.0	1.008	65-95	impervious	Drying
2								Wetting
3							pervious	Drying
4								Wetting
5	SW_L_IOF-B_4_3	0.814	44.9	26.3	1.008	65-95	pervious	Drying
6	SW_L_IOF-B_2_2	1.214	54.8	21.3	1.008	40-95	pervious	Drying

6.4 Results–contour figures of final water head distribution

In this section, the contour figures of water head distribution in the heap (Figs. 6-4~6-9) at the final state (at 1000 hours) are displayed. The legends shown in the figures indicate the magnitude of the water head. It should be noted, however, that because of the limitation of the software, the same color in different contour figures (e.g. green color in Figs. 6-7 a and 6-7 b, blue color in Figs. 6-7 c and 6-8 c, etc.) does not always represent the same value of water head, thus the direct comparison of water head between figures is difficult. This issue may not be serious since these contour figures are only used for general observation of simulation results in this section. The symbols of water table are placed on each contour figure to qualitatively distinguish the interface between the saturated zone and the unsaturated zone (or the zone with positive water head and zone with negative water head). The quantitatively analysis of simulation results are presented in later sections.

Figs. 6-4~6-9 show that the patterns of water head distribution are different depending on the Sr_{ini}. The water head seems to be proportional to the elevation when Sr_{ini} is relatively low; while the zones where the water head values are similar (e.g. the zone in red trapezoid in Fig. 6-4 d) are observed for the cases with relatively high Sr_{ini}. The results may be related to the SWCC curves as shown in Fig. 6-3. For the conditions with relatively low values of Sr_{ini} (e.g. $Sr_{ini}\leq 70\%$ in Case 1-4, $Sr_{ini}=65\%$ in Case 5 and $Sr_{ini}=42\%$ in Case 6), the values of Sr_{ini} are all close to their corresponding residual values of Sr, which means the slight change in Sr will induce significant change in suction or water head. As a result, the equilibrium between suction and Sr can be achieved with only slight change of Sr from Sr_{ini}. While for the conditions with relatively high Sr_{ini}, in order to achieve equilibrium between suction and Sr, more water needs

to move, during which the seepage in the heap may be affected by other issues as explained in the following content.

For some cases with the pervious boundaries in Figs. 6-6~6-9, the water head in the zone slightly above the water table (e.g. zone in black closed curve in Fig. 6-6 d) seems dryer than the zone above it. It may be caused by the difference of permeability in the heap. Since the permeability of IOF-B in the saturated zone is higher than that in the unsaturated zone, water in the unsaturated zone near the water table may be easier to drain out along the water table than that in some other unsaturated areas. Because water in the zone near the drainage boundaries may also be easier to drain out, as a result, the Sr value in these zones is lower than that in any other places in the unsaturated zone. However, these zones with low permeability (trap circle, the zone slightly above water table and the zone near the boundary) may stop the water drainage inside this circle.

6.5 Results- time histories of the bottom center point O

Fig. 6-10 shows the water head change of point O at the bottom center of the heap with time for 6 cases, which indicates the time history of the height of the saturated zone. It is noticed that for conditions with relatively low Sr_{ini}, the water head at point O may momentarily becomes negative (e.g. black lines in Figs 6-10 a, b, c, d and f) and it takes longer time for stabilization (e.g. red lines in Figs 6-10 a, b, c and d; black line in Figs 6-10 e and f) than those conditions with relatively high Sr_{ini}. The longer duration of the stabilization may be attributed to the low permeability in the conditions with low Sr_{ini}. Another finding in Fig 6-10 being worth mentioning is that there are cases that the final water head at point O for a lower Sr_{ini} is higher than that for a higher Sr_{ini} (e.g. Fig.6-10 b, red line vs blue line; Fig. 6-10c, pink line vs green line; Fig. 6-10d, red line vs blue line and pink line vs green line; Fig. 6-10e, pink line vs blue line), which may be affected by formation of the trap circle observed in Figs. 6-4~6-9. Regarding the effect of different boundary conditions, it seems that there is no reduction of the water head histories (Figs. 6-10 a and b) in cases with the impervious boundaries, while the reduction from peak values are observed in cases with pervious boundary (Figs. 6-10 c-e). However, no reduction is observed for the Case 6 (loosest condition) even for a very high water head at point O (Fig. 6-10 f, dark blue and green lines). It may be related to the permeability difference near the drainage boundaries, where slight difference in Sr may cause significant change in permeability for the loose IOF-B due to its low air entry value, by which the drainage may be clocked by the less permeable areas at, such as, the two toes of the heap.

6.6 Discussion

Considering the safety of the ship in the ocean with iron ore fines, it is necessary to think of the critical condition the ship may experience. The highest water table in the heap of IOF-B for a given Sr_{ini} is compared among 6 cases of the seepage analysis. According to the results described in the previous sections, the maximum height of water table (H_{Max}) is assumed to be the maximum water head at bottom center point (point O).

Fig. 6-11(a) shows the relationship between Sr_{ini} and H_{Max} for Cases 1 and 2 which are of impervious boundaries. Case1 used the parameters obtained from drying curve of SWCC and those of Case2 are from wetting curve of SWCC. It shows that values of H_{Max} in these cases are close to each other when Sr_{ini} is relatively low; while the values of H_{Max} for Case 1 are much higher (about 1.5m higher) than those of Case 2 for the same Sr_{ini} when Sr_{ini} is relatively high. It implies that the two parameters, α and n in the Van Genuchten model, may significantly affect the distribution of Sr. It can be seen from Figs. 6-5 (d) and (e) that the size of arrows, which represent the flow speed of the pore water, in the unsaturated zone are not very uniform as compared with that shown in Figs. 6-4 (d) and (e). It also indicates that the seepage may be affected by the parameters, α and n.

The relationship between Sr_{ini} and H_{Max} for Cases 1-4 in Fig. 6-11(b) shows that, using parameters, α and n, obtained from drying curve of SWCC also produces the higher H_{Max} for the cases with pervious boundaries; on the other hand, the H_{Max} is lower for the conditions with pervious boundaries.

Fig. 6-11(c) summarizes the H_{Max} of Cases 3, 5 and 6 of which the boundary conditions are the same and the parameters, α and n, are obtained from the drying curves of SWCCs. Though the data scattered severely, an envelope can be drawn which shows the relationship between Sr_{ini} and possible maximum value of H_{Max} regardless of density of IOF-B. Four points near the envelope (three points from Case 3 and one point from Case 5 as shown in Fig. 11c) are picked up to analyze the distribution of Sr along vertical center line of the heap at the moment when the H_{Max} condition is reached as shown in Fig. 6-12. It can be seen that the Sr in the unsaturated zone is rather uniform for a given Sr_{ini}, which is about 5%-10% less than Sr_{ini}. By using the results of Fig. 6-12, the distribution of Sr in the heap can be estimated for different Sr_{ini} values.

6.7 Chapter conclusions

In this chapter, seepage analysis is performed to study the water content distribution in the heap of iron ore fines type B (IOF-B). The analysis results show that the water in the unsaturated zone may be trapped inside the heap for a relatively high initial Sr (Sr_{ini}) due probably to the formation of zones with low permeability (trap circle); the height of water table may largely depends on the formation of this trap circle. An envelope is drawn on the relationship between Sr_{ini} and possible maximum water table regardless of density of IOF-B. The distribution in the unsaturated zone may be rather stable and can be roughly estimated according to the values of Sr_{ini}.

Reference

1. DSC 18/INF.11. (2013). The Technical Working Group (TWG) Report #2 Marine Report. International Maritime Organization.
2. Van Genuchten, M. Th. (1980) A closed-form equation for predicting the hydraulic conductivity of unsaturated soils, Soil Sci. Soc. Am. J., 892-898.

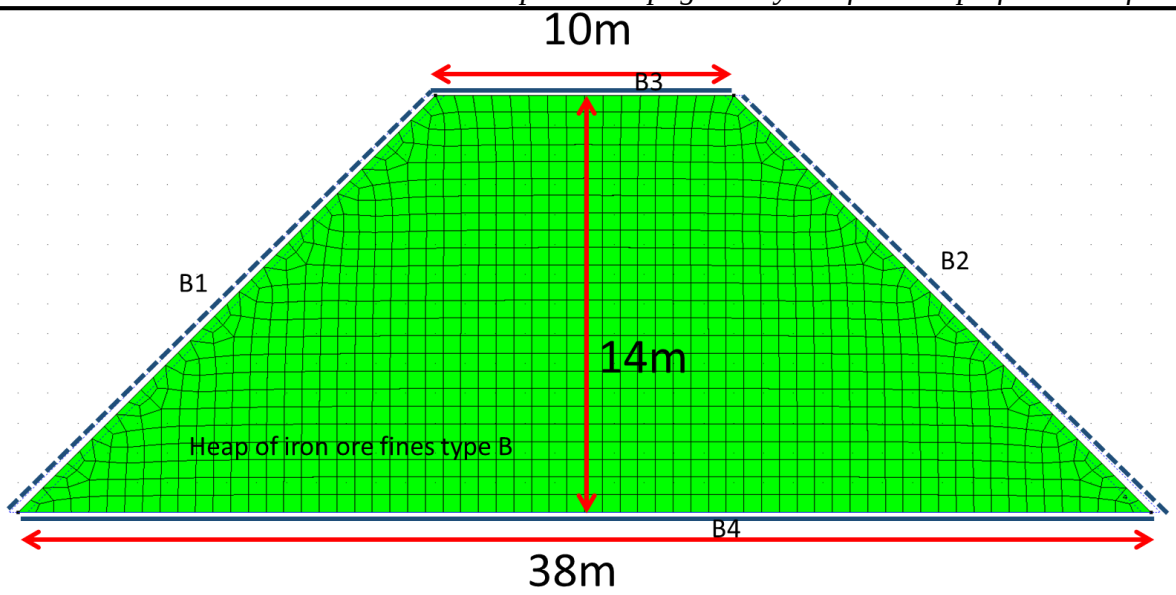

Fig. 6-1 Model of heap of IOF-B for seepage analysis

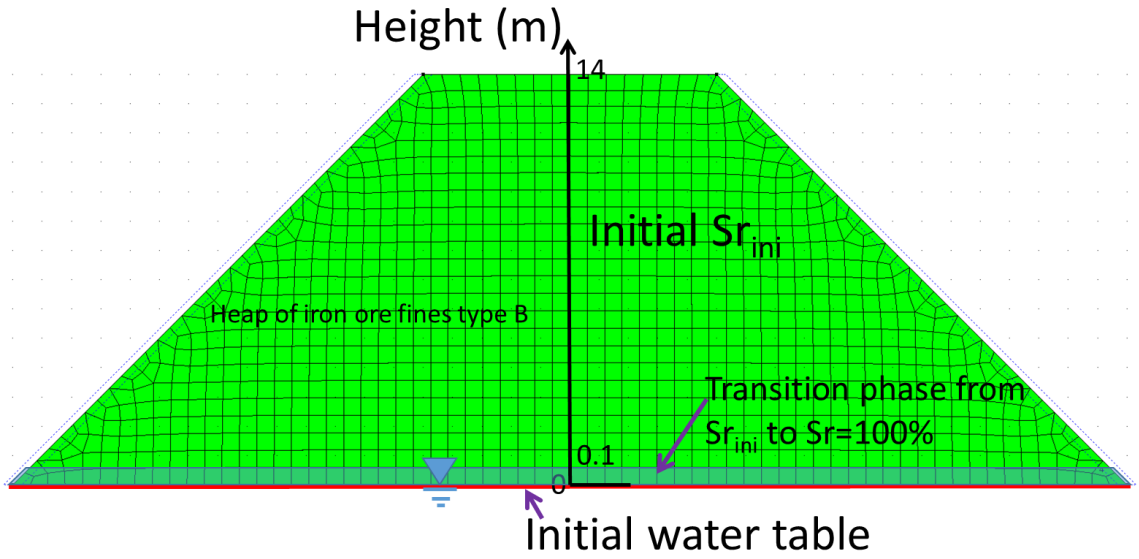

Fig. 6-2 Heap dimensions and boundary conditions

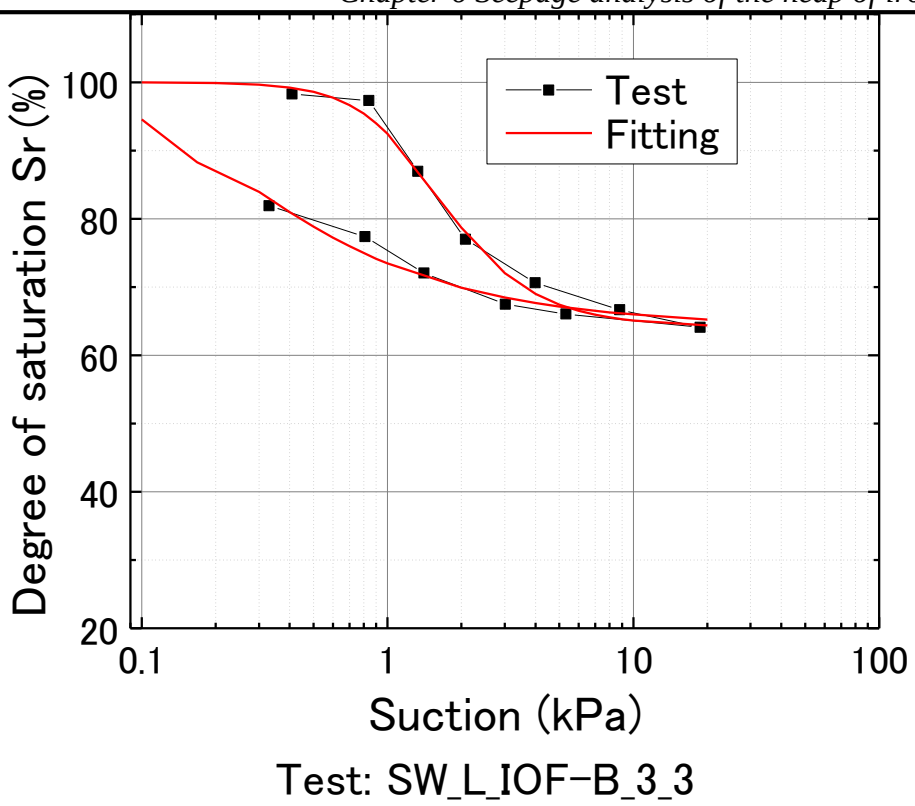

Fig. 6-3 (a) Fitting of SWCC of SW_L_IOF-B_3_3

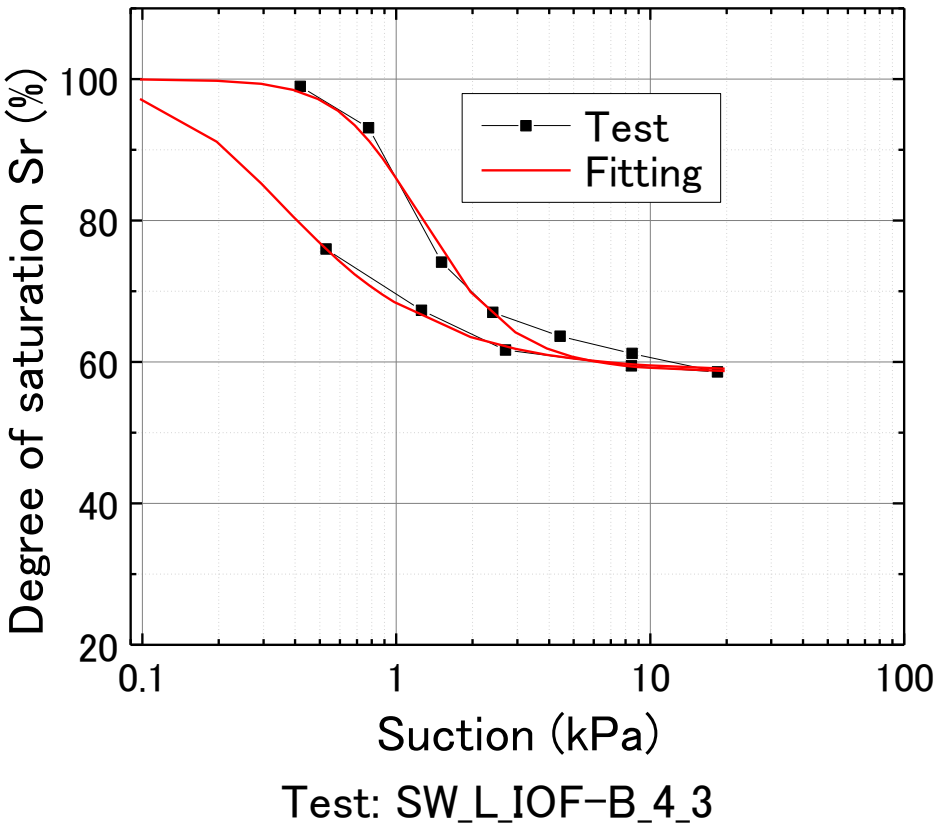

Fig. 6-3 (b) Fitting of SWCC of SW_L_IOF-B_4_3

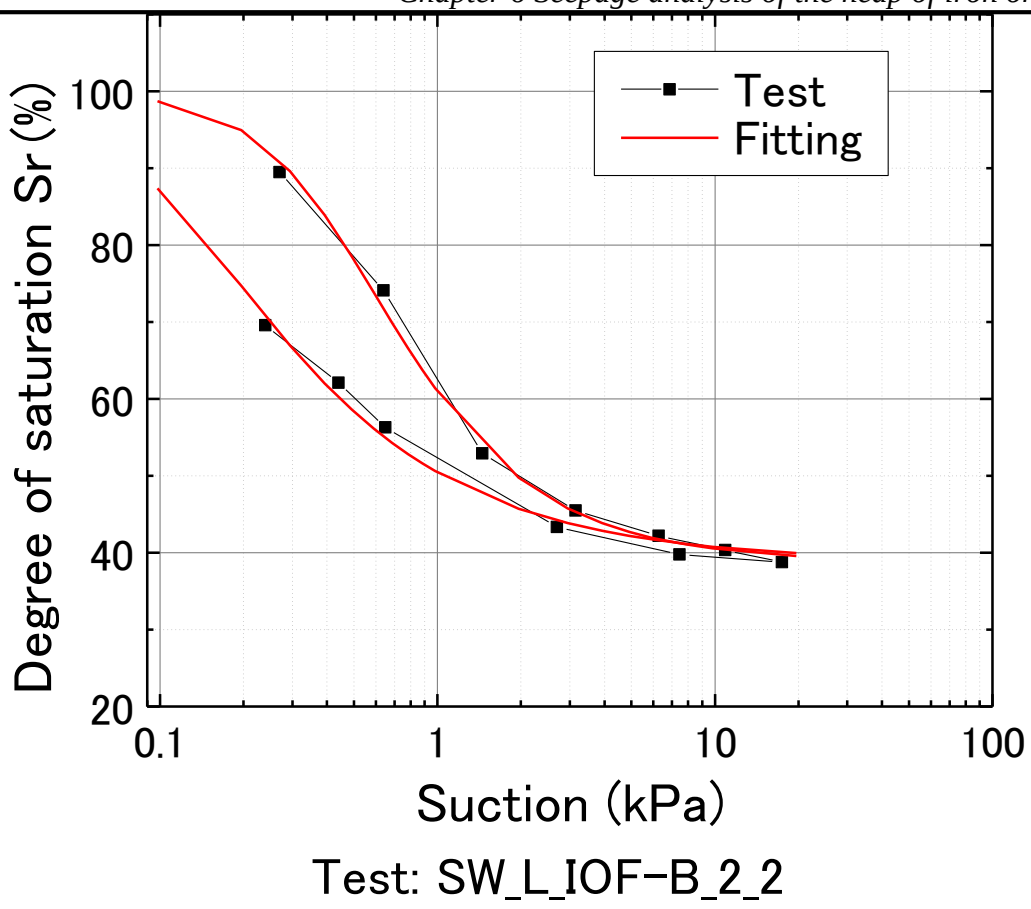

Fig. 6-3 (c) Fitting of SWCC of SW_L_IOF-B_2_2

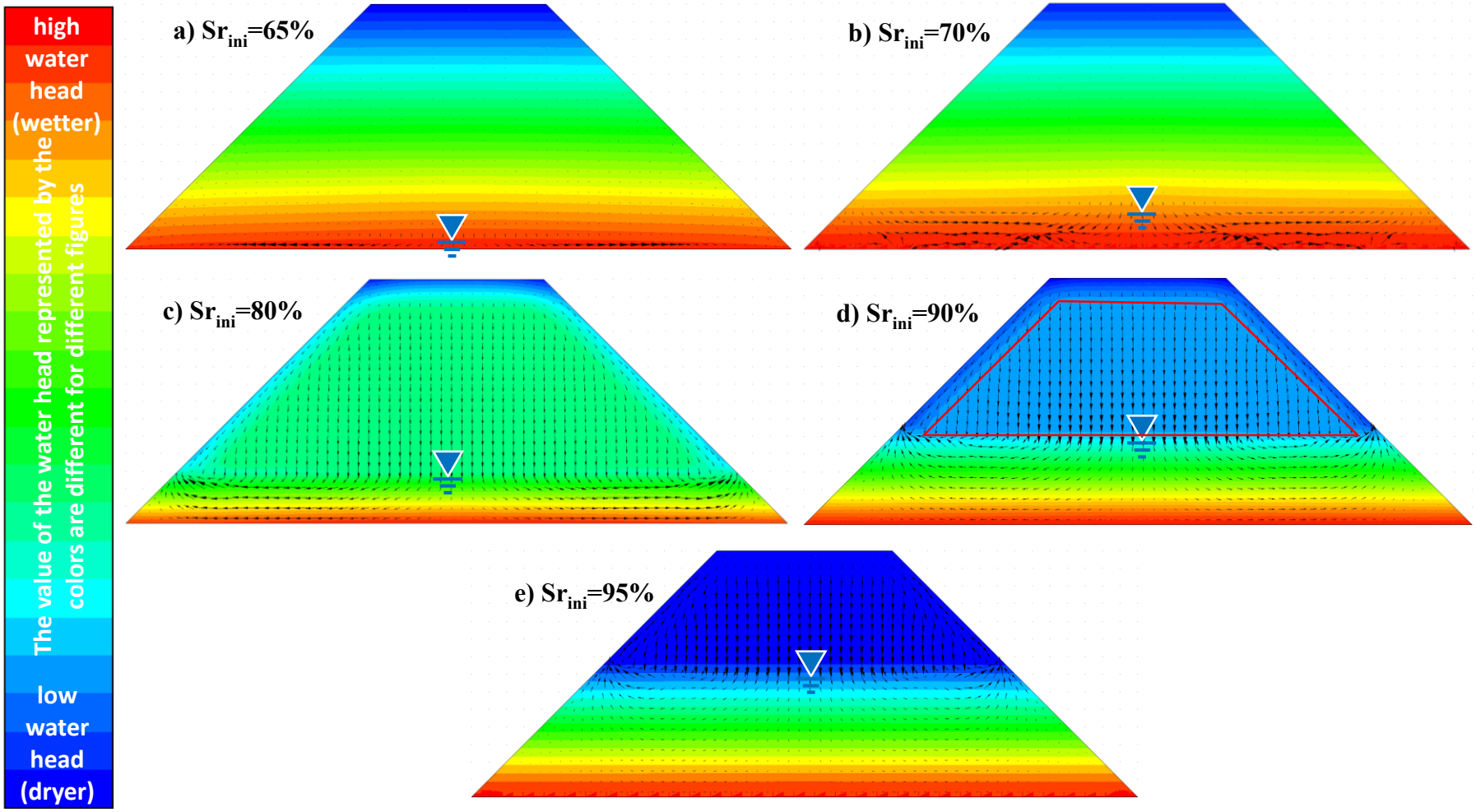

Fig. 6-4 Water head distribution for different initial degree of saturation in Case 1

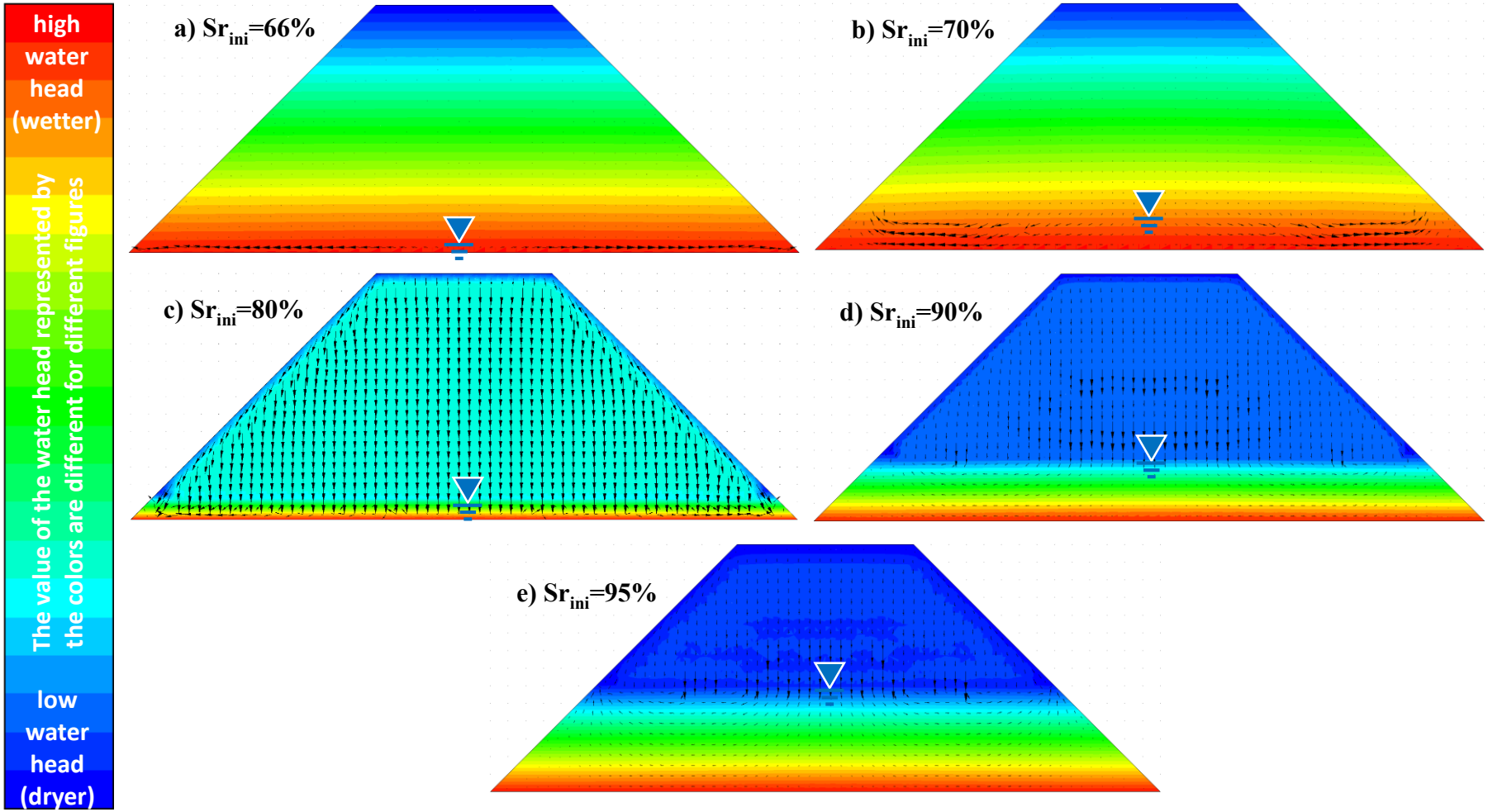

Fig. 6-5 Water head distribution for different initial degree of saturation in Case 2

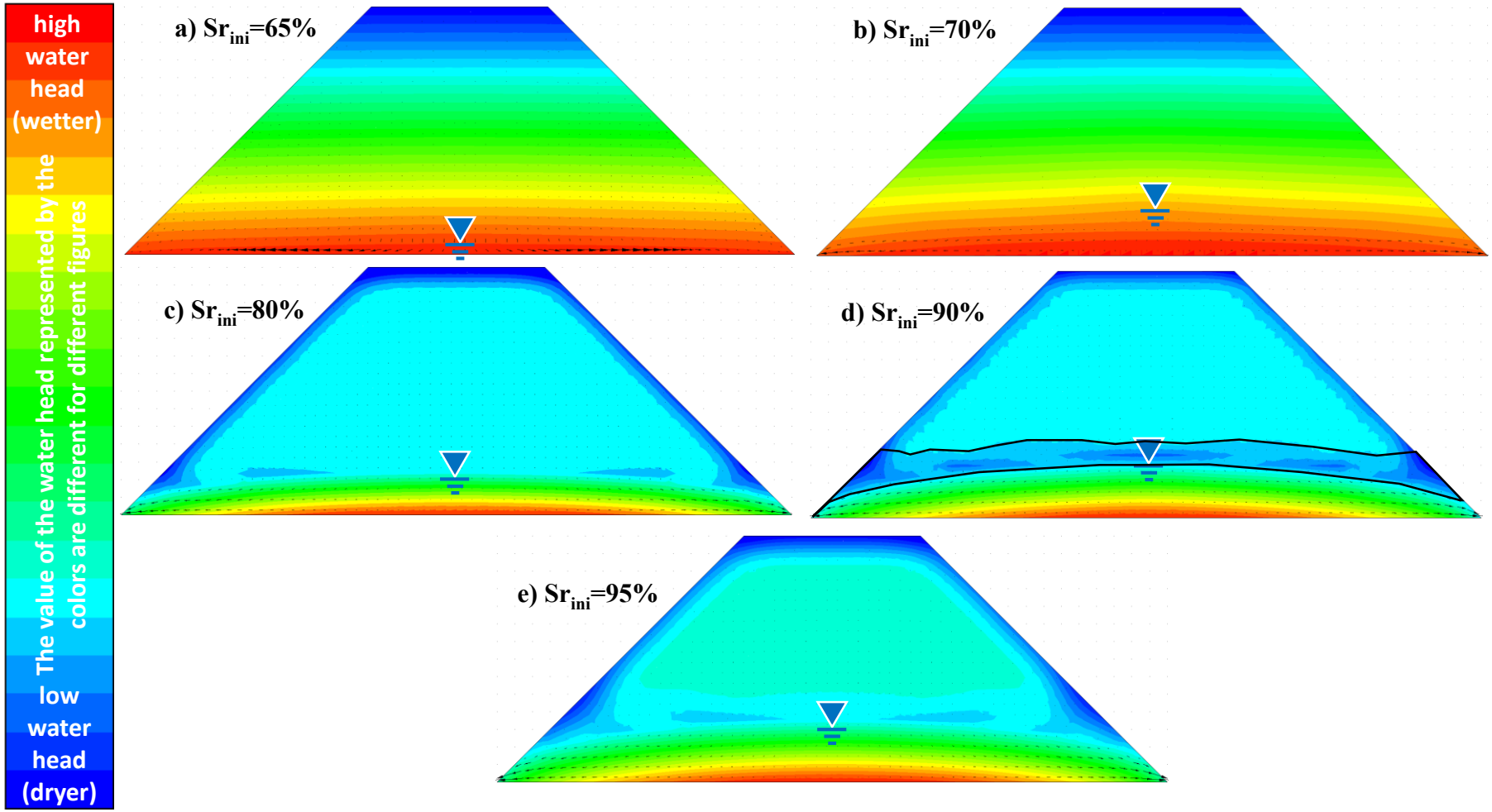

Fig. 6-6 Water head distribution for different initial degree of saturation in Case 3

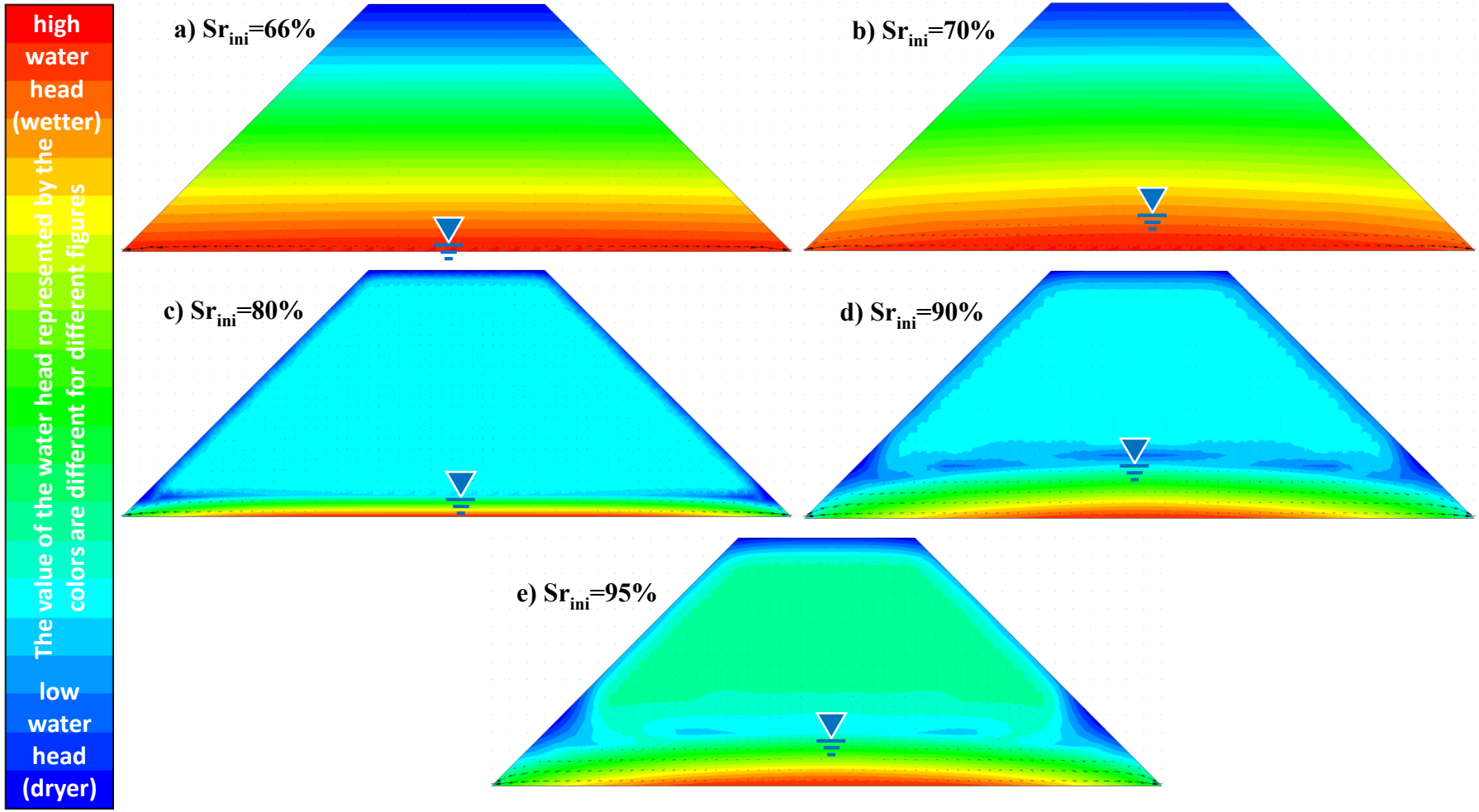

Fig. 6-7 Water head distribution for different initial degree of saturation in Case 4

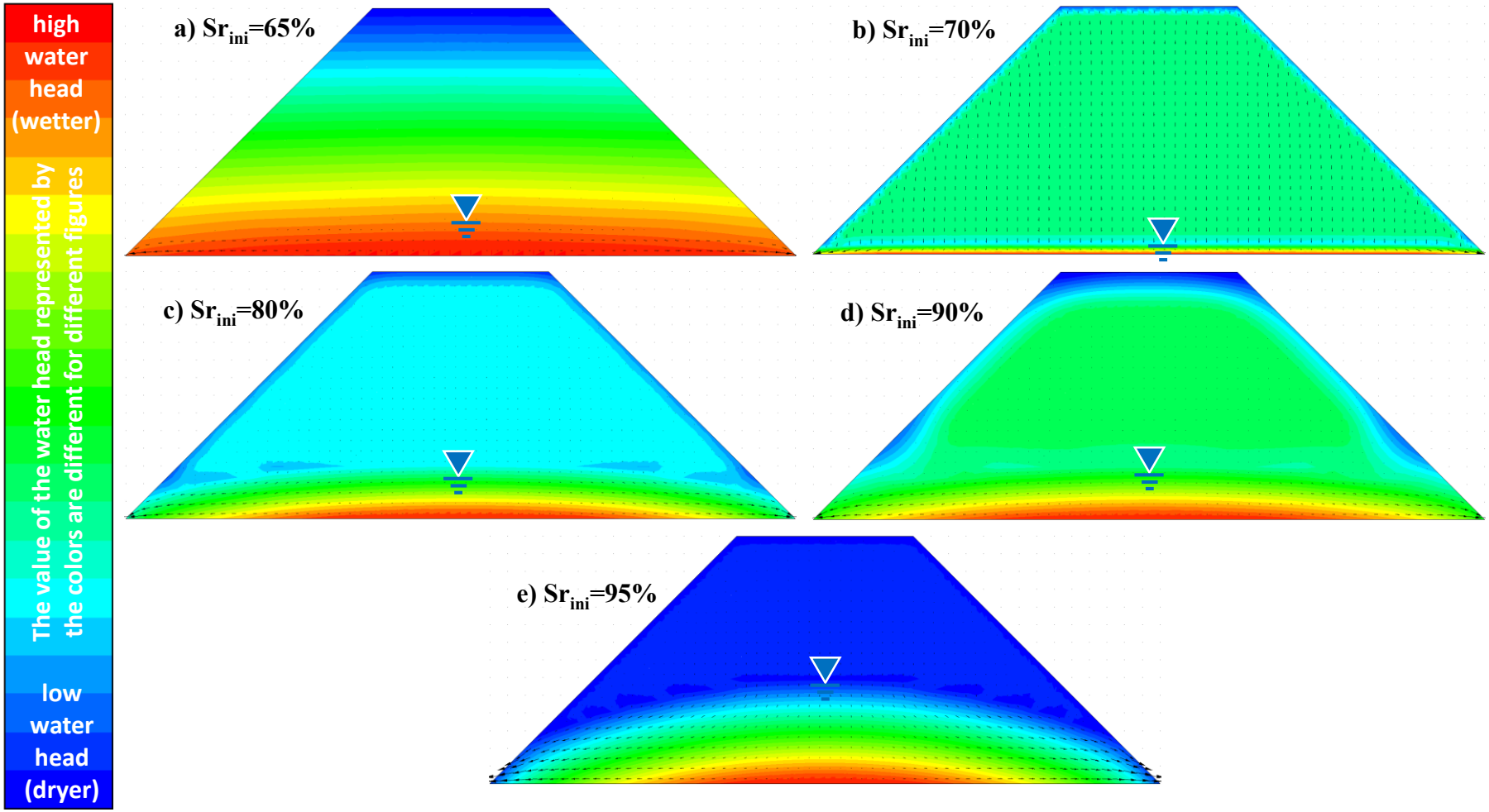

Fig. 6-8 Water head distribution for different initial degree of saturation in Case 5

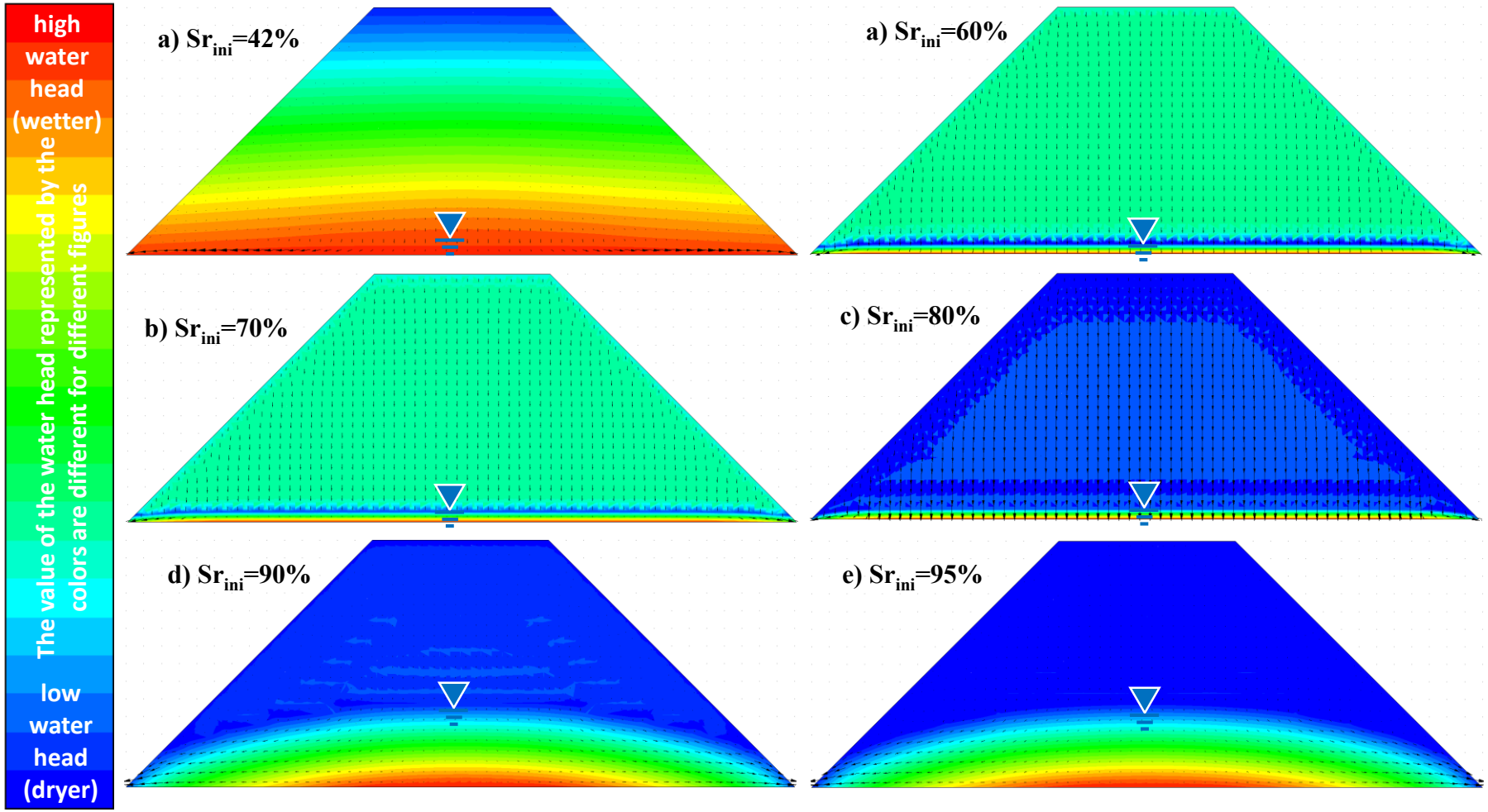

Fig. 6-9 Water head distribution for different initial degree of saturation in Case 6

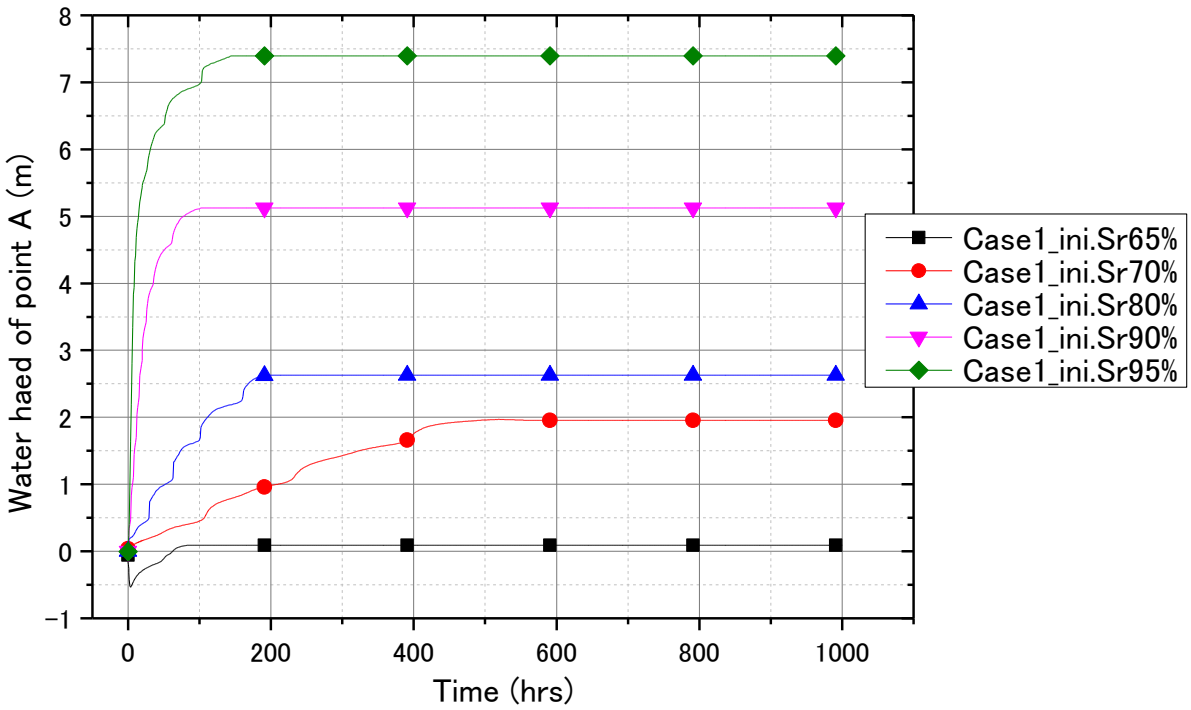

Fig. 6-10 (a) Time history of water head at bottom center point O for Case 1

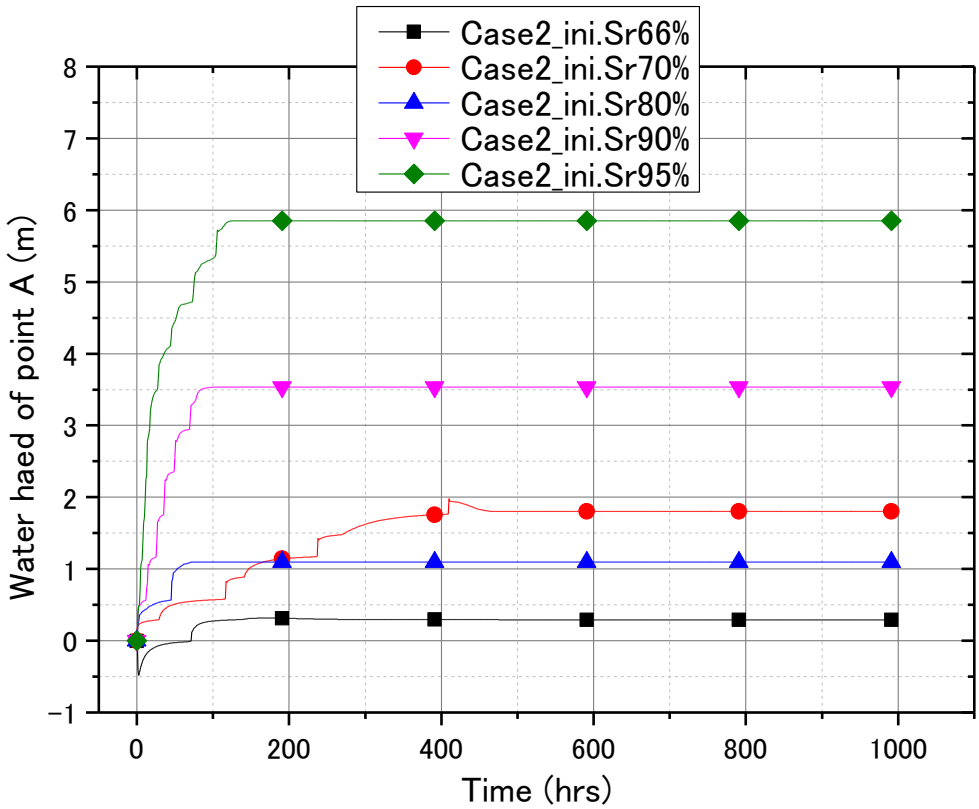

Fig. 6-10 (b) Time history of water head at bottom center point O for Case 2

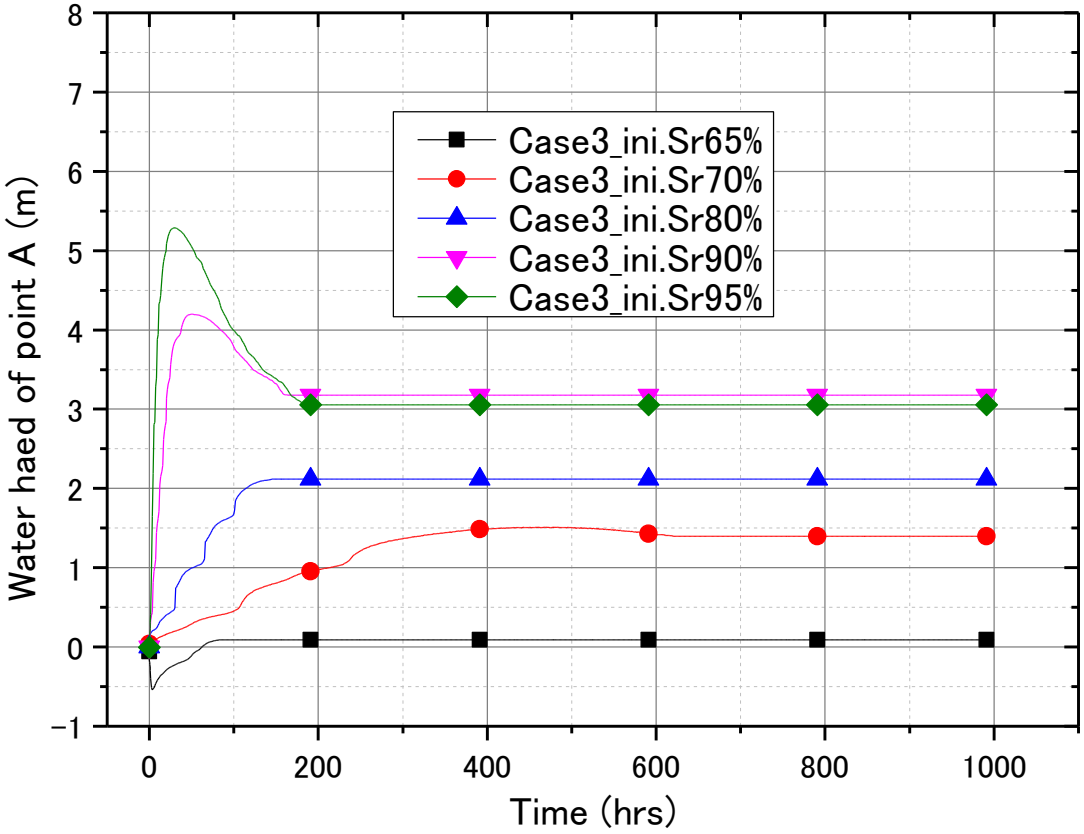

Fig. 6-10 (c) Time history of water head at bottom center point O for Case 3

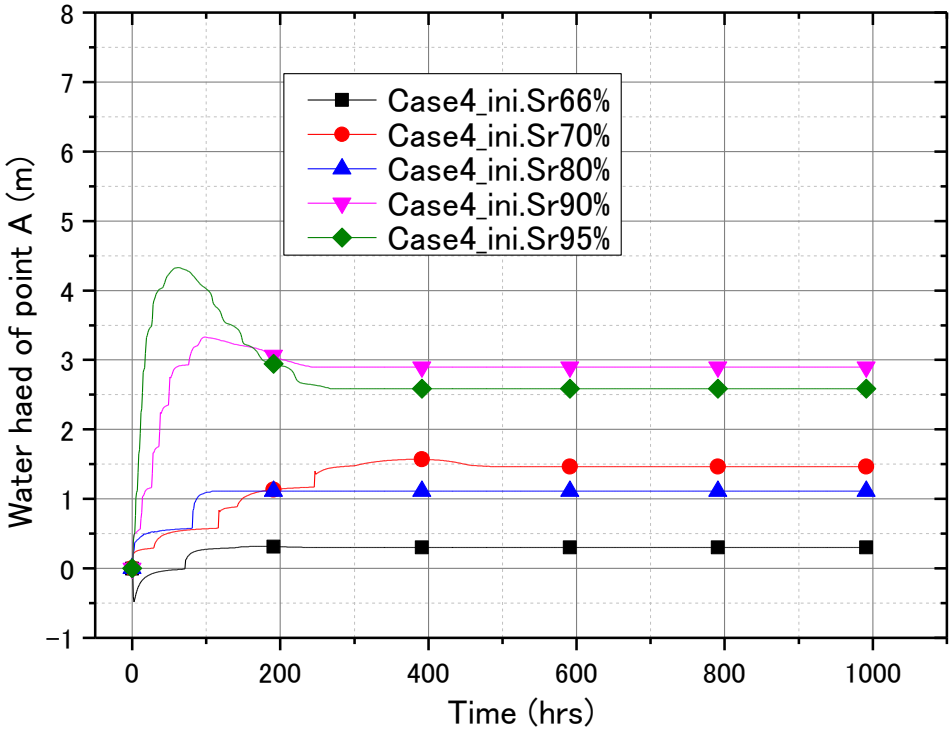

Fig. 6-10 (d) Time history of water head at bottom center point O for Case 4

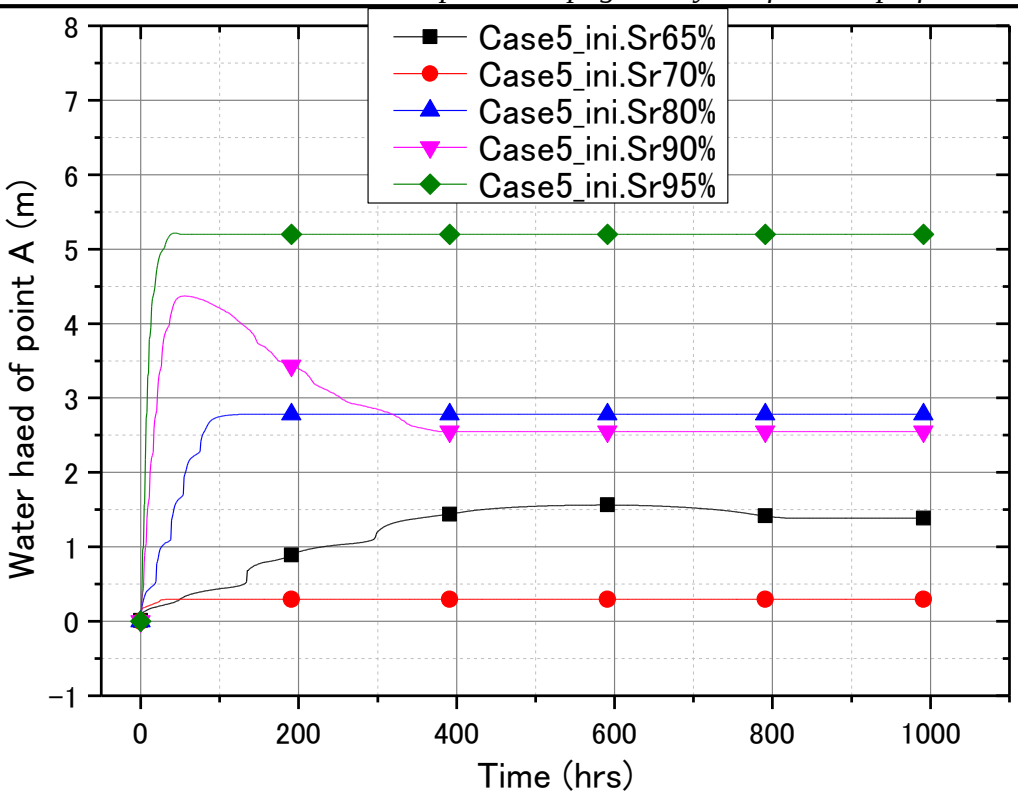

Fig. 6-10 (e) Time history of water head at bottom center point O for Case 5

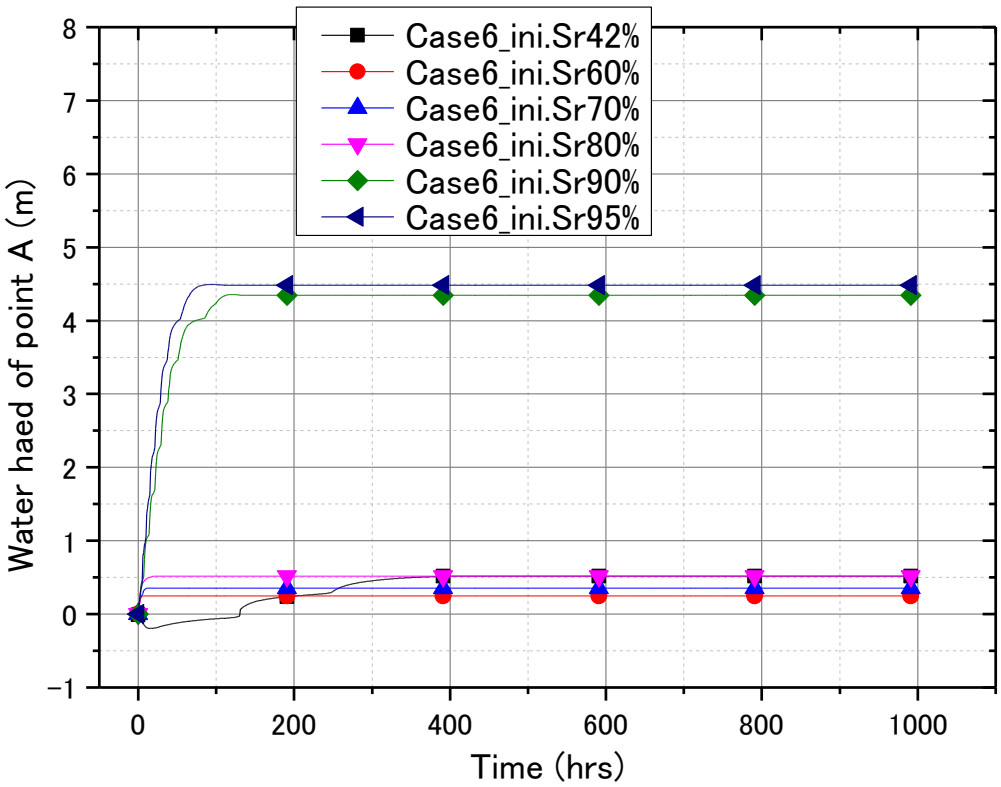

Fig. 6-10 (f) Time history of water head at bottom center point O for Case 6

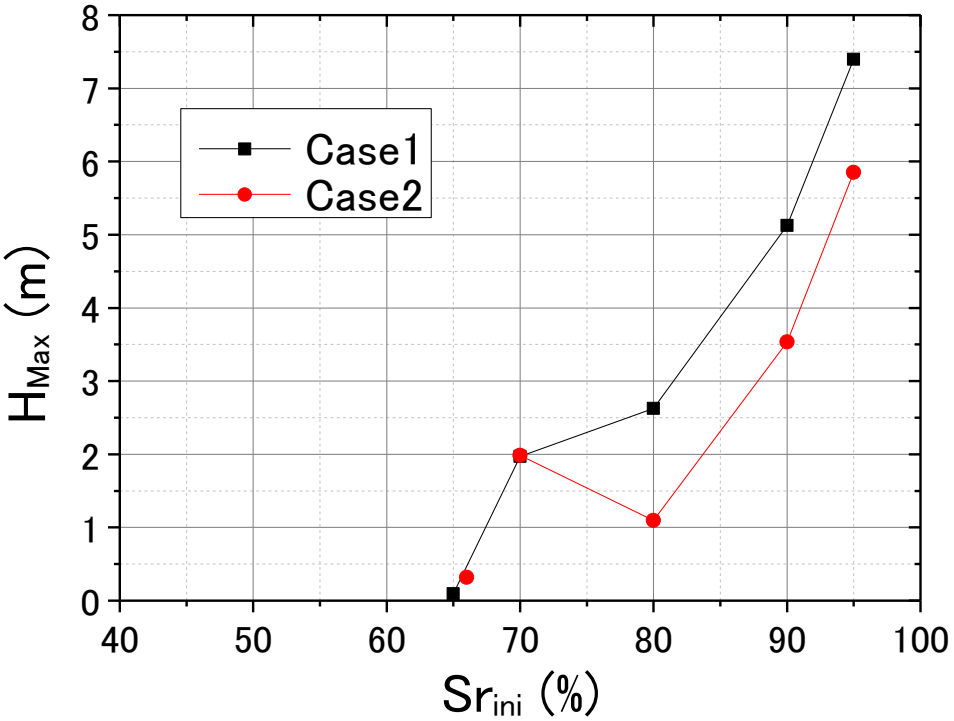

Fig. 6-11 (a) Maximum height of saturated zone for Case 1 and Case 2

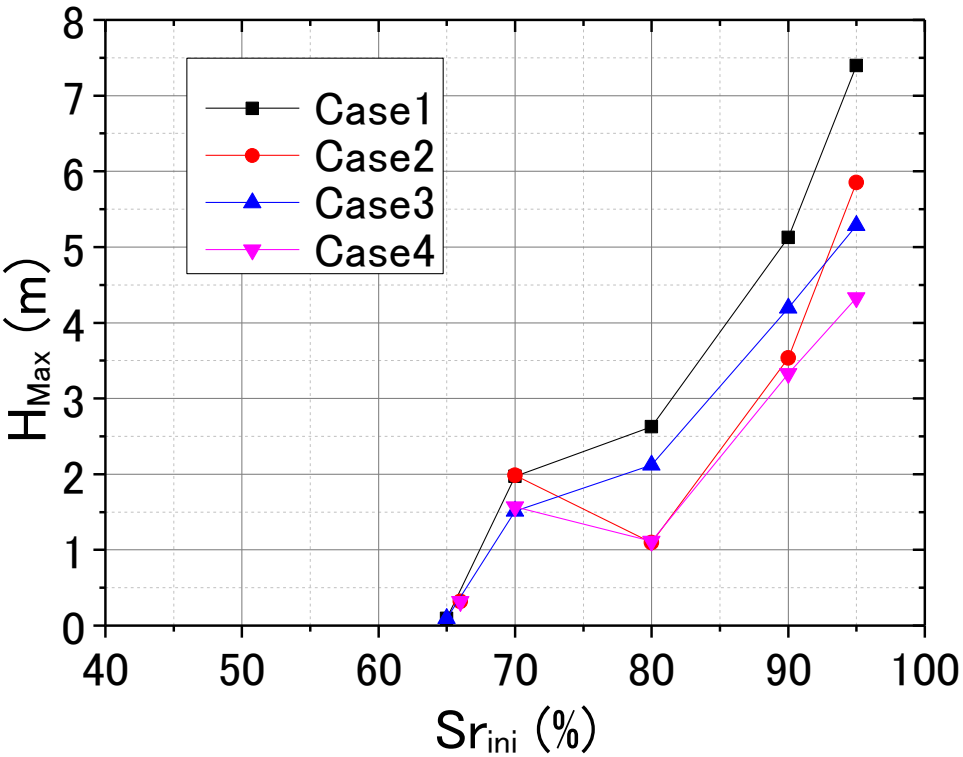

Fig. 6-11 (b) Maximum height of saturated zone for Cases 1-4

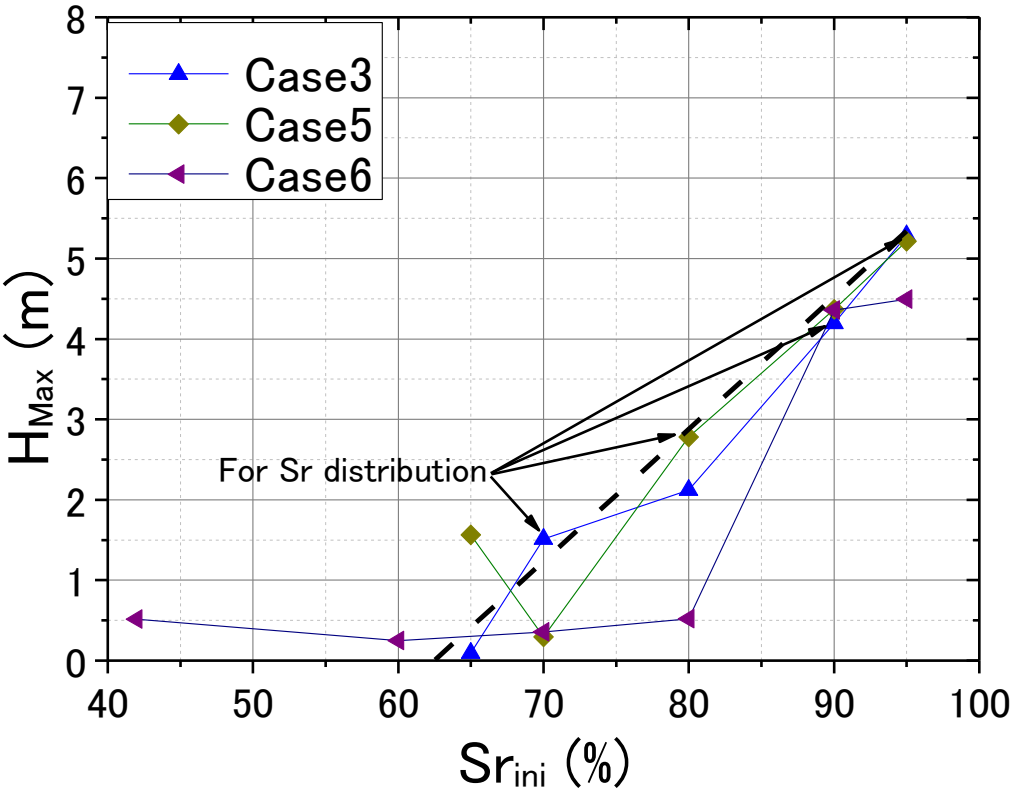

Fig. 6-11 (c) Maximum height of saturated zone for Cases 3-6

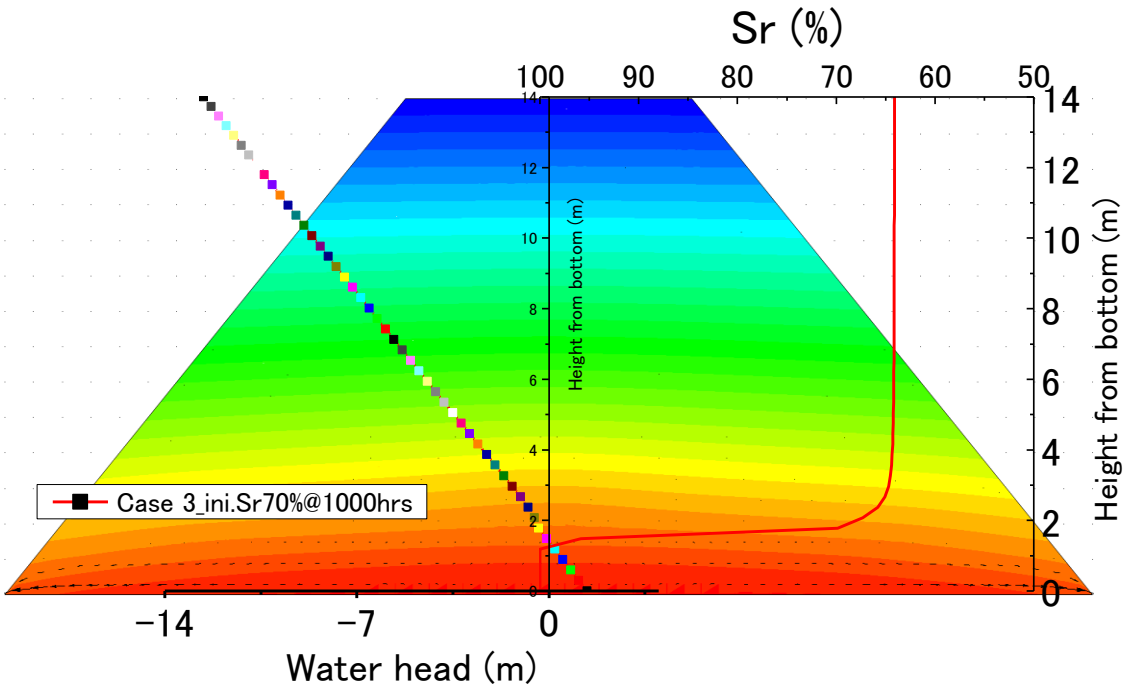

Fig. 6-12 (a) Water head and degree of saturation distribution along vertical center line for Case 3 with Sr_{ini} of 70% at 1000th hour

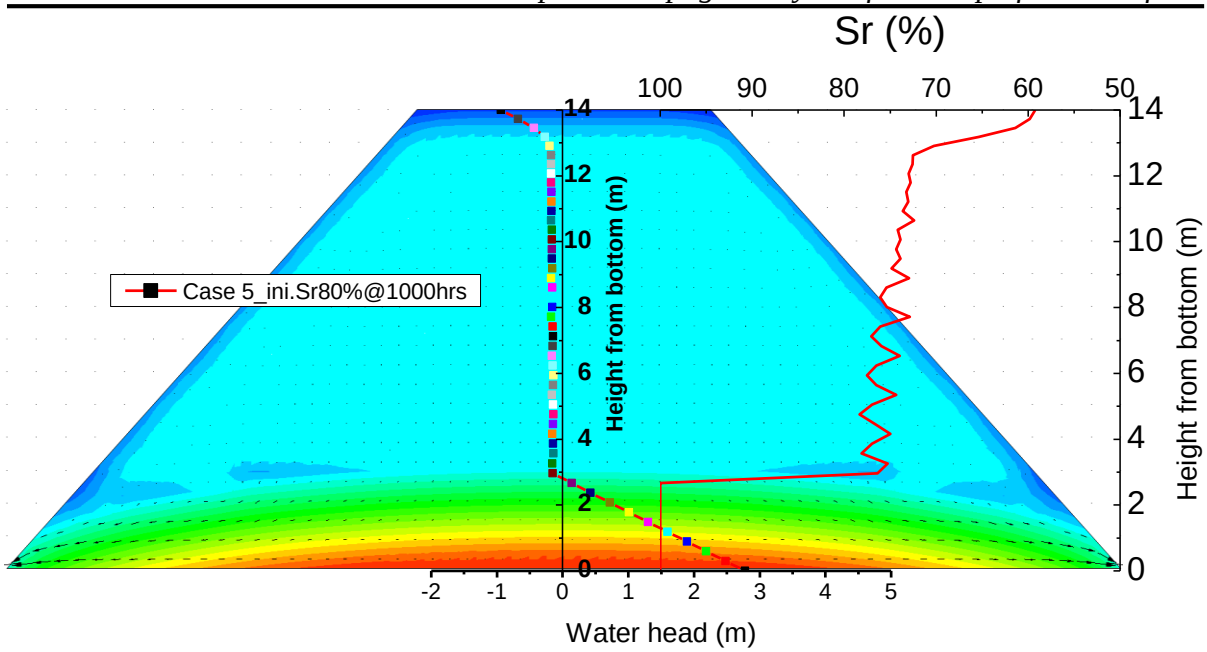

Fig. 6-12 (b) Water head and degree of saturation distribution along vertical center line for Case 5 with Sr_{ini} of 80% at 1000th hour

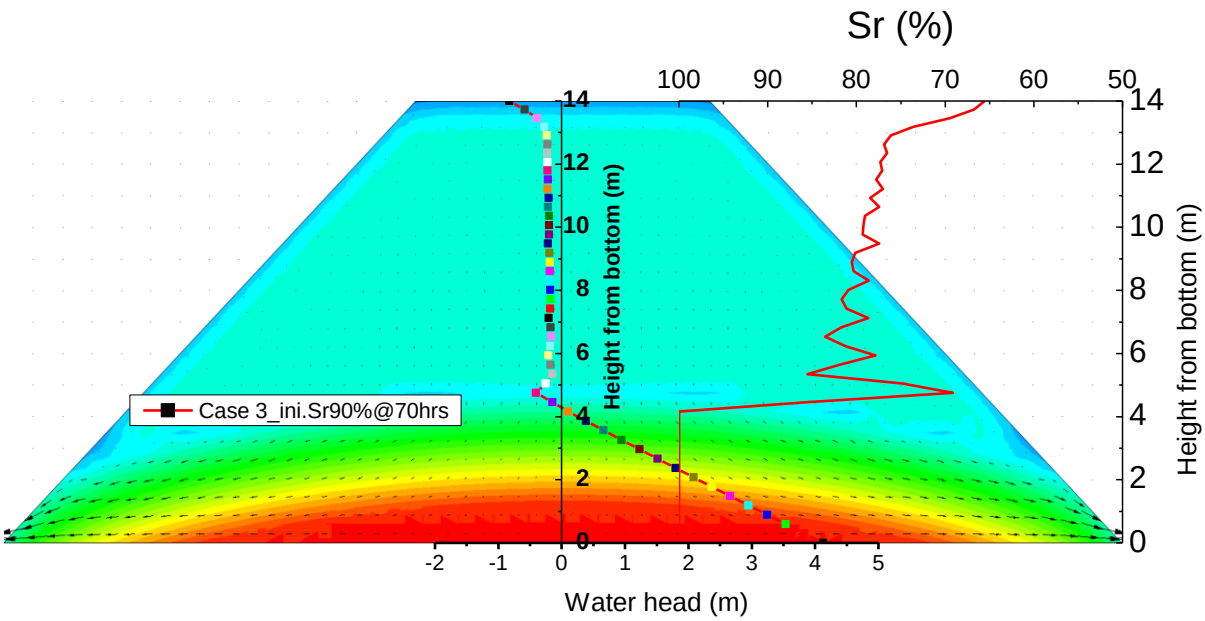

Fig. 6-12 (c) Water head and degree of saturation distribution along vertical center line for Case 3 with Sr_{ini} of 90% at 70th hour

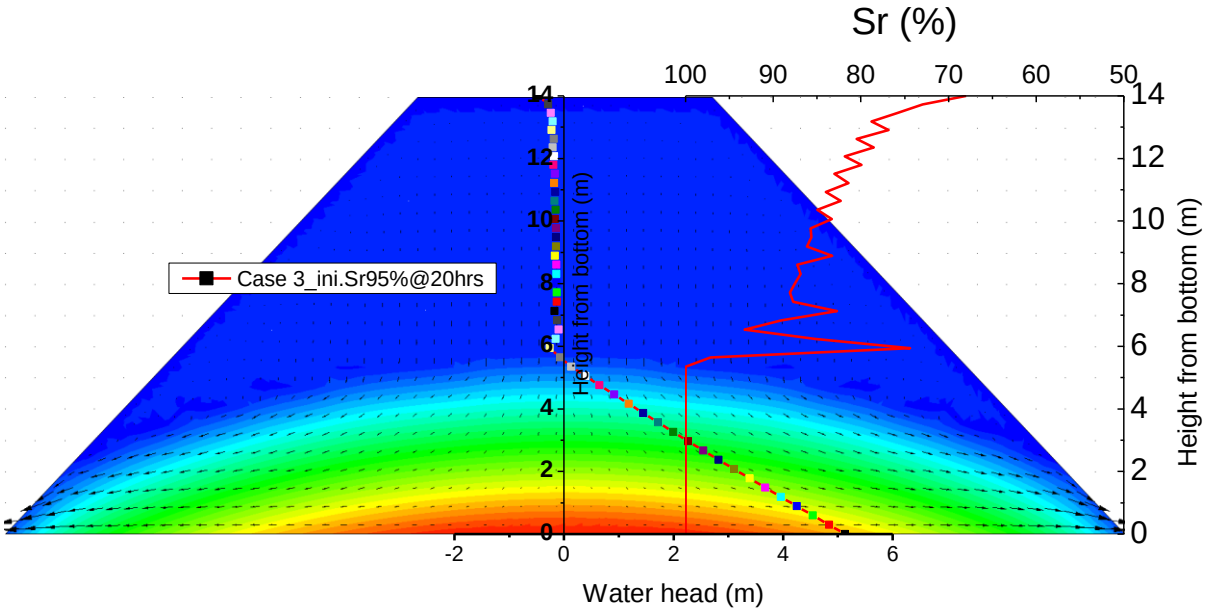

Fig. 6-12 (d) Water head and degree of saturation distribution along vertical center line for Case 3 with Sr_{ini} of 95% at 20th hour

Chapter 7. Dynamic response analysis of the heap of iron ore fines

Contents

7.1 Introduction

In Chapter 6, the seepage in the heap of iron ore fines type B (IOF-B) is analyzed numerically based on the results of the SWCC and permeability tests described in Chapter 4. The results in Chapter 6 provide reference data, such as the height of the water table, distribution of degree of saturation (Sr) in the heap etc. for the dynamic response analysis of the heap. Together with the results of the undrained monotonic loading and cyclic loading tests of IOF-B addressed in Chapter 5, the liquefaction potential of the partially saturated heap of IOF-B is evaluated for a given initial and boundary conditions. Though for the liquefaction problem of iron ore fines during transportation at sea, a wide range of knowledge needs to be covered for comprehensive understanding, the problem is simplified from the view point of geotechnical engineering as described in Chapter 1. The assumptions made in Chapter 1 are repeated herein to provide the general conditions of the simulation described in this Chapter:

1) The material for the simulation in this chapter is IOF-B;
2) The simulation only focuses on individual heaps of IOF-B, thus, other issues such as the responses of multiple heaps in the ship, the stability of the ship after liquefaction of the heaps etc. are out of the scope of this analysis;
3) There are six types of motions the ship may experience in a voyage (Fig. 1-1 in Chapter 1), while maritime reports show that the rolling motion is predominant (DSC 18/INF.11., 2013). Thus, the analysis in this study only considers the rolling motion;
4) According to the Maritime reports, the statistic data shows that the frequency of the rolling motion is 0.1 Hz (DSC 18/INF.11., 2013) which is also assumed to be the case in this study;
5) There is no very clear description in the maritime reports about the roll angle and the number of cycles of rolling motion the heap may experience. In this study, 200 cycles of sinusoidal rolling motion with constant amplitude are applied to the model.

7.2 Simulation program and model

The commercial software, UWLC Ver. 2 was used for the determination of the parameters used in the constitutive models, the initialization of the static stress distribution and the post process. The rolling motion was applied by a separate program provided by Associate Professor F. Cai from Gunma University, Japan. Both the software and the program used to simulate the rolling motion were for two dimensional analysis.

Fig. 7-1 shows the model and the local coordinate axes of the heap used for simulation. The dimensions of the model are the same as those used in the seepage analysis introduced in

Chapter 6, which are typical for heaps in Capesize type of bulk carriers (typically 150 kDWT or more). The heap is set to roll around a center point "O", which is 1.6 m above the crest of the heap. The model is divided into 3 zones, which are assigned to different properties. Zone 1 is the saturated zone with a maximum height of 3 m. The shape of the water table is a simplified version according to the results of the seepage analysis shown in Fig. 6-12 in Chapter 6. Zone 2 is the unsaturated zone and the hat-shaped Zone 3 is deliberately set to be the non-liquefiable zone to avoid insufficient confining pressure at the surface of the liquefiable zones. The density of the heap is set to be uniform and with medium dense condition (ρ_d=2.56 g/cm^3, Dc=91.7%). The bottom boundary is fixed without allowing any movement and the rest of the boundaries are set free.

7.3 Simulation conditions and constitutive models

Table 7-1 shows the general conditions considered in the simulation. In Case 1, Zone 1 is assumed to be liquefiable and the other two zones are assumed to be non-liquefiable, through which the responses of the heap with liquefaction potential only in the saturated zone are studied; while in Case 2 and Case 3, unsaturated Zone 2 is also assumed to be liquefiable, which is more realistic since the potential of liquefaction of unsaturated IOF-B is observed, as discussed in Chapter 5. The drainage boundaries used in the simulation are indicated in Table 7-1 and Fig. 7-1. The only difference between Case 2 and Case 3 is the values of permeability. The permeability in saturated Zone 1 (k_{sat}) is 1.008×10^{-3} cm/s for all 3 cases, which corresponds to the permeability of the fully saturated medium dense specimen of IOF-B (Dc = 91.7%) under confining pressure of 100 kPa, as addressed in Chapter 4. The permeability of unsaturated Zone 2 (k_{unsat}) in Case 2 and Case 3 are 1.008×10^{-3} cm/s ($k_{unsat}= k_{sat}$) and 1.5×10^{-5} cm/s ($k_{unsat}< k_{sat}$), respectively, to consider the effect of permeability on the responses of the heap. The value 1.5×10^{-5} cm/s corresponds to the permeability of the unsaturated medium dense specimen of IOF-B (Dc = 92.7%) with Sr of 84.3% under confining pressure of 100 kPa. For each simulation, 200 cycles of rolling motion were applied to the heap with a rolling angle from 5°-30°.

Table 7-1 Simulation conditions

Case	Zone1	Zone2		Zone3	Drainage boundary	Roll angle (°)	Cycle number
1	Saturated Liquefiable zone	Non-liquefiable zone		Non-liquefiable zone	1	5, 10, 15, 20, 25, 30	200
2		Unsaturated liquefiable zone	$k_{unsat}= k_{sat}$		2		
3			$k_{unsat}< k_{sat}$				

The built-in constitutive model, PZ-sand model, is used for the liquefiable zones. PZ-sand model is a generalized model developed by Pastor et al. (1990). It has 15 parameters as shown in Table 7-2. The first 12 parameters were determined according to the undrained monotonic loading tests of saturated IOF-B and the last 3 parameters were determined based on the undrained cyclic loading tests. PZ-sand model is essentially used for the saturated soils, while in order to consider the unsaturated condition of IOF-B the parameters were adjusted to match the liquefaction resistance curve of unsaturated IOF-B.

Table 7-2 Parameters of PZ-sand model

Parameters	Saturated liquefiable zone	Unsaturated liquefiable zone
M_f: Slope of failure line in p'-q plane	1.8	1.8
M_g: Slope of the critical state line in p'-q plane	1.88	1.88
C: Ratio of Mg in extension side of triaxial test to the in compression side	0.6	0.6
α_f: Parameter related to yield	0.45	0.45
α_g: Parameter related to plastic flow	0.45	0.45
K_{evo}: Coefficient of bulk modulus	400	400
G_{eso}: Coefficient of shear modulus	800	800
m_v: Exponent of bulk modulus	0.5	0.5
m_s: Exponent of shear modulus	0.5	0.5
β_0: Parameter related to soil softening	99	99
β_1: Parameter related to soil softening	0.001	0.001
H_0: Coefficient of loading plastic modulus	20000	20000
H_{U0}: Unloading plastic modulus (kPa)	3000	3000
γ: Parameter related to reloading plastic deformation	9	30
γ_u: Parameter related to unloading plastic modulus	9	30

Fig. 7-2 compares the effective stress paths and the stress strain relationships of IOF-B under undrained monotonic loading between the simulation and the test results. The test conditions are described in Table 5-1 in Chapter 5. Fig 7-2 shows that the simulation results match the

overall trend of the behaviors of IOF-B; however, the peaks of shear stress and the strain softening behavior are not well captured. The predicted peak deviator stress is lower than the test result for the condition with low confining pressure, while it is higher than the test result for high confining pressure. On the other hand, as discussed in Section 5.3.2, the strain softening behavior of medium dense IOF-B appears after the phase transformation points, which is the point that the soils behavior transforms from contraction to dilatancy (Ishihara, 1993). The classical behaviors of sands show that the dilatancy behavior is usually associated with stable behavior (Lade and Yamanuro, 1997) under the undrained condition. For PZ-sand model, it may be unable to simulate the behaviors of dilatancy and strain softening at the same time.

Fig. 7-3 compares the simulated and test results of the undrained behavior of saturated medium dense IOF-B under the cyclic loading. Three tests were picked from Set 4 with confining pressure of 100 kPa, as shown in Table 5-3 in Chapter 5. Detailed information about the tests can be found from Appendix G according to the names of the tests. The simulation results show that the effective stress paths are roughly consistent with the test results; while the stress strain behaviors may not be properly simulated. The test results show that axial strain is progressively developed under the cyclic loading; while the predicted axial strain is very small in the early stage of cyclic loading and it is developed (Fig. 7-3b) or tends to be developed (Figs. 7-3d and f) suddenly when the effective stress approaches zero. It implies that, in the simulation, large deformation could be suddenly trigged either locally or universally when the effective stress reaches zero.

Fig. 7-4 shows the predicted undrained behavior for unsaturated medium dense IOF-B under the cyclic loading. The three tests were picked from Set 4 with Sr of 84%, as shown in Table 5-3. Since the PZ-sand model is for saturated soils, as can be expected, the predicted effective stress reduces to zero under cyclic loading, which is not the case for the tests. Similar to the stress strain relationships shown in Fig. 7-3, the sudden development of axial strain for unsaturated IOF-B (Figs. 7-4b and f) may also cause problems in the simulation.

Fig. 7-5 compares the liquefaction resistance curves of the test results and the simulations for both saturated and unsaturated conditions of medium dense IOF-B. The number of cycles (N) of the saturated tests are defined in two ways (1) 5% double amplitude of axial strain ($N_{DA=5\%}$, solid squares); (2) reduction of effective mean principle stress (p') to $0.01p_0$' ($N_{p'\rightarrow 0.01p_0'}$, half solid squares, p_0' is the initial value of p'). N is defined by the reduction of p' to 0 ($N_{p'\rightarrow 0}$) for the simulations result since $N_{DA=5\%}$ is not available, as shown in Figs. 7-3 and 7-4. For the tests

with unsaturated conditions, $N_{DA=5\%}$, is used since $N_{p'\rightarrow 0.01p0'}$ is not available. Though the definitions of N are different for the test and the simulation, Fig. 7-5 shows that liquefaction resistance curves roughly match when N is higher than 10. More importantly, the predicted resistance against liquefaction under unsaturated conditions is much higher than that under saturated conditions.

Comparisons between the test and simulation results discussed above show that the parameters used for the PZ-sand model may not be very appropriate to predict the real behaviors of medium dense IOF-B. They may need to be further optimized. However, the simulations in this study focus on the responses of the heap with or without considering the liquefaction potential of unsaturated IOF-B and the effect of permeability on the response of the heap, of which the difference of the responses among the 3 cases may not be significantly affected by the parameters of the PZ-sand model.

For the non-liquefiable zone, an elastic model was used for simplicity. The Young's modulus and Poisson's ratio are 160 MPa and 0.45, respectively.

7.4 Initial stress distribution

It is necessary to initialize the stress distribution in the heap before applying dynamic motion. Fig. 7-6 shows the initial distribution of p_0' and the normalized initial shear stress ratio τ_0/p_0' (τ_0 is in xy direction) for Cases 1-3. It can be seen that generally the distribution of p_0' is proportional to the gravity force and that of τ_{xy0}' is symmetric. Discontinuity of p_0' along the interface between the liquefiable zone and the non-liquefiable zone is also observed. The value of p_0' at the side of the non-liquefiable zone seems larger than that at the side of the liquefiable zone. This irregular distribution may be caused by the Young's modulus assigned to the elastic model in the non-liquefiable zone, which may be too large and as a result the non-liquefiable zone forms a hard shell bearing overmuch loading. The distribution of τ_0/p_0' seems not to be significantly affected by the discontinuity of p_0', while the slight concentration of τ_0/p_0' observed in Case1 at the two toes of the liquefiable zone may be problematic in the dynamic analysis.

7.5 Results-deformation divergence

For each simulation in the three cases, 200 rolling motion cycles at a frequency of 0.1 Hz were applied to the IOF-B heap. However, deformation divergence was observed before the completion of the 200 cycles in some simulations. Fig. 7-7 shows an example of the

deformation divergence, of which 200 cycles of rolling motion with rolling angle (θ) of 20° were applied to the model of Case 1. Figs. 7-7 (a), (b), (c) and (d) show the deformed grids (grids with blue color) at the 86.6th, 87.0th, 87.3rd and 87.8th cycle, respectively. The grids in grey color are the initial grid before applying cyclic motion. The deformation of the grid was very small after applying 86.6 cycles of motion (Fig. 7-7a), while the deformation of the nodes near the crest of the saturated liquefiable zone developed devastatingly and the divergent deformation spreads to the whole grid in a very short time thereafter (7-7b, c and d). Fig. 7-8 shows the vertical stress (σ_y) of a Gauss point (no. 2) of element 262 and the vertical displacement of node 773, as indicated in Fig. 7-7 (a). It seems that the program terminated the computation of σ_y at the Gauss point on the 86.6th cycle before large deformation was observed, while the displacement of the node was not ceased. As a result, the displacement of the node becomes extremely large.

It was found that computations of stress and strain on the Gauss points were automatically stopped before the deformation divergence, while the computations of displacement on the nodes continue until the end of the assigned motion. The computation of pore water pressure (PWP) was also not ceased, which resulted in extremely large PWP at the end of the rolling motion in many cases. The large deformation may be trigged sooner or later depending on the input motion, and the treatment after the large deformation may vary depending on the algorithm of the programs. For the program used in this study, the large deformation or failure may be indicated by the number of cycles at the terminal ($N_{terminal}$), after which the computation of stress and strain is terminated. The values of $N_{terminal}$ of three cases under the different rolling degrees (θ) are summarized in Table 7-3 ($N_{terminal}$=200 means that no large deformation was developed after 200 rolling cycles).

The relationship between θ and $N_{terminal}$ is plotted in Fig. 7-9. It shows that the values of $N_{terminal}$ are very different for the three cases when θ≤ 20°, while the difference of $N_{terminal}$ becomes smaller when θ ≥ 25°. The results imply that the resistance of the heap against rolling motion may be highest for the case only considering the liquefaction potential of the saturated zone (Case 1); the resistance may decrease when further considering the liquefaction potential of the unsaturated zone (Case 2); the resistance may become even lower when both the liquefaction potential and the permeability of the unsaturated zone are taken into account (Case 3), which is the most realistic condition among the 3 cases.

Table 7-3 Values of $N_{terminal}$ in three cases under different rolling angle (θ)

θ (°) / Case	5	10	15	20	25	30
1	200	200	200	86.6	8.6	5.1
2	200	200	98.8	53.6	19.4	12.3
3	200	93.9	56.4	47.2	29.7	8.5

7.6 Strain distribution in the heap

Figs. 7-11 through 7-17 show the distributions of strain (normal strain in the x direction, normal strain in the y direction and shear strain in the xy direction) in the heap at the terminals for Case 1 with different rolling angles, which considers the liquefaction potential of the saturated zone only. The interfaces between the saturated liquefiable zone and the non-liquefiable zone are indicated by the black and red lines in each figure, respectively. It can be seen that the magnitude of strain are relatively small for the heaps that experienced rolling motion with an angle of 5°, 25° or 30°, while it is very severe for the heap that experienced the rolling motion with an angle of 15°. These observations imply that the strain inside the heap may be related to both the rolling angle and the number of rolling motions. In addition, the strain in the areas near the toes seems larger than that in the areas near the center.

Figs. 7-18 through 7-25 show the distributions of strain at the terminals for Case 2, which considers the liquefaction potential of both the saturated and the unsaturated zone; however the low permeability of the unsaturated zone is not considered. The interfaces between three zones are indicated by the black or red lines in each figure. The results show that the magnitude of strain, similarly as Case 1, is smaller for the heaps that experienced the rolling motion with an angle of 5°, 25° or 30° compared with the heap that experienced the rolling motion with an angle of 10°, 15° or 20°. Regarding the locations where large normal and shear strains are mobilized, very clear failure planes running through both the saturated liquefiable zone and the unsaturated liquefiable zone are observed in Fig. 7-20, 7-21 and 7-23. Though the predicted liquefaction resistance of unsaturated IOF-B (Fig. 7-5) is about 1.7 times higher than that of the saturated condition according to the definition of liquefaction resistance ratio (LRR) defined by Eq. 5-4 in Chapter 5, it seems that the mobilized strain is not restricted by the higher resistance. Compared with Case 1, the results of Case 2 indicate that with the consideration of liquefaction potential of the unsaturated zone, the area of instability of the heap may become much broader rather than limited to the local areas near the toes. The comparison suggests that

it is very necessary to consider the liquefaction potential of the unsaturated zone when analyzing the responses of the heap under the rolling motion.

Figs. 7-26 through 7-33 show the distributions of strain at the terminals in Case 3, which considers the liquefaction potential of the saturated zone and the unsaturated zone, as well as the effect of low permeability of the unsaturated zone. Fig. 7-27 shows that the magnitude of strain in the heap under the 200 cycles of rolling motion with a rolling angle of 5° becomes much larger than that in Case 2 (Fig. 7-19). Though it is difficult to compare the strain between Case 2 and Case 3 for other rolling angles since the development of strain may be also related to the number of cycle of rolling motion, results in Case 3 imply that with the consideration of the low permeability of the unsaturated zone, the heap may become weaker to resist the rolling motion than that predicted in Case 2. Another evidence for this inference may be the locations of the failure planes. The results of Case 3 show that the intersection point of two failure planes becomes deeper with an increase in rolling angle, which is not clearly observed in Case 2. The deeper failure planes imply a vaster instable area of the heap. The comparison between Case 2 and Case 3 suggests that the permeability of the unsaturated zone may be an important factor for the response of the heap under the rolling motion.

7.7 Liquefaction potential of the heap

Four parameters had been considered to represent the liquefaction potential of the heap:

1. Maximum pore water pressure ratio (PWP_{max}/p_0'): it is the ratio of maximum value of PWP during cyclic rolling motion to the initial effective mean principle stress (p_0'). This is a widely used term in both laboratory tests and numerical simulations; however, it is difficult to use this parameter for the cases where large deformation was observed before completion of the assigned 200 cycles of rolling motion. Since PWP in the computation unreasonably increases or decreases, in order to use this parameter, a huge amount of data needs to be processed manually to extract PWP_{max} from the data before the development of large deformation. In addition, this parameter may not be a good parameter to be used for this simulation, since PWP may also be generated by the change of total stress, and thus the parameter may become larger than unity.
2. Terminal pore water pressure ratio (PWP_t/p_0'): this is a ratio of PWP at terminal, where the program stops the computation of stress and strain, to p_0'. Since PWP changes sinusoidally with the rolling motion, PWP could not represent the PWP_{max}.

3. Maximum effective stress reduction ratio ($1-p'_{min}/p_0'$): This parameter represents the maximum reduction in effective stress. It equals to unity when the minimum value of p' (p'_{min}) reduces to 0 kPa (liquefaction). Since there is no direct way to obtain p'_{min} by using the current software, processing a huge amount of data limits the use of this ratio.
4. Terminal effective stress reduction ratio ($1-p_t'/p_0'$): This parameter represents the effective stress reduction at the terminal. Since the effective stress usually decreases with an increase in the number of rolling motions, $1-p_t'/p_0'$ may be a good representative value of $1-p'_{min}/p_0'$. This parameter is used in this study to show the liquefaction potential of the heap.

Figs. 7-34 through 7-36 show the contour figures of the parameter $1-p_t'/p_0'$ for the three cases. The results show some similarities: (1) The two toes of the heap show high liquefaction potential; (2) Liquefaction potential of the heap seems to be related to the rolling angles as well as the number of rolling cycles; (3) the areas with relatively large strain also show high liquefaction potential. Since the liquefaction potential of the heap seems to be related to the number of rolling cycles, the comparisons are made between Case1 and Case2 for a rolling angle of 5° and 10° (Fig. 7-34a vs Fig. 7-35a, Fig. 7-34b vs Fig. 7-35b), respectively. They show that the area with relatively high liquefaction potential in the saturated liquefiable zone become smaller in Case 2 compared with that in Case 1; however liquefaction potential in a vast area of the unsaturated zone is as high as that in the saturated zone in Case 2. Case 2 and Case 3 are compared for the condition with a rolling angle of 5° (Fig. 7-35a vs Fig. 7-36a), which shows that the area with high liquefaction potential increases significantly in the unsaturated zone of the heap in Case 3, implying that the permeability of the unsaturated zone may significantly affect the liquefaction potential of the heap.

7.8 Discussion

In this chapter, the number of rolling cycles before development of large deformation, the strain distribution and the liquefaction potential distribution are analyzed based on the simulation results of three cases with considerations of the effects of liquefaction potential and the permeability of the unsaturated zone. The analysis results imply that, though the liquefaction resistance of unsaturated IOF-B is higher than that of the saturated condition, the unsaturated zone may have similar liquefaction potential as that in the saturated zone probably due to the positions of the failure planes, where the strain extensively develops. The analysis also shows that there are some properties of IOF-B that may significantly affect the overall liquefaction potential of the heap, such as permeability. Fig. 7-37 describes the general conditions of the

laboratory test programs and numerical simulations performed on IOF-B in this study. As can be seen, the conditions for the dynamic simulation discussed in this chapter need to be determined carefully according to the laboratory tests as well as the numerical simulations in order to correctly capture the behavior of the heap under the rolling motion. The dynamic response analysis addressed in this chapter does not comprehensively consider the density condition of the heap. Most parameters are determined based on the test results of medium dense IOF-B, of which the resistance against either monotonic loading or cyclic loading may be much higher than that of loose IOF-B, as concluded from Chapter 5. Thus, the heap with a loose condition may be weaker to resist the rolling motion. The real density condition of the heap of iron ore fines may vary depending on the source country of the products, the process procedure, the methods of loading etc., which is not easy to be determined. However, since there is a limited number of iron ore producers, which provide most of the iron ore fines used in the whole steel industry of the world, considering the significance of the liquefaction problem of iron ore fines, it would be worth studying more before proposing a simplified evaluation procedure.

The common way to avoid the liquefaction of liquefiable cargoes during maritime transportation executed among IMO and the related organizations is to set a Transportable Moisture Limit (TML). If the moisture content of a liquefiable cargo does not exceed its TML value, it could be allowed to be loaded to the ship; otherwise it should not be allowed. The Technical Work Group (TWG) proposed a modified Proctor test to determine the TML value for iron ore fines, as presented in Appendix A. Fig. 7-38 shows the compaction curve of IOF-B obtained in this study (Chapter 3) for the illustration of the proposal. The TML is set as the moisture content corresponding to the intersection point between the compaction curve and the line of Sr = 80%. However, the proposed compaction energy is about 20 times less than that used in this study. The compaction curve produced by small compaction energy is usually located at the bottom right hand side of the curve with higher energy, as schematically illustrated in Fig. 7-39, where the density is expressed in terms of compaction degree (Dc). The density of iron ore fines would decrease with a decrease in compaction energy. According to the author's survey experiences, the density of iron ore fines at least on the surface of the heap can be very loose, under which condition the heap with initial Sr of 80% may not be robust enough to resist motions experienced during voyages. Since the well documented data on the density condition of the heaps of iron ore fines are not available, future studies on the density effect are highly recommended.

7.9 Chapter conclusions

The following conclusions can be derived from the numerical simulations addressed in this chapter:

1. The predictions of the cyclic behaviors of IOF-B by using the PZ-sand model qualitatively match the experimental results, while the parameters used in this study may need to be optimized in order to produce better results;
2. With the considerations of liquefaction potential and permeability of the unsaturated zone in the heap of IOF-B, the overall liquefaction potential of the heap may become much higher than that without considering them.
3. The effect of IOF-B density may need to be considered in future studies by not only numerical simulation but also field investigation in order to properly evaluate the responses of the heap of iron ore fine and to verify the suitability of current proposal made by the relevant groups concerning the liquefaction problem of iron ore fines.

References

1. DSC 18/INF.11. (2013). The Technical Working Group (TWG) Report #2 Marine Report. International Maritime Organization.
2. Ishihara, K. (1993). Liquefaction and flow failure during earthquakes. Geotechnique, Vol. 43, No. 3, 351-415.
3. Lade, P.V. and Yamamuro, J.A. (1997). Effects of nonplastic fines on static liquefaction of sand. Can. Geotech. J., Vol. 34, 918-928.
4. Pastor, M., Zienkiewicz, O.C. and Chan, A.H.C. (1990) Generalized plasticity and the modelling of soil behaviour. Int. J. Numer. Anal. Meth. Geomech. 14 (3): 151–190

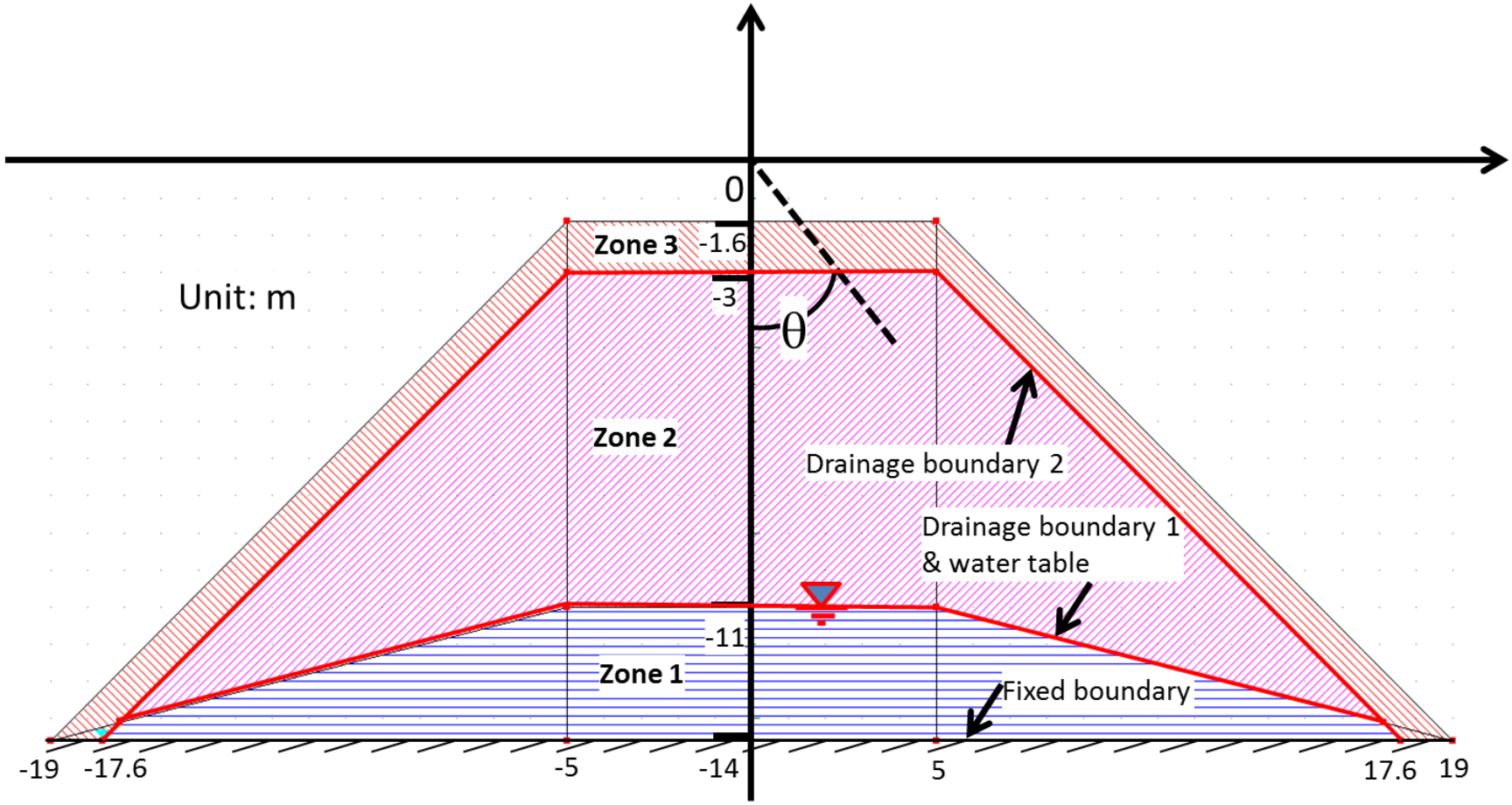

Fig. 7-1 Heap of IOF-B for simulation

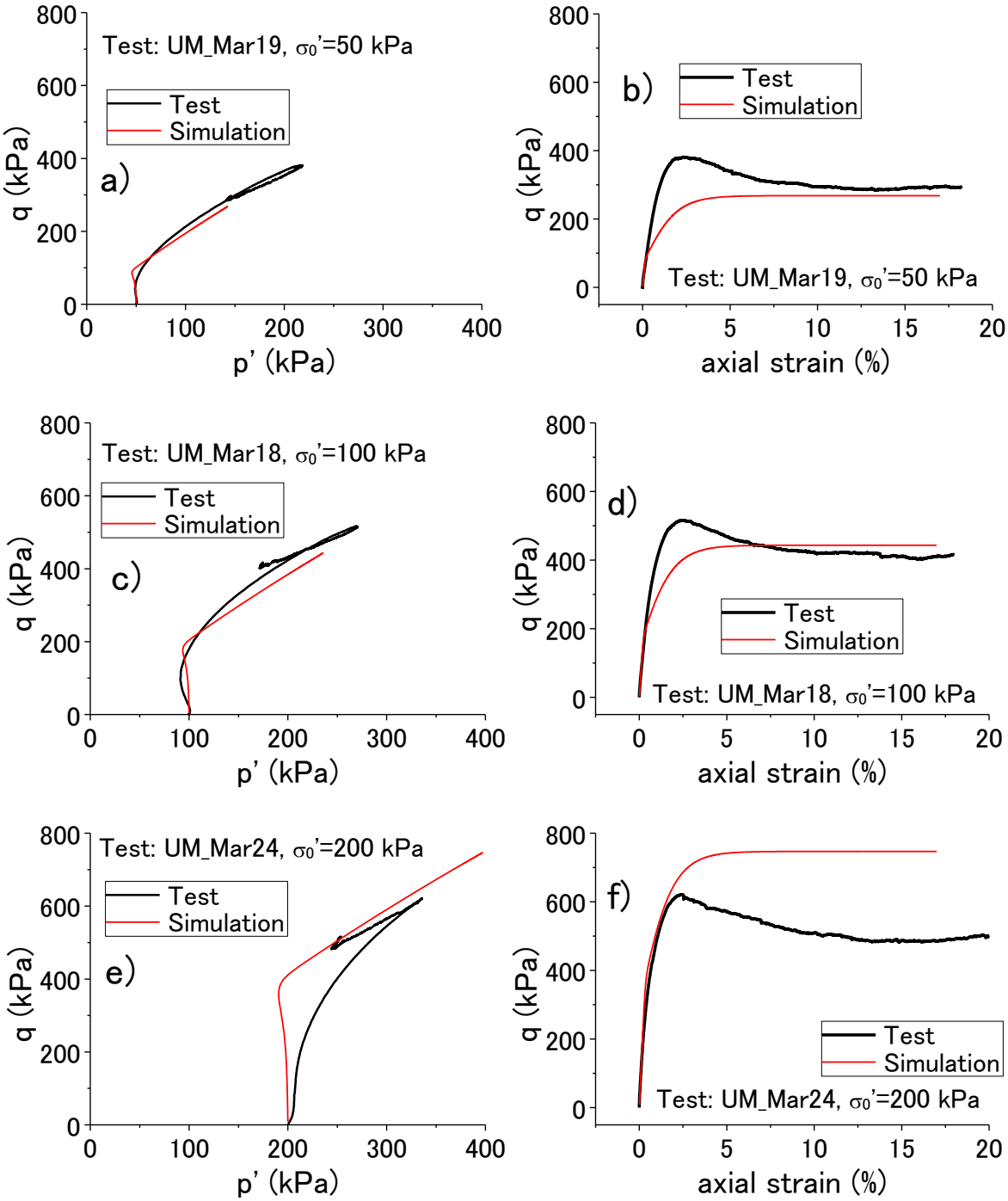

Fig. 7-2 Comparison between test and simulation for the undrained monotonic loading test of saturated IOF-B: a) Effective stress paths and b) Stress strain relationship under confining pressure of 50 kPa; c) Effective stress paths and d) Stress strain relationship under confining pressure of 100 kPa; e) Effective stress paths and f) Stress strain relationship under confining pressure of 200 kPa;

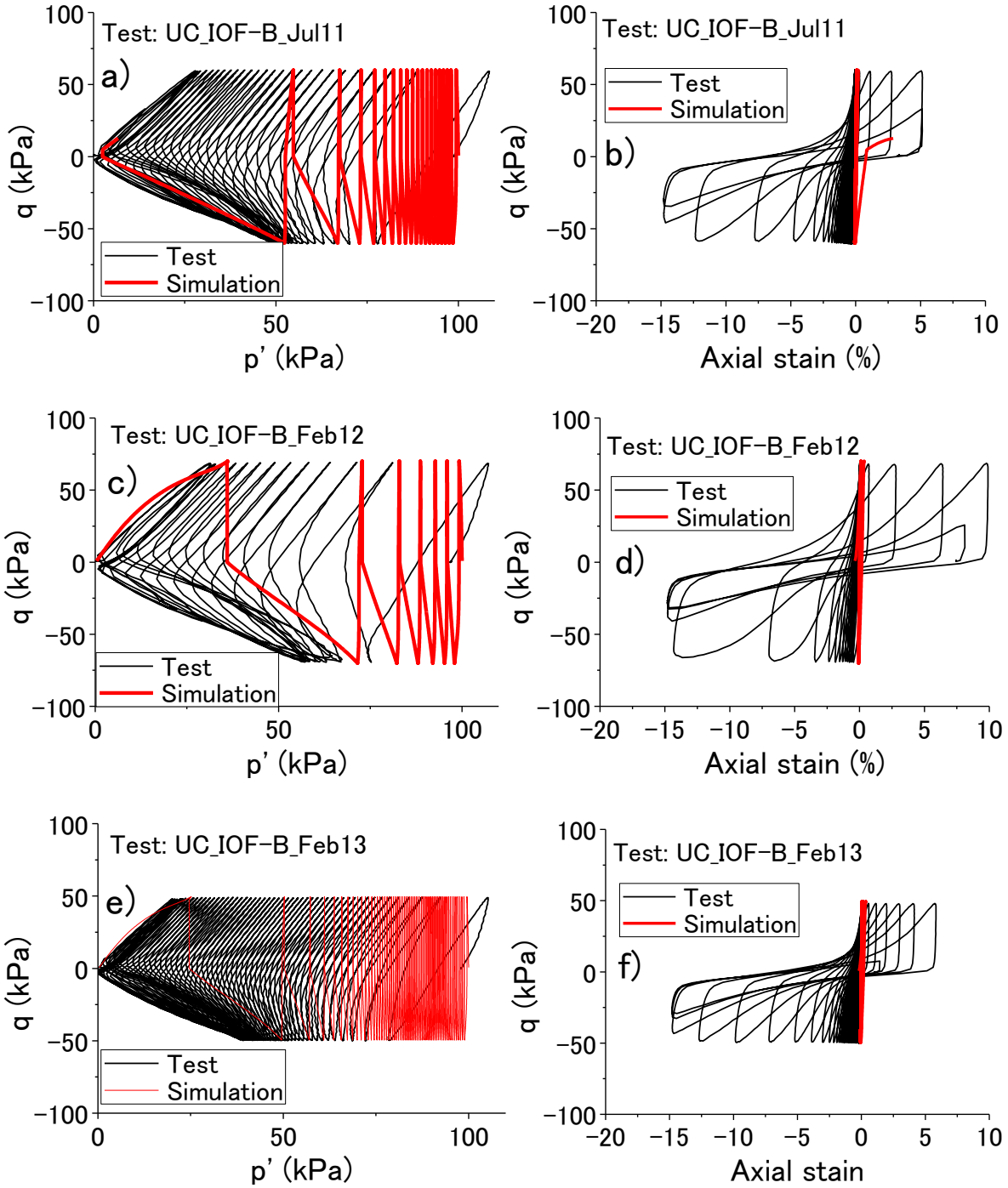

Fig. 7-3 Comparison between test and simulation for the undrained cyclic loading test of saturated IOF- under confining pressure of 100 kPa: a) Effective stress paths and b) Stress strain relationship of test UC_IOF-B_Feb-11; c) Effective stress paths and d) Stress strain relationship of test UC_IOF-B_Feb-12; e) Effective stress paths and f) Stress strain relationship of test UC_IOF-B_Feb-13;

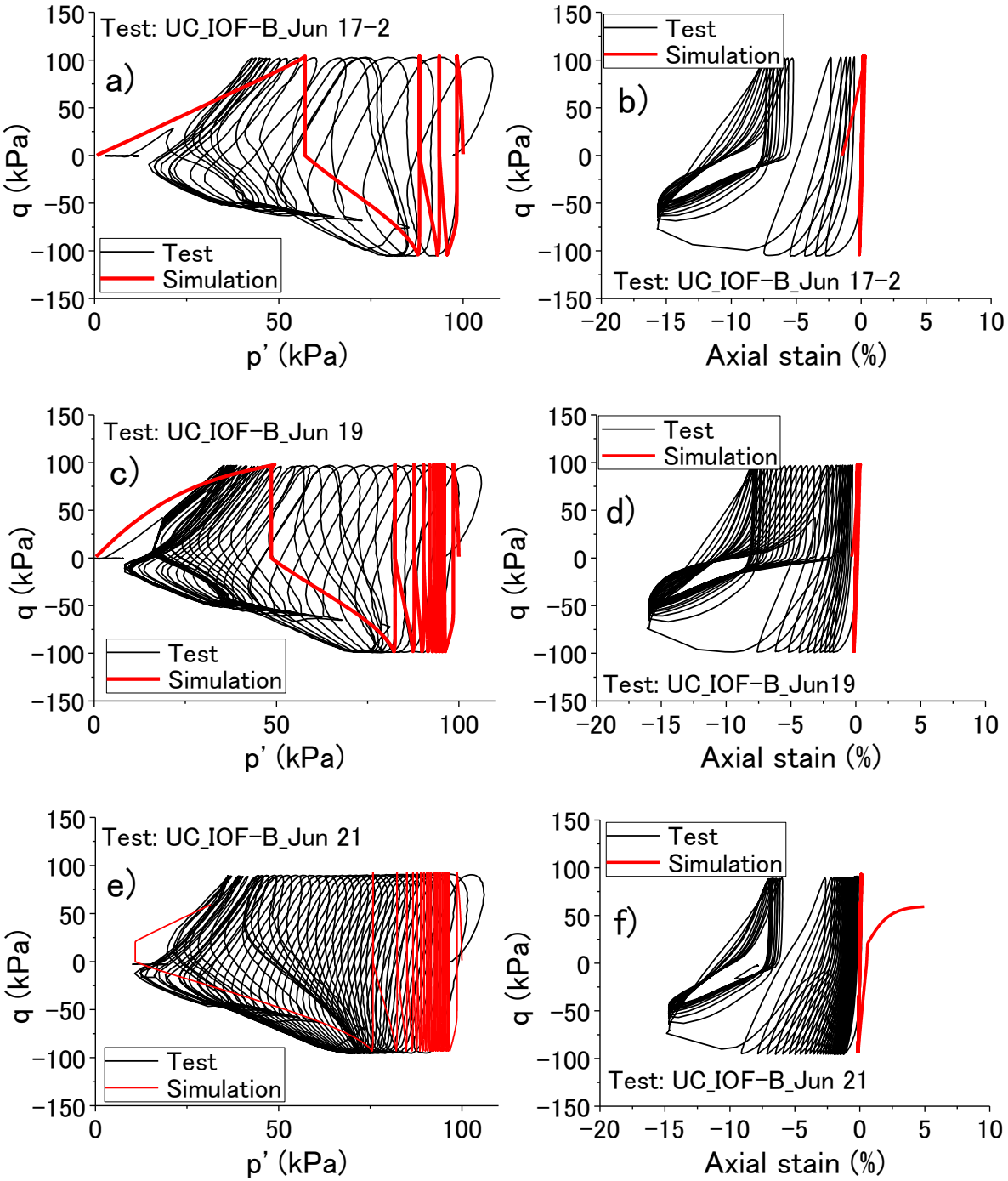

Fig. 7-4 Comparison between test and simulation for the undrained cyclic loading test of unsaturated IOF- under confining pressure of 100 kPa: a) Effective stress paths and b) Stress strain relationship of test UC_IOF-B_Jun-17-2; c) Effective stress paths and d) Stress strain relationship of test UC_IOF-B_ Jun-19; e) Effective stress paths and f) Stress strain relationship of test UC_IOF-B_ Jun-21;

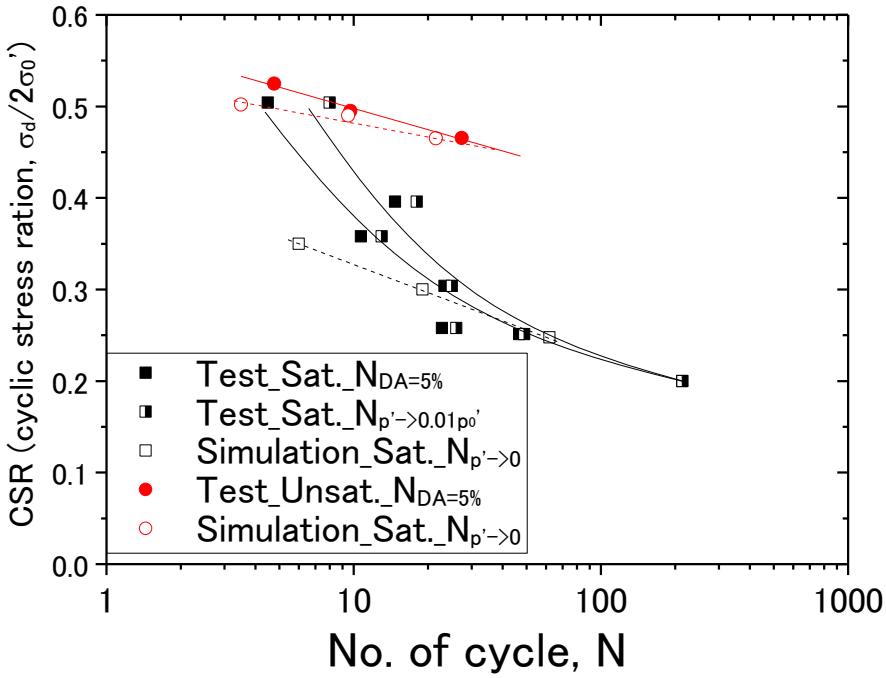

Fig. 7-5 Comparisons of liquefaction curves of IOF-B between the test and simulation results

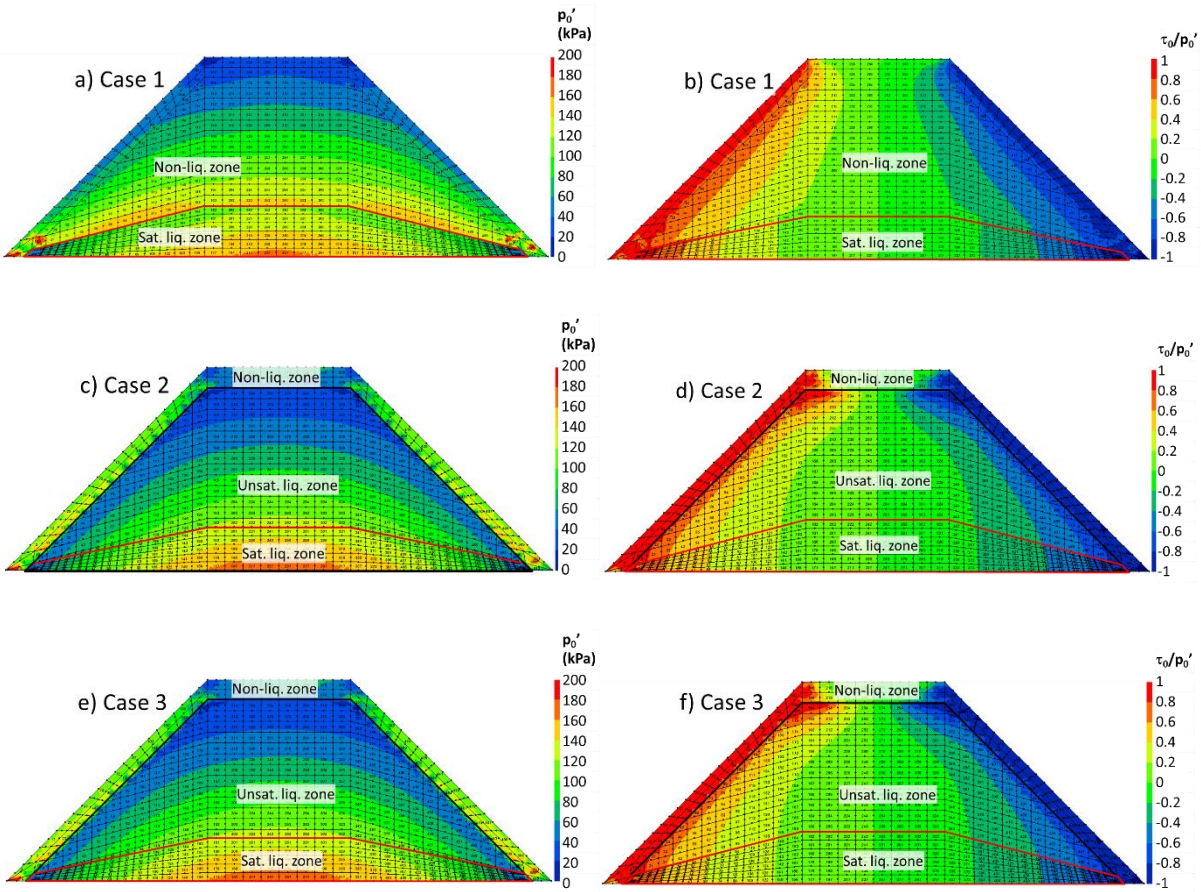

Fig. 7-6 Initial effective stress distribution and normalized initial shear stress distribution for: a) and b) Case1; c) and d) Case2; e) and f) Case3

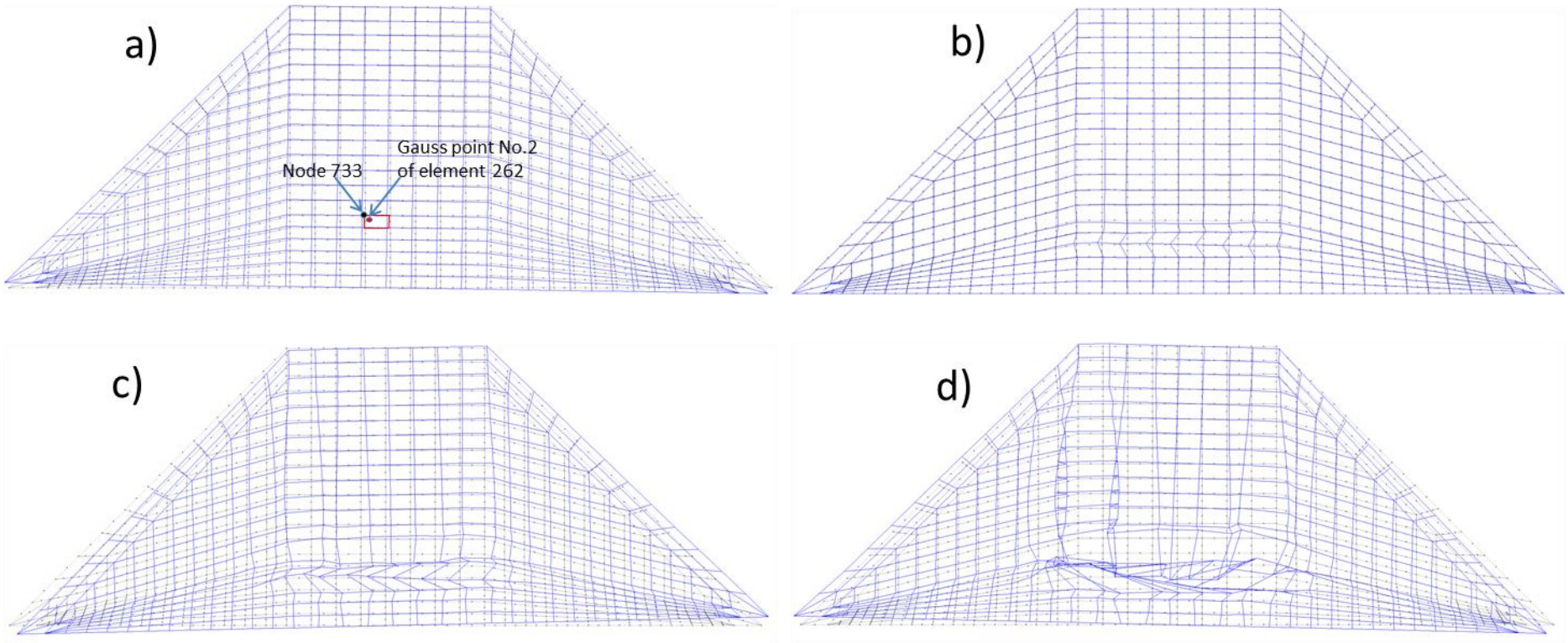

Fig. 7-7 Grid deformation of Case1 under 20° rolling angle at a) 86.6th cycle, b) 87.0th cycle, c) 87.3rd cycle and d) 87.8th cycle

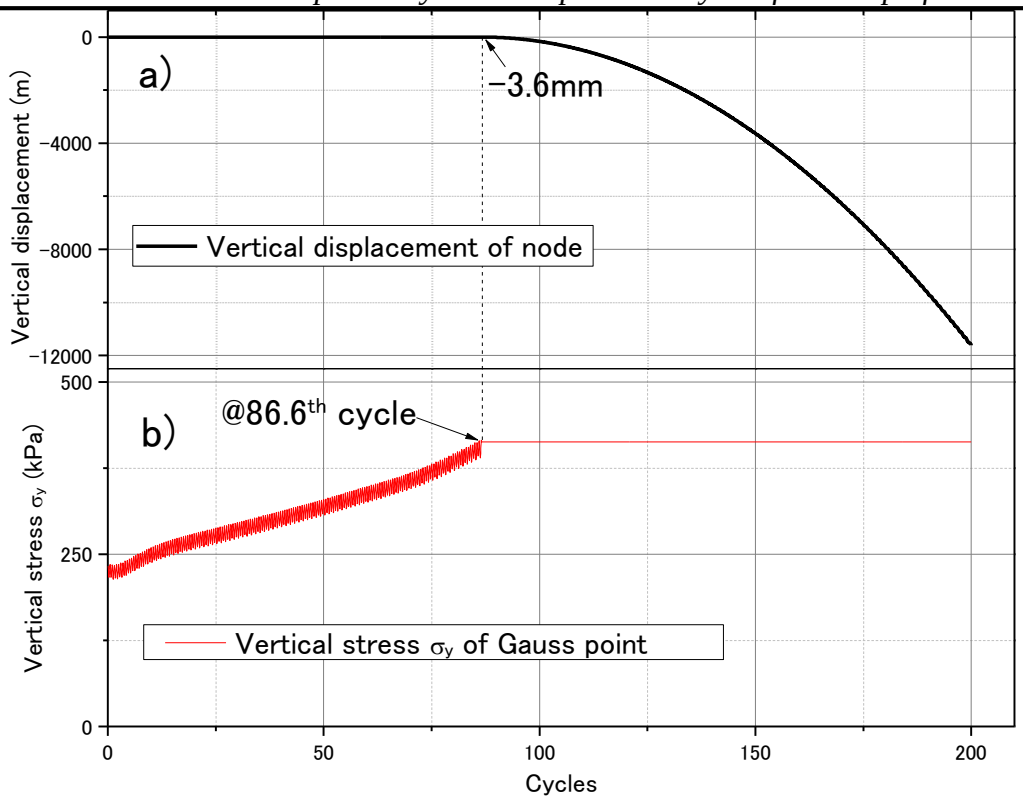

Fig. 7-8 a) Vertical displacement of a node and b) vertical stress of a gauss point in Case1 under 20° rolling angle

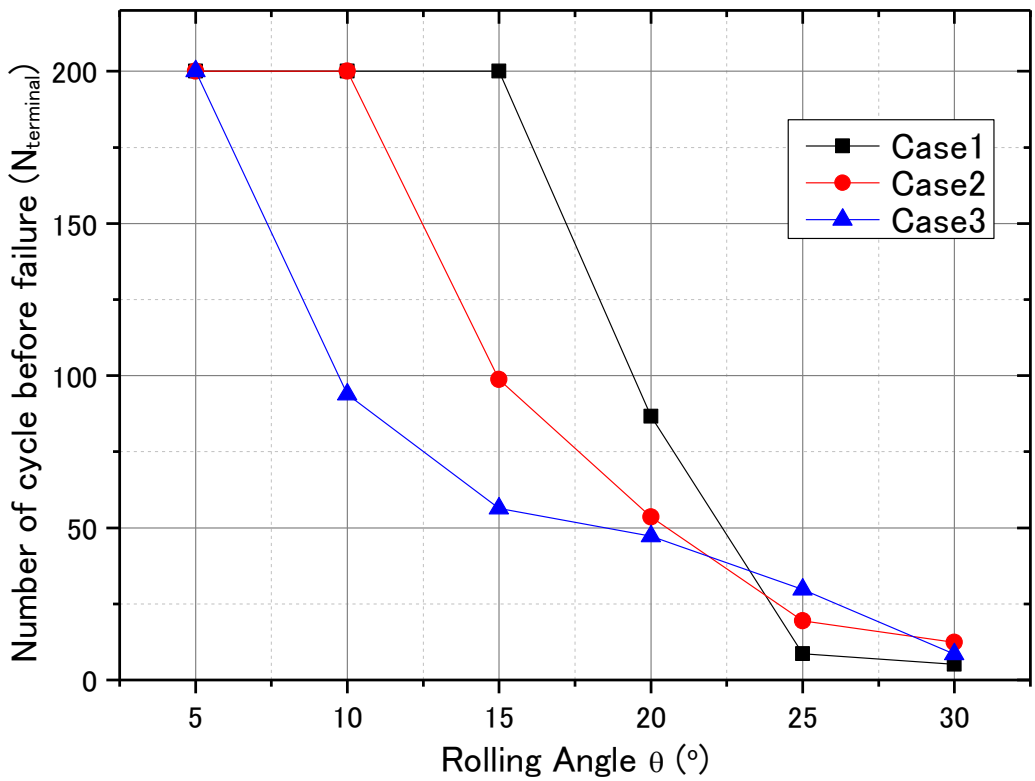

Fig. 7-9 Relationship between rolling angle and number of cycles before failure of the heap

ε_x (%)	5	4	3	2	1	0	-1	-2	-3	-4	-5
ε_y (%)	5	4.5	4	3.5	3	2.5	2	1.5	1	0.5	0
γ_{xy} (%)	5	4	3	2	1	0	-1	-2	-3	-4	-5

Fig. 7-10 Legend for contour figures of ε_x, ε_y and γ_{xy}

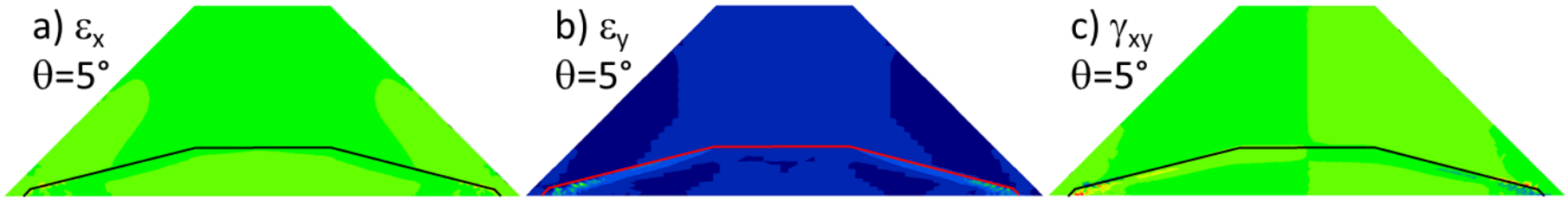

Fig. 7-11 Contour of strain at failure under 5° rolling angle for Case1

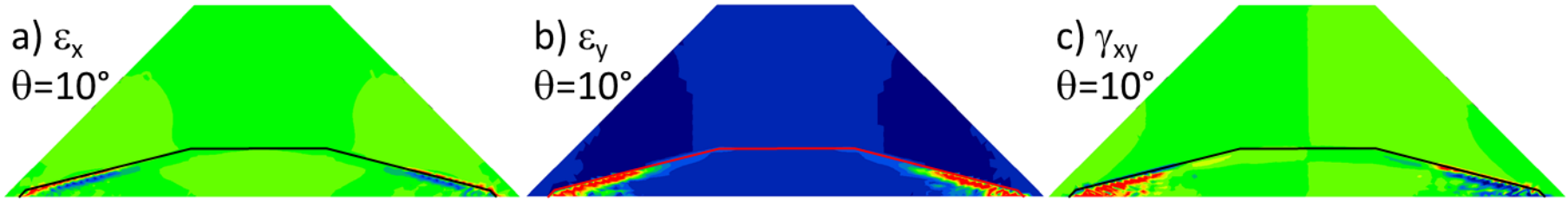

Fig. 7-12 Contour of strain at failure under 10° rolling angle for Case1

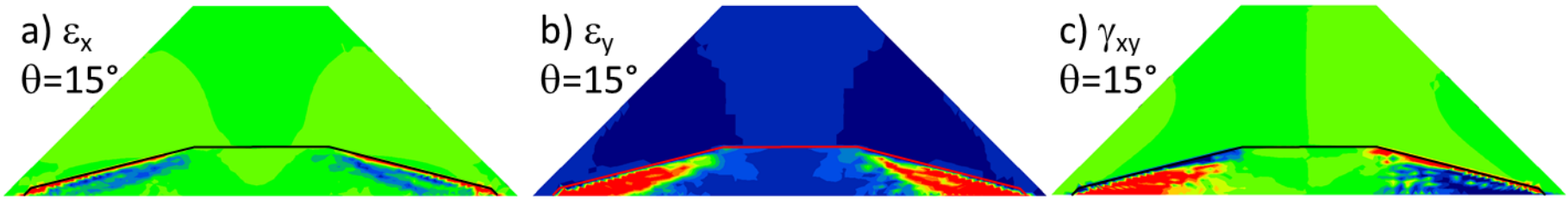

Fig. 7-13 Contour of strain at failure under 15° rolling angle for Case1

ε_x (%)	5	4	3	2	1	0	-1	-2	-3	-4	-5
ε_y (%)	5	4.5	4	3.5	3	2.5	2	1.5	1	0.5	0
γ_{xy} (%)	5	4	3	2	1	0	-1	-2	-3	-4	-5

Fig. 7-14 Legend for contour figures of ε_x, ε_y and γ_{xy}

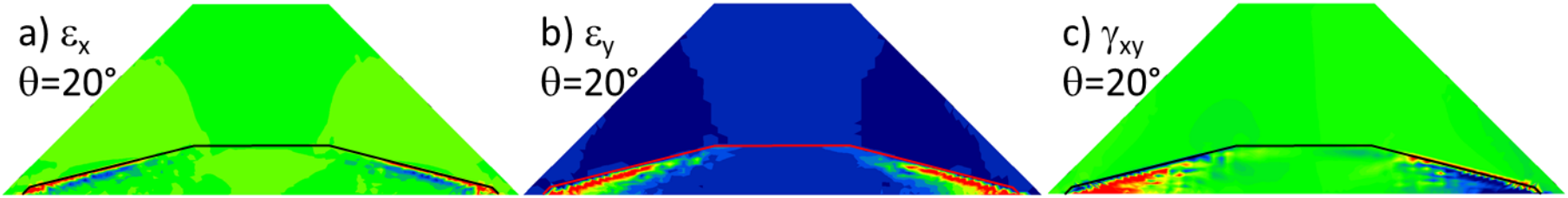

Fig. 7-15 Contour of strain at failure under 20° rolling angle for Case1

Fig. 7-16 Contour of strain at failure under 25° rolling angle for Case1

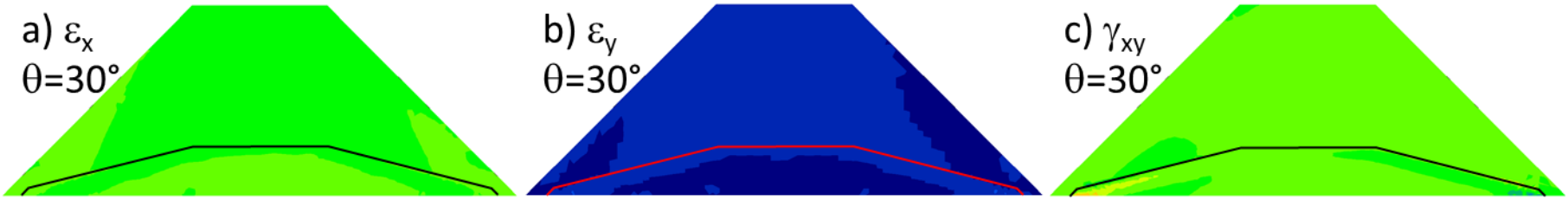

Fig. 7-17 Contour of strain at failure under 30° rolling angle for Case1

ε_x (%)	5	4	3	2	1	0	-1	-2	-3	-4	-5
ε_y (%)	5	4.5	4	3.5	3	2.5	2	1.5	1	0.5	0
γ_{xy} (%)	5	4	3	2	1	0	-1	-2	-3	-4	-5

Fig. 7-18 Legend for contour figures of ε_x, ε_y and γ_{xy}

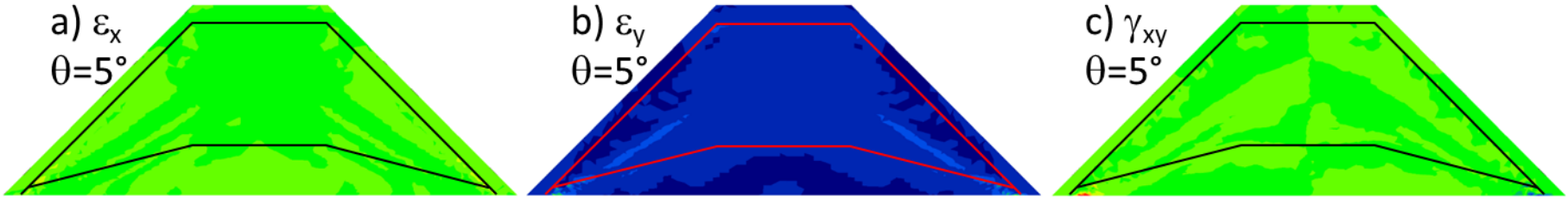

Fig. 7-19 Contour of strain at failure under 5° rolling angle for Case2

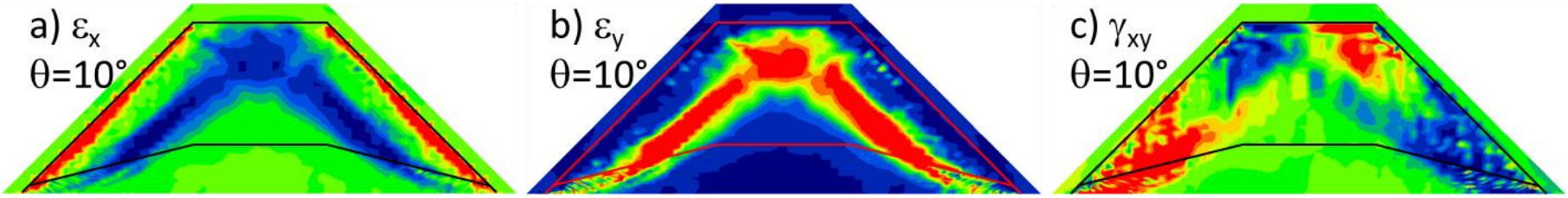

Fig. 7-20 Contour of strain at failure under 10° rolling angle for Case2

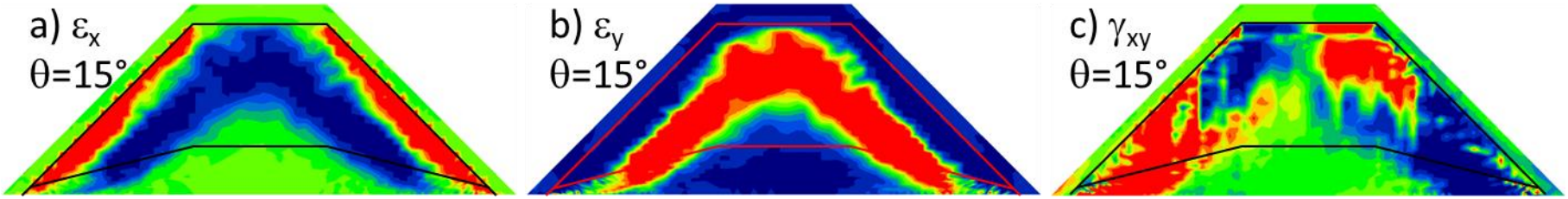

Fig. 7-21 Contour of strain at failure under 15° rolling angle for Case2

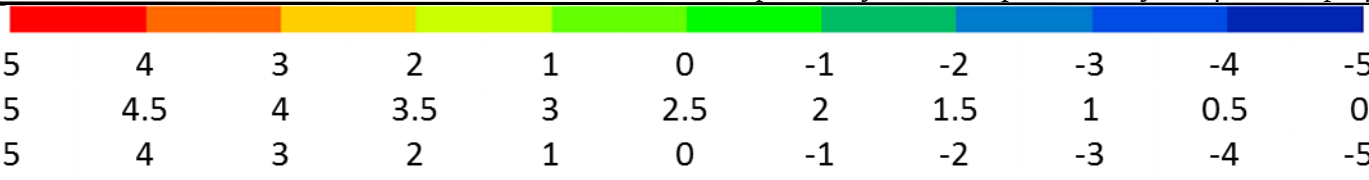

Fig. 7-22 Legend for contour figures of ε_x, ε_y and γ_{xy}

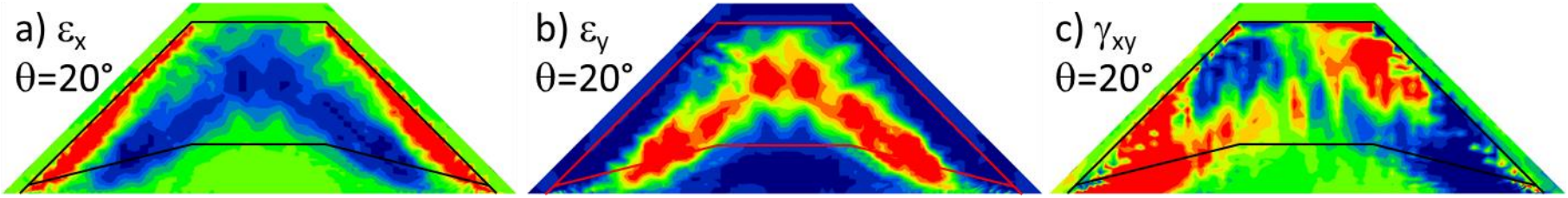

Fig. 7-23 Contour of strain at failure under 20° rolling angle for Case2

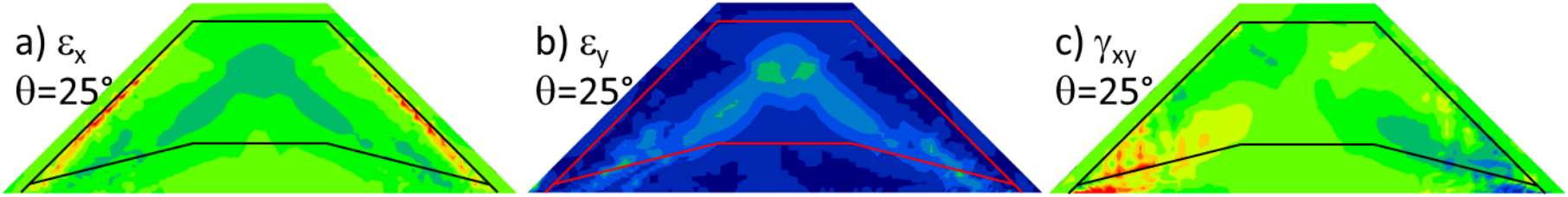

Fig. 7-24 Contour of strain at failure under 25° rolling angle for Case2

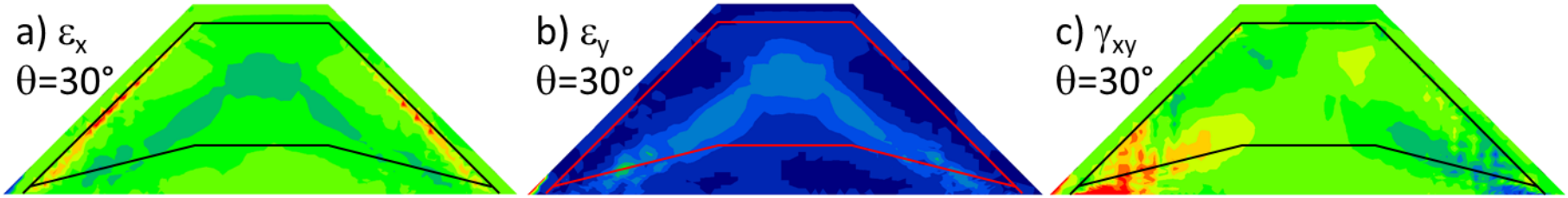

Fig. 7-25 Contour of strain at failure under 30° rolling angle for Case2

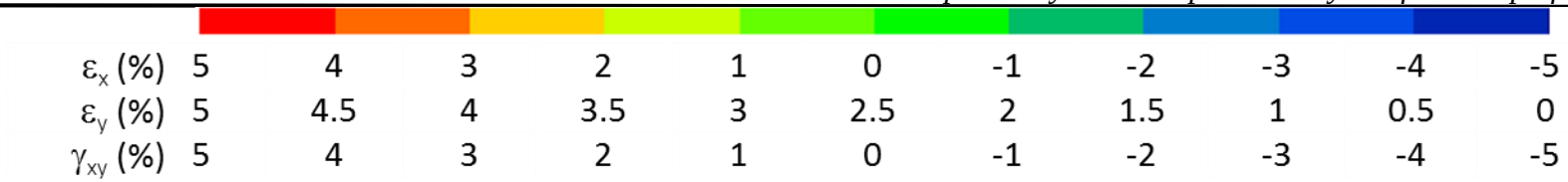

Fig. 7-26 Legend for contour figures of ε_x, ε_y and γ_{xy}

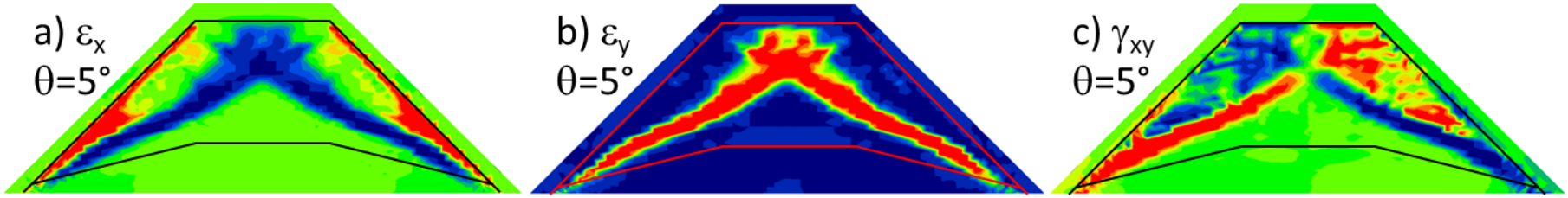

Fig. 7-27 Contour of strain at failure under 5° rolling angle for Case3

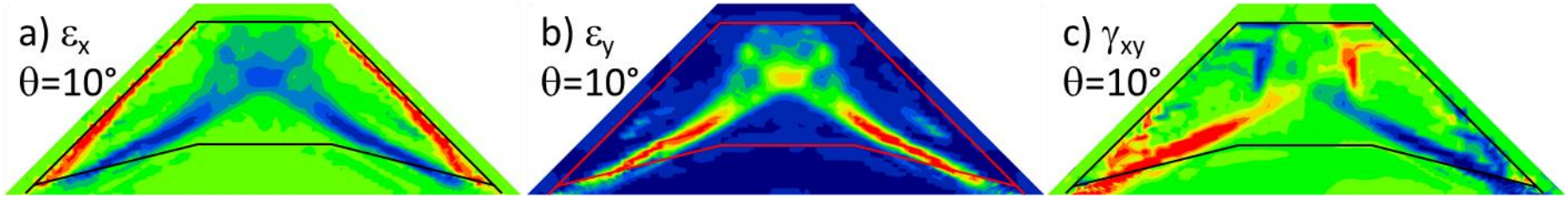

Fig. 7-28 Contour of strain at failure under 10° rolling angle for Case3

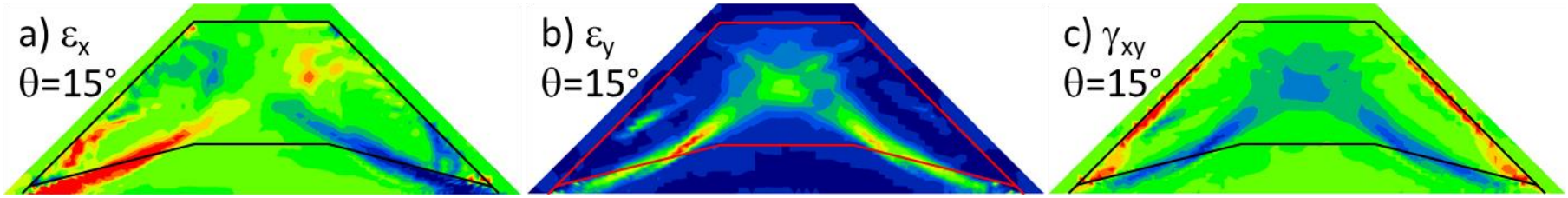

Fig. 7-29 Contour of strain at failure under 15° rolling angle for Case3

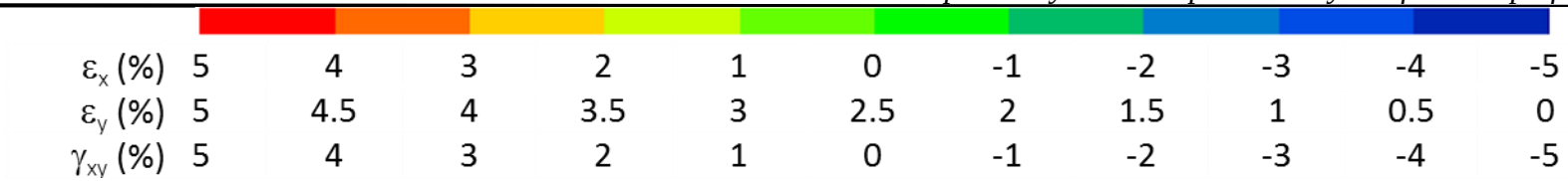

Fig. 7-30 Legend for contour figures of ε_x, ε_y and γ_{xy}

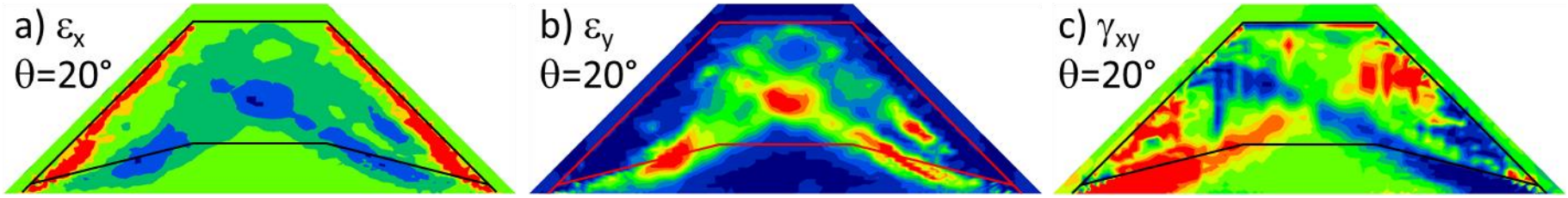

Fig. 7-31 Contour of strain at failure under 20° rolling angle for Case3

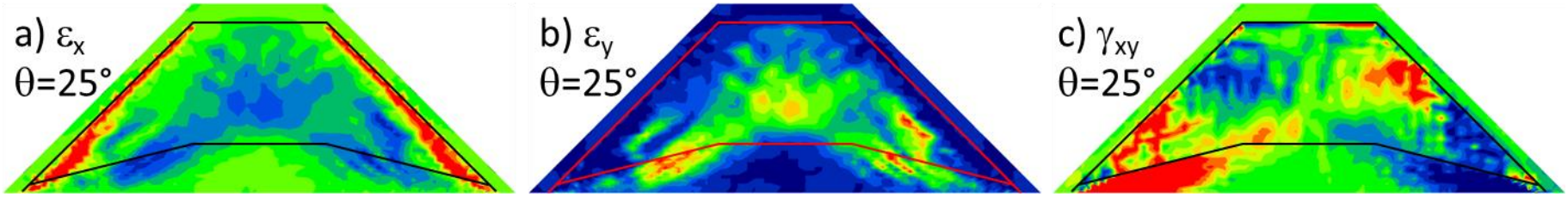

Fig. 7-32 Contour of strain at failure under 25° rolling angle for Case3

Fig. 7-33 Contour of strain at failure under 30° rolling angle for Case3

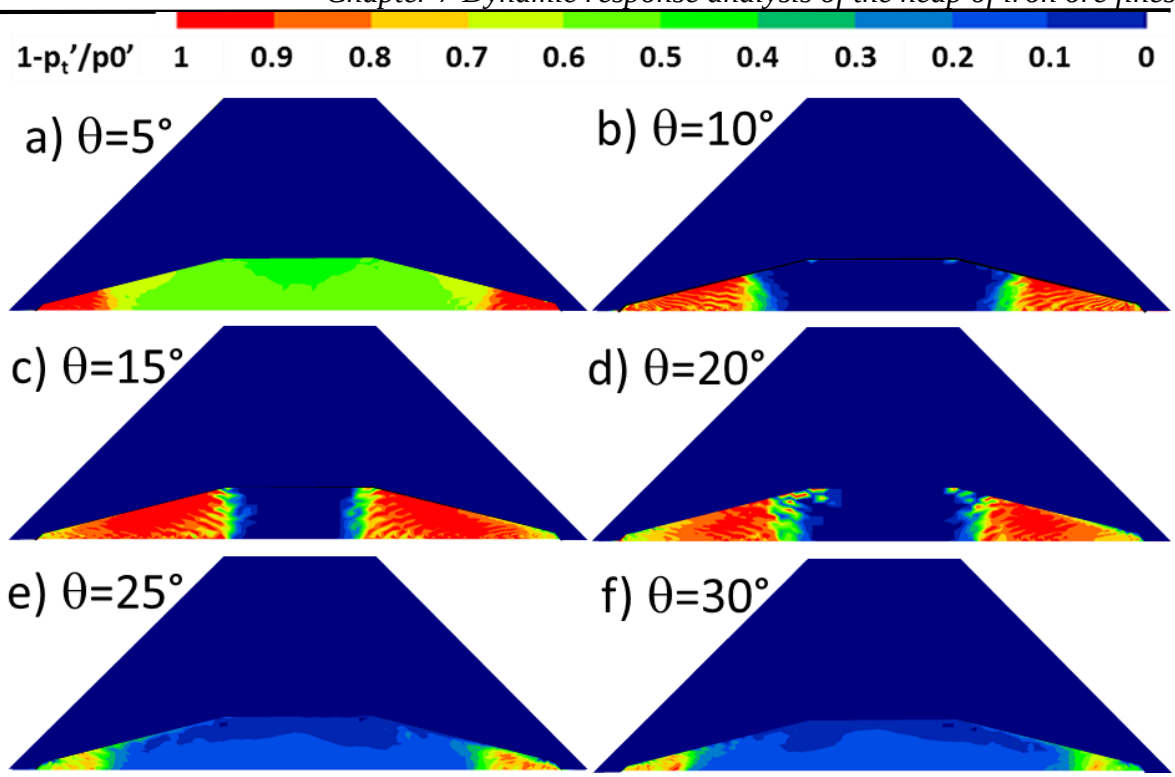

Fig. 7-34 Contour of effective stress reduction ratio failure for Case1 with rolling angle of: a) 5°; b) 10°; c) 15°; d) 20°; e) 25°; f) 30°

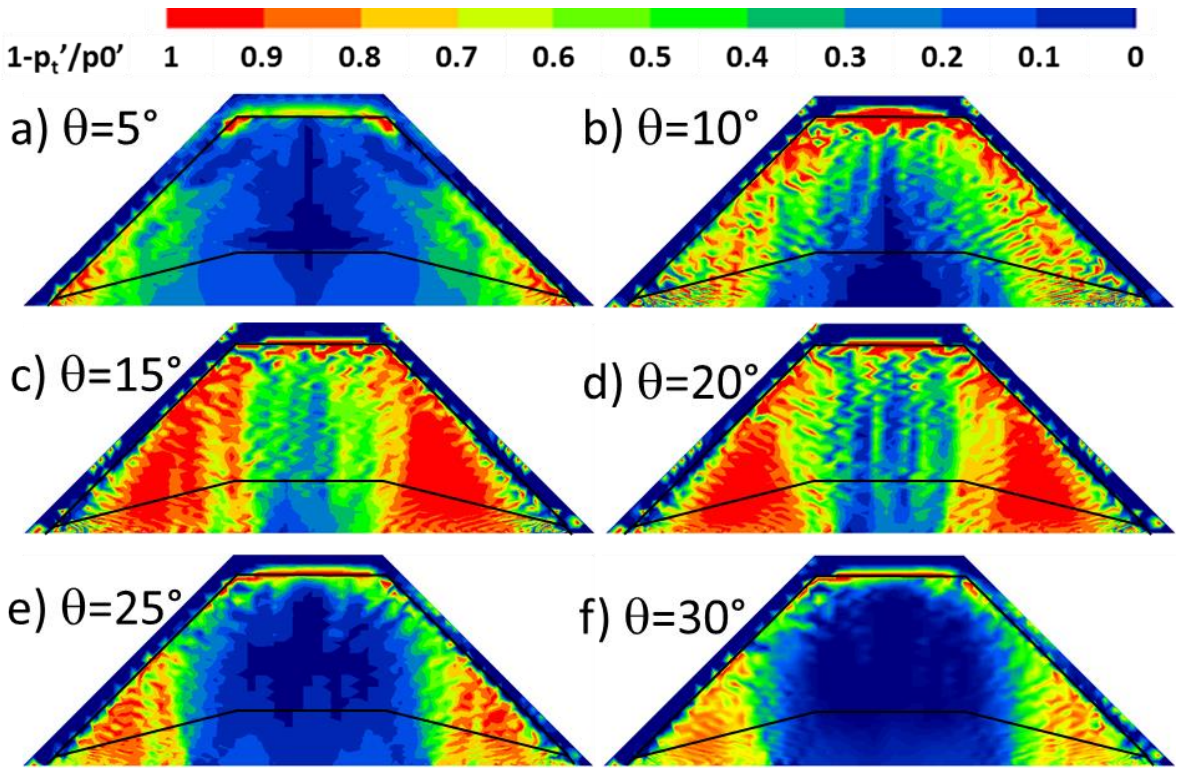

Fig. 7-35 Contour of effective stress reduction ratio failure for Case2 with rolling angle of: a) 5°; b) 10°; c) 15°; d) 20°; e) 25°; f) 30°

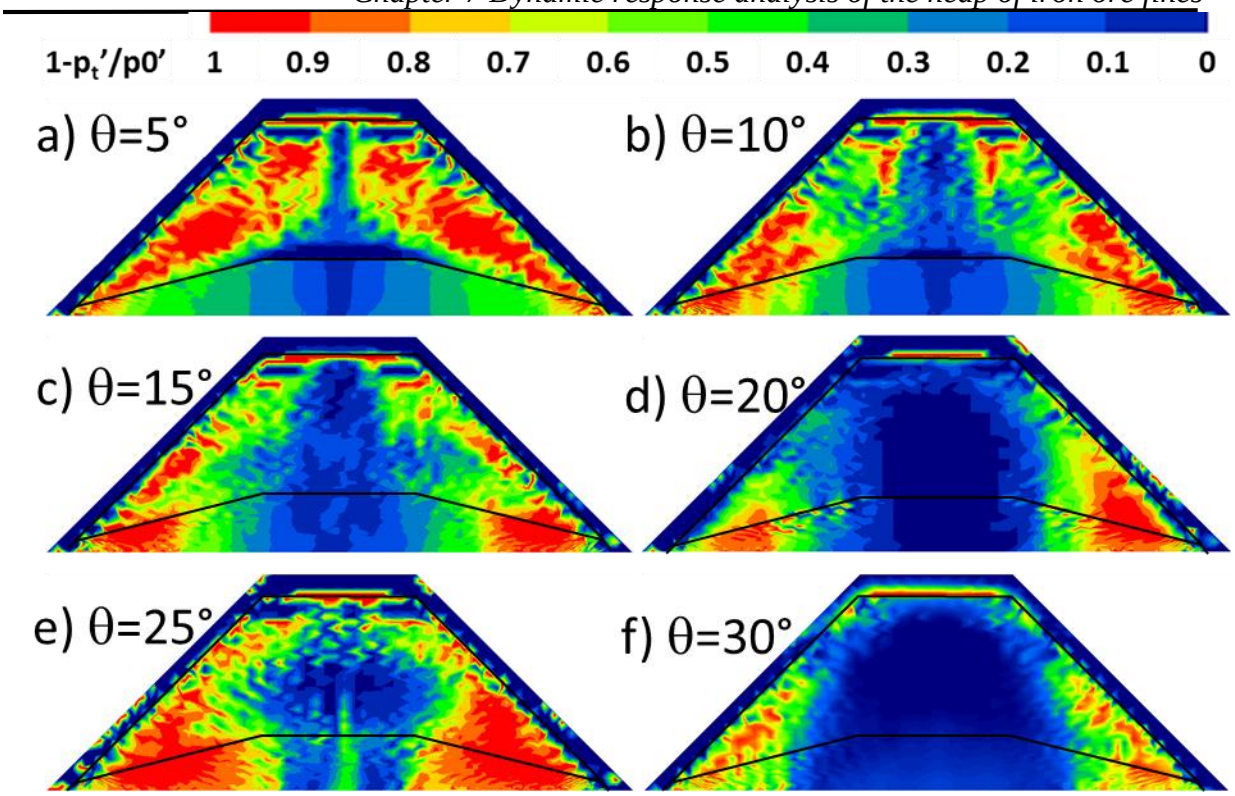

Fig. 7-36 Contour of effective stress reduction ratio failure for Case3 with rolling angle of: a) 5°; b) 10°; c) 15°; d) 20°; e) 25°; f) 30°

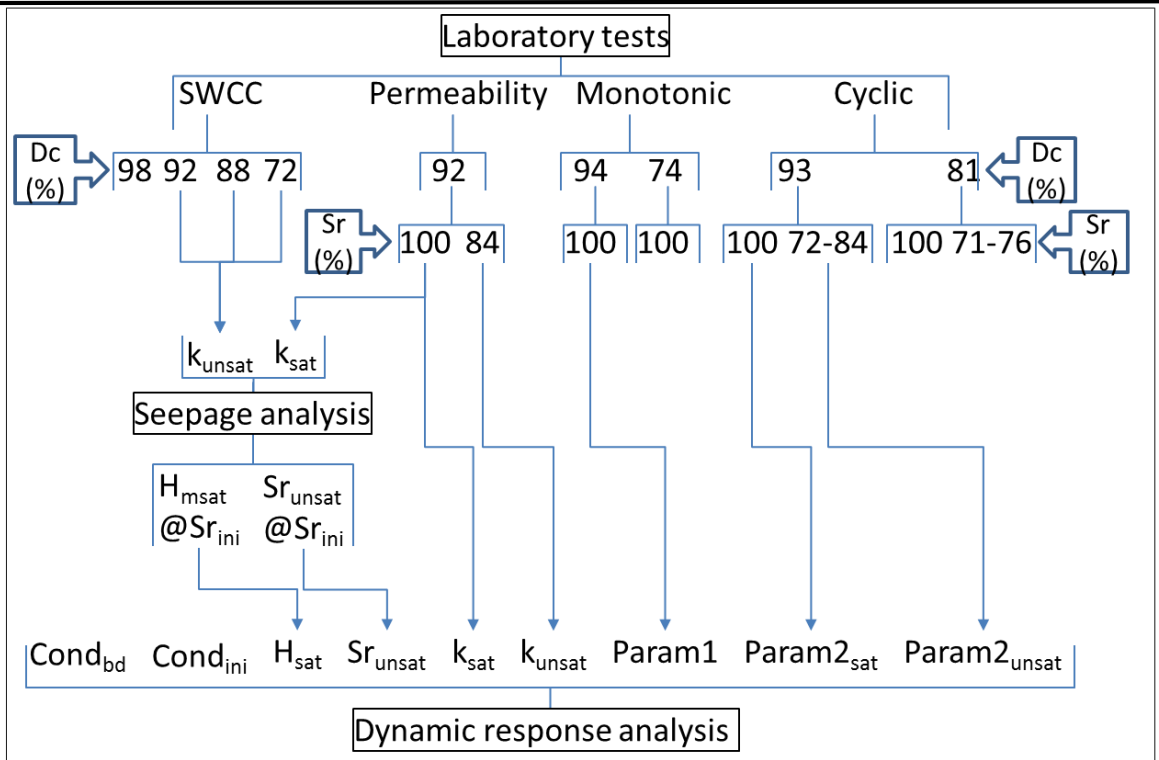

Notes: SWCC, SWCC test; Permeability, permeability test; Monotonic, undrained monotonic loading test; Cyclic, undrained cyclic loading test; Dc, compaction degree; Sr, degree of saturation; k_{unsat}, permeability of the unsaturated IOF-B; k_{sat}, permeability of the saturated IOF-B; H_{msat}, possible maximum height of water table in the heap of IOF-B for a given Sr_{ini}; Sr_{unsat}, distribution of Sr in the unsaturated zone of the heap of IOF-B for a given Sr_{ini}; Sr_{ini}, initial Sr of the heap of IOF-B; $Cond_{bd}$, boundary conditions; $Cond_{ini}$, initial conditions; H_{sat}, height of the water table in the heap; Param1, parameters of the constitutive model part 1 obtained from monotonic loading test; $Param2_{sat}$, parameters of the constitutive model part 2 obtained from cyclic loading test of the saturated IOF-B; $Param2_{unsat}$, parameters of the constitutive model part 2 obtained from cyclic loading test of the unsaturated IOF-B.

Fig. 7-37 General conditions of the laboratory test programs and numerical simulations performed on IOF-B

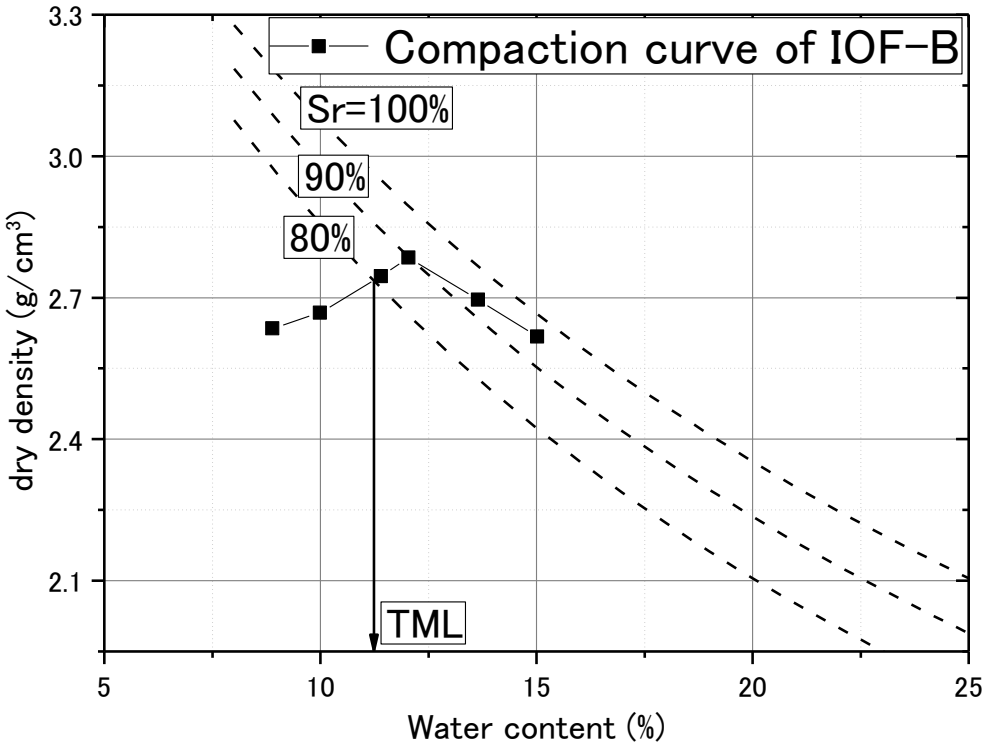

Fig. 7-38 Compaction curve of IOF-B

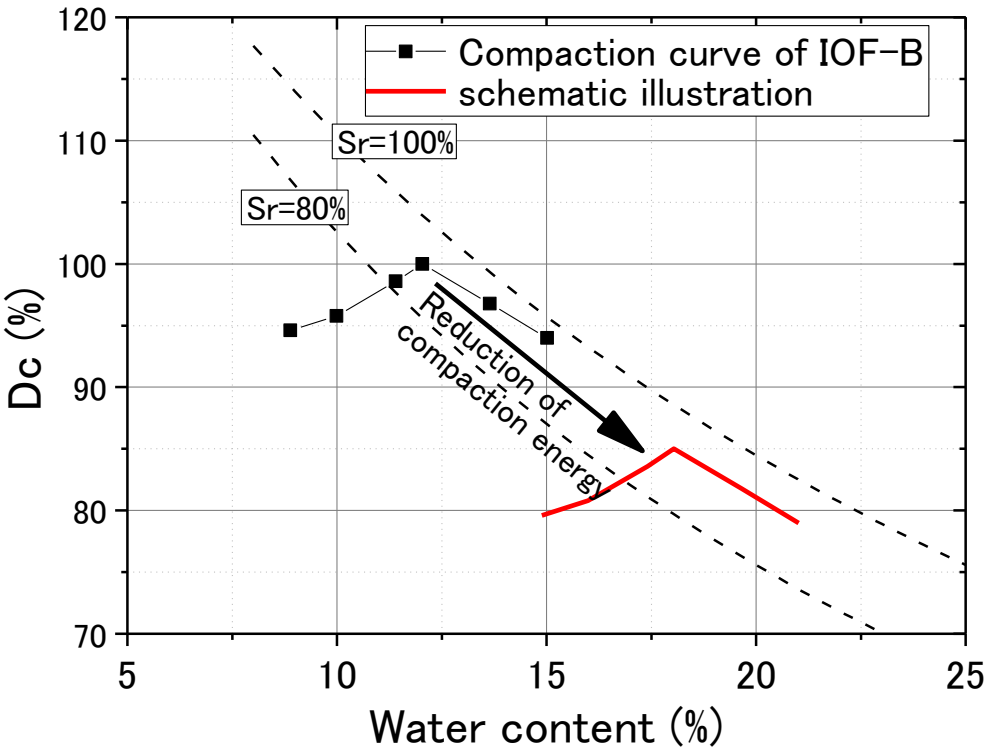

Fig. 7-39 Compaction curve of IOF-B expressed by compaction degree Dc

Chapter 8. Conclusions and recommendations

Contents

8.1 Conclusions

With the motivation of evaluating liquefaction potential of the partially saturated heap of iron ore fines suffering from the dynamic motions at sea, experimental studies and numerical simulations were performed in this study. Fig. 8-1 show the main contents involved in this study. Since a number of different tests are involved in this study, attempts were also made to develop more advanced testing techniques.

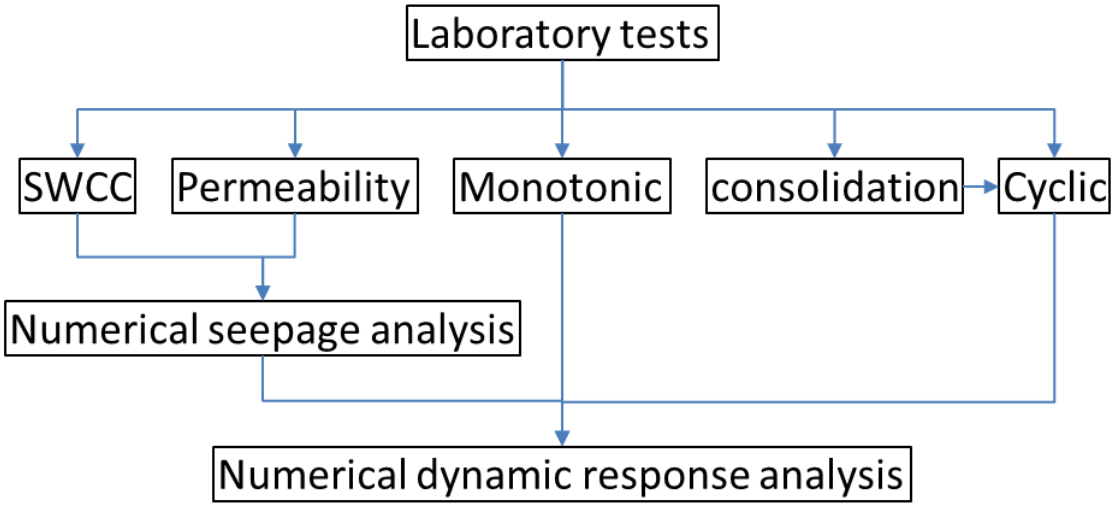

Fig. 8-1 Flow chart followed in this study

From this study, the following conclusions can be drawn:

Soil Water Characteristic Curve (SWCC)

1. Regarding the effect of void ratio on the water retention ability of iron ore fines type B (IOF-B) in the suction range of 0.1-20kPa, IOF-B with less void can retain more water in terms of the relationships between degree of saturation (Sr) and volumetric water content (θ) than that with more void under the same suction; IOF-B with less void can retain less water in terms of gravimetric water content (ω) than that with more void under the same suction less than 1.5 kPa, however, the volume of void affects ω insignificantly under the same suction higher than 1.5 kPa.
2. The membrane filter technique is efficient and reliable to measure SWCC of IOF-B within the suction range up to 20 kPa
3. The effects of gradation, void ratio and the type of sandy soils on SWCC may be insignificant in the high suction range (10^3-10^6 kPa).

4. Two types of iron ore fines tested possess higher water retention ability than their reference soil mixtures in the suction range of 0.1-100 kPa.

Permeability of soils (*k*)

1. For the permeability measurement system, such as the triaxial apparatus used in this study, the system head loss and filter clogging need to be considered carefully for the soils with relatively high permeability in order to evaluate *k* in an accurate manner.
2. Seepage in the soil specimens may take some time for stabilization and a constant hydraulic gradient applied to the soil specimens may be necessary to measure the stabilized permeability.
3. Permeability could be measured accurately on the saturated soils in this study, while it may be necessary to confirm the measurements of the unsaturated soils in the future study.

Undrained behaviors of soils under monotonic loading

1. The undrained shear strength of saturated IOF-B is closely related to the initial and residual effective stress, and the amount of axial strain of saturated IOF-B may be governed by the ratio of the applied shear stress to the residual effective stress.
2. The undrained shear strength of saturated IOF-B may reduce significantly with a decrease in its density.

Volume change of soils due to consolidation

1. The volume changes of the saturated sandy soils during isotropic compression and swelling (loading and unloading) are very different among different types of soils with various densities.

Undrained behaviors of soils under cyclic loading

1. For the sandy soils with unsaturated condition, the rate of excess pore pressure generation and the tendency of contractive behavior may reduce as compared with their saturated condition under otherwise similar conditions.
2. It is necessary to efficiently control total mean principal stress (p) of the unsaturated sandy soils under undrained cyclic triaxial loading in order to properly evaluate their resistance against liquefaction.

3. Membrane filter technique performed well to measure negative pore water pressure of the unsaturated sandy soils under cyclic loading.
4. Suction of the unsaturated sandy soils is sustained under cyclic loading until the soils approach liquefaction
5. The resistance against liquefaction of the tested sandy soils with unsaturated condition ($R_{L,Unsat}$) is higher than that with saturated condition ($R_{L,Sat}$) under otherwise similar conditions.
6. A new parameter, volumetric strain ratio $R_{Vol,air/0.1p'}$, is proposed to correlate the liquefaction resistance ratio (LRR= $R_{L,Unsat}$ /$R_{L,Sat}$) that is affected by Sr. The new parameter shows better correlation with LRR than previous proposals.

Seepage in the heap of iron ore fines

1. The distribution of Sr in the heap of IOF-B is affected by the initial degree of saturation (Sr_{ini}) and density. An envelope was drawn on the relationship between Sr_{ini} and the maximum height of water table (H_{max}) in the heap indicating the possible maximum H_{max} for a given Sr_{ini}. The distribution of Sr in the unsaturated zone is rather uniform and can be roughly estimated according to the value of Sr_{ini}.

Liquefaction potential of partially saturated heap

1. The predictions of the cyclic behaviors of IOF-B by using PZ-sand model qualitatively match the experimental results, while the parameters used in this study may need to be optimized in order to produce better results.
2. With the considerations of liquefaction potential and permeability of the unsaturated zone, the overall liquefaction potential of the heap of IOF-B becomes much higher than that without considering them.
3. The effect of density of IOF-B may need to be considered in the future studies in order to properly evaluate the responses of the heap of iron ore fines and to verify the suitability of current proposal made by the relevant groups concerning on the liquefaction problem of iron ore fines.

8.2 Recommendations

With reference to the results in this study, the following issues are recommend for further investigation:

Membrane filter technique

Membrane filter technique applied in this study performed very well on measuring either SWCC or negative pore water pressure. However, the application is limited to the suction value up to 20 kPa in this study. Further development of the application of membrane filter technique is recommended.

Permeability test

The system used in this study could not measure the hydraulic gradient directly applied on the specimens, which causes difficulties, such as system head loose, filter clogging, etc., in measuring permeability of the saturated and unsaturated soils. Development of techniques for permeability test in the triaxial system are recommended in order to overcome the difficulties existed in this study.

$R_{Vol,\ air/0.1p'}$ vs LRR

A new parameter, $R_{Vol,\ air/0.1p'}$ is proposed to correlate LRR in this study. It may need to be verified by more experimental data in the future study.

Evaluation of the liquefaction potential of the heap of iron ore fines

Only limited number of cases were performed to analyze the response of the heap of IOF-B under cyclic rolling motion, further studies are recommend to optimize the parameters of used constitutive model and to consider the effects of boundary condition, initial condition, density, distribution of Sr, permeability, etc. in order to understand the responses of the heap comprehensively.

Appendix

Contents

Appendix A. Introduction of issues about IMO

IMO (International Maritime Organization) is the United Nations (UN) specialized agency with responsibility for the safety and security of shipping and the prevention of marine pollution by ships. IMO consists of an Assembly, a Council and five main committees: the Maritime Safety Committee (MSC); the Marine Environment Protection Committee (MEPC); the Legal Committee; the Technical Co-operation Committee and the Facilitation Committee. The MSC (Maritime Safety Committee) is the highest technical body of the Organization. It consists of all Member States. The functions of the Maritime Safety Committee are to consider any matter within the scope of the Organization concerned with aids to navigation, construction and equipment of vessels, manning from a safety standpoint, rules for the prevention of collisions, handling of dangerous cargoes, maritime safety procedures and requirements, hydrographic information, log-books and navigational records, marine casualty investigations, salvage and rescue and any other matters directly affecting maritime safety. The Committee is also required to provide machinery for performing any duties assigned to it by the IMO Convention or any duty within its scope of work which may be assigned to it by or under any international instrument and accepted by the Organization. It also has the responsibility for considering and submitting recommendations and guidelines on safety for possible adoption by the Assembly. The expanded MSC adopts amendments to conventions such as SOLAS and includes all Member States as well as those countries which are Party to conventions such as SOLAS even if they are not IMO Member States. In addition, the MSC is assisted in its work by a number of sub-committees which are also open to all Member States. The Sub-Committee on Dangerous Goods, Solid cargoes and Containers (DSC) is one of the sub-committees of MSC.

The SOLAS Convention (International Convention for the Safety of Life at Sea) in its successive forms is generally regarded as the most important of all international treaties concerning the safety of merchant ships. The first version was adopted in 1914, in response to the Titanic disaster. The 1974 version (fifth version) includes the tacit acceptance procedure - which provides that an amendment shall enter into force on a specified date unless, before that date, objections to the amendment are received from an agreed number of Parties. As a result the 1974 Convention has been updated and amended on numerous occasions. The Convention in force today is sometimes referred to as SOLAS, 1974, as amended.

All content above is referred to website of IMO (http://www.imo.org/Pages/home.aspx).

Appendix B. Membrane filter technique

For the unsaturated soils, pore water pressure (PWP) is usually lower than pore air pressure (PAP) because of capillary effect. In order to measure PWP, it is necessary to isolate air from entering the measurement system of PWP. The ceramic disk with a thickness of 4mm-8 mm is traditionally used as the isolator. However, it needs to be fixed on the pedestal permanently, which causes technical difficulties to saturate and to maintain saturated state of the ceramic disk before the tests. To overcome these difficulties, a flexible micro porous membrane filter was introduced in recent study (Nishimura et al, 2012). Its work principle is the same with the ceramic disk using the capillary force of the micro pores (Fig. B-1). Elaborately designed pedestal used in this study can seal the membrane filter and create a flat surface as shown in Fig. B-2. Observations of the membrane filter by using SEM (Scanning Electron Microscope) was conducted as shown in Fig. B-3, which clearly shows the porous structure of the membrane filter. The air entry value (AEV) of the membrane filter and the sustainable time duration of isolation need to be examined before utilizing the membrane filter in the tests.

1. Determination of AEV of membrane filter

   The AEV of the commercial membrane filters is usually provided, however, it may not reliable for the long term usage, e.g. several days. A simple device schematically shown in Fig. B-4 was manufactured to measure the AEV of the membrane filters used in this study.

   Saturated membrane filter was carefully fixed by a steel plate and an acrylic bottle was cupped on the steel plate. The gap between the open end of the bottle and the steel plate was sealed by grease. Constant air pressure was applied from the bottom of the acrylic container and photos were taken from the top of the acrylic bottle from the beginning of applying air pressure until the air bobbles were observed in the acrylic bottle.

   Three types of membrane filters of Supor series (Hydrophilic acrylic copolymer), Pall Corporation, were tested. Table B-1 shows the properties of the membrane filters and the test results. Fig. B-5 shows the typical photos of initial and final states of the test.

Table B-1 Properties of membrane filter and AEV test results

Membrane type	Membrane pore size (μm)	Membrane thickness (μm)	Provided AEV (kPa)	supplied air pressure (kPa)	Enduring time (hrs)
Supor 450	0.45	140	250	20	240
Supor 450	0.45	140	250	25	50
Supor 200	0.20	145	350	25	<120,>70
Supor 200	0.20	145	350	40	2
Supor100	0.10	132	--	40	40

Table B-1 shows that Supor series membrane filter is very sensitive to the magnitude of the supplied air pressure. A small pressure increment may cause significant reduction of the air diffusion duration. Since the suction value of the sandy soils used in this study was not expected to be very high, Supor 450 membrane filter was mainly used in this study. In addition, the time duration shown in Table B-1 may change even for the same type of membrane filter which may be caused by the variation of the pore size distribution in the filter, thus Table B-1 may only provide a reference of the AEV of the membrane filter.

2. Sustainable time duration on the measurement of pore water pressure

Though AEV is determined through the process introduced above, it does not mean that the PWP can be certainly measured continuously as long as those shown in Table B-1 even if the suction in the unsaturated specimens is lower than the supplied air pressure.

The PWP was recorded by confining a specimen of Inagi sand (material properties is introduced in Chapter 3 in detail) in the triaxial system while keeping the PAP equals to atmosphere pressure. Fig. B-6 shows the measurement of PWP of two types of membrane filters for the same specimen. Membrane filter Versapor 200 has a two-layer structure, one layer is made by the hydrophilic acrylic copolymer the same as Supor series and the other layer is made by non-woven as a strength support layer. As shown in Fig. B-6, the measurements were consistent initially, while both of them suddenly increased by approximately 1 kPa as shown in dash circles in the figures. After the jump points, they gradually approach to 0 kPa. Possible reasons were examined such as, the types of membrane filter, the area of membrane filter contacting the specimen, the degree of saturation of the specimens (suction level) as well as the type of soils contacting the membrane filter. Jumps were observed in all examined cases except the last factor. By

paving a layer of DL clay on the pedestal as shown in Fig. B-7, PWP of the specimen of Inagi sand was measured. The jump was not observed until the end of the test as shown in Fig. B-8.

During the measurement of PWP, the water in the membrane filter was expected to contact with the pore water network in the specimen, while there is a possibility that at some areas the contacts lost due to re-distribution of the pore water as schematically shown in Fig. B-9. The loss of contacts may cause the invasion of the pore air in the membrane filter. Since the average particle size of DL clay is much smaller than Inagi sand, the loss of contacts may not easily happen for DL caly.

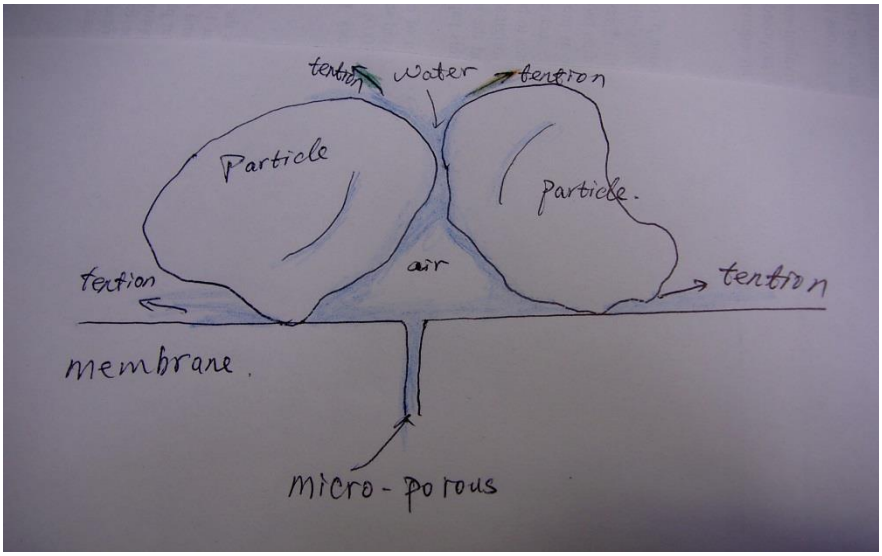

Fig. B-1 Illustration of suction in unsaturated soil

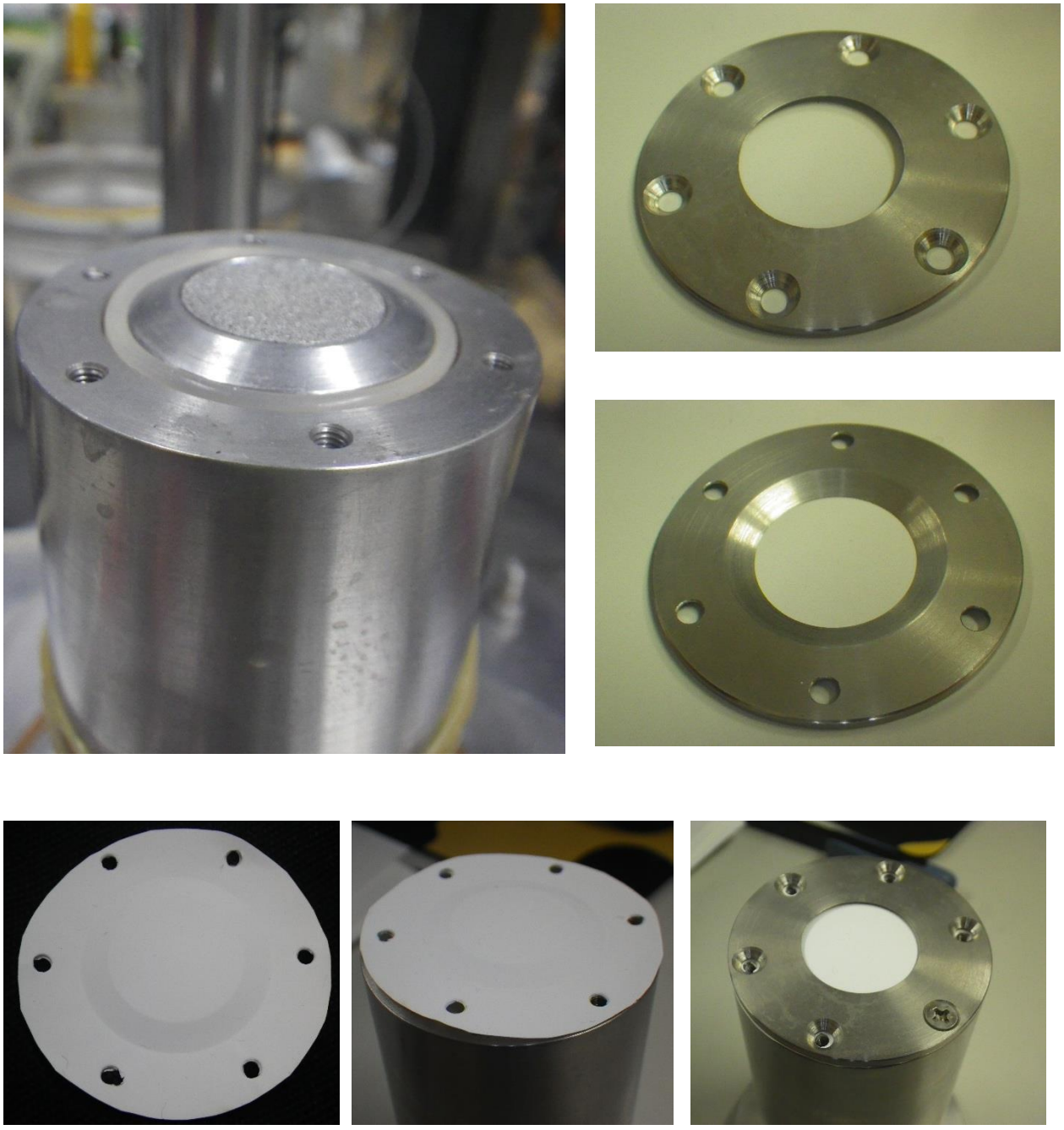

Fig. B-2 Components of pedestal in triaxial test for unsaturated soil

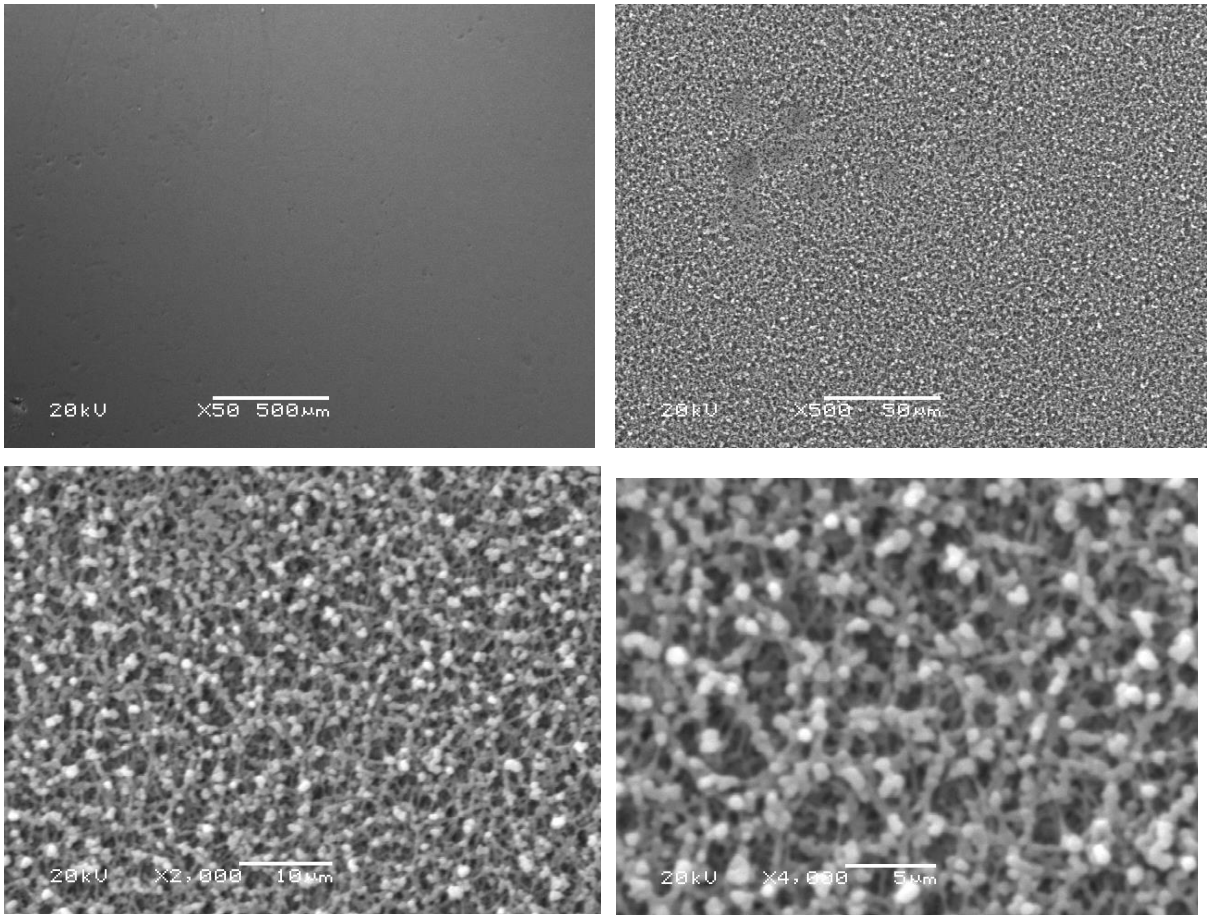

Fig. B-3 SEM image of porous structure of the membrane filter

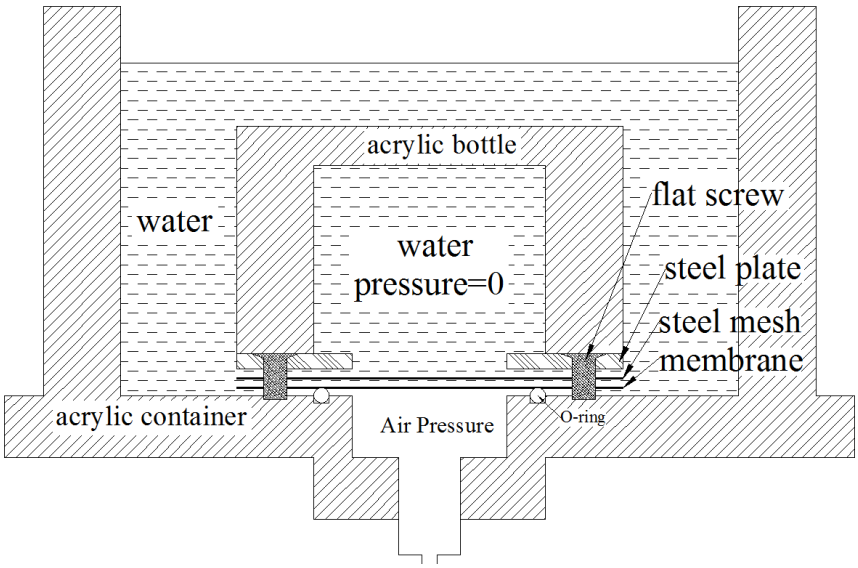

Fig. B-4 Schematic drawing of device measuring AEV

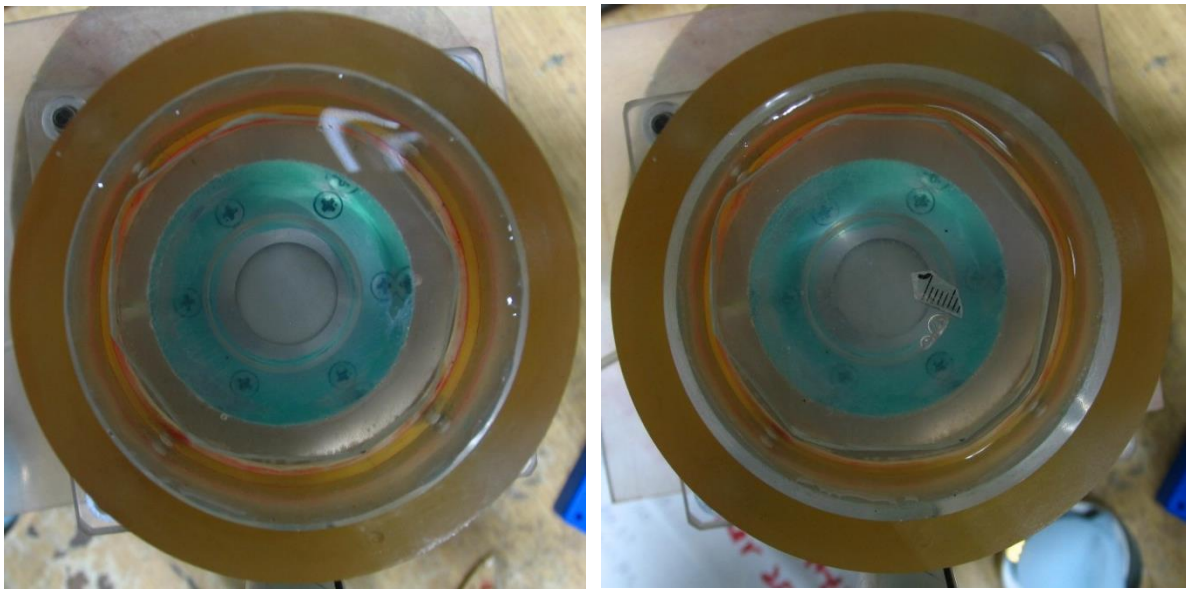

Fig. B-5 Initial and final states of test examining AEV of membrane filter

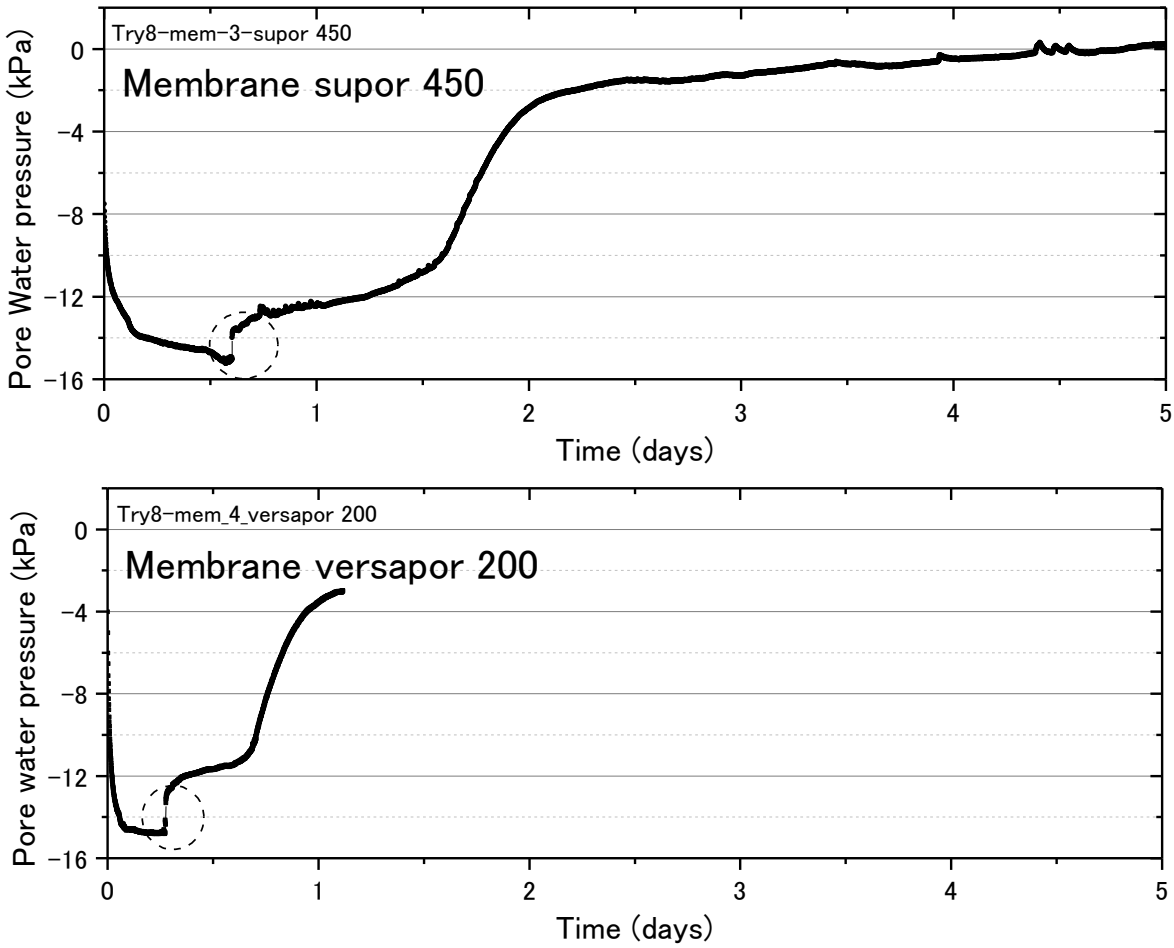

Fig. B-6 Pore water pressure measurements, a, supor 450 membrane, b, versapor 200 membrane

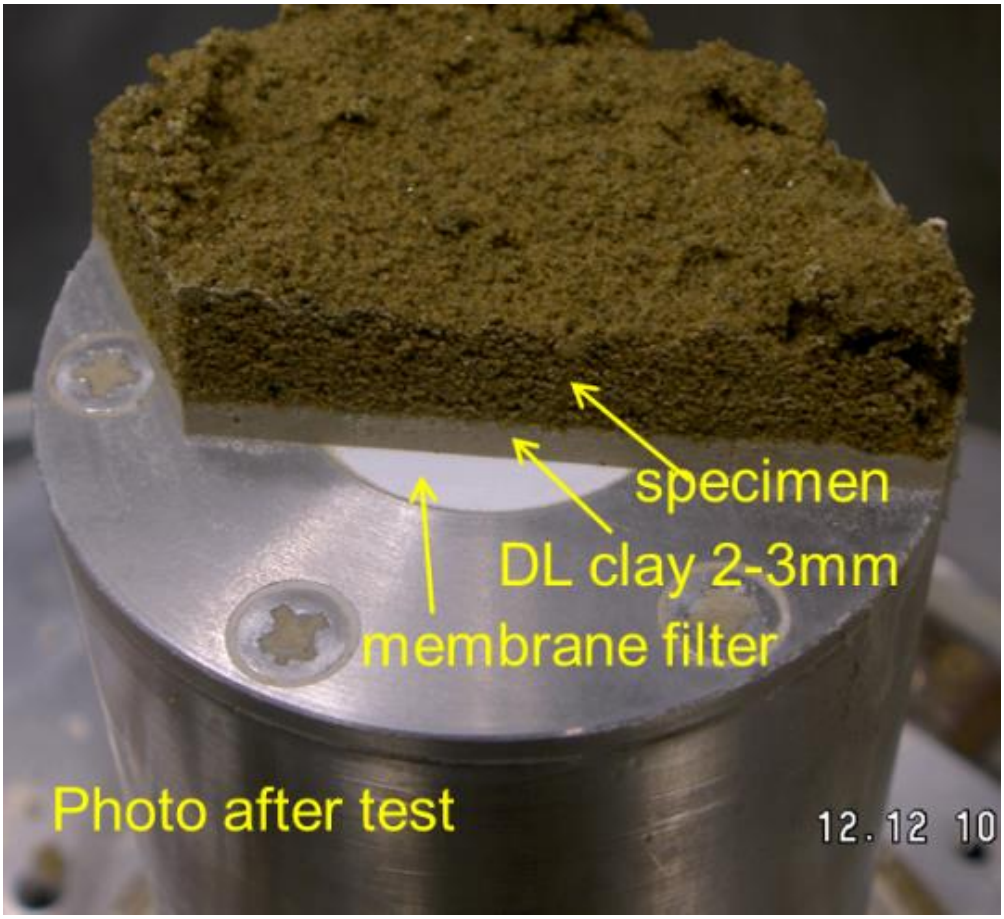

Fig. B-7 DL clay paved on pedestal (after test)

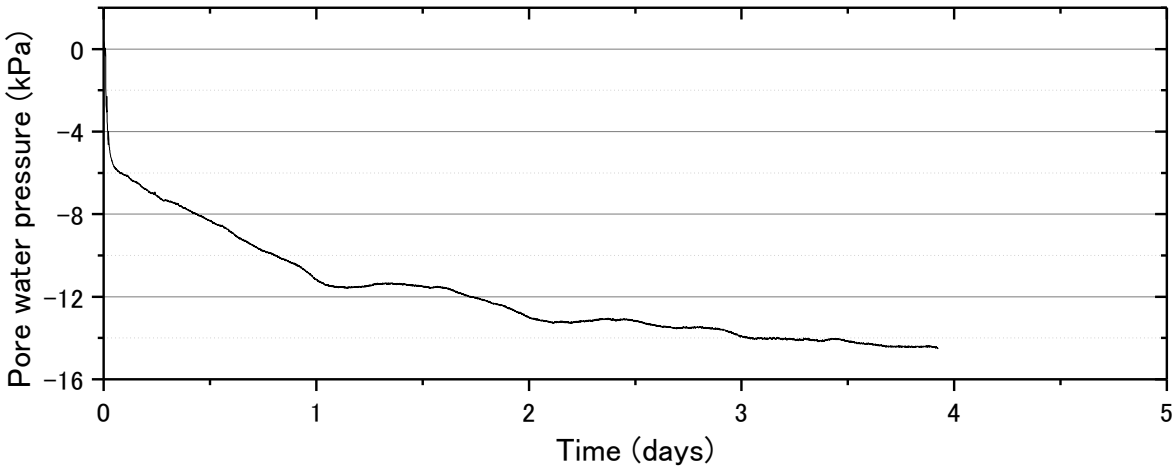

Fig. B-8 Pore water pressure measurement by paving DL

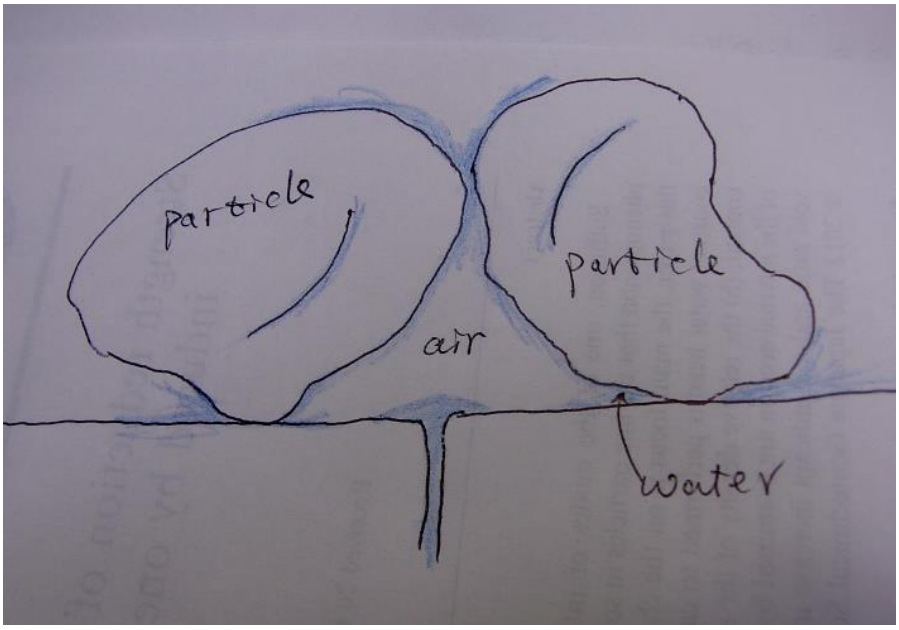

Fig. B-9 Loss of water connection

Appendix C. Volume measurement system

The double cell system to measure the volume change of the unsaturated specimens consists of an inner cell, a reference burette and a differential pressure transducer (DPT) as shown in Fig. C-1. The DPT measure the water level difference between the inner cell and the reference burette. The water level of the inner cell changes with the volume change of the specimen and movement of the top cap, and the water level in the reference burette is kept constant. The measured volume change from DPT (ΔV_{DPT}) is the summation of the volume change of the specimen ($\Delta V_{specimen}$) and the volume change induced by the movement of top cap (ΔV_{topcap}) which can be calculated from the readings of the vertical displacement transducer (LVDT):

$$\Delta V_{specimen} = \Delta V_{DPT} - \Delta V_{topcap} \qquad \text{(Eq. C-1)}$$

$$\Delta V_{topcap} = \Delta Disp_{LVDT} \times A_{topcap} \qquad \text{(Eq. C-2)}$$

where, $\Delta Disp_{LVDT}$ is the change of the vertical displacement measured by LVDT; A_{topcap} is the area of top cap.

The system can measure the overall volume change of the specimens, however, there is a problem for this system. The output of DPT is slightly slower than that of LVDT, which, according to Eqs. C-1 and C-2, introduces calculation error to the $\Delta V_{specimen}$.

Fig. C-2 shows the set-up of a trial test and the data measured by three transducers. For the test, a spring was sandwiched between the top cap and the pedestal, and sinusoidal loading from double action cylinder was applied to the spring. The water level change in the inner cell was monitored by the DPT and PWP (pore water pressure) transducers and the movement of the top cap was measured by the LVDT. The unit of y-axes are voltage and the scale were adjusted for comparison purpose. Fig. C-2 shows that the response of the PWP transducer is consistent the LVDT, while a output delay (Δt) is observed for the DPT. According to the outputs of DPT and LVDT, the volume change, ΔV_{DPT} and ΔV_{topcap}, together with the volumetric strain of the spring based on Eq. C-1 are plotted in Fig. C-3 (the dimensions of the spring are assumed to be 50mm in diameter and 100mm in height). The positive value of the volumetric strain in Fig. C-3 means volume compression. There are at least two types of errors induced by meniscus effect and DPT delay in Fig. C-3. The meniscus effect was difficult to avoid as far as the current measurement system is used. The DPT delay caused a error of around ±1% in this case.

To reduce the error induced by the output delay, the measured data of DPT were shifted backward slight. Fig. C-4 shows the results after shifting. The error caused by the output delay was mostly eliminated.

The effect of output delay can be eliminated for a mild change of the water level in the inner cell, such as the case illustrated in Fig. C-2, however, the water level also suddenly changes when, such as, the specimen is liquefied. To simulate this condition, rectangle loading was applied to the spring system shown in Fig. C-2. Fig. C-5 shows the recorded output of LVDT and DPT in terms of voltage after shifting DPT data backward for 0 s, 0.3 s and 0.6 s. When the water level suddenly changes, the response of DPT first shows the output delay of about 0.3s and then a gradually increase to the value corresponding to the input. During this progressive development process, an apparent error are introduced when calculating the volumetric strain no matter how to shift the data. This progressive development process is caused by the electric signal analysis process in the transducer, which may be a universal problem of this type DPT.

From the results shown above, it can be seen that at least three types of errors, meniscus effect, output delay and progressive development of output, involve in the volume change measurement system. The meniscus effect is difficult to remove by using current system. The error caused by output delay can be largely eliminated by shifting measured data. The error caused by progressive development of output due to the sudden change of the water level in the inner cell could not be efficiently reduced and the data measured under similar conditions for instance, during liquefaction, may have to be abandoned.

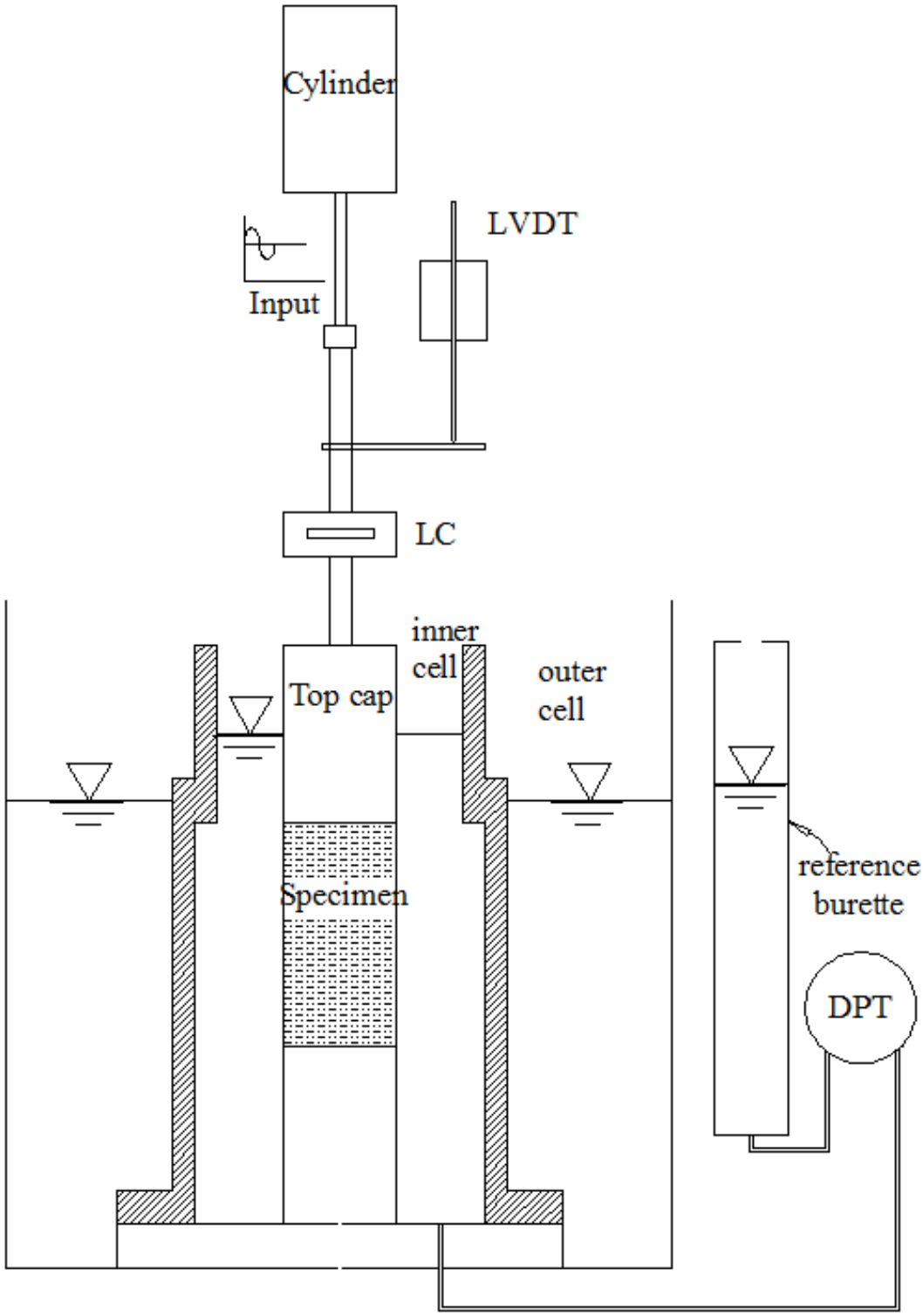

Fig. C-1 Volume change measurement system in trixial apparatus

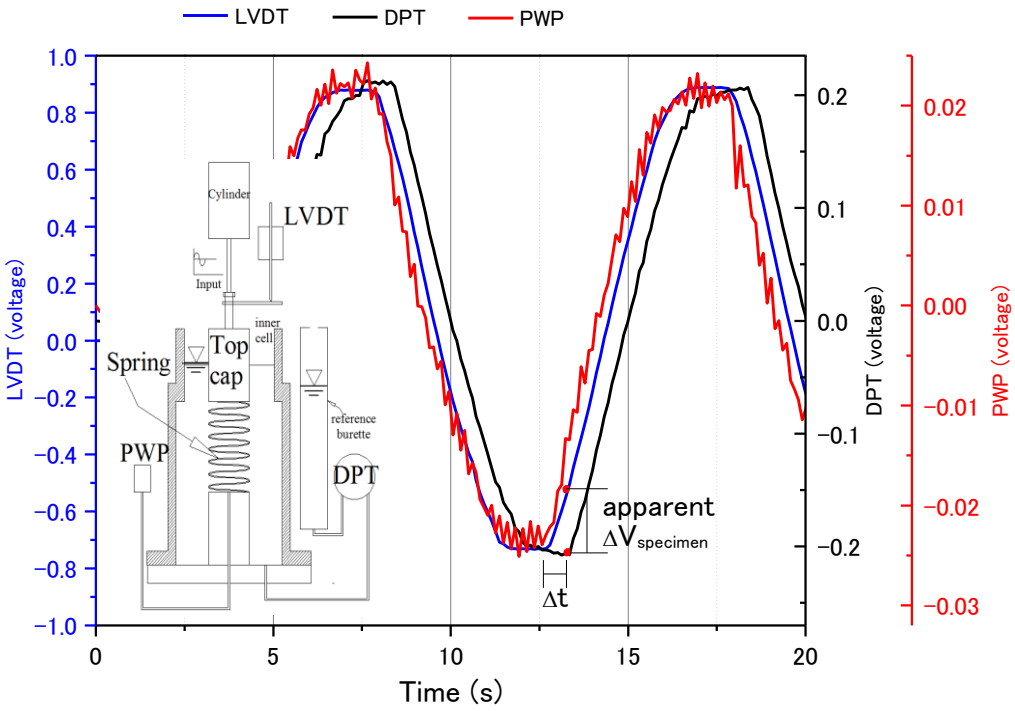

Fig. C-2 Output delay of DPT

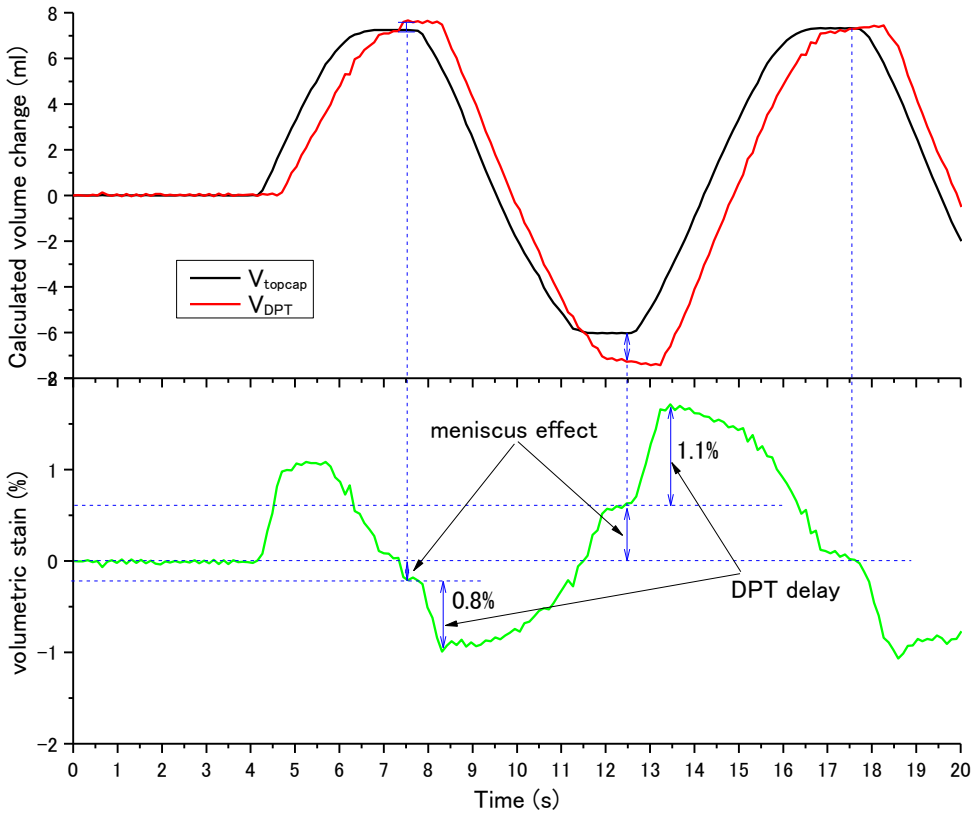

Fig. C-3 Errors for measurement of volumetric strain of a specimen

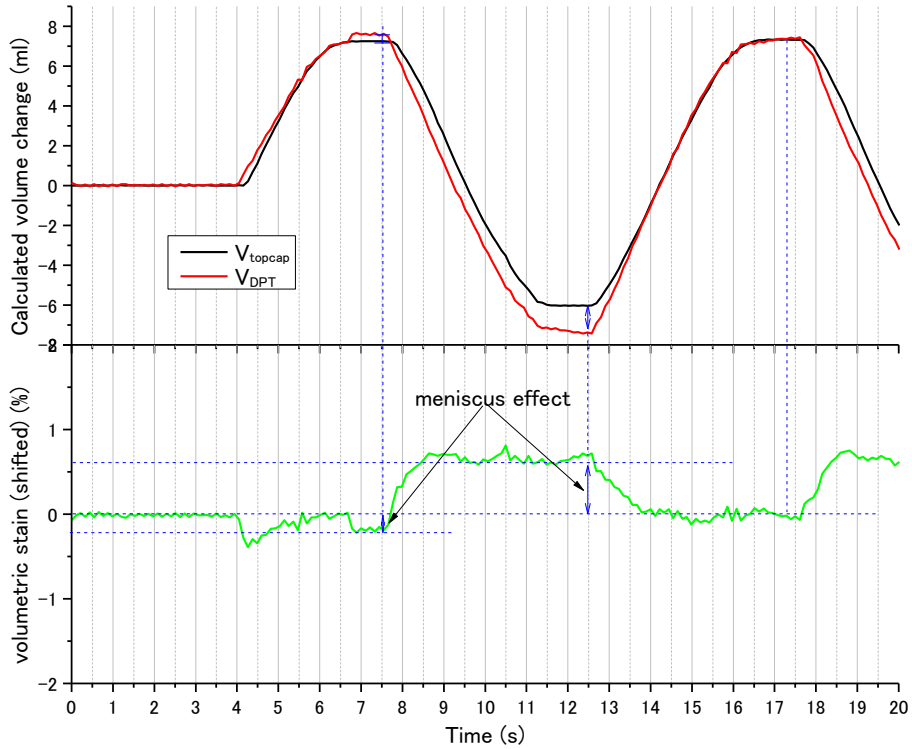

Fig. C-4 Error reduction by shifting data of DPT

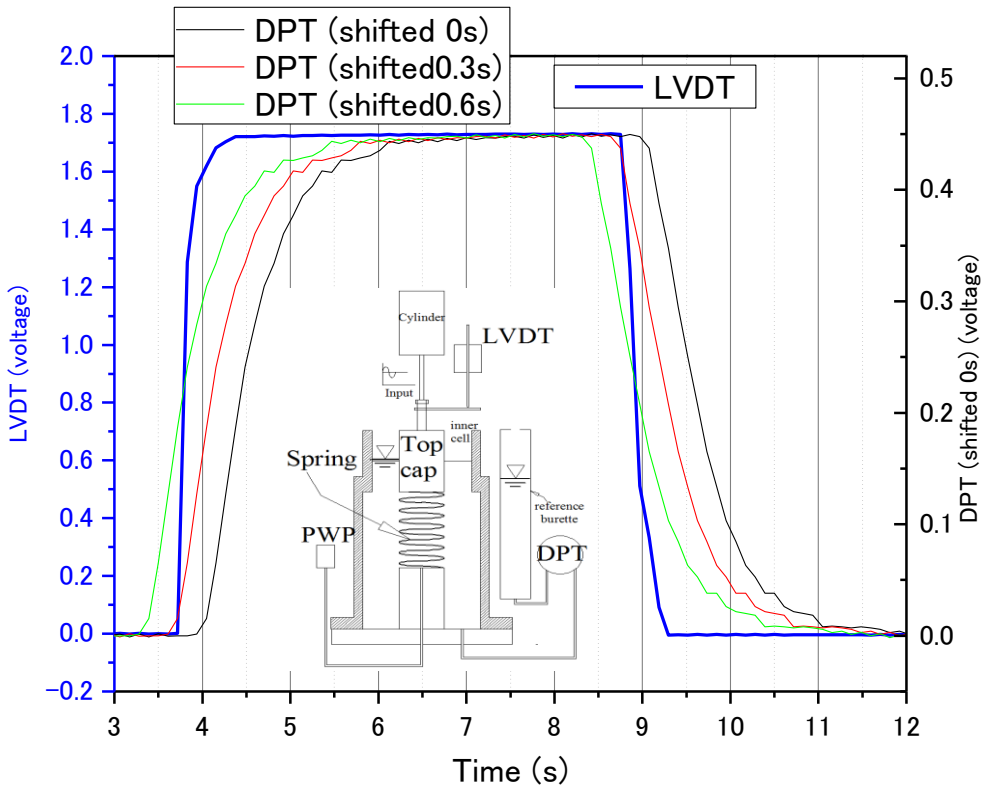

Fig. C-5 Errors for measurement of volumetric strain caused by sudden change of water level

Appendix D. Time histories of SWCC test in high suction range

The time histories of SWCC tests conducted in high suction range (10^3kPa-10^6kPa) are presented in this appendix. The related illustration and discussion are addressed in Chapter 4. Table D-1 lists the test conditions for all tested materials. There is a unique name for each individual test which contains some information about this test.

For each individual test, there are three identical specimens, the time histories of the three specimens are plotted in the same figure.

Test name	Specific gravity G_s	Void ratio e	Dry density ρ_d (g/cm3)	Compaction energy (kJ/m^3)
SW_H_IOF-A_D/W_XX	4.835	0.592	3.03	3.27
SW_H_NCD-A_D/W_XX	2.694	0.336	2.01	3.26
SW_H_IOF-A-4.75_D/W_XX	4.859	0.817	2.67	2.88
SW_H_IOF-A-2_D/W_XX	4.859	1.138	2.27	2.45
SW_H_IOF-B_D/W_XX	4.444	1.221	2.00	2.16
SW_H_NCD-B_D/W_XX	2.678	0.841	1.45	2.19

SW_H_XXX_D/W_XX:
SW_H_: stands for SWCC test in high suction level by vapor equilibrium technique.
XXX_: stands for material tested.
IOF-A_: iron ore fines type A with original gradation;
NCD-A_: common material mixture, reference for IOF-A;
IOF-A-4.75_: iron ore fines type A passing 4.75 mm sieve;
IOF-A-2_: iron ore fines type A passing 2 mm sieve;
IOF-B_: iron ore fines type B;
NCD-B_: common material mixture , reference for IOF-B;
D/W_: stands for Drying or Wetting process
XX: stands for value of relative humidity.

D-1 Iron ore fines type A (IOF-A)—drying process

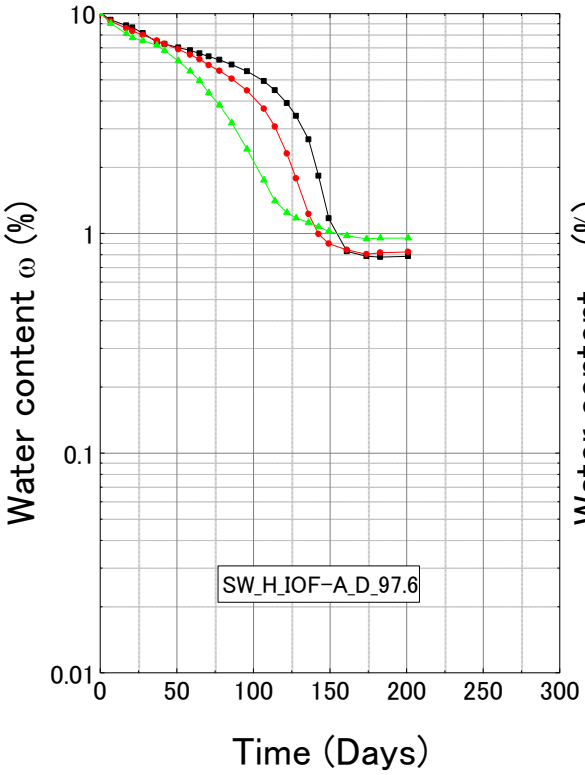

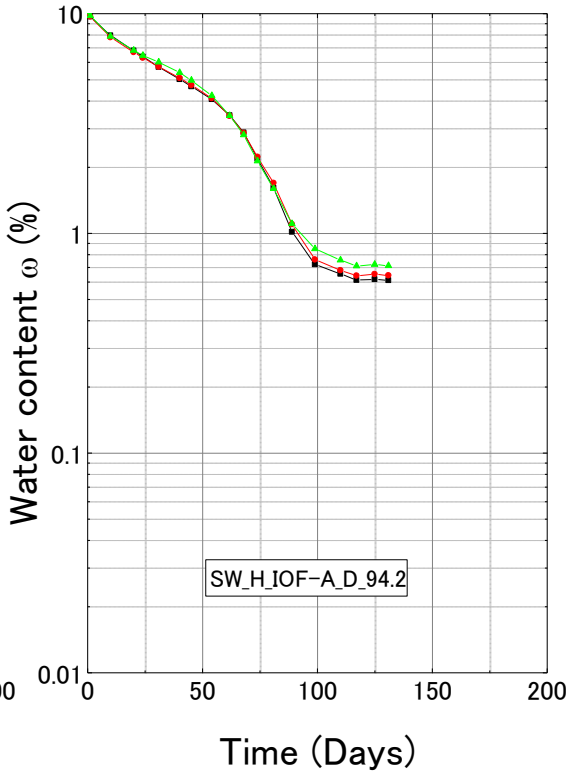

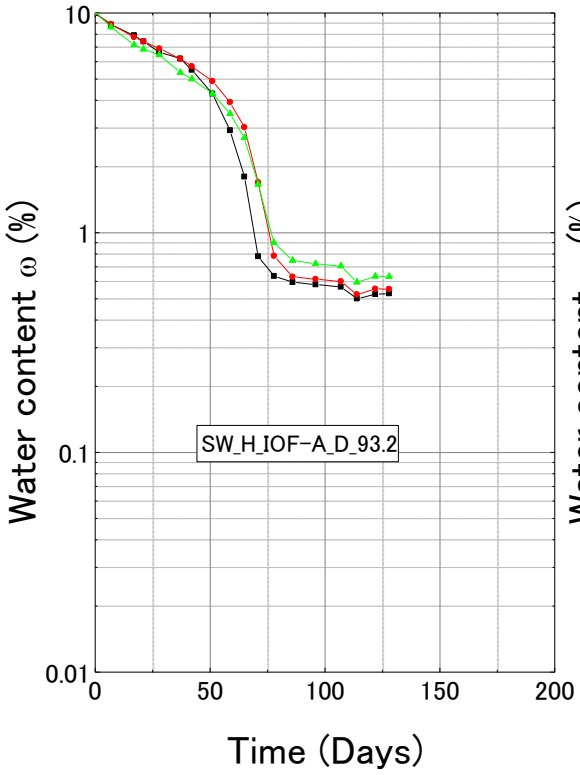

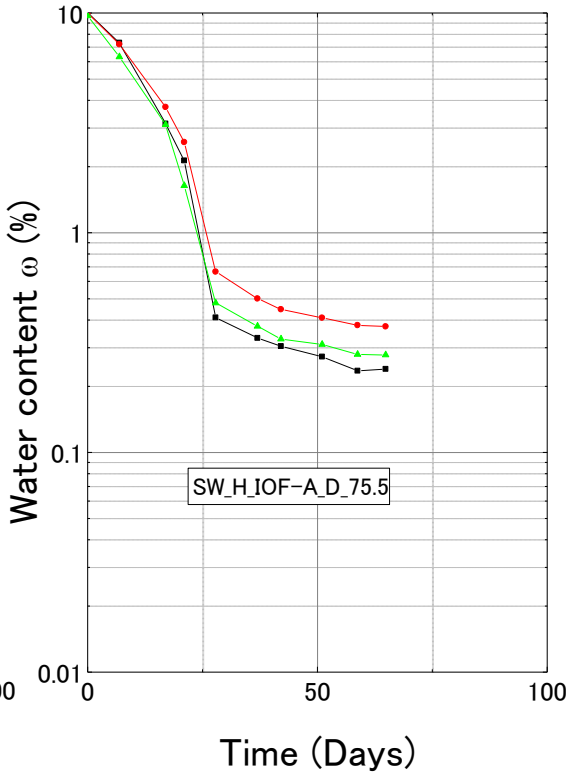

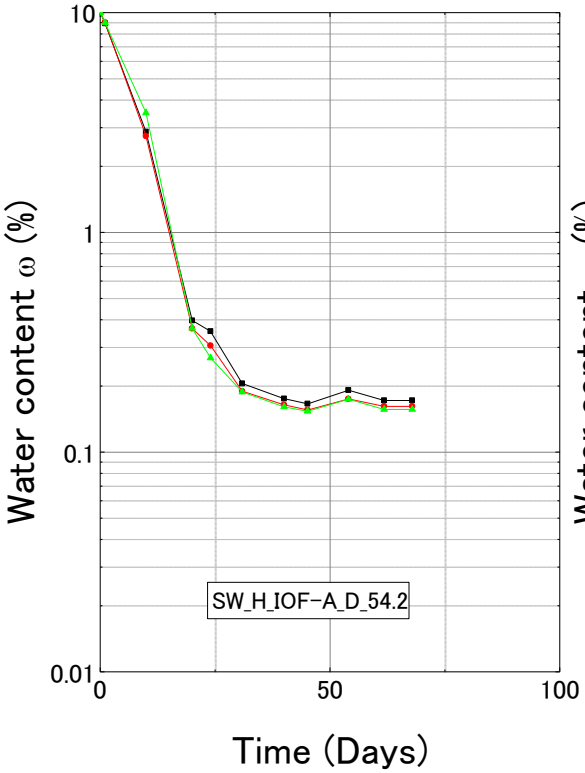
10
1
0.1
0.01
0
50
100
Water content ω (%)
Time (Days)
SW_H_IOF-A_D_54.2

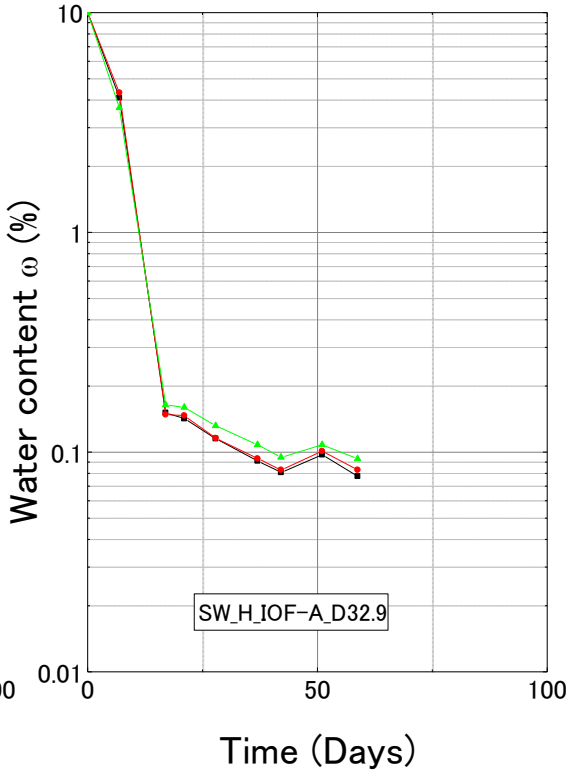
10
1
0.1
0.01
0
50
100
Water content ω (%)
Time (Days)
SW_H_IOF-A_D32.9

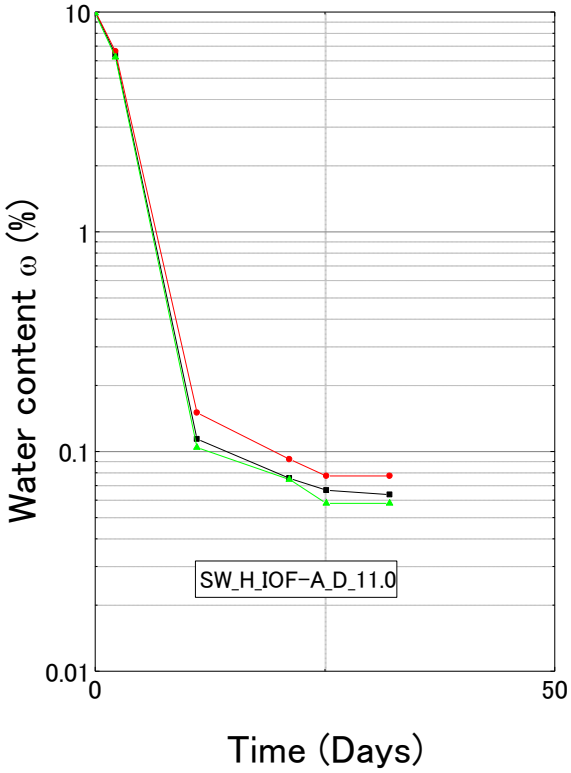
10
1
0.1
0.01
0
50
Water content ω (%)
Time (Days)
SW_H_IOF-A_D_11.0

D-2 Iron ore fines type A (IOF-A)—wetting process

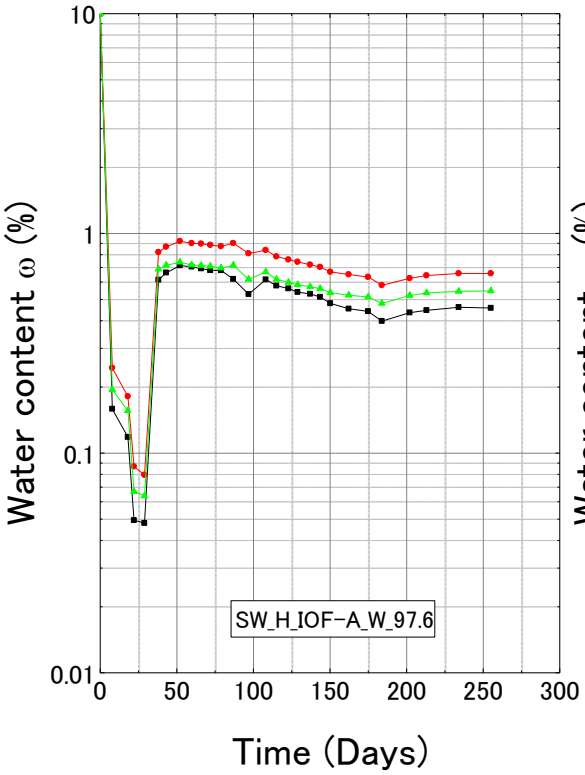

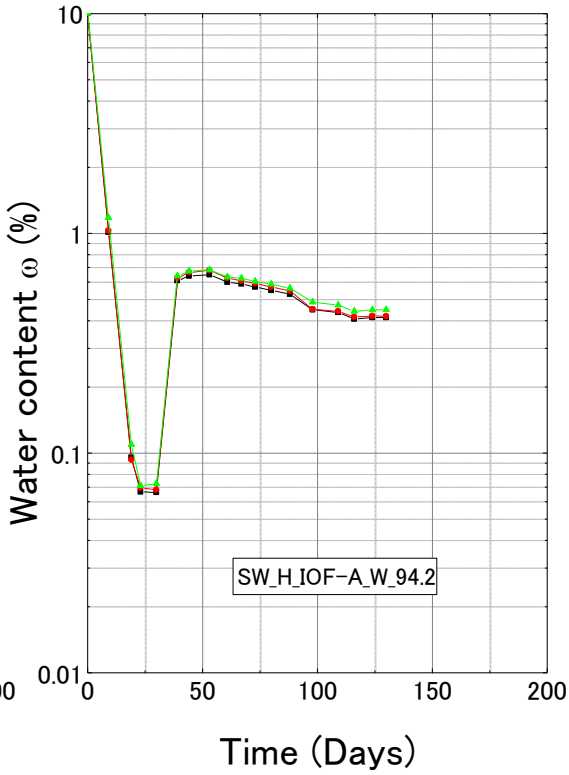

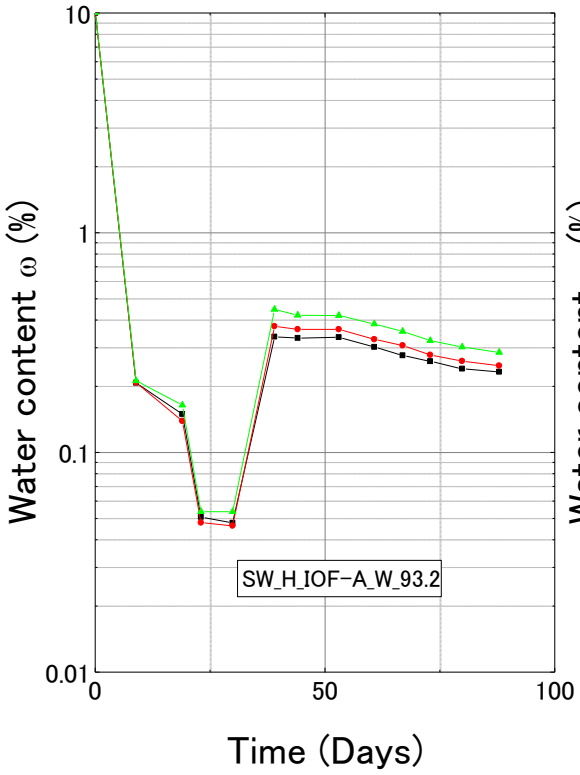

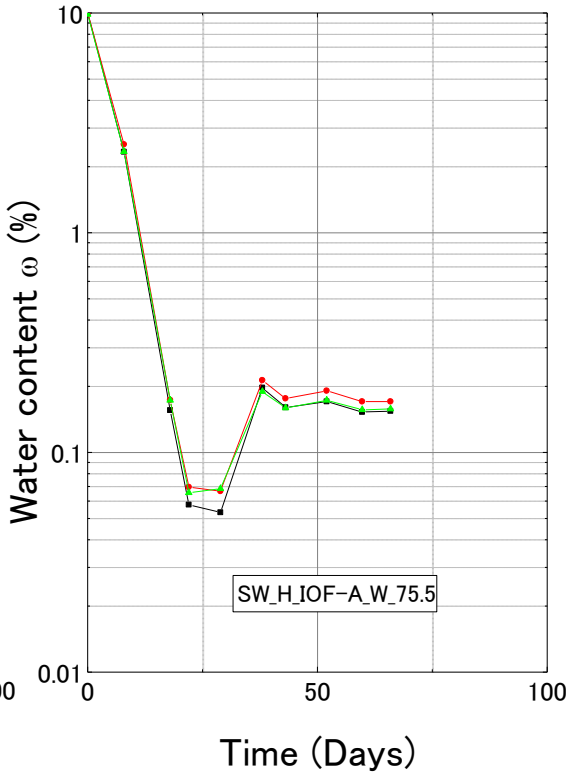

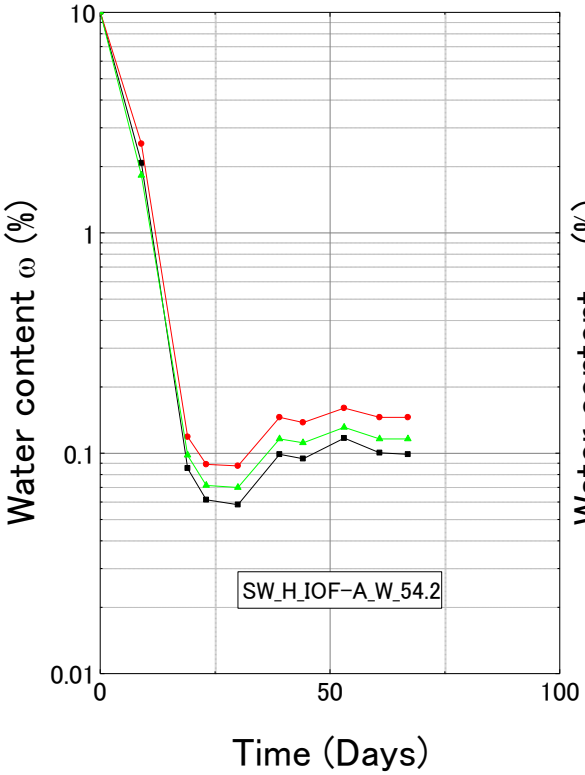
10
1
0.1
0.01
0
50
100
Water content ω (%)
Time (Days)
SW_H_IOF-A_W_54.2

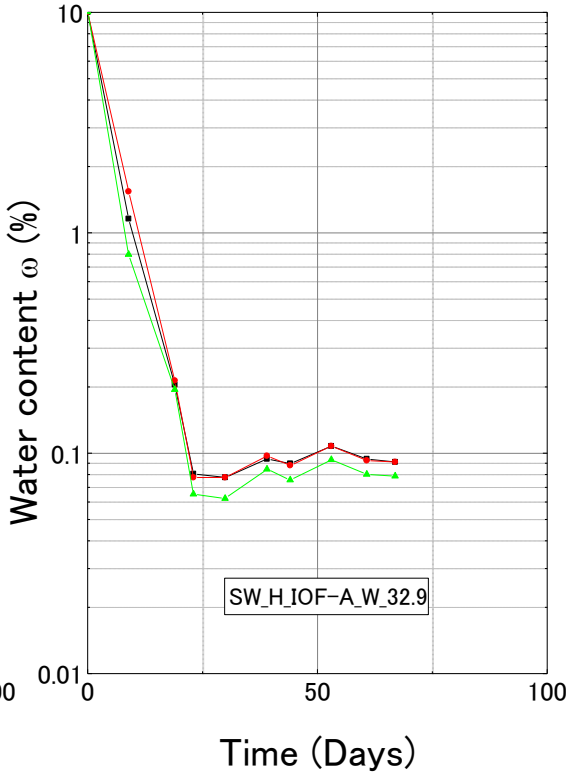
10
1
0.1
0.01
0
50
100
Water content ω (%)
Time (Days)
SW_H_IOF-A_W_32.9

D-3 Reference mater for IOF-A—drying process

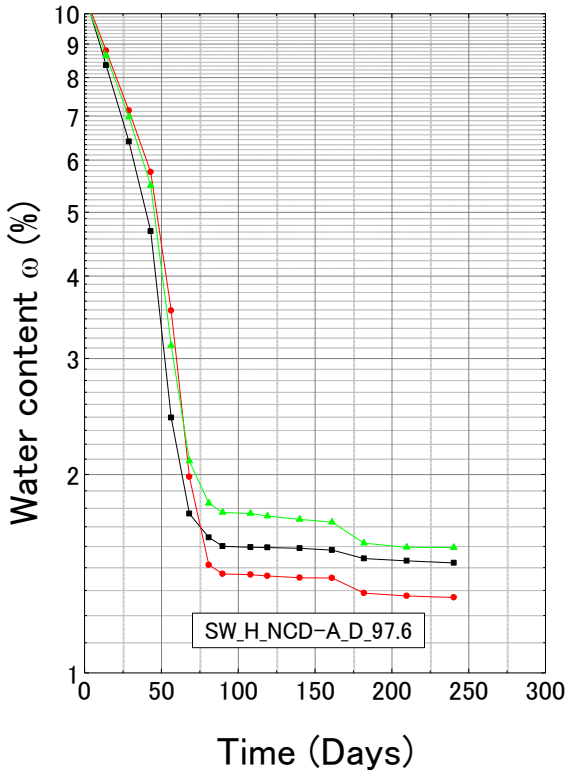

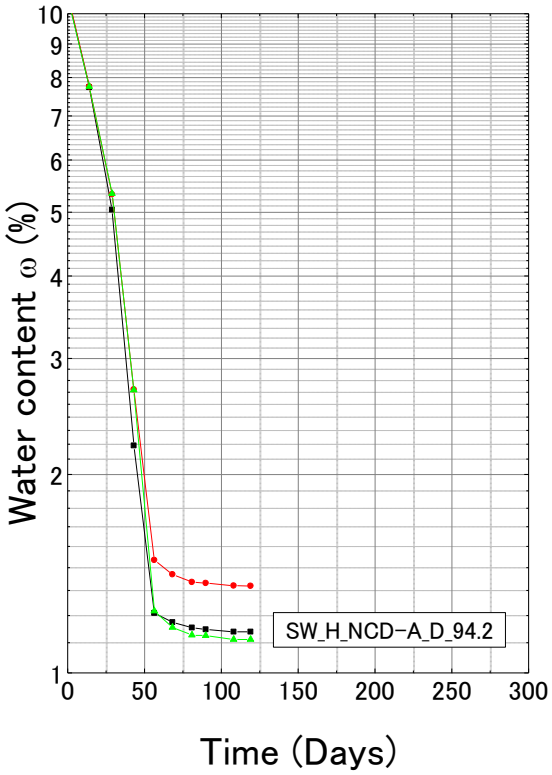

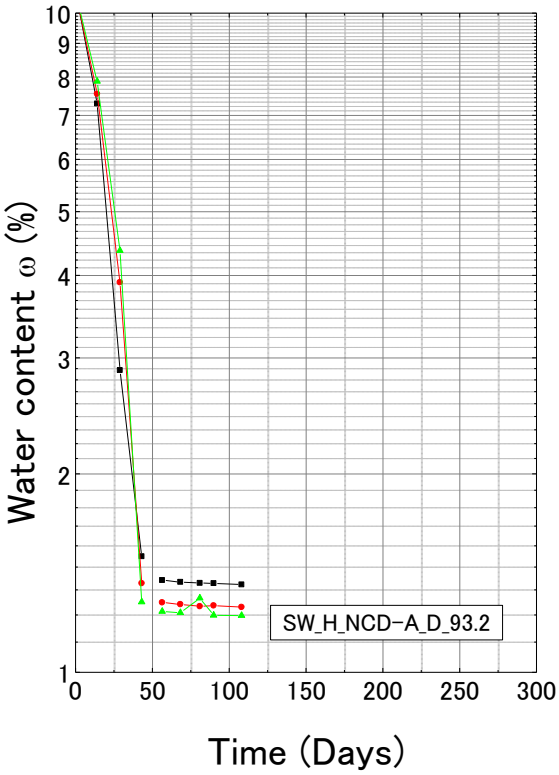

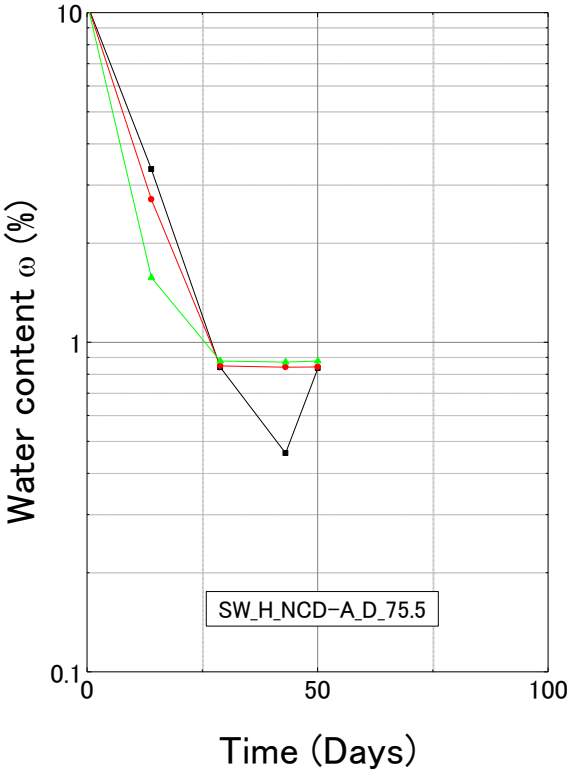
10
1
0.1
0
50
100
Water content ω (%)
Time (Days)
SW_H_NCD-A_D_75.5

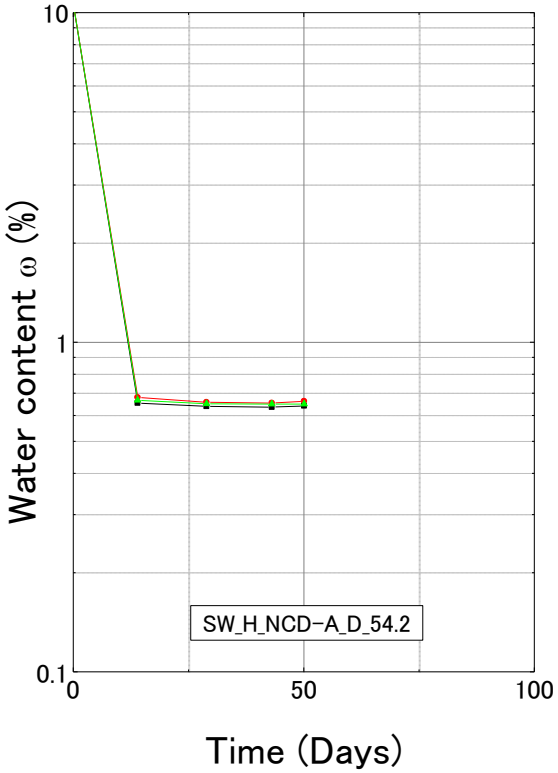
10
1
0.1
0
50
100
Water content ω (%)
Time (Days)
SW_H_NCD-A_D_54.2

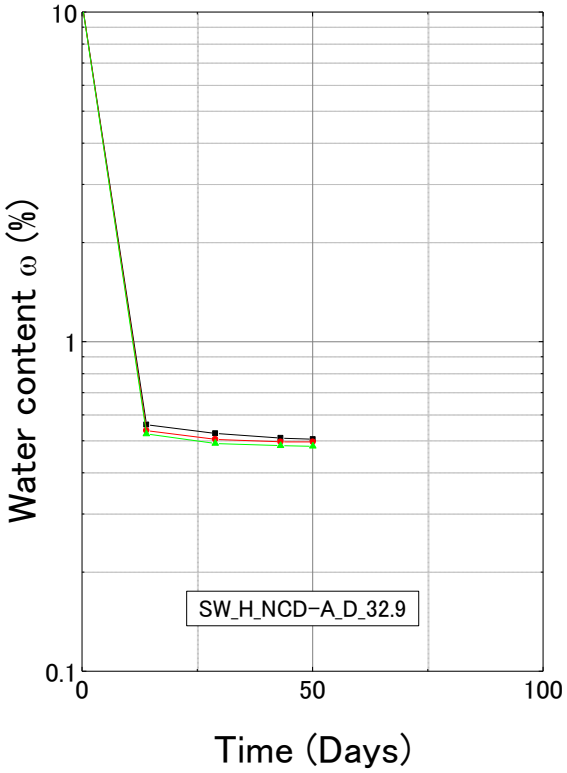
10
1
0.1
0
50
100
Water content ω (%)
Time (Days)
SW_H_NCD-A_D_32.9

D-4 Reference mater for IOF-A—wetting process

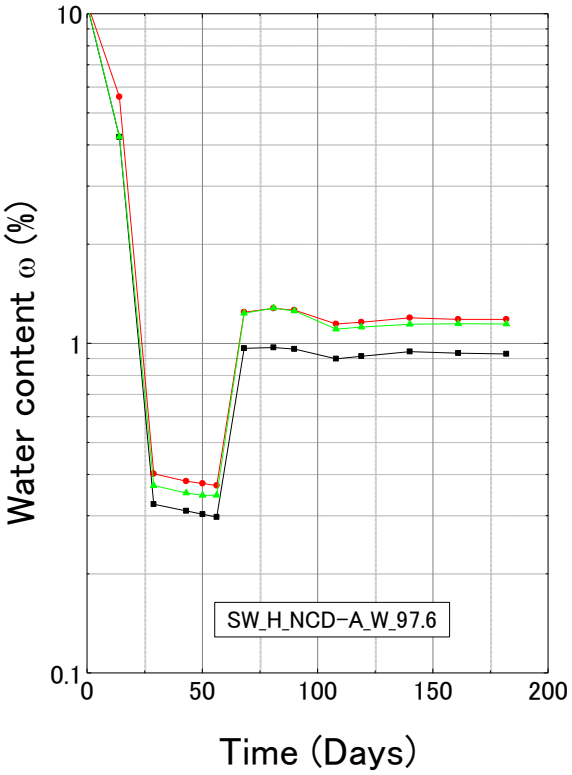

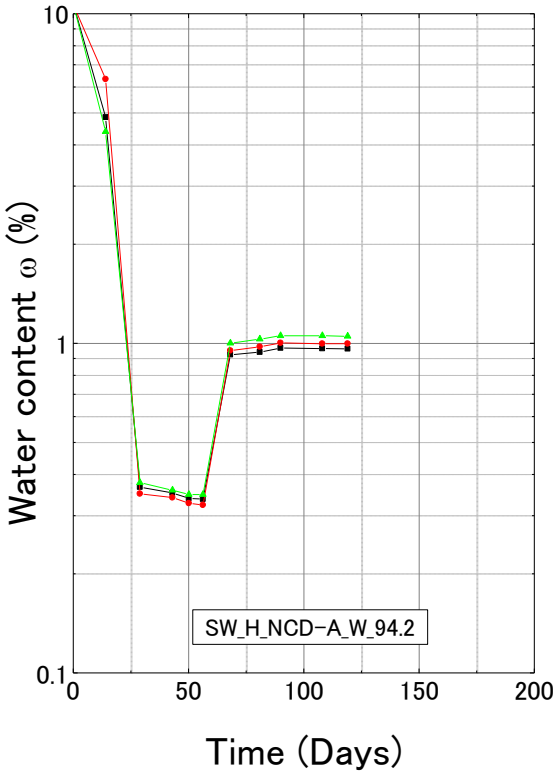

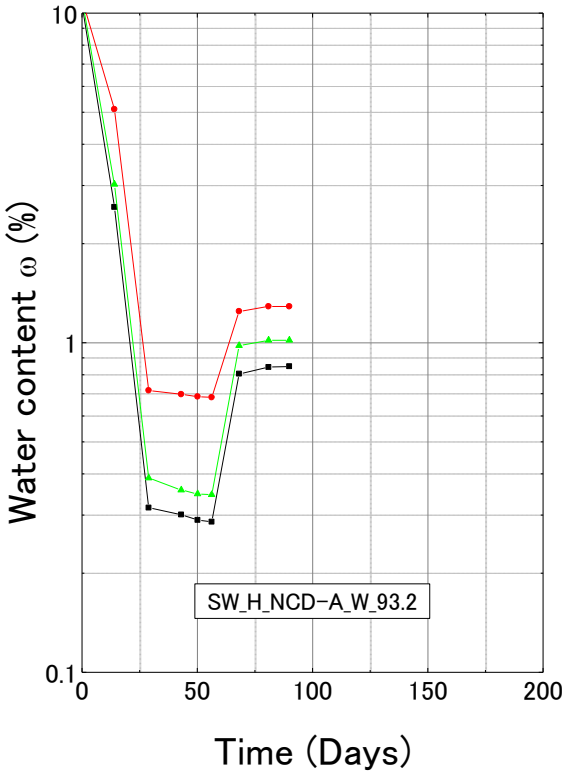

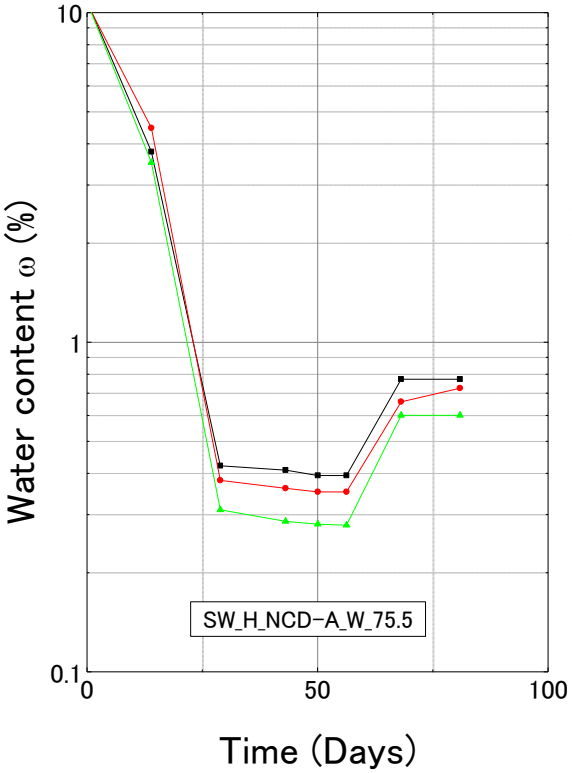
10
1
0.1
0
50
100
Water content ω (%)
Time (Days)
SW_H_NCD-A_W_75.5

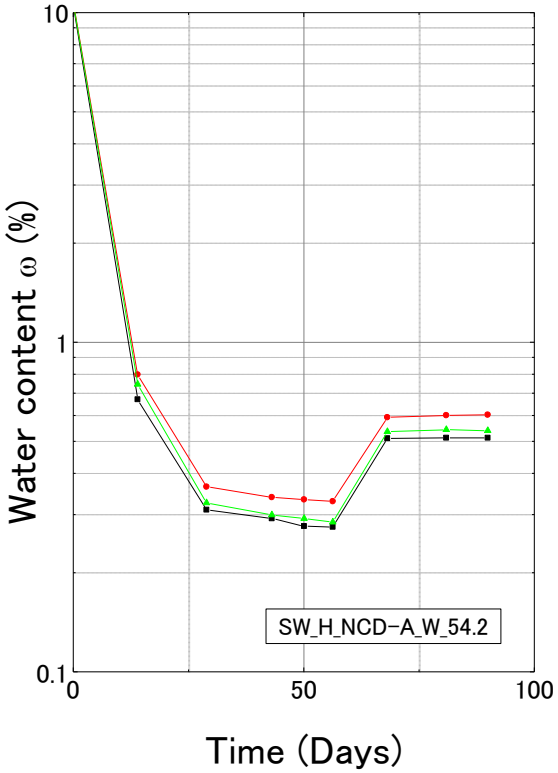
10
1
0.1
0
50
100
Water content ω (%)
Time (Days)
SW_H_NCD-A_W_54.2

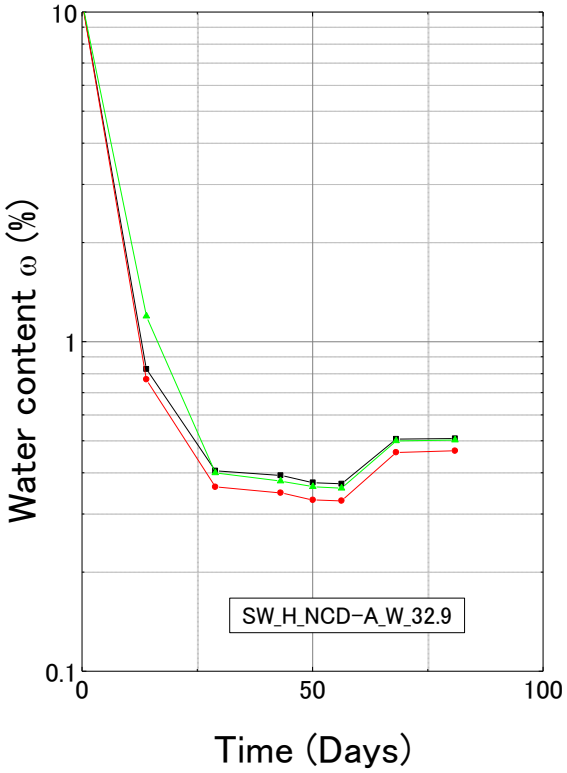
10
1
0.1
0
50
100
Water content ω (%)
Time (Days)
SW_H_NCD-A_W_32.9

D-5 IOF-A passing 4.75mm sieve—drying process

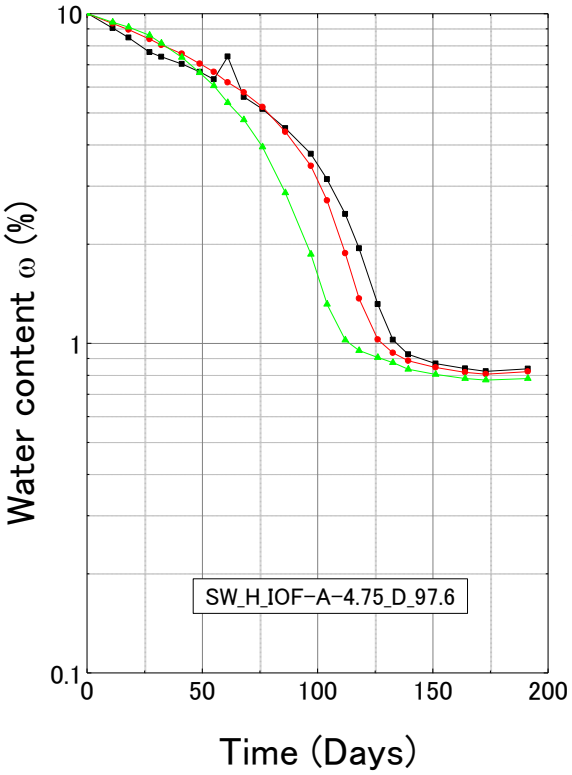

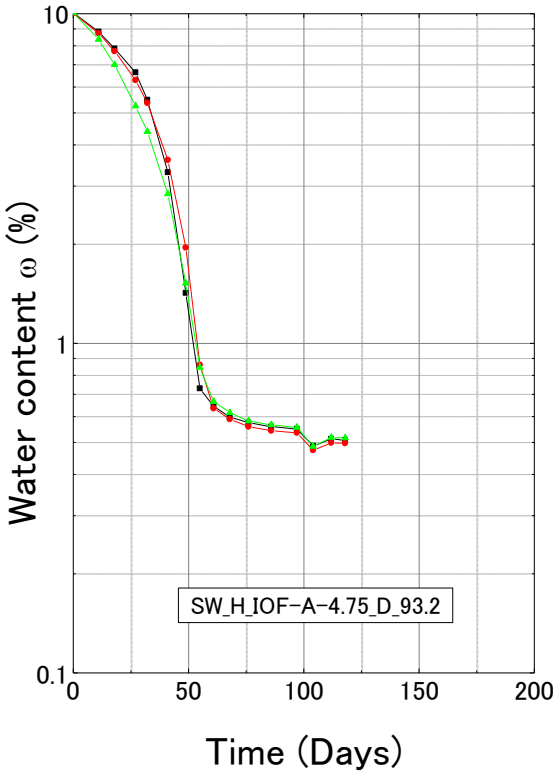

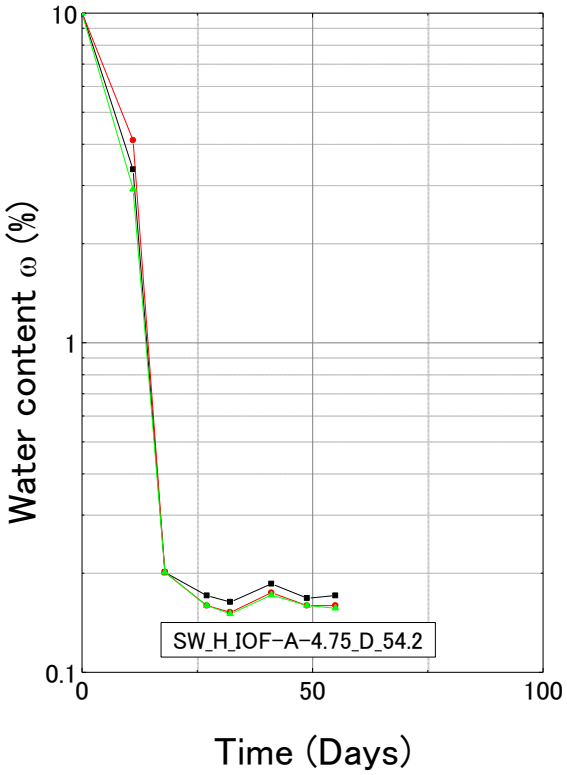

D-6 IOF-A passing 4.75mm sieve—wetting process

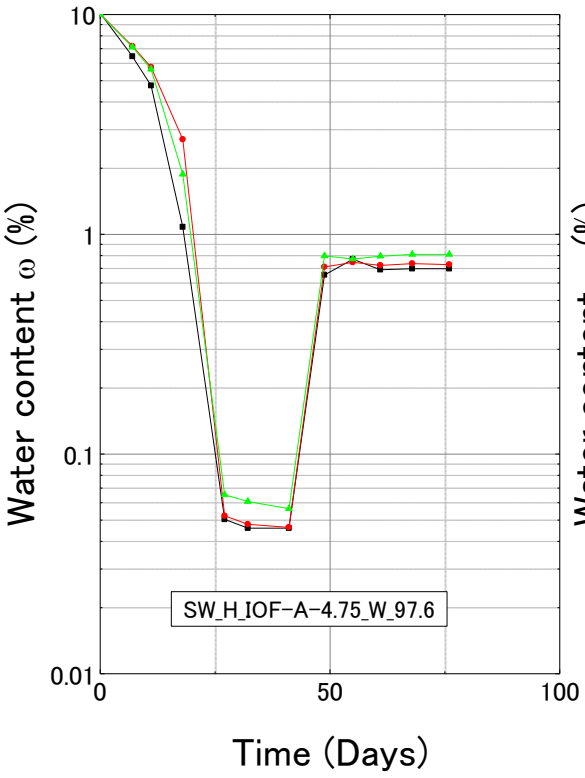

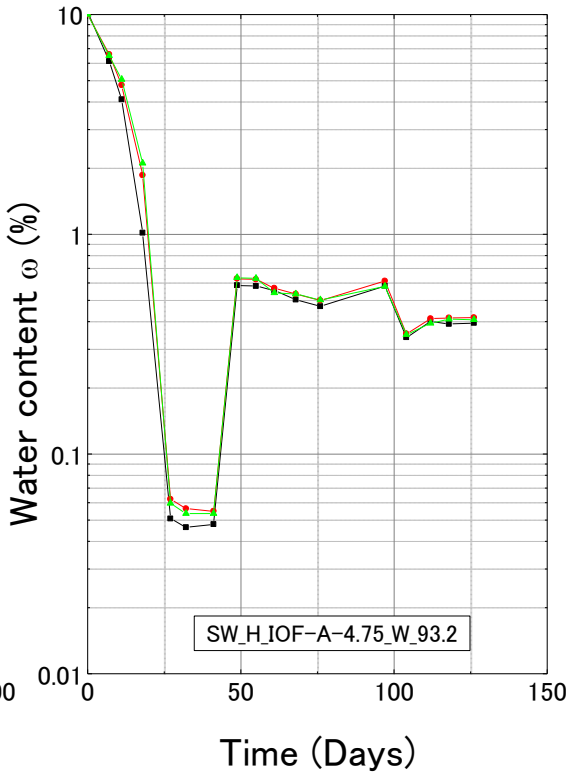

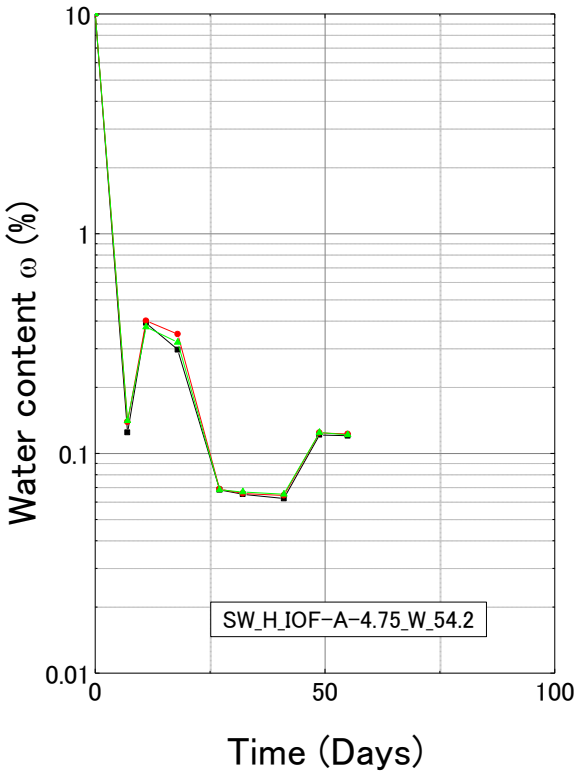

D-7 IOF-A passing 2mm sieve—drying process

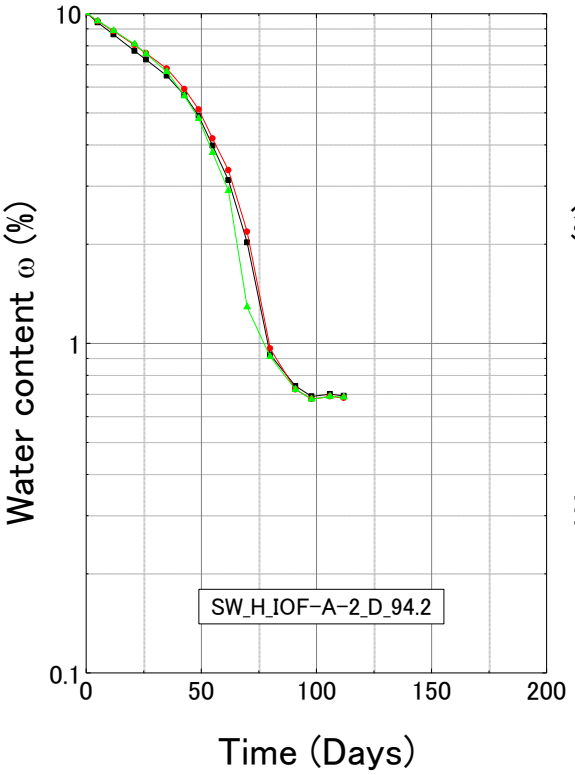

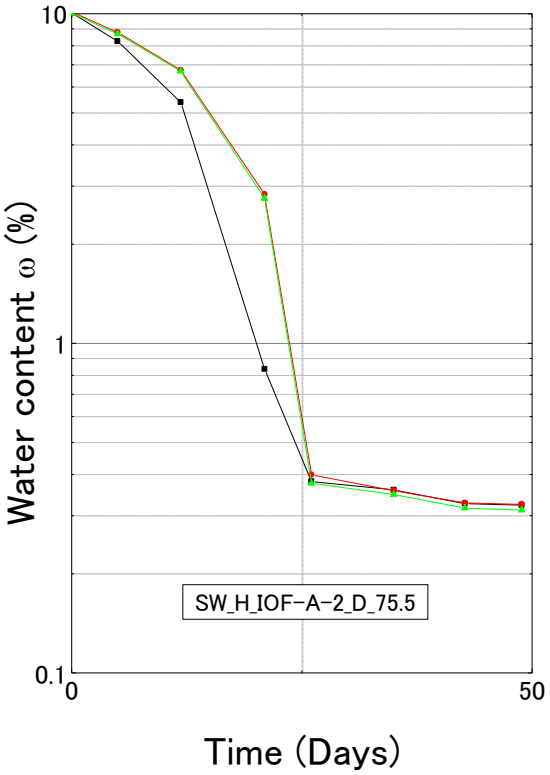

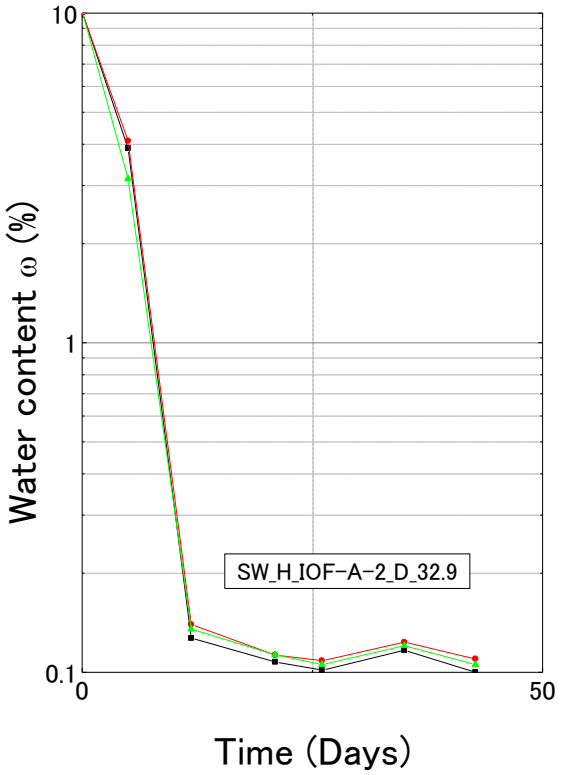

D-8 IOF-A passing 2mm sieve—wetting process

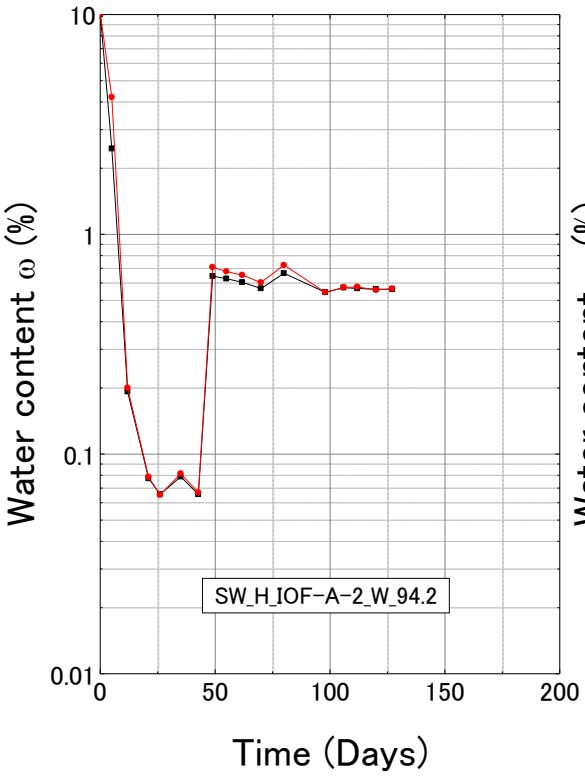

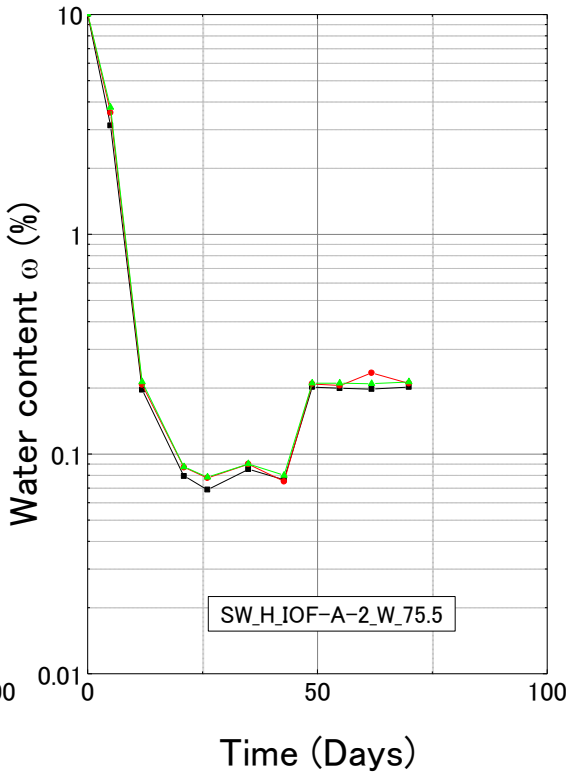

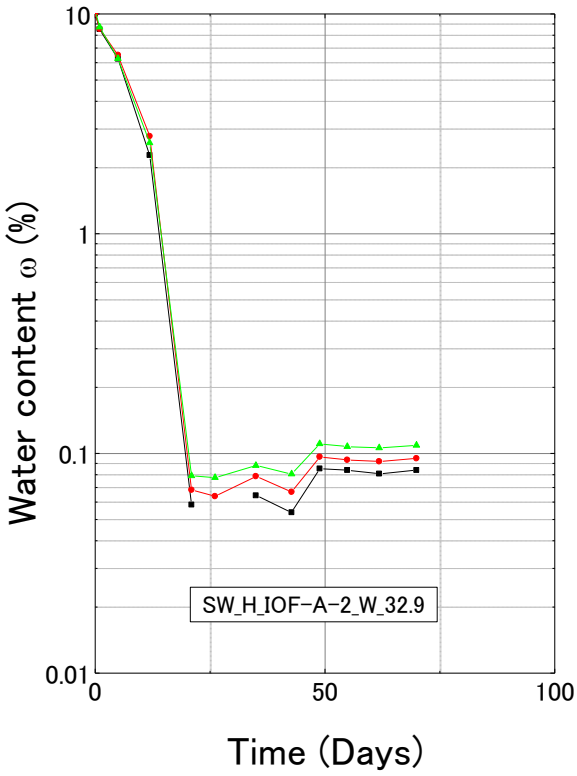

D-9 Iron ore fines type B (IOF-B)—drying process

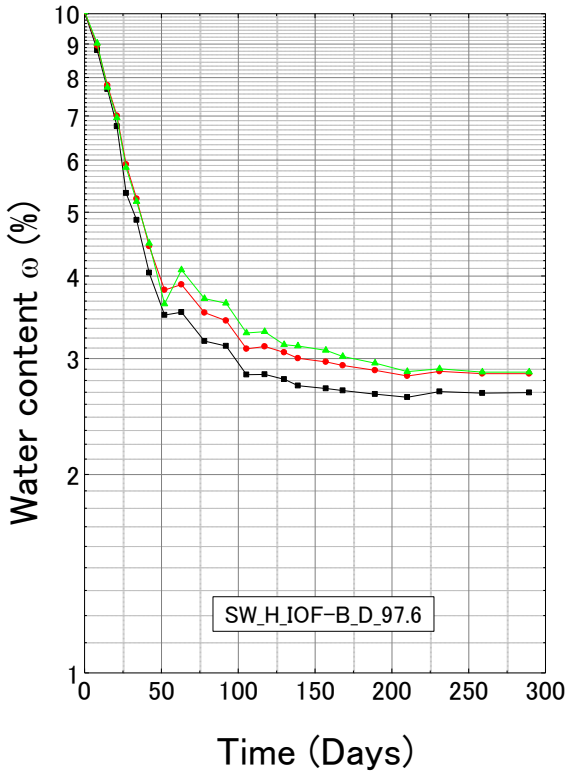

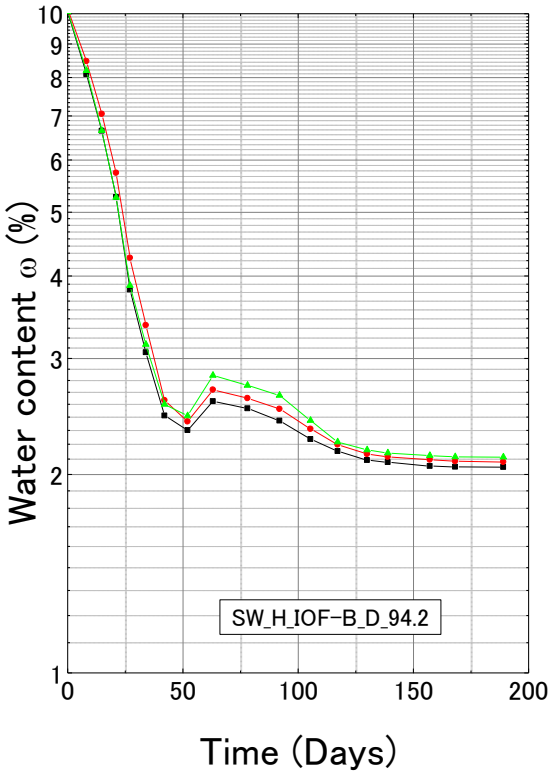

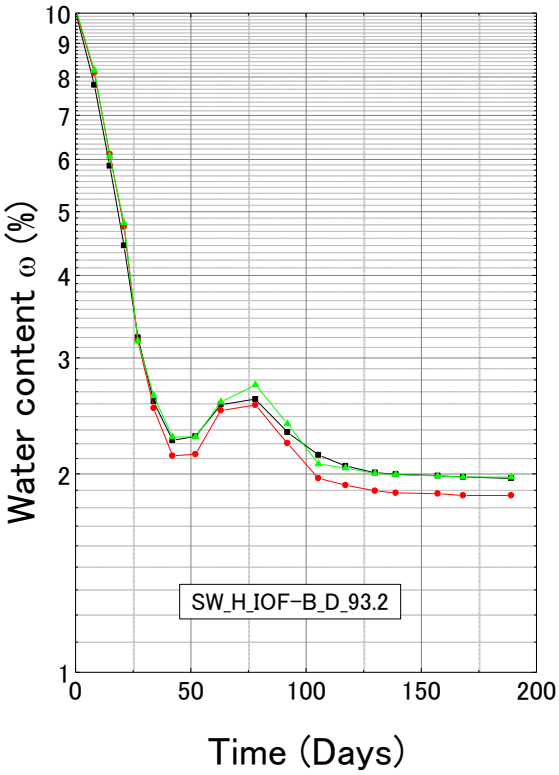

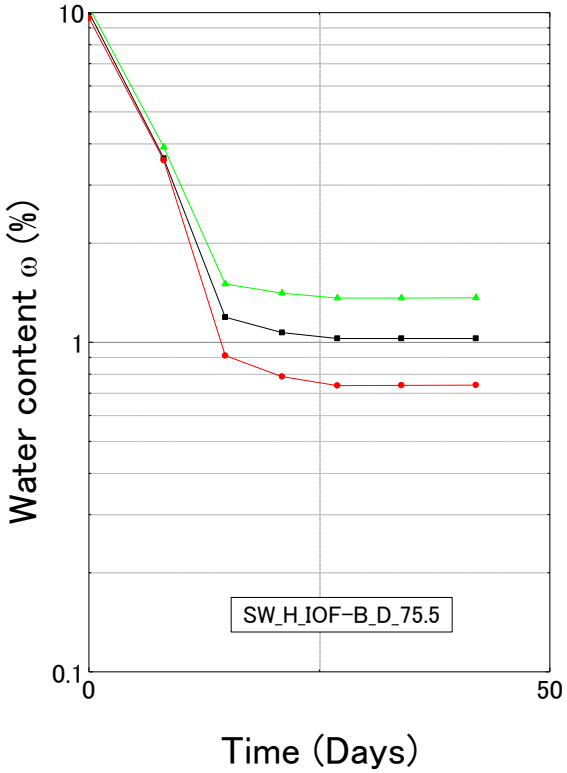
10
1
0.1
0
50
Water content ω (%)
Time (Days)
SW_H_IOF-B_D_75.5

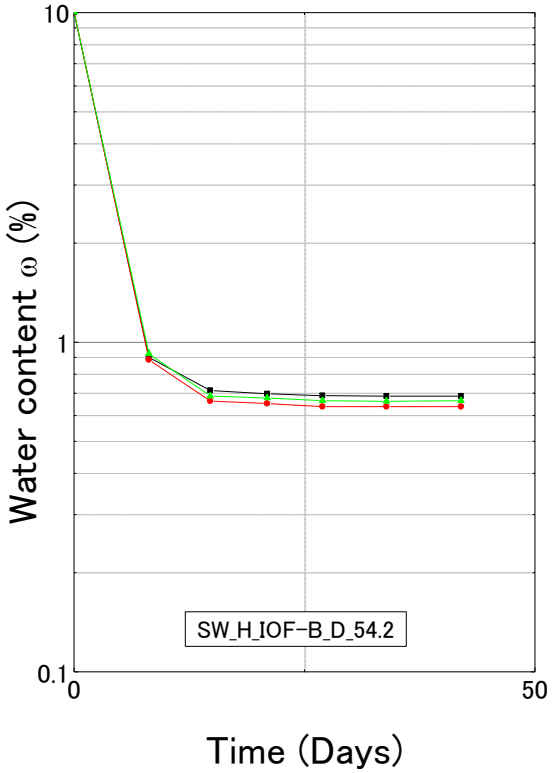
10
1
0.1
0
50
Water content ω (%)
Time (Days)
SW_H_IOF-B_D_54.2

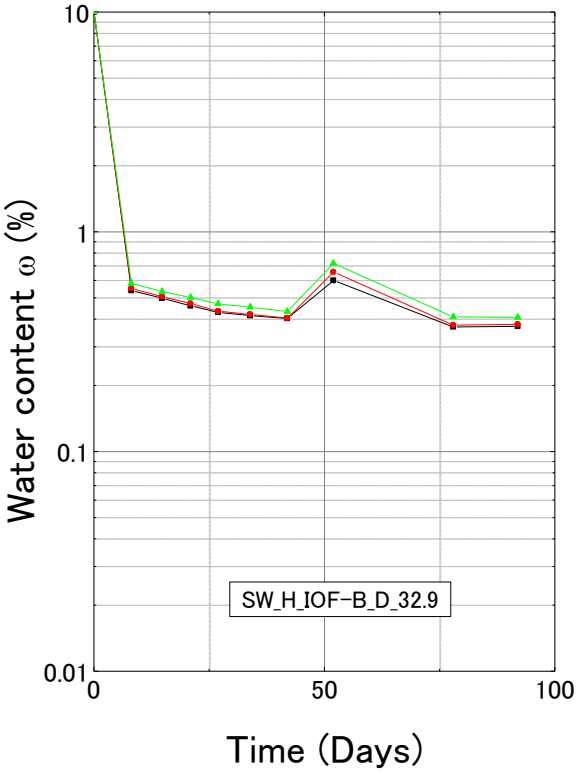
10
1
0.1
0.01
0
50
100
Water content ω (%)
Time (Days)
SW_H_IOF-B_D_32.9

D-10 Iron ore fines type B (IOF-B)—wetting process

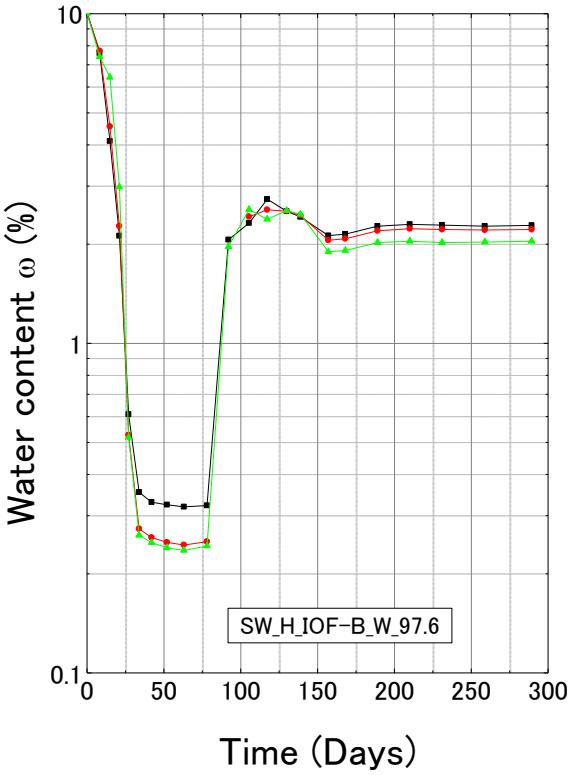

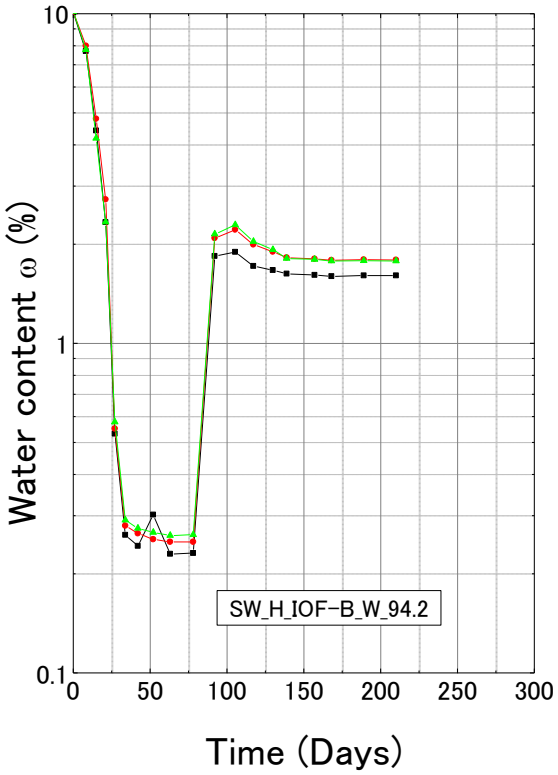

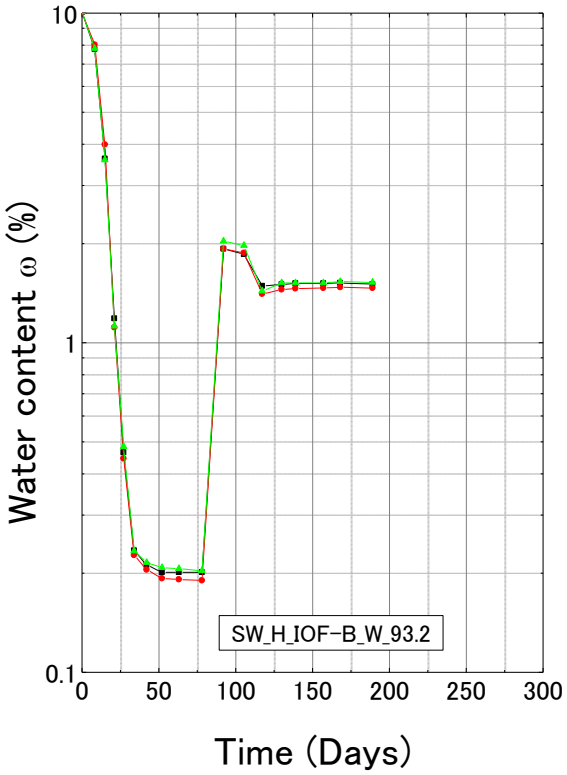

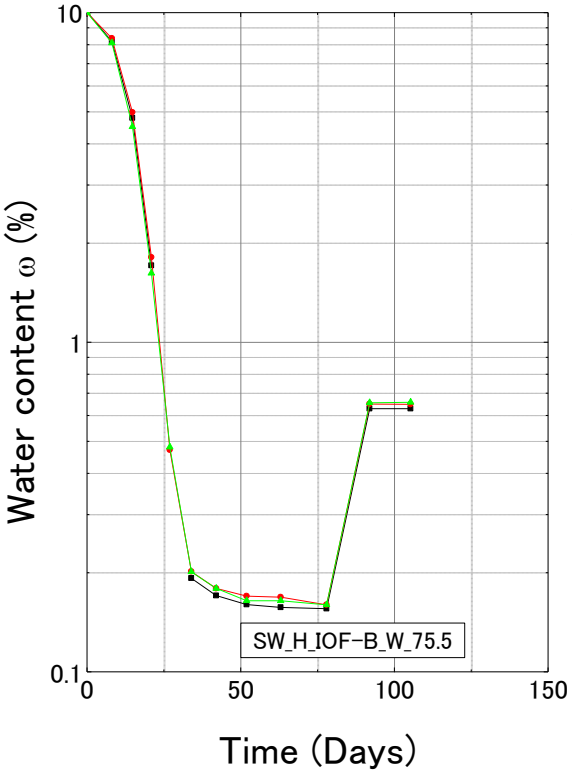
10
1
0.1
0
50
100
150
Water content ω (%)
Time (Days)
SW_H_IOF-B_W_75.5

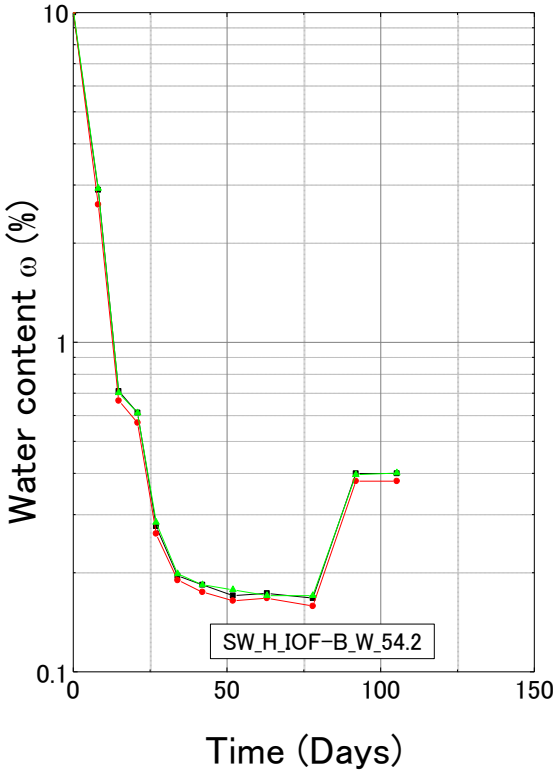
10
1
0.1
0
50
100
150
Water content ω (%)
Time (Days)
SW_H_IOF-B_W_54.2

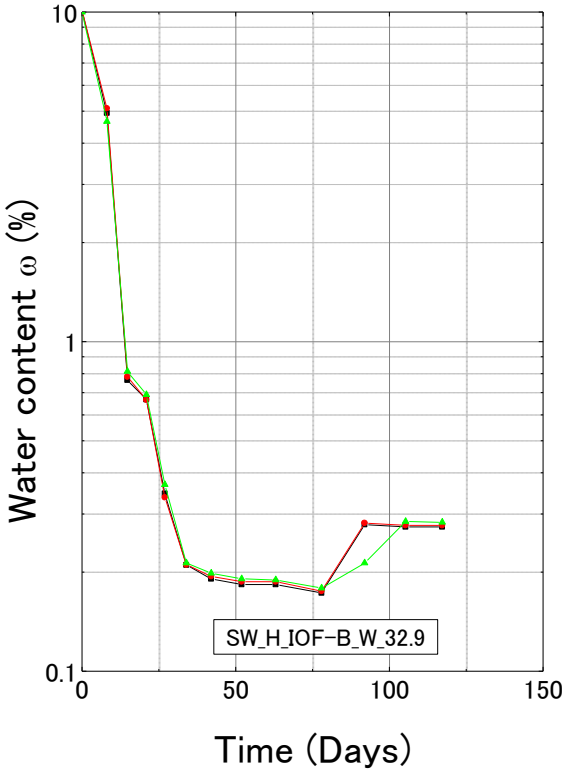
10
1
0.1
0
50
100
150
Water content ω (%)
Time (Days)
SW_H_IOF-B_W_32.9

D-11 Reference materials for IOF-B—drying process

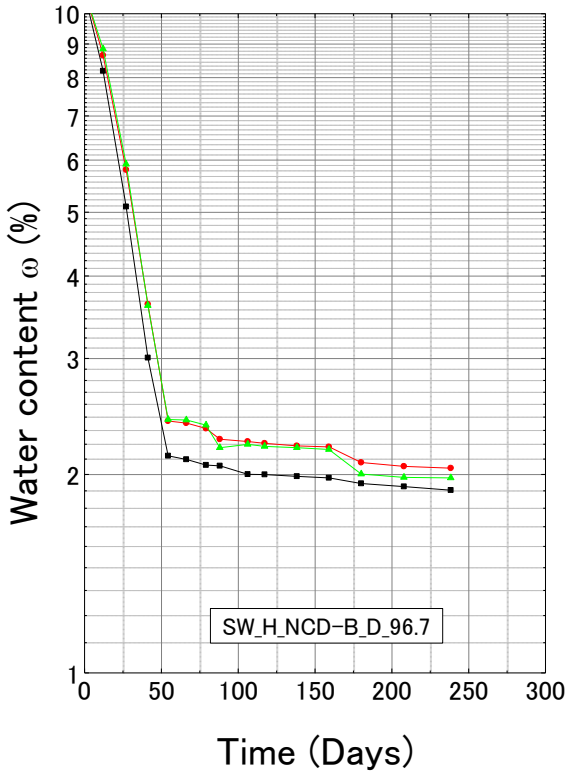

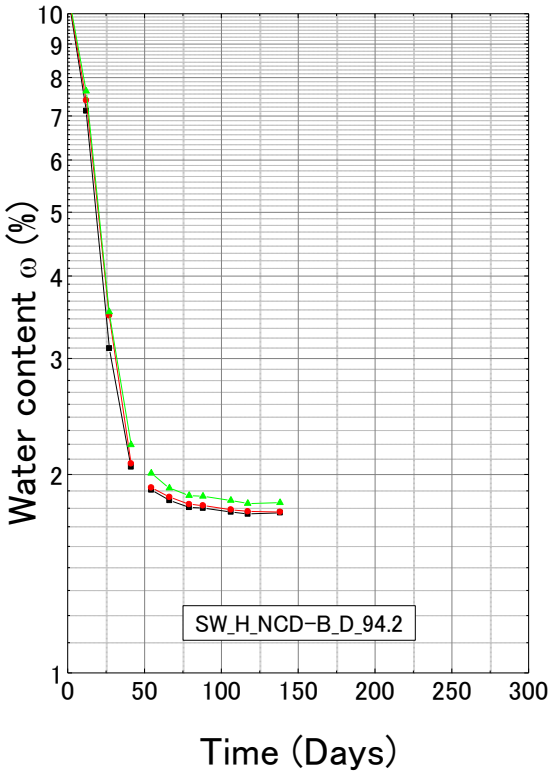

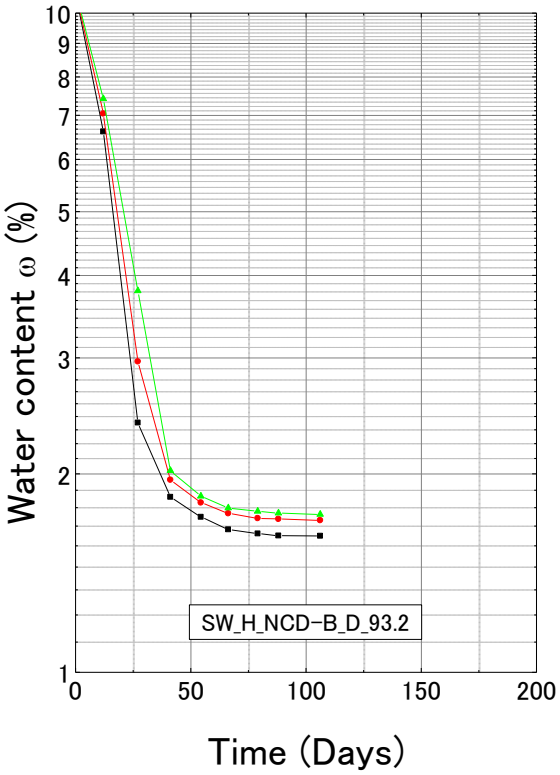

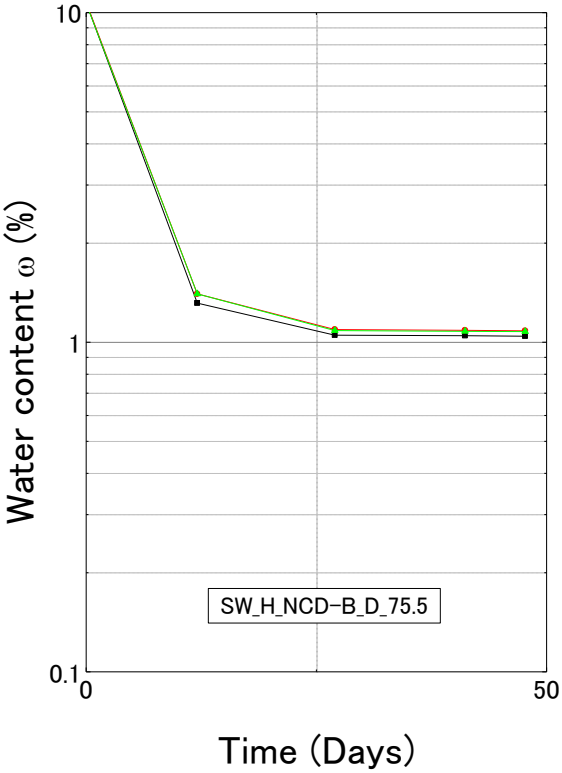
10
1
0.1
0
50
Water content ω (%)
Time (Days)
SW_H_NCD-B_D_75.5

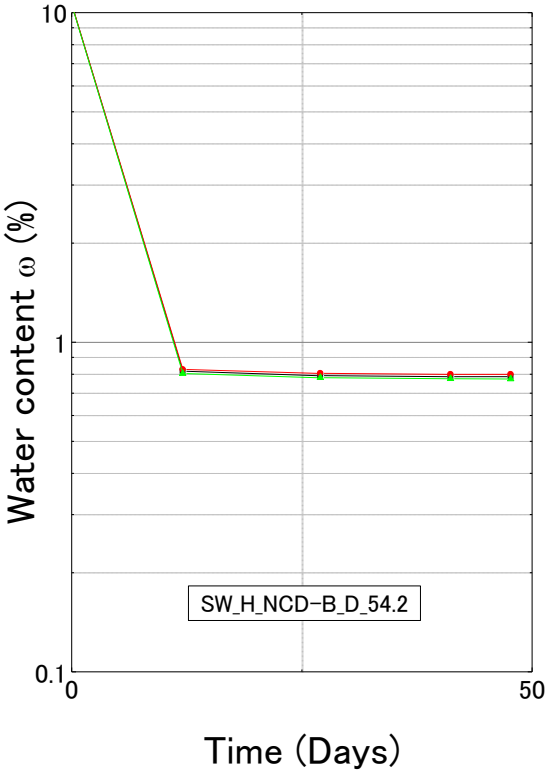
10
1
0.1
0
50
Water content ω (%)
Time (Days)
SW_H_NCD-B_D_54.2

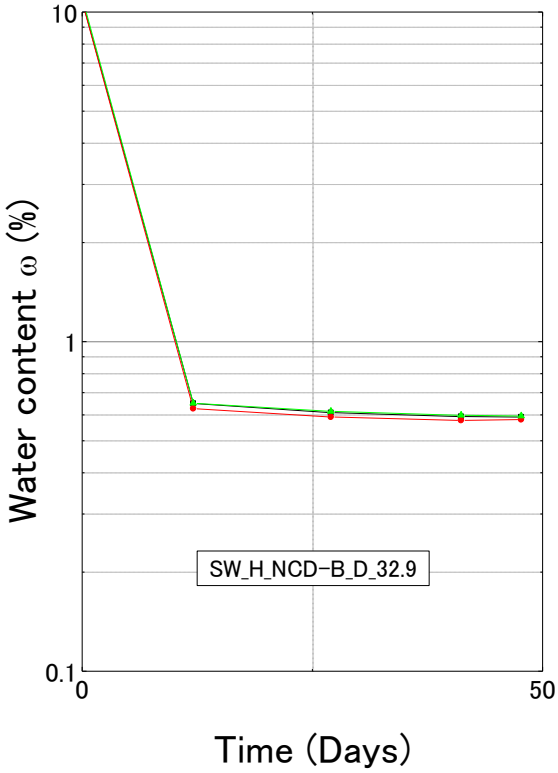
10
1
0.1
0
50
Water content ω (%)
Time (Days)
SW_H_NCD-B_D_32.9

D-12 Reference materials for IOF-B—wetting process

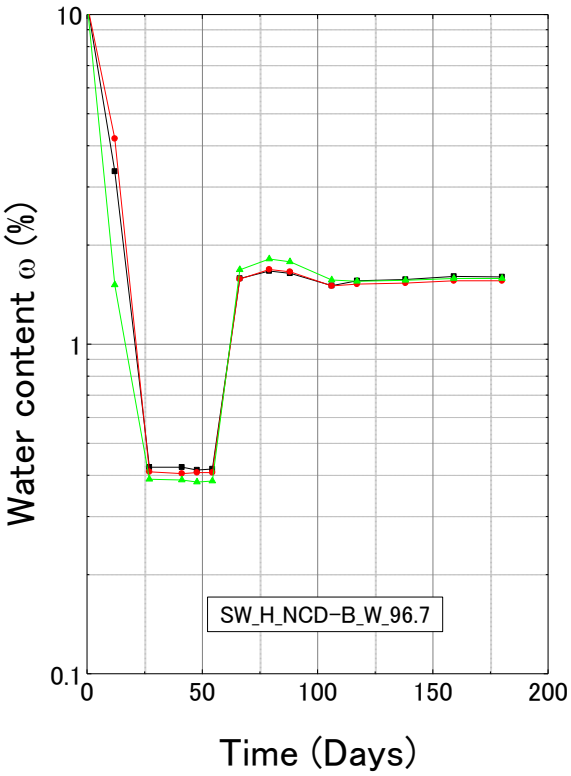

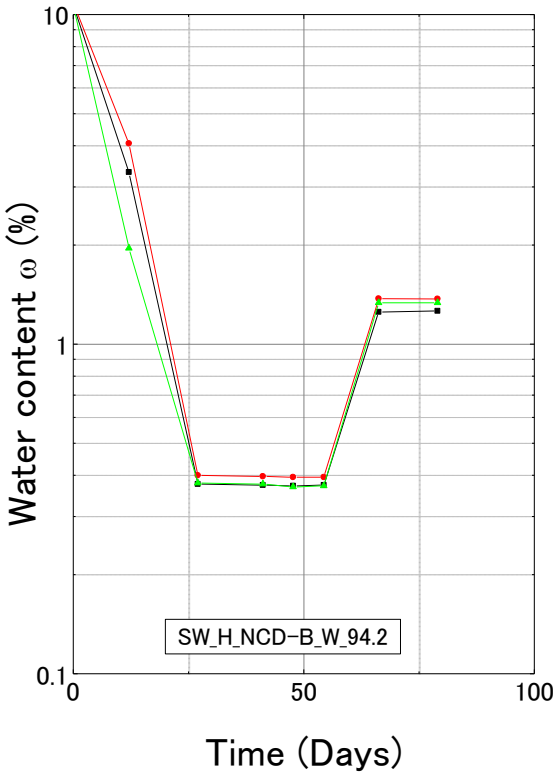

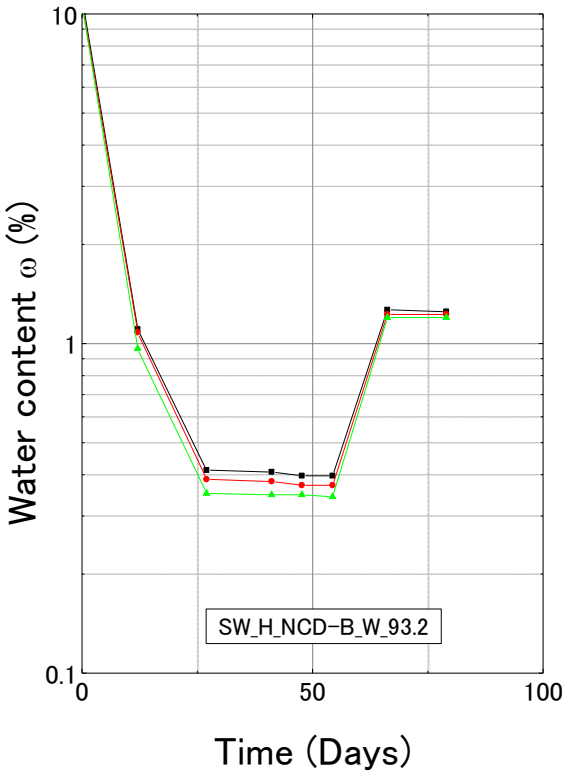

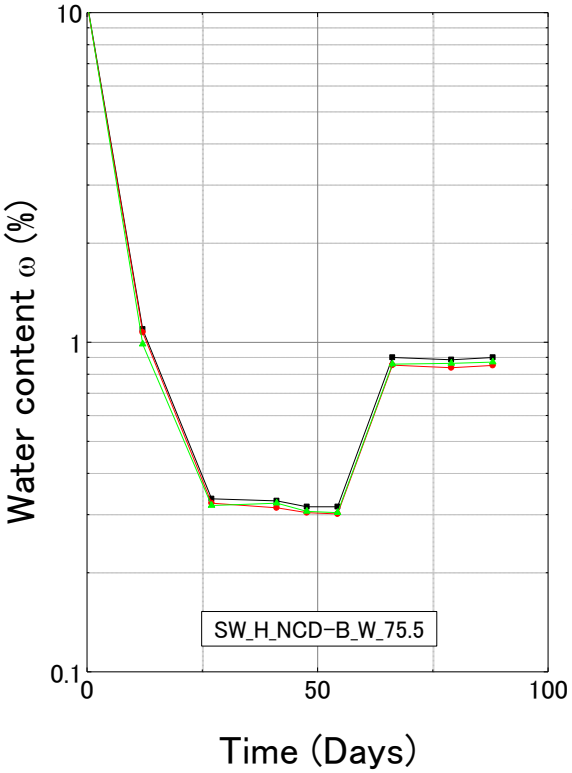
10
1
0.1
0
50
100
Water content ω (%)
Time (Days)
SW_H_NCD-B_W_75.5

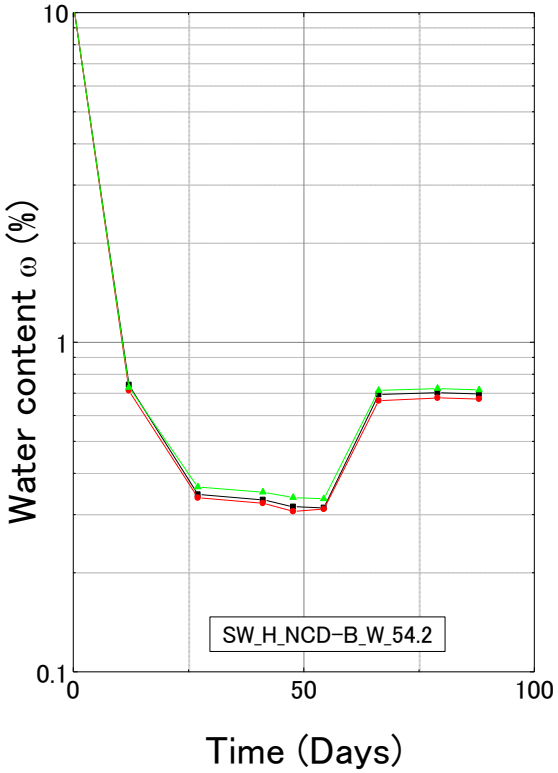
10
1
0.1
0
50
100
Water content ω (%)
Time (Days)
SW_H_NCD-B_W_54.2

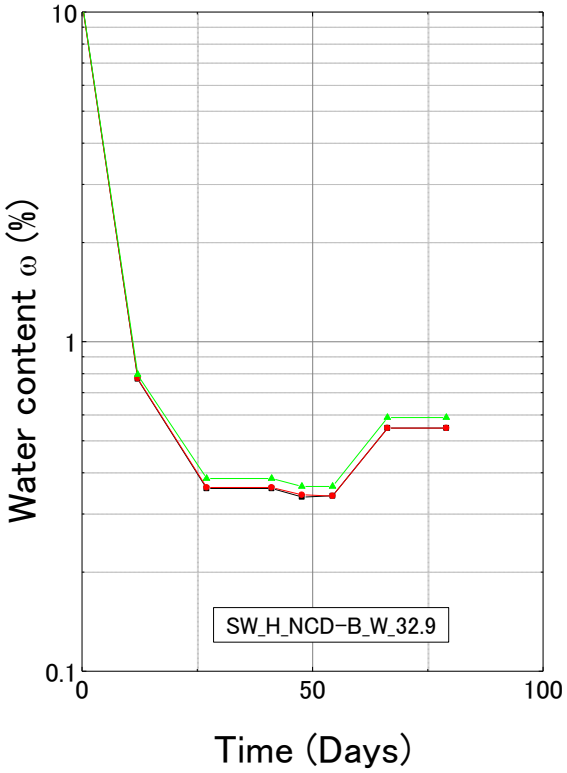
10
1
0.1
0
50
100
Water content ω (%)
Time (Days)
SW_H_NCD-B_W_32.9

Appendix E. Undrained cyclic loading test for Toyoura sand

Results of undrained cyclic loading tests conducted on Toyoura snad, Inagi sand and iron ore fines type B (IOF-B) are summarized in Appendixes E, F and G, respectively. Each test is assigned a unique name, of which "UC_" is used to stand for undrained cyclic loading test. The test materials Toyoura sand, Inagi sand and IOF-B are substituted by "T", "ING" and "IOF-B" in the test name for short. There is an information bar at the bottom of each figure to indicate the name and conditions of the test.

Tables E-1 and E-2 summarize the test conditions of all tests conducted on saturated and unsaturated Toyoura sand, respectively. Symbols in Table E-1 and E-2 are stand for:

e, ρ_d and Dr: void ration, dry density and relative density after consolidation;

CSR: cyclic stress ratio ($=\sigma_d/2\sigma_0'$, σ_d is single amplitude of cyclic loading);

$N_{DA=5\%}$: number of cycle which causes 5% double amplitude of axial strain;

σ_0': confining pressure before applying cyclic loading;

Sr: degree of saturation after consolidation;

$\varepsilon^*_{vol,air}$: maximum volumetric strain caused by pore air compression;

B: pore water pressure B;

Set: number of set classified in Table 5-3

Table E-1 Summary of test condition of saturated Toyoura sand

Test name	e	ρ_d (g/cm^3)	Dr (%)	CSR	$N_{DA=5\%}$	σ_0' (kPa)	Set
UC_T_Apr17	0.762	1.51	63.9	0.241	2.6	60.3	1
UC_T_Apr18	0.762	1.51	63.8	0.190	2.3	60.3	
UC_T_Apr19-1	0.753	1.52	66.5	0.147	32.1	60.9	
UC_T_Apr19-2	0.785	1.49	57.5	0.173	1.6	61.2	
UC_T_Apr26	0.773	1.50	60.7	0.163	8.6	59.5	
UC_T_Apr28	0.760	1.51	64.4	0.152	65.3	59.9	
UC_T_Oct13	1.008	1.32	-4.4	0.097	6.1	61.7	2
UC_T_Oct18	1.041	1.30	-13.7	0.090	11.1	60.8	
UC_T_Oct19	1.010	1.32	-5.0	0.065	53.7	60.5	
UC_T_Oct21	1.009	1.32	-4.6	0.078	19.1	60.9	

Table E-2 Summary of test condition of unsaturated Toyoura sand

test name	e	ρ_d (g/cm^3)	Dr (%)	σ_0' (kPa)	CSR	$N_{DA=5\%}$	Sr (%)	$\varepsilon^*_{vol,air}$ (%)	B	Set
UC_T_May8	0.751	1.52	66.8	61.7	0.353	15.8	91.6	1.35		1
UC_T_May10-1	0.746	1.52	68.4	61.3	0.352	18.9	91.7	1.32		
UC_T_May10-2	0.757	1.51	65.3	60.5	0.402	4.8	90.4	1.53		
UC_T_May10-3	0.753	1.52	66.5	61.8	0.327	18.3	91.1	1.41		
UC_T_May13-1	0.739	1.53	70.2	61.3	0.331	214.7	92.3	1.22		
UC_T_May13-2	0.749	1.52	67.5	61.5	0.345	138.9	91.2	1.39		
UC_T_Oct30	1.002	1.33	-2.8	61.3	0.185	92.9	79.0	3.92	0.07	2
UC_T_Oct31	1.006	1.32	-4.0	61.5	0.209	47.3	80.2	3.70	0.12	
UC_T_Nov1	1.026	1.31	-9.4	61.1	0.258	3.7	77.5	4.24	0.12	
UC_T_Nov4	1.004	1.33	-3.4	61.2	0.241	6.4	78.3	4.05	0.14	
UC_T_Nov3	1.008	1.32	-4.4	61.1	0.234	108.8	68.4	5.89	0.10	

E-1 Saturated Toyoura sand in Set 1

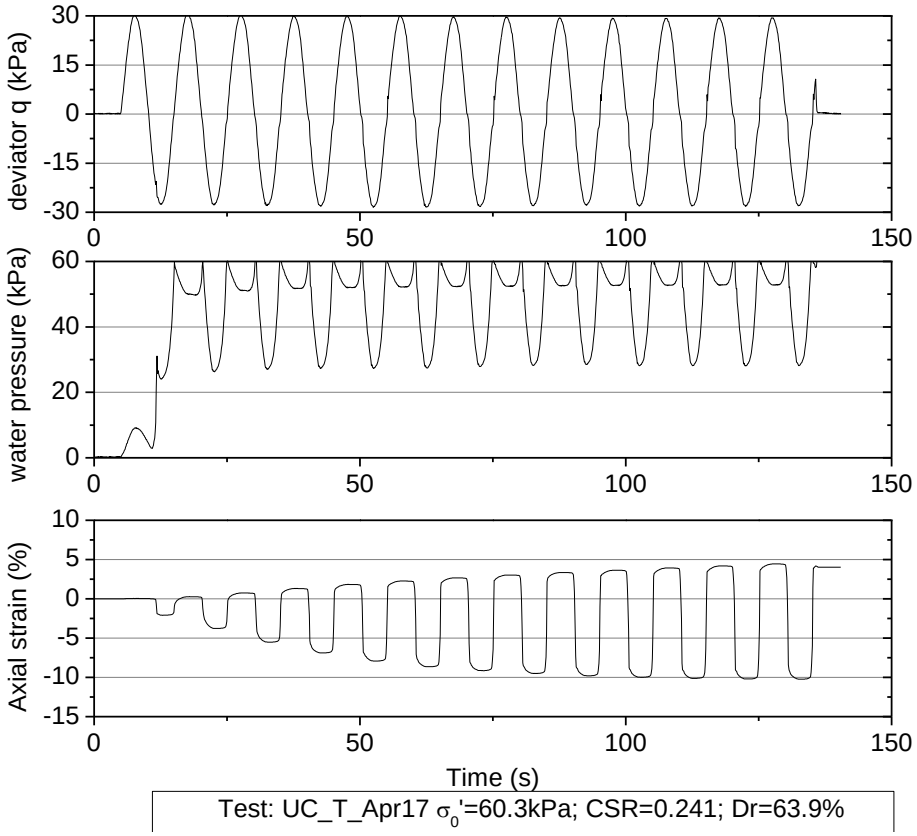

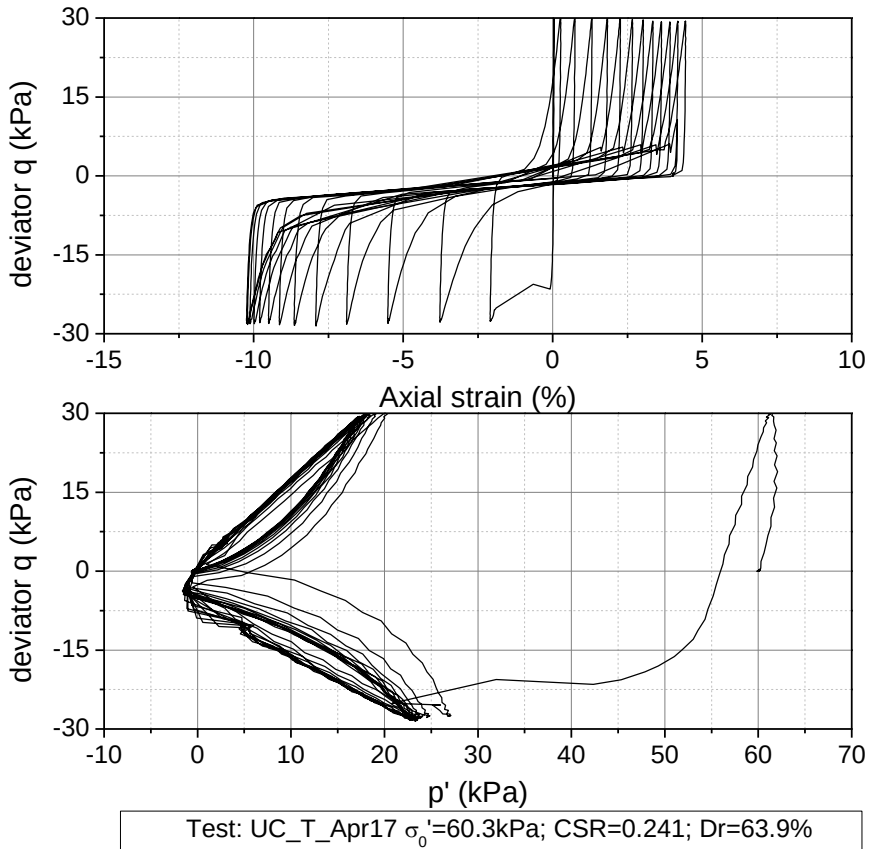

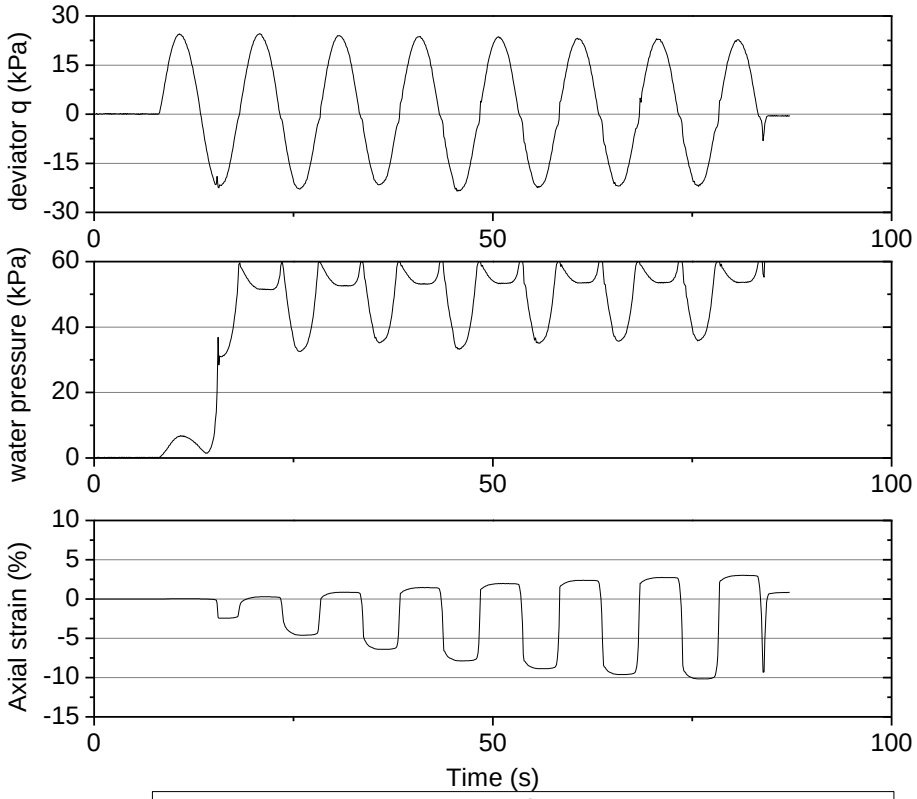

Test: UC_T_Apr18 σ_0'=60.3kPa; CSR=0.190; Dr=63.8%

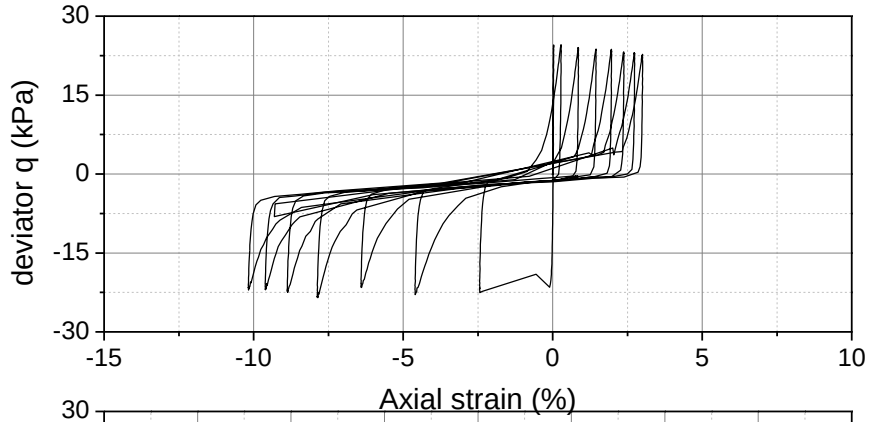

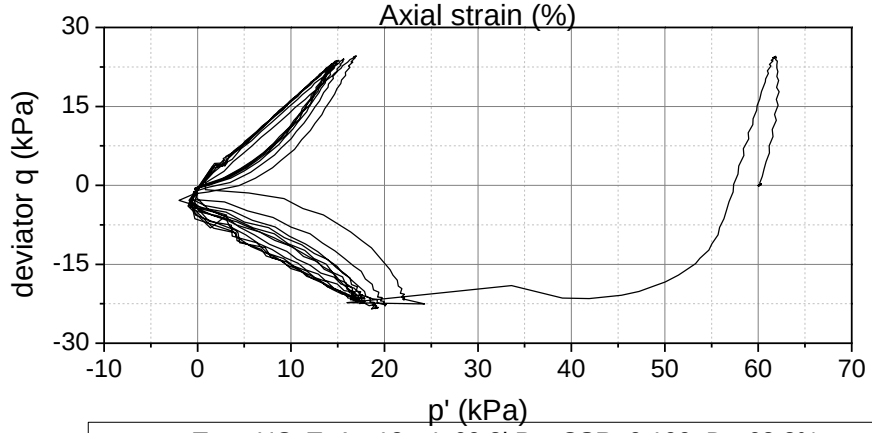

Test: UC_T_Apr18 σ_0'=60.3kPa; CSR=0.190; Dr=63.8%

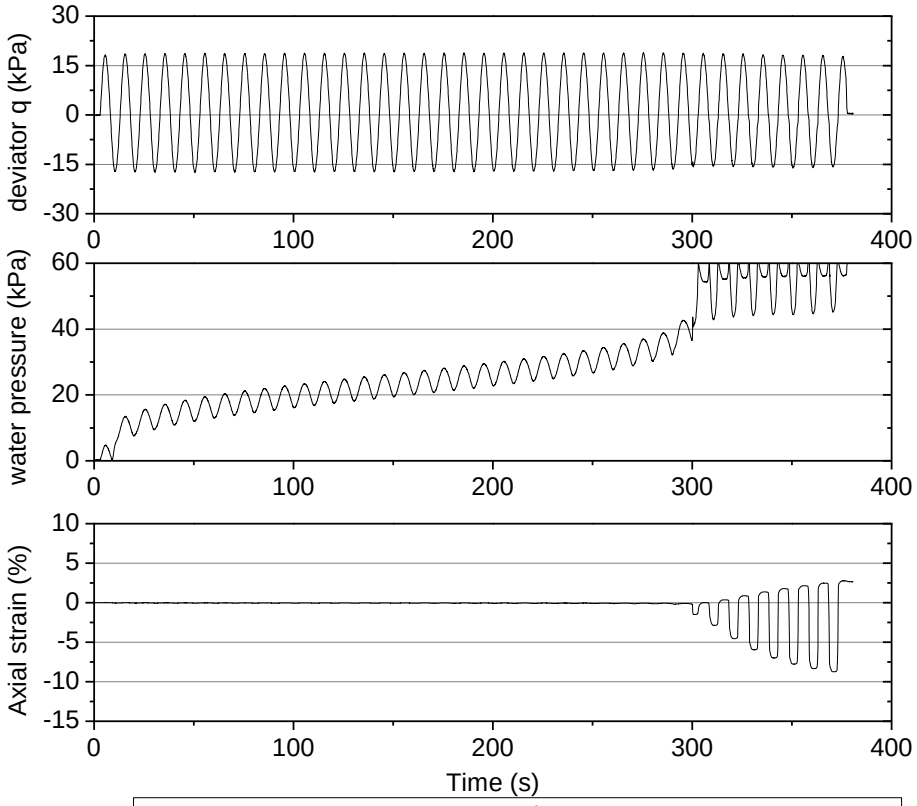

Test: UC_T_Apr19-1 σ_0'=60.9kPa; CSR=0.147; Dr=66.5%

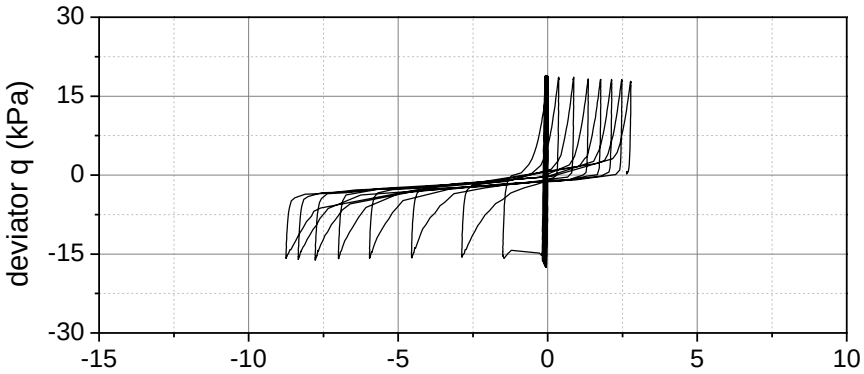

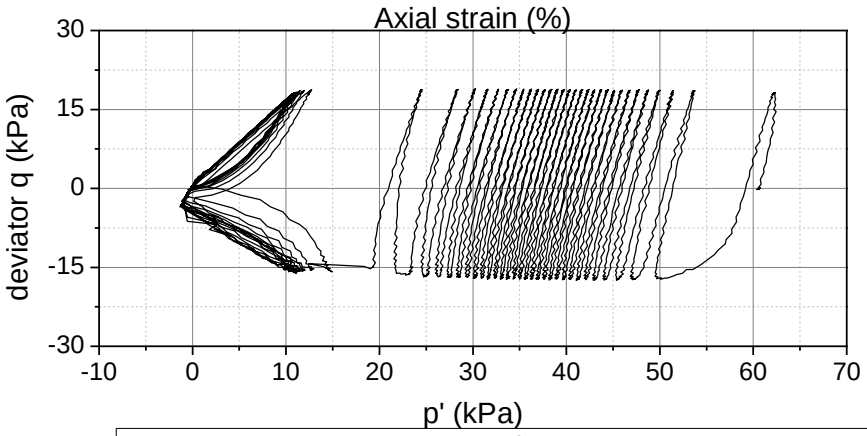

Test: UC_T_Apr19-1 σ_0'=60.9kPa; CSR=0.147; Dr=66.5%

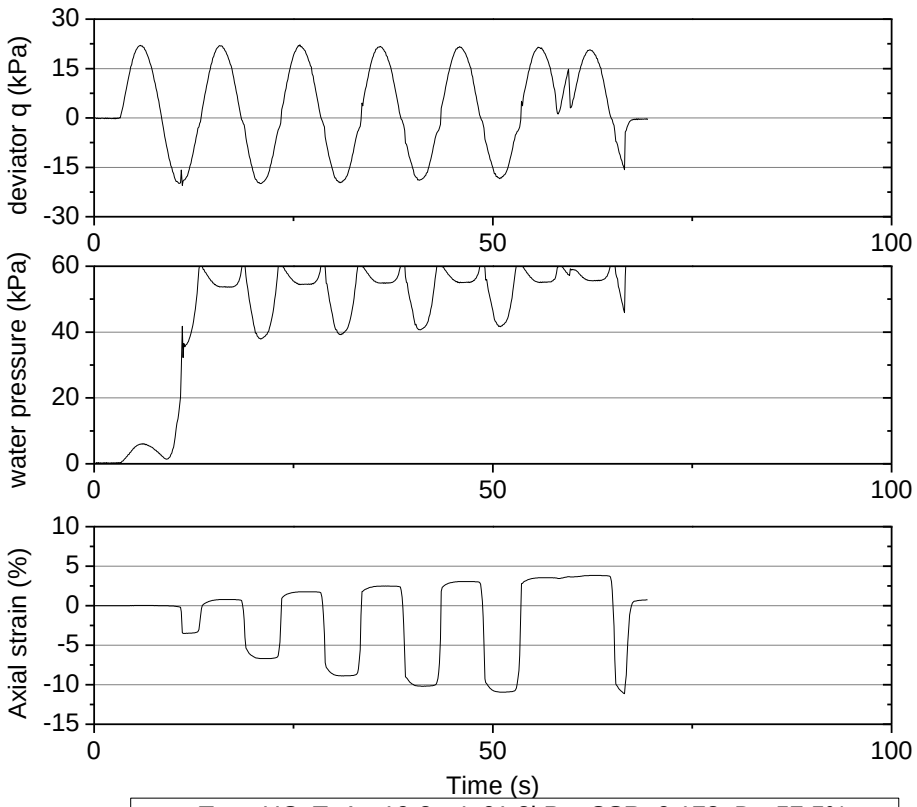

Test: UC_T_Apr19-2 σ_0'=61.2kPa; CSR=0.173; Dr=57.5%

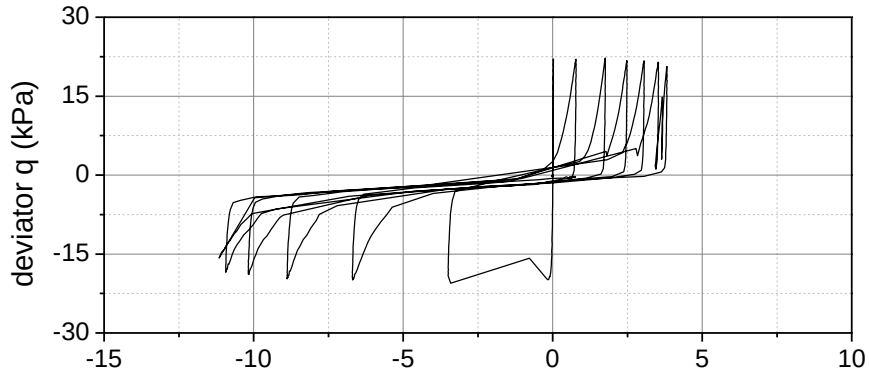

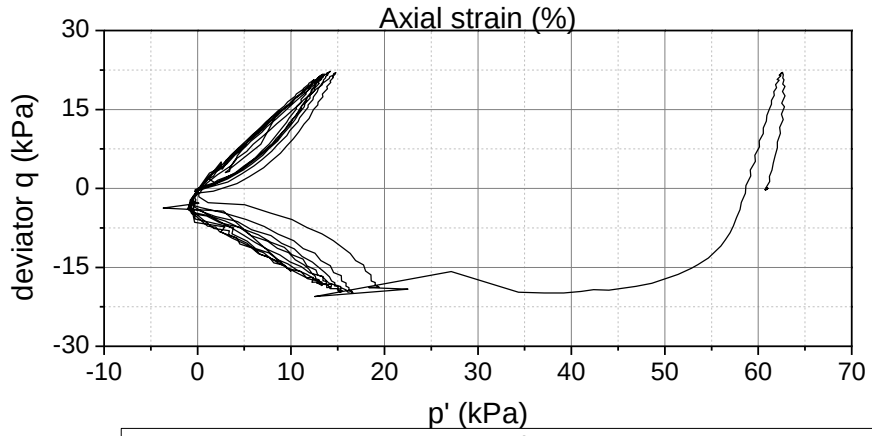

Test: UC_T_Apr19-2 σ_0'=61.2kPa; CSR=0.173; Dr=57.5%

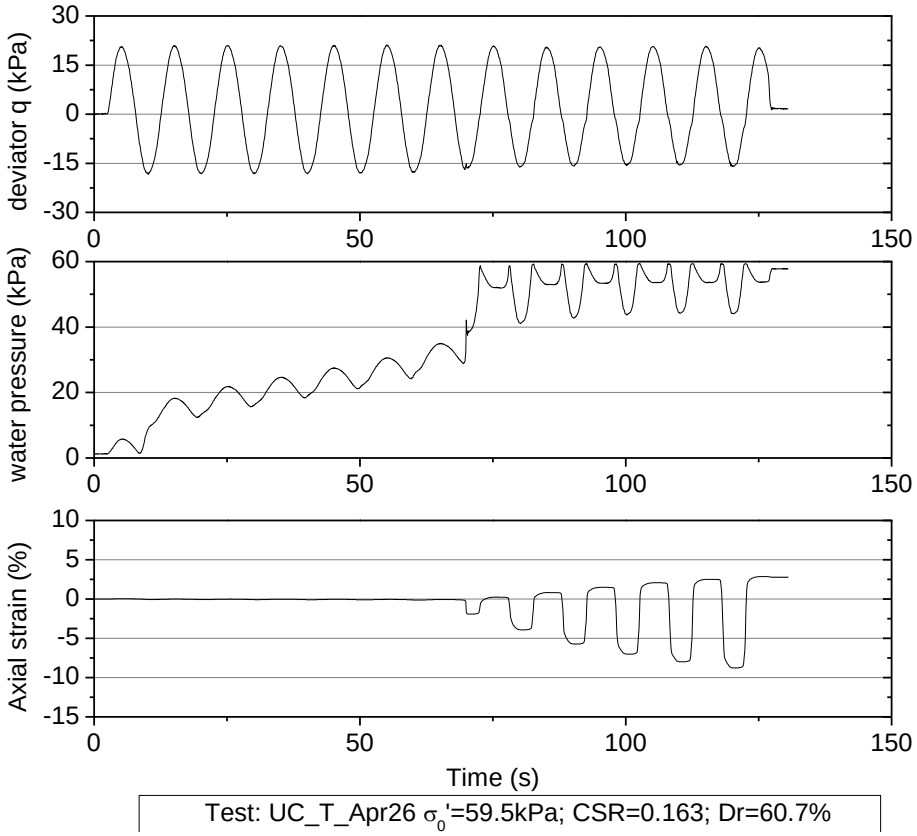
deviator q (kPa)
water pressure (kPa)
Axial strain (%)
Time (s)
Test: UC_T_Apr26 σ0'=59.5kPa; CSR=0.163; Dr=60.7%

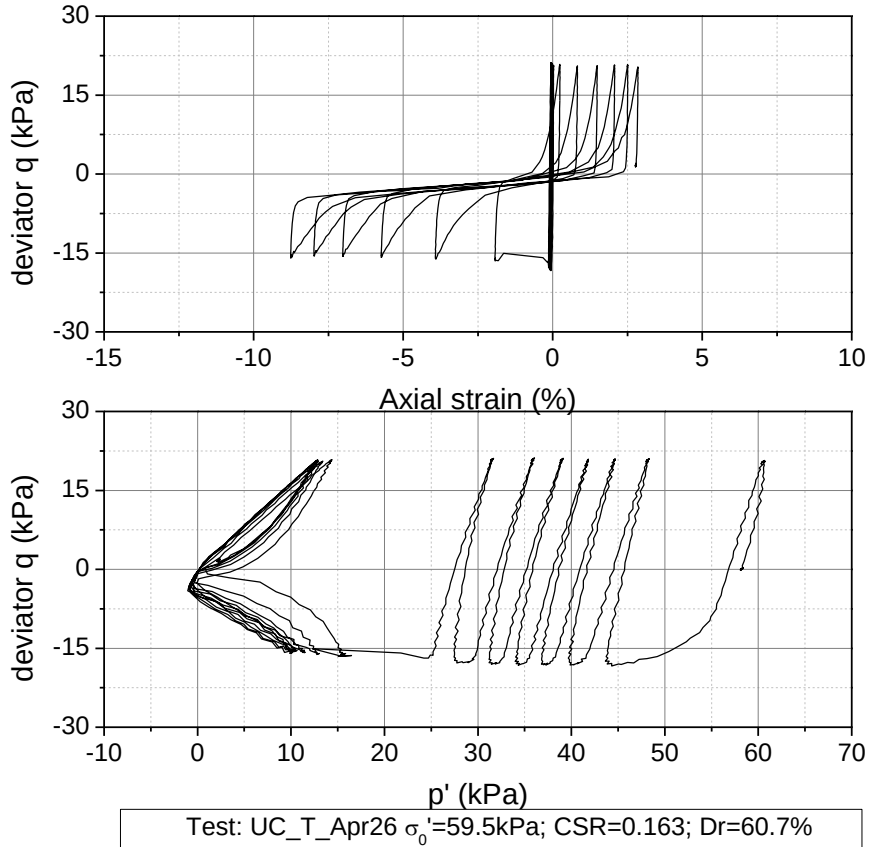
deviator q (kPa)
Axial strain (%)
deviator q (kPa)
p' (kPa)
Test: UC_T_Apr26 σ0'=59.5kPa; CSR=0.163; Dr=60.7%

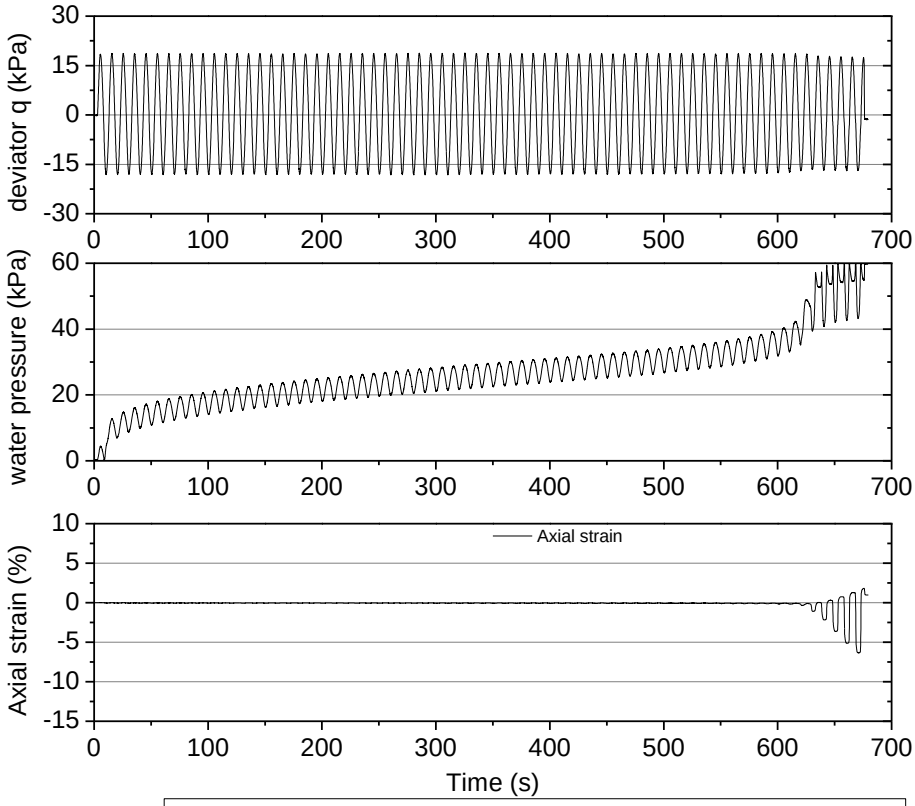

Test: UC_T_Apr28 σ_0'=59.9kPa; CSR=0.152; Dr=64.4%

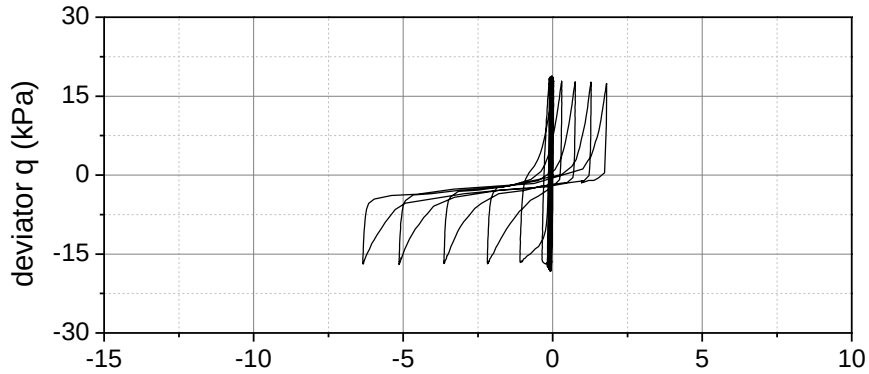

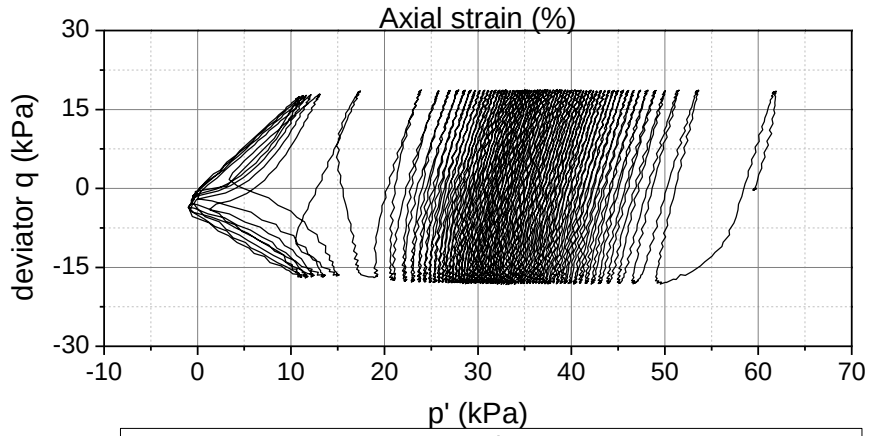

Test: UC_T_Apr28 σ_0'=59.9kPa; CSR=0.152; Dr=64.4%

E-2 Saturated Toyoura sand in Set 2

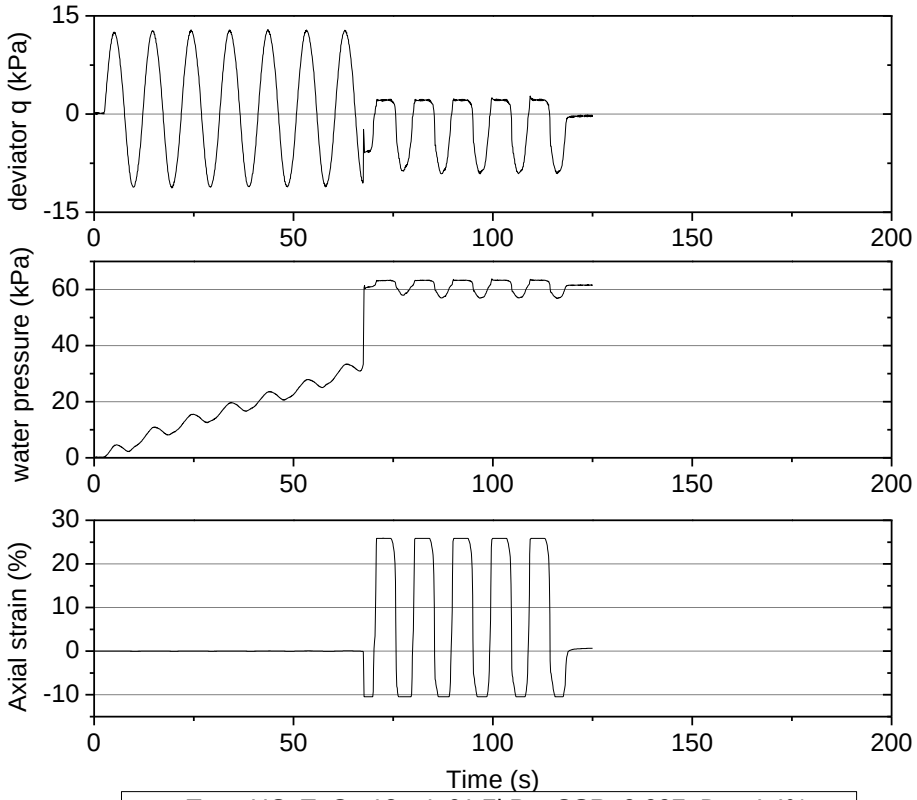

Test: UC_T_Oct13 σ_0'=61.7kPa; CSR=0.097; Dr=-4.4%

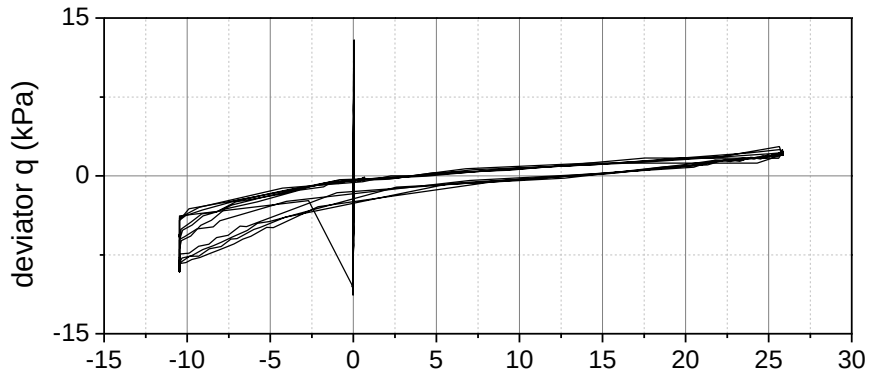

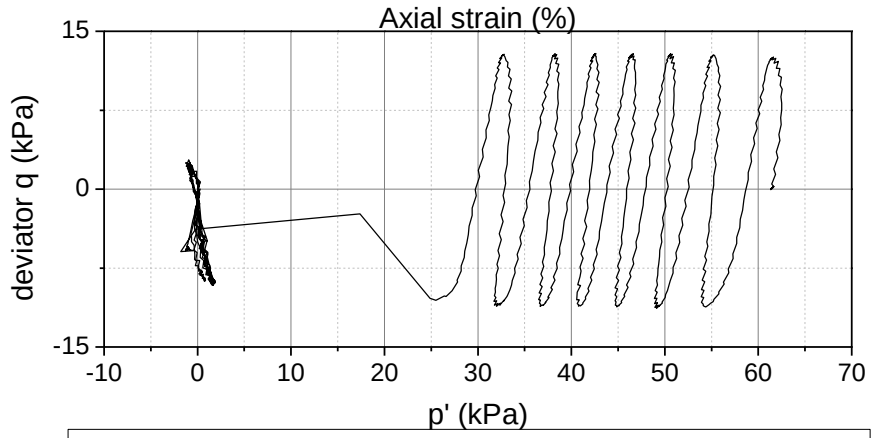

Test: UC_T_Oct13 σ_0'=61.7kPa; CSR=0.097; Dr=-4.4%

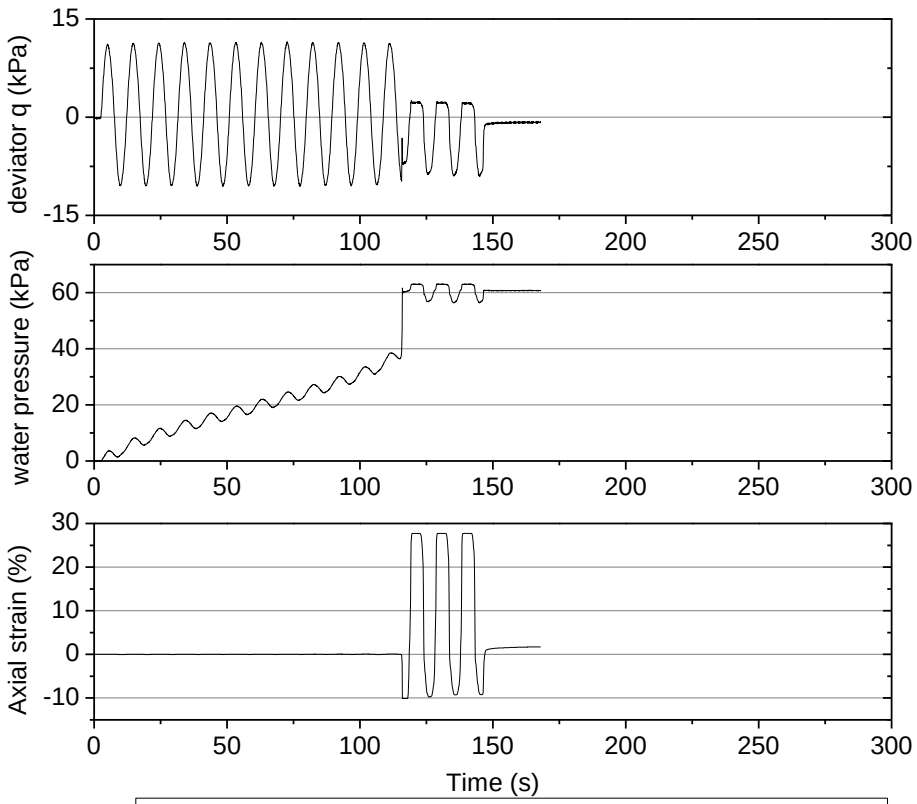

Test: UC_T_Oct18 σ_0'=60.8kPa; CSR=0.090; Dr=-13.7%

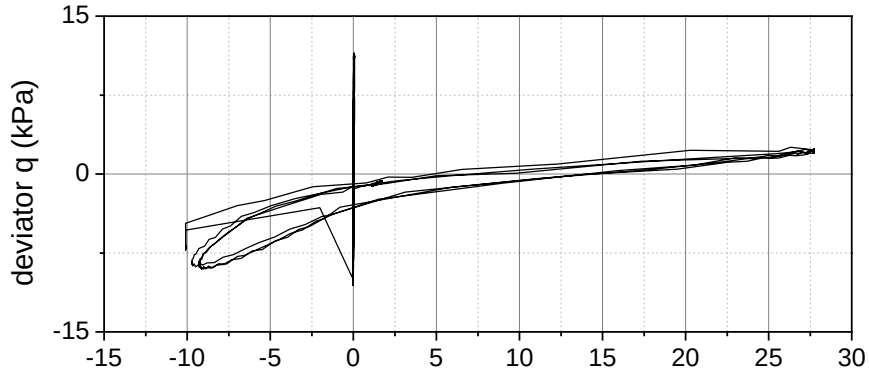

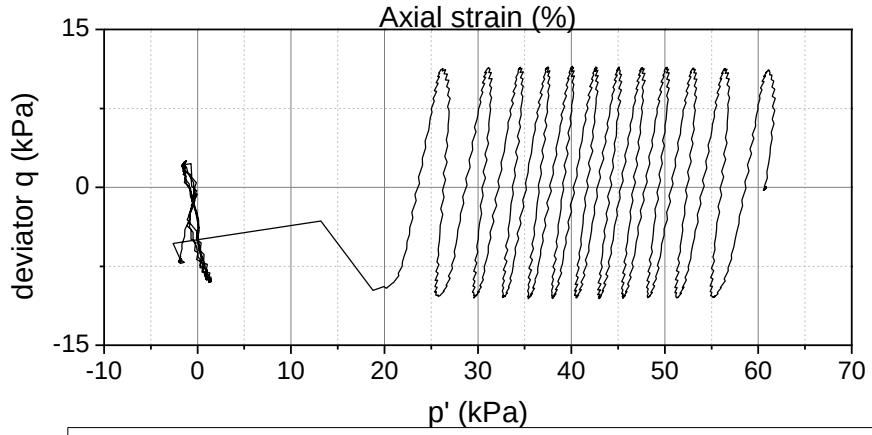

Test: UC_T_Oct18 σ_0'=60.8kPa; CSR=0.090; Dr=-13.7%

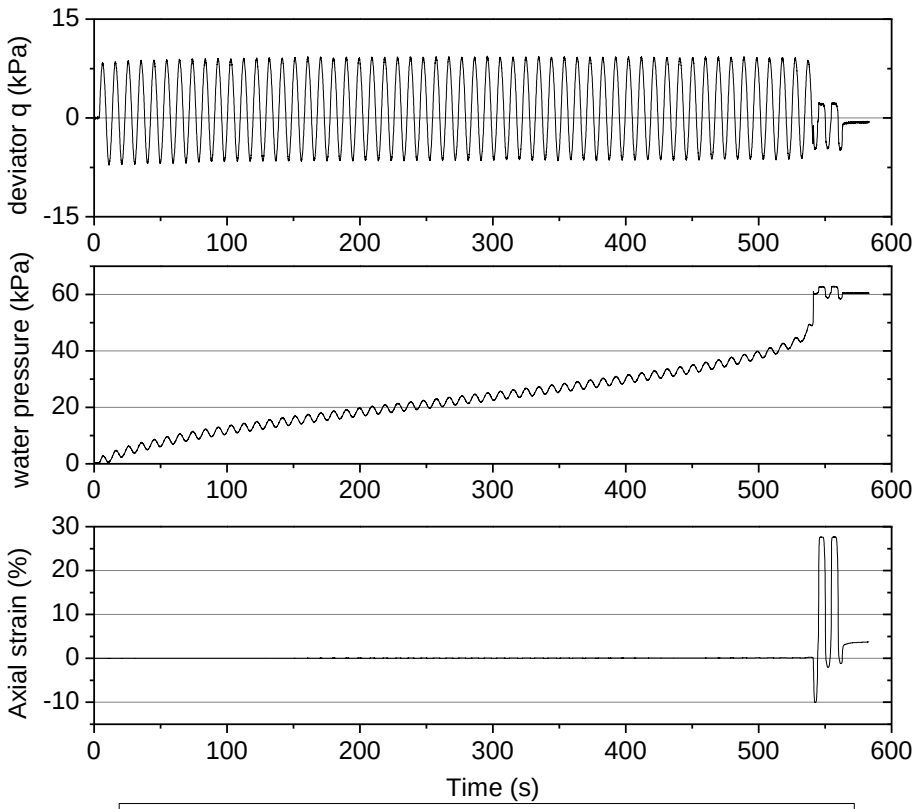

Test: UC_T_Oct19 σ_0'=60.5kPa; CSR=0.065; Dr=-5.0%

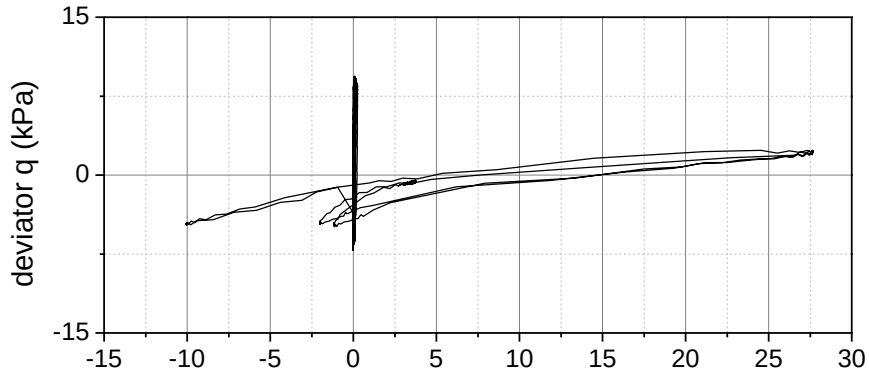

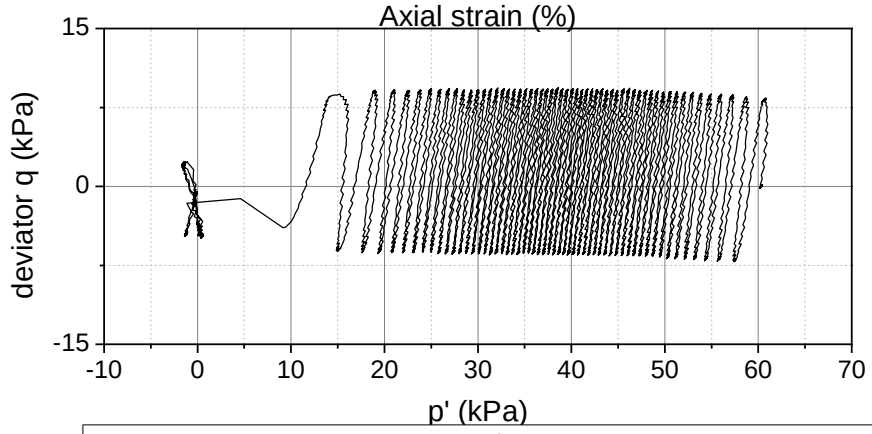

Test: UC_T_Oct19 σ_0'=60.5kPa; CSR=0.065; Dr=-5.0%

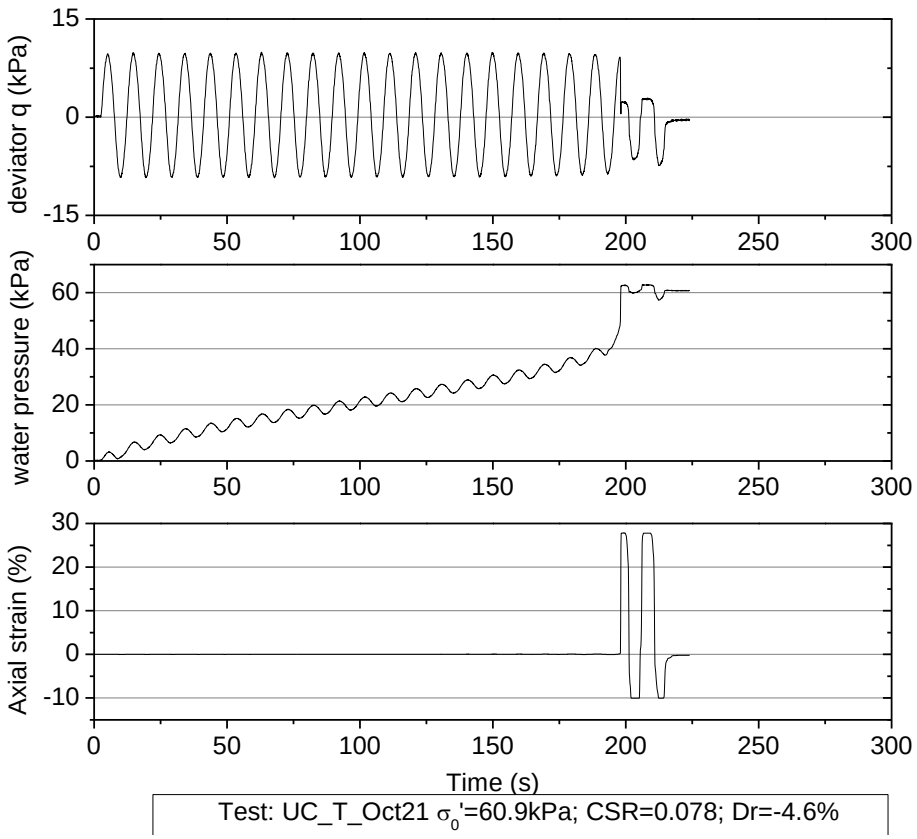
deviator q (kPa)
water pressure (kPa)
Axial strain (%)
Time (s)
Test: UC_T_Oct21 σ0'=60.9kPa; CSR=0.078; Dr=-4.6%

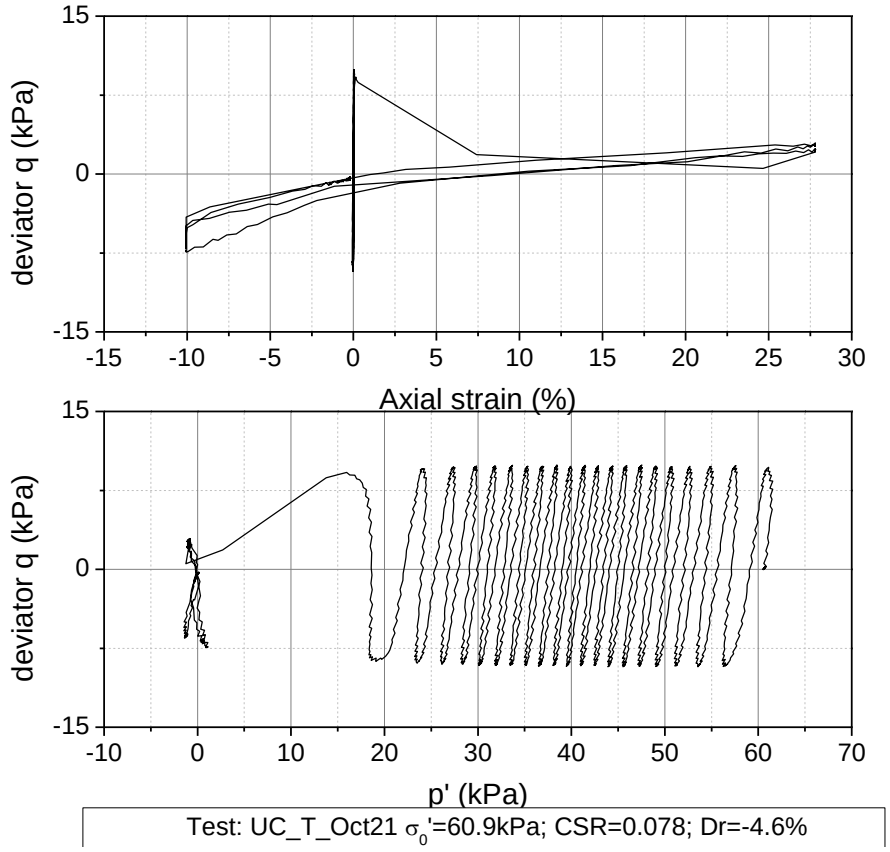
deviator q (kPa)
Axial strain (%)
deviator q (kPa)
p' (kPa)
Test: UC_T_Oct21 σ0'=60.9kPa; CSR=0.078; Dr=-4.6%

E-3 Unsaturated Toyoura sand in Set 1

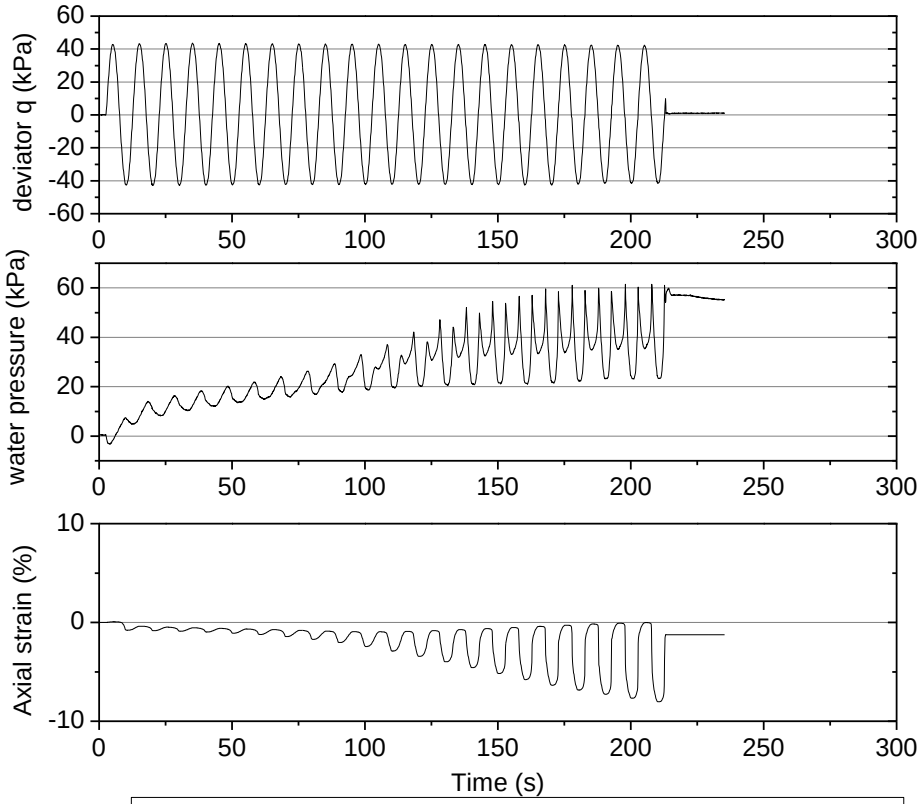

Test: UC_T_May8 σ_0'=61.7kPa; CSR=0.353; Dr=66.8%; Sr=91.6%

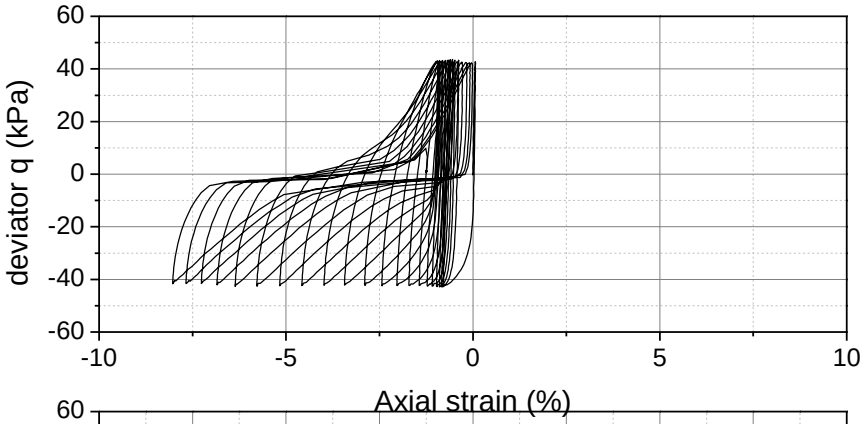

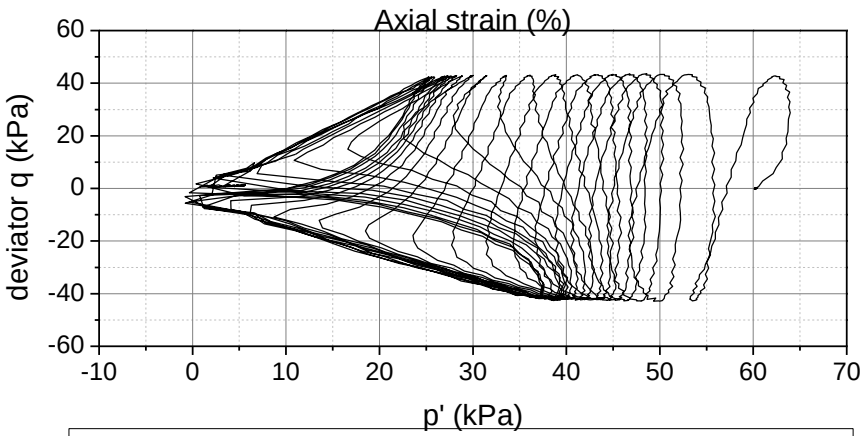

Test: UC_T_May8 σ_0'=61.7kPa; CSR=0.353; Dr=66.8%; Sr=91.6%

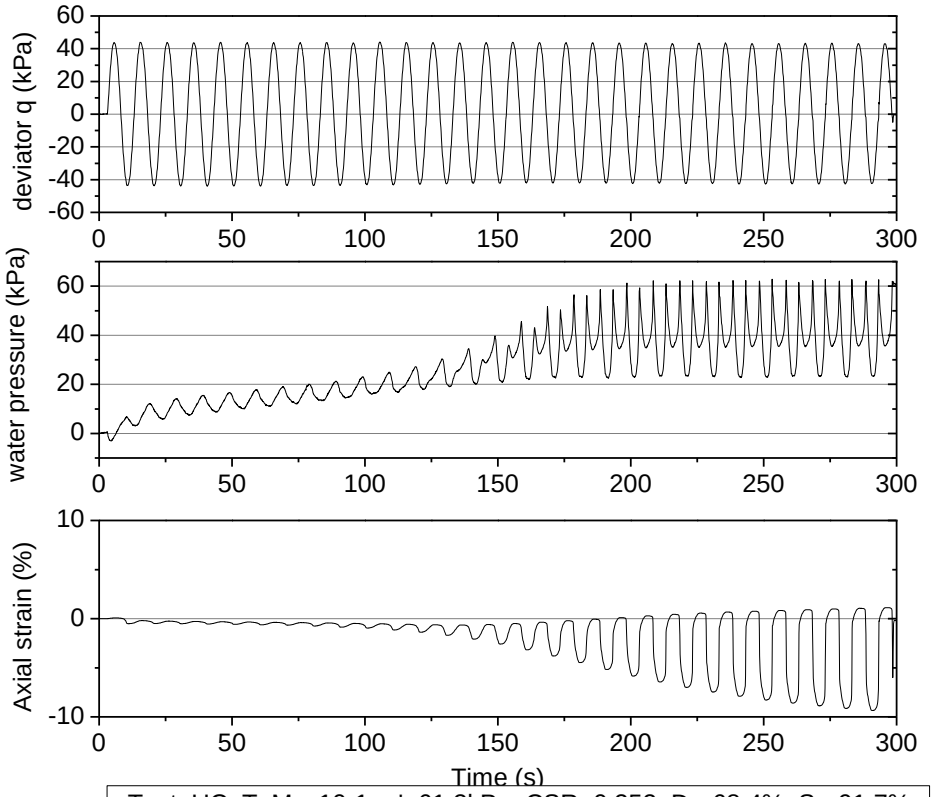

Test: UC_T_May10-1 σ_0'=61.3kPa; CSR=0.352; Dr=68.4%; Sr=91.7%

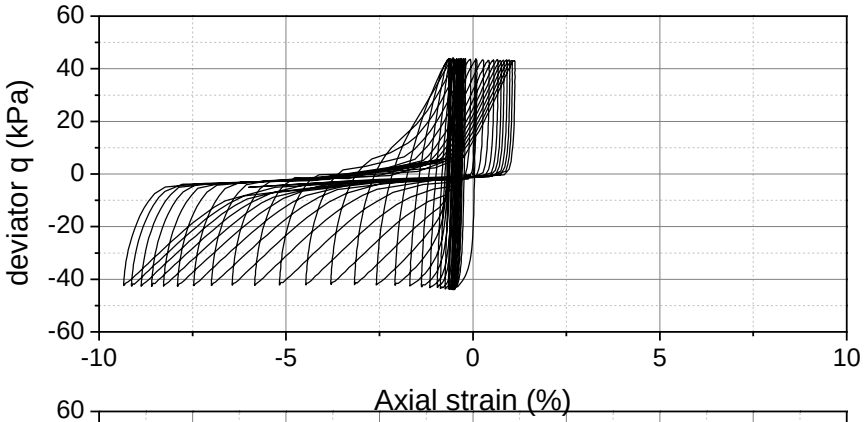

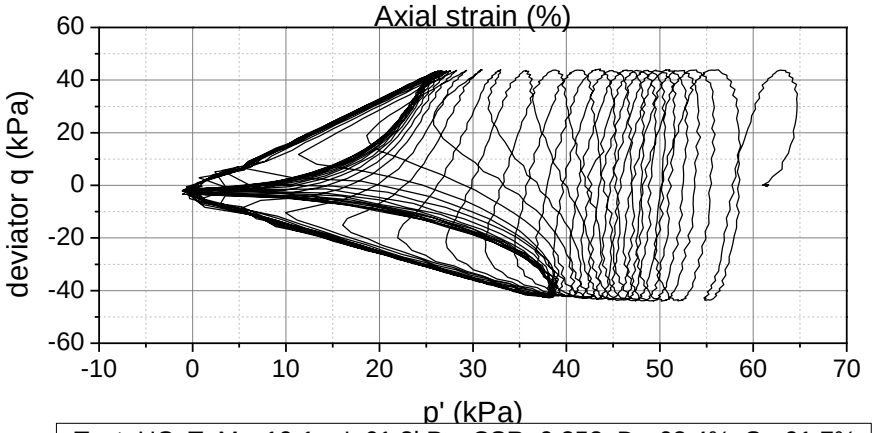

Test: UC_T_May10-1 σ_0'=61.3kPa; CSR=0.352; Dr=68.4%; Sr=91.7%

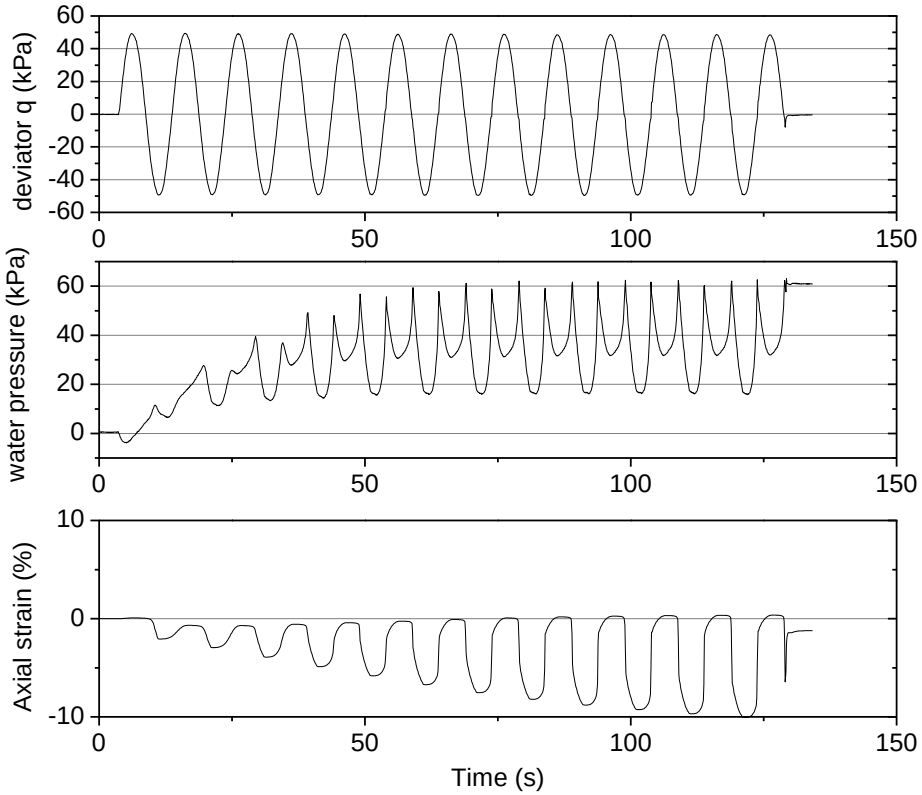

Test: UC_T_May10-2 σ_0'=60.5kPa; CSR=0.402; Dr=65.3%; Sr=90.4%

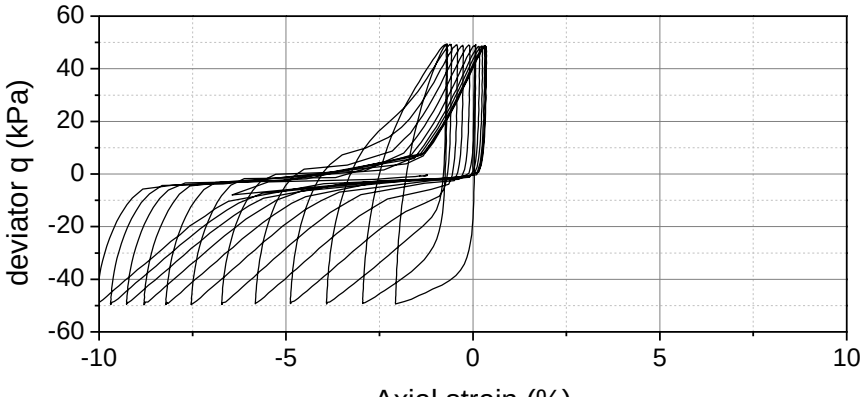

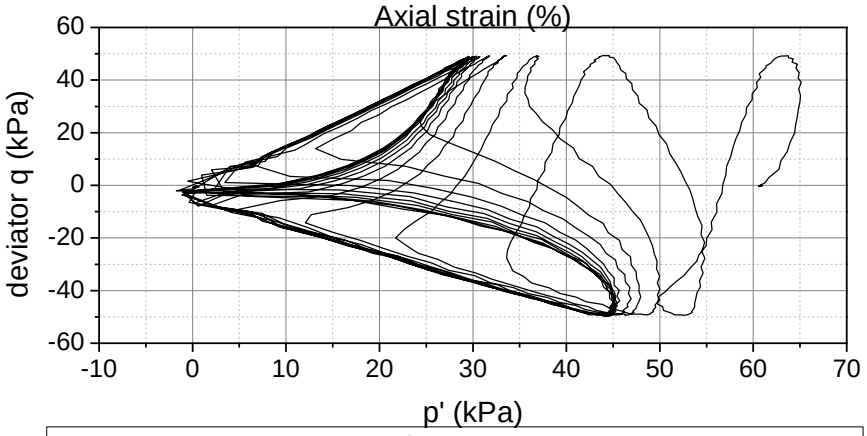

Test: UC_T_May10-2 σ_0'=60.5kPa; CSR=0.402; Dr=65.3%; Sr=90.4%

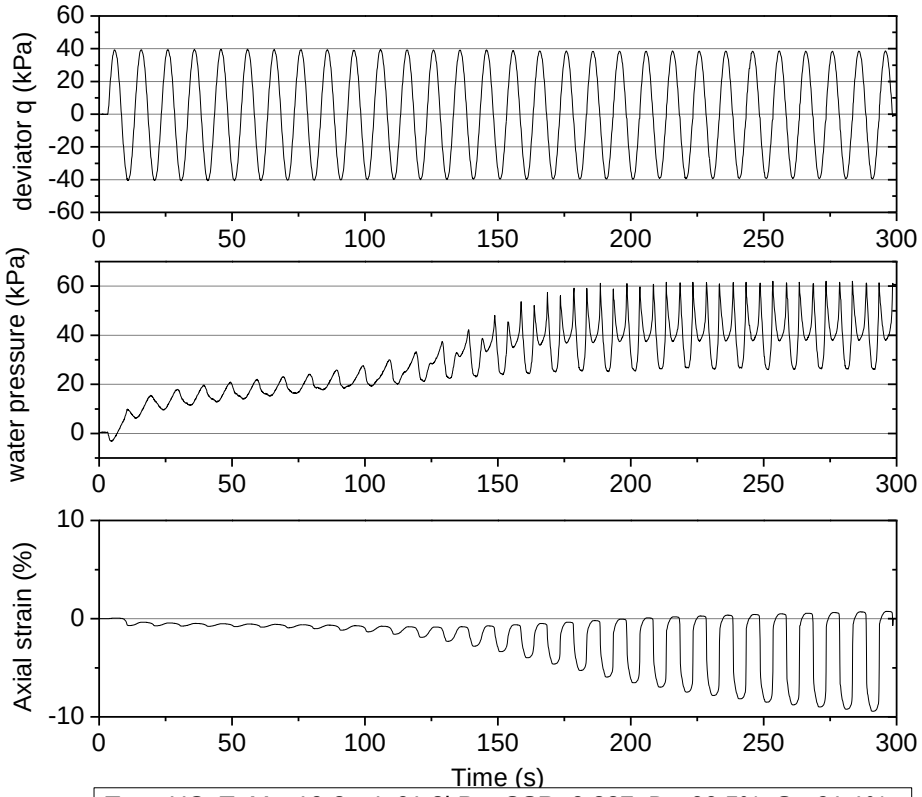

Test: UC_T_May10-3 σ_0'=61.8kPa; CSR=0.327; Dr=66.5%; Sr=91.1%

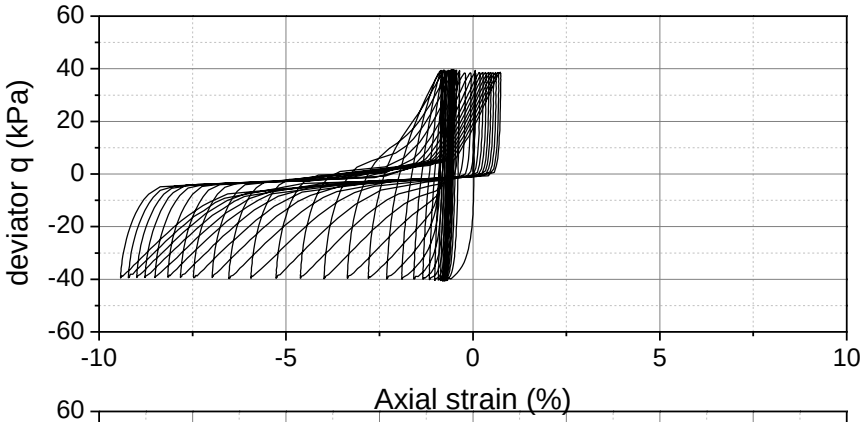

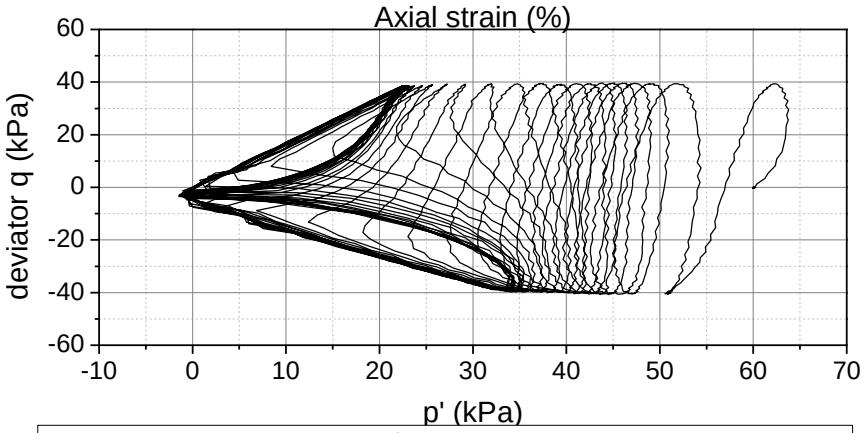

Test: UC_T_May10-3 σ_0'=61.8kPa; CSR=0.327; Dr=66.5%; Sr=91.1%

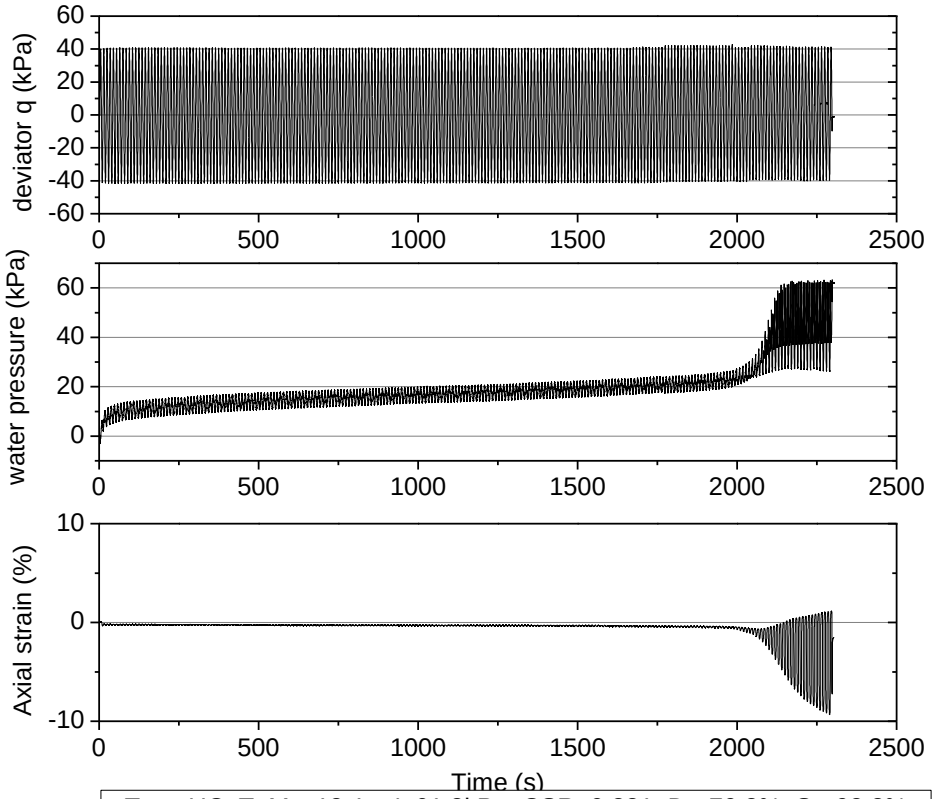

Test: UC_T_May13-1 σ_0'=61.3kPa; CSR=0.331; Dr=70.2%; Sr=92.3%

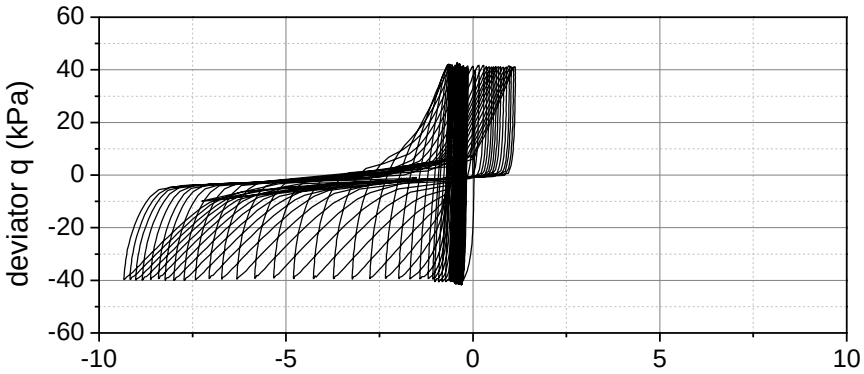

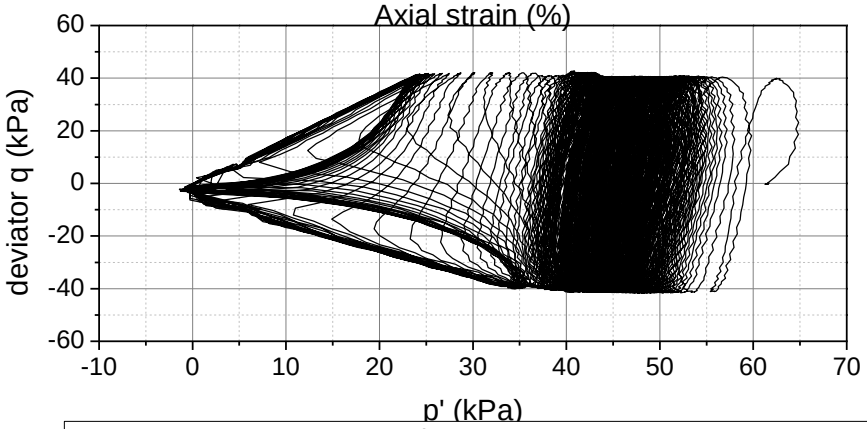

Test: UC_T_May13-1 σ_0'=61.3kPa; CSR=0.331; Dr=70.2%; Sr=92.3%

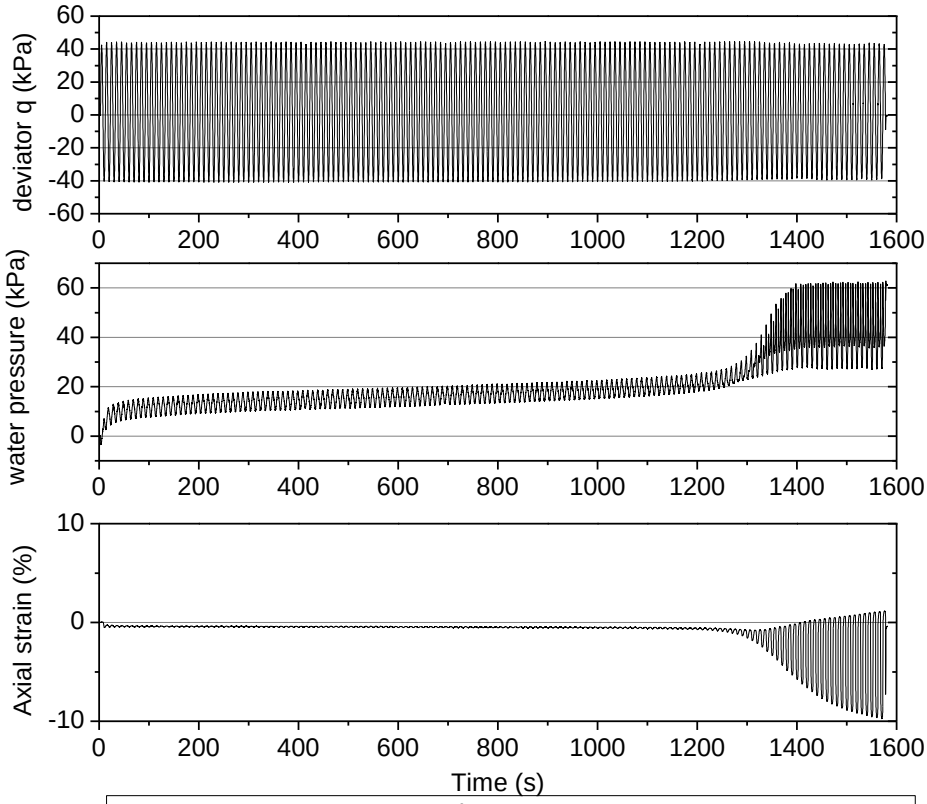

Test: UC_T_May13-2 σ_0'=61.5kPa; CSR=0.345; Dr=67.5%; Sr=91.2%

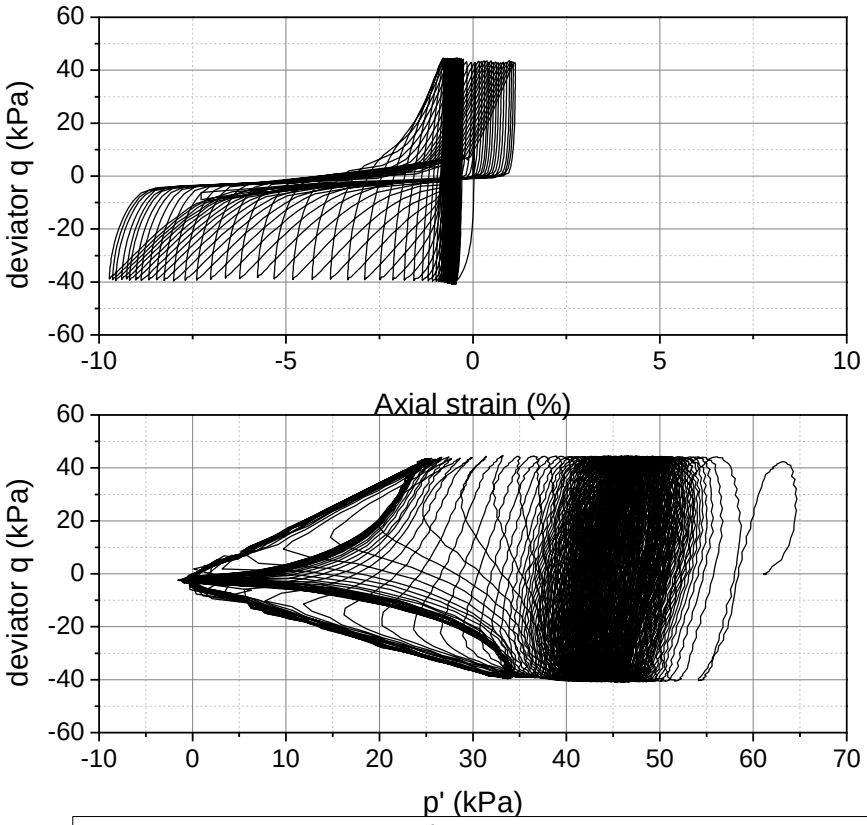

Test: UC_T_May13-2 σ_0'=61.5kPa; CSR=0.345; Dr=67.5%; Sr=91.2%

E-4 Unsaturated Toyoura sand in Set 2

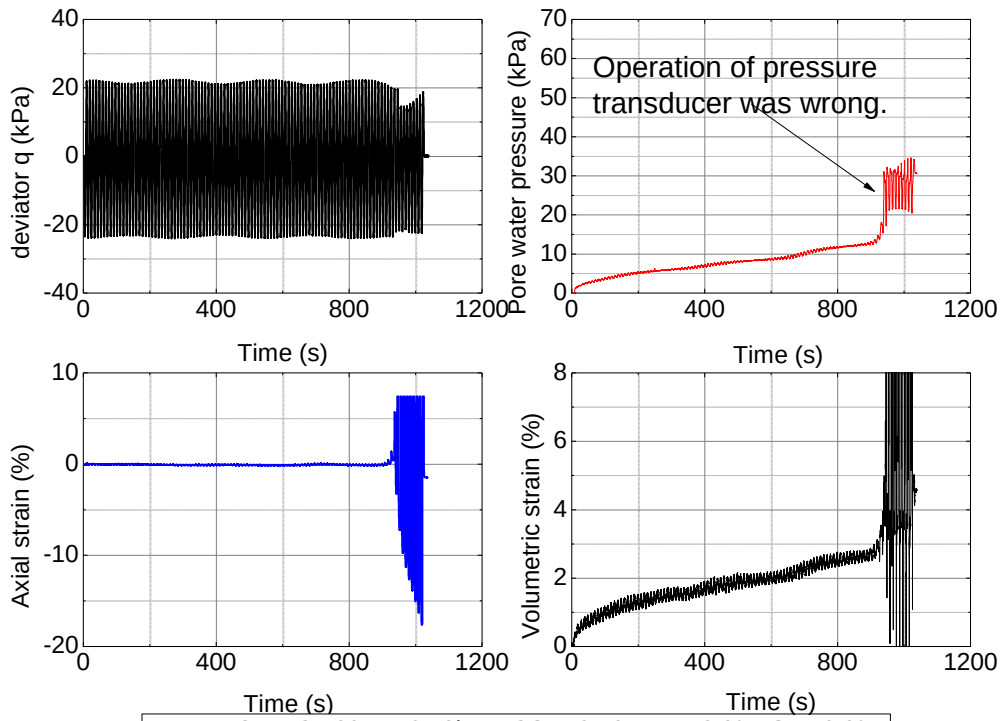

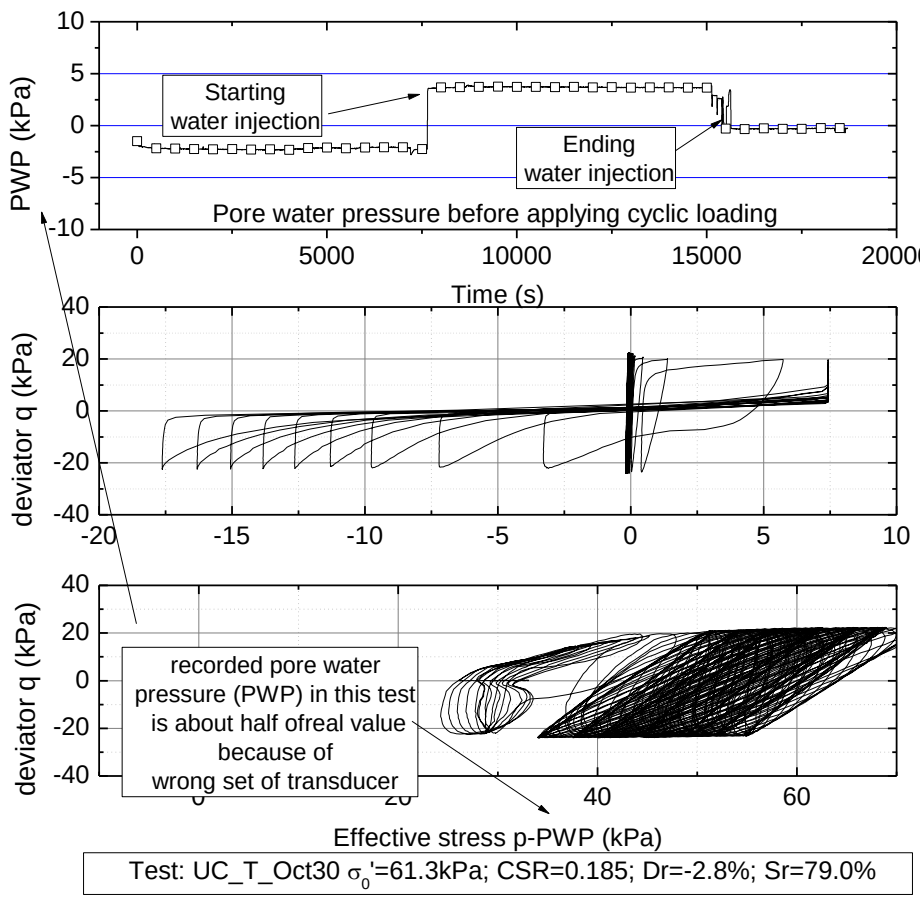

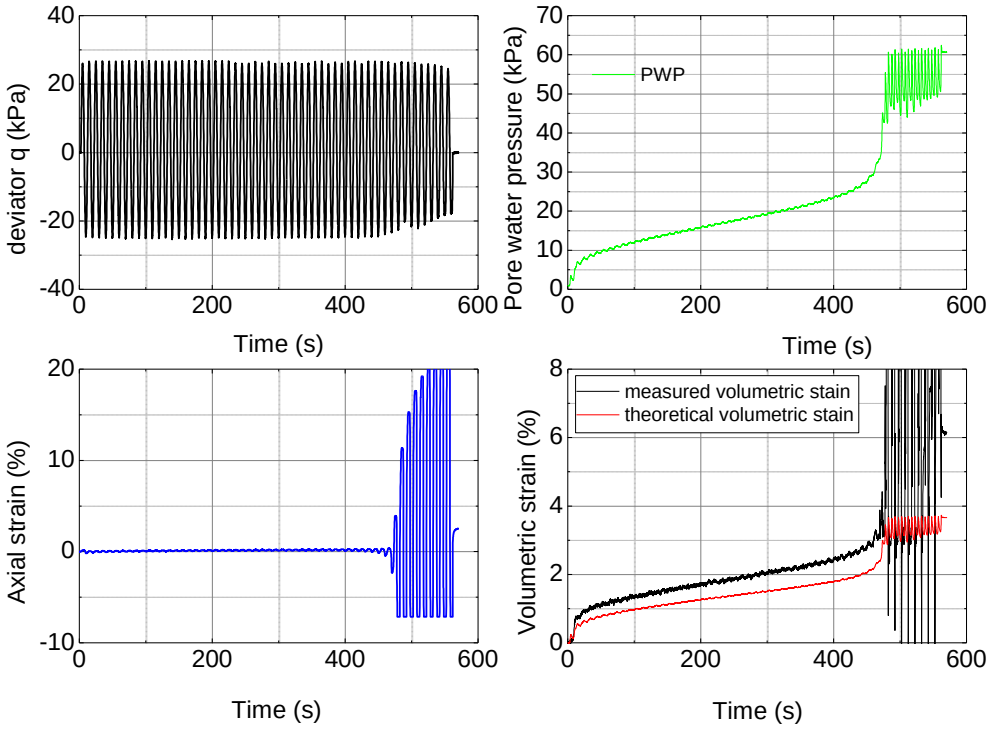

Test: UC_T_Oct31 σ_0'=61.5kPa; CSR=0.209; Dr=-4.0%; Sr=80.2%

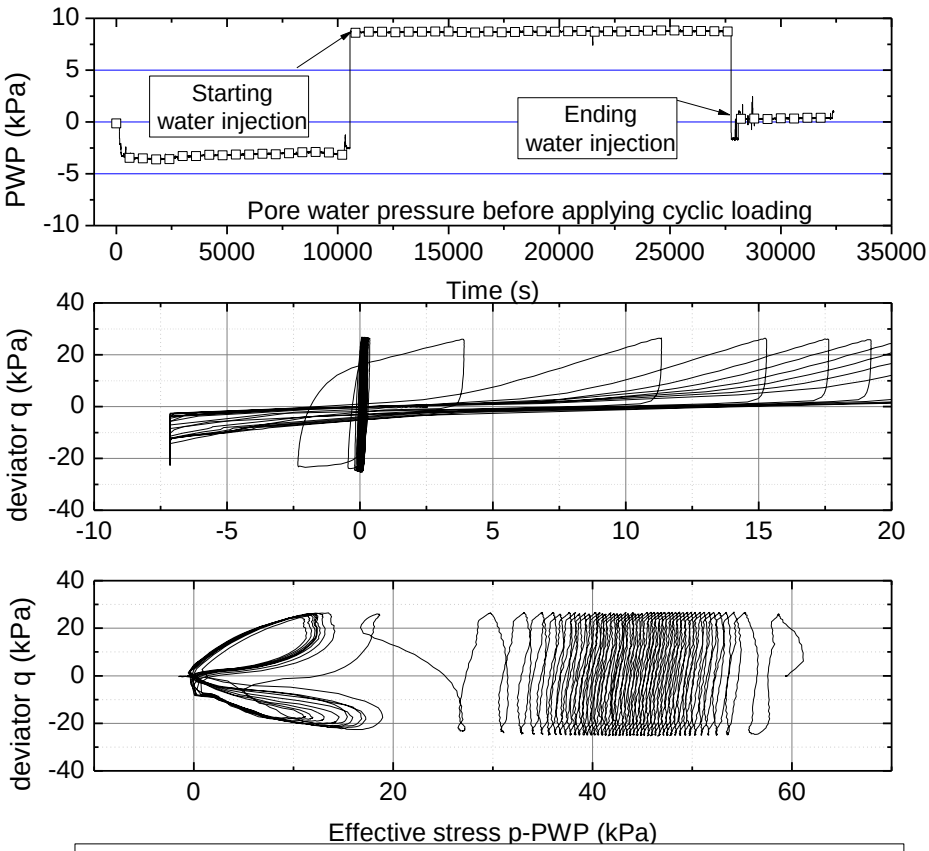

Test: UC_T_Oct31 σ_0'=61.5kPa; CSR=0.209; Dr=-4.0%; Sr=80.2%

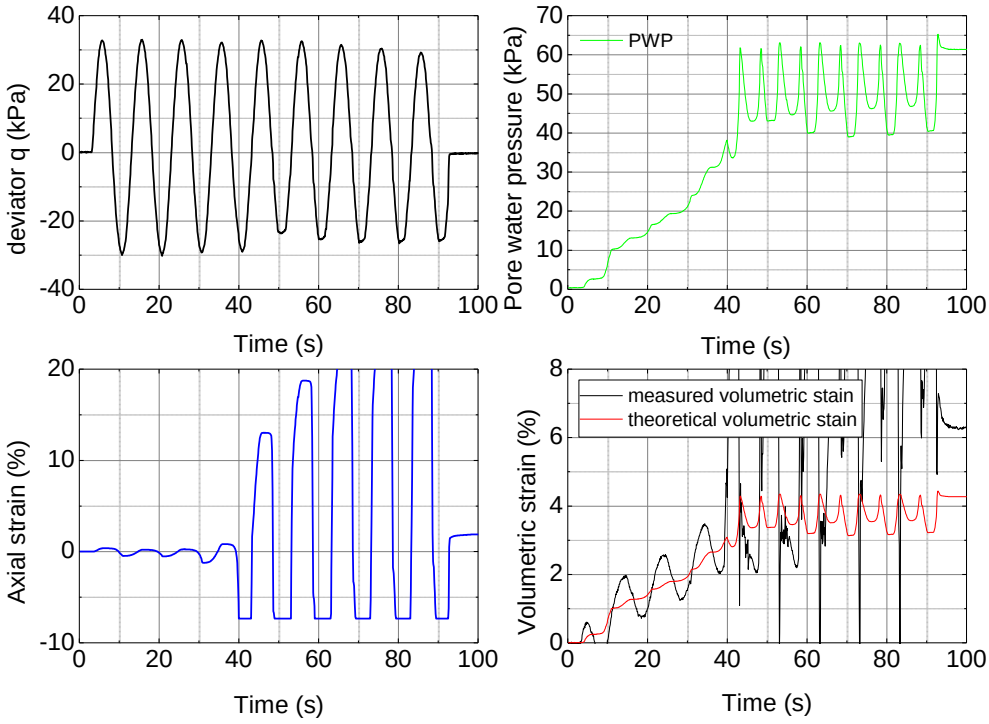

Test: UC_T_Nov1 σ_0'=61.1kPa; CSR=0.258; Dr=-9.4%; Sr=77.5%

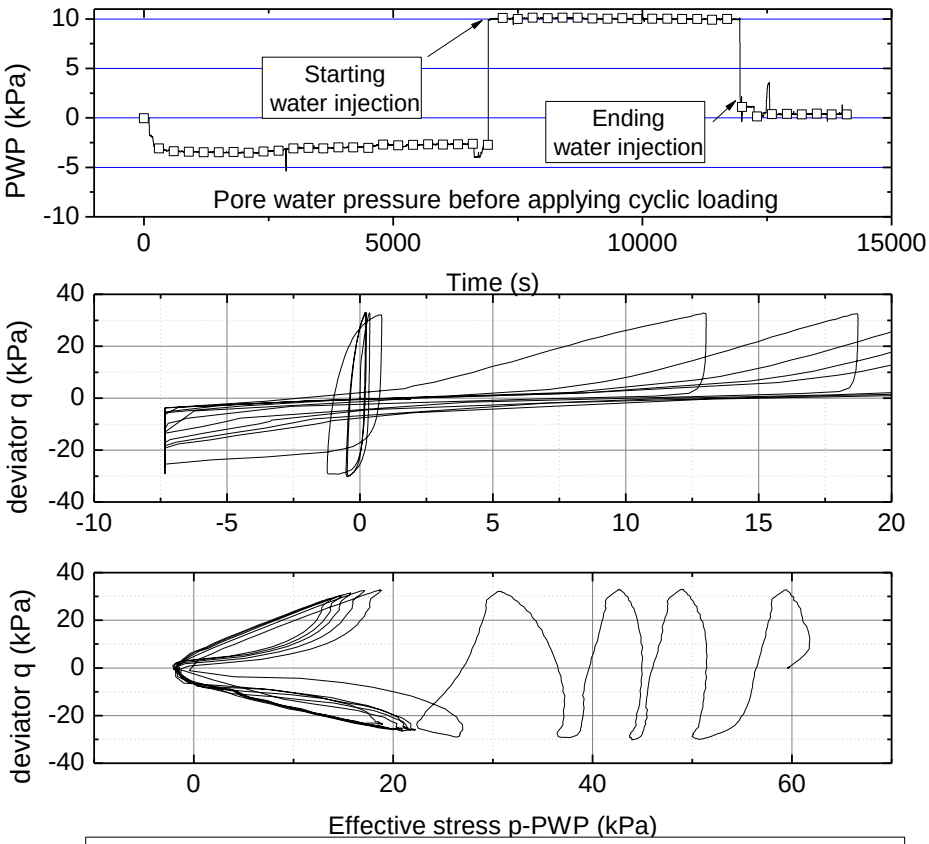

Test: UC_T_Nov1 σ_0'=61.1kPa; CSR=0.258; Dr=-9.4%; Sr=77.5%

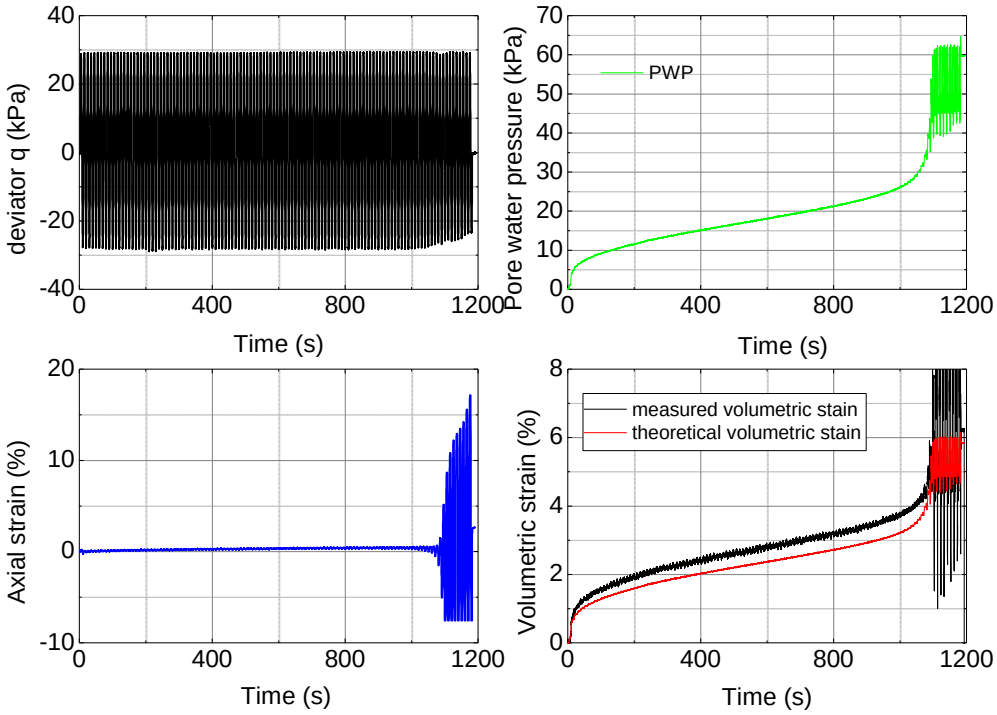

Test: UC_T_Nov3 σ_0'=61.1kPa; CSR=0.234; Dr=-4.4%; Sr=68.4%

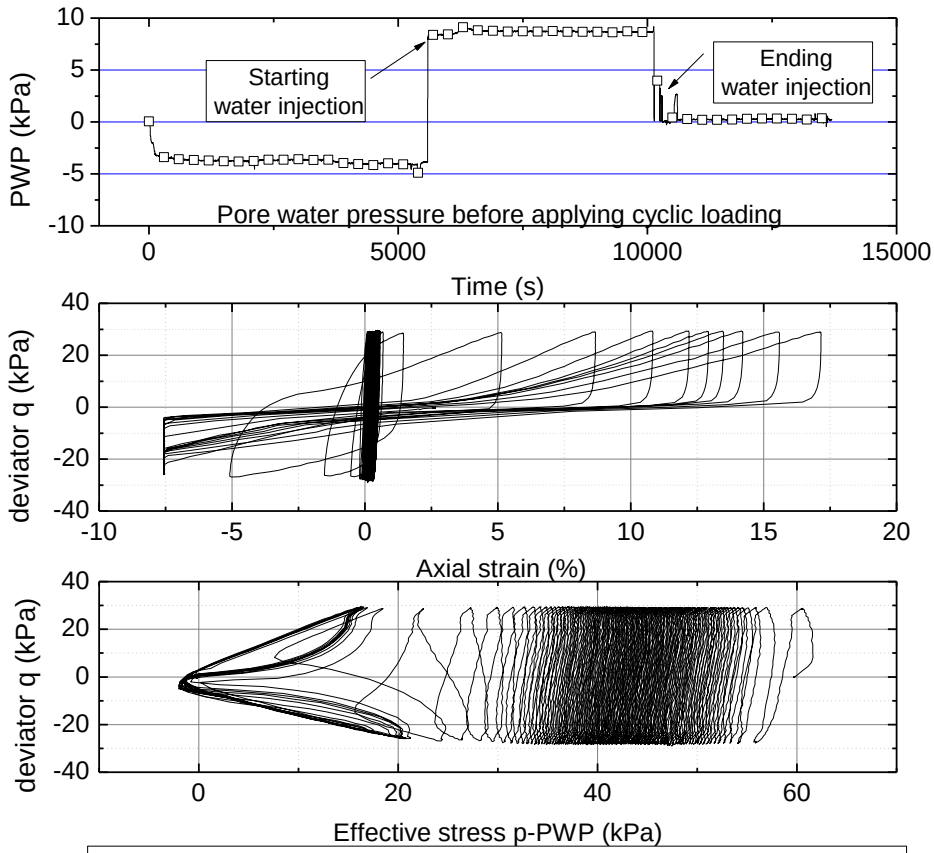

Test: UC_T_Nov3 σ_0'=61.1kPa; CSR=0.234; Dr=-4.4%; Sr=68.4%

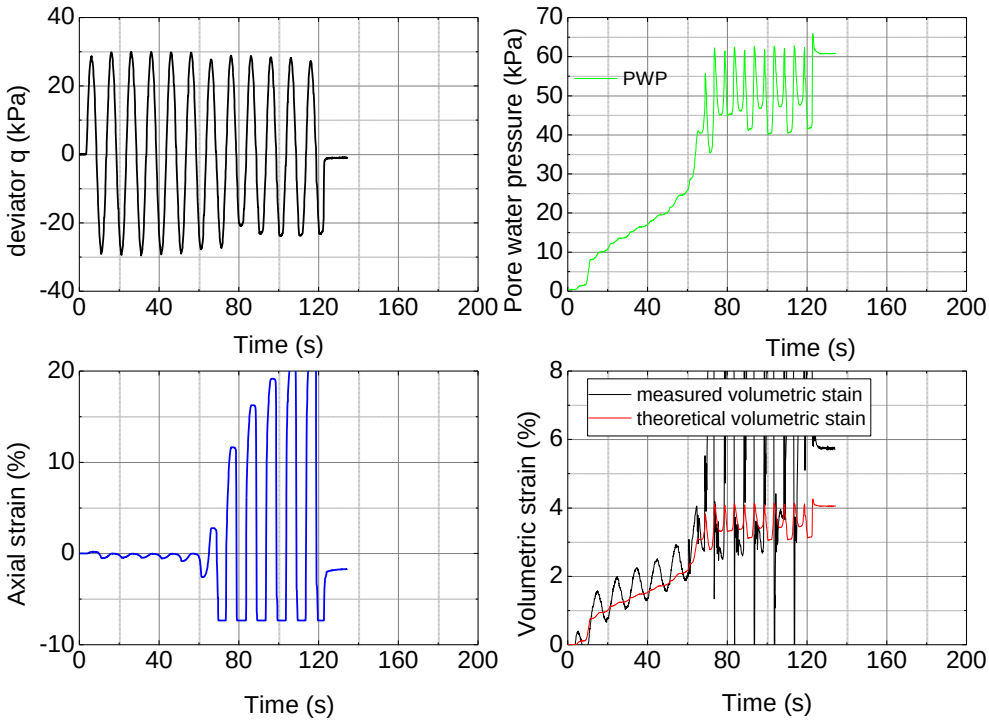

Test: UC_T_Nov4 σ_0'=61.2kPa; CSR=0.241; Dr=-3.4%; Sr=78.3%

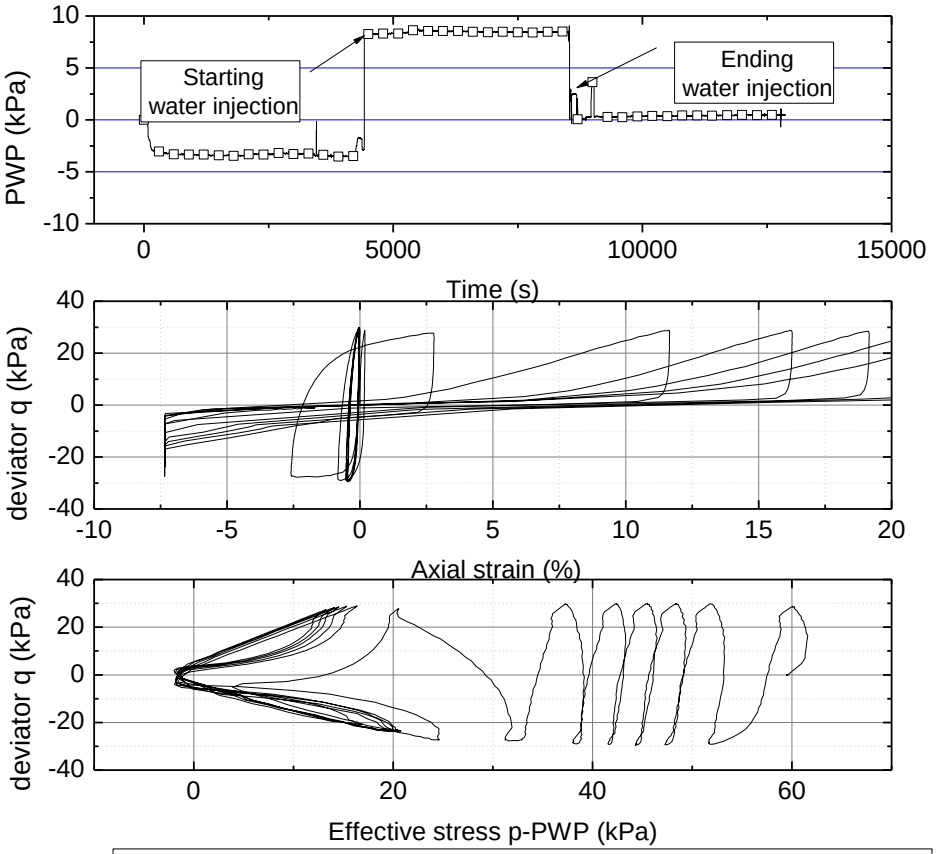

Test: UC_T_Nov4 σ_0'=61.2kPa; CSR=0.241; Dr=-3.4%; Sr=78.3%

Appendix F. Undrained cyclic loading test for Inagi sand

Results of undrained cyclic loading tests conducted on Toyoura snad, Inagi sand and iron ore fines type B (IOF-B) are summarized in Appendixes E, F and G, respectively. Each test is assigned a unique name, of which "UC_" is used to stand for undrained cyclic loading test. The test materials Toyoura sand, Inagi sand and IOF-B are substituted by "T", "ING" and "IOF-B" in the test name for short. There is an information bar at the bottom of each figure to indicate the name and conditions of the test.

Tables F-1 and F-2 summarize the test conditions of all tests conducted on saturated and unsaturated Inagi sand, respectively. Symbols in Table F-1 and F-2 are stand for:

e, ρ_d and Dr: void ration, dry density and relative density after consolidation;

CSR: cyclic stress ratio ($=\sigma_d/2\sigma_0'$, σ_d is single amplitude of cyclic loading);

$N_{DA=5\%}$: number of cycle which causes 5% double amplitude of axial strain;

T_{consld}: time duration for consolidation. Specimens were normally consolidated for two hours; while there are three tests, of which specimens were consolidated for one night (approximately 10 hours).

σ_0': confining pressure before applying cyclic loading;

Sr: degree of saturation after consolidation;

$\varepsilon^*_{vol,air}$: maximum volumetric strain caused by pore air compression;

B: pore water pressure B;

p: condition of total mean principal stress. ○ means cell pressure was controlled and p was kept constant; ● means cell pressure was not controlled and p changed during applying cyclic loading.

Set: number of set classified in Table 5-3

Table F-1 Summary of test condition of saturated Inagi sand

test name	e	ρ_d (g/cm^3)	Dr (%)	σ_0' (kPa)	CSR	$N_{DA=5\%}$	T_{consld}	Set
UC_ING_Dec30	1.092	1.27	74.9	58.3	0.213	1.0	2 hours	3
UC_ING_Dec31	1.091	1.27	75.1	57.7	0.160	6.7	2 hours	
UC_ING_Jan2	1.173	1.22	63.9	57.0	0.157	8.4	2 hours	
UC_ING_Jan3	1.159	1.23	65.8	57.0	0.149	13.6	2 hours	
UC_ING_Jan4	1.166	1.23	64.8	57.2	0.125	39.9	2 hours	
UC_ING_Jan5	1.169	1.22	64.4	56.0	0.173	10.3	one night	3
UC_ING_Jan7	1.174	1.22	63.9	55.3	0.179	7.3	one night	
UC_ING_Jan14	1.154	1.23	66.5	59.2	0.136	32.6	one night	

Table F-2 Summary of test condition of unsaturated Inagi sand

Test name	e	ρ_d (g/cm^3)	Dr (%)	σ_0' (kPa)	CSR	$N_{DA=5\%}$	Sr (%)	$\varepsilon^*_{vol,air}$ (%)	p	Set
UC_ING_Nov23	1.112	1.26	72.2	58.0	0.241	40.2	69.3	6.00	●	3
UC_ING_Nov26	1.125	1.25	70.4	60.1	0.264	11.3	68.8	6.15	●	
UC_ING_Dec28	1.123	1.25	70.7	58.8	0.270	7.2	67.3	6.44	●	
UC_ING_Mar19	1.101	1.26	73.7	59.5	0.354	0.8	72.0	5.46	○	3
UC_ING_Mar21	1.101	1.26	73.7	59.8	0.299	6.0	72.2	5.42	○	
UC_ING_Mar24	1.077	1.28	77.0	59.0	0.248	44.9	73.7	5.08	○	
UC_ING_Mar25	1.069	1.28	78.1	59.6	0.274	12.9	74.1	4.98	○	
UC_ING_Mar28	1.109	1.26	72.6	59.3	0.245	3.3	83.4	3.25	○	3
UC_ING_Mar29	1.098	1.27	74.1	59.5	0.197	13.1	84.0	3.11	○	
UC_ING_Apr8	1.067	1.29	78.3	59.0	0.172	126.9	84.9	2.90	○	

F-1 Saturated Inagi sand for two hours consolidation in Set 3

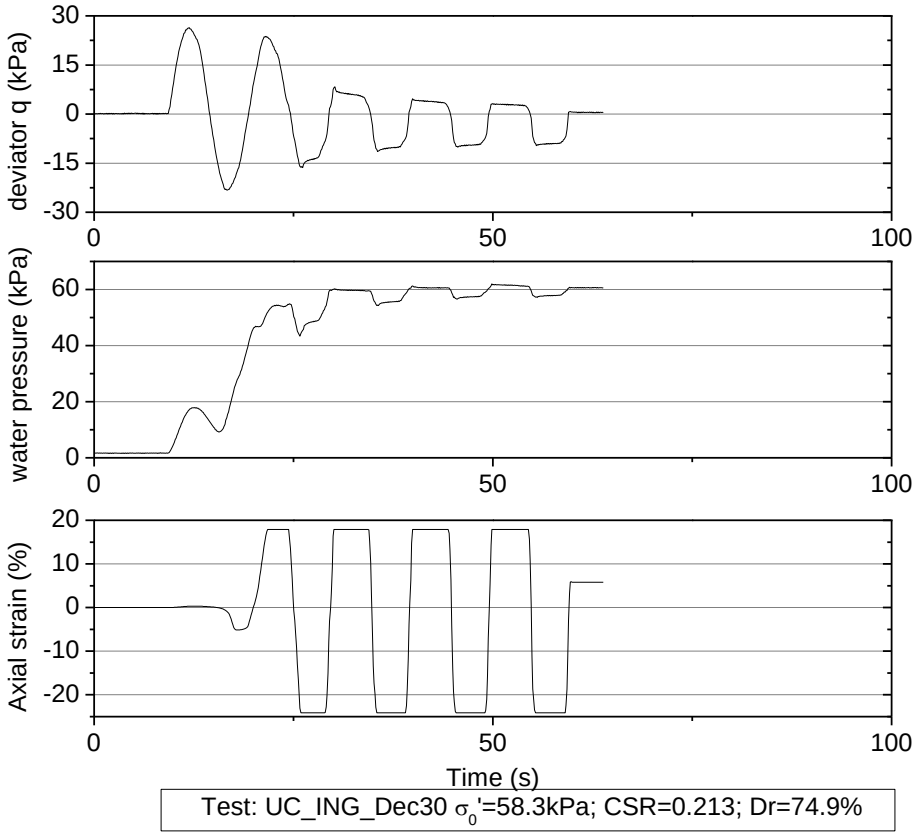

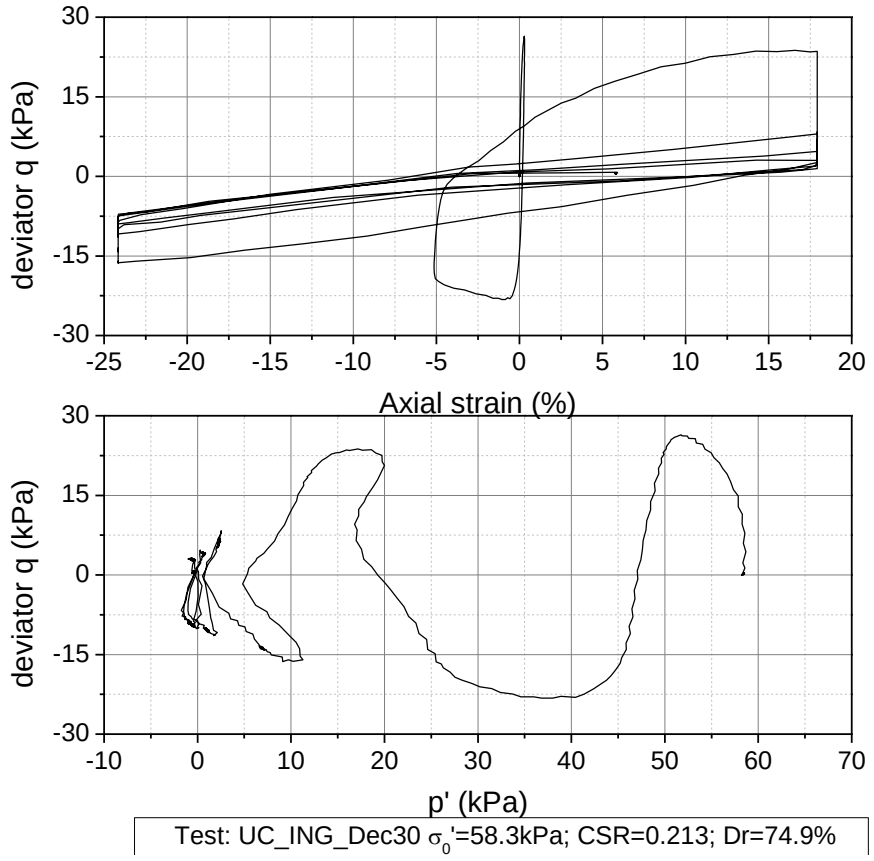

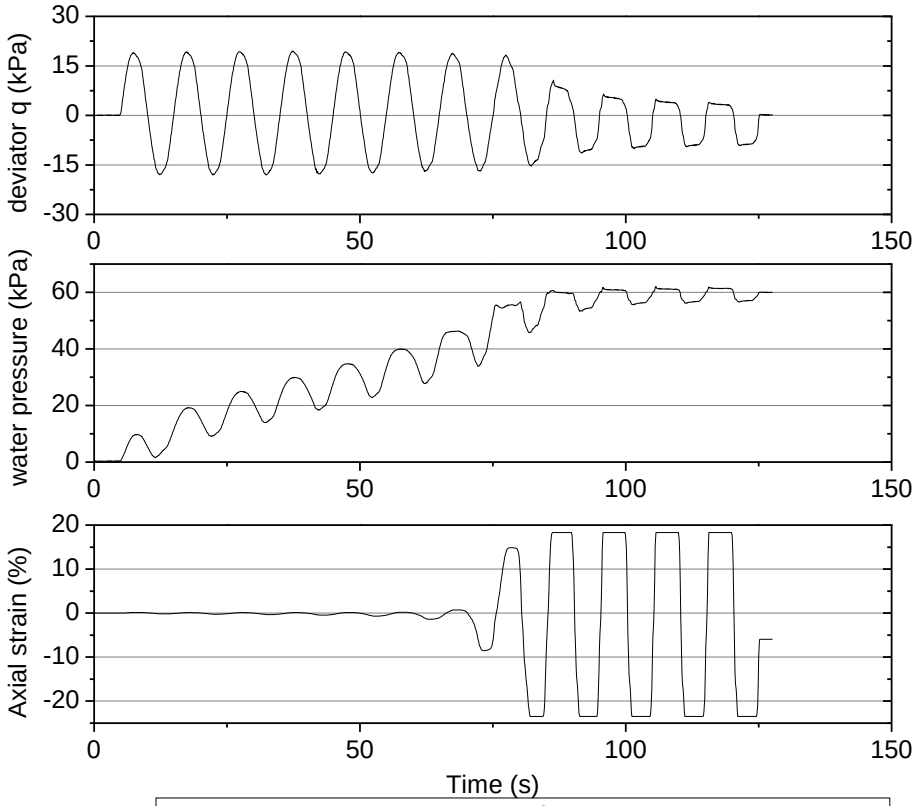

Test: UC_ING_Dec31 σ_0'=57.7kPa; CSR=0.160; Dr=75.1%

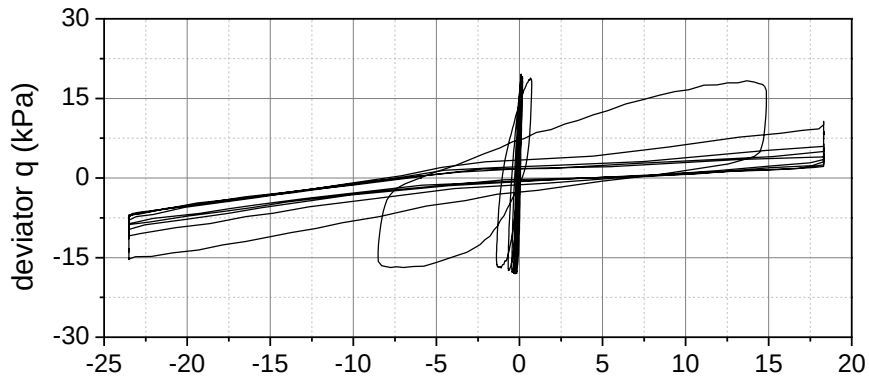

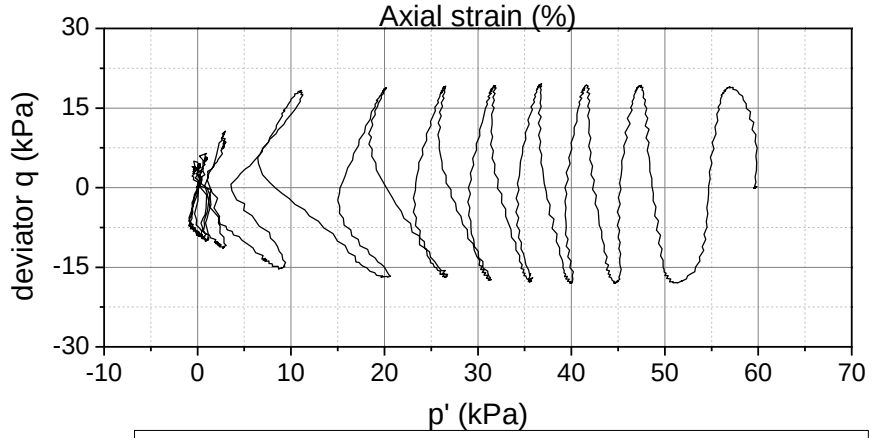

Test: UC_ING_Dec31 σ_0'=57.7kPa; CSR=0.160; Dr=75.1%

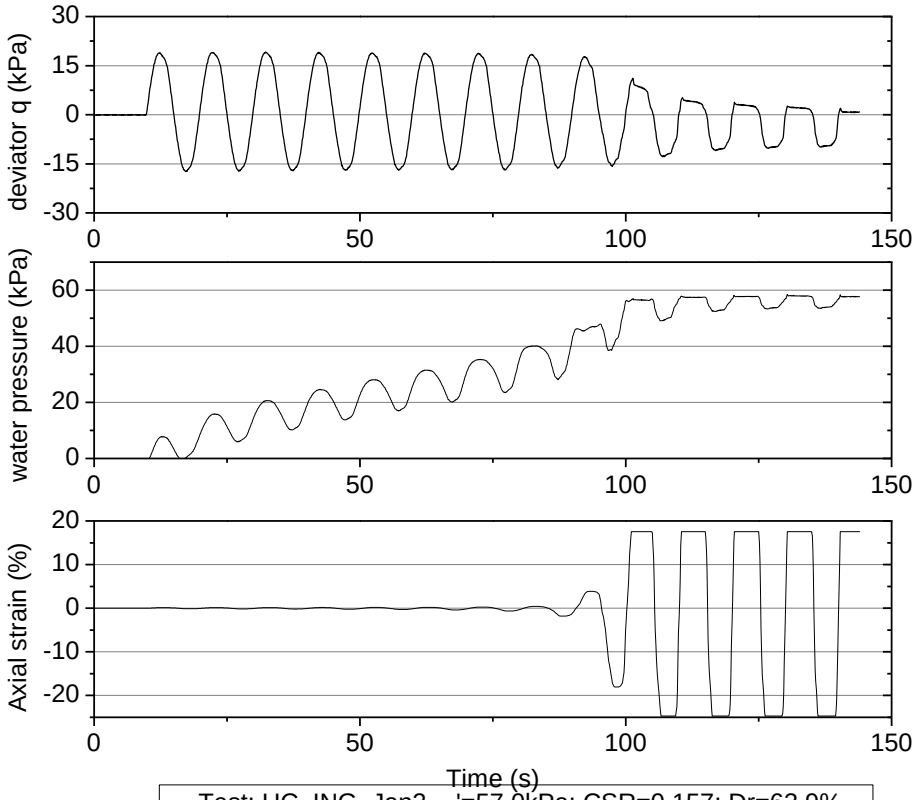

Test: UC_ING_Jan2 σ_0'=57.0kPa; CSR=0.157; Dr=63.9%

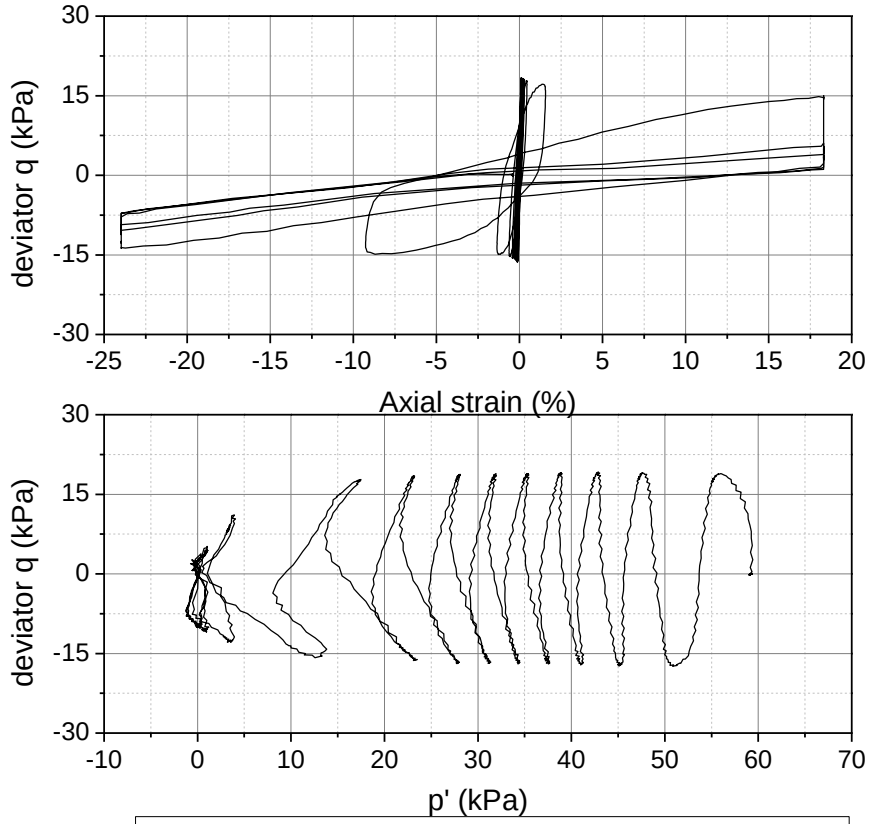

Test: UC_ING_Jan2 σ_0'=57.0kPa; CSR=0.157; Dr=63.9%

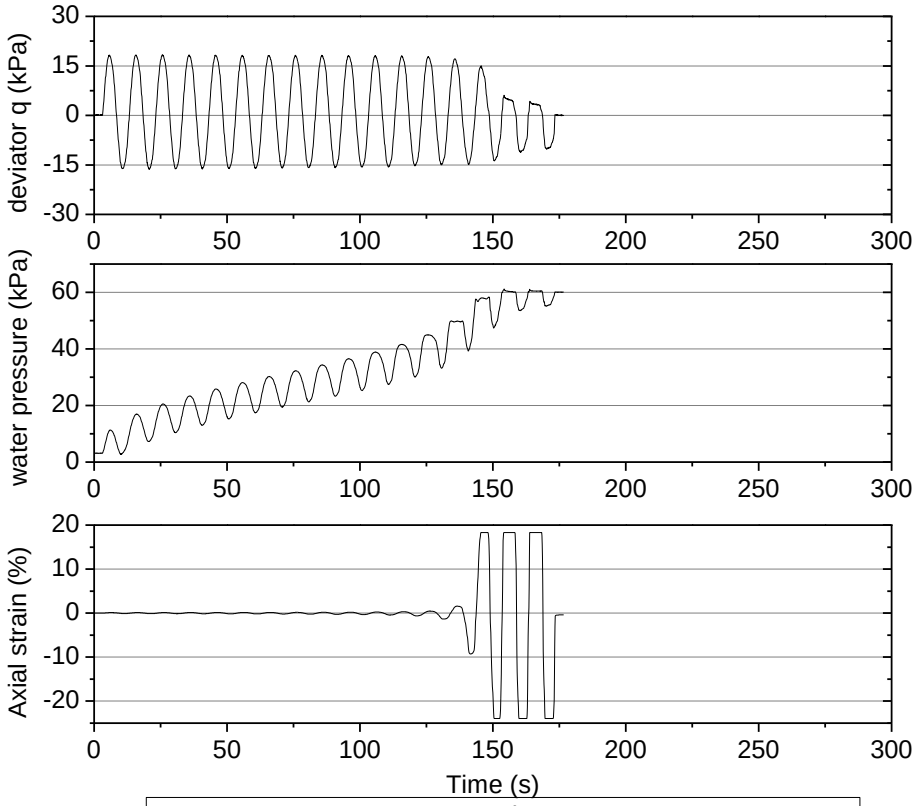

Test: UC_ING_Jan3 σ_0'=57.0kPa; CSR=0.149; Dr=65.8%

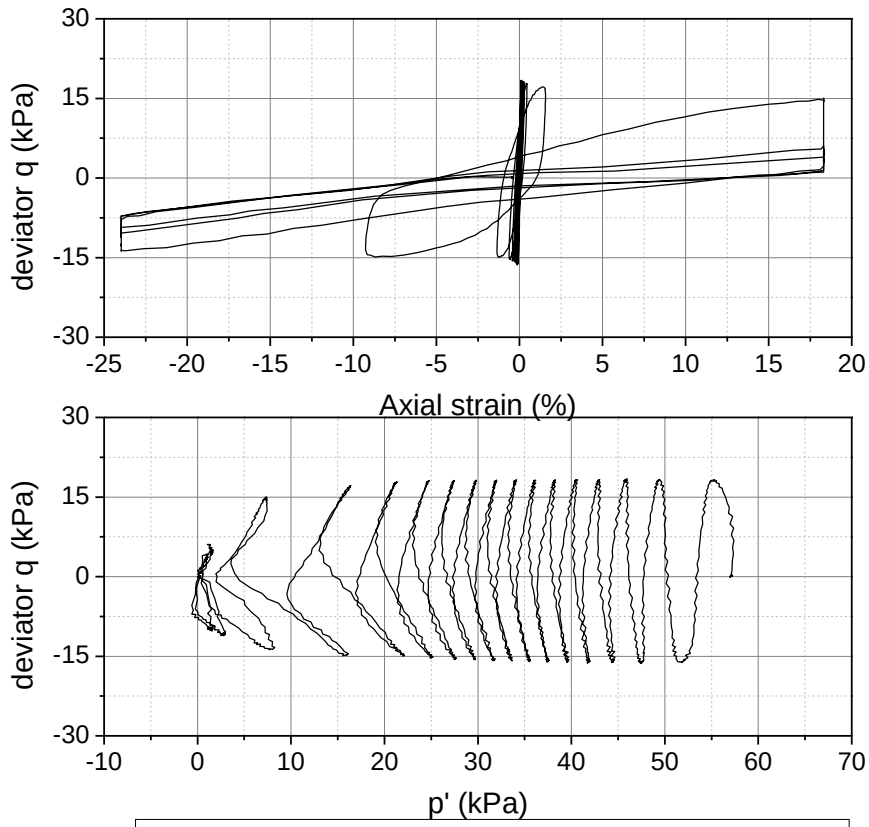

Test: UC_ING_Jan3 σ_0'=57.0kPa; CSR=0.149; Dr=65.8%

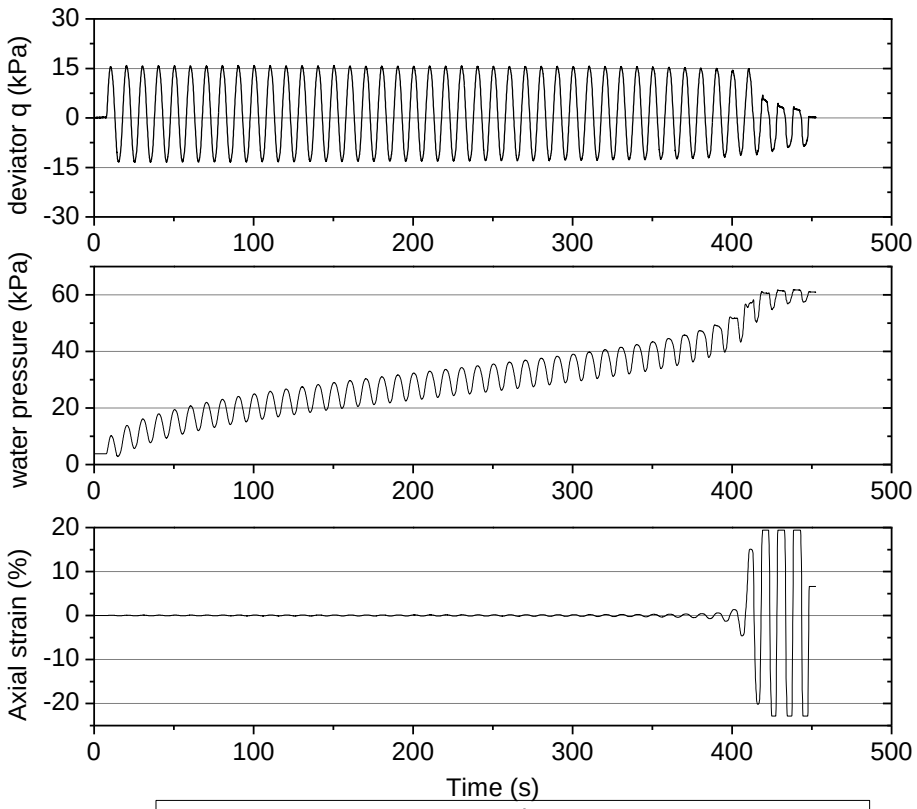

Test: UC_ING_Jan4 σ_0'=57.2kPa; CSR=0.125; Dr=64.8%

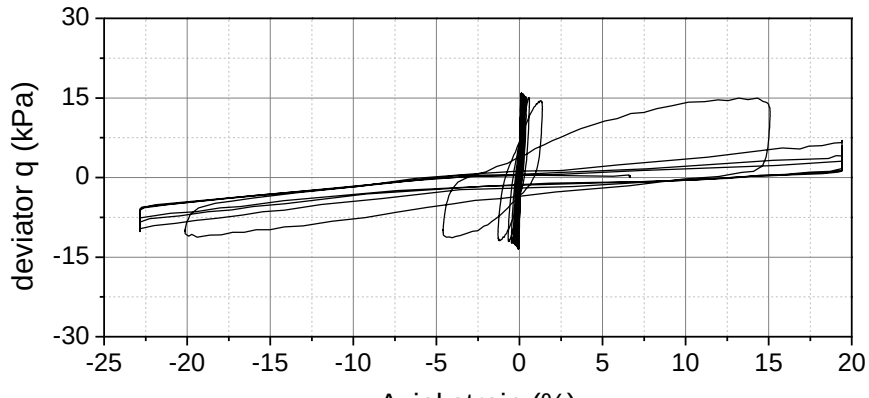

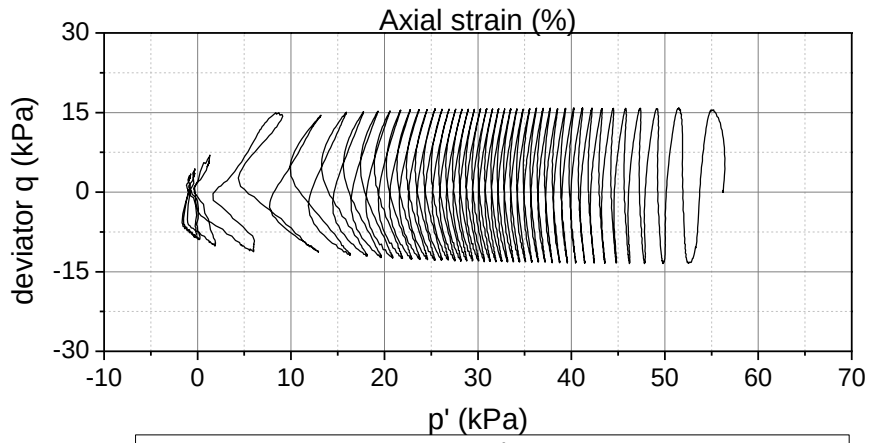

Test: UC_ING_Jan4 σ_0'=57.2kPa; CSR=0.125; Dr=64.8%

F-2 Saturated Inagi sand for overnight consolidation in Set 3

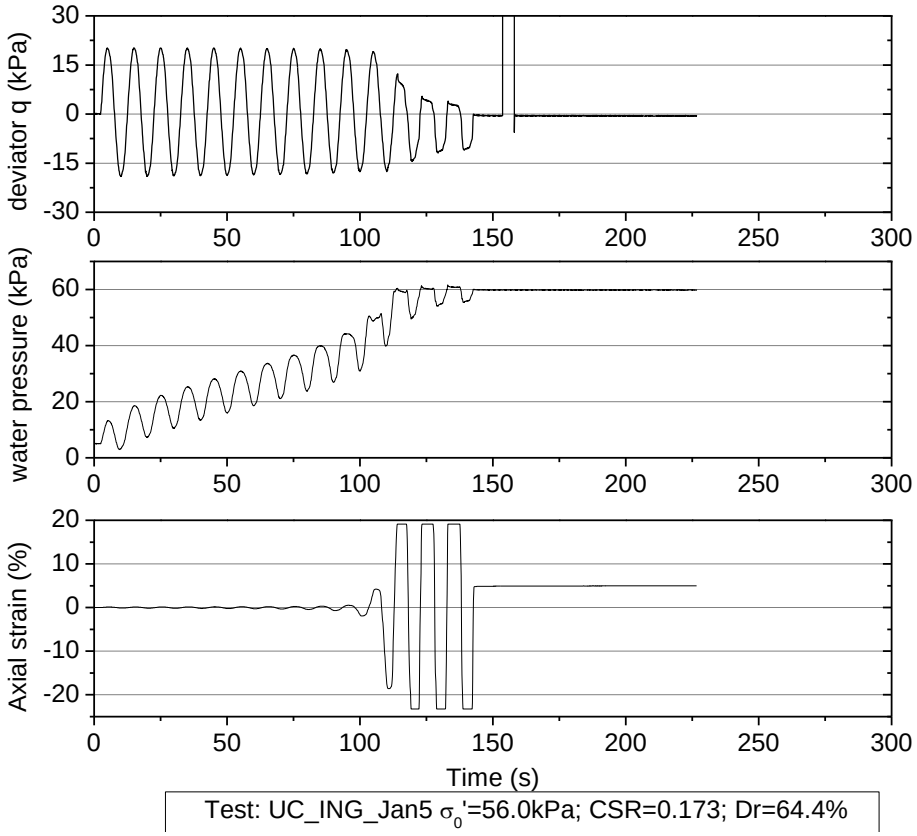

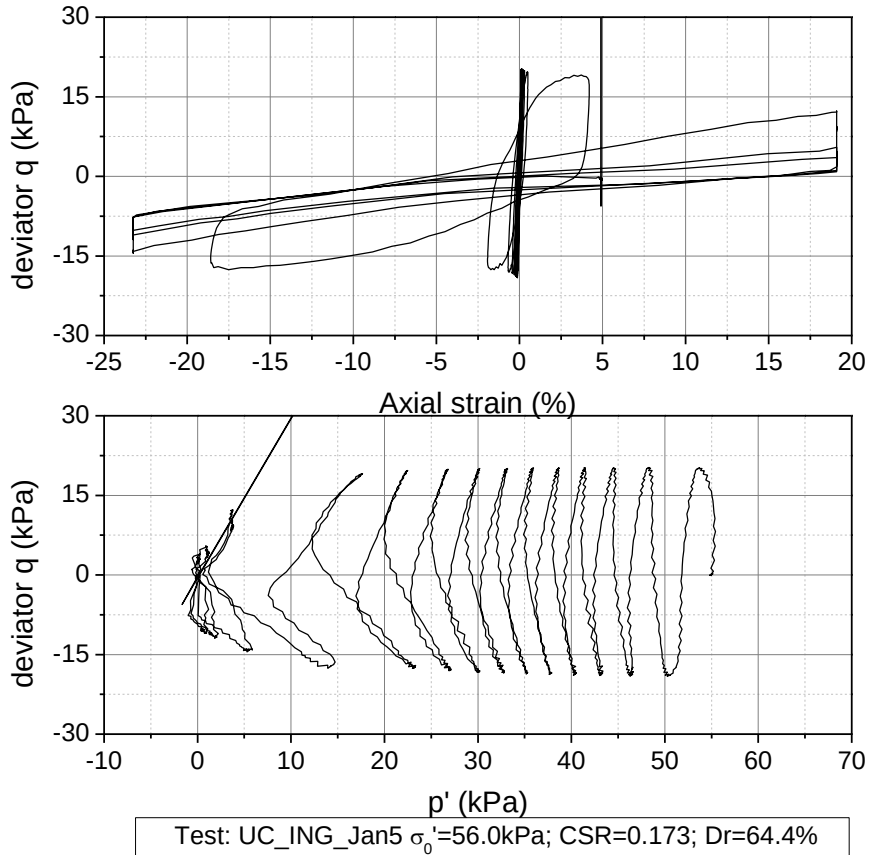

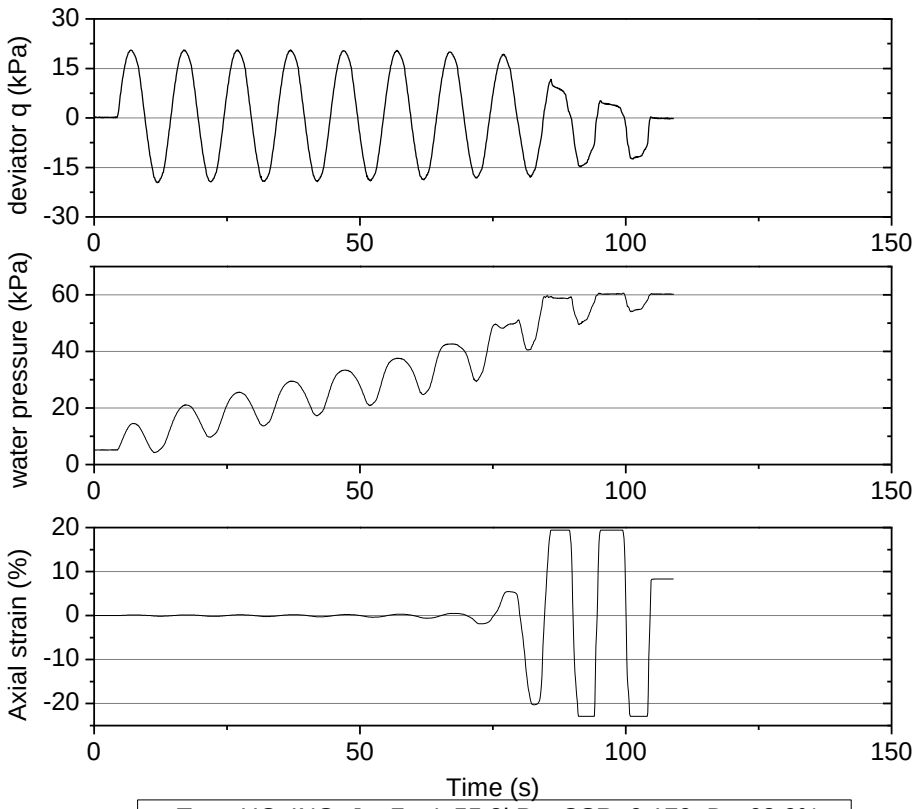

Test: UC_ING_Jan7 σ_0'=55.3kPa; CSR=0.179; Dr=63.9%

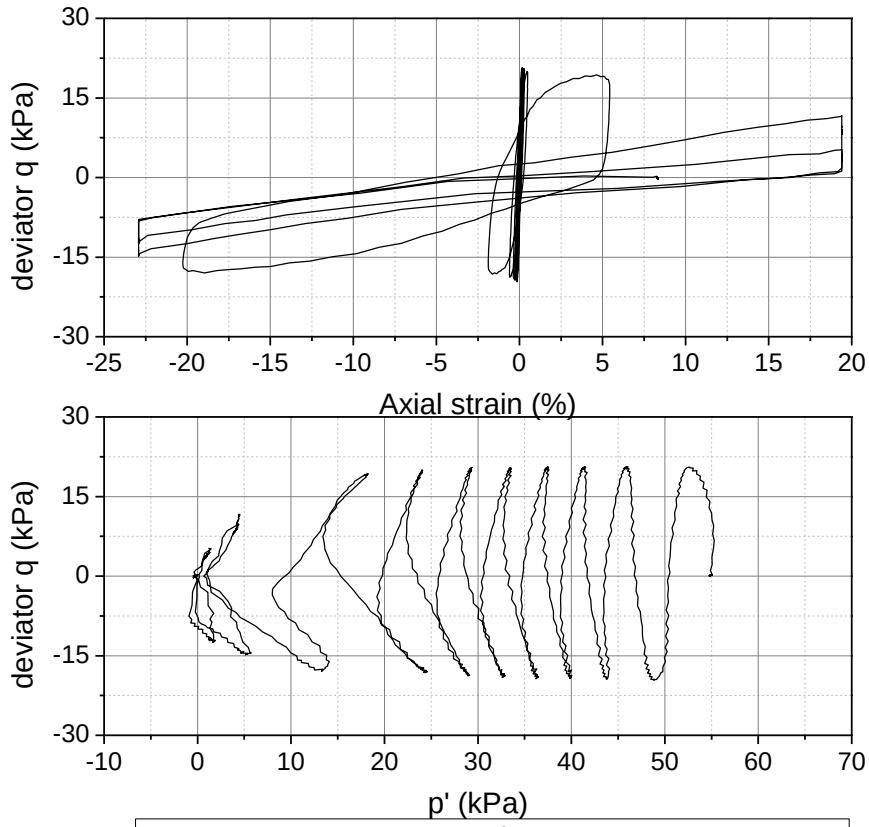

Test: UC_ING_Jan7 σ_0'=55.3kPa; CSR=0.179; Dr=63.9%

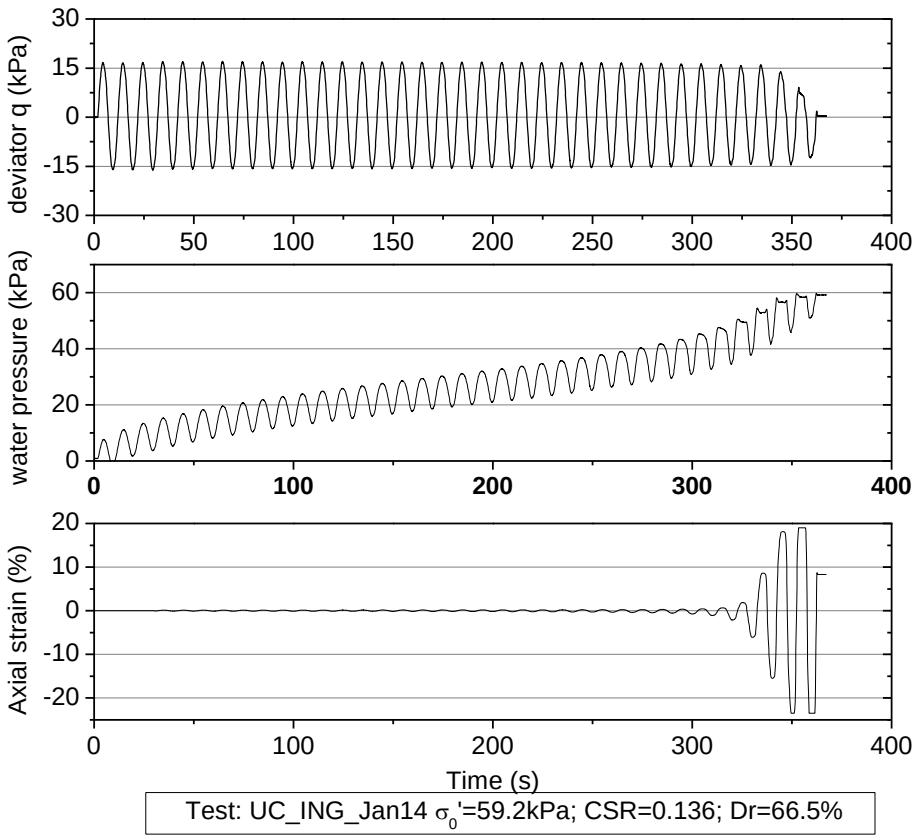
deviator q (kPa)
water pressure (kPa)
Axial strain (%)
Time (s)
Test: UC_ING_Jan14 σ0'=59.2kPa; CSR=0.136; Dr=66.5%

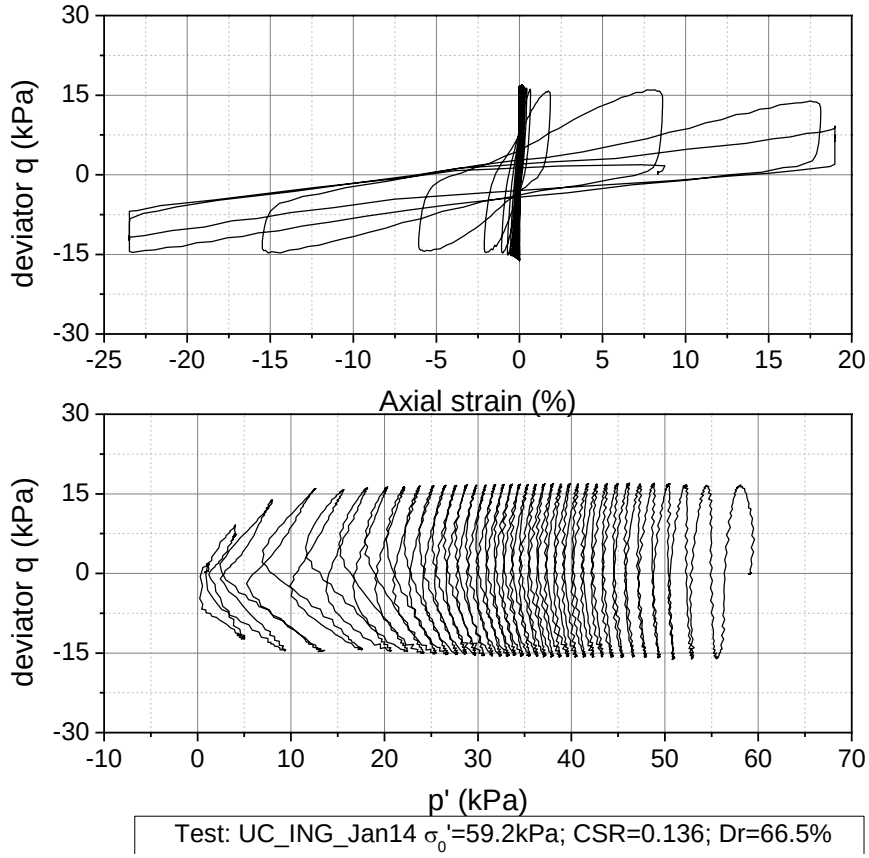
deviator q (kPa)
Axial strain (%)
deviator q (kPa)
p' (kPa)
Test: UC_ING_Jan14 σ0'=59.2kPa; CSR=0.136; Dr=66.5%

F-3 Unsaturated Inagi sand with Sr of 69%, p change in Set 3

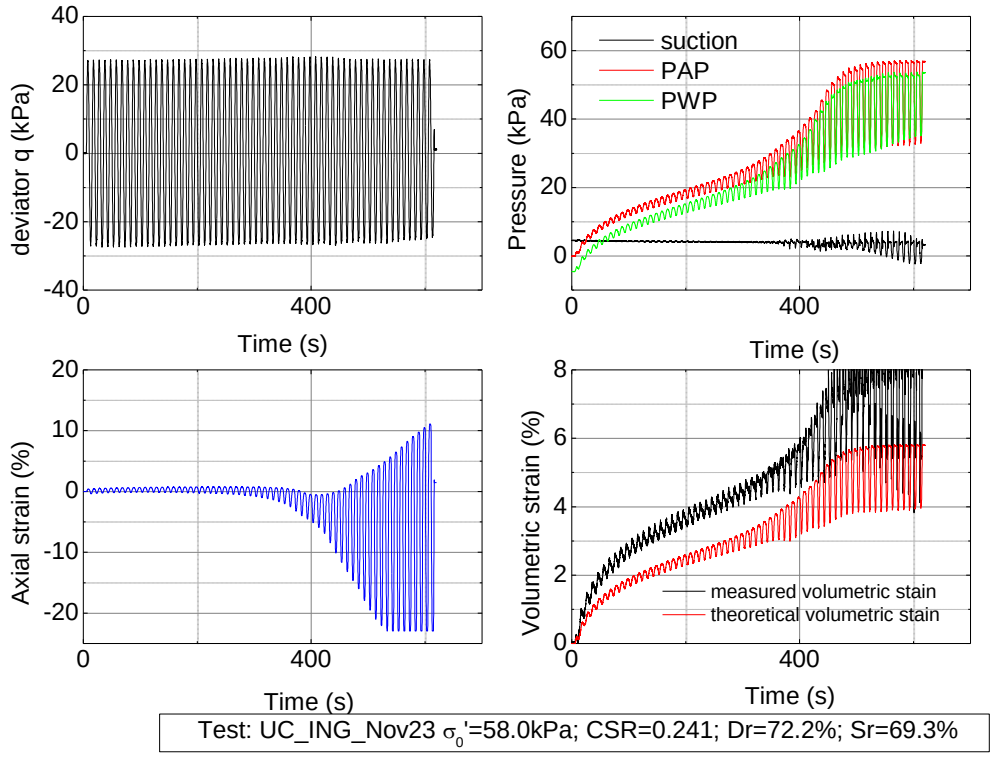

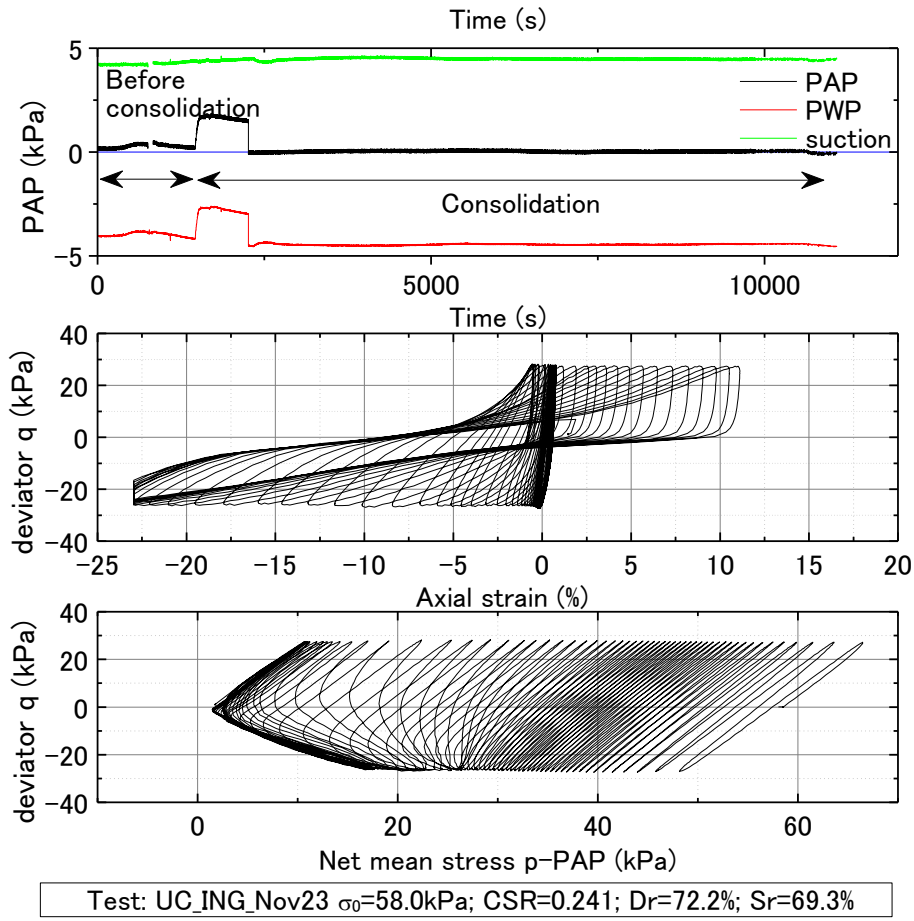

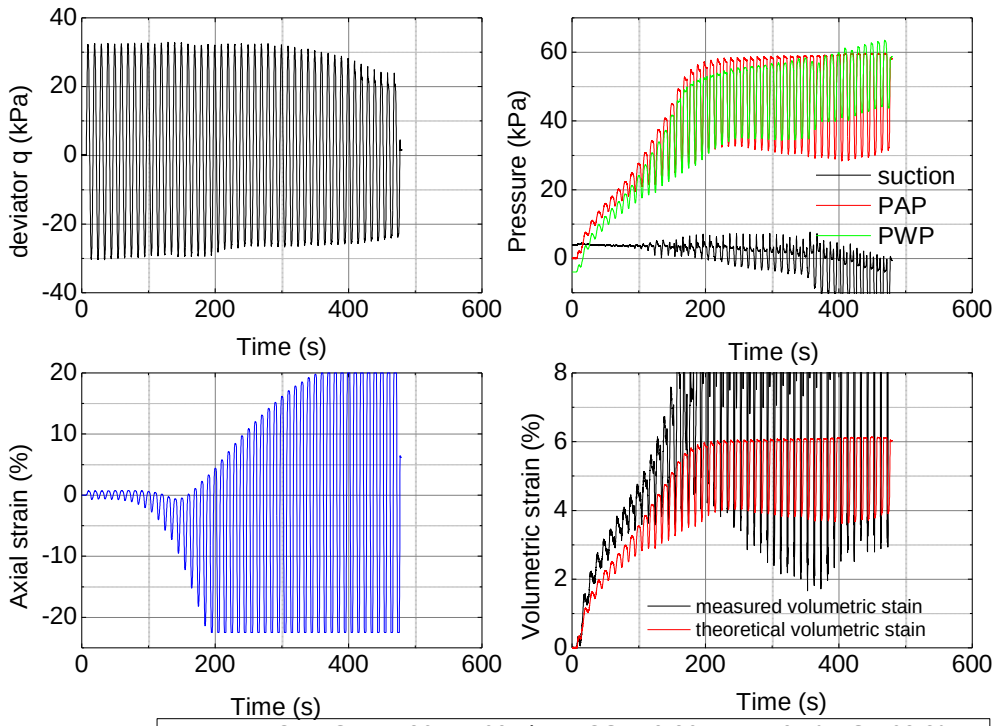

Test: UC_ING_Nov26 σ_0'=60.1kPa; CSR=0.264; Dr=70.4%; Sr=68.8%

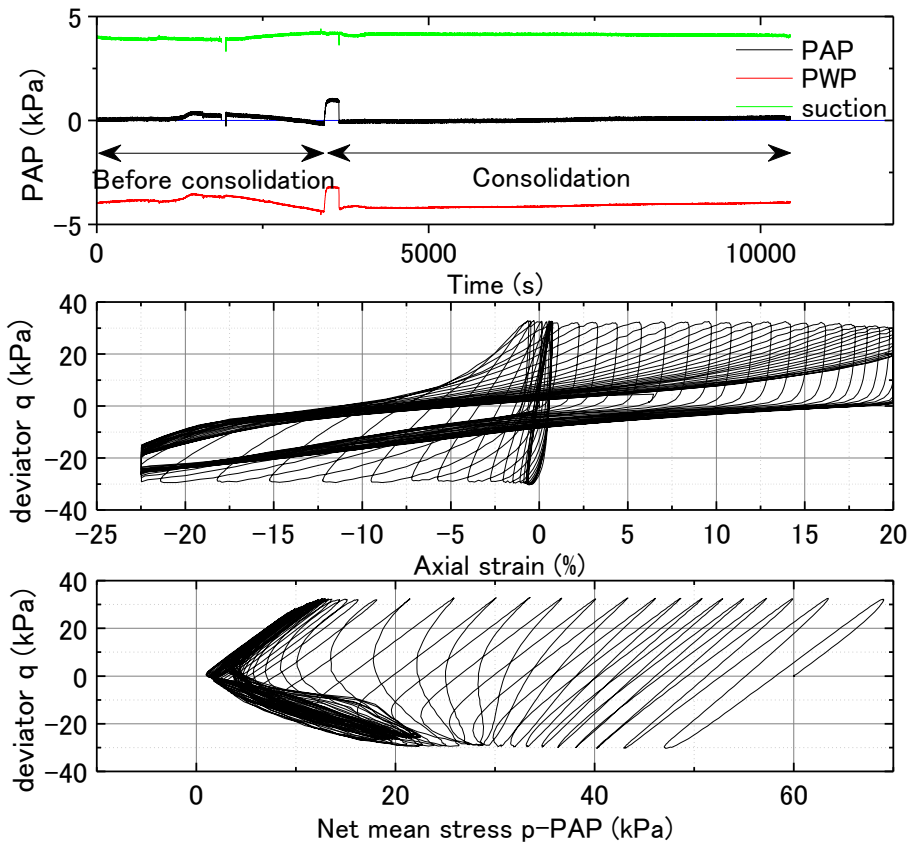

Test: UC_ING_Nov26 σ_0=60.1kPa; CSR=0.264; Dr=70.4%; Sr=68.8%

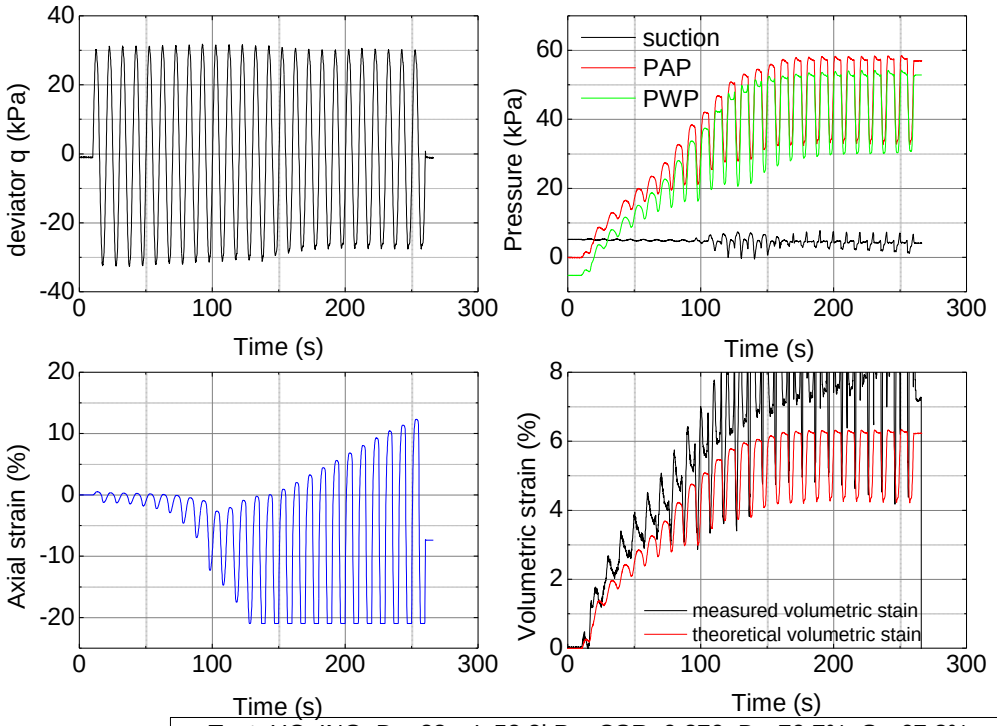

Test: UC_ING_Dec28 σ_0'=58.8kPa; CSR=0.270; Dr=70.7%; Sr=67.3%

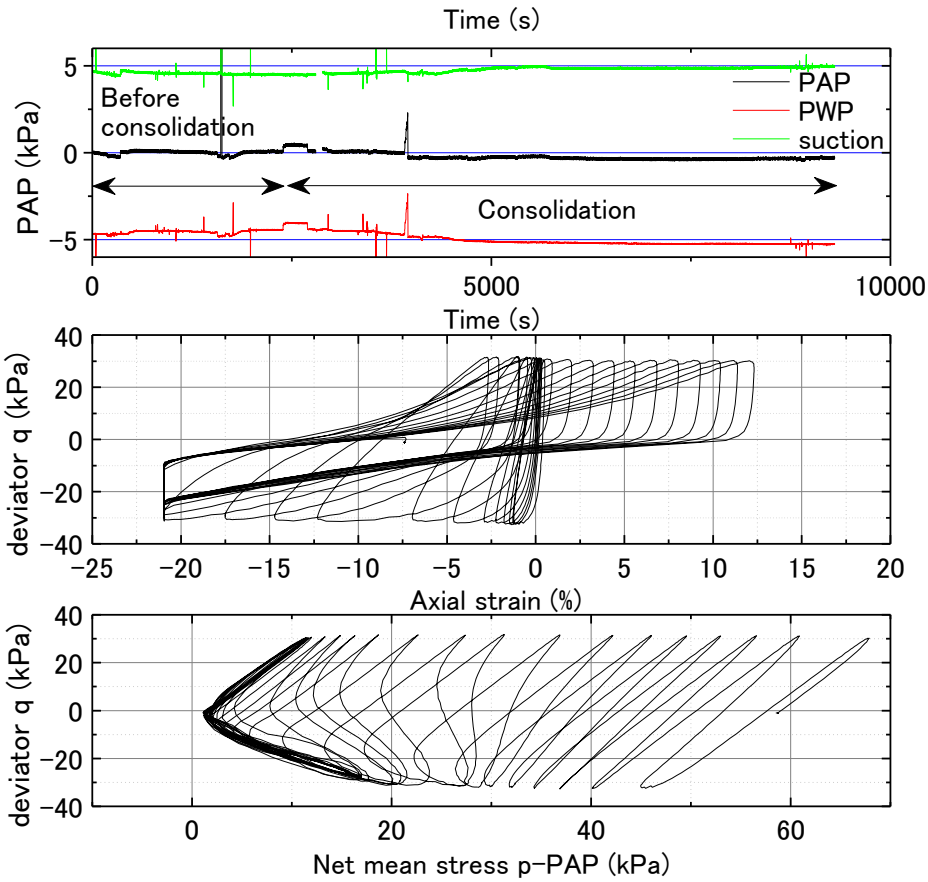

Test: UC_ING_Dec28 σ_0=58.8kPa; CSR=0.270; Dr=70.7%; Sr=67.3%

F-4 Unsaturated Inagi sand with Sr of 73%, p constant in Set 3

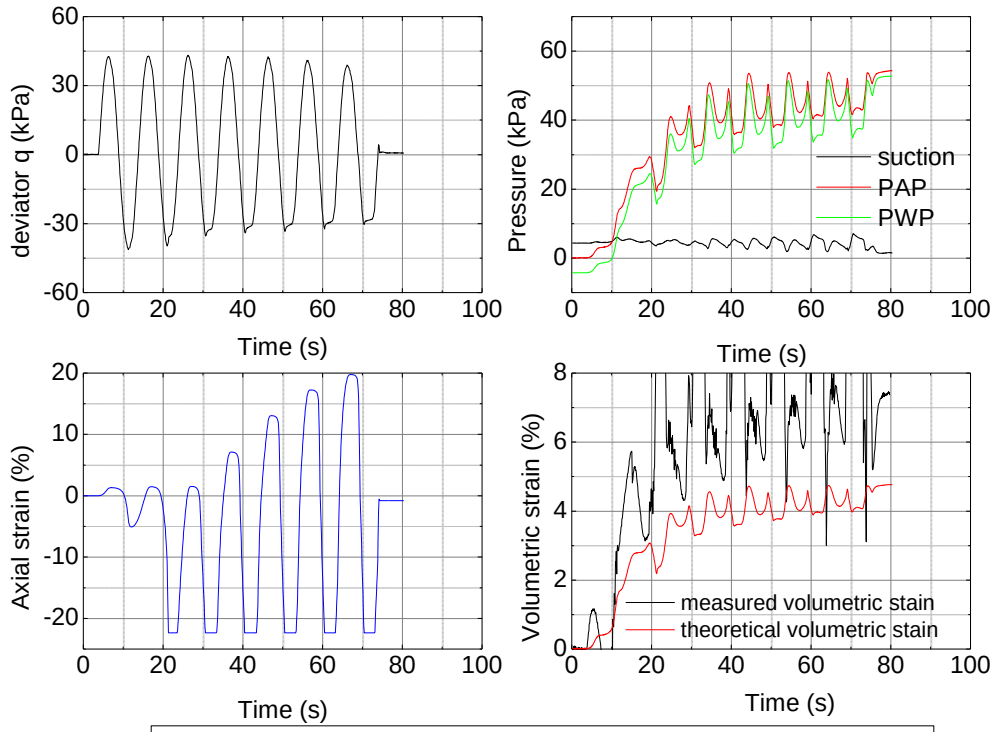

Test: UC_ING_Mar19 σ_0'=59.5kPa; CSR=0.354; Dr=73.7%; Sr=72.0%

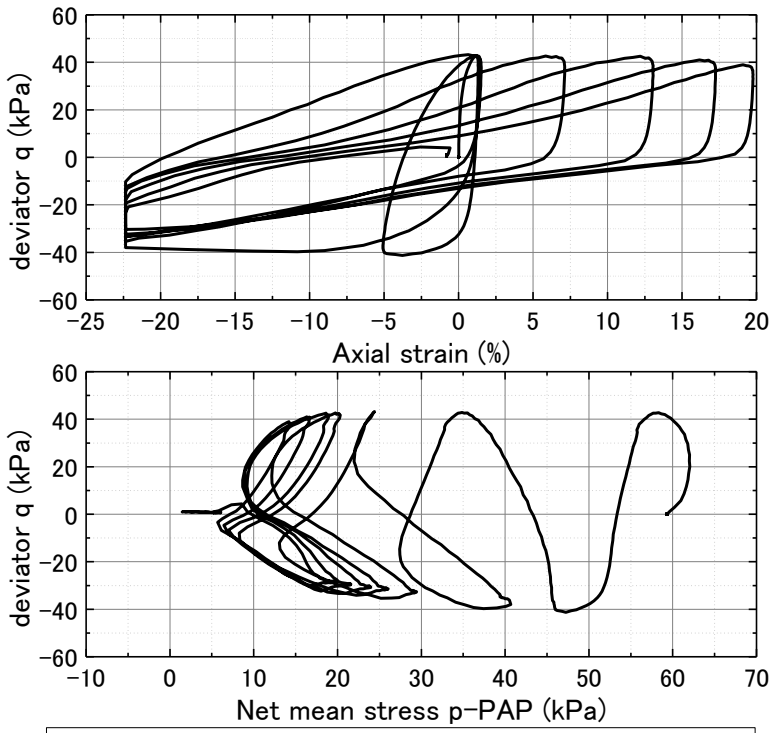

Test: UC_ING_Mar19 σ_0=59.5kPa; CSR=0.354; Dr=73.7%; Sr=72.0%

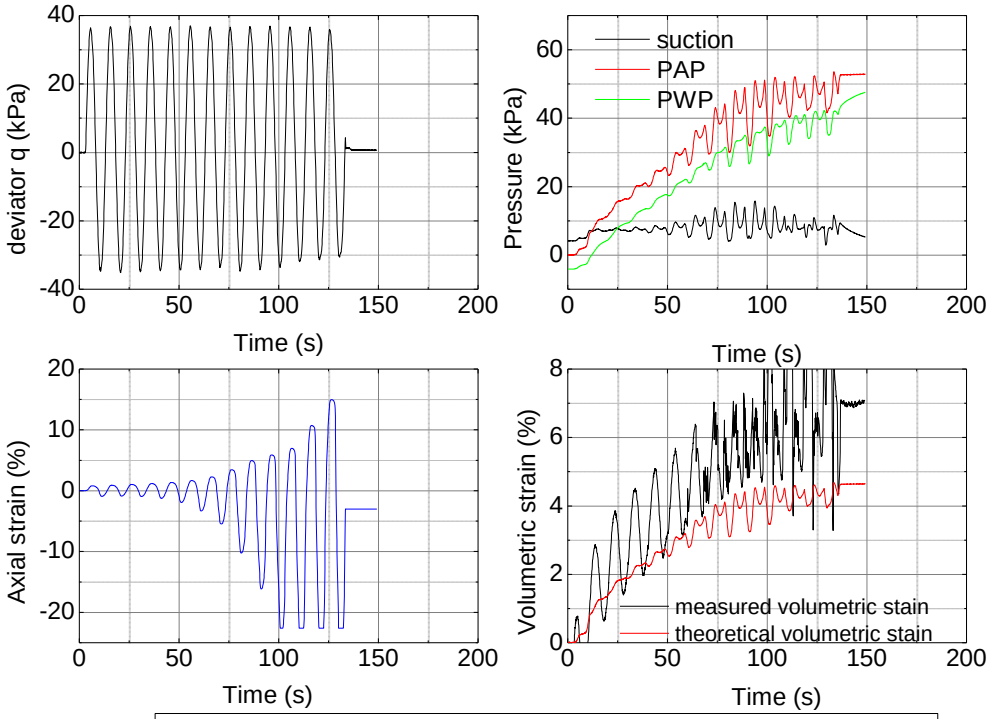

Test: UC_ING_Mar21 σ_0'=59.8kPa; CSR=0.299; Dr=73.7%; Sr=72.2%

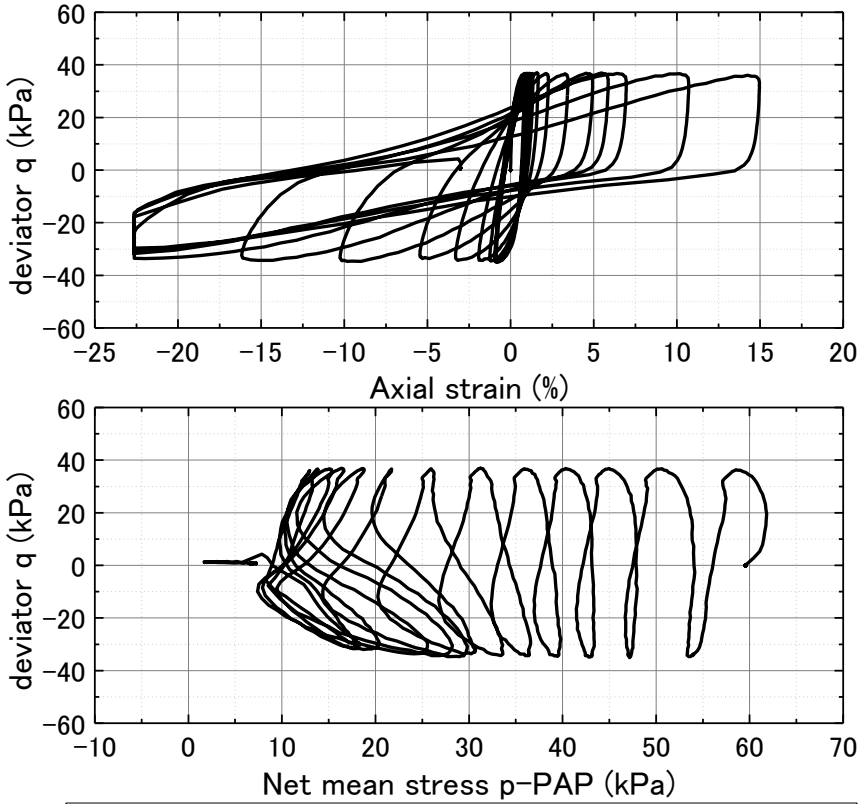

Test: UC_ING_Mar21 σ_0=59.8kPa; CSR=0.299; Dr=73.7%; Sr=72.2%

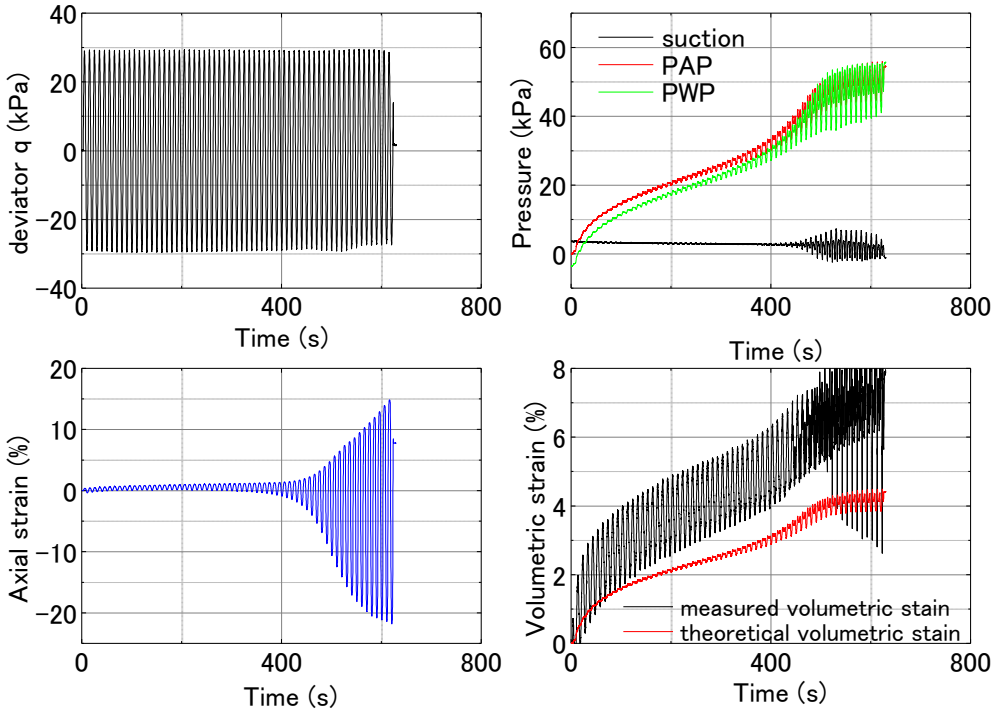

Test: UC_ING_Mar24 σ_0'=59.0kPa; CSR=0.248; Dr=77.0%; Sr=73.7%

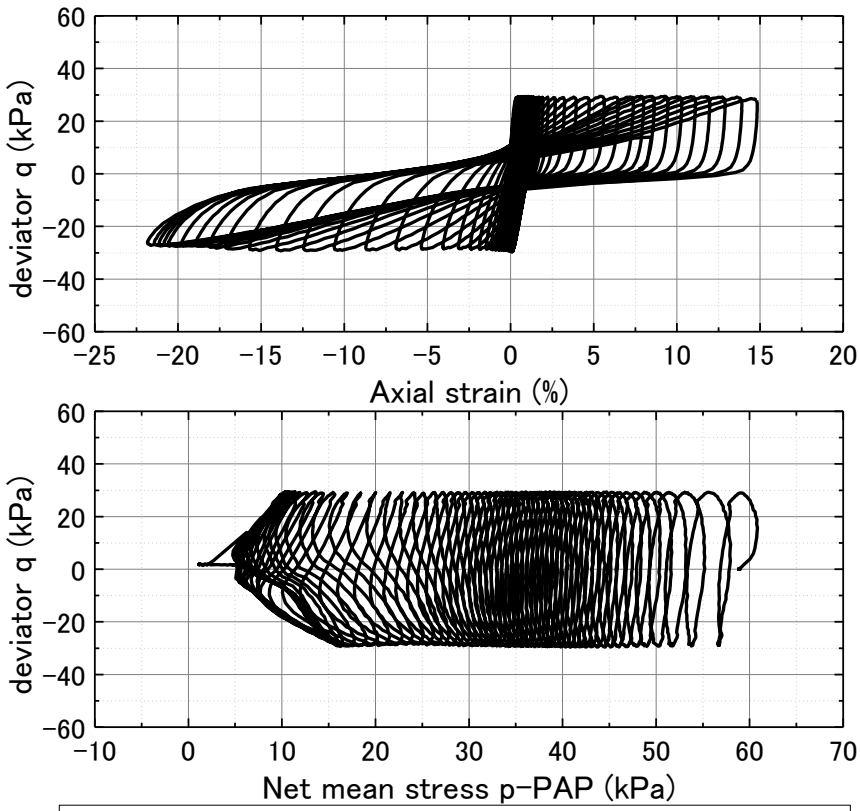

Test: UC_ING_Mar24 σ_0=59.0kPa; CSR=0.248; Dr=77.0%; Sr=73.7%

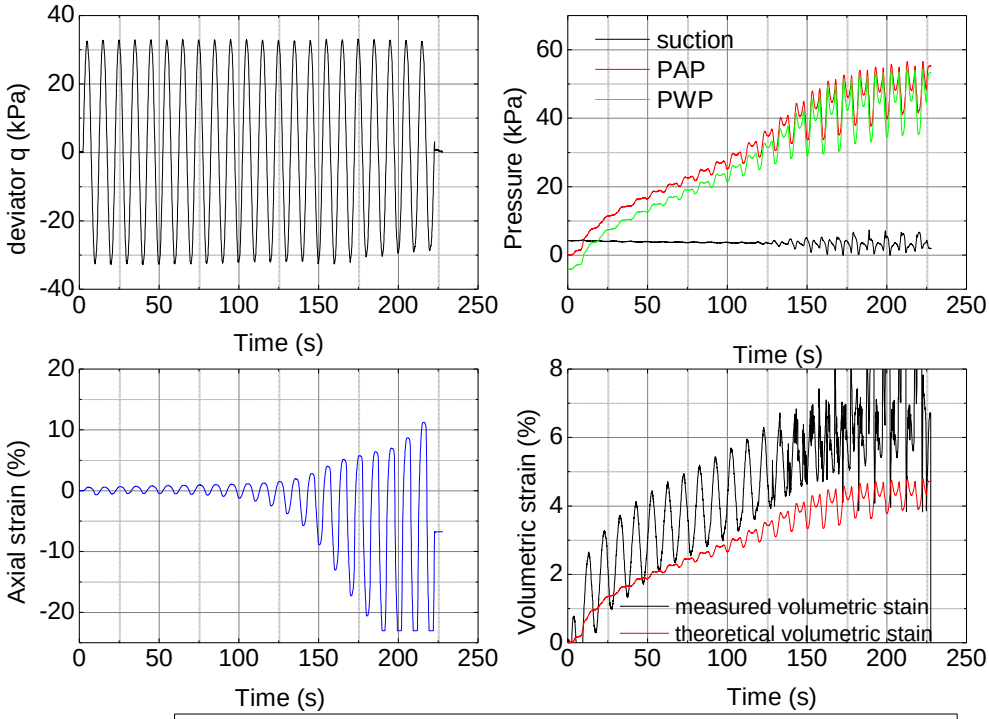

Test: UC_ING_Mar25 σ_0'=59.6kPa; CSR=0.274; Dr=78.1%; Sr=74.1%

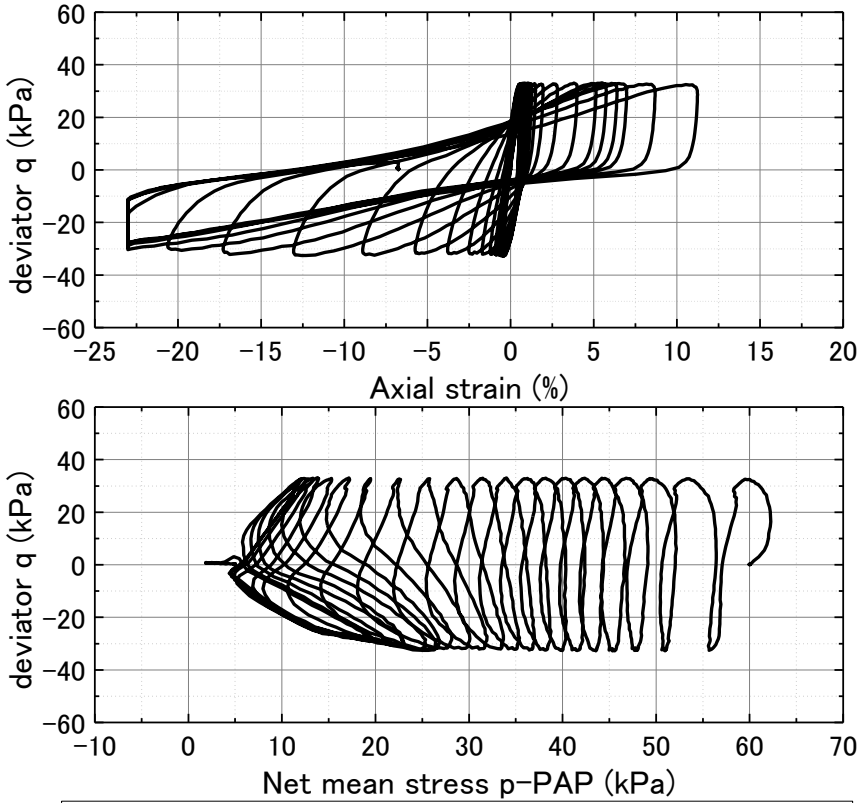

Test: UC_ING_Mar25 σ_0=59.6kPa; CSR=0.274; Dr=78.1%; Sr=74.1%

F-5 Unsaturated Inagi sand with Sr of 84%, p constant in Set 3

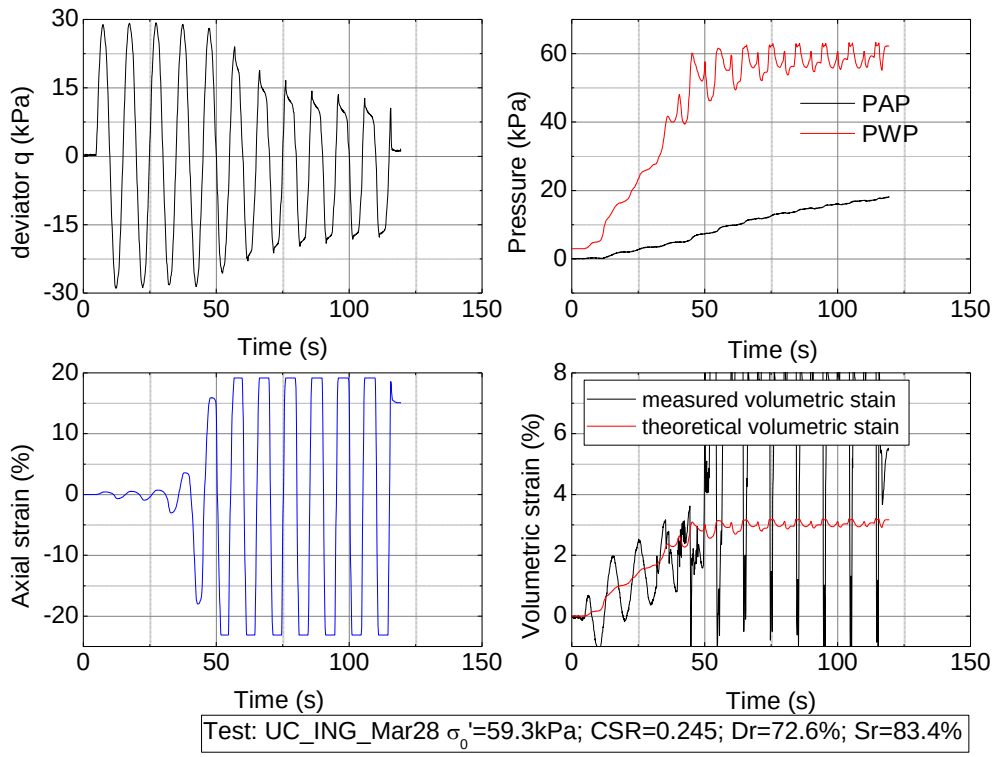

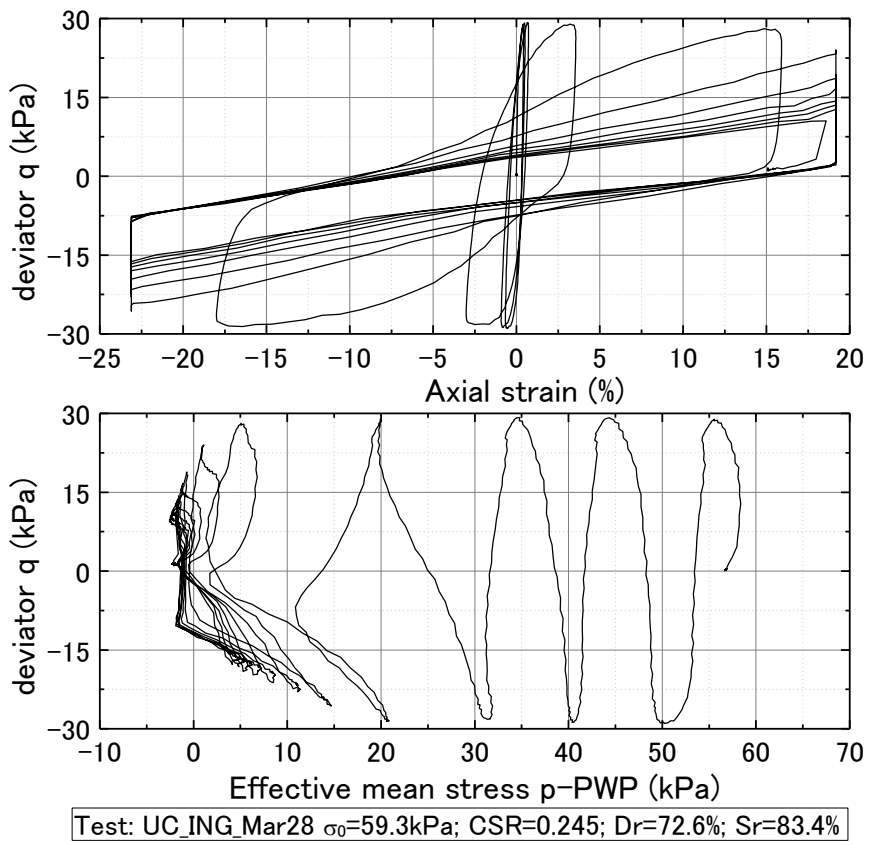

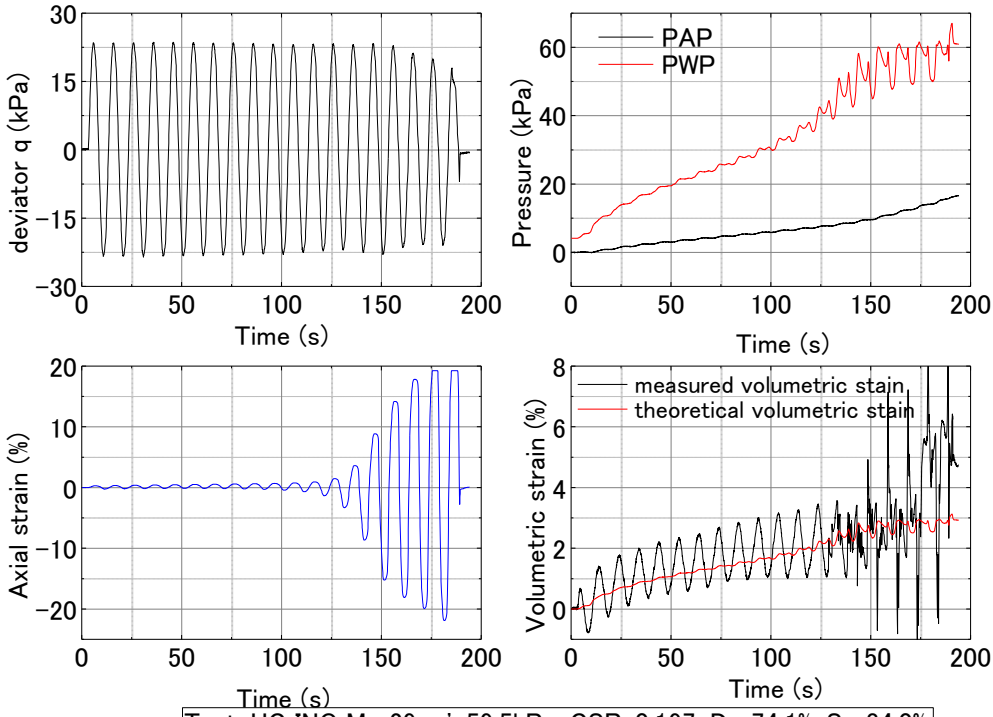

Test: UC_ING_Mar29 σ_0'=59.5kPa; CSR=0.197; Dr=74.1%; Sr=84.0%

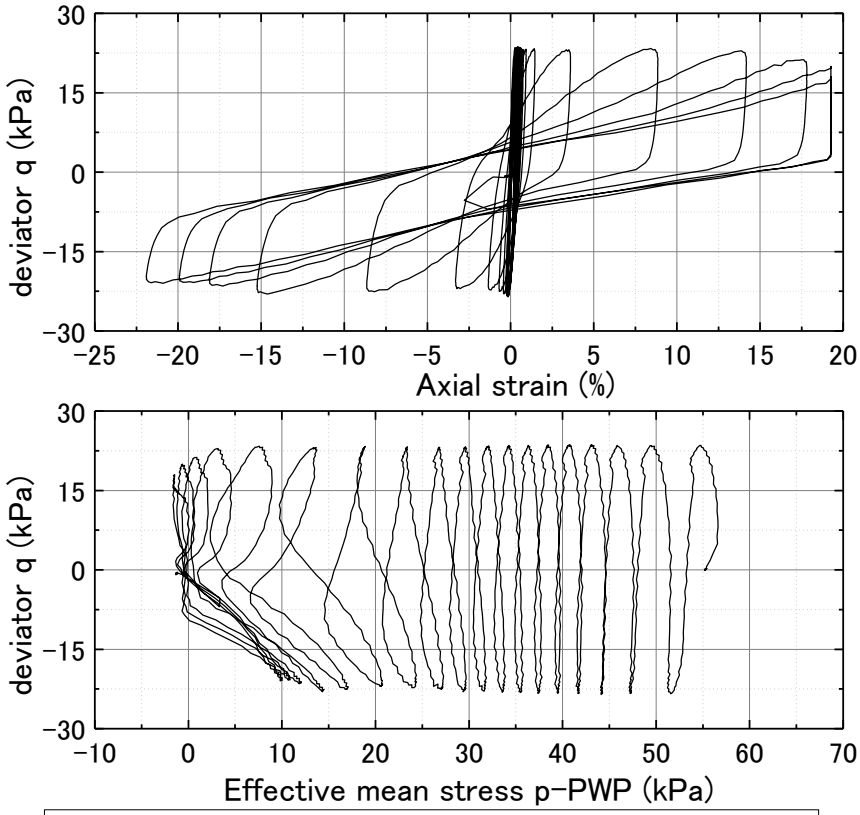

Test: UC_ING_Mar29 σ_0=59.5kPa; CSR=0.197; Dr=74.1%; Sr=84.0%

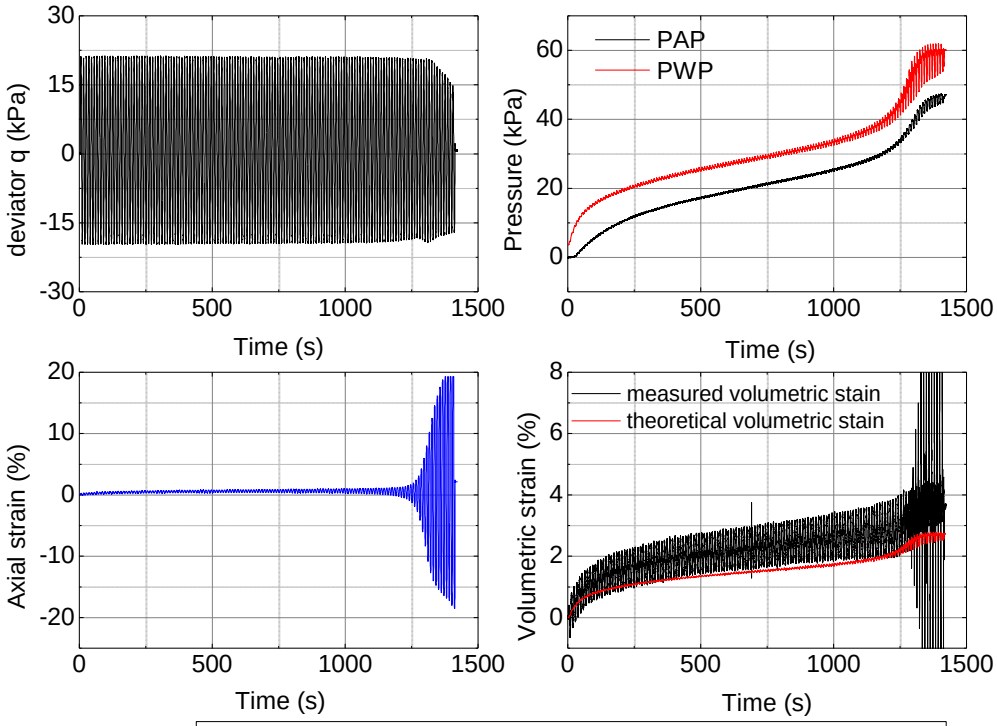

Test: UC_ING_Apr8 σ_0'=59.0kPa; CSR=0.172; Dr=78.3%; Sr=84.9%

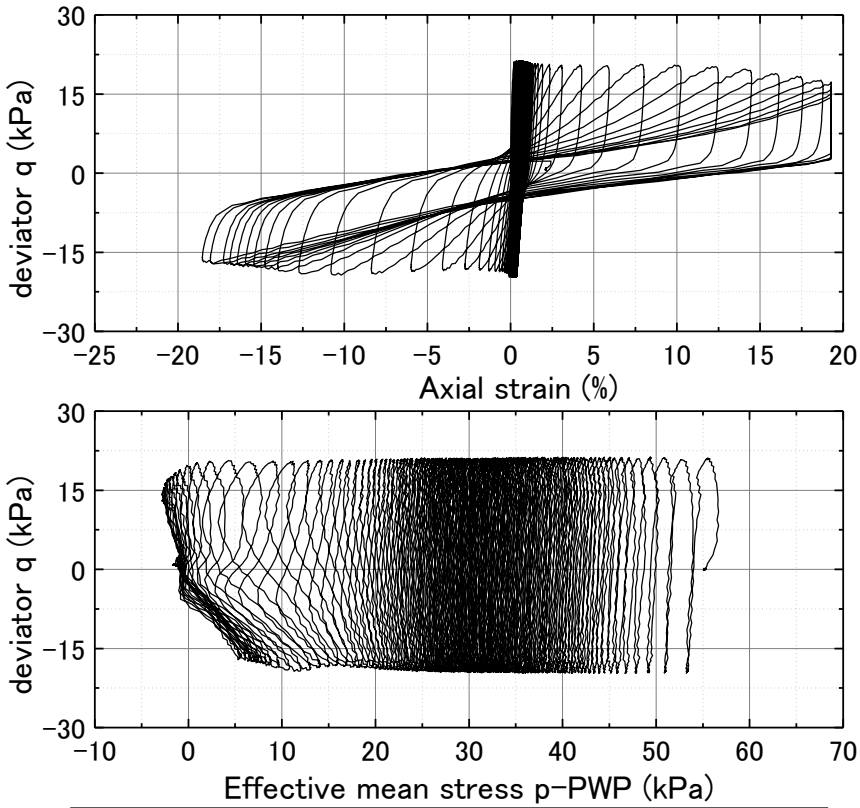

Test: UC_ING_Apr8 σ_0=59.0kPa; CSR=0.172; Dr=78.3%; Sr=84.9%

Appendix G.Undrained cyclic loading test for Iron ore fines type B

Results of undrained cyclic loading tests conducted on Toyoura snad, Inagi sand and iron ore fines type B (IOF-B) are summarized in Appendixes E, F and G, respectively. Each test is assigned a unique name, of which "UC_" is used to stand for undrained cyclic loading test. The test materials Toyoura sand, Inagi sand and IOF-B are substituted by "T", "ING" and "IOF-B" in the test name for short. There is an information bar at the bottom of each figure to indicate the name and conditions of the test.

Tables G-1 and G-2 summarize the test conditions of all tests conducted on saturated and unsaturated IOF-B, respectively. Symbols in Table G-1 and G-2 are stand for:

e, ρ_d and Dc: void ration, dry density and compection degree after consolidation;

CSR: cyclic stress ratio (=$\sigma_d/2\sigma_0$', σ_d is single amplitude of cyclic loading);

$N_{DA=5\%}$: number of cycle which causes 5% double amplitude of axial strain;

σ_0': confining pressure before applying cyclic loading;

Sr: degree of saturation after consolidation;

$\varepsilon^*_{vol,air}$: maximum volumetric strain caused by pore air compression;

B: pore water pressure B;

Set: number of set classified in Table 5-3

Table G-1 Summary of test condition of saturated IOF-B

test Name	e	ρ_d (g/cm^3)	Dc (%)	σ_0'(kPa)	$N_{DA=5\%}$	CSR	Set
UC_IOF-B_Feb6	0.737	2.56	91.9	97.5	22.8	0.258	4
UC_IOF-B_Feb8	0.722	2.58	92.7	98.2	213.6	0.200	
UC_IOF-B_Feb11	0.724	2.58	92.6	98.9	23.3	0.304	
UC_IOF-B_Feb12	0.725	2.58	92.5	97.2	10.7	0.358	
UC_IOF-B_Feb13	0.733	2.56	92.1	98.7	46.8	0.251	
UC_IOF-B_Feb17	0.717	2.59	92.9	98.7	14.7	0.396	
UC_IOF-B_Feb19	0.729	2.57	92.3	98.8	4.5	0.504	
UC_IOF-B_Jul1	1.015	2.21	79.2	100.2	1.6	0.171	5
UC_IOF-B_Jul3	0.984	2.24	80.4	100.7	4.6	0.152	
UC_IOF-B_Jul4	1.030	2.19	78.6	100.2	19.7	0.119	
UC_IOF-B_Aug19	0.701	2.61	93.8	50.2	34.8	0.300	6
UC_IOF-B_Aug21	0.744	2.55	91.5	51.2	16.7	0.346	
UC_IOF-B_Aug22	0.751	2.54	91.1	51.3	6.5	0.444	
UC_IOF-B_Sep10	1.064	2.15	77.3	50.2	27.1	0.104	7
UC_IOF-B_Sep12	1.135	2.08	74.7	50.5	7.1	0.131	
UC_IOF-B_Sep17	0.937	2.29	82.4	50.5	6.1	0.140	
UC_IOF-B_Sep18	0.973	2.25	80.9	49.5	35.3	0.112	

Table G-2 Summary of test condition of unsaturated IOF-B

test Name	e	ρ_d	Dc (%)	σ_0' (kPa)	$N_{DA=5\%}$	CSR	Sr (%)	$\varepsilon^*_{vol,air}$ (%)	Set
UC_IOF-B_Jun12-1	0.720	2.58	92.7	100.5	25.7	0.540	71.8	5.86	4
UC_IOF-B_Jun12-2	0.719	2.59	92.8	99.5	10.6	0.562	72.1	5.79	
UC_IOF-B_Jun13	0.722	2.58	92.7	99.4	2.6	0.572	73.3	5.57	
UC_IOF-B_Jun17-2	0.710	2.60	93.3	99.2	4.8	0.525	83.2	3.47	4
UC_IOF-B_Jun19	0.709	2.60	93.4	99.0	9.7	0.495	83.8	3.34	
UC_IOF-B_Jun21	0.698	2.62	93.9	99.6	27.4	0.465	84.4	3.20	
UC_IOF-B_Jun26	0.925	2.31	82.9	99.1	20.7	0.201	75.2	5.91	5
UC_IOF-B_Jun27	0.908	2.33	83.6	99.4	465.2	0.159	76.8	5.48	
UC_IOF-B_Jun28-1	0.897	2.34	84.1	99.0	3.9	0.229	75.8	5.70	
UC_IOF-B_Aug7	0.720	2.58	92.8	49.5	104.6	0.479	81.9	3.76	6
UC_IOF-B_Aug8	0.719	2.58	92.8	49.2	78.9	0.501	80.0	4.16	
UC_IOF-B_Aug12	0.721	2.58	92.7	49.8	119.7	0.517	77.1	4.76	
UC_IOF-B_Aug13	0.721	2.58	92.7	49.8	20.7	0.525	77.9	4.60	
UC_IOF-B_Aug17	0.724	2.58	92.6	49.7	17.1	0.534	81.4	3.88	
UC_IOF-B_Aug4	0.951	2.28	81.8	50.4	74.8	0.192	70.9	7.04	7
UC_IOF-B_Aug6	0.946	2.28	82.0	49.3	7.6	0.208	71.8	6.81	

G-1 Saturated IOF-B in Set 4

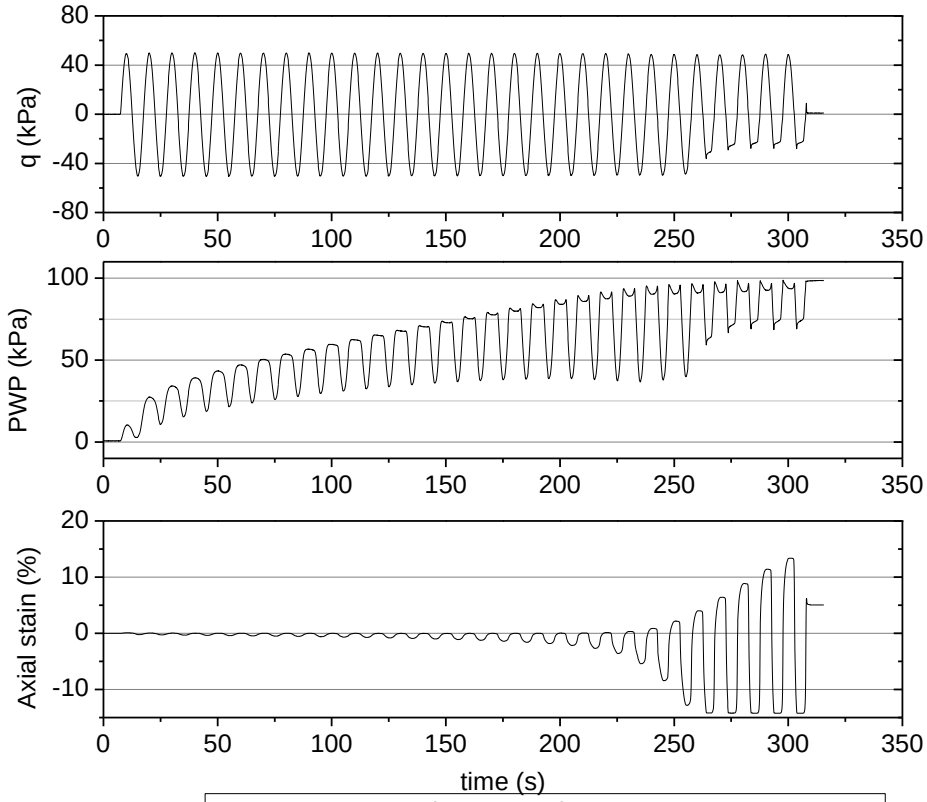

Test: UC_IOF-B_Feb6 σ_0'=97.5kPa; CSR=0.258; Dc=91.9%

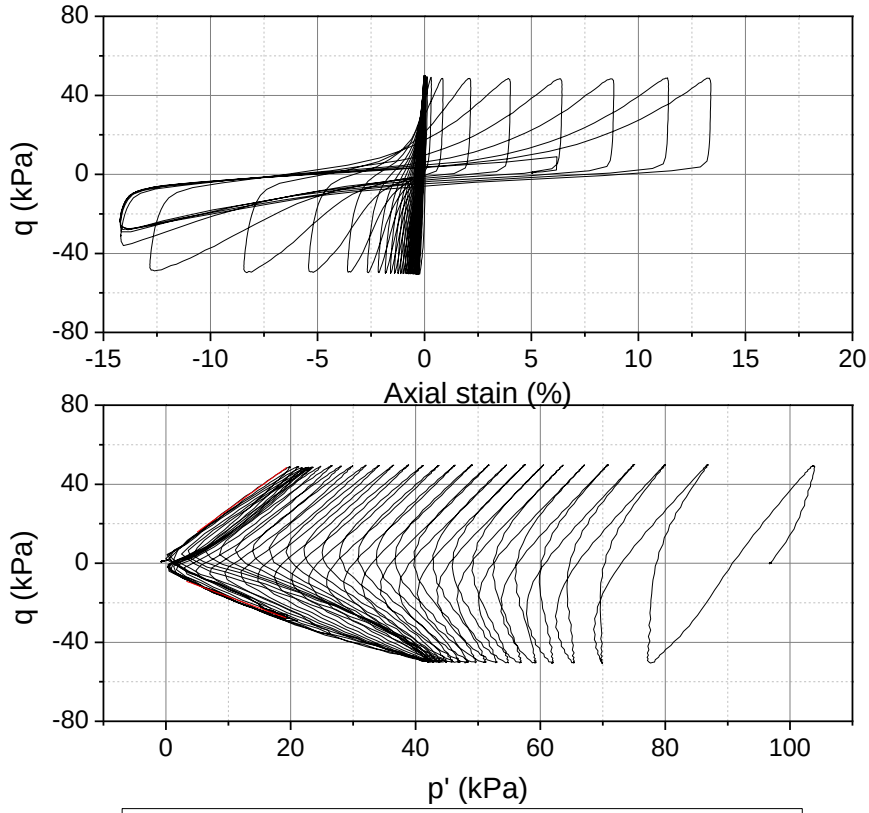

Test: UC_IOF-B_Feb6 σ_0'=97.5kPa; CSR=0.258; Dc=91.9%

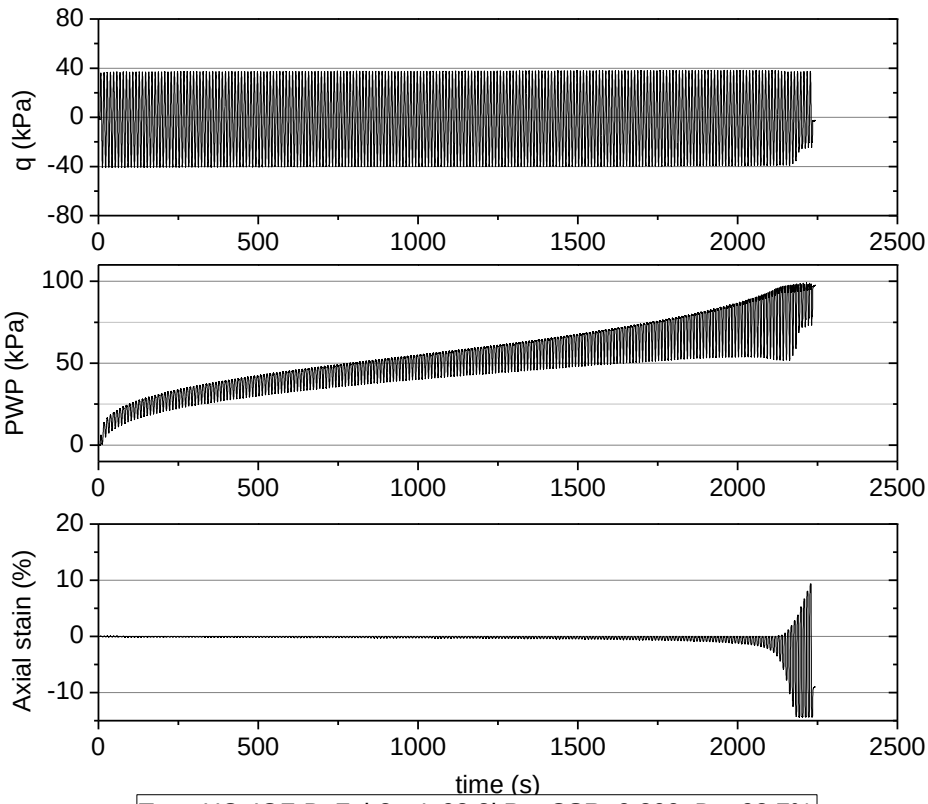

Test: UC_IOF-B_Feb8 σ_0'=98.2kPa; CSR=0.200; Dc=92.7%

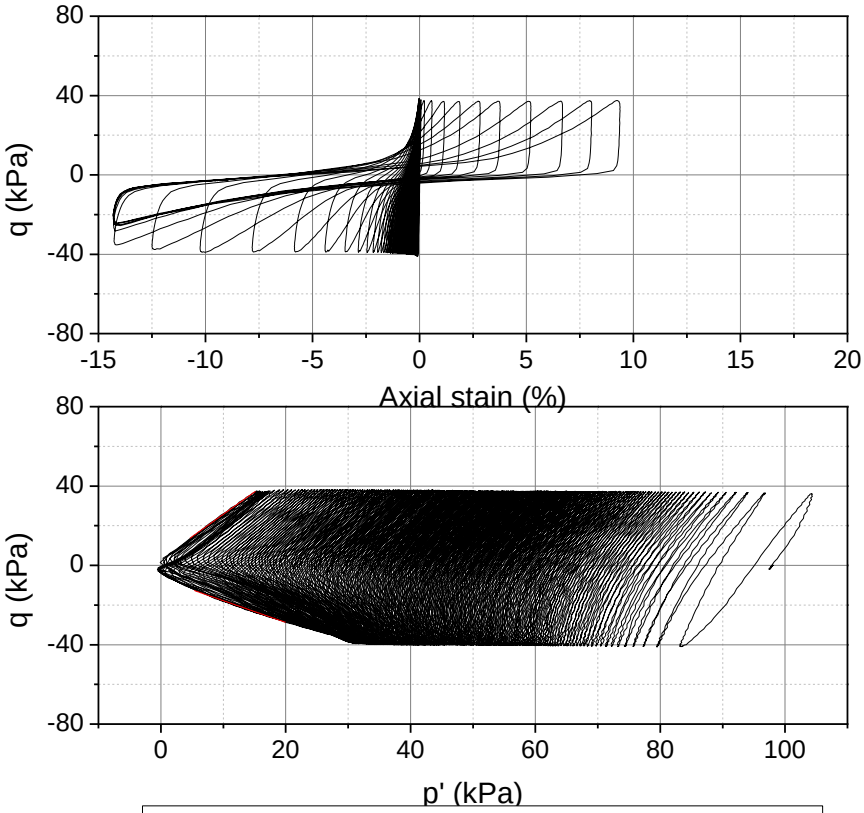

Test: UC_IOF-B_Feb8 σ_0'=98.2kPa; CSR=0.200; Dc=92.7%

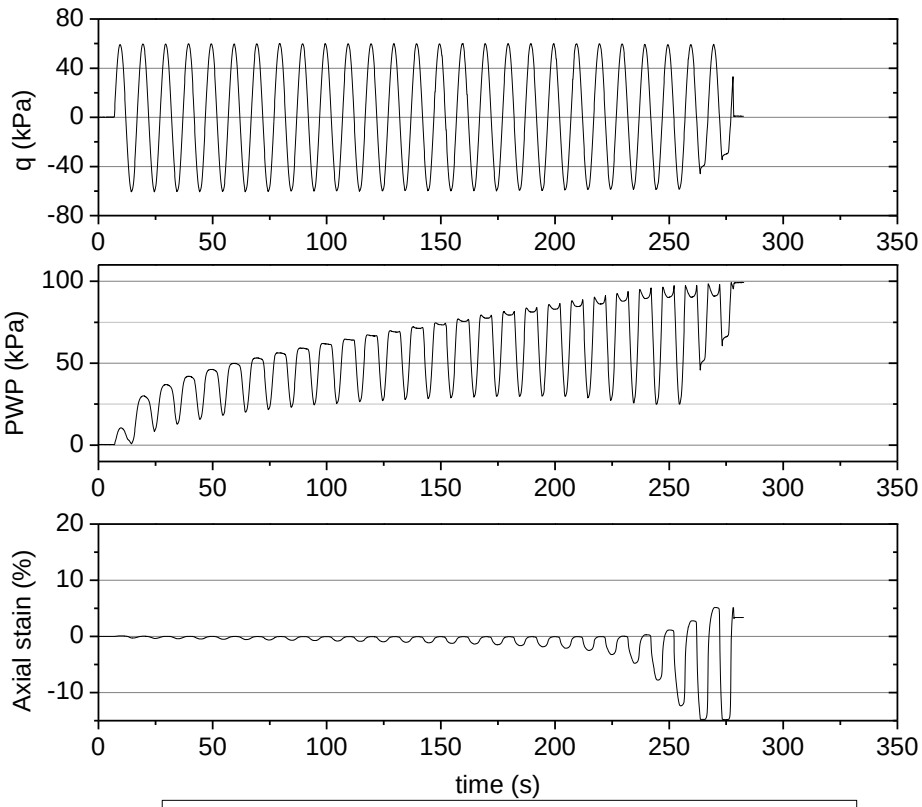

Test: UC_IOF-B_Feb11 σ_0'=98.9kPa; CSR=0.304; Dc=92.6%

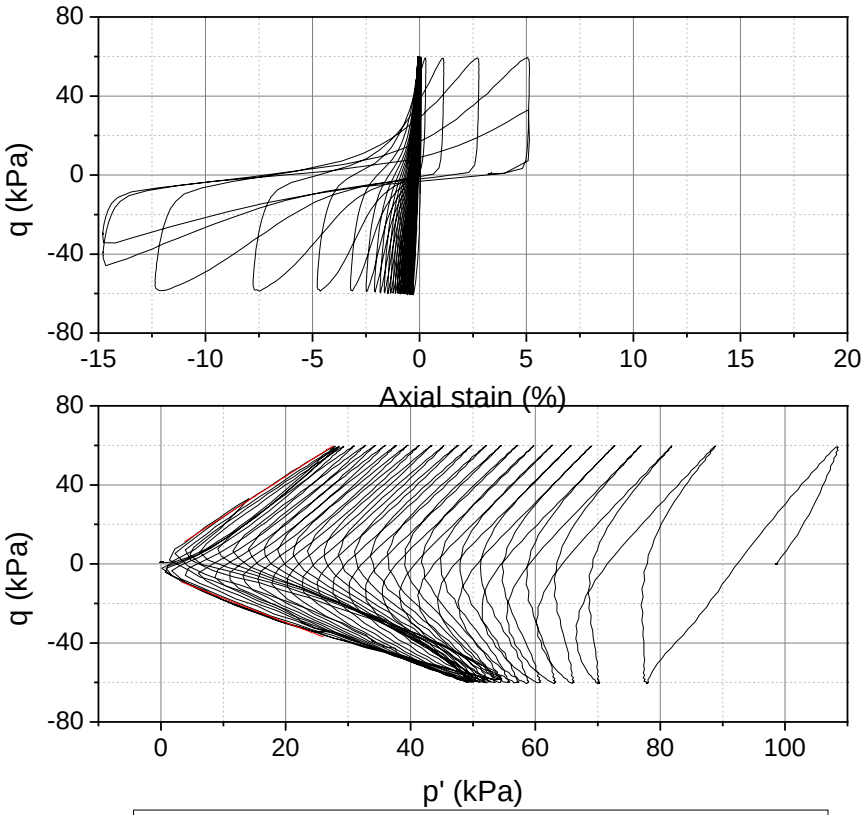

Test: UC_IOF-B_Feb11 σ_0'=98.9kPa; CSR=0.304; Dc=92.6%

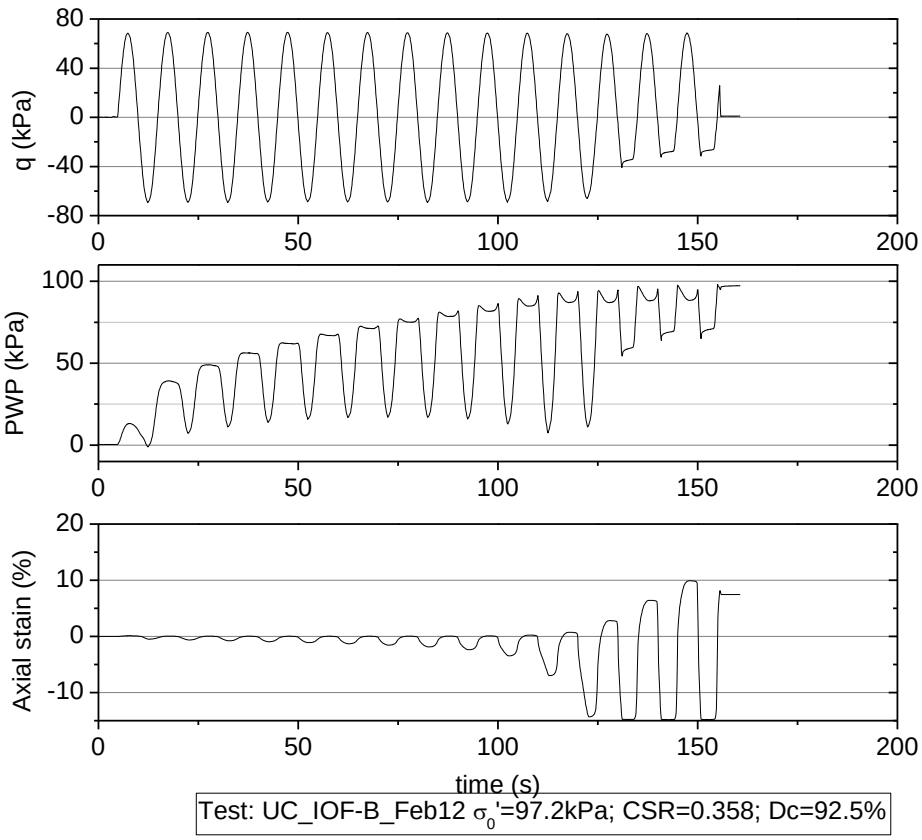
q (kPa)
PWP (kPa)
Axial stain (%)
time (s)
Test: UC_IOF-B_Feb12 σ0'=97.2kPa; CSR=0.358; Dc=92.5%

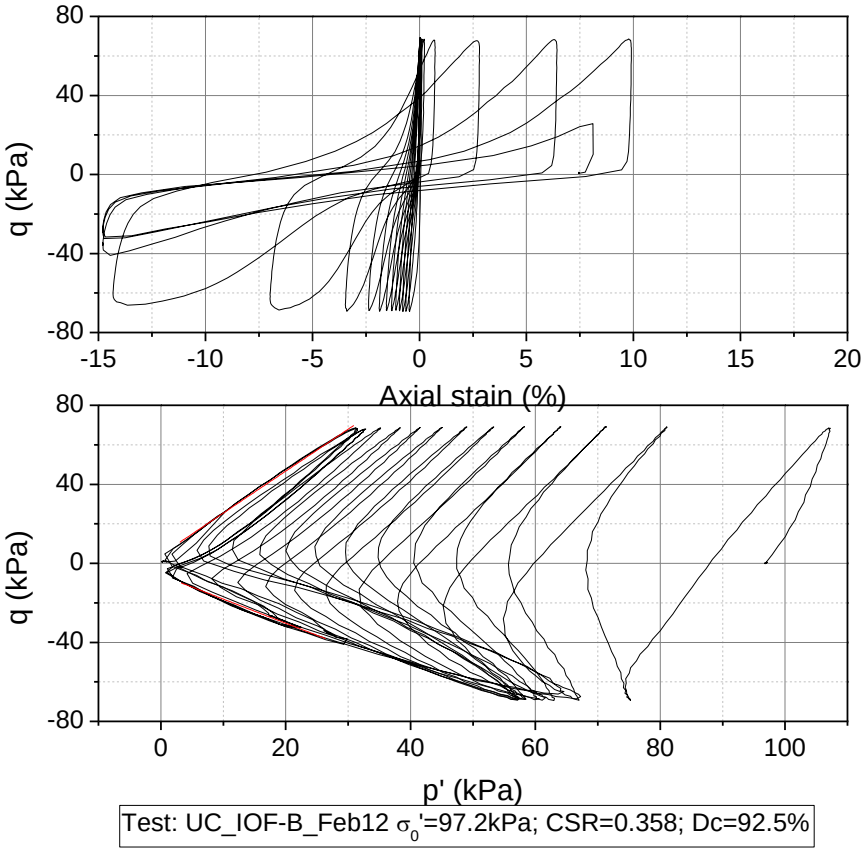
q (kPa)
Axial stain (%)
q (kPa)
p' (kPa)
Test: UC_IOF-B_Feb12 σ0'=97.2kPa; CSR=0.358; Dc=92.5%

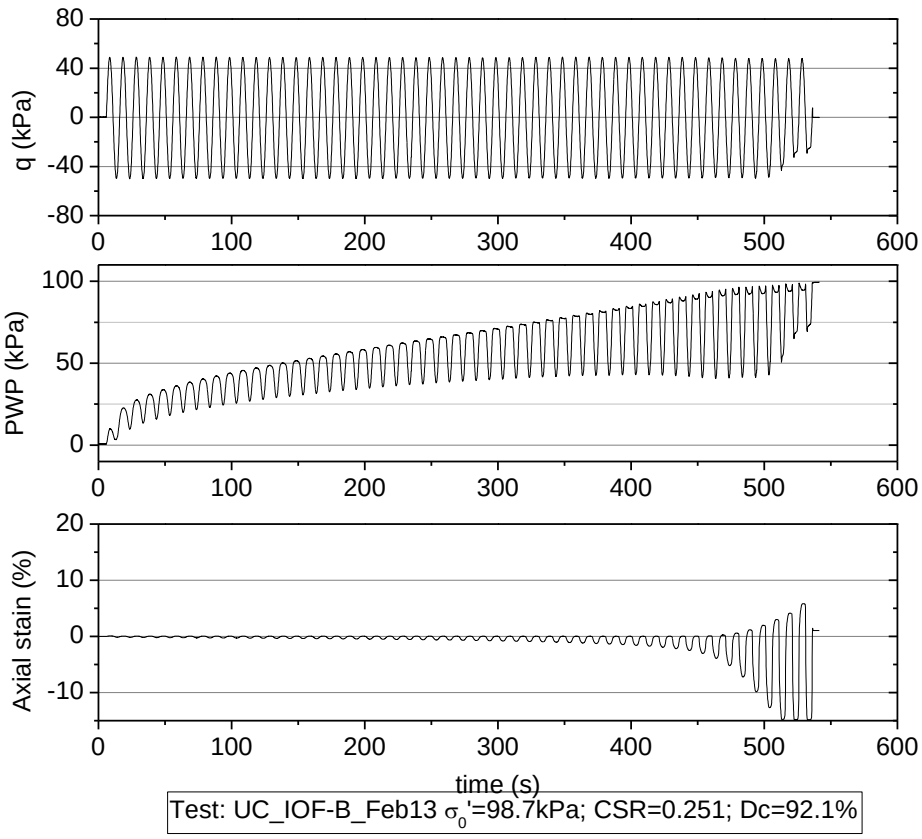

Test: UC_IOF-B_Feb13 σ_0'=98.7kPa; CSR=0.251; Dc=92.1%

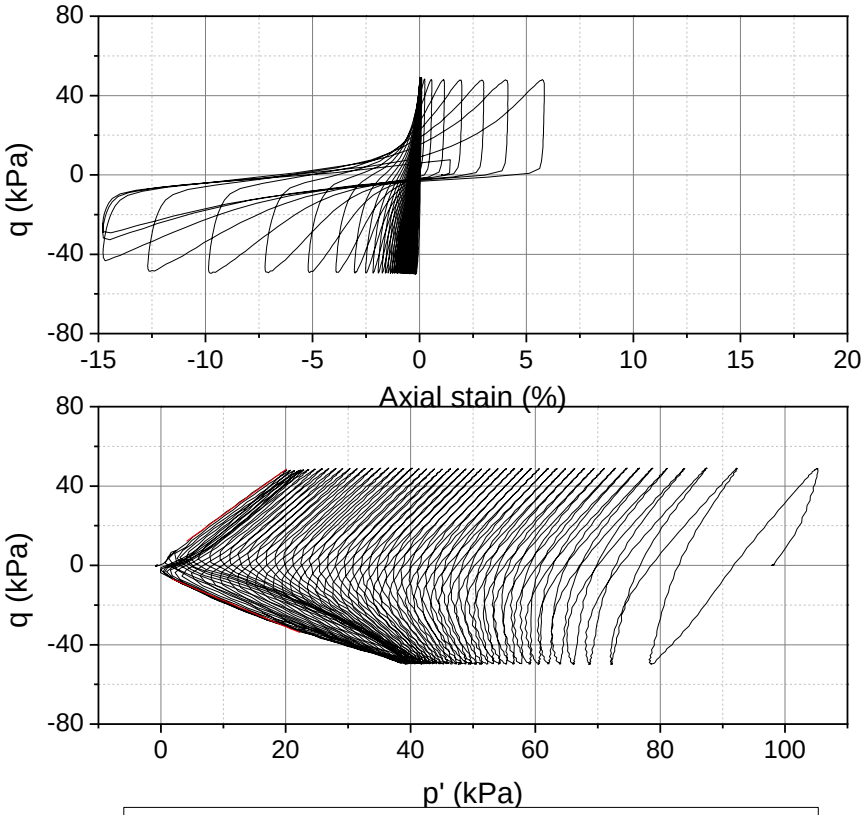

Test: UC_IOF-B_Feb13 σ_0'=98.7kPa; CSR=0.251; Dc=92.1%

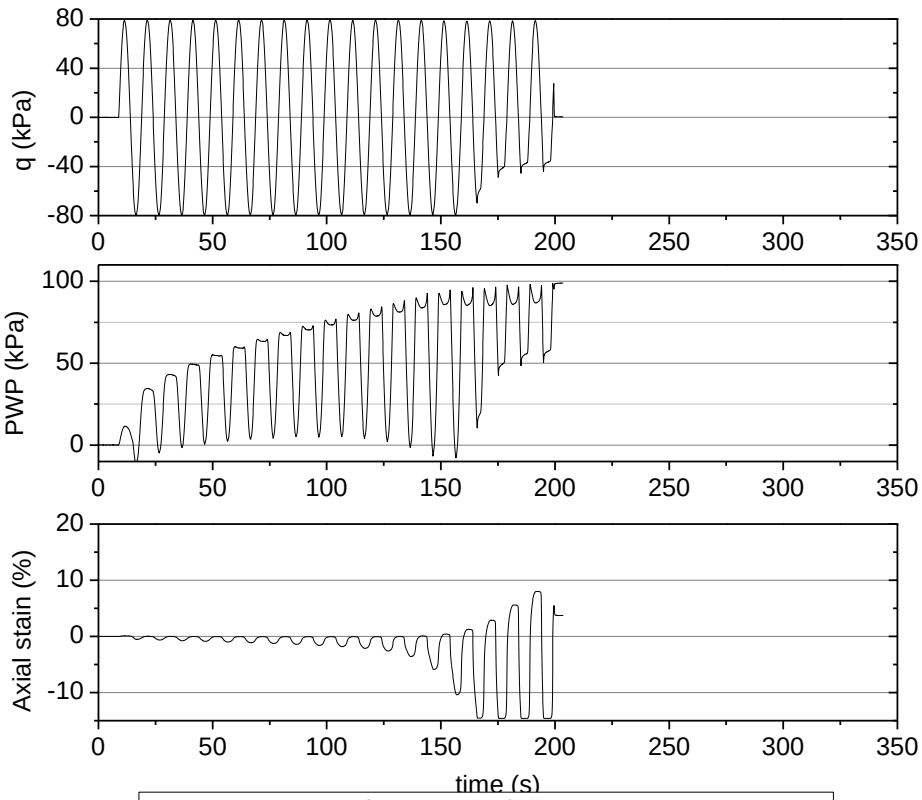

Test: UC_IOF-B_Feb17 σ_0'=98.7kPa; CSR=0.396; Dc=92.9%

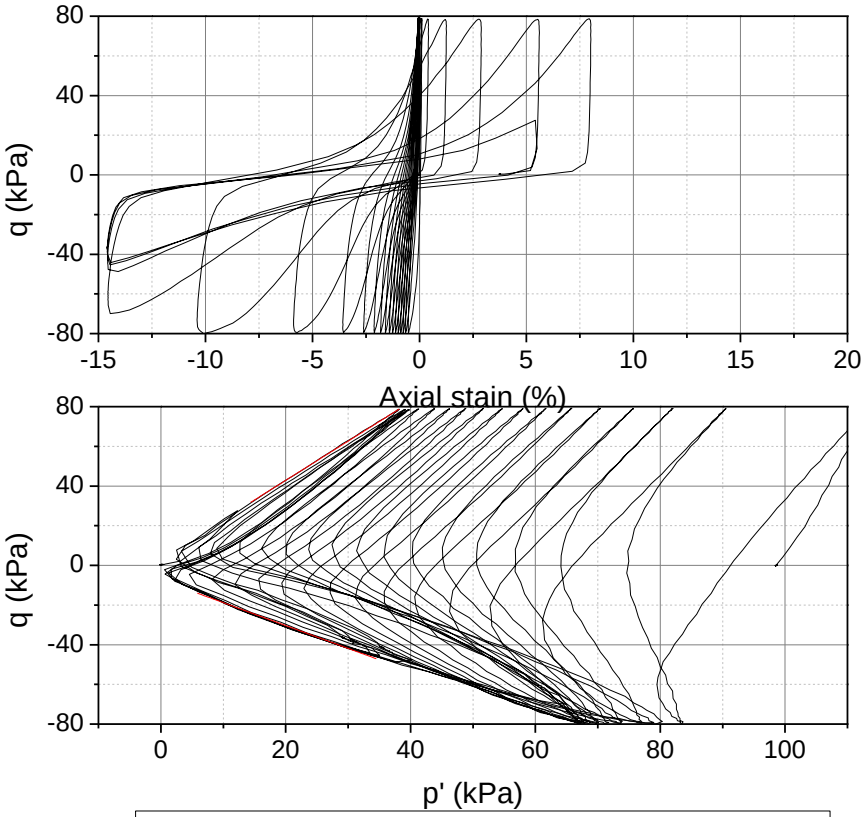

Test: UC_IOF-B_Feb17 σ_0'=98.7kPa; CSR=0.396; Dc=92.9%

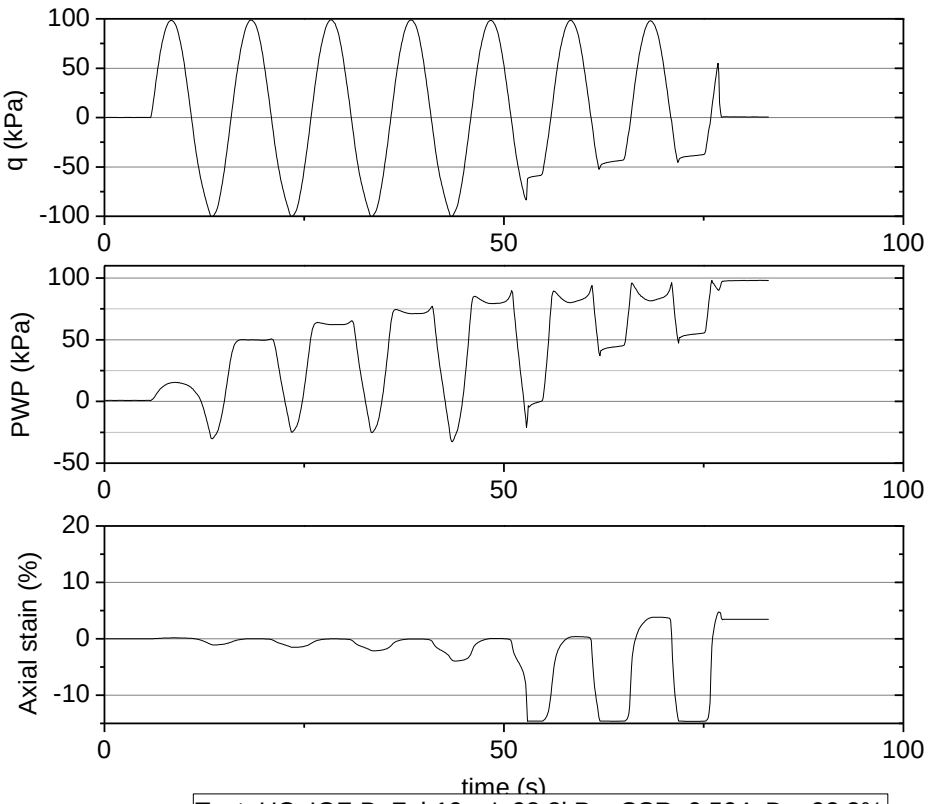

Test: UC_IOF-B_Feb19 σ_0'=98.8kPa; CSR=0.504; Dc=92.3%

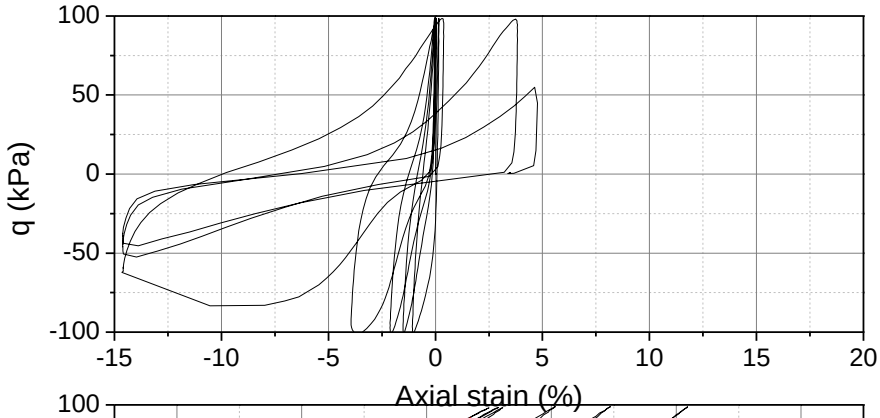

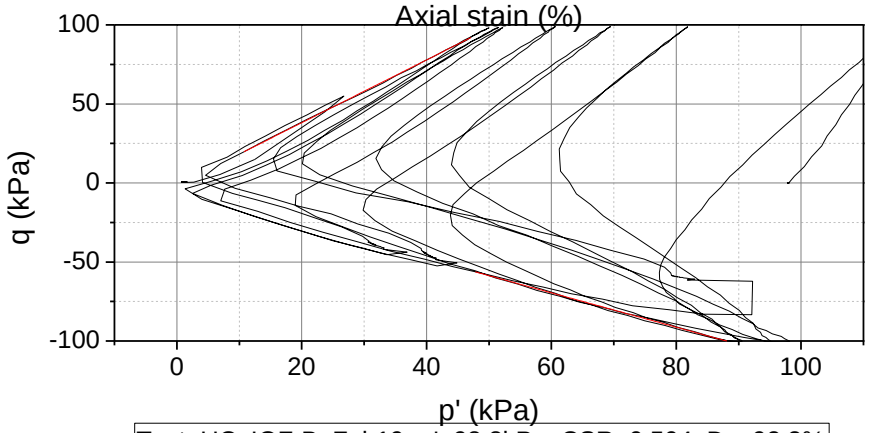

Test: UC_IOF-B_Feb19 σ_0'=98.8kPa; CSR=0.504; Dc=92.3%

G-2 Saturated IOF-B in Set 5

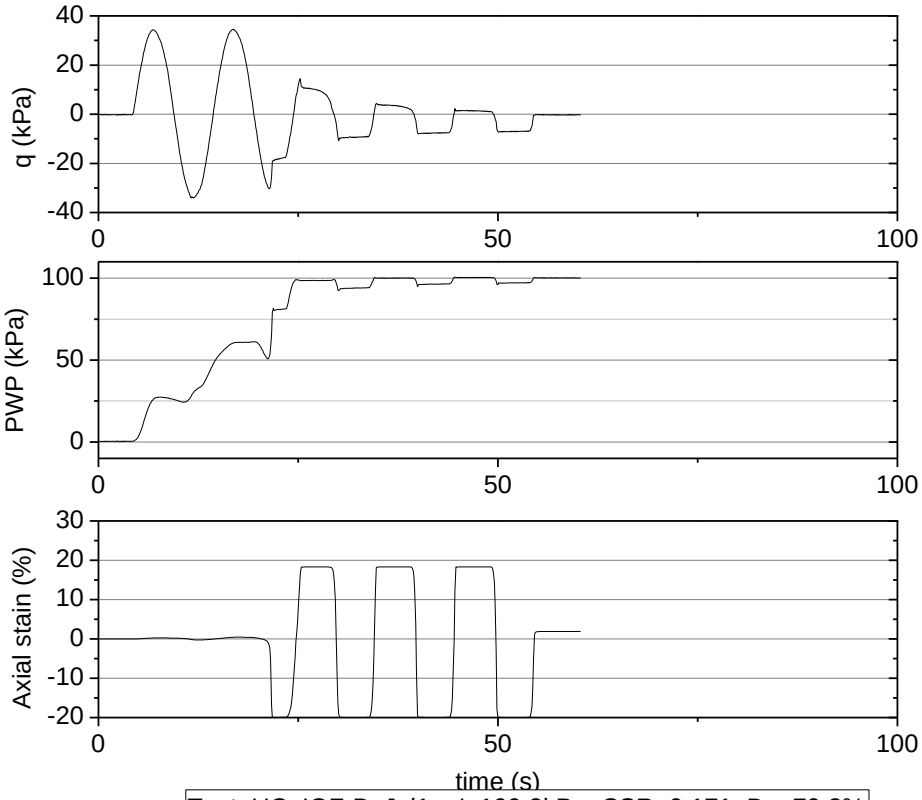

Test: UC_IOF-B_Jul1 σ_0'=100.2kPa; CSR=0.171; Dc=79.2%

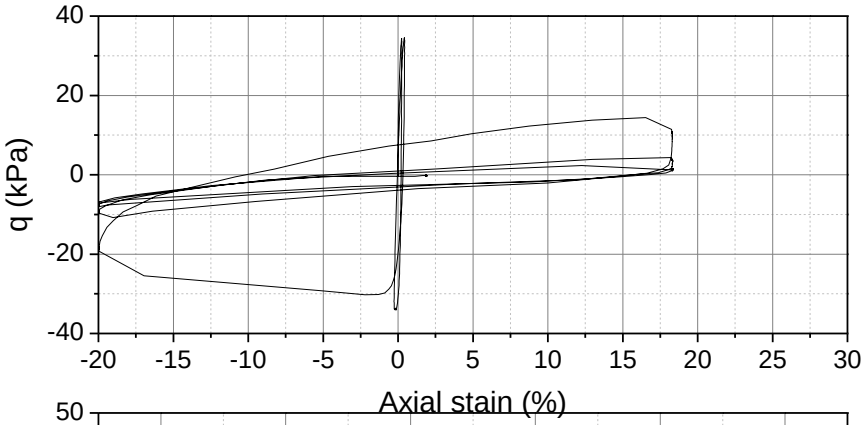

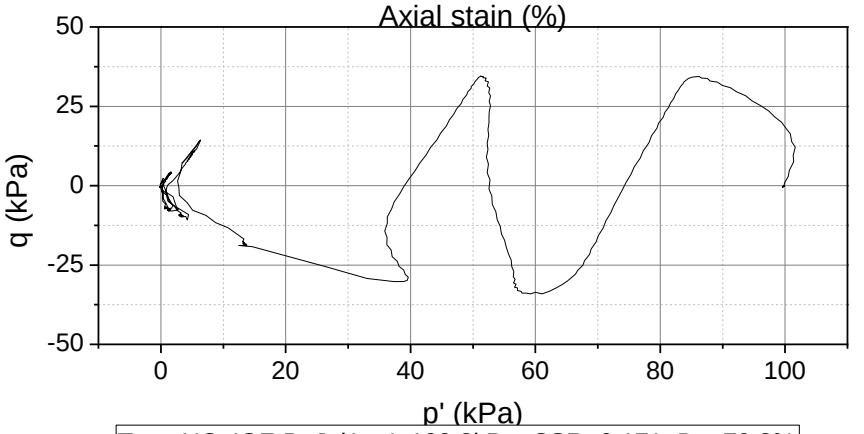

Test: UC_IOF-B_Jul1 σ_0'=100.2kPa; CSR=0.171; Dc=79.2%

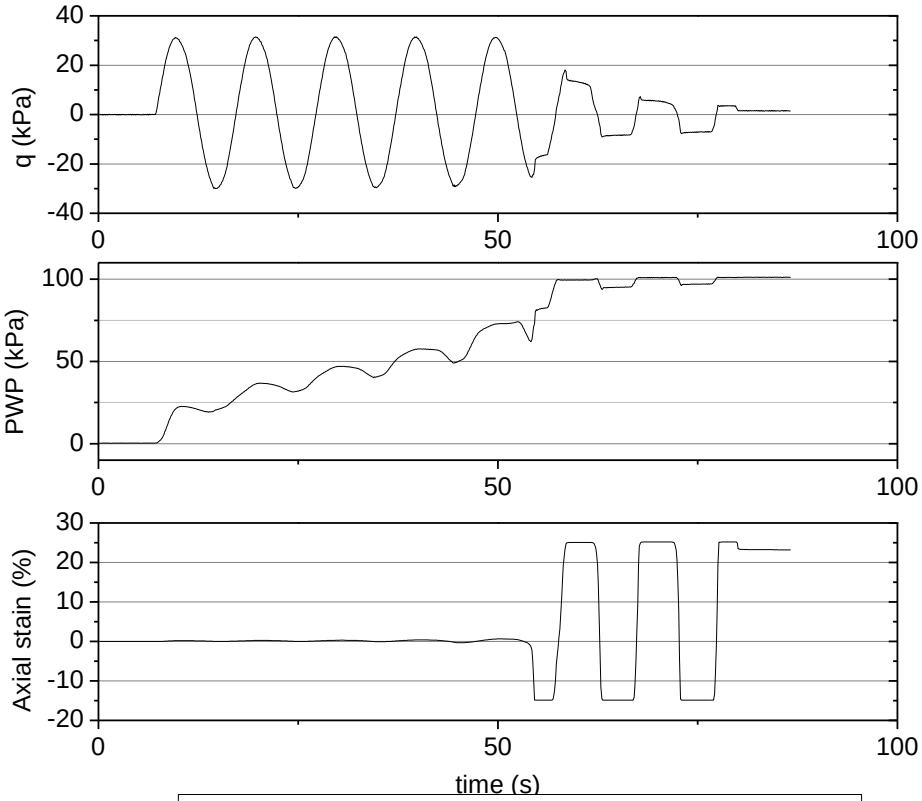

Test: UC_IOF-B_Jul3 σ_0'=100.7kPa; CSR=0.152; Dc=80.4%

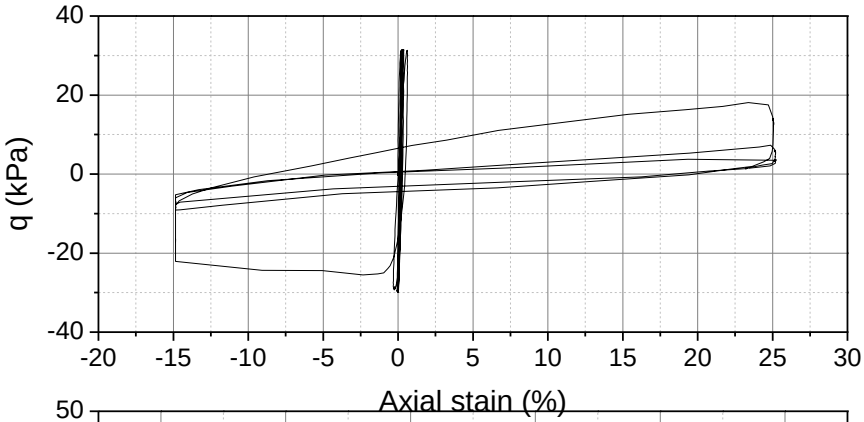

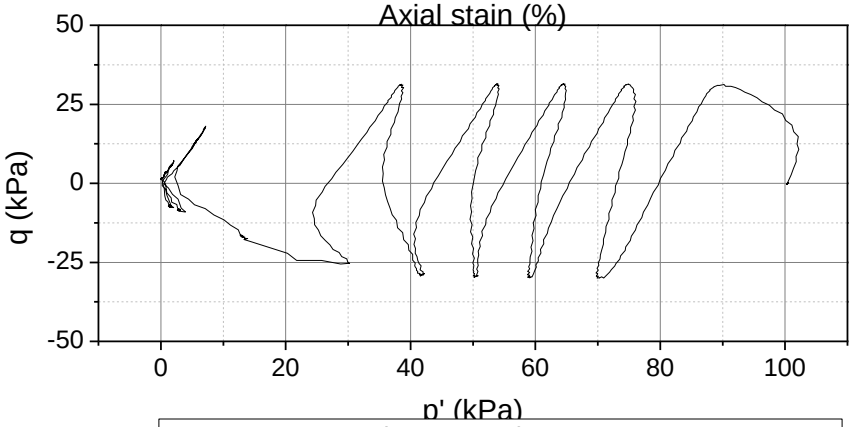

Test: UC_IOF-B_Jul3 σ_0'=100.7kPa; CSR=0.152; Dc=80.4%

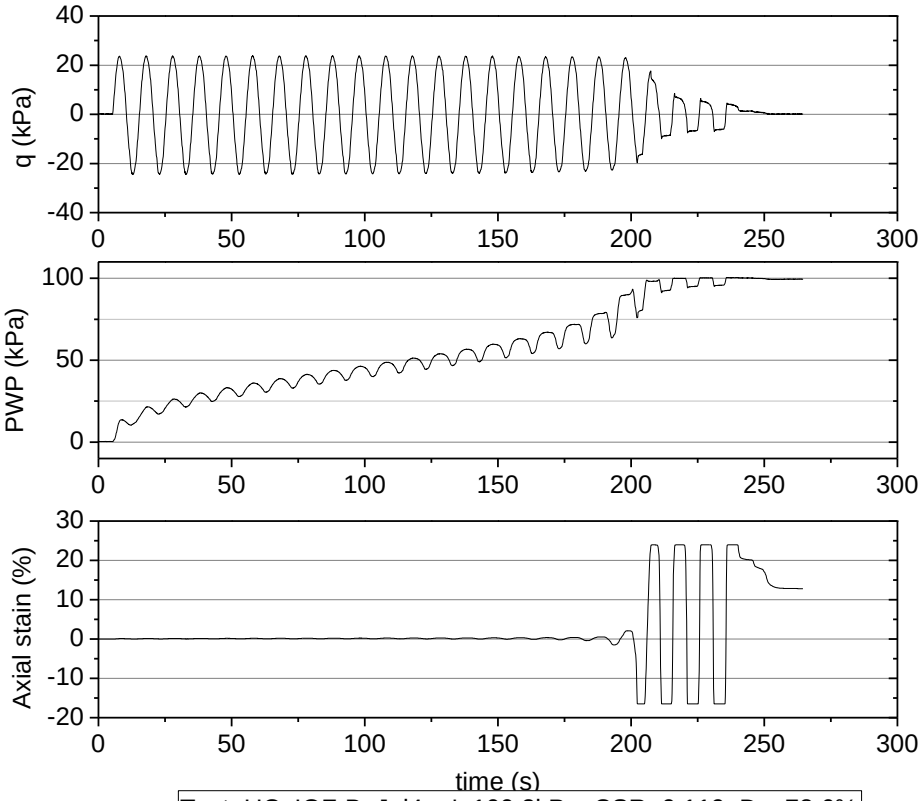

Test: UC_IOF-B_Jul4 σ_0'=100.2kPa; CSR=0.119; Dc=78.6%

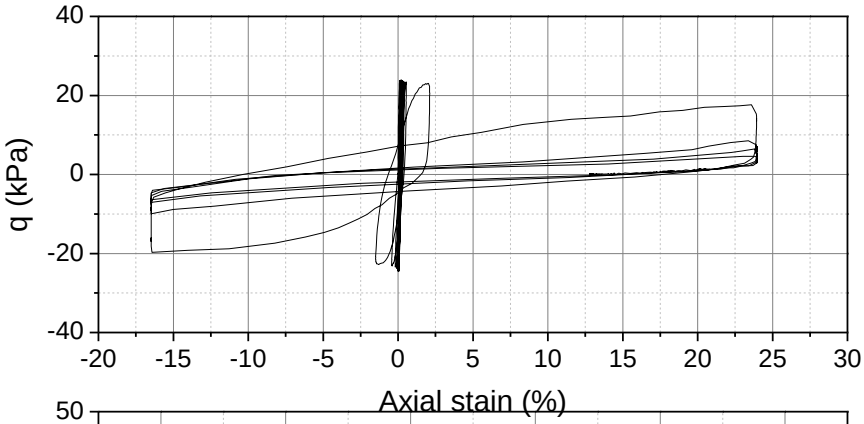

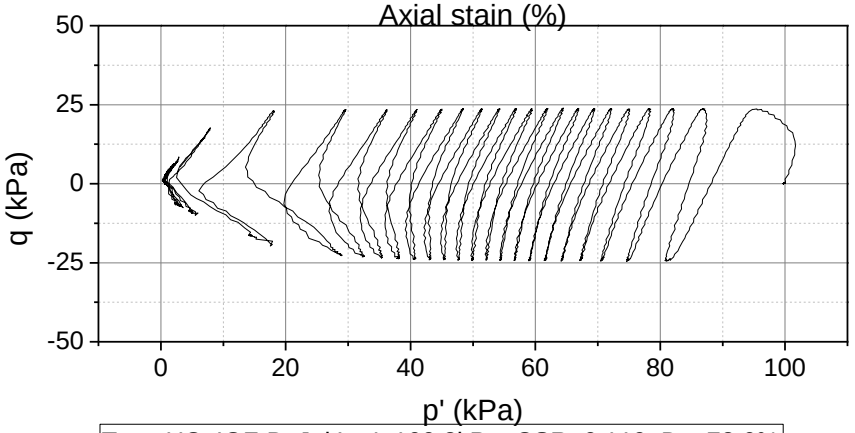

Test: UC_IOF-B_Jul4 σ_0'=100.2kPa; CSR=0.119; Dc=78.6%

G-3 Saturated IOF-B in Set 6

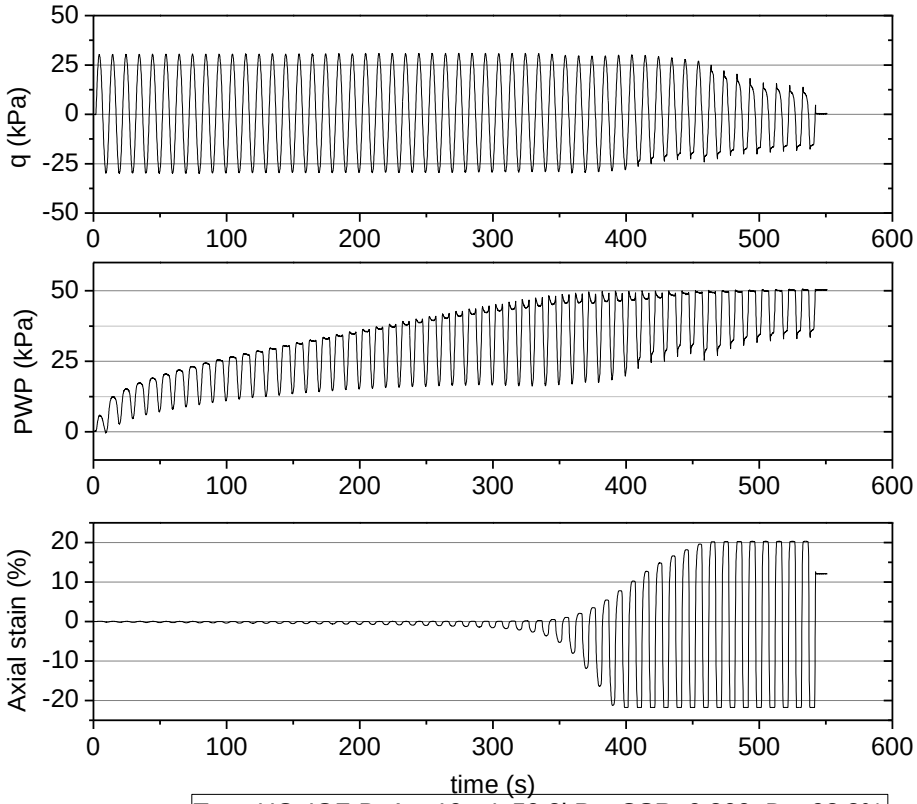

Test: UC_IOF-B_Aug19 σ_0'=50.2kPa; CSR=0.300; Dc=93.8%

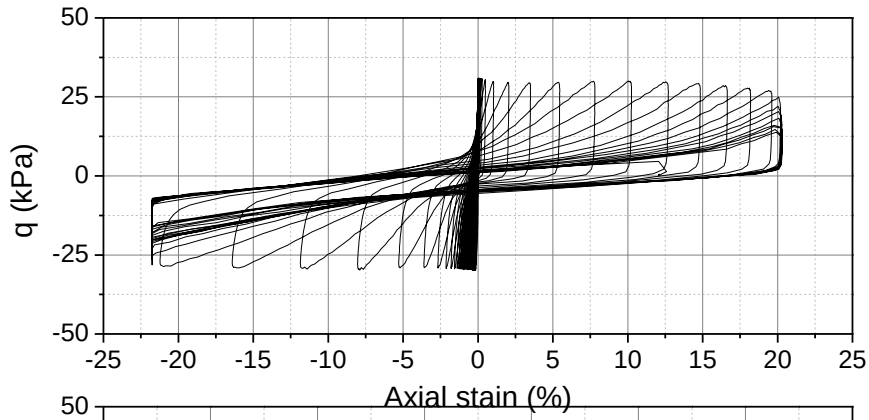

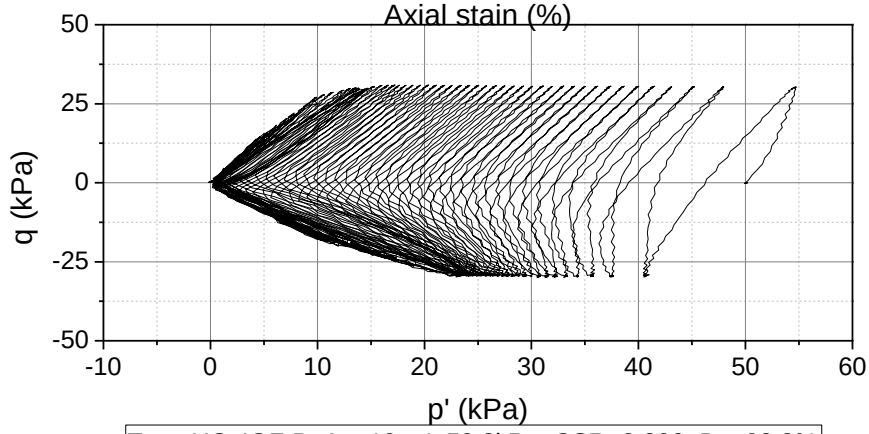

Test: UC_IOF-B_Aug19 σ_0'=50.2kPa; CSR=0.300; Dc=93.8%

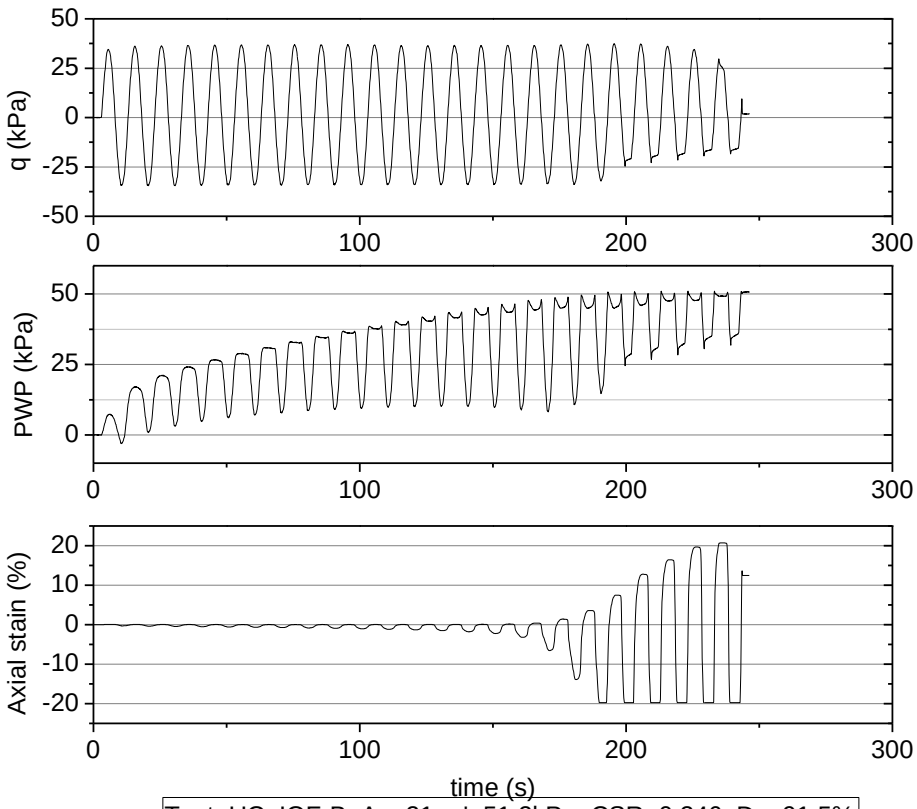

Test: UC_IOF-B_Aug21 σ_0'=51.2kPa; CSR=0.346; Dc=91.5%

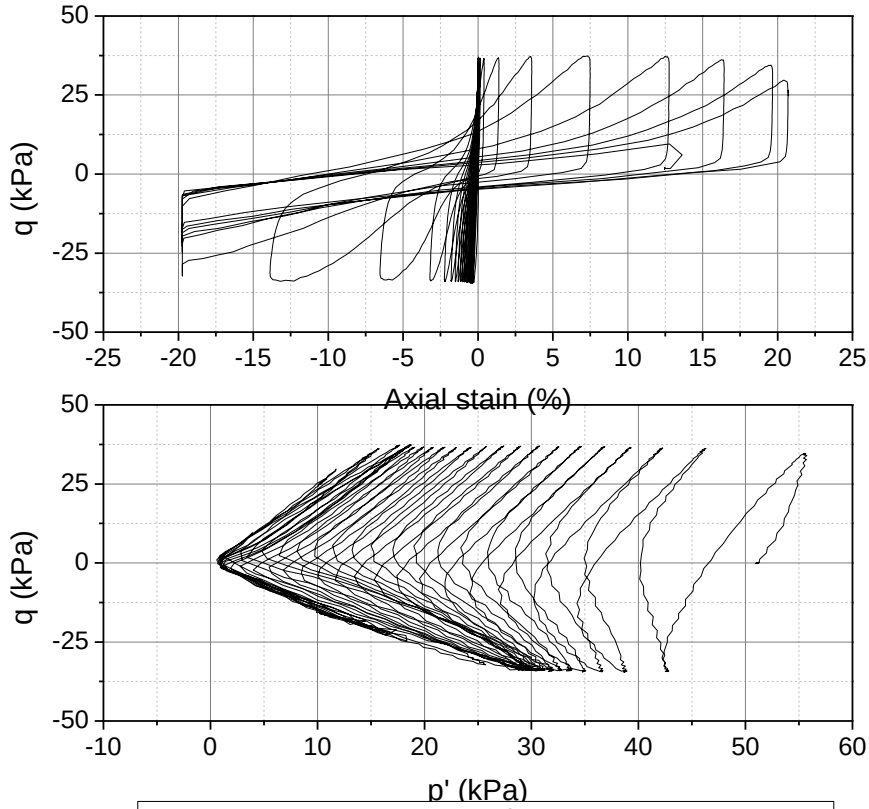

Test: UC_IOF-B_Aug21 σ_0'=51.2kPa; CSR=0.346; Dc=91.5%

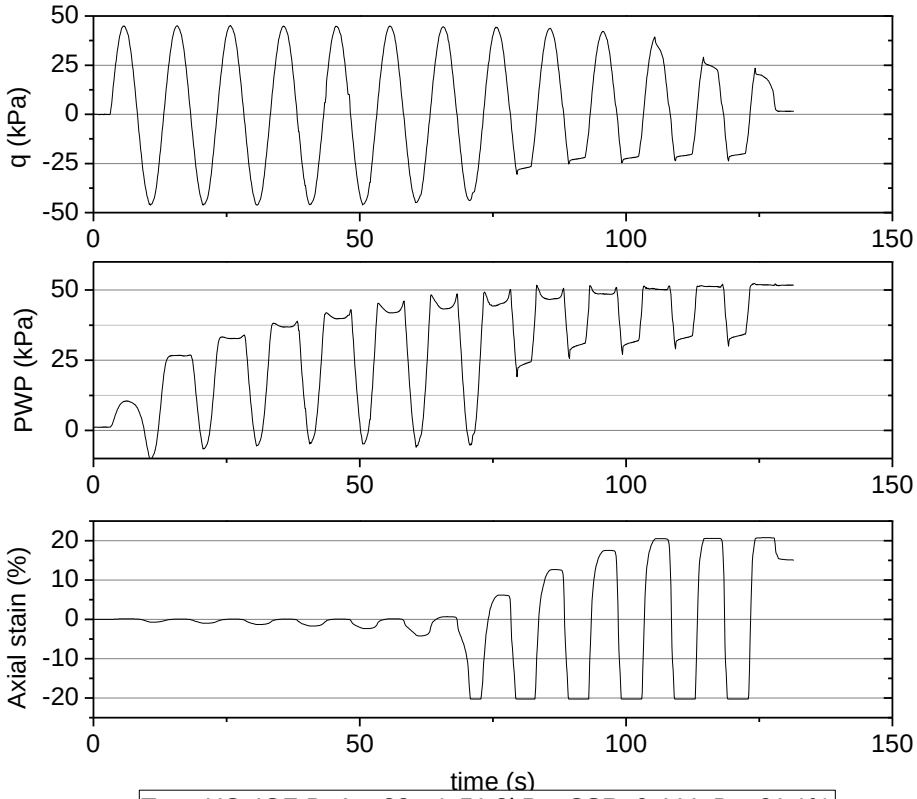

Test: UC_IOF-B_Aug22 σ_0'=51.3kPa; CSR=0.444; Dc=91.1%

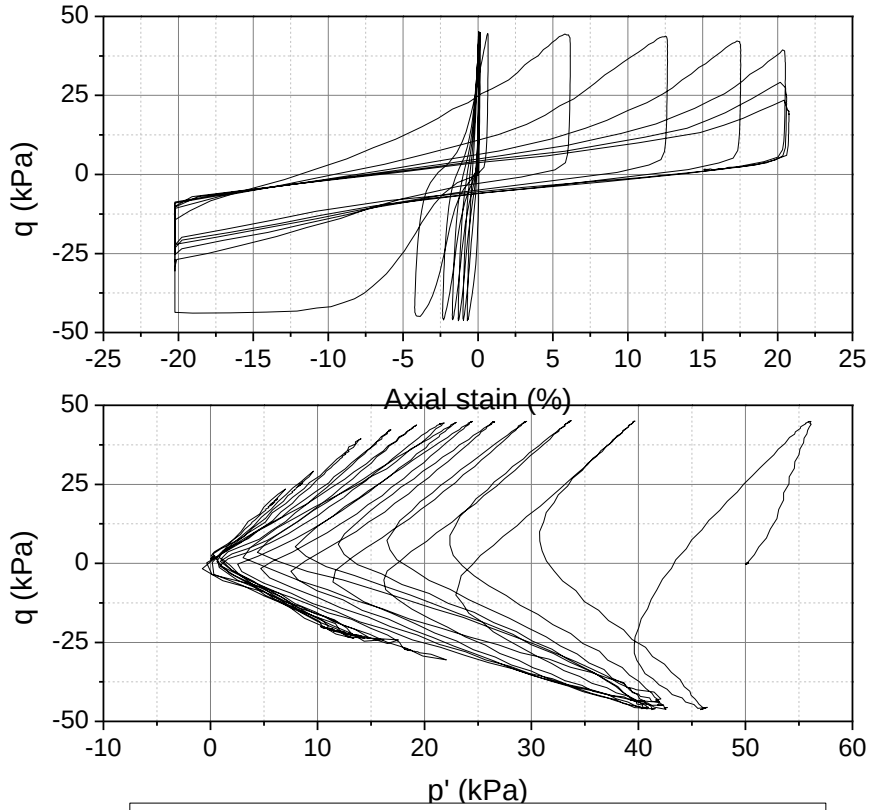

Test: UC_IOF-B_Aug22 σ_0'=51.3kPa; CSR=0.444; Dc=91.1%

G-4 Saturated IOF-B in Set 7

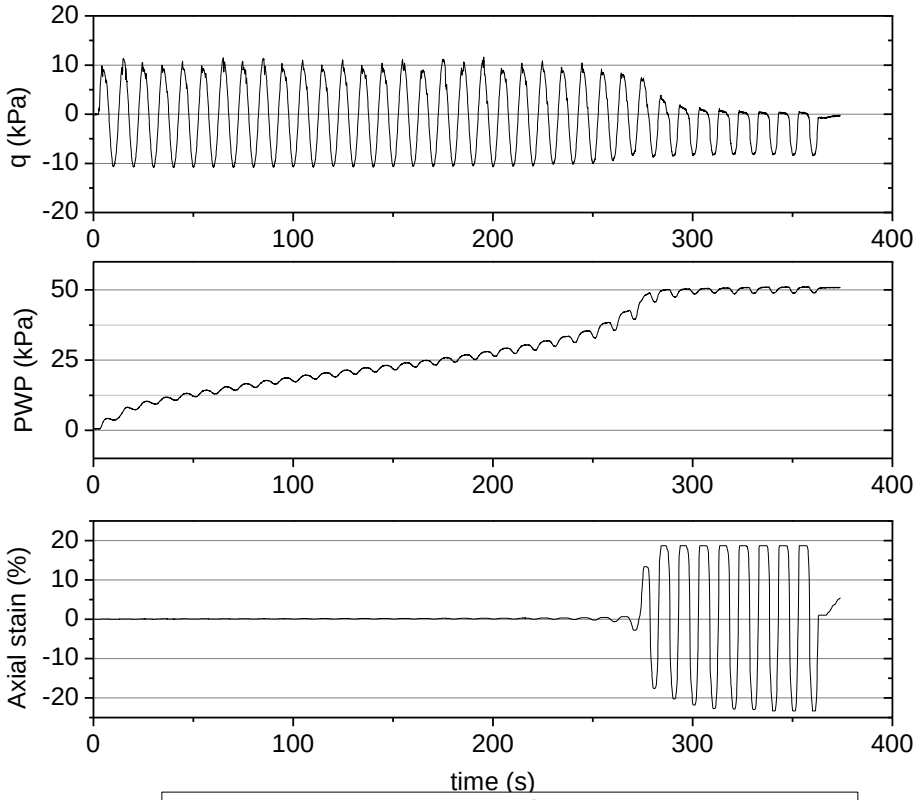

Test: UC_IOF-B_Sep10 σ_0'=50.2kPa; CSR=0.104; Dc=77.3%

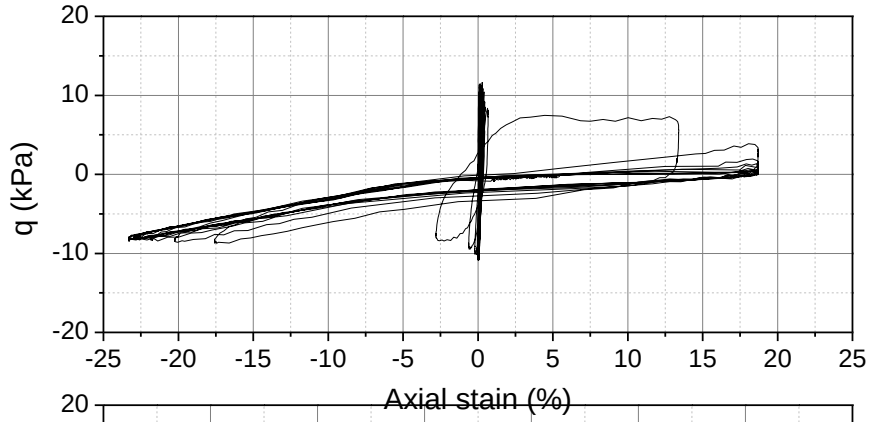

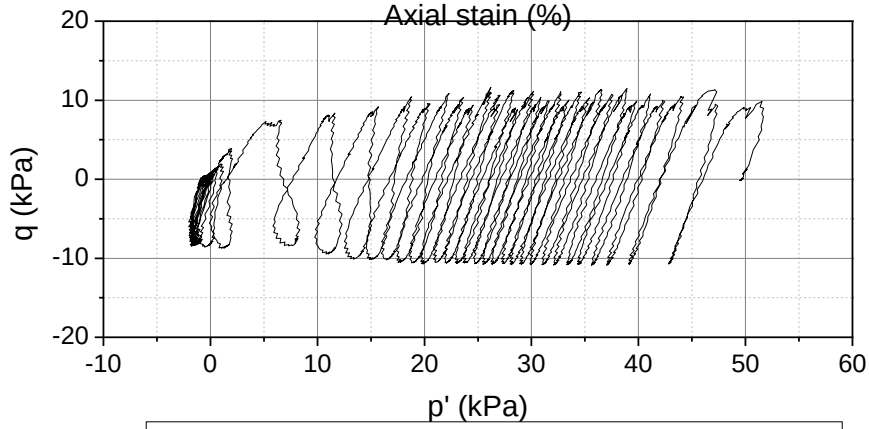

Test: UC_IOF-B_Sep10 σ_0'=50.2kPa; CSR=0.104; Dc=77.3%

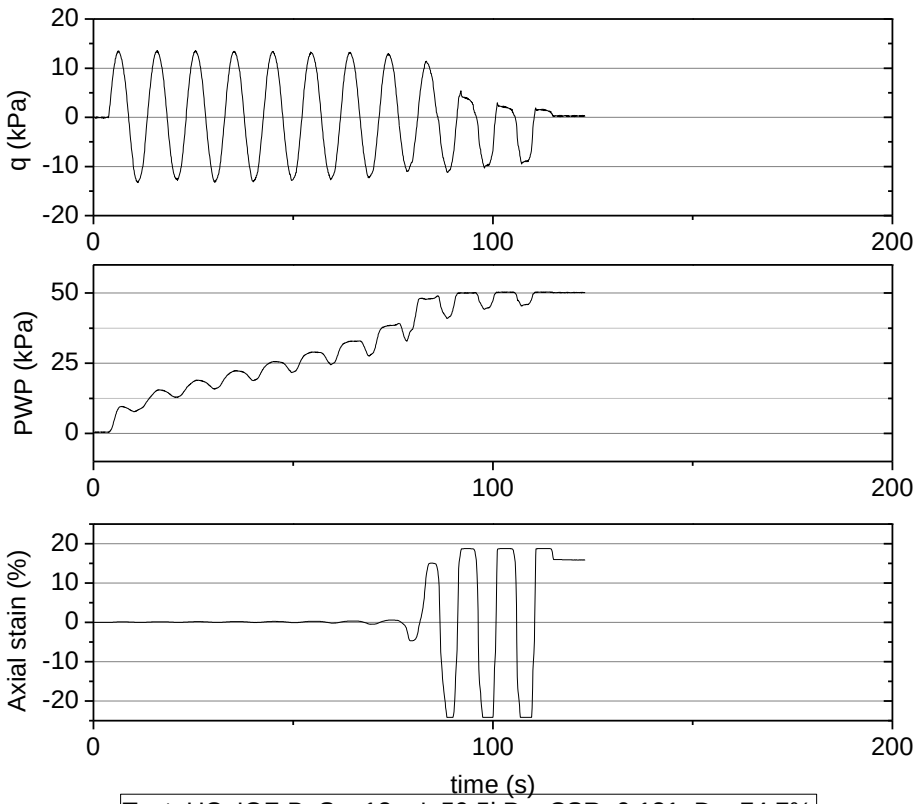

Test: UC_IOF-B_Sep12 σ_0'=50.5kPa; CSR=0.131; Dc=74.7%

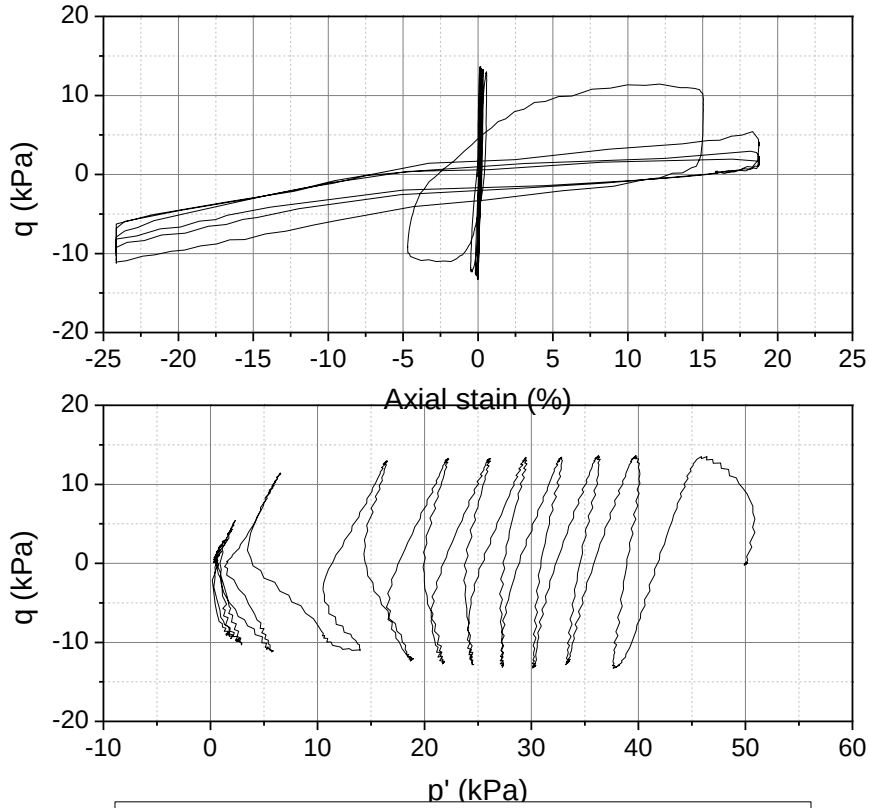

Test: UC_IOF-B_Sep12 σ_0'=50.5kPa; CSR=0.131; Dc=74.7%

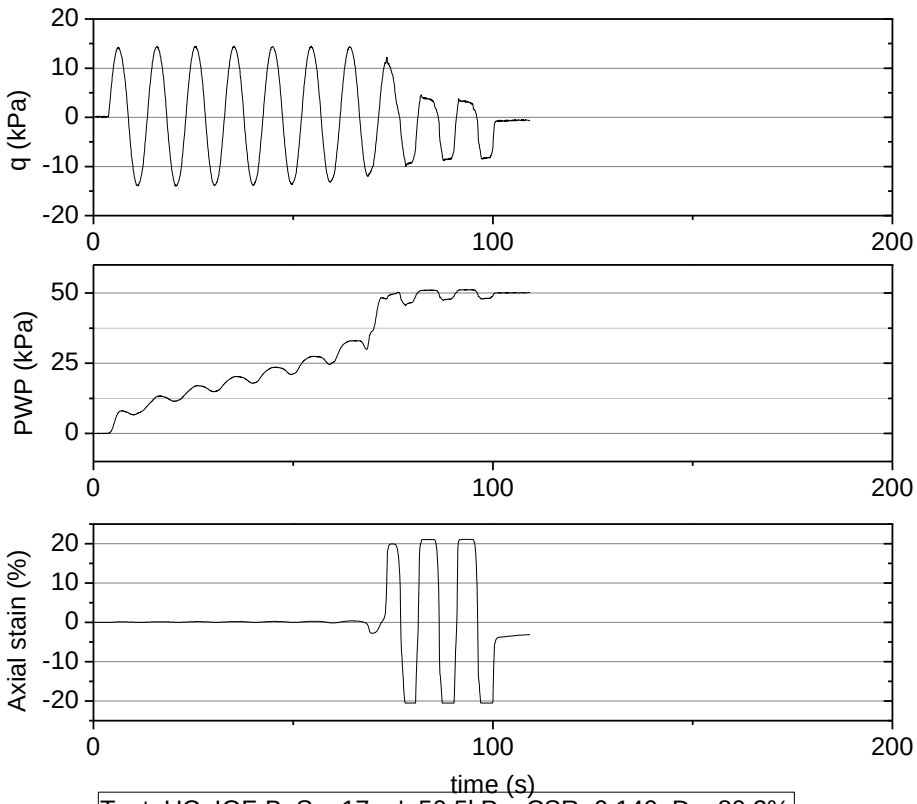

Test: UC_IOF-B_Sep17 σ_0'=50.5kPa; CSR=0.140; Dc=80.2%

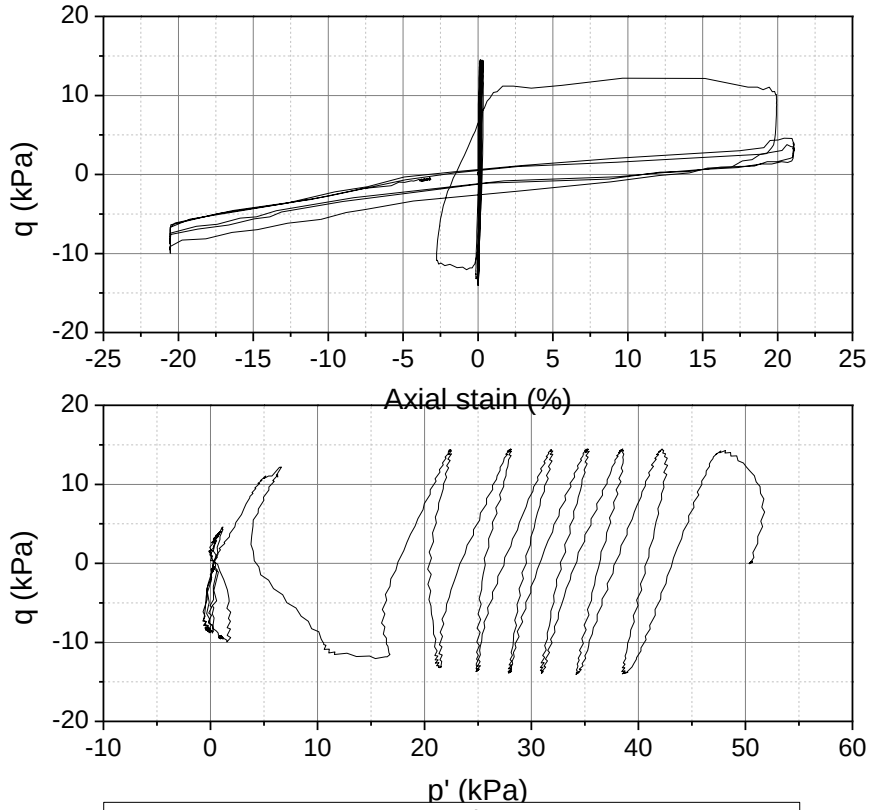

Test: UC_IOF-B_Sep17 σ_0'=50.5kPa; CSR=0.140; Dc=80.2%

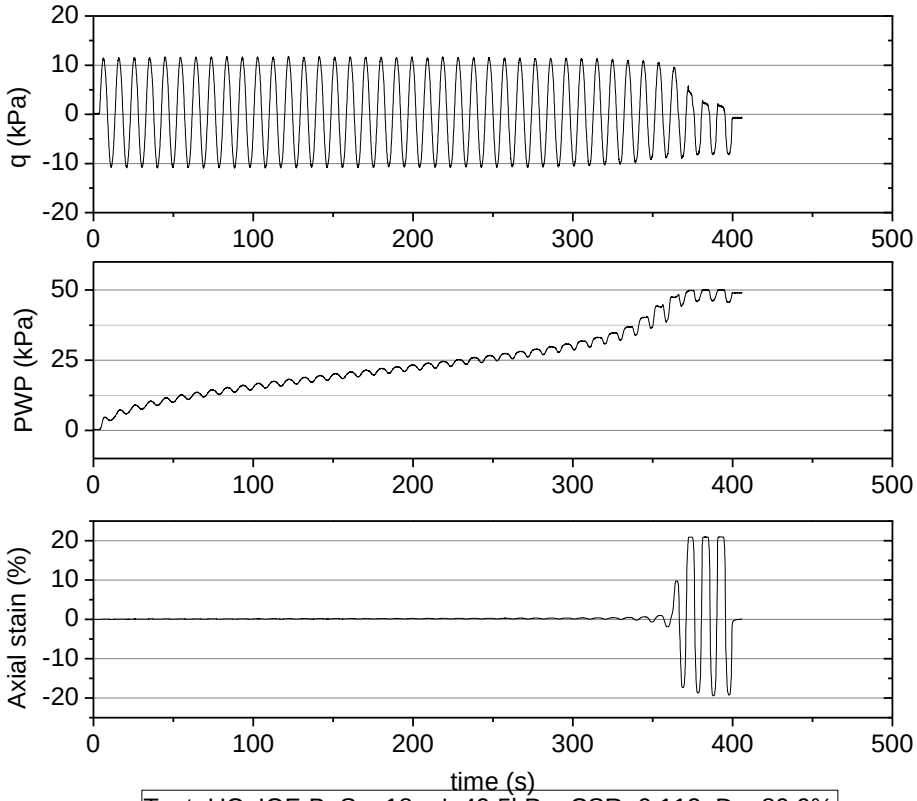

Test: UC_IOF-B_Sep18 σ_0'=49.5kPa; CSR=0.112; Dc=80.9%

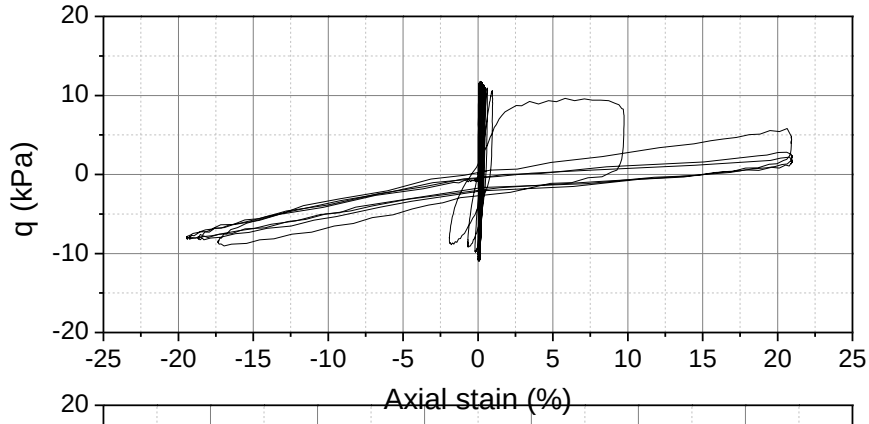

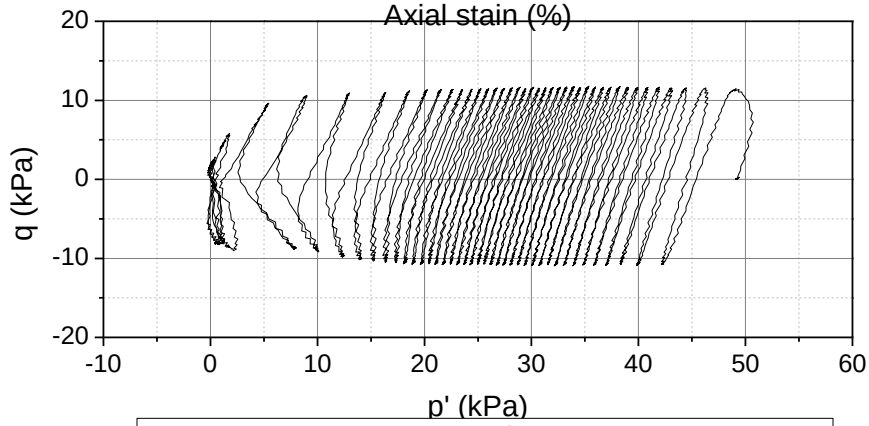

Test: UC_IOF-B_Sep18 σ_0'=49.5kPa; CSR=0.112; Dc=80.9%

G-5 Unsaturated IOF-B with Sr of 72% in Set 4

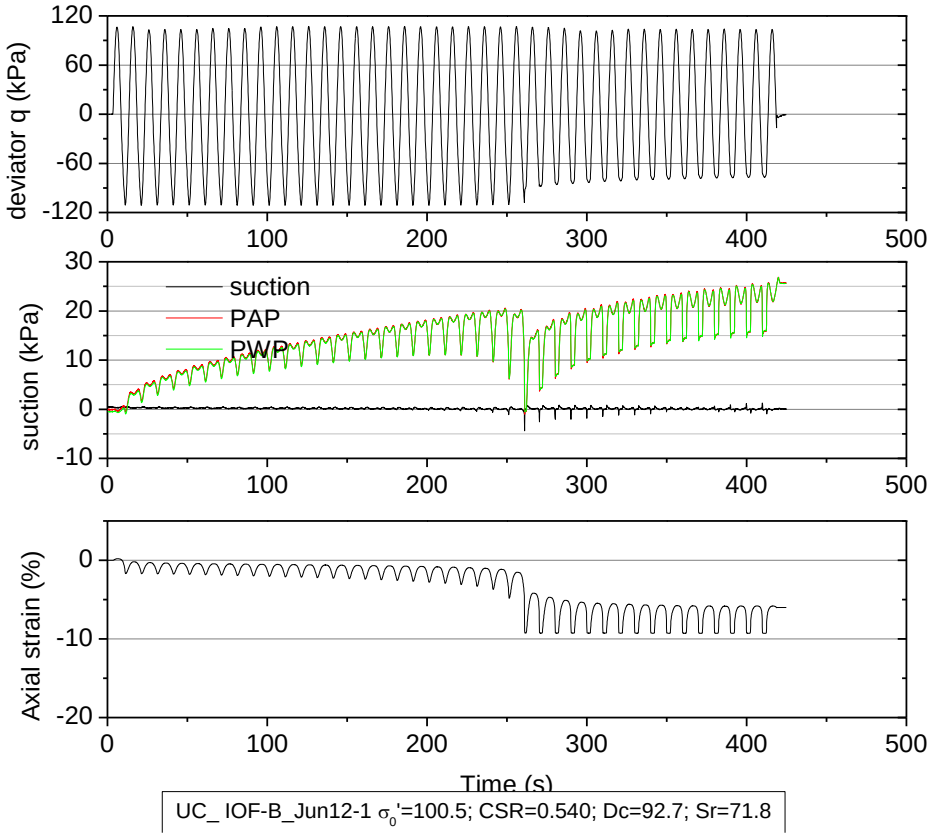

UC_ IOF-B_Jun12-1 σ_0'=100.5; CSR=0.540; Dc=92.7; Sr=71.8

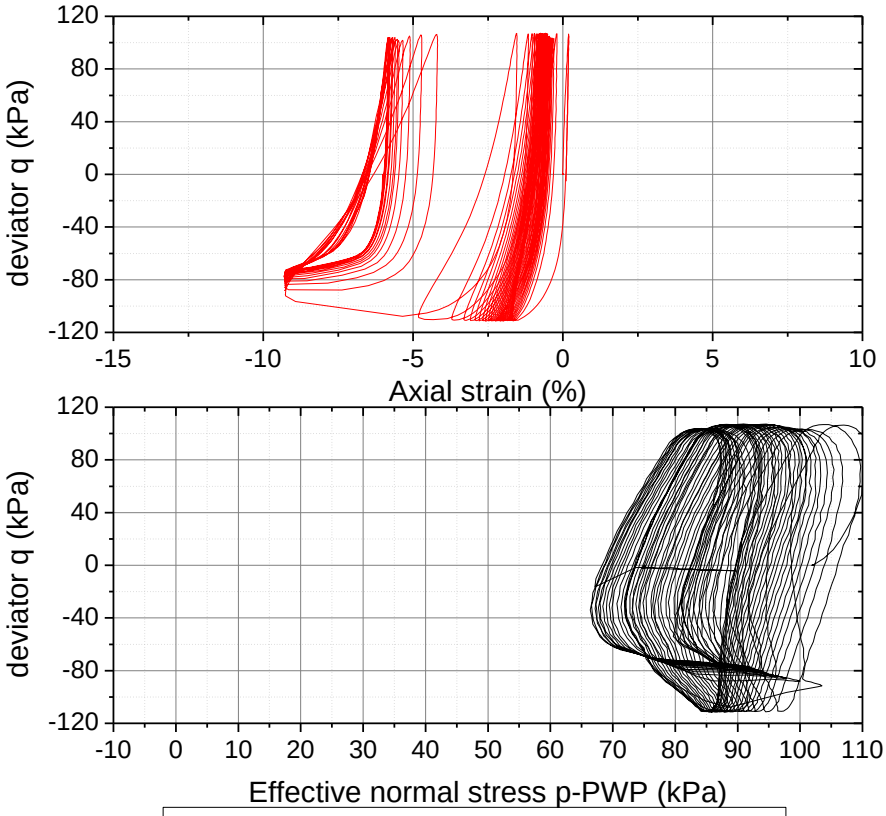

UC_ IOF-B_Jun12-1 σ_0'=100.5; CSR=0.540; Dc=92.7; Sr=71.8

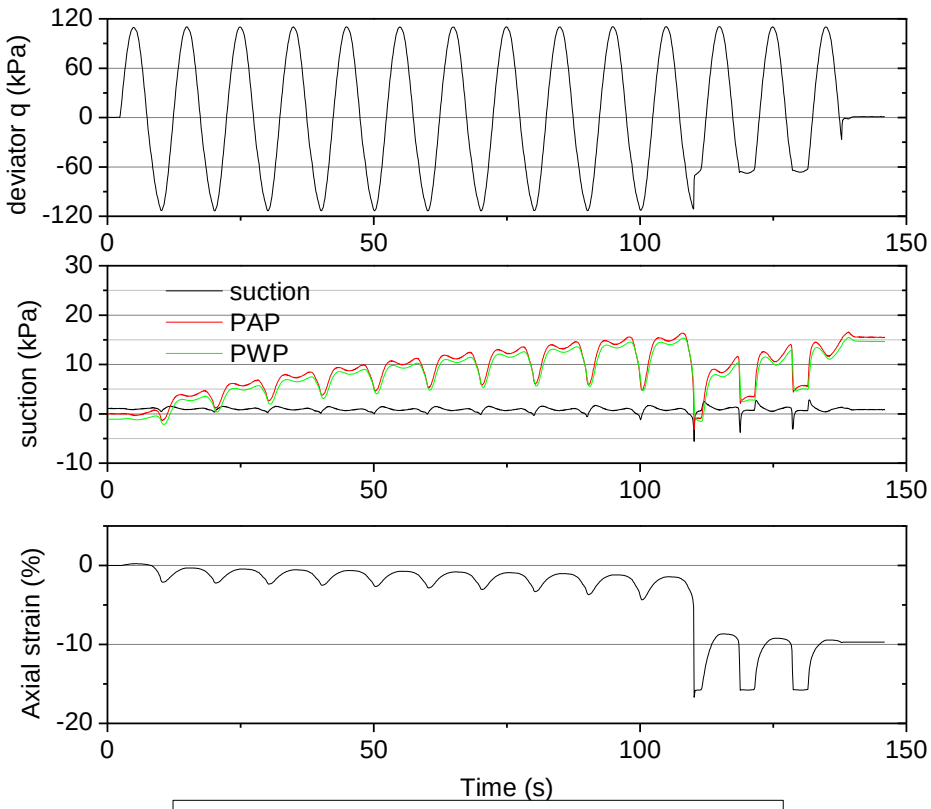

UC_ IOF-B_Jun12-2 σ_0'=99.5; CSR=0.562; Dc=92.8; Sr=72.1

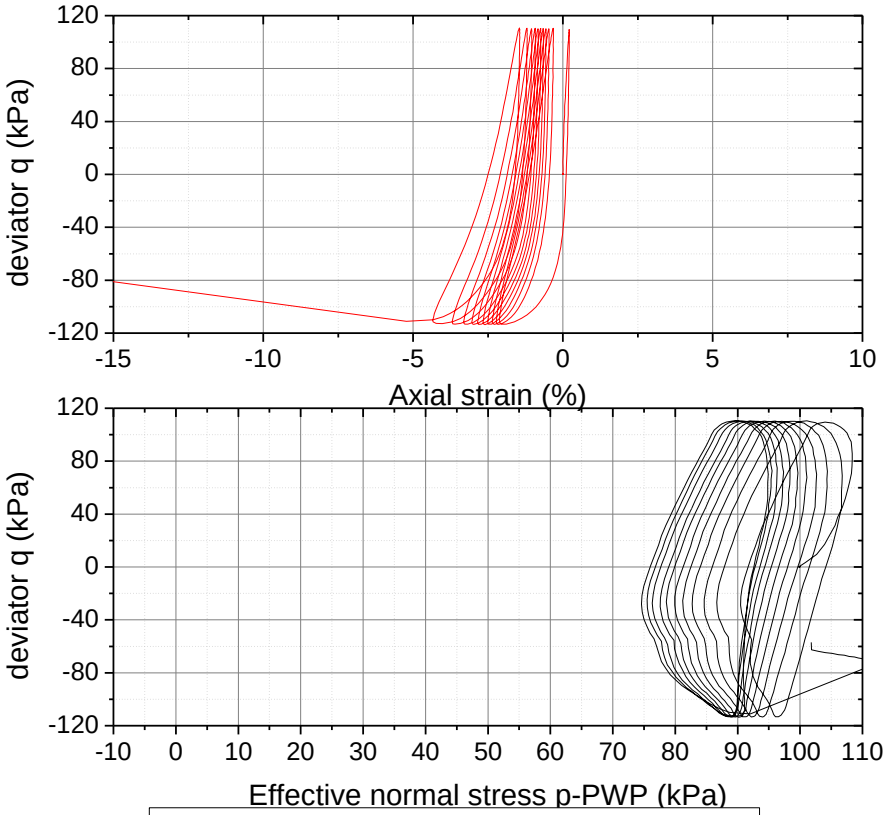

UC_ IOF-B_Jun12-2 σ_0'=99.5; CSR=0.562; Dc=92.8; Sr=72.1

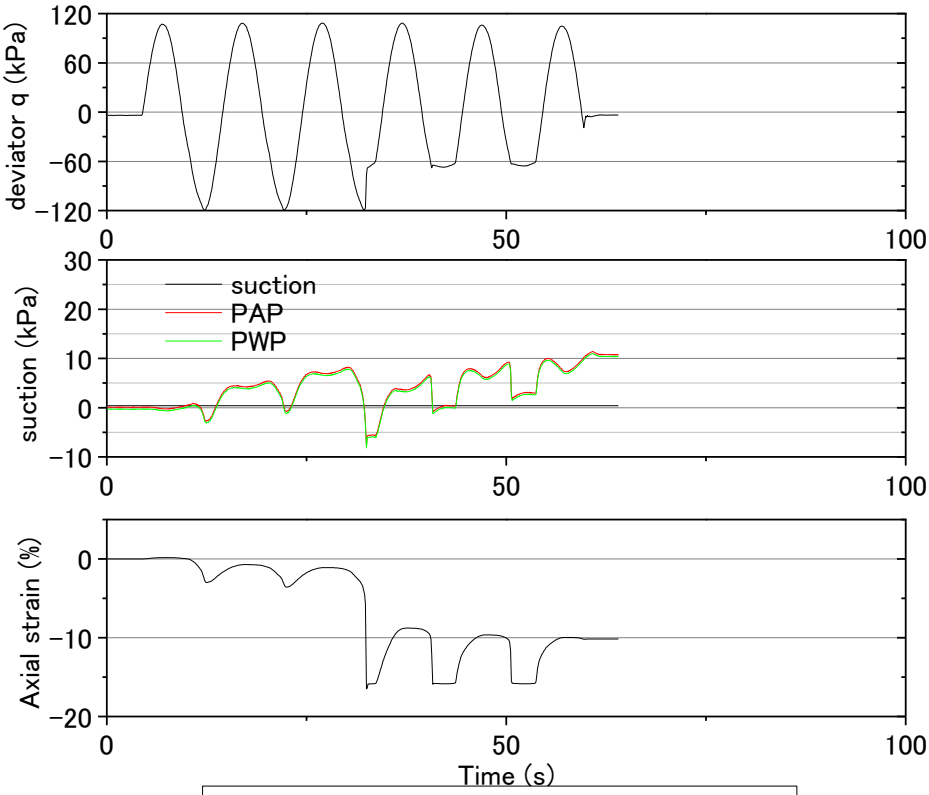

UC_ IOF-B_Jun13 σ_0'=99.4; CSR=0.572; Dc=92.7; Sr=73.3

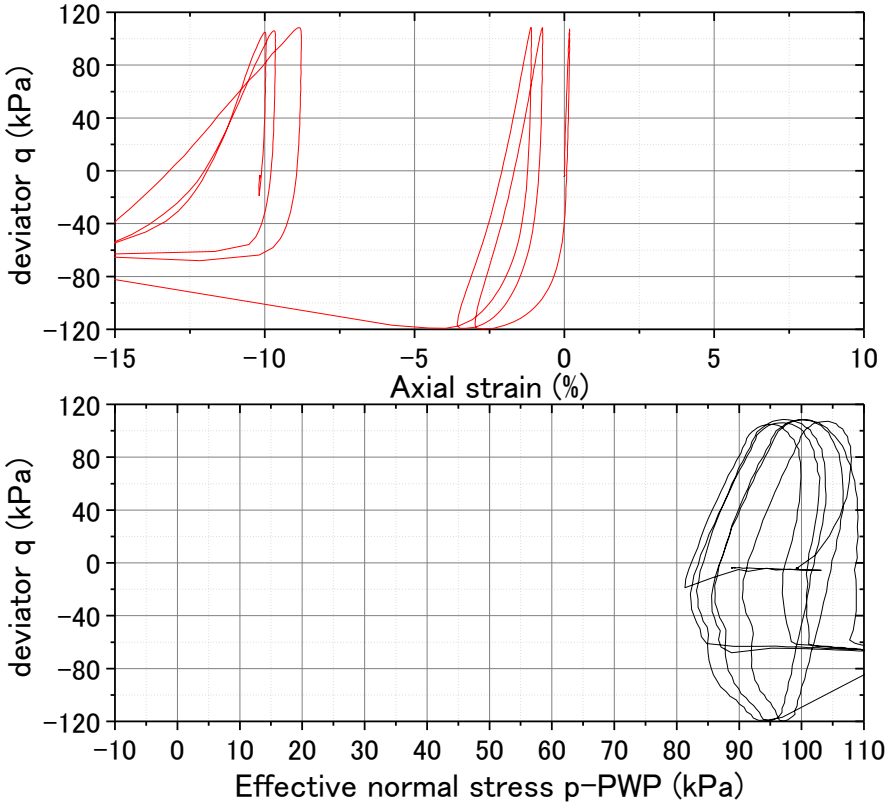

UC_ IOF-B_Jun13 σ_0'=99.4; CSR=0.572; Dc=92.7; Sr=73.3

G-6 Unsaturated IOF-B with Sr of 84% in Set 4

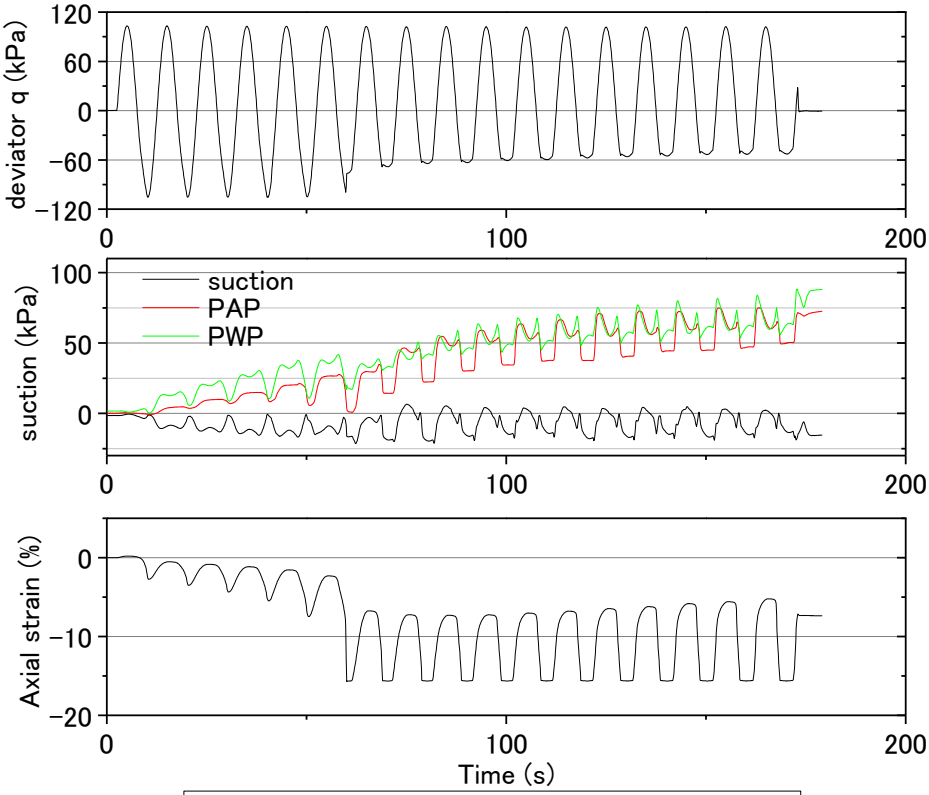

UC_ IOF-B_Jun17-2 σ_0'=99.2; CSR=0.525; Dc=93.3; Sr=83.2

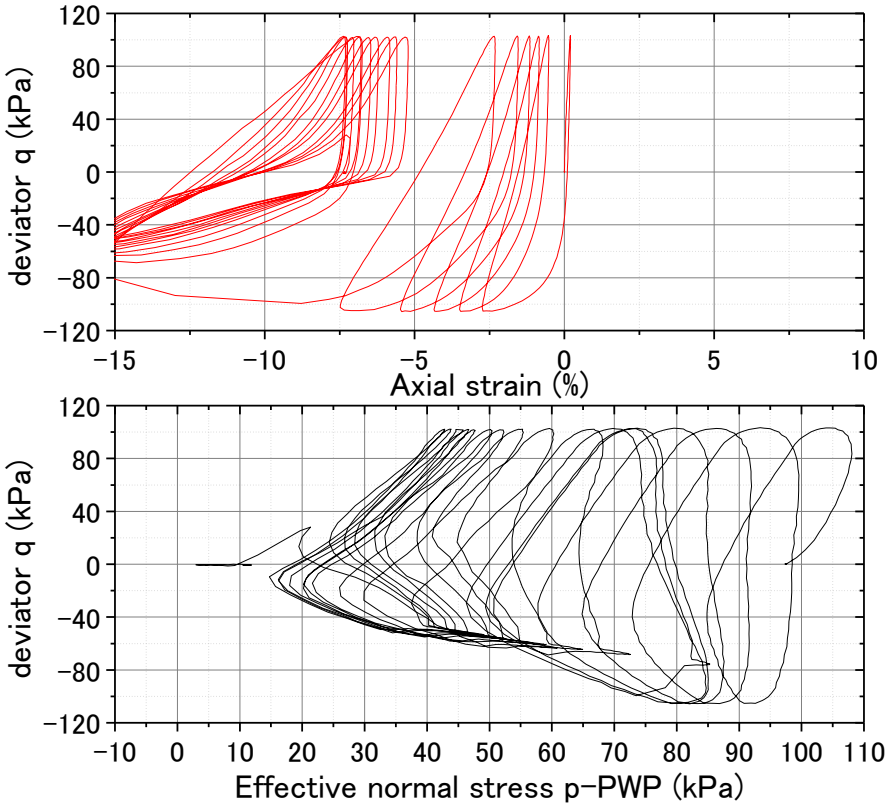

UC_ IOF-B_Jun17-2 σ_0'=99.2; CSR=0.525; Dc=93.3; Sr=83.2

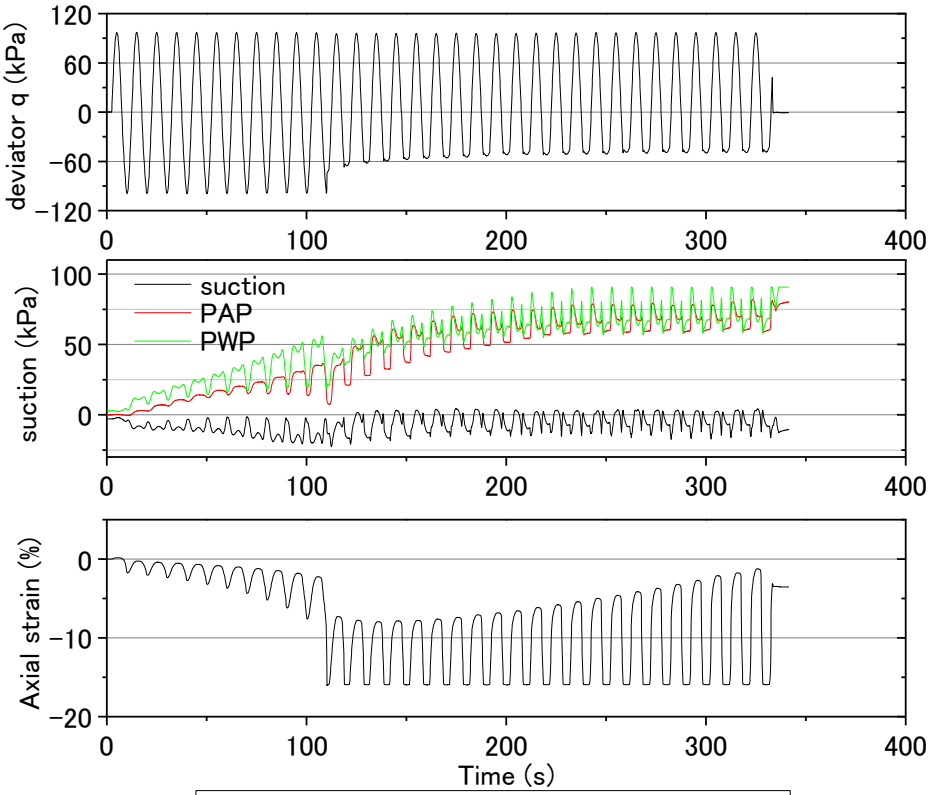

UC_ IOF-B_Jun19 σ0'=99.0; CSR=0.495; Dc=93.4; Sr=83.8

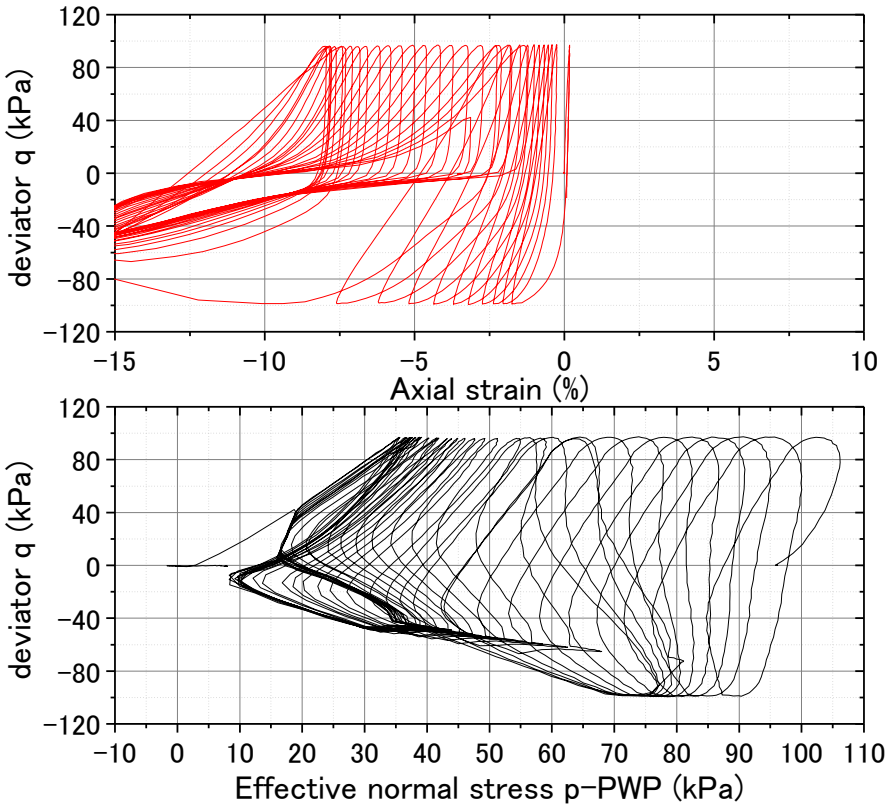

UC_ IOF-B_Jun19 σ0'=99.0; CSR=0.495; Dc=93.4; Sr=83.8

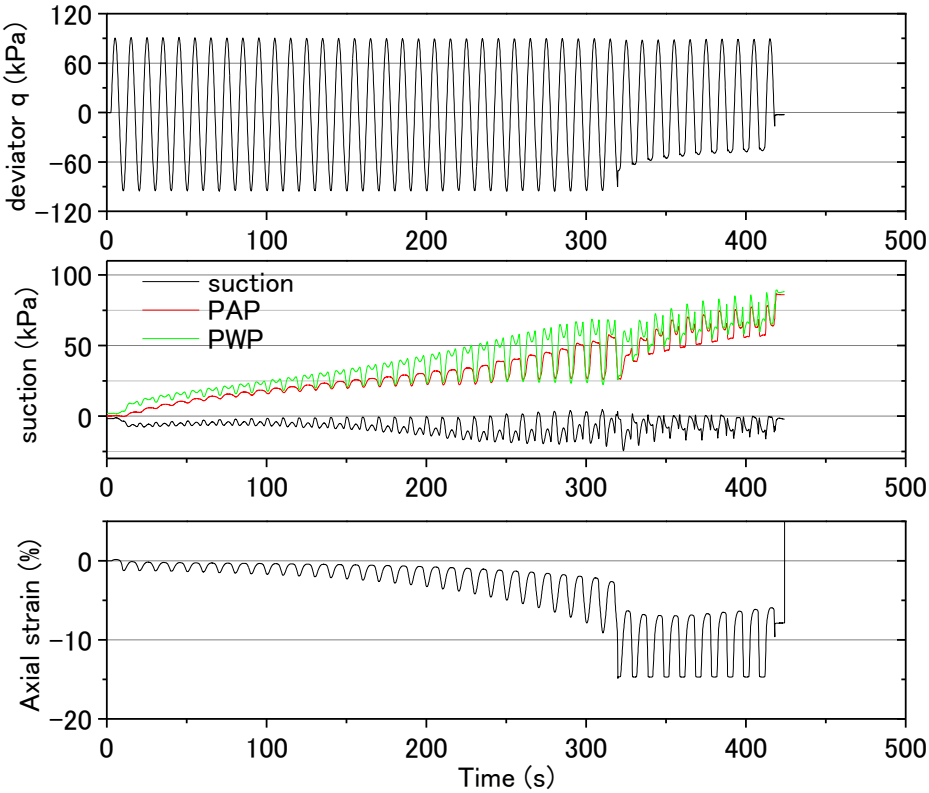

UC_ IOF-B_Jun21 σ0'=99.6; CSR=0.465; Dc=93.9; Sr=84.4

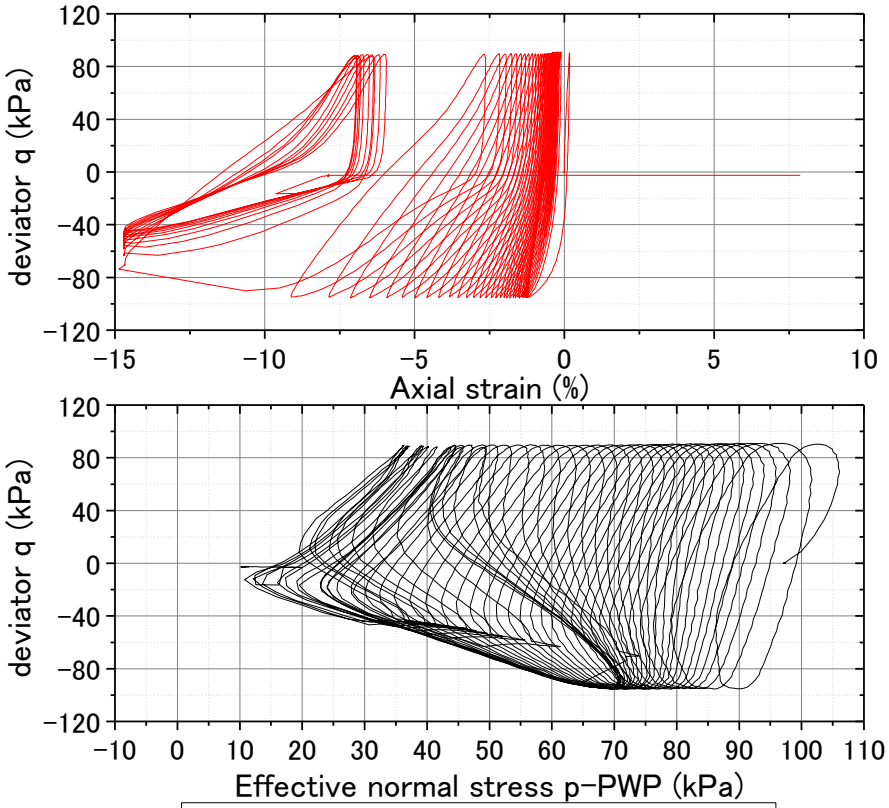

UC_ IOF-B_Jun21 σ0'=99.6; CSR=0.465; Dc=93.9; Sr=84.4

G-7 Unsaturated IOF-B with Sr of 76% in Set 5

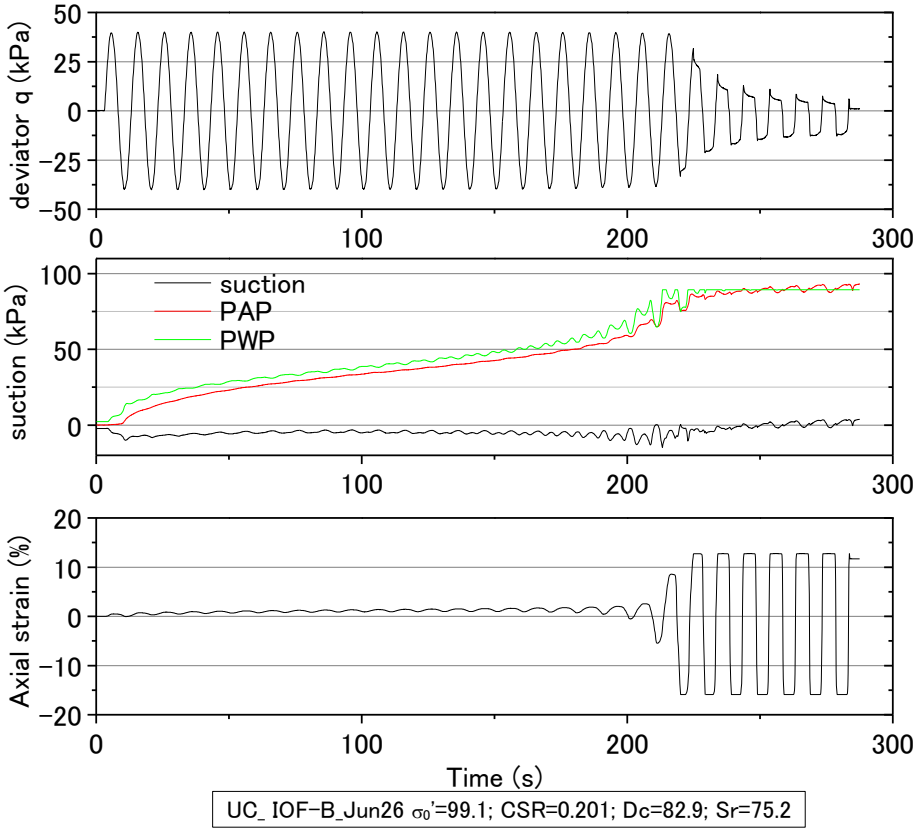

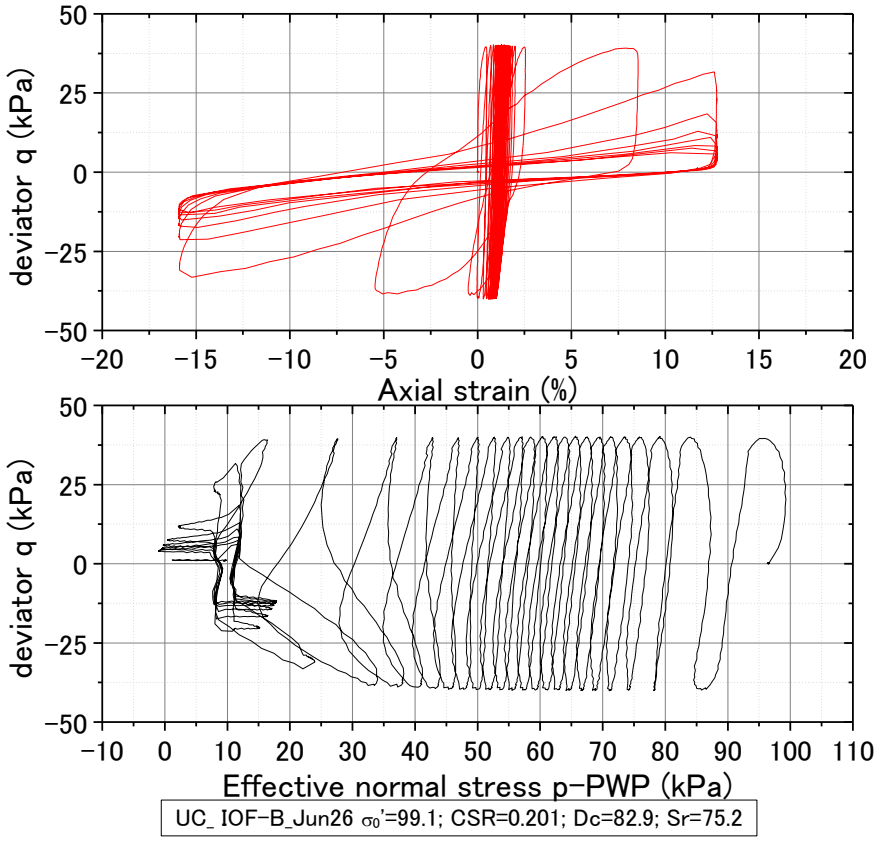

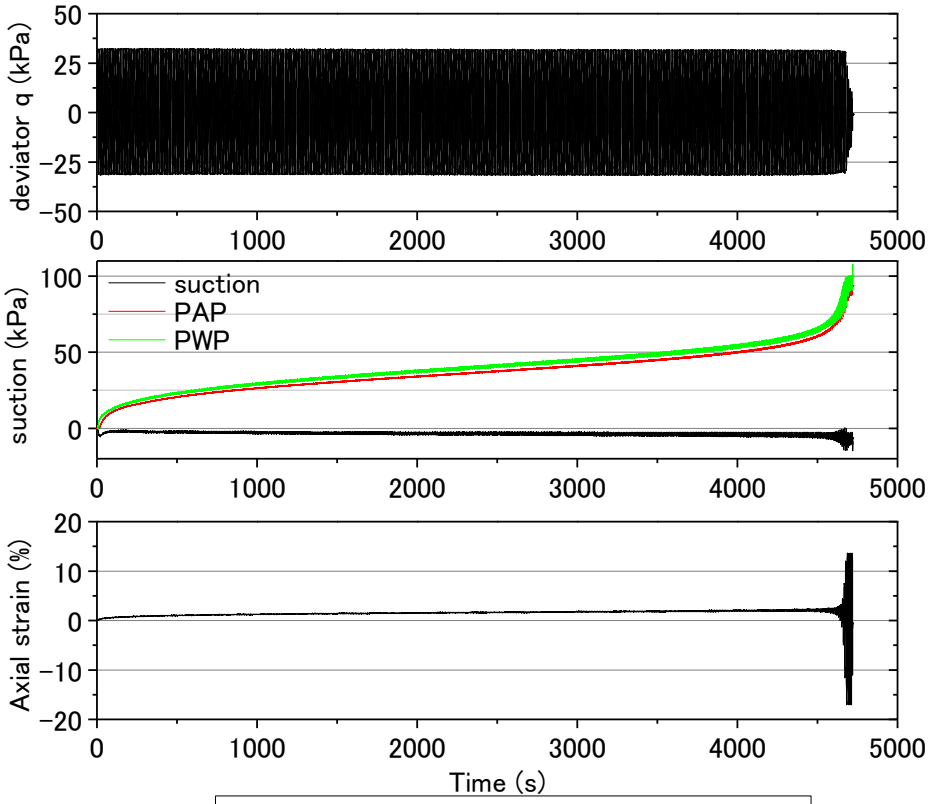

UC_ IOF-B_Jun27 σ_0'=99.4; CSR=0.159; Dc=83.6; Sr=76.8

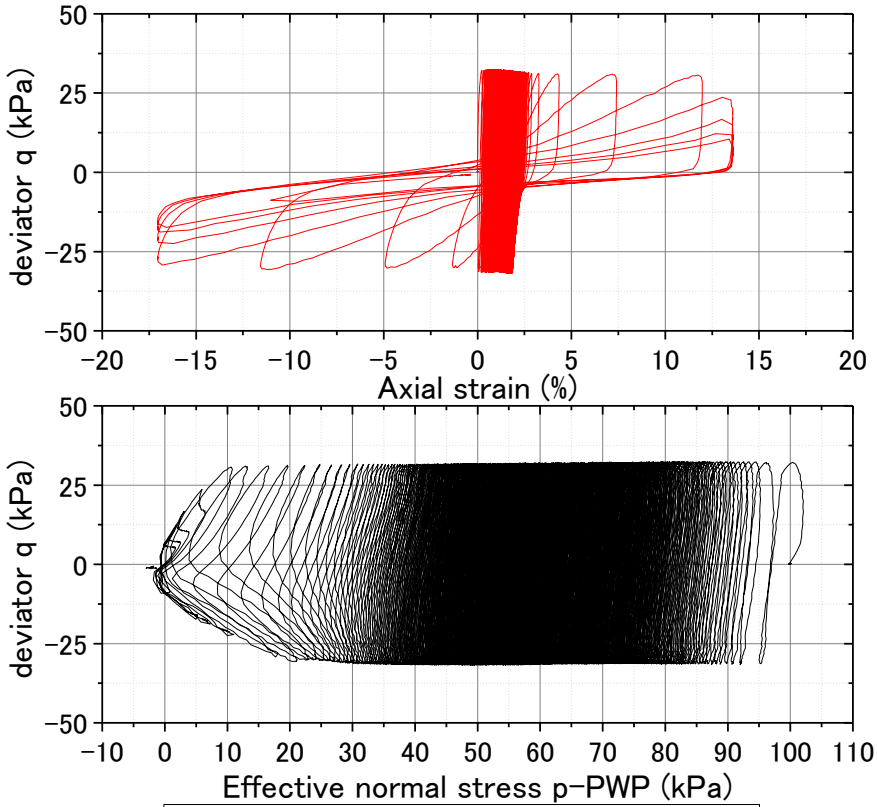

UC_ IOF-B_Jun27 σ_0'=99.4; CSR=0.159; Dc=83.6; Sr=76.8

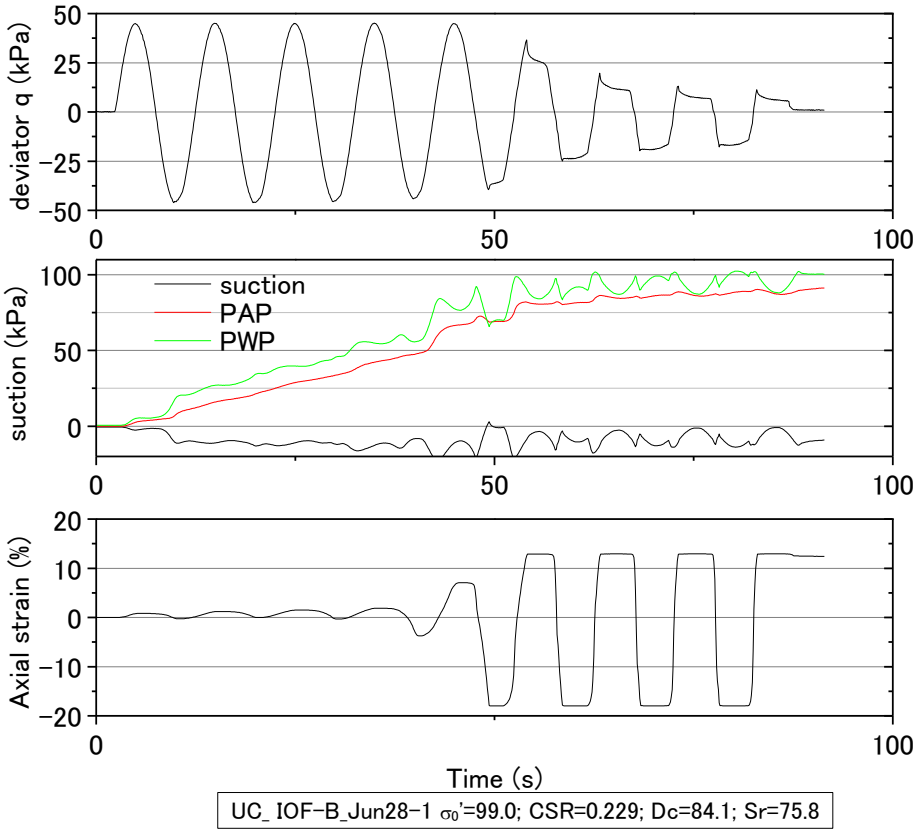

UC_ IOF-B_Jun28-1 σ0'=99.0; CSR=0.229; Dc=84.1; Sr=75.8

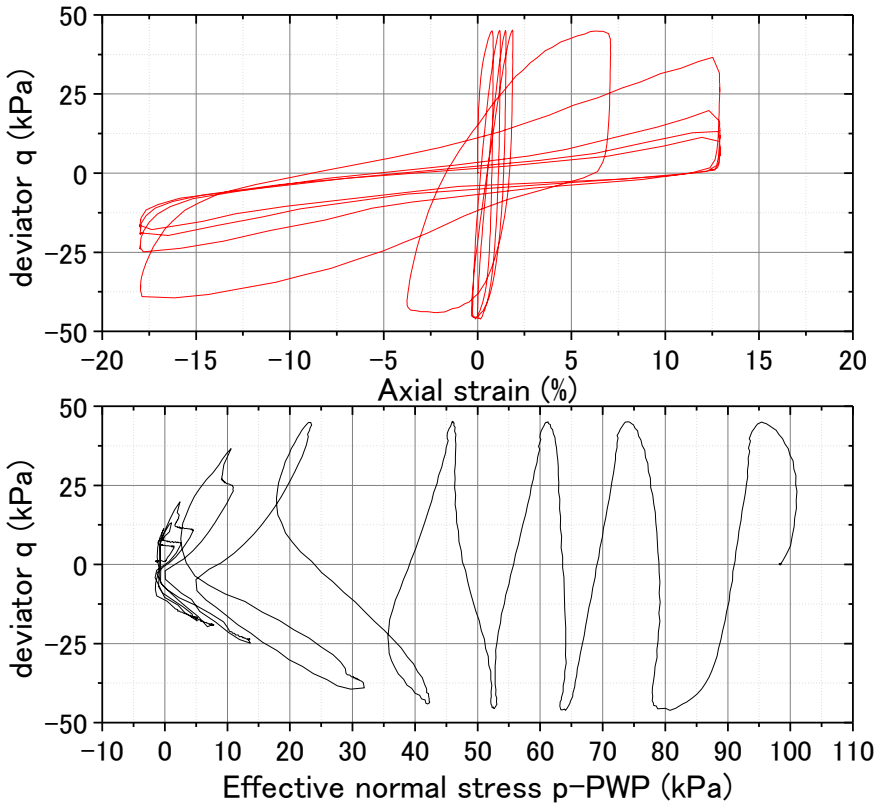

UC_ IOF-B_Jun28-1 σ0'=99.0; CSR=0.229; Dc=84.1; Sr=75.8

G-8 Unsaturated IOF-B with Sr of 77%-82% in Set 6

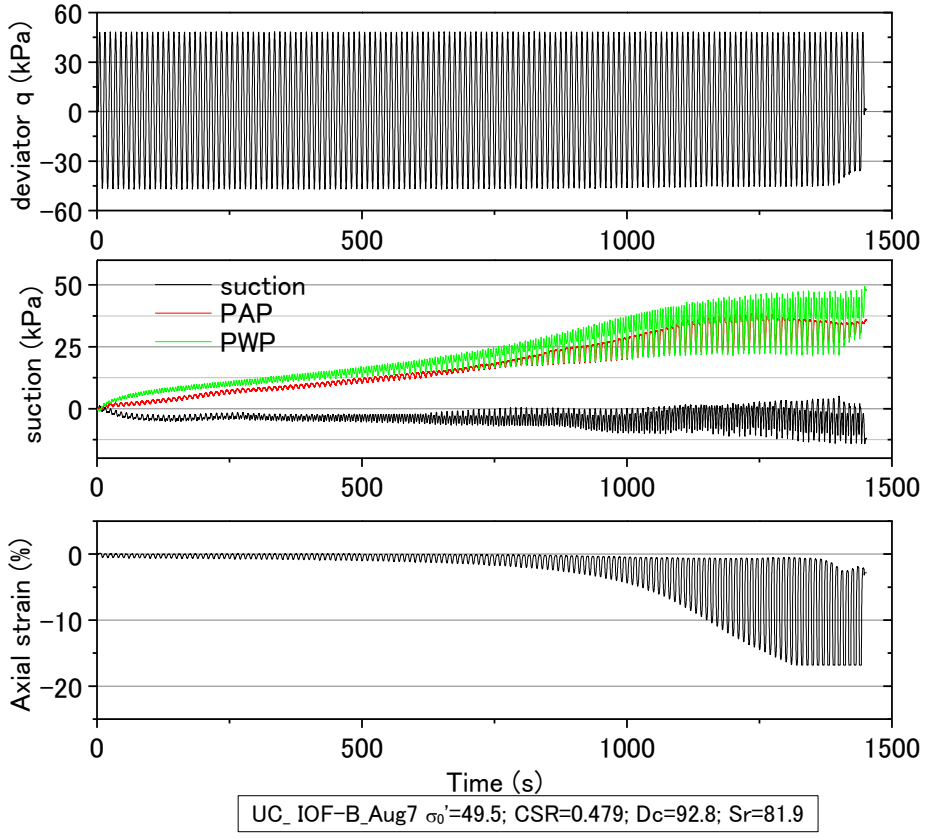

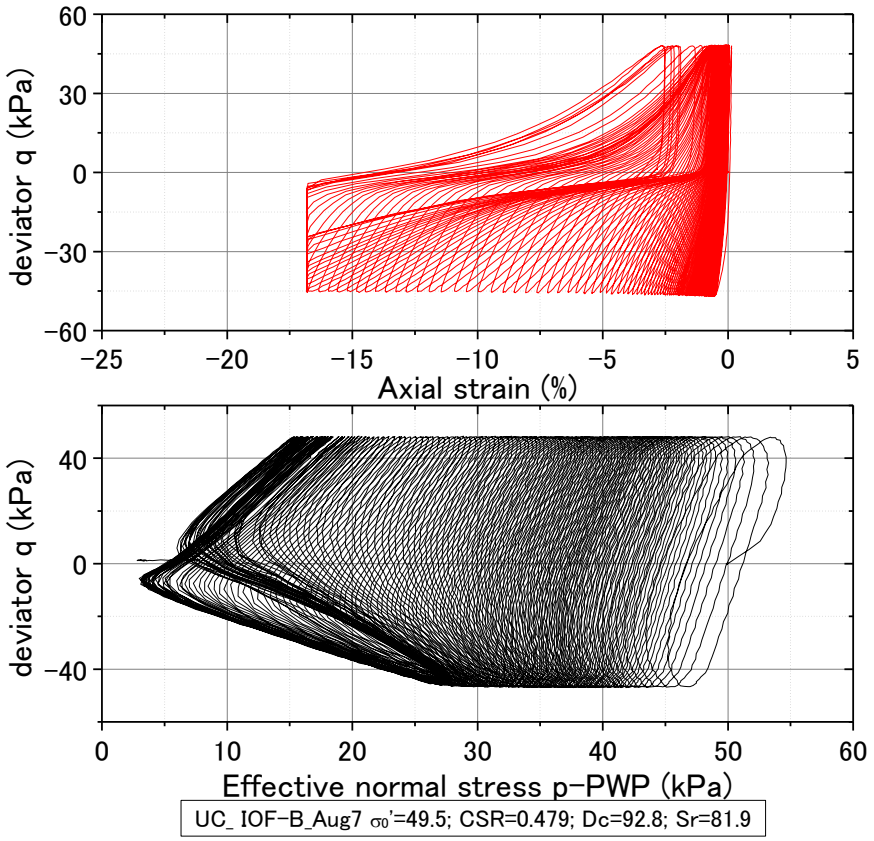

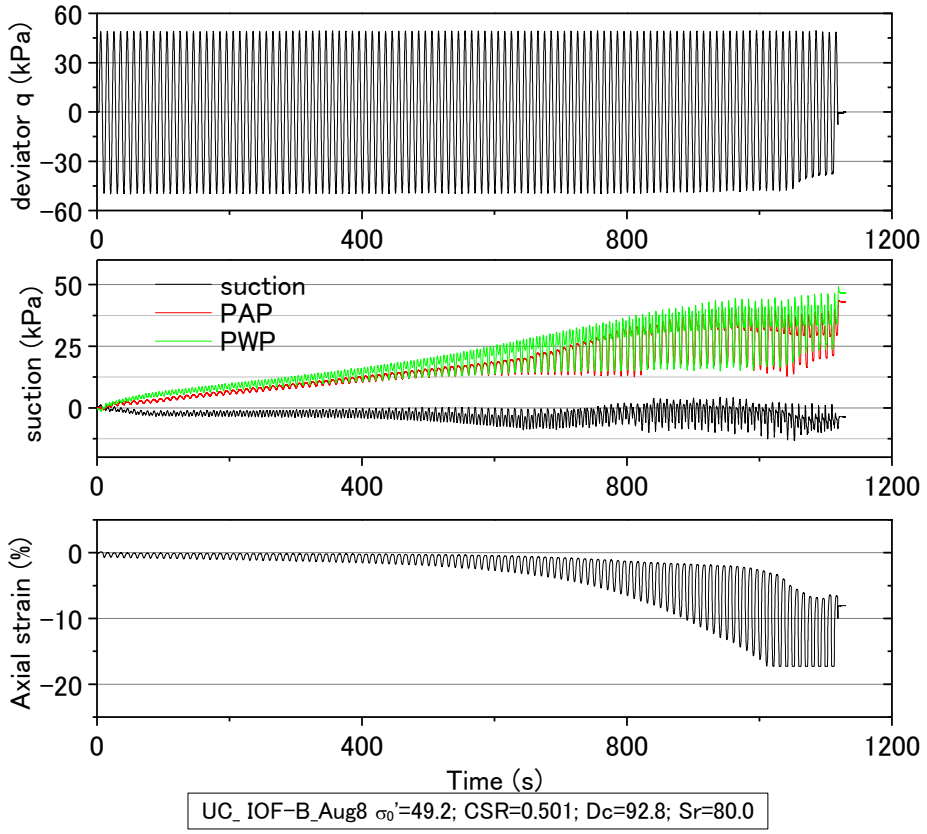

UC_ IOF-B_Aug8 σ_0'=49.2; CSR=0.501; Dc=92.8; Sr=80.0

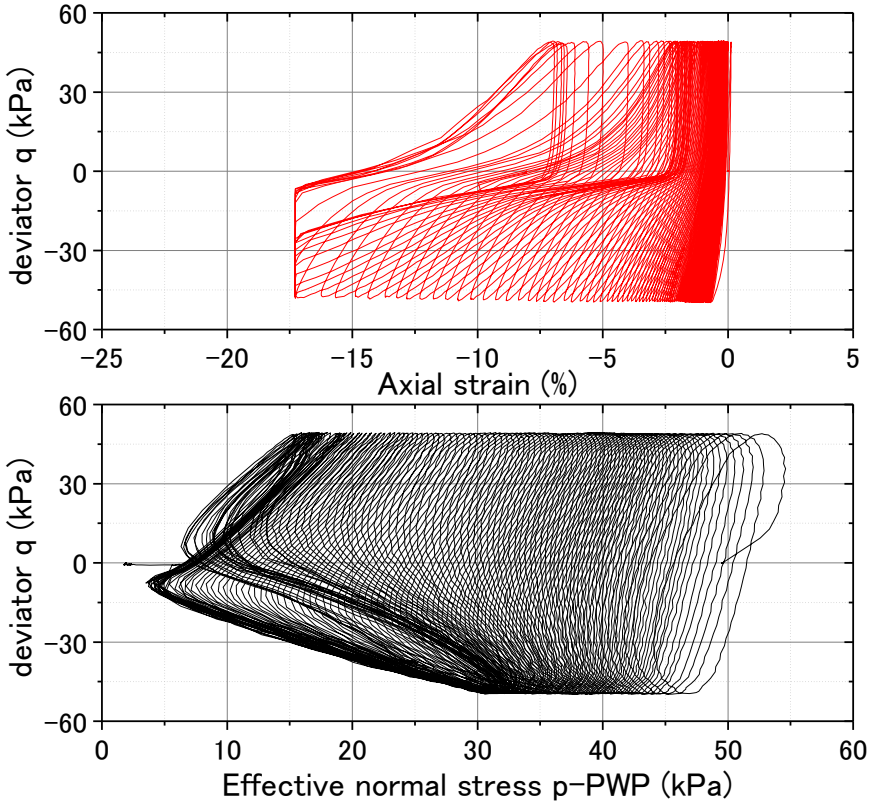

UC_ IOF-B_Aug8 σ_0'=49.2; CSR=0.501; Dc=92.8; Sr=80.0

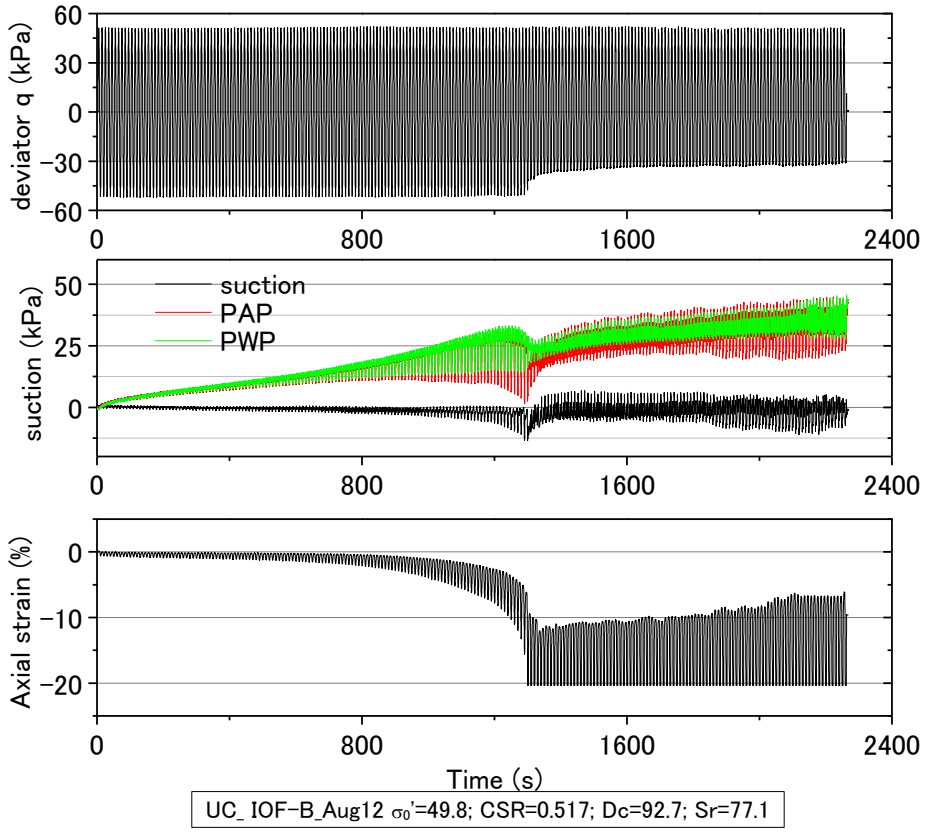

UC_ IOF-B_Aug12 σ_0'=49.8; CSR=0.517; Dc=92.7; Sr=77.1

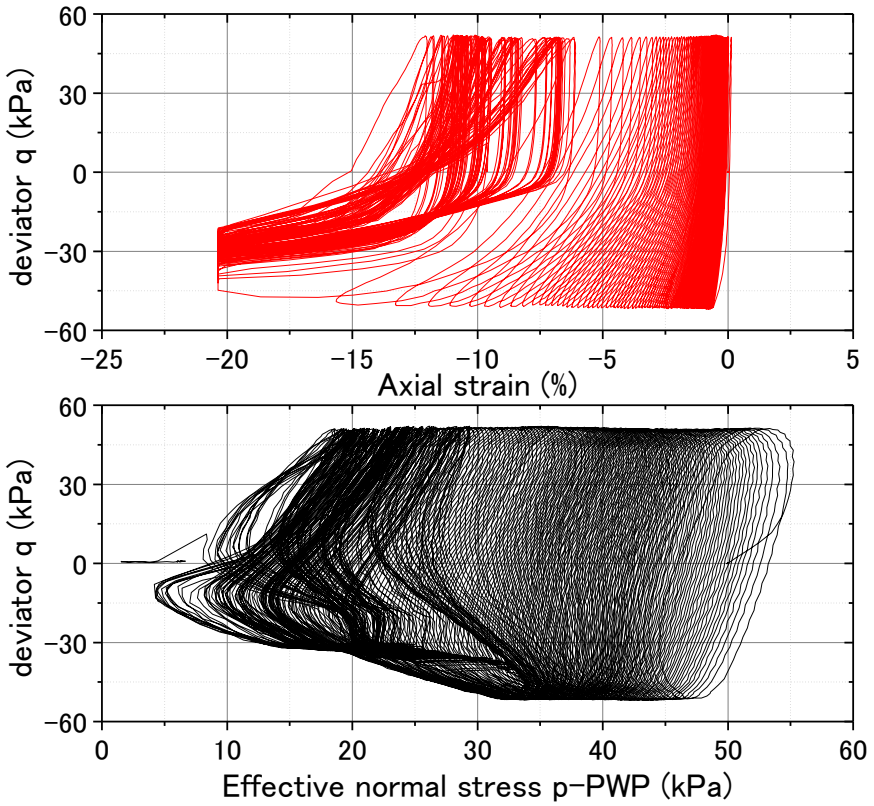

UC_ IOF-B_Aug12 σ_0'=49.8; CSR=0.517; Dc=92.7; Sr=77.1

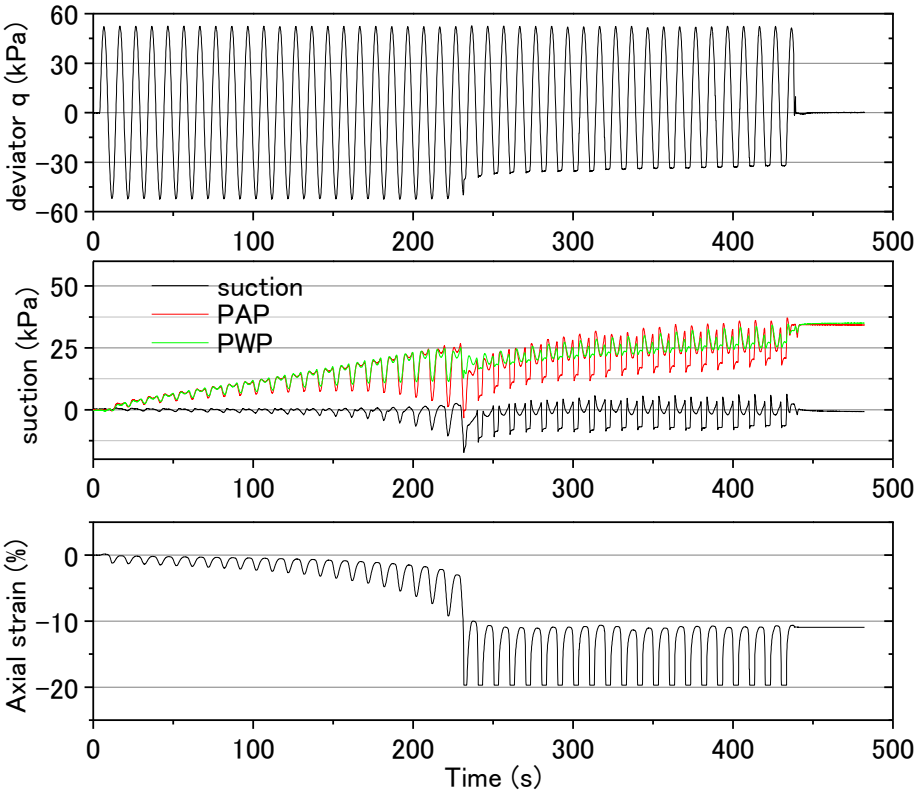

UC_ IOF-B_Aug13 σ_0'=49.8; CSR=0.525; Dc=92.7; Sr=77.9

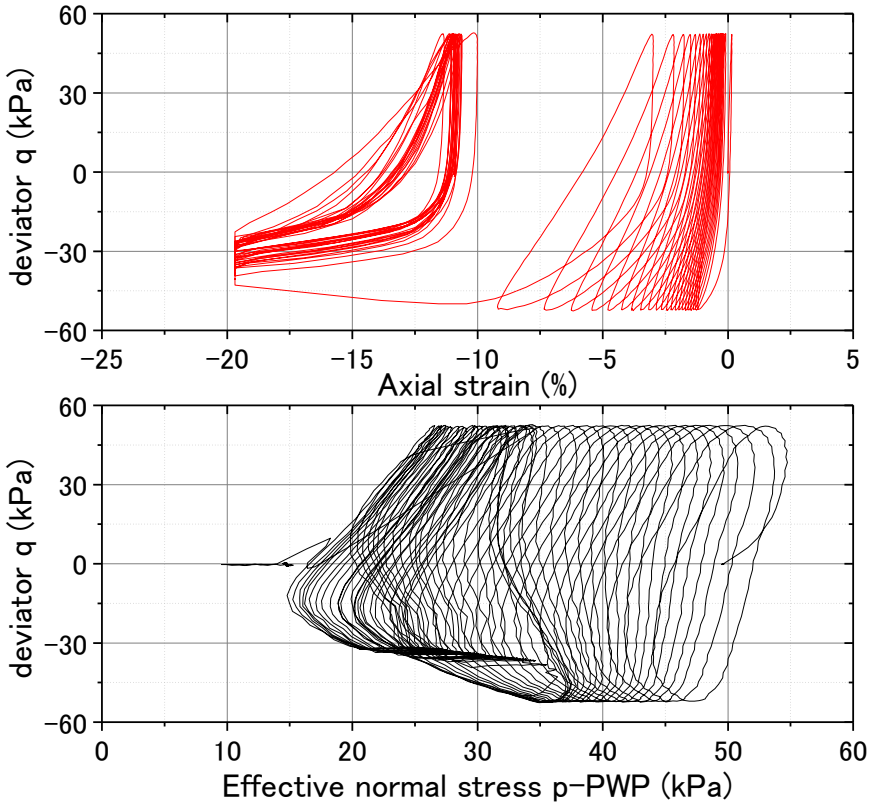

UC_ IOF-B_Aug13 σ_0'=49.8; CSR=0.525; Dc=92.7; Sr=77.9

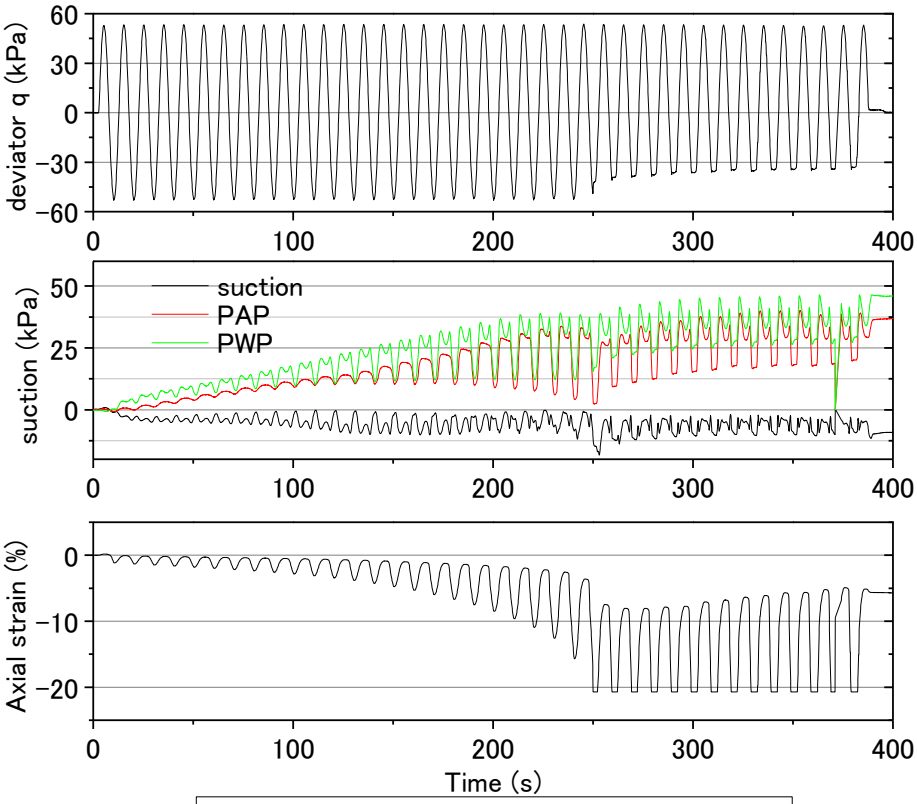

UC_ IOF-B_Aug17 σ_0'=49.7; CSR=0.534; Dc=92.6; Sr=81.4

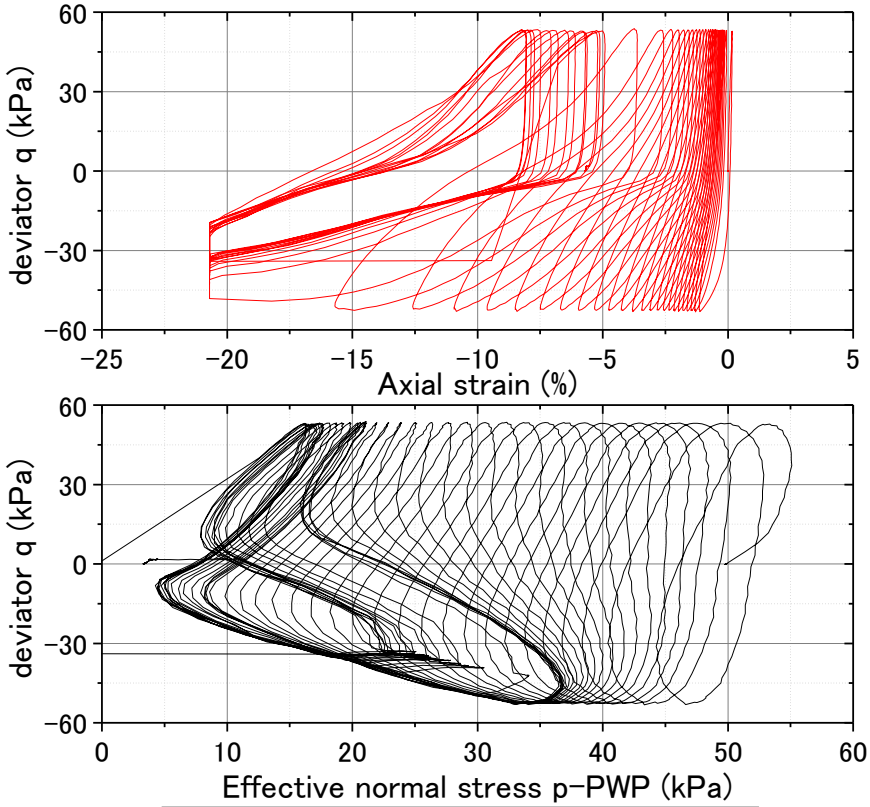

UC_ IOF-B_Aug17 σ_0'=49.7; CSR=0.534; Dc=92.6; Sr=81.4

G-9 Unsaturated IOF-B with Sr of 71% in Set 7

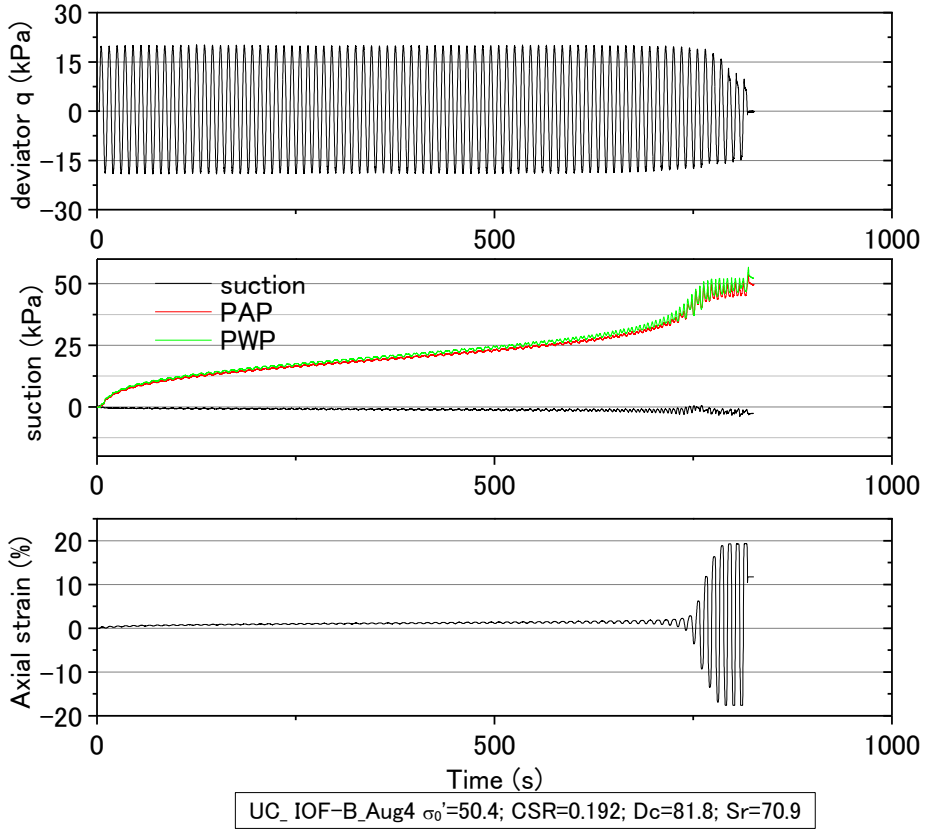

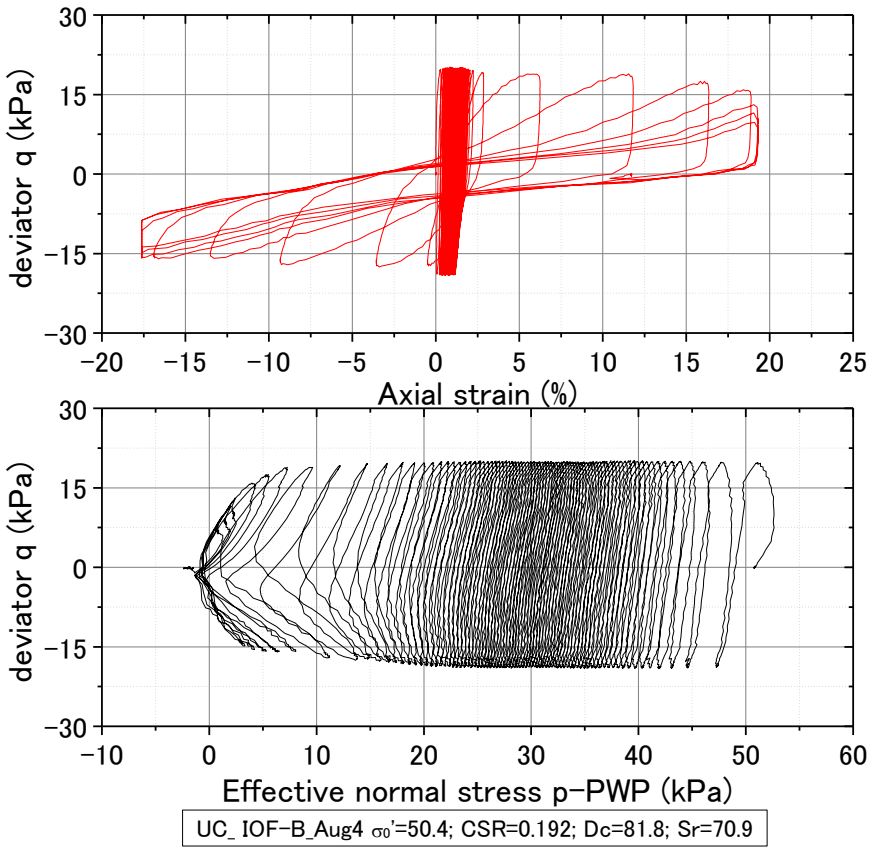

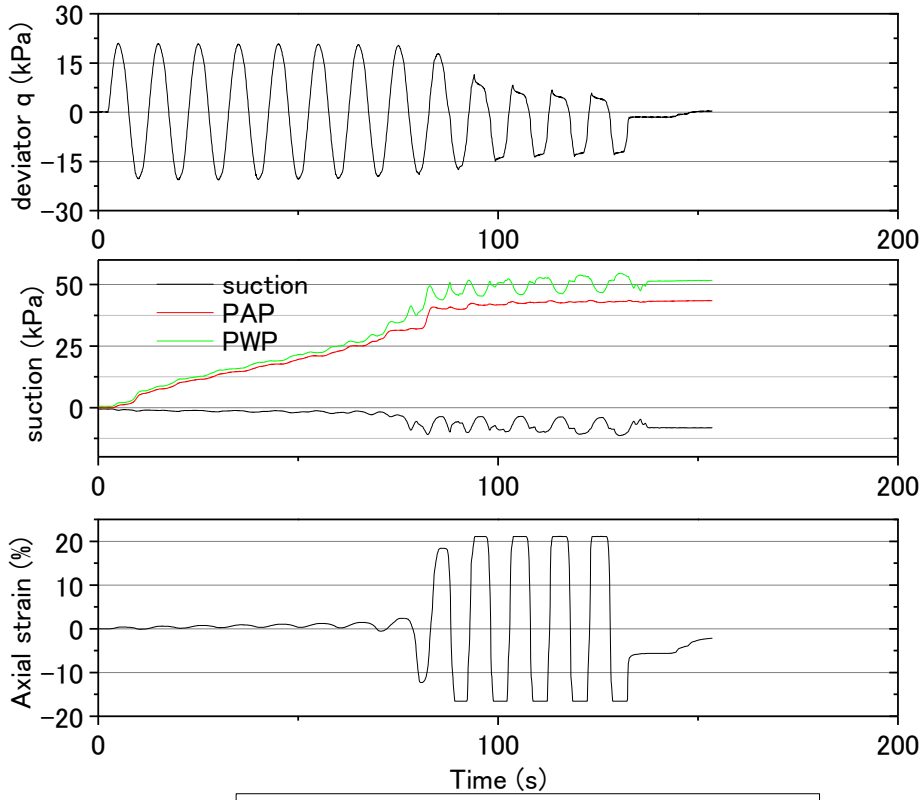

UC_ IOF-B_Aug6 σ_0'=49.3; CSR=0.208; Dc=82.0; Sr=71.8

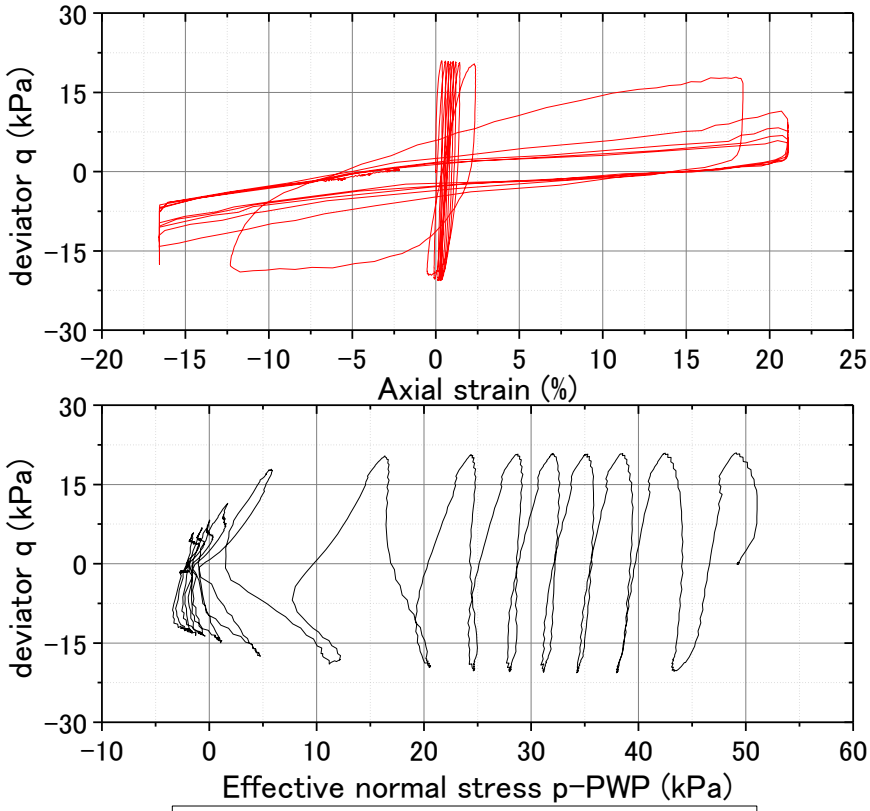

UC_ IOF-B_Aug6 σ_0'=49.3; CSR=0.208; Dc=82.0; Sr=71.8